Biochemical and Biophysical Studies on the *Escherichia coli* AmpC β-Lactamase



A thesis submitted to
the Board of the Faculty of Mathematical, Physical and Life Sciences
at the University of Oxford
in partial fulfilment of the requirements for the degree of Doctor of Philosophy.

Pauline Annemarie Lang
Pembroke College
Trinity Term 2022

Abstract

Antimicrobial resistance is one of the major global health concerns of the 21st century. While β-lactam antibiotics remain the most important class of antibacterials, their clinical use is increasingly compromised by resistance, most importantly through β-lactamase catalysed hydrolysis. More than 4000 different β-lactamases have been identified, which can collectively inactivate all clinically used β-lactam antibiotics. One successful strategy to combat resistance through β-lactamases is a combination therapy consisting of a β-lactam antibiotic and a β-lactamase inhibitor. However, β-lactamases are evolving rapidly, both adapting to new β-lactam antibiotics, and becoming resistant to inhibition by established β-lactamase inhibitors. This work describes biochemical and biophysical studies on interactions of the *Escherichia coli* AmpC β-lactamase ($AmpC_{EC}$) with new and established β-lactamase inhibitors as well as β-lactam antibiotics.

Studies on the inhibition of $AmpC_{EC}$ by the clinical candidate enmetazobactam as described in Chapter 2 lead to a re-evaluation of the mechanism by which not just $AmpC_{EC}$, but serine β-lactamases (SBLs) from all classes, are inhibited both by enmetazobactam and by the structurally related and most widely clinically used β-lactamase inhibitors, *i.e.* sulbactam, tazobactam, and clavulanic acid. The results suggest that previously reported substantial scaffold fragmentation likely does not (at least generally) contribute to transient β-lactamase inhibition by these inhibitors and reveal caveats on the interpretation of widely used mass spectrometric techniques to study SBL inhibition through covalent modification. Further they demonstrate scope for further development of penam sulfones and clavams for irreversible SBL inhibition. In Chapter 3 studies on $AmpC_{EC}$ inhibition by the clinically relevant diazabicyclooctanes (DBOs) avibactam, relebactam, nacubactam, and zidebactam are described. The results reveal significantly enhanced potency of zidebactam compared to the other DBOs, resulting from improved stabilisation of the tetrahedral transition state involved in generation of the covalent enzyme-DBO complex. However, the results also show potential for further DBO optimisation for $AmpC_{EC}$ inhibition by C2 acyl side chain optimisation. Chapter 4 focuses on $AmpC_{EC}$ inhibition by (bi)cyclic boronates, comparing taniborbactam, the first clinically approved dual-action inhibitor, acting on both SBLs and the mechanistically distinct metallo β-lactamases (MBLs), to structurally related compounds CB2 and CB3. Unexpectedly, next to the bicyclic taniborbactam bound to the nucleophilic serine of $AmpC_{EC}$, structural studies on $AmpC_{EC}$ interaction with taniborbactam reveal a second taniborbactam molecule bound non-covalently at the $AmpC_{EC}$ surface, apparently in a tricyclic form. Structural analysis reveals that this tricyclic form is likely not accommodated at SBL active sites, but may contribute to inhibition of some MBLs, thus explaining the unusually broad spectrum of β-lactamase inhibition by taniborbactam. Preliminary structural studies on $AmpC_{EC}$ interactions with β-lactam antibiotics, as described in Chapter 5, demonstrate that apparently subtle changes both in the core motifs and the sidechains of the β-lactam antibiotics can have a drastic impact on the conformation of the β-lactam derived acyl-enzyme species with potential implications for their hydrolytic stability. Chapter 6 describes initial steps to study $AmpC_{EC}$ catalysis and inhibition through time-resolved serial crystallography. A micro-crystallisation protocol is developed for $AmpC_{EC}$ and used to study $AmpC_{EC}$ interaction with inhibitors at room temperature in the 100 ms – 30 min timeframe.

Overall, the work presented gives new insight into the molecular basis of $AmpC_{EC}$ inhibition by all currently clinically relevant classes of inhibitors, as well as $AmpC_{EC}$ conferred antimicrobial resistance. The results provide guidance for the further development of β-lactamase resistant antimicrobials and improved β-lactamase inhibitors to counteract antimicrobial resistance.

Für meine Eltern

Acknowledgements

This work was supervised by Prof. Christopher J. Schofield and Dr Jürgen Brem at the Department of Chemistry of the University of Oxford. It was funded by the Medical Research Foundation as part of the National PhD Programme in Antimicrobial Resistance Research, led by Prof. Matthew B. Avison and Dr Claire Spreadbury (University of Bristol).

Parts of the work described in this thesis have been conducted within the context of a number of large multidisciplinary collaborations. A summary of these is given below. Detailed individual contributions of collaborators are highlighted at the beginning of each chapter and throughout the thesis.

Non-denaturing MS and LC-MS/MS analysis in Chapter 2 were done in collaboration with Dr Ritu Raj under supervision of Prof. Carol V. Robinson (University of Oxford). SPE-MS analyses was developed in collaboration with Dr Anthony Tumber (University of Oxford) and NMR assays were supported by Dr Christopher T. Lohans and Prof. Timothy D. W. Claridge (both University of Oxford). LC-MS analysis was supported by Dr Patrick Rabe (University of Oxford). Initial crystallisation and structure solution of $AmpC_{EC}$ was supported by Dr Thomas M. Leissing (University of Oxford). Follow-up non-denaturing MS experiments were conducted in collaboration with Mariska de Munnik (University of Oxford).

Microbiological studies described in Chapter 3 were supported by Dr Karina Calvopiña (University of Oxford). The work was guided with help from Prof. Malcom G. P. Page (Jacobs University Bremen). Studies on KPC inhibition by diazabicyclooctanes were done in collaboration with Catherine L. Tooke and Prof. James Spencer (University of Bristol).

Serial synchrotron crystallography experiments were conducted in collaboration with the UK XFEL hub, led by Dr Allen M. Orville (Diamond Light Source), as well as the I24 Beamline scientists at Diamond Light Source, led by Dr Robin L. Owen. Data processing was done by members of the XFEL hub and Dr Nicholas Devenish (Diamond Light Source).

Serial femtosecond crystallography experiments were conducted in collaboration with the UK XFEL hub at Diamond Light Source, led by Dr Allen M. Orville, the research group of Dr Jan Kern (Lawrence Berkeley National Laboratory), and the beamline scientists at the MFX beamline at the Linac Coherent Light Source, the BL3 beamline at the SPring-8 Angstrom Compact free electron Laser, and the NCI beamline at Pohang Accelerator Laboratory X-ray Free Electron Laser. Processing of serial data-sets was done by the research group of Dr Nicholas K. Sauter (Lawrence Berkeley National Laboratory).

The work on 2OG oxygenases described in the Appendix was additionally supported by Dr Patrick Rabe, Dr Anthony Tumber, Dr Zhihong Zhang, Dr Thomas M. Leissing, and Dr Michael A. McDonough (all University of Oxford). Structural studies on pcPAL were conducted in collaboration with the research group of Dr László C. Bencze (Babes-Bolyai University).

Thank you, Chris, for all the opportunities given, the experiences made, and the lessons learned. Thank you, for all your guidance and advice throughout the past years.

Thank you, Jürgen, for all your time, your patience, and advice. Thank you, for becoming both a mentor and a good friend.

Thank you, Patrick, for making the start into the DPhil so much easier by being a piece of home away from home. Thank you, for some great teamwork.

Thank you, Mariska, for all your help with tying up loose ends in the final stages.

Thank you, Thomas, for showing me the job of a computer person.

Thank you, Gareth, for helping me find my way during the first months in the biochemistry lab.

Thank you, Tony, for all the time you spent with me at the RapidFire.

Thank you, Karina, for explaining all things microbiology with never ending patience.

Thank you, Allen, Pierre, and Agata, for introducing me to the world of serial crystallography.

Thank you, Ian, for your help with data processing and for keeping billy running for me.

Thank you, Adam, for countless problems solved.

Thank you, Zahn and Jenny, for all your help with the administrational side of the work.

Thank you, Aistė, Gonzalo, Jos, Jürgen, Karina, Mariska, Patrick, Tharindi, and Thomas for all the good times, both inside and outside the lab.

Thank you, Lydia and Regina, for staying close wherever I go.

Thank you, Aarne, for going together with me through the good, the bad, and the ugly. It means the world to me.

Thank you, Mama and Papa, for being my constant source of comfort and support through all these years.

Publications

Primary Contributions

Pauline A. Lang, Ritu Raj, Anthony Tumber, Christopher T. Lohans, Patrick Rabe, Carol V. Robinson, Jürgen Brem, and Christopher J. Schofield, Studies on enmetazobactam clarify mechanisms of widely used β-lactamase inhibitors, *Proc. Natl. Acad. Sci. U.S.A*, **2022**, 119(18), e2117310119. https://doi.org/10.1073/pnas.2117310119.

Pauline A. Lang, Thomas M. Leissing, Malcolm M.G.P. Page, Christopher J. Schofield, and Jürgen Brem, Structural investigations of the inhibition of *Escherichia coli* AmpC β-Lactamase by diazabicyclooctanes, *Antimicrob. Agents Chemother.*, **2021**, 65(2) e02073-20. https://doi.org/10.1128/AAC.02073-20**.**

Pauline A. Lang, Anete Parkova, Thomas M. Leissing, Karina Calvopiña, Ricky Cain, Alen Krajnc, Tharindi D. Panduwawala, Jules Philippe, Colin W. G. Fishwick, Peteris Trapencieris, Malcolm G. P. Page, Christopher J. Schofield, and Jürgen Brem, Bicyclic Boronates as Potent Inhibitors of AmpC, the Class C β-Lactamase from *Escherichia coli*, *Biomolecules*, **2020**, 10(6), 899. https://doi.org/10.3390/biom10060899.

Alen Krajnc*, **Pauline A. Lang***, Tharindi D. Panduwawala*, Jürgen Brem*, and Christopher J. Schofield*, Will morphing boron-based inhibitors beat the β-lactamases? *Current Opin. Chem. Biol.* **2019**, 50, 101-110. ttps://doi.org/10.1016/j.cbpa.2019.03.001. **All authors contributed equally.*

Additional Contributions

Jürgen Brem, Tharindi Panduwawala, Jon Ulf Hansen, Joanne Hewitt, Edgars Liepins, Pawel Donets, Laura Espina, Alistair Farley, Kirill Shubin, Gonzalo Gomez Campillos, Paula Kiuru, Shifali Shishodia, Daniel Krahn, Rob Lesniak, Juliane Schmidt (Adrian), Karina Calvopina, Mari Carmen Turrientes, Madeline E. Kavanagh, Dmitrijs Lubriks, Philip Hinchliffe, Gareth W. Langley, Ali F. Aboklaish, Anders Eneroth, Maria Backlund, Andrei G. Baran, Elisabet Nielsen, Michael Speake, Janis Kuka, John Robinson, Solveiga Grinberga, Lindsay Robinson, Michael McDonough, Anna Rydzik, Thomas Leissing, Juan Carlos Jimenez-Castellanos, Matthew B. Avison, Solange Da Silva Pinto, Andrew D. Pannifer, Marina Martjuga, Emma Widlake, Martins Priede, Iva Hopkins Navratilova, Marek Gniadkowski, Anna Karin Belfrage, Peter Brandt, Jari Yli-Kauhaluoma, Eric Bacque, Malcolm G. P. Page, Fredrik Björkling, Jonathan M. Tyrrell, James Spencer, **Pauline A. Lang**, Pawel Baranczewski, Rafael Canton, Stuart P. McElroy, Philip S. Jones, Fernando Baquero, Edgars Suna, Angus Morrison, Timothy R. Walsh, and Christopher J. Schofield, Imitation of β-Lactam binding enables broad spectrum metallo-β-Lactamase inhibitors, *Nat. Chem.*, **2022**, 14, 1, 15-24. https://doi.org/10.1038/s41557-021-00831-x.

Agata Butryn, Philipp S. Simon, Pierre Aller, Philip Hinchliffe, Ramzi N. Massad, Gabriel Leen, Catherine L. Tooke, Isabel Bogacz, In-Sik Kim, Asmit Bhowmick, Aaron S. Brewster, Nicholas E. Devenish, Jürgen Brem, Jos J. A. G. Kamps, **Pauline A. Lang**, Patrick Rabe, Danny Axford, John H. Beale, Bradley Davy, Ali Ebrahim, Julien Orlans, Selina L. S. Storm, Tiankun Zhou, Shigeki Owada, Rie Tanaka, Kensuke Tono, Gwyndaf Evans, Robin L. Owen, Frances A. Houle, Nicholas K. Sauter, Christopher J. Schofield, James Spencer, Vittal K. Yachandra,

Junko Yano, Jan F. Kern, and Allen M. Orville, An on-demand, drop-on-drop method for studying enzyme catalysis by serial crystallography, *Nat. Commun.*, **2021**, 12(1), 4461, https://doi.org/10.1038/s41467-021-24757-7.

Patrick Rabe, Jos J. A. G. Kamps, Kyle D. Sutherlin, James D. S. Linyard, Pierre Aller, Cindy C. Pham, Hiroki Makita, Ian Clifton, Michael A. McDonough, Thomas M. Leissing, Denis Shutin, **Pauline A. Lang**, Agata Butryn, Jürgen Brem, Sheraz Gul, Franklin D. Fuller, In-Sik Kim, Mun Hon Cheah, Thomas Fransson, Asmit Bhowmick, Iris D. Young, Lee O'Riordan, Aaron S. Brewster, Ilaria Pettinati, Margaret Doyle, Yasumasa Joti, Shigeki Owada, Kensuke Tono, Alexander Batyuk, Mark S. Hunter, Roberto Alonso-Mori, Uwe Bergmann, Robin L. Owen, Nicholas K. Sauter, Timothy D. W. Claridge, Carol V. Robinson, Vittal K. Yachandra, Junko Yano, Jan F. Kern, Allen M. Orville, and Christopher J. Schofield, X-ray free-electron laser studies reveal correlated motion during isopenicillin N synthase catalysis, *Sci. Adv.* **2021**, 7, eabh0250, https://doi.org/10.1038/s41467-021-24757-7.

Patrick Rabe, John H. Beale, Agata Butryn, Pierre Aller, Anna Dirr, **Pauline A. Lang**, Danny N. Axford, Stephen B. Carr, Thomas M. Leissing, Michael A. McDonough, Bradley Davy, Ali Ebrahim, Julien Orlans, Selina L. S. Storm, Allen M. Orville, Christopher J. Schofield, and Robin L. Owen, Anaerobic fixed-target serial crystallography, IUCrJ, **2020**, 7, 901-912, https://doi.org/10.1107/S2052252520010374.

Alen Krajnc, Jürgen Brem, Philip Hinchliffe, Karina Calvopiña, Tharindi D. Panduwawala, **Pauline A. Lang**, Jos J.A.G. Kamps, Jonathan Tyrell, Emma Widlake, Benjamin Saward, Timothy Walsh, James Spencer, and Christopher J. Schofield, Bicyclic Boronate VNRX-5133 Inhibits Metallo- and Serine-β-Lactamases. *J. Med. Chem*. **2019**, 6, 21, 88544-8556. https://doi.org/10.1021/acs.jmedchem.9b00911.

Emma Z.A. Nagy, Souad D. Tork, **Pauline A. Lang**, Alina Filip, Florin D. Irmie, László Poppe, Monica I. Tosa, Christopher J. Schofield, Jürgen Brem, Csaba Paizs, and László C. Bencze, Mapping the Hydrophobic Substrate Binding Site of Phenylalanine Ammonia-Lyase from Petroselinum crispum. *ACS Catal*. **2019** 9, 9, 8825-8834, https://doi.org/10.1021/acscatal.9b02108.

Catherine L. Tooke, Philip Hinchliffe, **Pauline A. Lang**, Adrian J. Mulholland, Jürgen Brem, Christopher J. Schofield, and James Spencer, Molecular Basis of Class A β-Lactamase Inhibition by Relebactam. *Antimicrob. Agents Chemother*. **2019**, 63, 10, e00564-19. https://doi.org/10.1128/AAC.00564-19.

Mariska De Munnik, Christopher T. Lohans, **Pauline A. Lang**, Gareth W. Langley, Tika Malla, Anthony Tumber, Christopher J. Schofield, and Jürgen Brem, Targeting the Mycobacterium tuberculosis Ldt_{Mt2} with cysteine-reactive inhibitors including ebselen, *Chem. Comm.* **2019**, 55, 69, 10181-10322. https://doi.org/10.1039/C9CC04145A

Abbreviations

(*v*/*v*)	volume per volume ratio	EDTA	ethylenediaminetetraacetic acid
(*w*/*v*)	weight per volume ratio	EP	enzyme-product complex
2OG	α-ketoglutarate	ERT	ertapenem
2TY	2 trypton yeast extract	ES	enzyme-substrate complex
6-APA	6-aminopenicillanic acid	ESAC	extended spectrum AmpC
7-ACA	7-aminocephalosporanic acid	ESBL	extended spectrum β-lactamase
ADE	acoustic droplet ejector	ESI	electrospray ionisation
AEC	acyl-enzyme complex	FAS	ferrous ammonium sulfate
$AmpC_{EC}$	*Escherichia coli* AmpC	FDA	Food and Drug Administration
AMR	antimicrobial resistance	FPLC	fast protein liquid chromatography
ASU	asymmetric unit	ft	fixed-target
AVI	avibactam	GTP	guanosine-5'-triphosphate
BCAA	branched chain amino acid	HEPES	4-(2-hydroxyethyl)-1-piperazineethanesulfonic acid
BL	β-lactamase	HIF	hypoxia-inducible factor
BLI	β-lactamase inhibitor	HPLC	high-performance liquid chromatography
BMD	broth micro dilution	IMP	imipenemase
BME	β-mercaptoethanol	IPTG	isopropyl β-D-1-thiogalactopyranoside
BSA	bovine serum albumin	KCX	carbamylated lysine residue
CAZ	ceftazidime	KPC	Klebsiella pneumoniae carbapenemase
CB	cyclic boronate	KPC	*Klebseiella pneumoniae* carbapenemase
CDC	Centers for Disease Control and Prevention	LAA	L-ascorbic acid
CLSI	Clinical and Laboratory Standards Institute	Lal	lysinoalanine
CMY	cephamycinase	LB	Lysogeny broth
CoA	coenzyme A	LBNL	Lawrence Berkeley National Laboratory
CTX-M	cefotaxime hydrolases from Munich	LC	liquid chromatography
CV	column volume	LCLS	Linac Coherent Light Source
DBO	diazabicyclooctane	LTV	lactivicin
Dha	dehydroalanine	MH	Müller-Hinton
DLS	Diamond Light Source	MIC	minimum inhibitory concentration
DNA	deoxyribonucleic acid	MRF	medical research foundation
DTT	dithiothreitol	MS	mass spectroscopy
DW	de-acylating water molecule	MWCO	molecular weight cut-off
E. coli	*Escherichia coli*	MX	macromolecular crystallography

NAC	nacubactam	SBLi	serine β-lactamase inhibitor
NAG	*N*-acetylglucosamine	SDS	sodium dodecyl sulfate
NAM	*N*-acetylmuramic acid	SEC	size exclusion chromatography
NCF	nitrocefin	SFX	serial femtosecond crystallography
NDM	New Delhi Metallo β-lactamase	SBL	serine β-lactamase
NMR	nuclear magnetic resonance	SHV	sulfuhydryl reagent variable
OD	optical density	SI	supplementary information
OXA	oxacillinase	SIN	succinate
PAGE	polyacrylamide gel electrophoresis	SOC	super optimal broth
PAHX	phytanoyl-CoA hydroxylase	SPE	solid phase extraction
PAL	phenylalanine ammonia-lyases	SSX	serial synchrotron crystallography
PAL XFEL	Pohang Accelerator Laboratory X-ray Free Electron Laser	SUMO	small ubiquitin-related modifier
PBP	penicillin binding protein	TAF	trifluoroacetic acid
PCR	polymerase chain reaction	TAN	taniborbactam
PDB	protein data bank	TEM	Temoneira
PDCA	pyridinedicarboxylic acid	TEMED	tetramethylethylenediamine
PEG	polyethylene glycol	TEV	tobacco etch virus
PEI	piezoelectric injector	Tm	melting point
PHD	prolyl hydroxylase domain	tr	time-resolved
ppm	parts per million	Tris	tris(hydroxymethyl)aminomethane
PUFA	poly unsaturated fatty acid	UPLC	ultra-performance liquid chromatography
REL	relebactam	UV	ultra violet
RMSD	root-mean square deviation	VAB	vaborbactam
RNA	ribonucleic acid	VIM	Verona Imipenemase
rpm	rounds per minute	Vis	visable
rt	room temperature	wt	wild-type
SACLA	SPring-8 Angstrom Compact free electron LAser	XES	X-ray emission spectroscopy
SAR	structure-activity relationship	X-FEL	X-ray free-electron laser
SAXs	Small Angle X-ray scattering	ZID	zidebactam

Standard abbreviations for amino acids, nucleotides, SI units/prefixes, and chemical elements are used throughout.

Contents

Abstract i
Acknowledgements v
Publications ix
Abbreviations xi

Chapter 1 - Introduction

1.1. Antimicrobial chemotherapy 3
1.2. β-Lactam antibiotics 4
1.2.1. Discovery and development 4
1.2.2. Mechanism of action of β-lactams 6
1.3. Antimicrobial resistance 7
1.3.1. Global impact 7
1.3.2. Mechanisms of AMR 8
1.4. β-Lactamases 8
1.4.1. Serine β-lactamases 9
1.4.1.1. Class A serine β-lactamases 10
Class C serine β-lactamases 11
1.4.1.2. Class D serine β-lactamases 12
1.4.2. Metallo β-lactamases 13
1.5. β-Lactamase inhibitors 14
1.5.1. Serine β-lactamase inhibitors 15
1.5.2. Metallo β-lactamase inhibitors 16
1.5.3. “Dual-action” β-lactamase inhibitors 17
1.6. Research objectives 18
1.7. References 18

Chapter 2 - Interactions of AmpC$_{EC}$ and other Serine β-Lactamases with β-Lactam containing Inhibitors

2.1. Introduction 30
2.2. Production, purification, and initial characterisation of β-lactamases 32
2.2.1. Production and purification 32
2.2.2. Steady-state-kinetics with reporter substrates 33
2.2.3. Crystallisation of AmpC$_{EC}$ 35
2.3. SBL inhibition by penam sulfones 38
2.3.1. Kinetic analyses of transient SBL inhibition by penam sulfones 38
2.3.1.1. Dose-dependence studies 38
2.3.1.2. Detailed kinetic analyses of transient inhibition 40
2.3.2. Mechanistic studies with penam sulfones 43
2.3.2.1. Solid-phase-extraction mass spectrometry (SPE-MS) show lack of penam sulfone derived acyl-enzyme fragmentation 44
2.3.2.2. Acyl-enzyme fragmentation is induced during LC-MS analyses 49
2.3.2.3. Further investigations into the +169 Da species 53
2.3.2.4. Prolonged reaction of SBLs with penam sulfones can lead to dehydration of the nucleophilic serine 57
2.3.2.5. Solution based NMR studies show turn-over to fragmented products 67
2.4. SBL inhibition by clavulanic acid 68
2.4.1. Kinetic analyses of transient SBL inhibition 69
2.4.1.1. Dose-dependence studies 69

2.4.1.2. Detailed kinetic analyses of transient SBL inhibition by clavulanic acid.....70
2.4.2. Mechanistic studies with clavulanic acid.....72
2.4.2.1. Covalently bound species depend on the mass spectrometric method.....72
2.4.2.2. AEC fragmentation is observed on prolonged reaction of Class A SBLs with clavulanic acid.....74
2.4.2.3. Solution based NMR studies on clavulanic acid hydrolysis.....77
2.5. Summary and Conclusion.....79
2.6. Materials and Methods.....82
2.6.1. Materials.....82
2.6.2. Recombinant enzyme production and purification.....82
2.6.3. Kinetic assays under steady state conditions.....83
2.6.3.1. Kinetic characterisation of reporter substrates.....83
2.6.3.2. Dose-dependence studies.....84
2.6.3.3. Pseudo first order rate constants and apparent inhibition constants.....84
2.6.3.4. Dissociation rates.....85
2.6.3.5. Partition ratios.....85
2.6.4. Mass spectrometry.....85
2.6.4.1. Solid phase extraction mass spectrometry.....85
2.6.4.2. Liquid chromatography mass spectrometry.....86
2.6.4.3. Non-denaturing mass spectrometry.....86
2.6.5. Crystallography.....87
2.6.5.1. Crystallisation of AmpC$_{EC}$.....87
2.6.5.2. Crystallisation of OXA-10.....87
2.6.5.3. Data collection and processing.....88
2.6.6. Nuclear magnetic resonance spectrometry.....88
2.6.7. Tryptic digestion and LC-MS/MS analyses.....88
2.7. References.....89

Chapter 3 - Interactions of AmpC$_{EC}$ with Diazabicyclooctanes

3.1. Introduction.....97
3.2. Steady-state kinetics of AmpC$_{EC}$ inhibition by diazabicyclooctanes.....98
3.3. Microbiological analyses.....101
3.4. Mass spectrometry.....102
3.4.1. Analysis of SBL modifications observed on reaction with DBOs.....102
3.4.2. Mass spectrometric assay to study relative thermodynamic stability of AmpC$_{EC}$-DBO complexes.....106
3.5. Structural characterisation of AmpC$_{EC}$-DBO interactions.....109
3.5.1. Crystal structure of AmpC$_{EC}$ in complex with avibactam.....109
3.5.2. Crystal structure of AmpC$_{EC}$ in complex with relebactam.....110
3.5.3. Crystal structure of AmpC$_{EC}$ in complex with nacubactam.....111
3.5.4. Crystal structure of AmpC$_{EC}$ in complex with zidebactam.....112
3.5.5. Comparison of DBO binding modes at AmpC$_{EC}$ active site.....114
3.6. Summary and Conclusions.....118
3.7. Materials and Methods.....119
3.7.1. Materials.....119
3.7.2. Recombinant enzyme production and purification.....119
3.7.3. Kinetics.....120
3.7.4. Mass spectrometry.....120
3.7.5. Antimicrobial susceptibility testing.....120
3.7.6. X-ray crystallography.....120
3.8. References.....121

Chapter 4 - Interactions of AmpC$_{EC}$ with Cyclic Boronates

4.1. Introduction 127
4.2. Steady-state kinetics of SBL inhibition by cyclic boronates 129
4.2.1. Bicyclic boronates inhibit all classes of SBLs 129
4.2.2. Detailed kinetic studies for AmpC$_{EC}$ inhibition by cyclic boronates 130
4.3. Cyclic boronates restore ceftazidime activity in AmpC$_{EC}$ expressing *E. coli* 131
4.4. Structural characterisation of AmpC$_{EC}$-boronate interactions 132
4.4.1. Crystal structures of AmpC$_{EC}$-CB2 complex 132
4.4.2. Crystal structure of the AmpC$_{EC}$-CB3 complex 136
4.4.3. Crystal structure of AmpC$_{EC}$-TAN complex 138
4.4.4. Comparison of binding modes of bicyclic boronates 143
4.5. Summary and Conclusions 144
4.6. Materials and Methods 145
4.6.1. Materials 145
4.6.2. Recombinant enzyme production and purification 145
4.6.3. Kinetics 145
4.6.4. Antimicrobial Susceptibility Testing 146
4.6.5. Crystallography 146
4.7. References 146

Chapter 5 - Interactions of AmpC$_{EC}$ with β-Lactam Antibiotics

7.1. Introduction 151
7.2. AmpC$_{EC}$ interactions with penicillins 151
7.2.1. Nuclear magnetic resonance spectroscopy-based penicillin turnover assays 152
7.2.2. Structural studies 153
7.3. AmpC$_{EC}$ interactions with cephalosporins and cephamycins 157
7.3.1. Structure of cephamycin derived acyl-enzyme species 157
7.3.2. Structure of cephalosporin and cephamycin derived product complexes 159
7.4. AmpC$_{EC}$ interactions with penems and carbapenems 161
7.5. AmpC$_{EC}$ interactions with lactivicin derivative LTV-13 164
7.6. Summary and conclusions 166
7.7. Materials and Methods 167
7.7.1. Materials 167
7.7.2. Enzyme production and purification 167
7.7.3. Crystallography 167
7.7.4. NMR based turnover assays 168
7.8. References 168

Chapter 6 - Towards studying β-Lactamases with Time-Resolved Crystallography

6.1. Introduction 173
6.1.1. Serial crystallography 173
6.1.2. Sample requirements, delivery and reaction initiation 174
6.1.3. Time-resolved serial crystallography studies on β-lactamases 176
6.2. First SACLA experiment 176
6.2.1. AmpC$_{EC}$ crystallisation 177
6.2.2. OXA-48 expression and purification 178
6.2.3. OXA-48 crystallisation 178
6.2.4. Data collection at SACLA 181
6.3. LCLS experiment 182
6.3.1. Establishing a second crystal form for AmpC$_{EC}$ 182
6.3.2. Single crystal soaking experiments 185

6.3.3. Fixed-target SSX experiments....191
6.3.4. Data collection at LCLS....196
6.4. Conclusions and Future work....202
6.5. Materials and Methods....203
6.7.1. Materials....203
6.7.2. Enzyme production and purification....203
6.7.1. Crystallisation....204
6.7.2. Data collection and processing....206
6.7.2. Data analysis....207
6.7. References....207

Chapter 7 – Summary and Conclusions

7.1. AmpC$_{EC}$ inhibition by clinically relevant β-lactamase inhibitors....213
7.2. AmpC$_{EC}$ interactions with β-lactam antibiotics....214
7.3. Serial crystallography approaches to study AmpC$_{EC}$....215
7.4. Conclusions....216
7.5. References....216

Appendix

Appendix I – Summary of non-β-lactamase related work....219
8.1. Structural studies on the *Escherichia coli* AlkB DNA demethylase....219
8.2. Structural and functional studies on the phytanoyl-CoA hydroxylase....222
8.3. Structural studies on the *Petersilium crispum* phenylalanine ammonia-lyase....223
8.4. Materials and Methods....224
8.4.1. Materials....224
8.4.2. Enzyme production and purification....224
8.4.3. RapidFire MS based PAHX activity assay....225
8.4.4. X-ray Crystallography....226
8.4.4.1. Crystallisation of AlkB....226
8.4.4.1.1. Generation of apo AlkB....226
8.4.4.1.2. Crystallisation....227
8.4.4.1.3. Data collection, processing, and analysis....228
8.4.4.2. Crystallisation of PAHX....228
8.4.4.2.1. Generation of apo PAHX....228
8.4.4.2.2. Thermal shift assays....228
8.4.4.2.3. Anaerobic PAHX crystallisation....229
8.4.4.2.4. Aerobic PAHX crystallisation....229
8.4.4.2.5. Data collection, processing, and analysis....229
8.4.4.3. Crystallisation of pcPAL....230
Appendix II – General Methods....231
9.1. General....231
9.2. Microbiology....231
9.2.1. Bacterial Growth Media....231
9.2.2. Plasmid DNA isolation....231
9.2.3. Agarose Gel Electrophoresis....231
9.3. Protein Production and Purification....232
9.3.1. Preparation of competent cells....232
9.3.2. Transformation....232
9.3.3. Starter cultures....232
9.3.4. Glycerol Stocks....232
9.3.5. Bacterial growth and expression....232
9.3.6. Purification....233
9.3.7. SDS-PAGE....233

Appendix III – Supplementary Information for Chapter 2 234
Appendix IV – Supplementary Information for Chapter 3 251
Appendix V – Sequences of protein constructs 252
References 254

Chapter 1

Introduction

Contents

1.1. Antimicrobial chemotherapy 3
1.2. β-Lactam antibiotics 4
1.2.1. Discovery and development 4
1.2.2. Mechanism of action of β-lactams 6
1.3. Antimicrobial resistance 7
1.3.1. Global impact 7
1.3.2. Mechanisms of AMR 8
1.4. β-Lactamases 8
1.4.1. Serine β-lactamases 9
1.4.1.1. Class A serine β-lactamases 10
Class C serine β-lactamases 11
1.4.1.2. Class D serine β-lactamases 12
1.4.2. Metallo β-lactamases 13
1.5. β-Lactamase inhibitors 14
1.5.1. Serine β-lactamase inhibitors 15
1.5.2. Metallo β-lactamase inhibitors 16
1.5.3. “Dual-action” β-lactamase inhibitors 17
1.6. Research objectives 18
1.7. References 18

1.1. Antimicrobial chemotherapy

Less than a century ago infectious diseases were the leading cause of deaths worldwide, including in the western world[1]. Since then antimicrobial chemotherapy, together with other advances such as vaccines and improved sanitation have drastically increased the average life expectancy in middle- and high-income countries[2].

The concept of antimicrobial chemotherapy was first introduced by Paul Ehrlich at the beginning of the 20th century; he researched the toxicity of chemical agents against pathogens and was the first to envisage drugs that selectively kill the pathogen without harming the host cell[3]. In collaboration with the chemist Alfred Bertheim and bacteriologist Sahachiro Hata, Ehrlich performed the first systematic screen of hundreds of synthetic organoarsenic compounds with the aim of identifying a drug to treat syphilis. This work led to "Ehrlich's preparation 606" (arsphenamine)[3] which was later marketed by Hoechst as Salvarsan. Salvarsan (and the more soluble Neosalvarsan) quickly became the most frequently prescribed drug until its replacement by penicillin in the 1940s[4], despite the treatment suffering from significant side-effects[5]. Ehrlich's success inspired further systematic drug screens which in 1935 led to the discovery of the first sulfonamide antimicrobial (Prontosil) by Bayer, which had significantly less side-effects than Salvasan[6]. This breakthrough was followed by the discovery and unmatched success story of β-lactam antibiotics (see below). The commercial success of penicillin initiated the "Golden Age" of antimicrobial development, comprising about two decades of tremendous innovation (Figure 1), involving the discovery of aminoglycosides (e.g. streptomycin), tetracyclines, macrolides, glycopeptides and polyenses, as well as new and improved β-lactams[7].

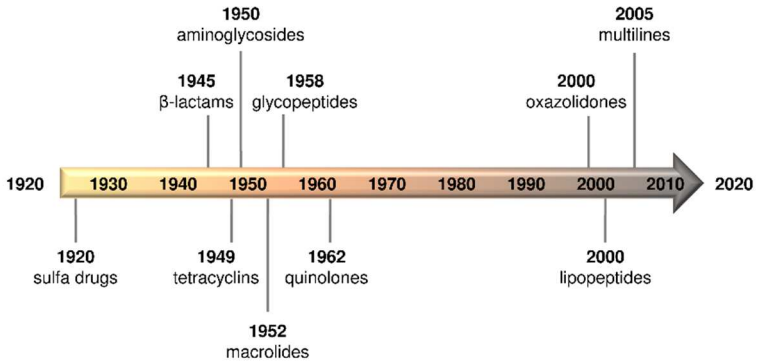


Figure 1: Timeline of antibacterial chemotherapy. The period between 1940-1960 is considered to be the "Golden Age" of antimicrobial development; this was followed by an "innovation gap" from the 1970s-2000s[7]. Years shown mark the clinical introduction of the first antibacterial from each new class.

By the 1960s infectious diseases were widely declared to be defeated[8], leading to decreased research, resulting in an "innovation gap" (Figure 1), with no new classes of antibiotics discovered for the remainder of the century (Figure 1). While resistance mechanisms to each of the clinically used antibiotic classes were discovered either before, or shortly after their

clinical introduction[7], initially resistance garnered little attention. It was only at the start of the 2000s with continuously increasing reports of treatment failure due to emerging resistance, that widespread interest in antibiotic development picked up again leading to the development and use of new classes such as oxazolidones and daptomycin (though these were discovered earlier)[9].

Today antimicrobial chemotherapy is one of the corner stones of modern medicine, not only by treating infections, but also by preventing them in immuno compromised patients, thereby enabling many other advances in medicine such as organ transplantation, cancer chemotherapy, and modern surgery[10].

1.2. β-Lactam antibiotics

While being one of the first classes of modern antimicrobials to be discovered, the β-lactams still remain the most important antimicrobials in clinical use, making up 65% of the antimicrobial market, amounting to ~ 15 billion USD worth in sales each year[11]. In addition to their medical use in humans, β-lactams are also used in substantial amounts in the agricultural industry[12].

1.2.1. Discovery and development

β-Lactams are natural compounds that are produced predominantly by fungi and also by certain bacteria[13]. Already in ancient Egypt, mouldy bread was pressed against open wounds, to help treat infections[14]. However, Alexander Flemings now famous observation of *Penicillium notatum* mould inhibiting bacterial growth in 1928[15] is generally considered to be the birth of penicillin, though his work was pre-dated and aided by work of others, who had made similar observations in the late 19th century[16].

The extraction and partial purification of penicillin by Howard Florey and Ernst Chain in 1940[17] enabled the first successful use in patients the following year[18]. A large international effort (in the context of World War II) then led to the development of large scale production of highly purified penicillin to make it accessible first to soldiers and finally to the broader public in 1946[19,20].

In 1949, a crystal structure of a penicillin was solved by Dorothy Crowfoot Hodgkin[21,22], making it one of the first chemical structures to be solved by X-ray crystallography. Hodgkin's work revealed the penicillin core to consist of a β-lactam ring fused to a thiazolidine ring (as predicted by Edward Abraham), with a C3 carboxy group and a C6 acyl side chain (Figure 2). This inspired medicinal chemistry efforts to further develop β-lactams.

Early studied penicillin extracts were likely mixtures of multiple penicillin derivatives with varying C6 acyl side chains[23]. Initial efforts to optimise the chemical structures of penicillins involved alteration of the fermentation broth which affected the nature of this side chain. For example, it was found that addition of cornsteep liquor (or phenylalanine, the sidechain precursor the liquor contains) favoured the production of penicillin G, with a benzylamido sidechain[24,25]. The isolation of 6-aminopenicillanic acid (6-APA)[26] then paved the path for semi-synthetic penicillins with new amido-sidechains such as carboxy-penicillins that showed broader antimicrobial spectrum, including against Gram-negative bacteria, and appeared more resistant towards inactivation[27,28].

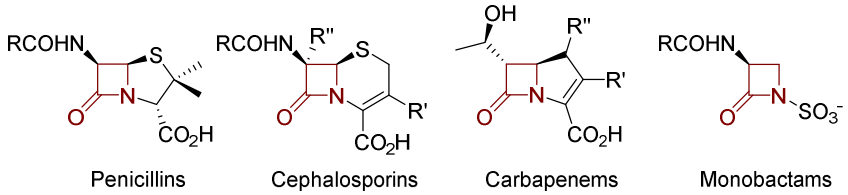


Figure 2: Major classes of β-Lactam antibiotics in clinical use. The β-lactam motif is highlighted in red.

The first cephalosporin (cephalosporin C), which contained a 4-6 ring system rather than the 4-5 system of penicillins, with a dihydrothiazine ring fused to the β-lactam ring (Figure 2), was isolated from *Cephalosporin acremonium* in 1948[29]. While cephalosporin C showed relatively low antibacterial activity, subsequent development of semi-synthetic cephalosporins based on fermented 7-aminocephalosporanic acid (7-ACA) resulted in potent, broad-spectrum antimicrobial activity[30]. Today, cephalosporins are the most widely used β-lactam antibiotics[11].

Carbapenems were isolated from *Streptomyces spp.* in the 1970s[31,32]. They contain a 4-5 ring system similar to that of penicillins, where the sulfur atom is replaced with a carbon and the five-membered ring is unsaturated (Figure 2). Carbapenems are active against a broad spectrum of pathogens and today are considered antibiotics of last resort, in part due to their relatively good stability against early identified β-lactamases[33] (see below).

The last major class of β-lactams to be discovered were the monobactams in the 1980s[34]. Monobactams are the only monocyclic β-lactam antibiotics to be used clinically and contain a sulfonic acid instead of the C3 carboxylic acid (Figure 2). Currently, the only clinically used monobactam is aztreonam, which is notable as it is the only β-lactam antibiotic which is not efficiently hydrolysed by metallo β-lactamases[35,36] (see below).

1.2.2. Mechanism of action of β-lactams

β-Lactam antimicrobials inhibit bacterial cell-wall biosynthesis by acylating penicillin-binding proteins (PBPs) which (among a wide range of cellular functions[37]) catalyse essential transpeptidase and carboxypeptidase steps in the biosynthesis of the periplasmatic side of the cell wall[37,38]. The bacterial cell wall is built of alternating *N*-acetylmuramic acid (NAM) and *N*-acetylglucosamine (NAG) units. Each of the NAM units is connected to a L-Ala-D-Glu-mDAP-D-Ala-D-Ala pentapeptide (mDAP: meso-diaminopimelic acid), which are crosslinked to other NAM units through PBP catalysed transpeptidase reaction (Figure 3). These crosslinks are thought to be continuously broken down and renewed to facilitate cell growth and division[39].

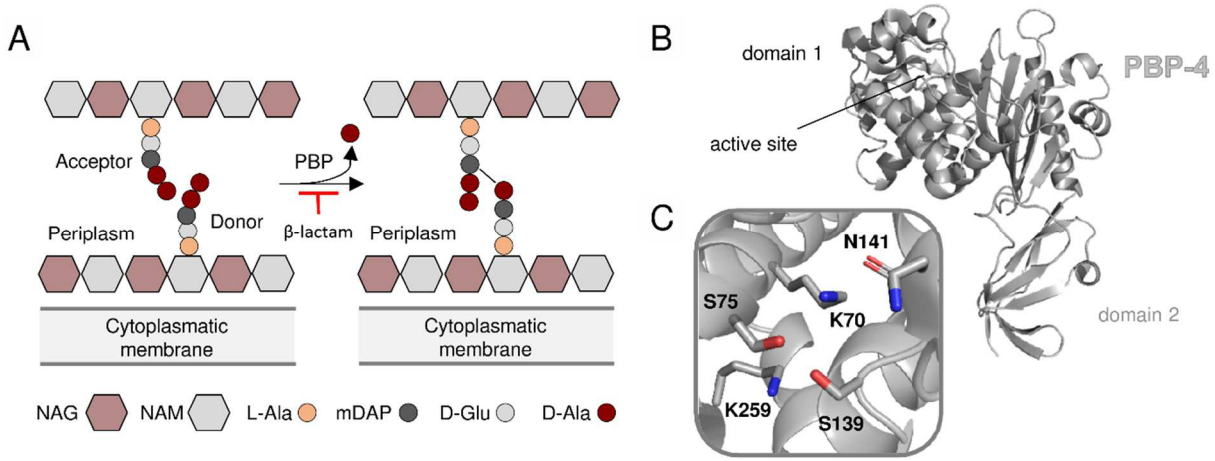


Figure 3: Role of penicillin binding proteins (PBPs) in bacterial cell wall synthesis. (A) Schematic of the PBP catalysed transpeptidase reaction, which involves crosslinking of two *C*-terminal pentapeptides with loss of the terminal D-Ala residue of the donor pentapeptide. (B) Overview of a crystal structure of *Staphylococcus aureus* PBP-4 (PDB: 6C39[40]). (C) Active site view of PBP-4 showing the nucleophilic Ser75 and other key active site residues. NAG: *N*-acetylglucosamine, NAM: *N*-acetylmuramic acid, mDAP: meso-diaminopimelic acid.

PBP catalysis proceeds via attack of a nucleophilic Ser residue on the *C*-terminal amide of the donor peptide, proceeding via a tetrahedral intermediate ([EI^1] in Figure 4) to give an acyl-enzyme complex (EI), with loss of the *C*-terminal D-Ala residue of the donor peptide.

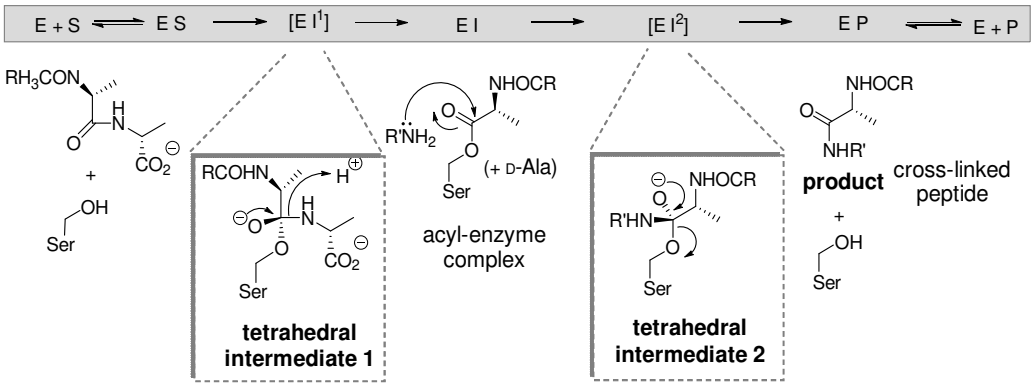


Figure 4: Outline mechanism of PBP catalysed transpeptidase crosslinking of bacterial cell wall.

In a second step the primary amine of the mDAP sidechain of the acceptor peptide reacts with the ester carbonyl of the acyl-enzyme complex, leading to a second tetrahedral intermediate (([EI^2]), followed by release of the cross-linked peptide (P, Figure 4)[38]. The resulting crosslinks are essential for the integrity of the bacterial cell wall[39].

β-Lactam antibiotics are proposed to mimic the D-Ala-D-Ala motif of the pentapeptide (Figure 5A) and work by reacting with the nucleophilic Ser of PBPs to form hydrolytically stable acyl-enzyme complexes (Figure 5B), leading to PBP inactivation[41]. This results in a blockage of cell wall synthesis, while peptidoglycan autolysis continues, which leads to increased permeability of the bacterial cell wall and eventually cell lysis due to increased osmotic pressure[38].

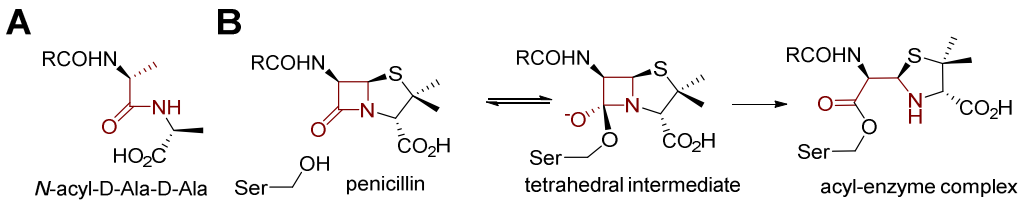


Figure 5: Mechanism of PBP inhibition by β-lactams. (A) The *N*-acyl-D-Ala-D-Ala PBP substrate has structural similarity with a β-lactam. (B) The mechanism of PBP inhibition by β-lactams proceeds through nucleophilic attack of the catalytic Ser residue on the β-lactam carbonyl, followed by formation of a tetrahedral intermediate leading to a hydrolytically stable acyl-enzyme complex.

1.3. Antimicrobial resistance

Bacterial resistance to antimicrobials (produced by fungi and soil bacteria) is an ancient, naturally occurring phenomenon, by far pre-dating the human use of antimicrobials[42]. However, since the introduction of antibiotics for medical and agricultural use, selective pressure has likely increased antimicrobial resistance (AMR), which is now a continuously growing global health problem[43]. Since the beginning of the 21st century, AMR has repeatedly been named one of the top health challenges by major world health organizations.

1.3.1. Global impact

While it is commonly agreed that AMR poses a global public health threat, quantification of its current burden as well as its potential future impact is complex. A first review on the impact of AMR, commissioned by the UK government and published in 2016 estimated that while in 2016 AMR accounted for a minimum of 700,000 deaths worldwide, this number may rise to 10 million AMR associated deaths per year by 2050[44], though this work has received criticism by some[45]. However, more recently a comprehensive study has shown that in 2019 more than 1.27 million people died worldwide from infections caused by drug resistant

pathogens[46]. In addition to the cost in human life, AMR also results in substantial additional costs for the healthcare system and thereby society. The Centers for Disease Control and Prevention (CDC) estimate in the United States alone annual costs of about 20 billion dollar in direct healthcare due to AMR, with an additional 35 billion dollars lost due to reduced productivity[47].

1.3.2. Mechanisms of AMR

Antimicrobial resistance may result from both intrinsic mechanisms and acquired capabilities of bacteria[48]. While there are differences in the relative importance of resistance mechanisms for different bacteria, especially between Gram-positive and Gram-negative strains, it is proposed that common antimicrobial resistance mechanisms can be differentiated into three different groups[48].

(i) Reduction of drug uptake and increased drug efflux. The amount of antibacterial agents entering and remaining within bacterial cells can be regulated. Drug uptake may be limited through the intrinsic composition of the bacterial cell wall (resulting e.g. in changes in thickness and polarity), through modification / reduced production of porins, or through biofilm formation[48,49]. Alternatively, drug concentrations may be reduced through increasing drug efflux via expression of efflux pump proteins. These are commonly chromosomally encoded and may be expressed constitutively or inducible[49,50].

(ii) Modification of drug targets. Both changes in the molecular structure and expression level of antibiotic targets may also confer resistance. In Gram-positive bacteria mutations altering the PBP active site is one of the main mechanisms of resistance to β-lactam antibiotics[38].

(iii) Modification or destruction of drugs. Antibiotics may be inactivated via modifications catalysed by transferases (e.g. acetylation, phosphorylation, and adenylation)[51]. In the case of certain tetracyclines and β-lactams, inactivation may occur through enzyme catalysed hydrolysis[52,53]. Bacterial production of β-lactamases is the main mechanisms of β-lactam resistance in Gram-negative bacteria[53].

1.4. β-Lactamases

Since the first discovery of a penicillin hydrolysing enzyme in *Escherichia coli* (which pre-dated the medical use of penicillin)[54], the number of known β-lactamases has increased to > 4300 and the true number is likely significantly higher[55,56]. A number of different systems have been introduced to classify β-lactamases either according to their substrate specificity or to their sequence and structure[57-64]. In this work the most commonly used updated Ambler

system will be used, which divides β-lactamases into four different classes[57,58,64]. Class A, C, and D are serine β-lactamases (SBLs) that employ a nucleophilic serine residue in catalysis, while class B β-lactamases use either one or two divalent zinc ions in catalyses and are hence described as metallo β-lactamases (MBLs).

1.4.1. Serine β-lactamases

Presently, the serine β-lactamases (SBLs), which span the Ambler classes A, C, and D (Figure 6), are clinically the most important β-lactamases[53].

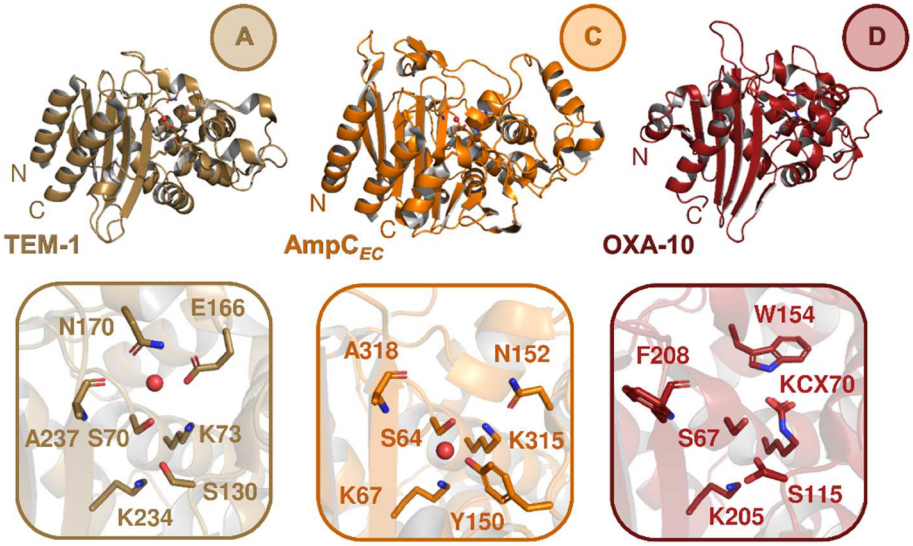


Figure 6: Structure of representative examples of SBLs from classes A, C, and D. Shown are views from crystal structures of TEM-1 (class A SBL, PDB: 1ZG4[65]), *Escherichia coli* AmpC (AmpC$_{EC}$, Class C SBL, PDB: 6T3D[66]), and OXA-10 (Class D SBL, PDB: 2X02[67]). The assigned 'de-acylating' water molecules are red spheres. KCX: carbamylated lysine.

SBLs catalyse β-lactam hydrolysis via an acyl-enzyme complex (AEC, Figure 7), which is similar to that involved in PBP catalysis and PBP inhibition by β-lactams, suggesting an evolutionary connection which is also supported by overall structural similarities between PBPs and some SBLs[68,69].

While with the PBPs, the β-lactam derived AEC are generally relatively hydrolytically stable (although exceptions have been reported e.g. with PBP2x from *Streptococcus pneumoniae*[70,71]), with β-lactamases hydrolysis of efficient substrates is fast, which is presumed to be aided by binding of a water molecule in close proximity to the nucleophilic Ser residue, named the de-acylating water molecule from here on[53,72]. In the case of class A and C SBLs binding of the de-acylating water molecule is conserved (Figure 6)[73,74], while with class D SBLs it is proposed to bind on formation of the AEC[75]. Notably, while in class A and D SBL catalysis the hydrolytic water molecule is proposed to react from the α-face of the active site[76], in case of the class C SBLs it is positioned on the β-face (Figure 6)[77].

After formation of the AEC (EI in Figure 7) via the first tetrahedral intermediate ([EI^1]), hydrolysis occurs on attack of the de-acylating water which is activated by a general base. Hydrolysis proceeds via a second tetrahedral intermediate ([EI^2]) to give the hydrolysed β-lactam product (P) and the re-generated β-lactamase (Figure 7). The nature of the general base activating the de-acylating water varies between different SBL classes and is still debated in some cases (see below).

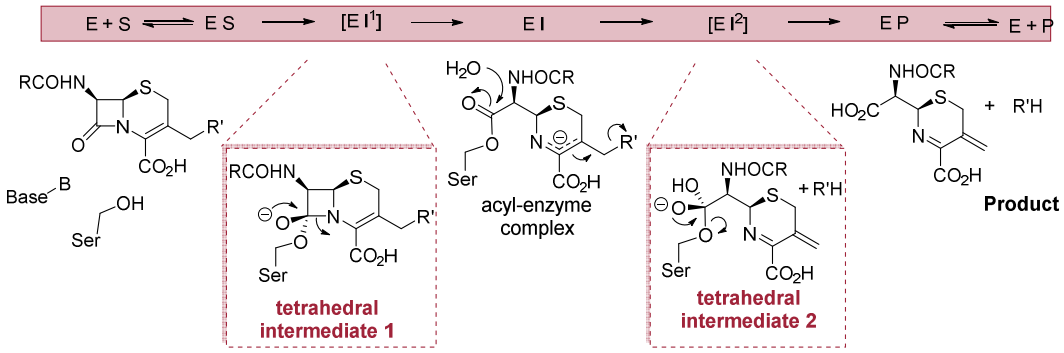


Figure 7: Outline mechanism of SBL catalysed β-lactam hydrolysis exemplified with a cephalosporin substrate. Binding of the β-lactam at the SBL active site to give a non-covalent complex is followed by nucleophilic attack of the catalytic Ser residue, proceeding vis a first tetrahedral intermediate to give an acyl-enzyme complex (AEC), analogous to β-lactam binding to PBPs. The AEC is hydrolysed by attack of a conserved water molecule, proceeding via a second tetrahedral intermediate to give the hydrolysed β-lactam and the re-activated SBL. In the case of cephalosporins AEC formation can be accompanied by the loss of the C3' / R2 sidechain.

1.4.1.1. Class A serine β-lactamases

Class A SBLs are the most common and best studied class of SBLs; they are widely disseminated on plasmids[53]. They include originally classical penicillinases such as the Temoneira (TEM, named after the patient whose cultures the enzyme was first identified in)[78] and sulfuhydryl reagent variable (SHV) β-lactamases[79], which have evolved into extended spectrum β-lactamases (ESBLs). These ESBLs have similar substrate scopes as the cefotaxime hydrolases from Munich (CTX-M)[80,81], which also belong to Ambler class A and hydrolyse both penicillins and extended spectrum cephalosporins as well as the monobactam aztreonam[82]. Further, class A SBLs also include carbapenemases such as the *Klebseiella pneumoniae* carbapenemases (KPCs)[83].

Structurally, class A SBLs are all relatively similar (sharing a 40-60% sequence identity) and contain one αβ domain and a second domain made of 8 α-helices[53]. Both the acylation and de-acylation steps of class A SBLs likely involve general acid/base catalysis involving conserved Glu166 and Lys73 residues[55].

Class C serine β-lactamases

After class A SBLs, the class C enzymes are the second most abundant class of β-lactamases[53]. Out of all β-lactamases, class C SBLs are thought to be most closely evolutionary related to PBPs[72]. The majority of class C enzymes are chromosomally encoded and summarised under the AmpC term, which traces back to the initial nomenclature introduced for ampicillin resistant *E. coli* strains[84]. These chromosomal AmpC enzymes are usually expressed at low levels, but may be induced by β-lactams or hyperproduced on mutations in the promoter or attenuator regions[85]. Class C SBLs confer resistance to most cephalosporins, including cephamycins (but not oxyiminocephalosporins like cefepime) and hydrolyse penicillins, although slowly[85]. Chromosomal AmpC β-lactamases usually bind carbapenems with high affinity, but form very hydrolytically stable acyl-enzyme complexes with them, preventing their efficient hydrolysis[86]. AmpC β-lactamases have, however, been associated with carbapenem resistance in some cases in which very high expression levels of AmpC were observed in combination with decreased outer membrane permeability through loss or alteration of porins and increased efflux[87-89].

Chromosomally encoded extended spectrum AmpC β-lactamases (ESACs) have emerged, with a broader hydrolysis spectrum, conferring resistance to fourth generation zwitterionic oxyiminocephalosporins such as cefepime and cefpirome[90,91] and (in combination with alterations in porins) also carbapenems[91]. Plasmid encoded class C β-lactamases have become common, including CMY, FOX, and MOX (termed after activity towards cephamycins, cefoxitin and moxalactam, respectively), as well as the AmpC type (ACT) SBLs[92]. In addition to cephalosporinase activity, these plasmid encoded AmpC variants usually also display carbapenemase activity[92]. While the carbapenem turn-over by plasmid encoded AmpCs is generally faster than with chromosomal AmpC, it is still not as effective as by carbapenemases from other Ambler classes (e.g. class B)[33]. Similarly to the chromosomal encoded AmpC, carbapenemase resistance associated with plasmid encoded class C SBLs is thus often observed in combination with decreased outer membrane permeability[93,94].

1.4.1.1.1. Mechanism of class C SBL catalysed β-lactam hydrolysis

By contrast with class A and D SBLs, the identity of the general base involved in both acylation and de-acylation of class C β-lactamases remain unclear, with two distinct potential mechanisms being proposed; a conjugated base mechanism involving Lys67 and Tyr150[72,95,96] (Figure 8A) or a substrate assisted mechanism involving the nitrogen of the β-lactam derived imine of the acyl-enzyme species[97,98] (Figure 8B).

Both Lys67 and Tyr150 are highly conserved within the class C SBL family and mutation of Tyr150 has been shown to reduce their activity in varying degrees depending on the substrate,

but not fully block it[77]. However, Tyr150 is likely neutral under physiologically relevant conditions (at least in the absence of substrate) as shown via ultra-high resolution crystallography and NMR[99,100], which would disfavour Tyr150 as the sole catalytic base.

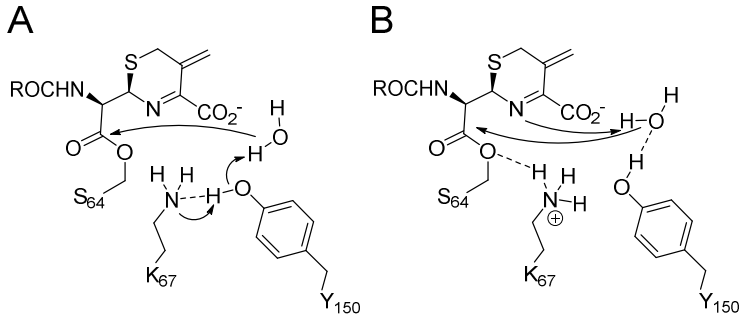


Figure 8: Proposed deacylation mechanisms for class C SBL acyl-enzyme complexes. (A) Conjugated base mechanism. (B) Substrate assisted mechanism.

1.4.1.1.2. The *Escherichia coli* AmpC β-lactamase

E. coli is currently the leading pathogen for deaths associated with resistance[46] and a chromosomal AmpC β-lactamase is present in most *E. coli*. The chromosomal *E. coli* AmpC β-lactamase (for clarity denoted as $AmpC_{EC}$ throughout this work), which is a focus of this work, was the first β-lactamase to be discovered in 1940[54], though it's full sequence was only reported in 1981[101]. $AmpC_{EC}$ production is not inducible by treatment with β-lactam antibiotics, but hyperproduction of $AmpC_{EC}$ occurs on mutations in the promoter (creating close homologies with the perfect consensus sequence of *E. coli*) or attenuator (destabilising the mRNA hairpin structure) regions in pathogenic *E. coli*[102,103]. Like most chromosomal class C SBLs, $AmpC_{EC}$ preferentially hydrolyses cephalosporins and cephamycins, and (less efficiently) penicillins and the monobactam aztreonam, while carbapenems inhibit $AmpC_{EC}$ through formation of hydrolytically stable acyl-enzyme complexes[104-106].

1.4.1.2. Class D serine β-lactamases

Class D SBLs are predominantly encoded for on plasmids and are all named OXA, after their ability to hydrolyse oxacillin, which differentiated them from early class A penicillinases such as TEM[107]. However, this may be misleading as class D SBLs manifest a higher level of diversity than the A and C subgroups. The substrate scope of OXA enzymes varies, with early variants hydrolysing predominantly penicillins, while newer variants have emerged with ESBL and carbapenemase activities[107].

As a distinctive difference to other SBLs, OXA β-lactamases utilise a carbamylated Lysine residue (Lys70) as the general base during catalysis[108]. Lys carbamylation occurs post-

translationally by reaction of Lys70 with a (bi)carbonate ion and is reversible under acidic conditions, leading to OXA inactivation[108,109]. Lys carbamylation of OXA SBLs is inhibited by high concentrations of halide ions, which bind in the OXA active sites in close proximity to the carbamylated Lys[109].

1.4.2. Metallo β-lactamases

Proteins with an αββα core fold, commonly known as metallo β-lactamase (MBL) fold enzymes, are common in many organisms and involved in a range of different cellular processes[110]. Although initially identified as class B β-lactamases, metallo β-lactamases (MBLs) display equally diverse structurally and mechanistically sub-groups as the SBLs, and have since been differentiated as B1, B2, and B3 MBLs based on their structure, metal binding ligands, and number of bound metal ions[111]. While the B1 and B3 MBLs utilise two divalent zinc ions in catalysis, B3 MBLs are reported to only require one Zn^{2+} to be catalytically viable[111,112]. Presently, the B1 MBL subgroup encloses the majority of the clinically relevant MBLs, *i.e.* the Verona Imipenemases (VIMs), New Delhi Metallo β-lactamases (NDMs), and imipenemases (IMPs). While B2 and B3 MBLs are almost exclusively chromosomally encoded, B1 MBLs are also widely disseminated on mobile plasmids[112].

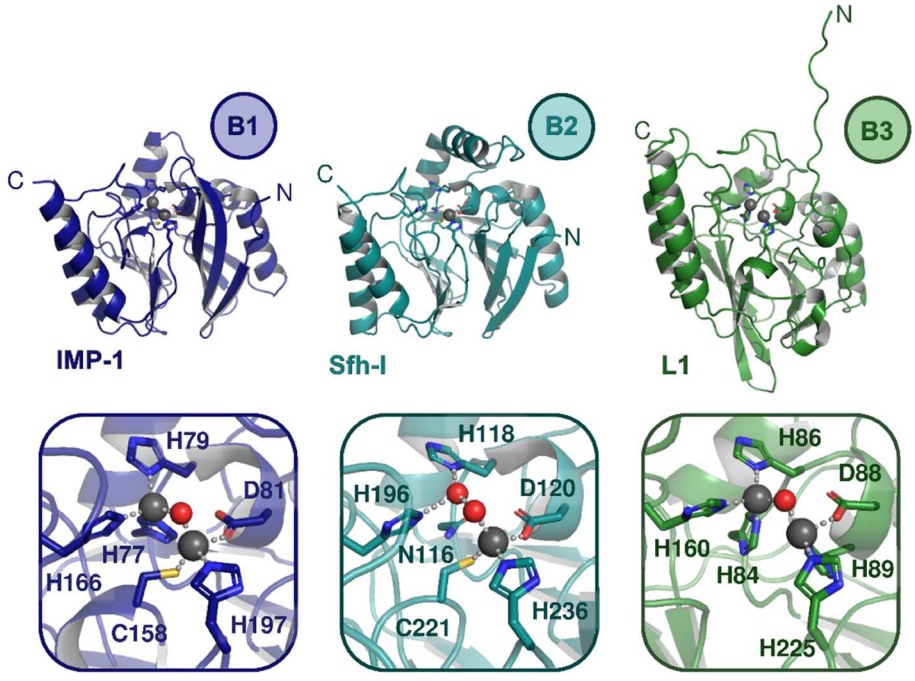


Figure 9: Structures of representative examples of MBLs from classes B1, B2, and B3. Shown are views from crystal structures of IMP-1 (B1 MBL, PDB: 5EV6[113]), Sfh-I (B2 MBL, PDB: 3SD9), and L1 (B3 MBL, PDB: 1SML[114]). Zn^{2+} ions are grey spheres; water molecules are red spheres. Coordination spheres are indicated as dashes.

In B1 and B3 MBL catalysis the two divalent Zn ions have a central role in catalysis, though activity with other divalent metals such as cadmium[115], cobalt[116], and iron[117] has also been observed with some MBLs. While both Zn ions are needed for optimal MBL activity, low activity has been proposed to occur on binding of a single Zn ion for example with the B1 MBL BCII, likely maintaining residual MBL activity under low zinc concentrations[118].

On binding of the β-lactam (S in Figure 10), nucleophilic attack of the μ2 bridging water, which is likely present as a hydroxide ion at physiologically pH, on the β-lactam carbonyl leads to a tetrahedral anionic intermediate ([EI[1]]), related to those observed in SBL catalysis)[119]. This is followed by opening of the β-lactam ring to give the hydrolysed product (P, Figure 10).

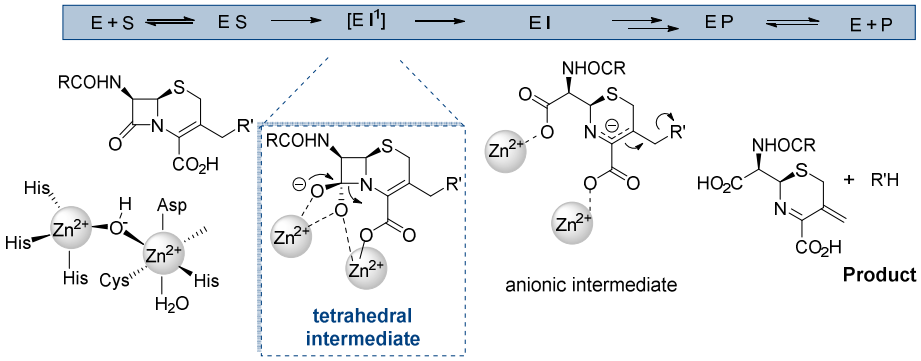


Figure 10: Outline mechanism of MBL catalysed β-lactam hydrolysis exemplified with a cephalosporin substrate. Binding of the β-lactam at the MBL active site to give a Michaelis complex is followed by nucleophilic attack of the μ2 di-zinc bridging water, proceeding via a tetrahedral intermediate to give an anionic intermediate, which is released to give the hydrolysed β-lactam. In the case of cephalosporins β-lactam hydrolysis is often accompanied by the loss of the C3' / R2 sidechain.

Collectively, MBLs can hydrolyse almost all clinically used β-lactam antibiotics, including penicillins, cephalosporins, and carbapenems, but not (efficiently) the monobactam aztreonam[111]. However, due to their originally very low dissemination they have long not been considered a threat[53]. This has changed drastically in recent years, with increasing MBL dissemination developing into a major threat to the clinical use of β-lactam antibiotics[111].

1.5. β-Lactamase inhibitors

Presently one of the most successful ways to combat β-lactamase facilitated antimicrobial resistance in the clinic is to use a combination therapy of a β-lactam antibiotic with a β-lactamase inhibitor[120]. While initially only inhibitors with relatively narrow spectrum of activity against some SBLs were available, more recently clinically useful inhibitors have also become available with broad spectrum SBL or dual SBL and MBL inhibition[55].

1.5.1. Serine β-lactamase inhibitors

As with the β-lactam antibiotics, β-lactamase inhibitors likely existed in nature long before humans started to use them. The first focused β-lactamase inhibitor to be discovered, clavulanic acid[121], is a natural product, produced by soil bacteria such as *Streptomyces clavuligerus*[122]. Clavulanic acid is approved for clinical use either in combination with amoxicillin (Augmentin, approved in 1984) or ticarcillin (Timentin, approved in 1997). It contains the β-lactam scaffold and is closely structurally related to penicillin (Figure 11). Clavulanic acid is reported to inhibit SBLs through acylation followed by further reaction of the nascent acyl-enzyme complex to give relatively stable complexes[120], which will be discussed in detail in Chapter 2. The penam sulfones (Figure 11) sulbactam[123] (in combination with ampecillin, Ampictam, approved in 1987) and tazobactam[124] (in combination with piperacillin, Tazocin, approved in 1993), are thought to inhibit SBLs through similar mechanisms as clavulanic acid[120], as also discussed in detail in Chapter 2. Further optimisation of the penam sulfone scaffold afforded enmetazobactam (Figure 12) which in combination with cefepime (Exblifep) has successfully completed clinical trials for complicated urinary tract infections including acute pyelonephritis in 2021[125]. Both penam sulfones and clavulanic acid are potent inhibitors of most SBLs from Ambler classes A and D, but generally lack activity against class C SBLs[120].

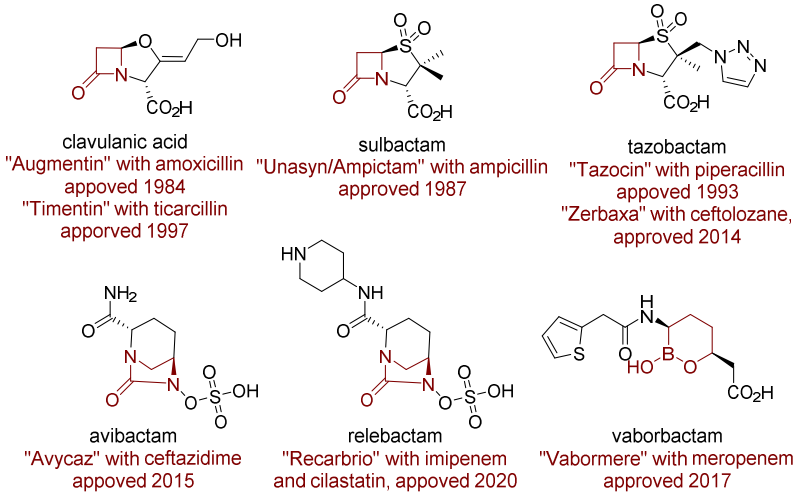


Figure 11: Clinically used serine β-lactamase inhibitors and their clinically used combinations with β-lactam antibiotics. Years refer to date of FDA approval. SBL binding motifs are highlighted in red.

Recently, synthetic β-lactamase inhibitors without a β-lactam ring have emerged. These include the mono-cyclic boronate vaborbactam (formerly RPX7009, used in combination with meropenem, Vabomere, Figure 11) and the diazabicyclooctane (DBO) avibactam (formerly NXL-104, used in combination with ceftazidime, marketed as Avycaz, Figure 11) which reached FDA approval in 2015[126]. Both vaborbactam and DBOs inhibit a wide range of class A and C and some class D SBLs[127,128] through reversible mechanisms[127,129-131], which will be discussed in detail in Chapters 3 and 4, respectively. The success of avibactam

has inspired extensive medicinal chemistry efforts to further optimise the relatively compact DBO core, leading to the clinical introduction of relebactam [132] (formerly MK-7655, used in combination with imipenem and cilastatin, Recarbrio, Figure 11). Further efforts on optimisation of the C2 amido sidechain have led to the discovery of nacubactam[133] (formerly OP-0595, Figure 12) and zidebactam[134] (formerly WCK-5107, Figure 12), both currently in Phase II clinical trials. Optimisation of the DBO core motif has yielded durlobactam[135] and ETX0282 (which is an orally available isopropyl ester pro-drug of the active SBLi ETX1317, Figure 12)[136]. Notably, all these next generation DBOs also show significant antimicrobial properties through PBP inhibition[133-135].

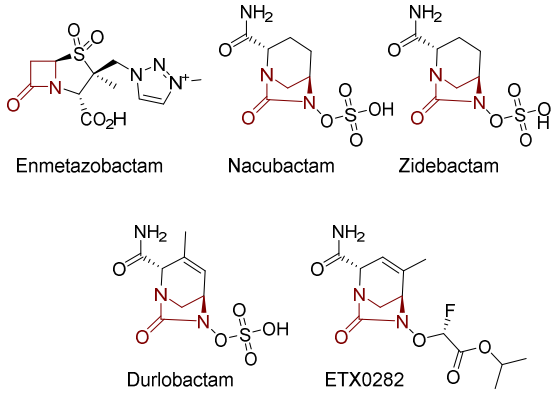


Figure 12: Serine β-lactamase inhibitors in clinical development. SBL binding motifs are highlighted in red.

1.5.2. Metallo β-lactamase inhibitors

For a long time MBL inhibitors were principally limited to general metallo-enzyme inhibitors such as metal chelating agents like EDTA[137], hydroxamic acids, and thiols[113,138,139], which have been used in diagnostics[140], but not as drugs, although a study has suggested EDTA use may be feasible for MBL inhibition in a mouse model[141]. However, the growing MBL dissemination has led to an urgent clinical need for MBL inhibitors[142] and recent efforts have resulted in more drug-like MBL inhibitors which are currently in pre-clinical development (Figure 13).

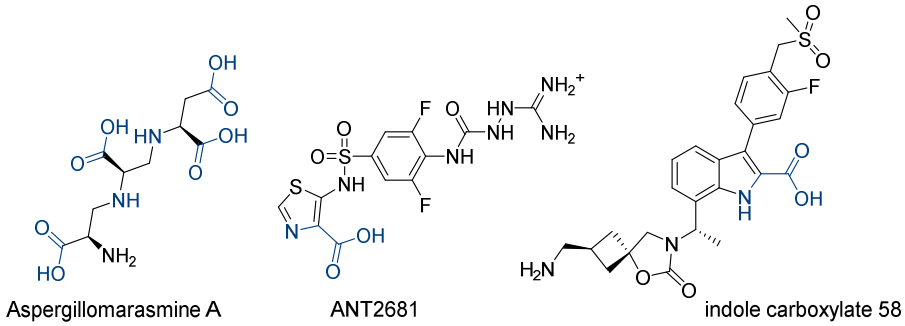


Figure 13: Selected metallo β-lactamase inhibitors in pre-clinical development. Metal chelating motifs are highlighted in blue.

Aspergillomarasmine A is a natural product which has been shown to inhibit B1 MBLs[143] by selectively sequestering Zn^{2+}[144]. The thiazole carboxylate ANT2681 is a product mimic adopting a similar binding mode as the hydrolysed carbapenem at the MBL active site[145]. ANT2681 has shown activity in mouse models and is currently in pre-clinical testing[145]. Indole carboxylates have been shown to confer broad-spectrum MBL inhibition through mimicking β-lactam binding at the MBL active site, with excellent activity in multiple mouse models with infection by carbapenem-resistant multi-drug resistant strains[146].

1.5.3. "Dual-action" β-lactamase inhibitors

Development of "dual" action pan-β-lactamase inhibitors that inhibit a wide range of SBLs and MBLs is complicated by the substantial structural and apparent mechanistic differences between both types of β-lactamases. However, due to the growing prevalence of pathogenic bacteria co-producing SBLs and MBLs there is an urgent clinical need, which has driven the development of taniborbactam, the first clinically useful β-lactamase inhibitor with activity against most SBLs and some MBLs[147].

Taniborbactam is a bicyclic boronate (Figure 14) which is proposed to inhibit both SBLs and MBLs by imitation of the tetrahedral transition states which are common to both SBL and MBL inhibition, the mechanisms of which will be discussed in detail in Chapter 4. Besides bicyclic boronates, a number of scaffolds can be used to mimic tetrahedral intermediates in β-lactamase catalysis, e.g. trifluoro methyl ketones, aldehydes, cyclobutanones, β-phospholactams and phosphonates[148-150]. However, to date bicyclic boronates are by far the most successful of these intermediate analogues. While early generations of cyclic boronic acids are ineffective against MBLs (see vaborbactam), bicyclic boronates show inhibition of a wide range of SBLs and some MBLs[151,152]. In addition to taniborbactam, which is used in combination with cefepime, two other bicyclic boronates have entered clinical testing; VNRX-5236 (Figure 14) has a smaller C3 amido sidechain compared to taniborbactam and is investigated in a prodrug form (VNRX-7145, Figure 14) in combination with ceftibuten[153]. QPX7728 (Xeruborbactam) is a tricyclic boronate with a cyclopropyl group fused to the C2/C3 carbons (Figure 14) and also currently in clinical development[154].

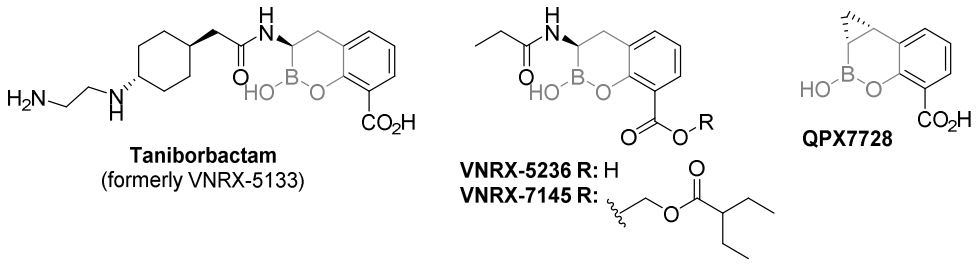


Figure 14: Dual serine- and metallo-β-lactamase inhibitors in clinical development. β-Lactamase binding motifs are highlighted in grey.

1.6. Research objectives

Much of the work described in this thesis aimed to characterise the class C *Escherichia coli* AmpC β-lactamase using a range of biophysical and biochemical techniques to investigate its interactions both with clinically useful β-lactamase inhibitors and with β-lactam antibiotics.

The work aimed to study $AmpC_{EC}$ inhibition by the β-lactam based β-lactamase inhibitors tazobactam, sulbactam, enmetazobactam, and clavulanic acid with focus on the nature of the hydrolytically stable acyl-enzyme species. Due to the unexpected results, the scope of the work was extended to re-evaluate the mechanism of inhibition of the β-lactam based inhibitors with other serine β-lactamases.

The diazabicyclooctanes avibactam, relebactam, nacubactam, and zidebactam were studied with respect of the influence of the different C2 amido sidechains on $AmpC_{EC}$ inhibition, both from structural, kinetic, and thermodynamic perspectives. Similarly, the bicyclic boronate taniborbactam was evaluated for $AmpC_{EC}$ inhibition in comparison to related boronates with varying C3 sidechains. In addition to studies with isolated $AmpC_{EC}$, the work aimed to evaluate $AmpC_{EC}$ inhibition in $AmpC_{EC}$ expressing *E. coli*.

Structural studies on the reaction of $AmpC_{EC}$ with different β-lactam antibiotics aimed to give insight into differences in the hydrolytic stability of the reacted acyl-enzyme species.

Finally, the work aimed to establish protocols to study $AmpC_{EC}$ inhibition and catalysis using time-resolved serial crystallography techniques.

Overall, the work aimed to provide new insights into the detailed mechanisms of $AmpC_{EC}$ inhibition and catalysis to aid SAR guided efforts to develop new β-lactam antibiotics with improved $AmpC_{EC}$ stability and improved $AmpC_{EC}$ inhibitors to counteract antimicrobial resistance.

1.7. References

1. CDC on Infectious Diseases in the United States: 1900–99. *Popul. Dev. Rev.* **1999**, *25*, 635-640.
2. Armstrong, G.L.; Conn, L.A.; Pinner, R.W. Trends in infectious disease mortality in the United States during the 20th century. *JAMA* **1999**, *281*, 61-66.
3. Ehrlich, P. Experimental Researches on Specific Therapy: On Immunity with special Reference to the Relationship between Distribution and Action of Antigens. In *The Collected Papers of Paul Ehrlich*, Himmelweit, F., Ed. Pergamon **1960**, pp. 106-117.
4. Mahoney, J.F.; Arnold, R.C.; Harris, A. Penicillin Treatment of Early Syphilis - A Preliminary Report. *Am. J. Public Health Nations Health* **1943**, *33*, 1387-1391.
5. Schwartz, R.S. Paul Ehrlich's Magic Bullets. *New Eng. J. Med.* **2004**, *350*, 1079-1080.
6. Domagk, G. Ein Beitrag zur Chemotherapie der bakteriellen Infektionen. *Dtsch. Med. Wochenschr.* **1935**, *61*, 250-253.
7. Hutchings, M.I.; Truman, A.W.; Wilkinson, B. Antibiotics: past, present and future. *Curr. Opin. Microbiol.* **2019**, *51*, 72-80.

8. Spellberg, B.; Taylor-Blake, B. On the exoneration of Dr. William H. Stewart: debunking an urban legend. *Infect. Dis. Poverty* **2013**, *2*, 3.
9. Donadio, S.; Maffioli, S.; Monciardini, P.; Sosio, M.; Jabes, D. Antibiotic discovery in the twenty-first century: current trends and future perspectives. *J. Antibiot.* **2010**, *63*, 423-430.
10. White, A.R.; Blaser, M.; Carrs, O.; Cassell, G.; Fishman, N.; Guidos, R.; Levy, S.; Powers, J.; Norrby, R.; Tillotson, G., et al. Effective antibacterials: at what cost? The economics of antibacterial resistance and its control. *J. Antimicrob. Chemother.* **2011**, *66*, 1948-1953.
11. Bush, K.; Bradford, P.A. β-Lactams and β-Lactamase Inhibitors: An Overview. *Cold Spring Harb. Perspect. Med.* **2016**, *6*, a025247.
12. Landers, T.F.; Cohen, B.; Wittum, T.E.; Larson, E.L. A Review of Antibiotic Use in Food Animals: Perspective, Policy, and Potential. *Public Health Rep.* **2012**, *127*, 4-22.
13. Hamed, R.B.; Gomez-Castellanos, J.R.; Henry, L.; Ducho, C.; McDonough, M.A.; Schofield, C.J. The enzymes of β-lactam biosynthesis. *Nat. Prod. Rep.* **2013**, *30*, 21-107.
14. Böttcher, H.M. *Wonder drugs: A history of antibiotics*; Lippincott, **1964**.
15. Fleming, A. On the Antibacterial Action of Cultures of a Penicillium, with Special Reference to their Use in the Isolation of *B. influenzæ*. *Br. J. Exp. Pathol.* **1929**, *10*, 226-236.
16. Kong, K.-F.; Schneper, L.; Mathee, K. Beta-lactam antibiotics: from antibiosis to resistance and bacteriology. *APMIS* **2010**, *118*, 1-36.
17. Chain, E.; Florey, H.W.; Gardner, A.D.; Heatley, N.G.; Jennings, M.A.; Orr-Ewing, J.; Sanders, A.G. Penicillin as a Chemotherapeutic Agent. *Lancet* **1940**, *236*, 226-228.
18. Abraham, E.P.; Chain, E.; Fletcher, C.M.; Florey, H.W.; Gardner, A.D.; Heatley, N.G.; Jennings, M.A. Further observations on penicillin. *Lancet* **1941**, *238*, 177-6736.
19. Macfarlane, G. *Howard Florey, the making of a great scientist*; Oxford University Press, **1979**.
20. Chain, E. The early years of the penicillin discovery. *Trends Pharmacol. Sci.* **1979**, *1*, 6-11.
21. Hodgkin, D.C. The X-ray analysis of the structure of penicillin. *Adv Sci.* **1949**, *6*, 85-89.
22. Crowfoot, D.; Bunn, C.W.; Rogers-Low, B.W.; Turner-Jones, A. XI. The X-Ray Crystallographic Investigation of the Structure of Penicillin. In *Chemistry of Penicillin*, Hans, T.C., Ed. Princeton University Press **2015**, pp. 310-366.
23. Demain, A.L.; Elander, R.P. The β-lactam antibiotics: past, present, and future. *Antonie Van Leeuwenhoek* **1999**, *75*, 5-19.
24. Moyer, A.J.; Coghill, R.D. Penicillin: VIII. Production of Penicillin in Surface Cultures. *J. Bacteriol.* **1946**, *51*, 57-78.
25. Moyer, A.J.; Coghill, R.D. Penicillin: IX. The Laboratory Scale Production of Penicillin in Submerged Cultures by Penicillium notatum Westling (NRRL 832). *J. Bacteriol.* **1946**, *51*, 79-93.
26. Batchelor, F.R.; Doyle, F.P.; Nayler, J.H.C.; Rolinson, G.N. Synthesis of Penicillin: 6-Aminopenicillanic Acid in Penicillin Fermentations. *Nature* **1959**, *183*, 257-258.
27. Sheehan, J.C. The Chemistry of Synthetic and Semisynthetic Penicillins. *Ann. N. Y. Acad. Sci.* **1967**, *145*, 216-223.
28. Acred, P.; Brown, D.M.; Knudsen, E.T.; Rolinson, G.N.; Sutherland, R. New Semi-synthetic Penicillin active against *Pseudomonas pyocyanea*. *Nature* **1967**, *215*, 25-30.
29. Abraham, E.P.; Newton, G.G.F. The structure of cephalosporin C. *Biochem. J.* **1961**, *79*, 377-393.
30. Chaudhry, S.B.; Veve, M.P.; Wagner, J.L. Cephalosporins: A Focus on Side Chains and β-Lactam Cross-Reactivity. *Pharmacy* **2019**, *7*, 103.
31. Nagarajan, R.; Boeck, L.D.; Gorman, M.; Hamill, R.L.; Higgens, C.E.; Hoehn, M.M.; Stark, W.M.; Whitney, J.G. β-Lactam antibiotics from *Streptomyces*. *J. Am. Chem. Soc.* **1971**, *93*, 2308-2310.
32. Kahan, J.S.; Kahan, F.M.; Goegelman, R.; Currie, S.A.; Jackson, M.; Stapley, E.O.; Miller, T.W.; Miller, A.K.; Hendlin, D.; Mochales, S., et al. Thienamycin, a new β-lactam

antibiotic. I. Discovery, taxonomy, isolation and physical properties. *J. Antibiot. (Tokyo)* **1979**, *32*, 1-12.
33. Papp-Wallace, K.M.; Endimiani, A.; Taracila, M.A.; Bonomo, R.A. Carbapenems: Past, Present, and Future. *Antimicrob. Agents Chemother.* **2011**, *55*, 4943-4960.
34. Sykes, R.B.; Cimarusti, C.M.; Bonner, D.P.; Bush, K.; Floyd, D.M.; Georgopapadakou, N.H.; Koster, W.H.; Liu, W.C.; Parker, W.L.; Principe, P.A., et al. Monocyclic β-lactam antibiotics produced by bacteria. *Nature* **1981**, *291*, 489-491.
35. Lohans, C.T.; Brem, J.; Schofield, C.J. New Delhi Metallo-β-Lactamase 1 Catalyzes Avibactam and Aztreonam Hydrolysis. *Antimicrob. Agents Chemother.* **2017**, *61*, e01224-01217.
36. Shields, R.K.; Doi, Y. Aztreonam Combination Therapy: An Answer to Metallo-β-Lactamase-Producing Gram-Negative Bacteria? *Clin. Infect. Dis.* **2019**, *71*, 1099-1101.
37. Sauvage, E.; Kerff, F.; Terrak, M.; Ayala, J.A.; Charlier, P. The penicillin-binding proteins: structure and role in peptidoglycan biosynthesis. *FEMS Microbiol. Rev.* **2008**, *32*, 234-258.
38. Zapun, A.; Contreras-Martel, C.; Vernet, T. Penicillin-binding proteins and β-lactam resistance. *FEMS Microbiol. Rev.* **2008**, *32*, 361-385.
39. Dörr, T.; Moynihan, P.J.; Mayer, C. Editorial: Bacterial Cell Wall Structure and Dynamics. *Front. Microbiol.* **2019**, *10*, 2051.
40. Alexander, J.A.N.; Chatterjee, S.S.; Hamilton, S.M.; Eltis, L.D.; Chambers, H.F.; Strynadka, N.C.J. Structural and kinetic analyses of penicillin-binding protein 4 (PBP4)-mediated antibiotic resistance in *Staphylococcus aureus*. *J. Biol. Chem.* **2018**, *293*, 19854-19865.
41. Tipper, D.J.; Strominger, J.L. Mechanism of action of penicillins: a proposal based on their structural similarity to acyl-D-alanyl-D-alanine. *Proc. Natl. Acad. Sci. U. S. A.* **1965**, *54*, 1133-1141.
42. D'Costa, V.M.; King, C.E.; Kalan, L.; Morar, M.; Sung, W.W.L.; Schwarz, C.; Froese, D.; Zazula, G.; Calmels, F.; Debruyne, R., et al. Antibiotic resistance is ancient. *Nature* **2011**, *477*, 457-461.
43. Prestinaci, F.; Pezzotti, P.; Pantosti, A. Antimicrobial resistance: a global multifaceted phenomenon. *Pathog. Glob. Health* **2015**, *109*, 309-318.
44. O'Neill, J. *Tackling drug-resistant infections globally: final report and recommendations*; Government of the United Kingdom, **2016**.
45. de Kraker, M.E.A.; Stewardson, A.J.; Harbarth, S. Will 10 Million People Die a Year due to Antimicrobial Resistance by 2050? *PLoS Med.* **2016**, *13*, e1002184.
46. Murray, C.J.L.; Ikuta, K.S.; Sharara, F.; Swetschinski, L.; Robles Aguilar, G.; Gray, A.; Han, C.; Bisignano, C.; Rao, P.; Wool, E., et al. Global burden of bacterial antimicrobial resistance in 2019: a systematic analysis. *Lancet* **2022**, *399*, 629-655.
47. Dadgostar, P. Antimicrobial Resistance: Implications and Costs. *Infect. Drug Resist.* **2019**, *12*, 3903-3910.
48. Reygaert, W.C. An overview of the antimicrobial resistance mechanisms of bacteria. *AIMS Microbiol.* **2018**, *4*, 482-501.
49. Kumar, A.; Schweizer, H.P. Bacterial resistance to antibiotics: Active efflux and reduced uptake. *Adv. Drug Del. Rev.* **2005**, *57*, 1486-1513.
50. Poole, K. Efflux pumps as antimicrobial resistance mechanisms. *Ann. Med.* **2007**, *39*, 162-176.
51. Egorov, A.M.; Ulyashova, M.M.; Rubtsova, M.Y. Bacterial Enzymes and Antibiotic Resistance. *Acta Naturae* **2018**, *10*, 33-48.
52. Gasparrini, A.J.; Markley, J.L.; Kumar, H.; Wang, B.; Fang, L.; Irum, S.; Symister, C.T.; Wallace, M.; Burnham, C.-A.D.; Andleeb, S., et al. Tetracycline-inactivating enzymes from environmental, human commensal, and pathogenic bacteria cause broad-spectrum tetracycline resistance. *Commun. Biol.* **2020**, *3*, 241.
53. Bush, K. Past and Present Perspectives on β-Lactamases. *Antimicrob. Agents Chemother.* **2018**, *62*, e01076-01018.
54. Abraham, E.P.; Chain, E. An Enzyme from Bacteria able to Destroy Penicillin. *Nature* **1940**, *146*, 837-837.

55. Tooke, C.L.; Hinchliffe, P.; Bragginton, E.C.; Colenso, C.K.; Hirvonen, V.H.A.; Takebayashi, Y.; Spencer, J. β-Lactamases and β-Lactamase Inhibitors in the 21st Century. *J. Mol. Biol.* **2019**, *431*, 3472-3500.
56. Naas, T.; Oueslati, S.; Bonnin, R.A.; Dabos, M.L.; Zavala, A.; Dortet, L.; Retailleau, P.; Iorga, B.I. Beta-lactamase database (BLDB) – structure and function. *J. Enzyme Inhib. Med. Chem.* **2017**, *32*, 917-919.
57. Bush, K.; Jacoby, G.A. Updated Functional Classification of β-Lactamases. *Antimicrob. Agents Chemother.* **2010**, *54*, 969-976.
58. Hall, B.G.; Barlow, M. Revised Ambler classification of β-lactamases. *J. Antimicrob. Chemother.* **2005**, *55*, 1050-1051.
59. Silveira, M.C.; Azevedo da Silva, R.; Faria da Mota, F.; Catanho, M.; Jardim, R.; R Guimarães, A.C.; de Miranda, A.B. Systematic Identification and Classification of β-Lactamases Based on Sequence Similarity Criteria: β-Lactamase Annotation. *Evol. Bioinform. Online* **2018**, *14*, Article 1176934318797351.
60. Bush, K. The ABCD's of β-lactamase nomenclature. *J. Infect. Chemother.* **2013**, *19*, 549-559.
61. Page, M.G.P. A Unified Numbering Scheme for Class C β-Lactamases. *Antimicrob. Agents Chemother.* **2020**, *64*, e02247-02219.
62. Sawai, T.; Mitsuhashi, S.; Yamagishi, S. Drug Resistance of Enteric Bacteria. *Jpn. J. Microbiol.* **1968**, *12*, 423-434.
63. Richmond, M.H.; Sykes, R.B. The β-Lactamases of Gram-Negative Bacteria and their Possible Physiological Role. In *Advances in Microbial Physiology*, Rose, A.H., Tempest, D.W., Eds. Academic Press **1973**, Vol. 9, pp. 31-88.
64. Ambler, R.P.; Baddiley, J.; Abraham, E.P. The structure of β-lactamases. *Philos. Trans. R. Soc. B* **1980**, *289*, 321-331.
65. Stec, B.; Holtz, K.M.; Wojciechowski, C.L.; Kantrowitz, E.R. Structure of the wild-type TEM-1 β-lactamase at 1.55 Å and the mutant enzyme Ser70Ala at 2.1 Å suggest the mode of noncovalent catalysis for the mutant enzyme. *Acta Crystallogr. D* **2005**, *61*, 1072-1079.
66. Lang, P.A.; Parkova, A.; Leissing, T.M.; Calvopina, K.; Cain, R.; Krajnc, A.; Panduwawala, T.D.; Philippe, J.; Fishwick, C.W.; Trapencieris, P., et al. Bicyclic Boronates as Potent Inhibitors of AmpC, the Class C β-Lactamase from *Escherichia coli*. *Biomolecules* **2020**, *10*, 899.
67. Vercheval, L., Kerff, F., Sauvage, E., Herman, R., Galleni, M., Charlier, P. Crystal structure of the class D β-lactamase OXA-10 at 1.35 Å resolution. **2010**, 10.2210/pdb2X02/pdb.
68. Massova, I.; Mobashery, S. Kinship and Diversification of Bacterial Penicillin-Binding Proteins and β-Lactamases. *Antimicrob. Agents Chemother.* **1998**, *42*, 1-17.
69. Meroueh, S.O.; Minasov, G.; Lee, W.; Shoichet, B.K.; Mobashery, S. Structural Aspects for Evolution of β-Lactamases from Penicillin-Binding Proteins. *J. Am. Chem. Soc.* **2003**, *125*, 9612-9618.
70. Di Guilmi, A.M.; Mouz, N.; Pétillot, Y.; Forest, E.; Dideberg, O.; Vernet, T. Deacylation Kinetics Analysis of *Streptococcus pneumoniae* Penicillin-Binding Protein 2x Mutants Resistant to β-Lactam Antibiotics Using Electrospray Ionization-Mass Spectrometry. *Anal. Biochem.* **2000**, *284*, 240-246.
71. Lu, W.-P.; Kincaid, E.; Sun, Y.; Bauer, M.D. Kinetics of β-Lactam Interactions with Penicillin-susceptible and -resistant Penicillin-binding Protein 2x Proteins from *Streptococcus pneumoniae*: Involvement of Acylation and Deacylation in β-Lactamase Resistance. *J. Biol. Chem.* **2001**, *276*, 31494-31501.
72. Lobkovsky, E.; Moews, P.C.; Liu, H.; Zhao, H.; Frere, J.M.; Knox, J.R. Evolution of an enzyme activity: crystallographic structure at 2 Å resolution of cephalosporinase from the ampC gene of *Enterobacter cloacae* P99 and comparison with a class A penicillinase. *Proc. Natl. Acad. Sci. U. S. A.* **1993**, *90*, 11257-11261.
73. Strynadka, N.C.J.; Adachi, H.; Jensen, S.E.; Johns, K.; Sielecki, A.; Betzel, C.; Sutoh, K.; James, M.N.G. Molecular structure of the acyl-enzyme intermediate in β-lactam hydrolysis at 1.7 Å resolution. *Nature* **1992**, *359*, 700-705.

74. Chen, Y.; McReynolds, A.; Shoichet, B.K. Re-examining the role of Lys67 in class C β-lactamase catalysis. *Protein Sci.* **2009**, *18*, 662-669.
75. Verma, V.; Testero, S.A.; Amini, K.; Wei, W.; Liu, J.; Balachandran, N.; Monoharan, T.; Stynes, S.; Kotra, L.P.; Golemi-Kotra, D. Hydrolytic Mechanism of OXA-58 Enzyme, a Carbapenem-hydrolyzing Class D β-Lactamase from *Acinetobacter baumannii*. *J. Biol. Chem.* **2011**, *286*, 37292-37303.
76. Golemi, D.; Maveyraud, L.; Vakulenko, S.; Tranier, S.; Ishiwata, A.; Kotra, L.P.; Samama, J.-P.; Mobashery, S. The First Structural and Mechanistic Insights for Class D β-Lactamases: Evidence for a Novel Catalytic Process for Turnover of β-Lactam Antibiotics. *J. Am. Chem. Soc.* **2000**, *122*, 6132-6133.
77. Dubus, A.; Normark, S.; Kania, M.; Page, M.G.P. The Role of Tyrosine 150 in Catalysis of β-Lactam Hydrolysis by AmpC β-Lactamase from *Escherichia coli* Investigated by Site-Directed Mutagenesis. *Biochemistry* **1994**, *33*, 8577-8586.
78. Datta, N.; Kontomichalou, P. Penicillinase Synthesis Controlled By Infectious R Factors In *Enterobacteriaceae*. *Nature* **1965**, *208*, 239-241.
79. Liakopoulos, A.; Mevius, D.; Ceccarelli, D. A Review of SHV Extended-Spectrum β-Lactamases: Neglected Yet Ubiquitous. *Front. Microbiol.* **2016**, *7*, 1374.
80. Bonnet, R. Growing Group of Extended-Spectrum β-Lactamases: the CTX-M Enzymes. *Antimicrob. Agents Chemother.* **2004**, *48*, 1-14.
81. Canton, R.; Gonzalez-Alba, J.M.; Galán, J.C. CTX-M Enzymes: Origin and Diffusion. *Front. Microbiol.* **2012**, *3*, 110.
82. Paterson, D.L.; Bonomo, R.A. Extended-Spectrum β-Lactamases: a Clinical Update. *Clin. Microbiol. Rev.* **2005**, *18*, 657-686.
83. Yigit, H.; Queenan, A.M.; Anderson, G.J.; Domenech-Sanchez, A.; Biddle, J.W.; Steward, C.D.; Alberti, S.; Bush, K.; Tenover, F.C. Novel Carbapenem-Hydrolyzing β-Lactamase, KPC-1, from a Carbapenem-Resistant Strain of *Klebsiella pneumoniae*. *Antimicrob. Agents Chemother.* **2001**, *45*, 1151-1161.
84. Burman, L.G.; Park, J.T.; Lindström, E.B.; Boman, H.G. Resistance of *Escherichia coli* to Penicillins: Identification of the Structural Gene for the Chromosomal Penicillinase. *J. Bacteriol.* **1973**, *116*, 123-130.
85. Jacoby, G.A. AmpC β-Lactamases. *Clin. Microbiol. Rev.* **2009**, *22*, 161-182.
86. Queenan, A.M.; Shang, W.; Flamm, R.; Bush, K. Hydrolysis and Inhibition Profiles of β-Lactamases from Molecular Classes A to D with Doripenem, Imipenem, and Meropenem. *Antimicrob. Agents Chemother.* **2010**, *54*, 565-569.
87. Lee, E.H.; Nicolas, M.H.; Kitzis, M.D.; Pialoux, G.; Collatz, E.; Gutmann, L. Association of two resistance mechanisms in a clinical isolate of *Enterobacter cloacae* with high-level resistance to imipenem. *Antimicrob. Agents Chemother.* **1991**, *35*, 1093-1098.
88. Xu, C.; Wang, D.; Zhang, X.; Liu, H.; Zhu, G.; Wang, T.; Cheng, Z.; Wu, W.; Bai, F.; Jin, Y. Mechanisms for Rapid Evolution of Carbapenem Resistance in a Clinical Isolate of *Pseudomonas aeruginosa*. *Front. Microbiol.* **2020**, *11*, 1390.
89. Quale, J.; Bratu, S.; Gupta, J.; Landman, D. Interplay of Efflux System, *ampC*, and *oprD* Expression in Carbapenem Resistance of *Pseudomonas aeruginosa* Clinical Isolates. *Antimicrob. Agents Chemother.* **2006**, *50*, 1633-1641.
90. Haenni, M.; Châtre, P.; Madec, J.-Y. Emergence of *Escherichia coli* producing extended-spectrum AmpC β-lactamases (ESAC) in animals. *Front. Microbiol.* **2014**, *5*, 53.
91. Mammeri, H.; Nordmann, P.; Berkani, A.; Eb, F. Contribution of extended-spectrum AmpC (ESAC) β-lactamases to carbapenem resistance in *Escherichia coli*. *FEMS Microbiol. Lett.* **2008**, *282*, 238-240.
92. Philippon, A.; Arlet, G.; Jacoby, G.A. Plasmid-Determined AmpC-Type β-Lactamases. *Antimicrob. Agents Chemother.* **2002**, *46*, 1-11.
93. Bradford, P.A.; Urban, C.; Mariano, N.; Projan, S.J.; Rahal, J.J.; Bush, K. Imipenem resistance in *Klebsiella pneumoniae* is associated with the combination of ACT-1, a plasmid-mediated AmpC β-lactamase, and the foss of an outer membrane protein. *Antimicrob. Agents Chemother.* **1997**, *41*, 563-569.

94. Stapleton, P.D.; Shannon, K.P.; French, G.L. Carbapenem Resistance in *Escherichia coli* Associated with Plasmid-Determined CMY-4 β-Lactamase Production and Loss of an Outer Membrane Protein. *Antimicrob. Agents Chemother.* **1999**, *43*, 1206-1210.
95. Oefner, C.; D'Arcy, A.; Daly, J.J.; Gubernator, K.; Charnas, R.L.; Heinze, I.; Hubschwerlen, C.; Winkler, F.K. Refined crystal structure of β-lactamase from *Citrobacter freundiiindicates* a mechanism for β-lactam hydrolysis. *Nature* **1990**, *343*, 284-288.
96. Tripathi, R.; Nair, N.N. Deacylation Mechanism and Kinetics of Acyl–Enzyme Complex of Class C β-Lactamase and Cephalothin. *J. Phys. Chem. B* **2016**, *120*, 2681-2690.
97. Bulychev, A.; Massova, I.; Miyashita, K.; Mobashery, S. Nuances of Mechanisms and Their Implications for Evolution of the Versatile β-Lactamase Activity: From Biosynthetic Enzymes to Drug Resistance Factors. *J. Am. Chem. Soc.* **1997**, *119*, 7619-7625.
98. Patera, A.; Blaszczak, L.C.; Shoichet, B.K. Crystal Structures of Substrate and Inhibitor Complexes with AmpC β-Lactamase: Possible Implications for Substrate-Assisted Catalysis. *J. Am. Chem. Soc.* **2000**, *122*, 10504-10512.
99. Chen, Y.; Minasov, G.; Roth, T.A.; Prati, F.; Shoichet, B.K. The Deacylation Mechanism of AmpC β-Lactamase at Ultrahigh Resolution. *J. Am. Chem. Soc.* **2006**, *128*, 2970-2976.
100. Kato-Toma, Y.; Iwashita, T.; Masuda, K.; Oyama, Y.; Ishiguro, M. pKa measurements from nuclear magnetic resonance of tyrosine-150 in class C β-lactamase. *Biochem. J.* **2003**, *371*, 175-181.
101. Jaurin, B.; Grundström, T. ampC cephalosporinase of *Escherichia coli* K-12 has a different evolutionary origin from that of β-lactamases of the penicillinase type. *Proc. Natl. Acad. Sci. U. S. A.* **1981**, *78*, 4897-4901.
102. Jaurin, B.; Grundström, T.; Edlund, T.; Normark, S. The *E. coli* β-lactamase attenuator mediates growth rate-dependent regulation. *Nature* **1981**, *290*, 221-225.
103. Nelson, E.C.; Elisha, B.G. Molecular Basis of AmpC Hyperproduction in Clinical Isolates of *Escherichia coli*. *Antimicrob. Agents Chemother.* **1999**, *43*, 957-959.
104. Galleni, M.; Amicosante, G.; Frère, J.M. A survey of the kinetic parameters of class C β-lactamases. Cephalosporins and other β-lactam compounds. *Biochem. J.* **1988**, *255*, 123-129.
105. Galleni, M.; Frère, J.M. A survey of the kinetic parameters of class C β-lactamases. Penicillins. *Biochem. J.* **1988**, *255*, 119-122.
106. Bauvois, C.; Ibuka, A.S.; Celso, A.; Alba, J.; Ishii, Y.; Frère, J.-M.; Galleni, M. Kinetic Properties of Four Plasmid-Mediated β-Lactamases. *Antimicrob. Agents Chemother.* **2005**, *49*, 4240-4246.
107. Evans, B.A.; Amyes, S.G.B. OXA β-Lactamases. *Clin. Microbiol. Rev.* **2014**, *27*, 241-263.
108. Golemi, D.; Maveyraud, L.; Vakulenko, S.; Samama, J.-P.; Mobashery, S. Critical involvement of a carbamylated lysine in catalytic function of class D β-lactamases. *Proc. Natl. Acad. Sci. U. S. A.* **2001**, *98*, 14280-14285.
109. Vercheval, L.; Bauvois, C.; di Paolo, A.; Borel, F.; Ferrer, J.-L.; Sauvage, E.; Matagne, A.; Frère, J.-M.; Charlier, P.; Galleni, M., et al. Three factors that modulate the activity of class D β-lactamases and interfere with the post-translational carboxylation of Lys70. *Biochem. J.* **2010**, *432*, 495-506.
110. Pettinati, I.; Brem, J.; Lee, S.Y.; McHugh, P.J.; Schofield, C.J. The Chemical Biology of Human Metallo-β-Lactamase Fold Proteins. *Trends Biochem. Sci.* **2016**, *41*, 338-355.
111. Bahr, G.; González, L.J.; Vila, A.J. Metallo-β-lactamases in the Age of Multidrug Resistance: From Structure and Mechanism to Evolution, Dissemination, and Inhibitor Design. *Chem. Rev.* **2021**, *121*, 7957-8094.
112. Boyd, S.E.; Livermore, D.M.; Hooper, D.C.; Hope, W.W. Metallo-β-Lactamases: Structure, Function, Epidemiology, Treatment Options, and the Development Pipeline. *Antimicrob. Agents Chemother.* **2020**, *64*, e00397-00320.
113. Hinchliffe, P.; González, M.M.; Mojica, M.F.; González, J.M.; Castillo, V.; Saiz, C.; Kosmopoulou, M.; Tooke, C.L.; Llarrull, L.I.; Mahler, G., et al. Cross-class metallo-β-

lactamase inhibition by bisthiazolidines reveals multiple binding modes. *Proc. Natl. Acad. Sci. U. S. A.* **2016**, *113*, e3745-3754.
114. Ullah, J.H.; Walsh, T.R.; Taylor, I.A.; Emery, D.C.; Verma, C.S.; Gamblin, S.J.; Spencer, J. The crystal structure of the L1 metallo-β-lactamase from *Stenotrophomonas maltophilia* at 1.7 Å resolution. *J. Mol. Biol.* **1998**, *284*, 125-136.
115. Paul-Soto, R.; Zeppezauer, M.; Adolph, H.W.; Galleni, M.; Frere, J.-M.; Carfi, A.; Dideberg, O.; Wouters, J.; Hemmingsen, L.; Bauer, R. Preference of Cd(II) and Zn(II) for the Two Metal Sites in *Bacillus cereus* β-Lactamase II: A Perturbed Angular Correlation of γ-rays Spectroscopic Study. *Biochemistry* **1999**, *38*, 16500-16506.
116. Badarau, A.; Damblon, C.; Page, Michael I. The activity of the dinuclear cobalt-β-lactamase from *Bacillus cereus* in catalysing the hydrolysis of β-lactams. *Biochem. J.* **2006**, *401*, 197-203.
117. Cahill, S.T.; Tarhonskaya, H.; Rydzik, A.M.; Flashman, E.; McDonough, M.A.; Schofield, C.J.; Brem, J. Use of ferrous iron by metallo-β-lactamases. *J. Inorg. Biochem.* **2016**, *163*, 185-193.
118. Wommer, S.; Rival, S.; Heinz, U.; Galleni, M.; Frère, J.-M.; Franceschini, N.; Amicosante, G.; Rasmussen, B.; Bauer, R.; Adolph, H.-W. Substrate-activated Zinc Binding of Metallo-β-lactamases: Physiological Importance of the Mononuclear Enzymes. *J. Biol. Chem.* **2002**, *277*, 24142-24147.
119. Page, M.I.; Badarau, A. The Mechanisms of Catalysis by Metallo β-Lactamases. *Bioinorg. Chem. Appl.* **2008**, *2008*, 576297.
120. Drawz, S.M.; Bonomo, R.A. Three decades of β-lactamase inhibitors. *Clin. Microbiol. Rev.* **2010**, *23*, 160-201.
121. Reading, C.; Cole, M. Clavulanic acid: a β-lactamase-inhibiting β-lactam from *Streptomyces clavuligerus*. *Antimicrob. Agents Chemother.* **1977**, *11*, 852-857.
122. Song, J.Y.; Jensen, S.E.; Lee, K.J. Clavulanic acid biosynthesis and genetic manipulation for its overproduction. *Appl. Microbiol. Biotechnol.* **2010**, *88*, 659-669.
123. English, A.R.; Retsema, J.A.; Girard, A.E.; Lynch, J.E.; Barth, W.E. CP-45,899, a β-Lactamase Inhibitor That Extends the Antibacterial Spectrum of β-Lactams: Initial Bacteriological Characterization. *J. Antimicrob. Chemother.* **1978**, *14*, 414-419.
124. Aronoff, S.C.; Jacobs, M.R.; Johenning, S.; Yamabe, S. Comparative activities of the β-lactamase inhibitors YTR 830, sodium clavulanate, and sulbactam combined with amoxicillin or ampicillin. *Antimicrob. Agents Chemother.* **1984**, *26*, 580-582.
125. Isler, B.; Harris, P.; Stewart, A.G.; Paterson, D.L. An update on cefepime and its future role in combination with novel β-lactamase inhibitors for MDR Enterobacterales and *Pseudomonas aeruginosa*. *J. Antimicrob. Chemother.* **2021**, *76*, 550-560.
126. Wang, D.Y.; Abboud, M.I.; Markoulides, M.S.; Brem, J.; Schofield, C.J. The road to avibactam: the first clinically useful non-β-lactam working somewhat like a β-lactam. *Future Med. Chem.* **2016**, *8*, 1063-1084.
127. Ehmann, D.E.; Jahic, H.; Ross, P.L.; Gu, R.F.; Hu, J.; Kern, G.; Walkup, G.K.; Fisher, S.L. Avibactam is a covalent, reversible, non-β-lactam β-lactamase inhibitor. *Proc. Natl. Acad. Sci. USA* **2012**, *109*, 11663-11668.
128. Hecker, S.J.; Reddy, K.R.; Totrov, M.; Hirst, G.C.; Lomovskaya, O.; Griffith, D.C.; King, P.; Tsivkovski, R.; Sun, D.; Sabet, M., et al. Discovery of a Cyclic Boronic Acid β-Lactamase Inhibitor (RPX7009) with Utility vs Class A Serine Carbapenemases. *J. Med. Chem.* **2015**, *58*, 3682-3692.
129. Ehmann, D.E.; Jahic, H.; Ross, P.L.; Gu, R.F.; Hu, J.; Durand-Reville, T.F.; Lahiri, S.; Thresher, J.; Livchak, S.; Gao, N., et al. Kinetics of avibactam inhibition against Class A, C, and D β-lactamases. *J. Biol. Chem.* **2013**, *288*, 27960-27971.
130. Choi, H.; Paton, R.S.; Park, H.; Schofield, C.J. Investigations on recyclisation and hydrolysis in avibactam mediated serine β-lactamase inhibition. *Org. Biomol. Chem.* **2016**, *14*, 4116-4128.
131. Tsivkovski, R.; Lomovskaya, O. Biochemical Activity of Vaborbactam. *Antimicrob. Agents Chemother.* **2020**, *64*, e01935-01919.

132. Blizzard, T.A.; Chen, H.; Kim, S.; Wu, J.; Bodner, R.; Gude, C.; Imbriglio, J.; Young, K.; Park, Y.-W.; Ogawa, A., et al. Discovery of MK-7655, a β-lactamase inhibitor for combination with Primaxin®. *Bioorg. Med. Chem. Lett.* **2014**, *24*, 780-785.
133. Morinaka, A.; Tsutsumi, Y.; Yamada, M.; Suzuki, K.; Watanabe, T.; Abe, T.; Furuuchi, T.; Inamura, S.; Sakamaki, Y.; Mitsuhashi, N., et al. OP0595, a new diazabicyclooctane: mode of action as a serine β-lactamase inhibitor, antibiotic and β-lactam 'enhancer'. *J. Antimicrob. Chemother.* **2015**, *70*, 2779-2786.
134. Moya, B.; Barcelo, I.M.; Bhagwat, S.; Patel, M.; Bou, G.; Papp-Wallace, K.M.; Bonomo, R.A.; Oliver, A. WCK 5107 (Zidebactam) and WCK 5153 are novel inhibitors of PBP2 showing potent "β-Lactam Enhancer" activity against *Pseudomonas aeruginosa*, including multidrug-resistant metallo-β-lactamase-producing high-risk clones. *Antimicrob. Agents Chemother.* **2017**, *61*, e02529-02516.
135. Durand-Réville, T.F.; Guler, S.; Comita-Prevoir, J.; Chen, B.; Bifulco, N.; Huynh, H.; Lahiri, S.; Shapiro, A.B.; McLeod, S.M.; Carter, N.M., et al. ETX2514 is a broad-spectrum β-lactamase inhibitor for the treatment of drug-resistant Gram-negative bacteria including *Acinetobacter baumannii*. *Nat. Microbiol.* **2017**, *2*, 17104.
136. Durand-Réville, T.F.; Comita-Prevoir, J.; Zhang, J.; Wu, X.; May-Dracka, T.L.; Romero, J.A.C.; Wu, F.; Chen, A.; Shapiro, A.B.; Carter, N.M., et al. Discovery of an Orally Available Diazabicyclooctane Inhibitor (ETX0282) of Class A, C, and D Serine β-Lactamases. *J. Med. Chem.* **2020**, *63*, 12511-12525.
137. Azumah, R.; Dutta, J.; Somboro, A.M.; Ramtahal, M.; Chonco, L.; Parboosing, R.; Bester, L.A.; Kruger, H.G.; Naicker, T.; Essack, S.Y., et al. *In vitro* evaluation of metal chelators as potential metallo-β-lactamase inhibitors. *J. Appl. Microbiol.* **2016**, *120*, 860-867.
138. Klingler, F.-M.; Wichelhaus, T.A.; Frank, D.; Cuesta-Bernal, J.; El-Delik, J.; Müller, H.F.; Sjuts, H.; Göttig, S.; Koenigs, A.; Pos, K.M., et al. Approved Drugs Containing Thiols as Inhibitors of Metallo-β-lactamases: Strategy To Combat Multidrug-Resistant Bacteria. *J. Med. Chem.* **2015**, *58*, 3626-3630.
139. Brem, J.; Berkel, S.S.v.; Zollman, D.; Lee, S.Y.; Gileadi, O.; McHugh, P.J.; Walsh, T.R.; McDonough, M.A.; Schofield, C.J. Structural Basis of Metallo-β-Lactamase Inhibition by Captopril Stereoisomers. *Antimicrob. Agents Chemother.* **2016**, *60*, 142-150.
140. Lee, K.; Lim, Y.S.; Yong, D.; Yum, J.H.; Chong, Y. Evaluation of the Hodge Test and the Imipenem-EDTA Double-Disk Synergy Test for Differentiating Metallo-β-Lactamase-Producing Isolates of *Pseudomonas* spp. and *Acinetobacter* spp. *J. Clin. Microbiol.* **2003**, *41*, 4623-4629.
141. Aoki, N.; Ishii, Y.; Tateda, K.; Saga, T.; Kimura, S.; Kikuchi, Y.; Kobayashi, T.; Tanabe, Y.; Tsukada, H.; Gejyo, F., et al. Efficacy of Calcium-EDTA as an Inhibitor for Metallo-β-Lactamase in a Mouse Model of *Pseudomonas aeruginosa* Pneumonia. *Antimicrob. Agents Chemother.* **2010**, *54*, 4582-4588.
142. Mojica, M.F.; Rossi, M.-A.; Vila, A.J.; Bonomo, R.A. The urgent need for metallo-β-lactamase inhibitors: an unattended global threat. *Lancet Infect. Dis.* **2022**, *22*, e28-34.
143. King, A.M.; Reid-Yu, S.A.; Wang, W.; King, D.T.; De Pascale, G.; Strynadka, N.C.; Walsh, T.R.; Coombes, B.K.; Wright, G.D. Aspergillomarasmine A overcomes metallo-β-lactamase antibiotic resistance. *Nature* **2014**, *510*, 503-506.
144. Sychantha, D.; Rotondo, C.M.; Tehrani, K.H.M.E.; Martin, N.I.; Wright, G.D. Aspergillomarasmine A inhibits metallo-β-lactamases by selectively sequestering Zn^{2+}. *J. Biol. Chem.* **2021**, *297*, 100918.
145. Davies, D.T.; Leiris, S.; Sprynski, N.; Castandet, J.; Lozano, C.; Bousquet, J.; Zalacain, M.; Vasa, S.; Dasari, P.K.; Pattipati, R., et al. ANT2681: SAR Studies Leading to the Identification of a Metallo-β-lactamase Inhibitor with Potential for Clinical Use in Combination with Meropenem for the Treatment of Infections Caused by NDM-Producing *Enterobacteriaceae*. *ACS Infect. Dis.* **2020**, *6*, 2419-2430.
146. Brem, J.; Panduwawala, T.; Hansen, J.U.; Hewitt, J.; Liepins, E.; Donets, P.; Espina, L.; Farley, A.J.M.; Shubin, K.; Campillos, G.G., et al. Imitation of β-lactam binding enables broad-spectrum metallo-β-lactamase inhibitors. *Nat. Chem.* **2022**, *14*, 15-24.

147. Liu, B.; Trout, R.E.L.; Chu, G.-H.; McGarry, D.; Jackson, R.W.; Hamrick, J.C.; Daigle, D.M.; Cusick, S.M.; Pozzi, C.; De Luca, F., et al. Discovery of Taniborbactam (VNRX-5133): A Broad-Spectrum Serine- and Metallo-β-lactamase Inhibitor for Carbapenem-Resistant Bacterial Infections. *J. Med. Chem.* **2020**, *63*, 2789-2801.
148. Krajnc, A.; Lang, P.A.; Panduwawala, T.D.; Brem, J.; Schofield, C.J. Will morphing boron-based inhibitors beat the β-lactamases? *Curr. Opin. Chem. Biol.* **2019**, *50*, 101-110.
149. Yang, K.-W.; Feng, L.; Yang, S.-K.; Aitha, M.; LaCuran, A.E.; Oelschlaeger, P.; Crowder, M.W. New β-phospholactam as a carbapenem transition state analog: Synthesis of a broad-spectrum inhibitor of metallo-β-lactamases. *Bioorg. Med. Chem. Lett.* **2013**, *23*, 5855-5859.
150. Abboud, M.I.; Kosmopoulou, M.; Krismanich, A.P.; Johnson, J.W.; Hinchliffe, P.; Brem, J.; Claridge, T.D.W.; Spencer, J.; Schofield, C.J.; Dmitrienko, G.I. Cyclobutanone Mimics of Intermediates in Metallo-β-Lactamase Catalysis. *Chem. Eur. J.* **2018**, *24*, 5734-5737.
151. Brem, J.; Cain, R.; Cahill, S.; McDonough, M.A.; Clifton, I.J.; Jiménez-Castellanos, J.-C.; Avison, M.B.; Spencer, J.; Fishwick, C.W.G.; Schofield, C.J. Structural basis of metallo-β-lactamase, serine-β-lactamase and penicillin-binding protein inhibition by cyclic boronates. *Nat. Commun.* **2016**, *7*, 12406.
152. Cahill, S.T.; Cain, R.; Wang, D.Y.; Lohans, C.T.; Wareham, D.W.; Oswin, H.P.; Mohammed, J.; Spencer, J.; Fishwick, C.W.G.; McDonough, M.A., et al. Cyclic Boronates Inhibit All Classes of β-Lactamases. *Antimicrob. Agents Chemother.* **2017**, *61*, e02260-02216.
153. Trout, R.E.; Zulli, A.; Mesaros, E.; Jackson, R.W.; Boyd, S.; Liu, B.; Hamrick, J.; Daigle, D.; Chatwin, C.L.; John, K., et al. Discovery of VNRX-7145 (VNRX-5236 Etzadroxil): An Orally Bioavailable β-Lactamase Inhibitor for *Enterobacterales* Expressing Ambler Class A, C, and D Enzymes. *J. Med. Chem.* **2021**, *64*, 10155-10166.
154. Hecker, S.J.; Reddy, K.R.; Lomovskaya, O.; Griffith, D.C.; Rubio-Aparicio, D.; Nelson, K.; Tsivkovski, R.; Sun, D.; Sabet, M.; Tarazi, Z., et al. Discovery of Cyclic Boronic Acid QPX7728, an Ultrabroad-Spectrum Inhibitor of Serine and Metallo-β-lactamases. *J. Med. Chem.* **2020**, *63*, 7491-7507.

Chapter 2

Interactions of AmpC$_{EC}$ and other Serine β-Lactamases with β-Lactam containing Inhibitors

The work in this chapter was carried out in conjunction with Dr Jürgen Brem, who advised on the experimental design and expressed and purified recombinant TEM-116, Dr Ritu Raj, who conducted non-denaturing MS and LC-MS/MS analyses under supervision of Prof. Carol V. Robinson, Dr Anthony Tumber, who advised on SPE-MS experiments, Dr Christopher T. Lohans and Prof. Timothy D. W. Claridge, who supported NMR experiments and Dr Patrick Rabe, who supported LC-MS experiments. Non-denaturing MS experiments with clavulanic acid were done in collaboration with Mariska de Munnik (University of Oxford). Part of the work described herein has been reported in the academic literature[1].

Contents

2.1. Introduction 30
2.2. Production, purification, and initial characterisation of β-lactamases 32
2.2.1. Production and purification 32
2.2.2. Steady-state-kinetics with reporter substrates 33
2.2.3. Crystallisation of $AmpC_{EC}$ 35
2.3. SBL inhibition by penam sulfones 38
2.3.1. Kinetic analyses of transient SBL inhibition by penam sulfones 38
2.3.1.1. Dose-dependence studies 38
2.3.1.2. Detailed kinetic analyses of transient inhibition 40
2.3.2. Mechanistic studies with penam sulfones 43
2.3.2.1. Solid-phase-extraction mass spectrometry (SPE-MS) show lack of penam sulfone derived acyl-enzyme fragmentation 44
2.3.2.2. Acyl-enzyme fragmentation is induced during LC-MS analyses 49
2.3.2.3. Further investigations into the +169 Da species 53
2.3.2.4. Prolonged reaction of SBLs with penam sulfones can lead to dehydration of the nucleophilic serine 57
2.3.2.5. Solution based NMR studies show turn-over to fragmented products 67
2.4. SBL inhibition by clavulanic acid 68
2.4.1. Kinetic analyses of transient SBL inhibition 69
2.4.1.1. Dose-dependence studies 69
2.4.1.2. Detailed kinetic analyses of transient SBL inhibition by clavulanic acid 70
2.4.2. Mechanistic studies with clavulanic acid 72
2.4.2.1. Covalently bound species depend on the mass spectrometric method 72
2.4.2.2. AEC fragmentation is observed on prolonged reaction of Class A SBLs with clavulanic acid 74
2.4.2.3. Solution based NMR studies on clavulanic acid hydrolysis 77
2.5. Summary and Conclusion 79
2.6. Materials and Methods 82
2.6.1. Materials 82
2.6.2. Recombinant enzyme production and purification 82
2.6.3. Kinetic assays under steady state conditions 83
2.6.3.1. Kinetic characterisation of reporter substrates 83
2.6.3.2. Dose-dependence studies 84
2.6.3.3. Pseudo first order rate constants and apparent inhibition constants 84
2.6.3.4. Dissociation rates 85
2.6.3.5. Partition ratios 85
2.6.4. Mass spectrometry 85
2.6.4.1. Solid phase extraction mass spectrometry 85
2.6.4.2. Liquid chromatography mass spectrometry 86

2.6.4.3. Non-denaturing mass spectrometry 86
2.6.5. Crystallography 87
2.6.5.1. Crystallisation of AmpC$_{EC}$ 87
2.6.5.2. Crystallisation of OXA-10 87
2.6.5.3. Data collection and processing 88
2.6.6. Nuclear magnetic resonance spectrometry 88
2.6.7. Tryptic digestion and LC-MS/MS analyses 88
2.7. References 89

2.1. Introduction

One of the most clinically successful strategies to overcome β-lactamase conferred resistance to β-lactam antibiotics is co-administration of a β-lactam antibiotic with a β-lactamase inhibitor[2-4]. The first clinically used serine β-lactamase inhibitor (SBLi) to acquire FDA approval was clavulanic acid[5] (a clavam) in 1984, followed by the penam sulfones sulbactam[6] and tazobactam[7] (Figure 1), all of which contain a β-lactam. They differ from penicillins, which are β-lactamase substrates, by the absence of a C6 amido sidechain and either substitution of the thiazolidine sulfur by oxygen to give a clavam (clavulanic acid), or oxidation of the thiazolidine sulfur to give the corresponding penam sulfones (sulbactam and tazobactam).

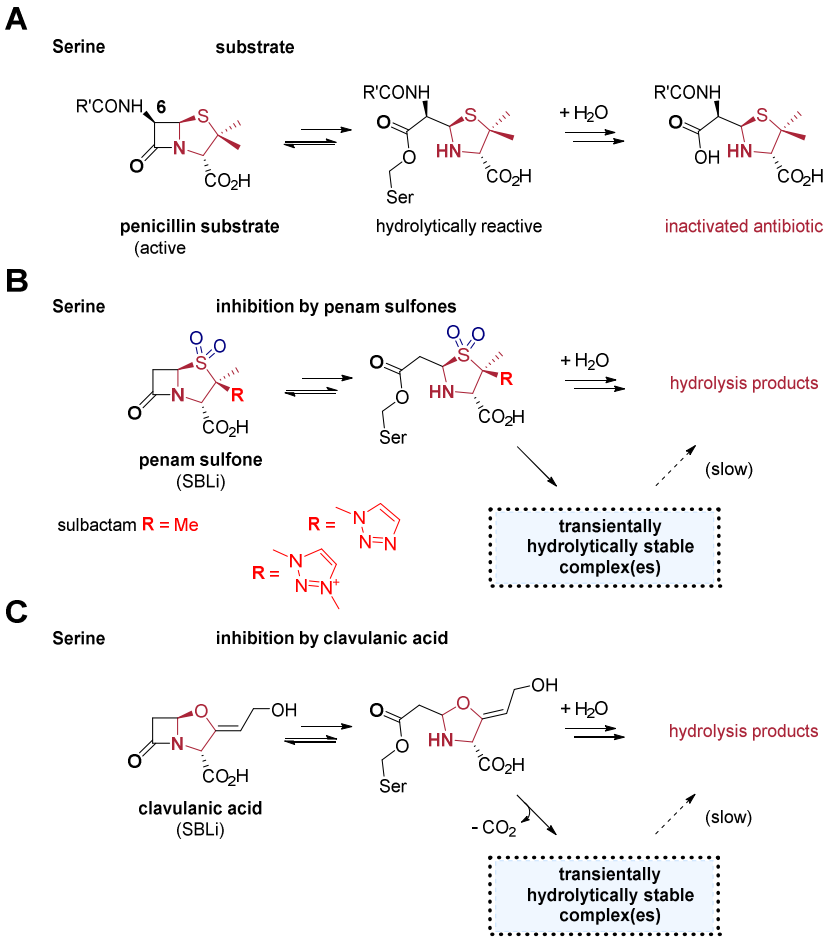


Figure 1: Sulfone derivatives of penicillins and clavulanic acid are potent mechanism-based inhibitors of serine β-lactamases. (A) Outline mechanism for penicillin hydrolysis as catalysed by a nucleophilic serine β-lactamase. Reaction proceeds via an acyl-enzyme complex, which is reactive to hydrolysis. (B) Sulfone derivatives of penicillins are inhibitors, their acyl-enzyme complex reacts to give hydrolytically stable complexes, the identity of which are the focus of our work. (C) The clavam clavulanic acid reacts with SBLs in a similar manner as penam sulfones, but with additional de-carboxylation of the acyl-enzyme complex. Note the initially formed hydrolysis products may react further. The figure and figure legend are adopted with permission from Lang *et al.* Proc. Natl. Acad. Sci. U.S.A., 2022, *119*, e2117310119.

These relatively subtle changes lead to bifurcation of the reaction of SBLi with SBLs after formation of the nascent acyl-enzyme complex (AEC). While in the case of efficient substrates this AEC is rapidly hydrolysed to reactivate the SBL, with SBLi, in addition to hydrolysis, further reactions can occur leading to relatively hydrolytically stable AECs, which confer transient inhibition of SBLs (Figure 1).

Due to their essential role in SBL inhibition, the nature of these transientally hydrolytically stable species has been of special interest and has been studied extensively using a wide range of biophysical techniques. Interestingly, there are substantial discrepancies between the results of studies on the mechanisms of SBL inhibition using denaturing liquid-chromatography mass spectrometry (LC-MS) and those employing UV/Vis and Raman spectroscopic methods:

In case of the penam sulfones, most Raman[8-14] and UV/Vis[10,15] spectroscopic studies in combination with other crystallographic studies[8,9,14-17] indicate inhibtion via formation of a *trans*-enamine species, which results from opening of the thiazolidine ring of the nascant AEC with subsequent tautomerisation and isomerisation, but without inhibitor scaffold fragmentation. However, by contrast, MS based studies[15,18-24] as well as some crystallographic studies[24-27] indicate substantial scaffold fragmentation following formation of the AEC.

In case of clavulanic acid, MS[15,21,24,28-34] and some crystallographic studies[27,30,35] have shown similar extensive scaffold fragmentation leading to the same transiently stable species bound to SBLs. Similar to the penam sulfones, spectroscopic studies[8,11,15], as well as some crystallographic studies[8,24,35,36], have, however, only indicated decarboxylation, likely at the stage of imine formation, and otherwise no further fragmentation reactions, leading to a decarboxylated *trans*-enamine as the major species for inhibition.

The work in this chapter was originally aimed at studying AmpC$_{EC}$ inhibition by enmetazobactam, a new penam sulfone SBLi, which differs from tazobactam solely by addition of a methyl group at the triazole sidechain, thereby conferring a permanent positive charge (Figure 1). In combination with cefepime, enmetazobactam is reported to manifest substantially better antimicrobial properties against class A extended spectrum β-lactamase (ESBL), but not carbapenemase, producing strains than the commonly used piperacillin/tazobactam combination[22,37,38] and the enmetazobactam/cefepime combination (marketed as EXBLIFEP) has recently successfully completed clinical trials for complicated urinary tract infections, including acute pyelonephritis[39].

However, protein observed MS based studies on reaction of AmpC$_{EC}$ with enmetazobactam showed significant differences to previous reports on SBL reaction both with

enmetazobactam[22] and sulbactam, and tazobactam[15,18-24], thus motivating a broader re-evaluation of the mechanism of all clinically used β-lactam containing SBLi, i.e. sulbactam, tazobactam, and clavulanic acid, with representative SBLs from all Ambler classes: TEM-116 (Class A), $AmpC_{EC}$ (class C), and OXA-10 (class D).

2.2. Production, purification, and initial characterisation of β-lactamases

2.2.1. Production and purification

Recombinant TEM-116 was produced and purified by Dr Jürgen Brem (Univeristy of Oxford) according to reported procedures[40]. The E. coli W3110 strain carrying the pAD7-$AmpC_{EC}$ plasmid was provided by Prof. Malcolm G. P. Page (Jacobs University Bremen). The OXA-10 pET22b-OXA-10 plasmid was provided by Dr Jürgen Brem (Univeristy of Oxford).

$AmpC_{EC}$ was expressed in *E. coli* W3110 harbouring the pAD7 plasmid[41] and purified via ion-exchange chromatography using modified reported procedures[42] as described in detail in the Materials and Methods.

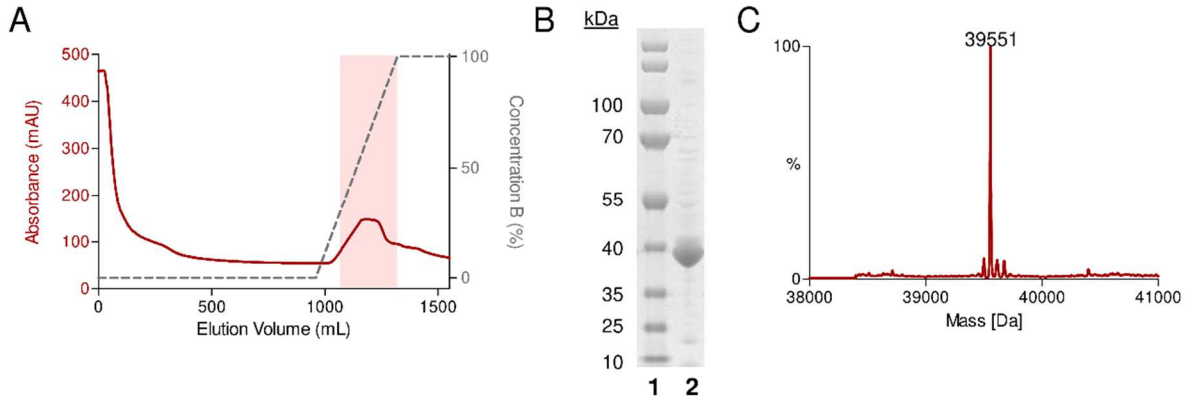


Figure 2: Purification of recombinant $AmpC_{EC}$. (A) UV-Trace of ion exchange chromatography used to purify $AmpC_{EC}$ from cell lysate. Column: SP Sepharose (GE Healthcare), 100 ml; Buffer A: 10 mM Tris pH 6.75; Buffer B: 100 mM Tris, pH 7.0. Highlighted elution volumes contained purified $AmpC_{EC}$. (B) SDS-PAGE analyses of purified $AmpC_{EC}$. Lane 1: PageRuler™ (Thermo Fisher Scientific). Lane 2: Purified $AmpC_{EC}$. (C) SPE-MS analysis of purified $AmpC_{EC}$. Shown is the deconvoluted spectrum obtained using the maximum entropy algorithm in the MassHunter Workstation Qualitative Analysis B.07.00 program (Agilent).

Recombinant OXA-10 was produced in *E. coli* BL21 DE using a pET22b vector carrying the OXA-10 gene and purified via ion-exchange and size-exclusion chromatography as previously reported[43] and as described in detail in the Materials and Methods.

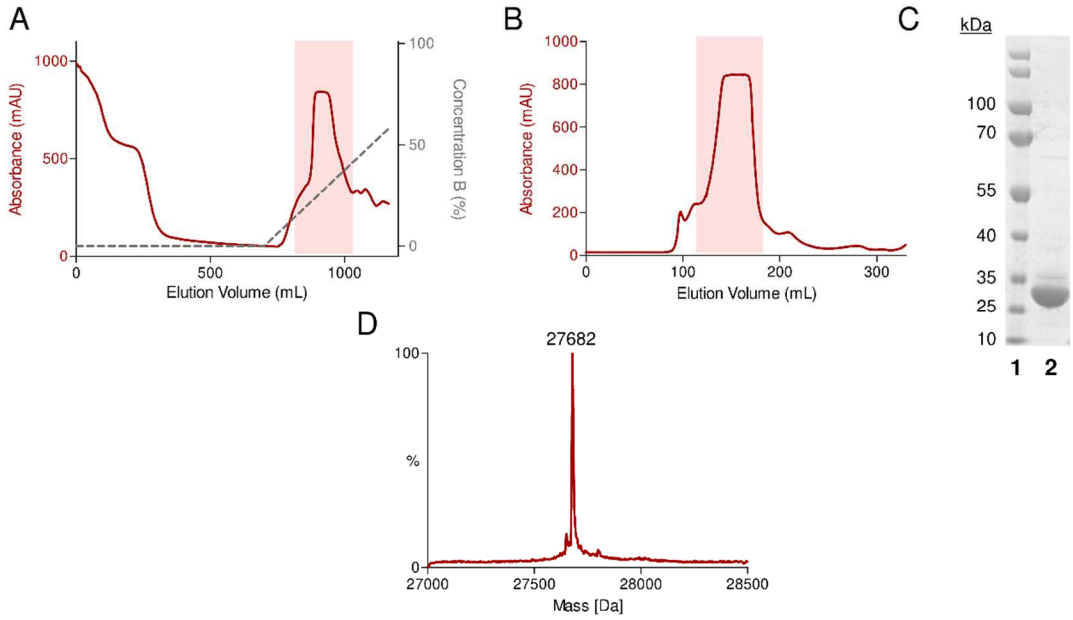


Figure 3: Purification of recombinant OXA-10. (A) UV-Trace of ion exchange chromatography used to purify OXA-10 from cell lysate. Column: SP Sepharose (GE Healthcare), 100 ml; Buffer A: 50 mM MES, pH 6.0; Buffer B: 50 mM MES, pH 6.0, 1 M NaCl. Highlighted elution volumes contained purified OXA-10. (B) UV-trace of size exclusion chromatography used to purify OXA-10. Column: Superdex 75, 300 ml, Buffer: 50 mM MES, pH 6.0, 100 mM NaCl. (C) SDS-PAGE analyses of purified OXA-10. Lane 1: PageRuler™ (Thermo Fisher Scientific). Lane 2: Purified OXA-10. (D) SPE-MS analysis of purified OXA-10. Shown is the deconvoluted spectrum obtained using the maximum entropy algorithm in the MassHunter Workstation Qualitative Analysis B.07.00 program (Agilent).

2.2.2. Steady-state-kinetics with reporter substrates

β-Lactamase activity was tested using the two reporter substrates nitrocefin (NCF) and FC-5[44]. While NCF and FC-5 are not clinically used β-lactam antibitiotics, they display favourable properties for spectroscopic assays and are thus commonly used to study kinetics of β-lactamase inhibition[44].

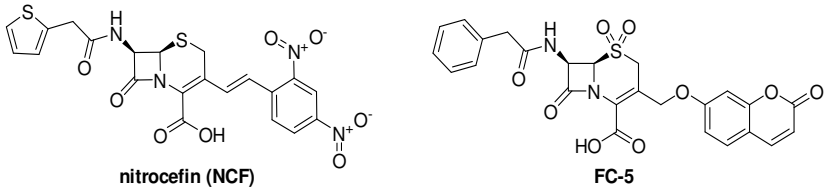


Figure 4: Reporter substrates nitrocefin (NCF) and FC-5.

Both NCF and the NCF derived hydrolysis products are strongly chromogenic, with λ_{max} = 390 nm and λ_{max} = 486 nm[45], respectively. FC-5 on the other hand releases 7-hydroxycoumarin on hydrolysis, which results in an increase in fluorescence (with λ_{ex} = 380 nm and λ_{em} = 460 nm)[44]. Hydrolysis of both β-lactams can therefore be monitored using a microplate-reader.

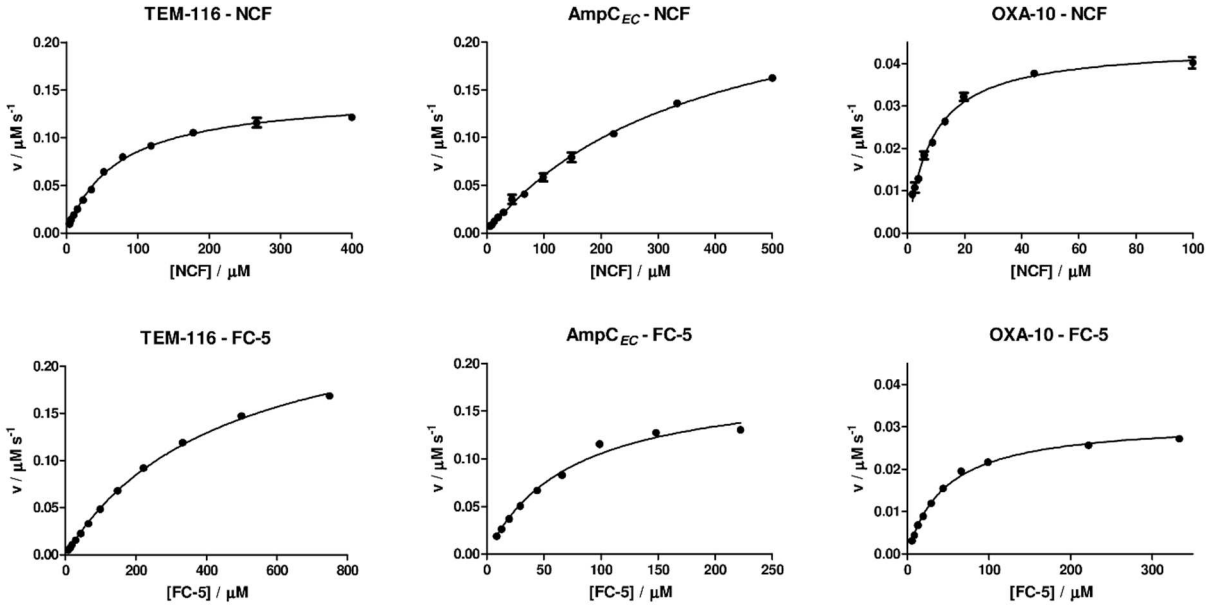


Figure 5: Kinetic characterisation of SBL catalysed hydrolysis of reporter substrates FC-5 and Nitrocefin (NCF). TEM-116 (1 nM), AmpC$_{EC}$ (500 pM), or OXA-10 (250 pM) were reacted with varying concentrations of NCF or FC-5. Buffer: 50 mM phosphate buffer, pH 7.5, 0.01% Triton X-100. For experiments with OXA-10 the buffer additionally contained 10 mM $NaHCO_3$. The figure and figure legend are adopted with permission from Lang *et al.* Proc. Natl. Acad. Sci. U.S.A., 2022, 119, e2117310119.

AmpC$_{EC}$ showed relatively fast turn-over rates for both substrates (k_{cat} 366 ± 11 s^{-1} and 563 ± 28 s^{-1}, for FC-5 and NCF, respectively), but significantly higher affinity towards FC-5, compared to NCF (K_m 74 ± 5 µM and 368 ± 31 µM, respectively), which results in more efficient turn-over of FC-5 (k_{cat}/K_m 5.0 ± 0.5 µM^{-1}s^{-1} and 1.5 ± 0.2 µM^{-1}s^{-1}, for FC-5 and NCF, respectively, Figure 5 and Table 1), making it the preferred reporter substrate to evaluate AmpC$_{EC}$ inhibition, which was used throughout Chapters 2-4.

Table 1: Steady-state kinetics for SBL catalysed hydrolysis of reporter substrates FC-5 and Nitrocefin (NCF). Values were obtained from non-linear regression shown in Figure 5.

	k_{cat} (s^{-1})	K_m (µM)	k_{cat}/K_m (µM^{-1} s^{-1})
TEM-116			
NCF	145.8 ± 2.9	70.7 ± 3.1	2.06 ± 0.12
FC-5	274.1 ± 3.6	448.8 ± 11.2	0.611 ± 0.023
AmpC$_{EC}$			
NCF	563.3 ± 27.6	367.5 ± 30.8	1.53 ± 0.20
FC-5	366.2 ± 10.9	73.6 ± 5.0	4.97 ± 0.49
OXA-10			
NCF	177.0 ± 3.6	8.5 ± 0.5	20.7 ± 1.7
FC-5	126.0 ± 2.4	46.4 ± 2.3	2.72 ± 0.18

For TEM-116 and OXA-10 NCF hydrolysis was more efficient than FC-5 hydrolysis (TEM-116 k_{cat}/K_m 2.1 ± 0.1 µM^{-1}s^{-1} 0.61 ± 0.02 and µM^{-1}s^{-1}, respectively; OXA-10 k_{cat}/K_m 21 ± 2 µM^{-1}s^{-1} and 2.7 ± 0.2 µM^{-1}s^{-1}, respectively) mainly due to significantly higher affinity (TEM-116 K_m: 71 ± 3 µM and 449 ± 11 µM, respectively; OXA-10 K_m: 8.5 ± 0.5 µM and 46 ± 2 µM, respectively). However, for consistency and due to the significantly better robustness of the

fluorescence based FC-5 assay, FC-5 was also used as the prefered reporter substrate for the kinetic studies with TEM-116 and OXA-10 described in this chapter, unless stated otherwise.

2.2.3. Crystallisation of AmpC$_{EC}$

As initial attempts to crystallise AmpC$_{EC}$ according to reported procedures[46] failed (see Chapter 5 for further information), a broad screen was used to identify new crystallisation conditions. A sparse matrix screen (spanning 480 different precipitant solution, screened each at 3 different protein-precipitant ratios), only afforded one hit (Pact Premier, Molecular Dimension, condition B12, 20% (w/v) PEG 6000, 100 mM MES pH 6.0, 10 mM $ZnCl_2$) yielding microcrystals (< 30 µm) after ~ 2 days of incubation at room temperature. A second, similar condition (Pact Premier, Molecular Dimensions, condition D12, 20 % (w/v) PEG 6000, 100 mM Tris pH 8.0, 2 mM $ZnCl_2$) gave microcrystals over ~ 2-3 weeks at room temperature.

The initial hit was optimised in a grid screen (22 – 27% (w/v) PEG 6000, 100 mM MES pH 6.0, 10 mM $ZnCl_2$) to give macrocrystals of AmpC$_{EC}$ (> 150 µm) reproducibly and reliably within ~2-7 days of incubation at room temperature. Due to the relatively high concentrations of PEG 6,000 in the precipitant solution, no further cryo-protectant was needed for storing crystals and collecting X-ray diffraction data at 100 K.

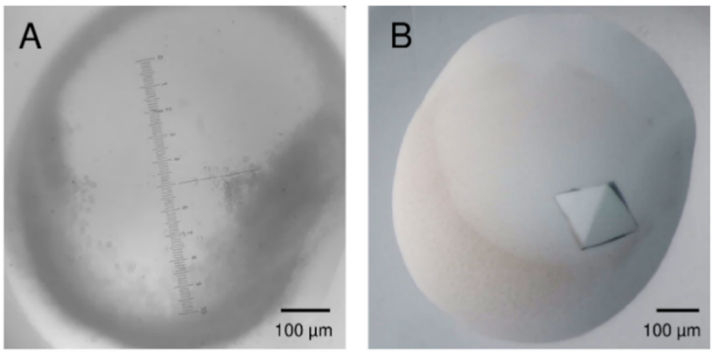


Figure 6: AmpC$_{EC}$ crystals from sitting-drop vapour diffusion experiments. (A) Initial hit from Pact Premier broad screen, condition B12 (20% (w/v) PEG 6000, 100 mM MES pH 6.0, 10 mM $ZnCl_2$) yielding microcrystals. (B) Optimised conditions from grid-screen yielding macro crystal. 200 nl of AmpC$_{EC}$ (20 mg ml^{-1}, in 50 mM Tris pH 7.0) were added to 200 nl of precipitant solution and incubated for ~2-7 days at room temperature.

The obtained crystals show high symmetry (space group $P4_32$) and usually diffracted to ~ 1.3 – 1.5 Å resolution. A structure with one molecule of unmodified AmpC$_{EC}$ per assymetric unit (ASU) was solved via molecular replacement (*by Dr Thomas Leissing, Univeristy of Oxford*), using a reported structure of AmpC$_{EC}$ (PDB: 1IEM[47]) as the starting model.

In the structure His13 of three symmetry related AmpC$_{EC}$ molecules coordinate to a Zn^{2+} ion, rationalising its essential role in the crystallisation process. Analysis of symmetry related molecules suggest that the AmpC$_{EC}$ active site is relatively accessible, and trials to obtain AmpC$_{EC}$-inhibitor and substrate complexes through soaking into crystals of unmodified AmpC$_{EC}$ were generally successful as described in Chapters 2-5. The soaking procedure was, however, limited by a relatively low tolerance of the crystals towards DMSO, as described in Chapter 4.

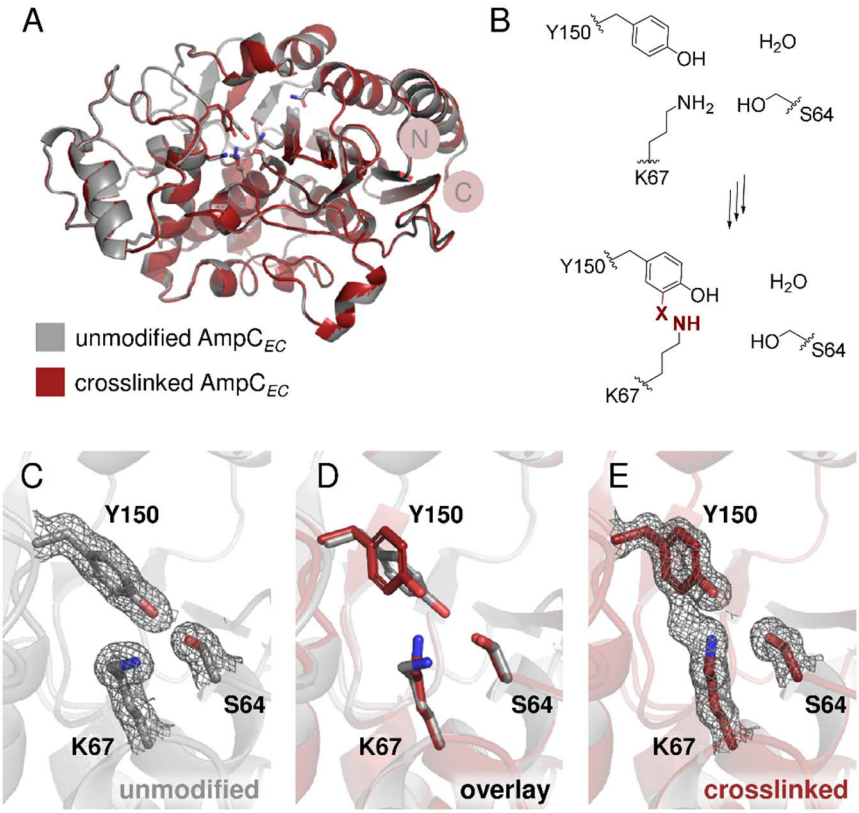


Figure 7: Views from AmpC$_{EC}$ crystal structures. (A) Overlay of general fold of unmodified AmpC$_{EC}$ as observed in fresh crystals and crosslinked AmpC$_{EC}$ as observed in crystals aged for 2 weeks of room temperature. (B) Crosslinking observed crystallographically at AmpC$_{EC}$ active site on crystal aging. (C-D) Active site views of unmodified and crosslinked AmpC$_{EC}$. $2mF_o$-DF_c maps are contoured at 1.0 σ and carved around active site residues. X: unknown heteroatom, may be CH_2 derived from formaldehyde (see text).

Notably, on aging of the crystals at room temperature for ~ 2 weeks, additional electron density was observed in the active site, indicating crosslinking of the Lys67 N^{ζ}-amine via an additional heteroatom to the Tyr150 located at the nucleophilic position *ortho* to the phenolic hydroxyl group. While this crosslink does not induce any changes in the overall fold of AmpC$_{EC}$ (main chain root mean square deviation (RMSD) of 0.193 Å, for crosslinked AmpC$_{EC}$ compared to unmodified AmpC$_{EC}$, Figure 7A), rotation of the Tyr150 phenol ring can be observed in the crosslinked AmpC$_{EC}$ active site compared to unmodified AmpC$_{EC}$, positioning it further away from the nucleophilic Ser64 (3.47 Å compared to 2.95 Å distance between the Ser64 and Tyr150 sidechain oxygen atoms, Figure 7C-D).

Table 2: Data collection and refinement statistics for the AmpC$_{EC}$ crystal.

Datasets	**AmpC$_{EC}$** (PDB: 6T3D)	**AmpC$_{EC}$ (crosslinked)**
Data Collection		
Beamline (Wavelength, Å)	DLS I03 (0.9763)	DLS I03 (0.9763)
Detector	Eiger2 XE 16M	Pilatus 6M-F
Data Processing	Xia2 3dii	Xia2
Space group	*P* 4$_3$ 3 2	*P* 4$_3$ 3 2
Cell dimensions		
- *a,b,c* (Å)	139.2, 139.2, 139.2	138.6,138.6, 138.6
- α, β, γ (°)	90, 90, 90	90, 90, 90
No. of molecules/ASU	1	1
No. reflections	73865 (5399)*	93055 (9144)*
Resolution (Å)	49.21-1.50 (1.54-1.50)*	48.99 - 1.38 (1.43 - 1.38)*
R_{meas}(I)	0.104 (6.300)*	0.155 (2.929)*
I/σI	29.3 (1.2)*	21.6 (2.1)*
$CC_{1/2}$	1.00 (0.51)*	1.000 (0.864)*
Completeness (%)	100 (100)*	99.9 (99.9)*
Multiplicity	76.6 (77.9)*	75.7 (75.1)*
Wilson B value (Å^2)	23.97	14.9
Refinement	PHENIX	PHENIX
R_{work}/R_{free}	0.1582/0.1777	0.1746/0.1810
No. atoms		
- Enzyme	2871	2744
- Water	343	443
Average B-factors		
- Enzyme	33.2	18.9
- Water	44.7	33.4
R.m.s deviations		
- Bond lengths (Å)	0.007	0.01
- Bond angles (°)	0.820	1.4

[#] ASU = asymmetric unit.
[$] RMS = root mean square.
*Highest resolution shell in parentheses.

Further studies are needed to verify the nature of the additional crosslinking atom, as well as the exact mechanism of crosslink formation. Previously, a similar Lys-Tyr crosslink has been observed crystallographically with the class C β-lactamase GC1 from *Enterobacter cloacae*, with the authors assuming a reaction with azide present in the crystal growth conditions[48]. However, as the precipitant solution used to crystallise AmpC$_{EC}$ does not contain azide, such reaction appears unlikely. A similar Lys-Tyr crosslink observed at the active site of a PBP[49] was suggested to result from Mannich reaction with formaldehyde. Formaldehyde is a known impurity / degradation product in Tris buffer and PEG[50,51], which were both used for AmpC$_{EC}$ crystallisation. Thus such a reaction may be plausible.

Both Tyr150 and Lys67 are of catalytic importance for hydrolysis of β-lactam derived $AmpC_{EC}$-acyl-enzyme complexes (see Chapter 1). Thus crystals of the crosslink modified $AmpC_{EC}$ can be used to obtain structures of otherwise short lived AEC species as will be shown in Chapter 5.

2.3. SBL inhibition by penam sulfones

2.3.1. Kinetic analyses of transient SBL inhibition by penam sulfones

2.3.1.1. Dose-dependence studies

Dose-dependent studies on $AmpC_{EC}$ inhibition by enmetazobactam, tazobactam, and sulbactam were carried out using FC-5[44] with variation of the enzyme-inhibitor pre-incubation time as well as the pH. Whilst $AmpC_{EC}$ appeared stable on incubation at room temperature (≥ 360 min), substantially increased or decreased pH, compared to the standard conditions (pH 7.5), resulted in high background, likely due to non-enzymatic degradation of the reporter substrate. Assays were therefore conducted only in a range of pH 7.0 – 8.0 (Table 3, Figure 8, and Appendix III, Figure S1-2).

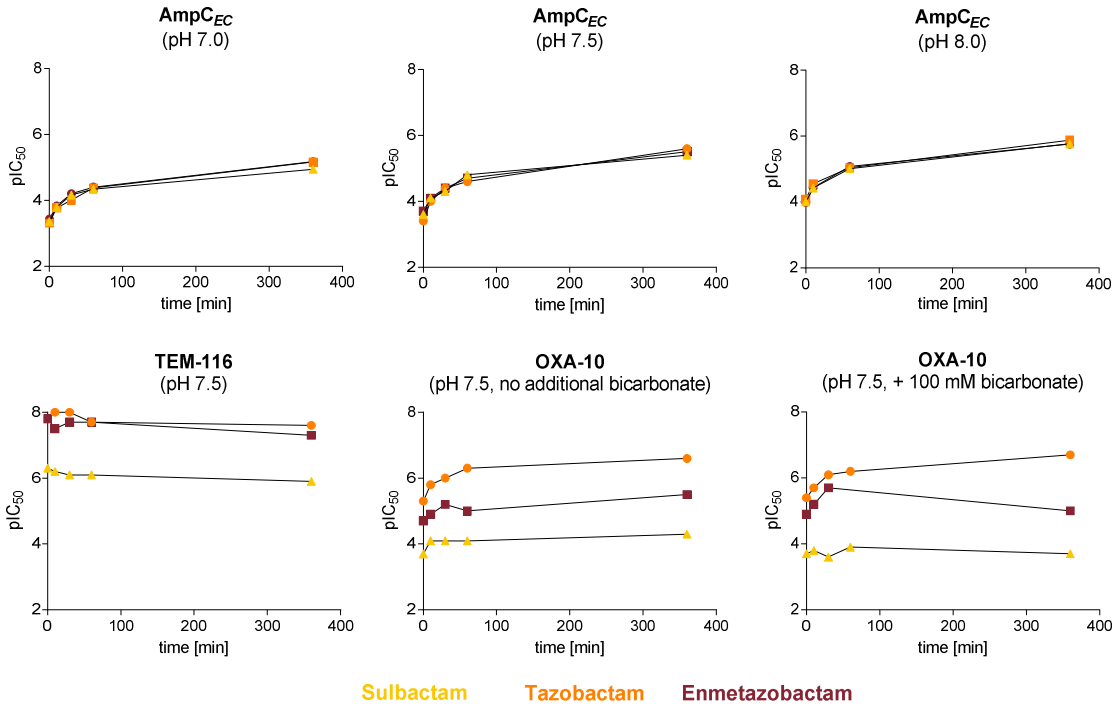


Figure 8: Time dependence of TEM-116, $AmpC_{EC}$, and OXA-10 inhibition by tazobactam, enmetazobactam, or sulbactam. Graphical presentation of time-dependencies of pIC_{50}s summarised in Table 3. The figure and figure legend are adopted with permission from Lang *et al.* Proc. Natl. Acad. Sci. U.S.A., 2022, 119, e2117310119.

All the penam sulfones showed comparably weak inhibition of AmpC$_{EC}$ (pIC$_{50}$ 3.4 – 3.6, at pH 7.5, without pre-incubation) with a 10 min preincubation time; this improved with prolonged pre-incubation (e.g. pIC$_{50}$ 3.4 compared to 5.6 for tazobactam, at pH 7.5, after 0 and 360 min pre-incubation, respectively). The inhibitors were more potent at higher pH (e.g. pIC$_{50}$ 4.6 compared to 3.8 for tazobactam, at pH 7.0 and 8.0, respectively, with 10 min preincubation), and prolonged pre-incubation improved penam sulfone potency across the tested pH span in a similar manner (Table 3 and Figure 8, top).

By comparison, studies with the class A SBL TEM-116 and the class D SBL OXA-10 showed substantially better inhibition (Table 3 and Figure 8, bottom). With OXA-10 tazobactam was most potent, followed by enmetazobactam and sulbactam (pIC$_{50}$s of 5.4, 4.9, and 3.7, respectively, without pre-incubation and addition of bicarbonate). While sulbactam potency appeared independent of the pre-incubation time, tazobactam and enmetazobactam showed analogous improvement with prolonged pre-incubation as observed with AmpC$_{EC}$. Assays in the presence of 100 mM bicarbonate (to ensure full carbamylation of the catalytic Lys70 residue[52]) showed no significant impact of bicarbonate concentration on OXA-10 inhibition.

Table 3: pIC$_{50}$ values for penam sulfone inhibition of TEM-116, AmpC$_{EC}$, and OXA-10. The enzymes (1 nM TEM-116, 500 pM AmpC$_{EC}$ or 250 pM OXA-10) in 50 mM phosphate buffer pH 7.5 (unless stated otherwise), 0.01% (v/v) Triton X-100 were pre-incubated with the inhibitors for the indicated times at room temperature, then assayed using 5 µM FC-5[44]. AmpC$_{EC}$ was screened at pH 7.0, 7.5, and 8.0. OXA-10 was also screened with 100 mM $NaHCO_3$ added. pIC$_{50}$s as determined using non-linear regression (Appendix III, Figure S1 and S2). Errors are standard errors of four technical replicates.

		pIC$_{50}$[a]					
			AmpC$_{EC}$		OXA-10[a]	OXA-10[b]	TEM-116
	time	pH 7.0	pH 7.5	pH 8.0	pH 7.5	pH 7.5	pH 7.5
tazobactam	0 min	3.31 ± 0.03	3.43 ± 0.04	4.09 ± 0.02	5.41 ± 0.07	5.30 ± 0.04	8.16 ± 0.05
	10 min	3.77 ± 0.03	4.04 ± 0.02	4.56 ± 0.02	5.72 ± 0.05	5.83 ± 0.06	7.98 ± 0.07
	30 min	4.01 ± 0.04	4.52 ± 0.02	N/D	6.07 ± 0.05	6.05 ± 0.06	7.97 ± 0.03
	60 min	4.38 ± 0.03	4.79 ± 0.02	5.04 ± 0.04	6.25 ± 0.07	6.34 ± 0.07	7.68 ± 0.07
	360 min	5.16 ± 0.03	5.59 ± 0.03	5.88 ± 0.01	6.69 ± 0.12	6.63 ± 0.08	7.60 ± 0.04
enmetazobactam	0 min	3.43 ± 0.03	3.66 ± 0.02	3.99 ± 0.01	4.86 ± 0.02	4.71 ± 0.04	7.77 ± 0.04
	10 min	3.83 ± 0.02	4.10 ± 0.02	4.44 ± 0.02	5.23 ± 0.08	4.90 ± 0.05	7.51 ± 0.12
	30 min	4.20 ± 0.03	4.55 ± 0.03	N/D	5.70 ± 0.08	5.24 ± 0.10	7.73 ± 0.05
	60 min	4.40 ± 0.02	4.81 ± 0.01	5.08 ± 0.05	4.75 ± 0.14	4.97 ± 0.14	7.65 ± 0.07
	360 min	5.17 ± 0.03	5.55 ± 0.02	5.76 ± 0.01	4.99 ± 0.19	5.49 ± 0.11	7.28 ± 0.09
sulbactam	0 min	3.35 ± 0.02	3.56 ± 0.03	4.01 ± 0.04	3.66 ± 0.01	3.69 ± 0.04	6.27 ± 0.03
	10 min	3.79 ± 0.02	4.08 ± 0.05	4.43 ± 0.02	3.85 ± 0.02	4.06 ± 0.03	6.23 ± 0.05
	30 min	4.16 ± 0.07	4.44 ± 0.03	N/D	3.58 ± 0.08	4.05 ± 0.10	6.08 ± 0.04
	60 min	4.34 ± 0.04	4.70 ± 0.02	5.01 ± 0.02	3.95 ± 0.05	4.12 ± 0.08	6.07 ± 0.04
	360 min	4.94 ± 0.04	5.38 ± 0.03	5.77 ± 0.03	3.69 ± 0.10	4.30 ± 0.08	5.89 ± 0.06

[a]With 100 mM added $NaHCO_3$.
[b]Without added $NaHCO_3$.

In agreement with previous reports[22,53], showing superior inhibition of class A SBLs, TEM-116 was the most potently inhibited out of the three enzymes tested (pIC_{50}s of 7.8, 8.2, and 6.3, for enmetazobactam, tazobactam, and sulbactam, respectively, without pre-incubation). In contrast to $AmpC_{EC}$ and OXA-10, the potency of TEM-116 inhibition did not increase with prolonged pre-incubation, but showed a slow decrease in potency with 10-360 min preincubation (e.g. pIC_{50} 8.2 and 7.6 for tazobactam after 0 min and 260 min pre-incubation, respectively) (Table 3 and Figure 8, bottom).

The similar potency observed with enmetazobactam compared to tazobactam is in agreement with a previous report[22]. The reported significantly enhanced potential of enmetazobactam *in cells*[37] and *in vivo*[54] may thus result primarily from improved properties with respect to variables other than potency against isolated SBLs, such as decreased β-lactamase induction or improved penetration / influx-efflux ratio, which may be a consequence of the permanent positive charge imposed by the *N*-methyl group on enmetazobactam compared to tazobactam.

2.3.1.2. Detailed kinetic analyses of transient inhibition

As described in the introduction to this chapter, the reaction of penam sulfones with SBLs bifurcates after formation of the initial acyl-enzyme complex, leading to either efficient hydrolysis of the AEC, transient inhibition, or, in rare cases, irreversible inhibition of the SBL. The different pathways proposed are summarised schematically in Figure 9.

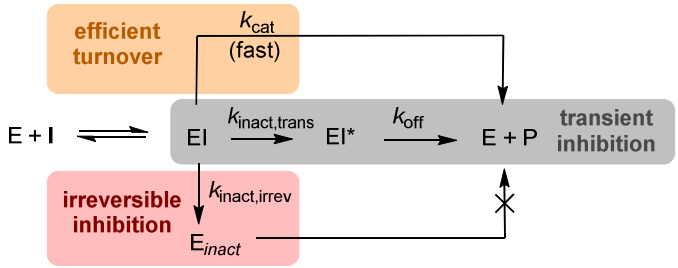


Figure 9: Bifurcating pathways of SBL inhibition by penam sulfones and penam sulfone hydrolysis by SBLs. E: enzyme; I: inhibitor; EI: initial acyl-enzyme complex; EI*: transiently stable acyl-enzyme species, E_{inact}: irreversibly inhibited enzyme, P: hydrolysis products.

Thus, more detailed kinetic studies were conducted to further understand the significant differences in potency of penam sulfone inhibition of SBLs from different classes, as well as to study potential differences in inhibition by tazobactam and enmetazobactam.

Binding (k_{inact}/K or k_2/K) and dissociation (k_{off}) rates, as well as apparent inhibition constants (K_{iapp}), can be determined from competition studies with reporter substrates such as nitrocefin and FC-5, as previously reported[55,56] and described in detail in the Materials and Methods.

While these techniques are most suited to study fully reversible inhibition (as described for AmpC$_{EC}$ inhibition by diazabicyclooctanes and cyclic boronates in Chapters 3 and 4), they can also be used to estimate kinetic constants for transient inhibition of suicide inhibitors with bifurcating pathways such as penam sulfones, under the condition that binding events leading to efficient hydrolysis of the inhibitors, as well as those leading to rare cases of irreversible inhibition, are either so fast or so rare that they are neglectable for inhibition within the observed timeframe.

Table 4: Kinetic parameters for SBL inhibition by penam sulfones. Values as determined from regressions in Figure 10.

	K_{iapp} (μM)	k_2/K (M^{-1} s^{-1})	k_{off} (M^{-1} s^{-1})	$t_{1/2}$ (min)	k_{cat}/k_{inact}
TEM-116					
Tazobactam	0.07 ± 0.01	(746 ± 32) x 10^3	(1.47 ± 0.04) x 10^{-3}	7.8 ± 0.2	9
Enmetazobactam	0.26 ± 0.04	(209 ± 5) x 10^3	(1.06 ± 0.03) x 10^{-3}	10.9 ± 0.3	4
Sulbactam	1.59 ± 0.28	(13.1 ± 0.1) x 10^3	(9.26 ± 0.56) x 10^{-3}	1.2 ± 0.1	240
AmpC$_{EC}$					
Tazobactam	1042 ± 242	7.6 ± 0.6	(6.62 ± 0.4) x 10^{-6}	1746 ± 10	9800
Enmetazobactam	7464 ± 985	4.1 ± 0.5	(14.4 ± 0.4) x 10^{-6}	803 ± 2	5100
Sulbactam	1577 ± 189	4.9 ± 0.3	(18.8 ± 0.4) x 10^{-6}	616 ± 1	3100
OXA-10					
Tazobactam	469 ± 80	138 ± 7	(1.21 ± 0.02) x 10^{-3}	9.6 ± 0.2	160
Enmetazobactam	4311 ± 365	42 ± 2	(1.36 ± 0.02) x 10^{-3}	8.5 ± 0.1	1700
Sulbactam	4916 ± 873	3.8 ± 0.1	(7.46 ± 0.75) x 10^{-3}	1.6 ± 0.2	53000

With OXA-10, significantly slower inactivation rates by penam sulfones (138 ± 7 M s^{-1}, 42 ± 2 M s^{-1}, and 3.8 ± 0.1 M s^{-1}, for tazobactam, enmetazobactam, and sulbactam, respectively) were observed compared to TEM-116 (746 ± 32 x10^3 M s^{-1}, 209 ± 5 x 10^3 M s^{-1}, and 13.1 ± 0.1 x 10^3 M s^{-1}, respectively), while dissociation rates showed no significant differences, with half-lives of the inhibited species ranging between 2-11 min (Figure 10 and Table 4). The partition ratios between acyl-enzyme hydrolysis and transient inhibition, which were estimated based on the inhibitor-enzyme ratio required to reduce SBL activity by 90% after 1 h of pre-incubation with the inhibitor (as previously described[22]), were higher for OXA-10 (160, 1700, and 5300, for tazobactam, enmetazobactam, and sulbactam, respectively) compared to TEM-116 (9, 4, 240, respectively) (Figure 10 and Table 4).

With AmpC$_{EC}$ very slow binding was observed (k_{inact}/K of 7.6 ± 0.6 M s^{-1}, 4.1 ± 0.5 M s^{-1}, and 4.9 ± 0.3 M s^{-1}, for tazobactam, enmetazobactam, and sulbactam, respectively), an observation which, together with very high partition ratios (988, 5100, 3100, respectively), rationalises the significantly reduced potency of the penam sulfones against AmpC$_{EC}$, compared to OXA-10 and TEM-116, despite the vastly reduced dissociation rates (with $t_{1/2}$

1746 ± 10 min, 803 ± 2 min, and 616 ± 1 min, respectively) compared to OXA-10 and TEM-116 (Figure 10 and Table 4).

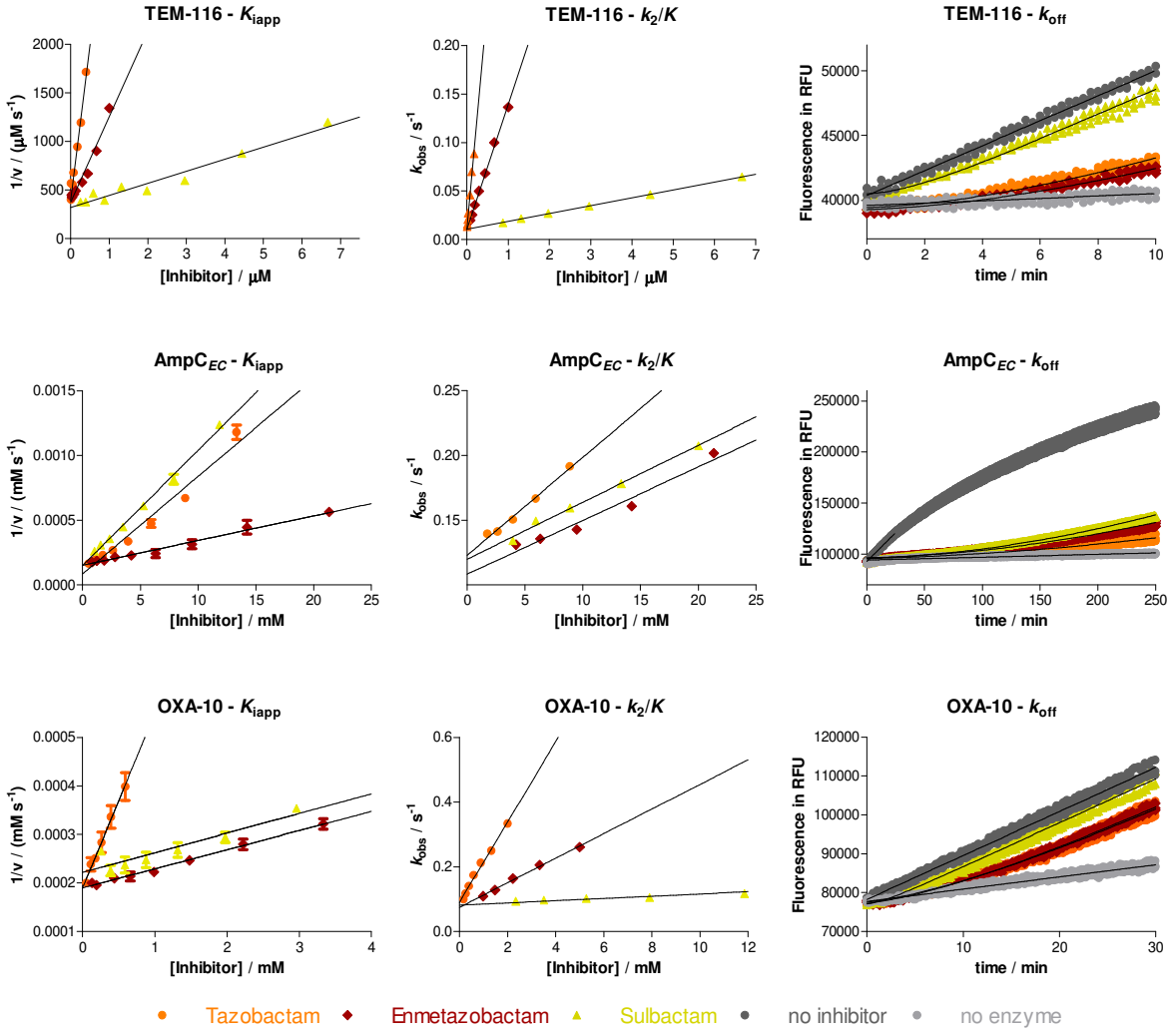


Figure 10: Kinetic characterisation of SBL inhibition by penam sulfones. Left column: Determination of K_{iapp} values for TEM-116 (1 nM) assayed with NCF (50 µM), AmpC$_{EC}$ (100 nM) assayed with FC-5 (5 µM), and OXA-10 (50 nM) assayed with FC-5 (5 µM). Middle column: Determination of Pseudo first-order rate (k_2/K) determination assayed with the same conditions used for K_{iapp} determination. Right column: Dissociation after 'jump-dilution' of TEM-116, AmpC$_{EC}$, or OXA-10 (3 µM) pre-incubated with penam sulfones, then diluted 100.000-300.000 fold and assayed with FC-5[44] (25 µM). Buffer: 50 mM phosphate buffer, pH 7.5, 0.01 % (v/v) Triton-X 100. For experiments with OXA-10 the buffer additionally contained 10 mM $NaHCO_3$. The figure and figure legend are adopted with permission from Lang *et al.* Proc. Natl. Acad. Sci. U.S.A., 2022, *119*, e2117310119.

2.3.2. Mechanistic studies with penam sulfones

The reaction of penam sulfones with the nucleophilic Ser residue of SBLs to give covalent complexes which are transiently hydrolytically stable is central to their inhibition of SBLs (Figure 11). Due to their importance for inhibition and thus for the rational design of new SBLi, the nature of these species and their mechanisms of formation have been of substantial interest.

However, while most spectroscopic studies[8-15] in combination with some crystallographic studies[8,9,14-17] indicate a *trans*-enamine species **5** (Figure 11) as the predominant species for SBL inhibition, MS based studies[15,18-24] as well as other crystallographic studies[24-27] indicate substantial scaffold fragmentation of the AEC to give transientally hydrolytically stable species **6**, **7**, and **8** (Figure 11).

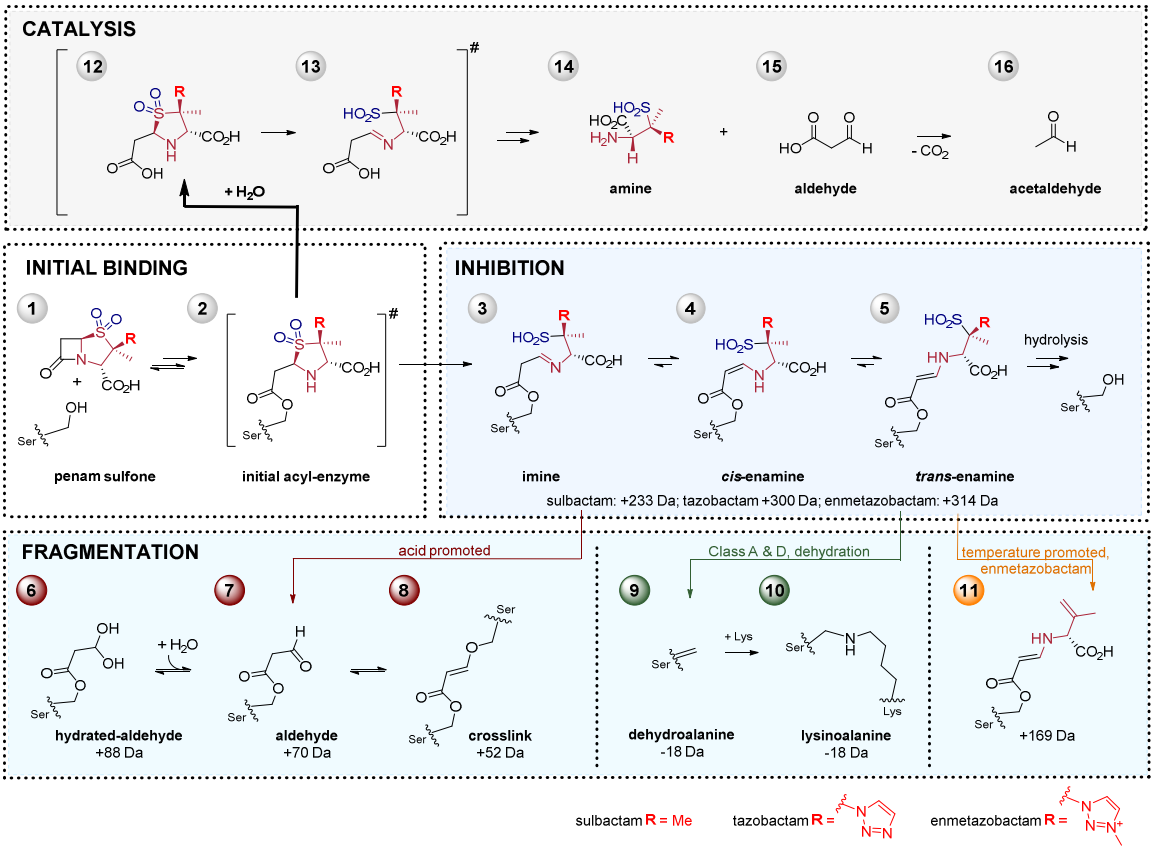


Figure 11: Pathways for reaction of penam sulfones with SBLs. Following initial acyl-enzyme **2** formation the main transient inactivation pathway occurs via thiazolidine ring opening to give species **3**-**5** which are relatively stable to hydrolysis. Fragmentation of **3**-**5** can occur in rare cases and is promoted by acid to give **6**-**8** or heat to give **11**. In rare cases fragmentation of **2**-**5** can result in irreversible inactivation of the SBL to give **9**-**10**. Efficient hydrolysis of the β-lactam occurs to give a β-amino acid product **12** which fragments in solution to give **13**-**16**. Our results imply biologically relevant inhibition involves **3**-**5** or equivalent mass species. The figure and figure legend are reproduced with permission from Lang *et al.* Proc. Natl. Acad. Sci. U.S.A., 2022, 119, e2117310119.

2.3.2.1. Solid-phase-extraction mass spectrometry (SPE-MS) show lack of penam sulfone derived acyl-enzyme fragmentation

SPE-MS studies were carried out with support from Dr Anthony Tumber (Univeristy of Oxford).

To investigate the identity of the transitory stable species, protein-observed denaturing ESI-MS experiments were carried out. Instead of a conventional liquid-chromatography MS (LC-MS) protocol, a solid-phase extraction MS (SPE-MS) protocol was set up to increase throughput (Figure 12-15). This set-up employs short plugs of resin (e.g. C4) instead of long chromatography columns. While this set-up reduces the separation efficiency, it drastically reduces the analysis time (~ 45 s, instead of 10-20 min per sample). However, as buffer components (e.g. Tris and salts) generally show a lot higher polarity than proteins, this simplified purification is sufficient to acquire good quality protein MS spectra. The shorter analysis time typically enables one to record spectra of up to 25 individual reactions in 20 min intervals, compared to a single reaction being monitored via continuous LC-MS analysis over the same duration. Therefore, it was possible to investigate reactions of AmpC$_{EC}$, TEM-116, and OXA-10 with enmetazobactam, tazobactam, and sulbactam, at two different concentrations (10 or 100 equivalents of enmetazobactam and tazobactam, and 100 or 500 equivalents of sulbactam) in parallel over a period of 24 h.

The reaction of TEM-116, AmpC$_{EC}$, and OXA-10 with 10 equivalents of enmetazobactam at room temperature resulted in apparent covalent modification (Figure 12, top). Full modification of TEM-116 was observed within 20 min. With OXA-10 low levels of modification were observed after 20 min, which continuously decreased on longer incubation, with full recovery of the unmodified OXA-10 after ~ 3 h. The reaction with AmpC$_{EC}$ was slower, reaching a maximum of ~95% modification ~ 3 h after reaction initiation, followed by almost complete recovery of unmodified AmpC$_{EC}$ over a period of 24 h. Surprisingly, and by contrast with a previous report[22], no significant amounts of +52 Da, +70 Da, or +88 Da species (likely correlating to **6**, **7**, and **8**) were observed. Instead, increments of +314 Da (compromising the full mass of enmetazobactam, correlating e.g. to *trans*-enamine **5**), and +169 Da (potentially correlating to elimination product **11,** see paragraph 2.3.2.3 for further discussion) were observed. While the ratio of the two different modifications varied slightly between different SBLs, it remained constant for each SBL over the analysed time.

Time courses recorded following incubation with a larger excess of enmetazobactam (100 equiv., Figure 12, bottom) showed full modification of all SBLs within 20 min. As in the previous experiments, only +169 (potentially correlating to **11**) and +314 Da (likely correlating to species **3**-**5**, or equivalent mass species) mass shifts were observed. However, relatively small amounts of a +52 Da mass shift were observed to accumulate over 12 h in the case of TEM-116. While modification of AmpC$_{EC}$ was stable over 24 h, +169 and +314 Da (and +52 Da)

adducts of TEM-116 and OXA-10 were only observed for 12-18 h. Interestingly, on hydrolysis both TEM-116 and OXA-10 partially showed a mass decrease of 18 Da (~50% of TEM-116 and ~60% of OXA-10); in a previous report this has been hypothesised to reflect dehydration of the nucleophilic Ser to give a dehydroalanine residue (Dha, **9**)[22].

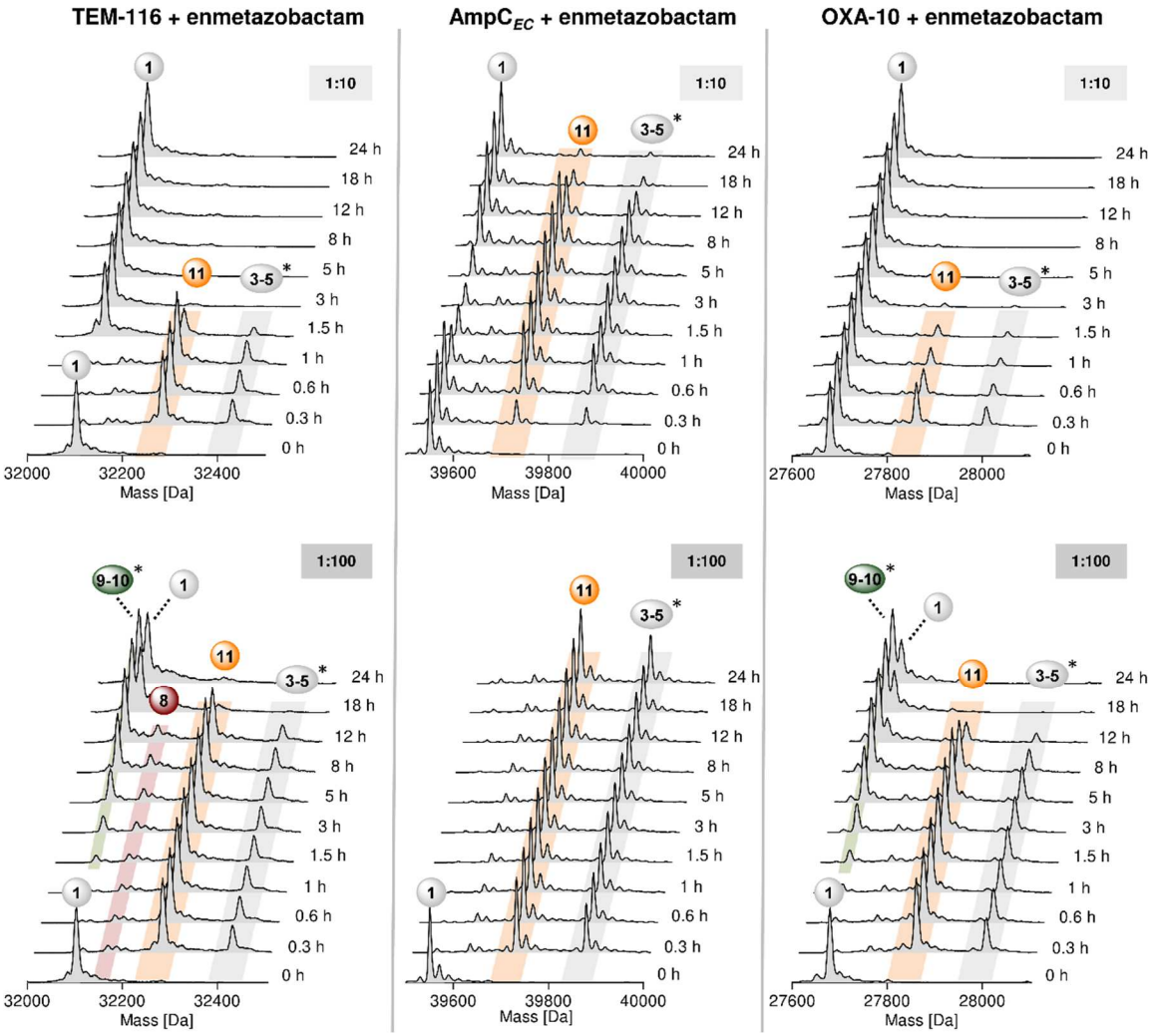


Figure 12: SPE-MS time courses of TEM-116, AmpC$_{EC}$, and OXA-10 modification by enmetazobactam. TEM-116, AmpC$_{EC}$, and OXA-10 (3 µM) were incubated with a 10 (top) or 100 (bottom) molar excess of enmetazobactam at r.t. Buffer: 50 mM Tris buffer pH 7.5. Spectra were acquired without the inhibitor (0 h) and after incubation for the indicated times. Deconvoluted spectra, obtained using the maximum entropy algorithm in the MassHunter Workstation Qualitative Analysis B.07.00 program (Agilent), are shown. Proposed structures corresponding to the labelled mass shifts are given in Figure 11. See Table 5 for summary of the calculated and observed masses and mass shifts. *Note mass shifts may reflect more than one species, e.g. **2**-**5** as well as **9**-**10** give the same mass shift. The figure and figure legend are adopted with permission from Lang *et al.* Proc. Natl. Acad. Sci. U.S.A., 2022, *119*, e2117310119.

The reaction of the SBLs with 10 or 100 equivalents of tazobactam (Figure 13) showed similar results to the observations with enmetazobactam, with some notable differences: no +169 Da adduct was observed, the lifetime of the observed modifications was slightly shorter than with enmetazobactam, and only small amounts of -18 Da modified TEM-116 were observed on

reaction with 100 equivalents of tazobactam, while almost full conversion to the -18 Da modified OXA-10 was observed.

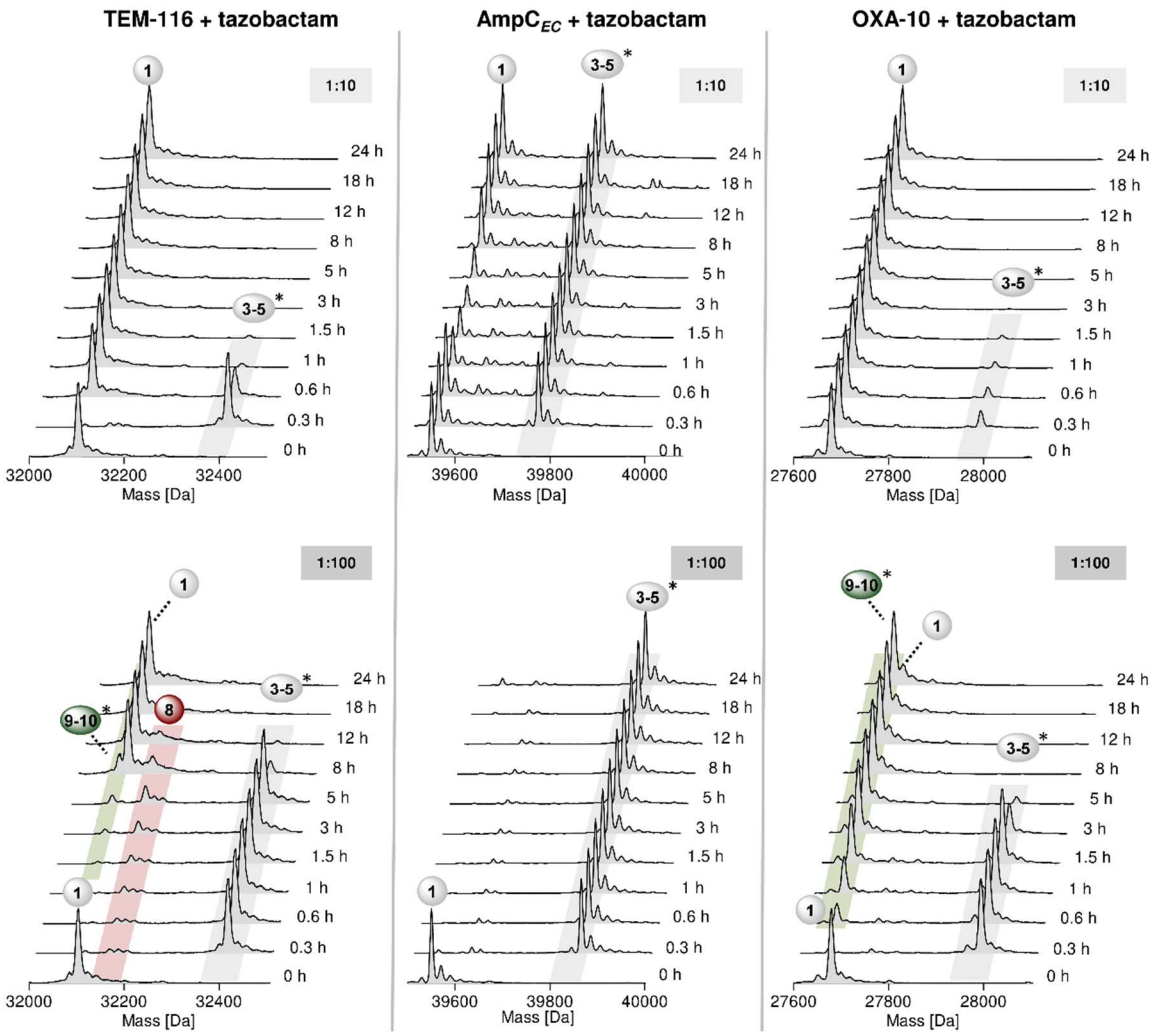


Figure 13: SPE-MS time courses of TEM-116, AmpC$_{EC}$, and OXA-10 modification by tazobactam. TEM-116, AmpC$_{EC}$, and OXA-10 (3 µM) were incubated with a 10- or 100-fold excess of tazobactam at r.t. Buffer: 50 mM Tris buffer pH 7.5. Mass spectra were acquired without the inhibitor (0 h) and after incubation for the indicated times. Deconvoluted spectra, obtained using the maximum entropy algorithm in the MassHunter Workstation Qualitative Analysis B.07.00 program (Agilent), are shown. Proposed structures corresponding to the labelled mass shifts are given Figure 11. See Table 5 for summary of the calculated and observed masses and mass shifts. *Note mass shifts may reflect more than one species, e.g. **2-5** as well as **9**-**10** give the same mass shift. The figure and figure legend are adopted with permission from Lang *et al.* Proc. Natl. Acad. Sci. U.S.A., 2022, 119, e2117310119.

In agreement with the lower potency against TEM-116 and OXA-10 observed for sulbactam compared to tazobactam and enmetazobactam (Table 3), less modification of these SBLs was observed on incubation with 100 or 500 equivalents of sulbactam (Figure 14). As observed with tazobactam, only adducts comprising the full mass of sulbactam (233 Da) were observed. On OXA-10 incubation with 500 equivalents of sulbactam low amounts of the -18 Da modified OXA-10 were generated within 5 h.

After recovery of the unmodified TEM-116 and presumed full turnover of 500 equivalents of sulbactam, additional adducts were observed 5-24 h after initiation of the reaction, potentially indicating slow reaction of TEM-116 with sulbactam degradation products present in solution (Figure 14, bottom).

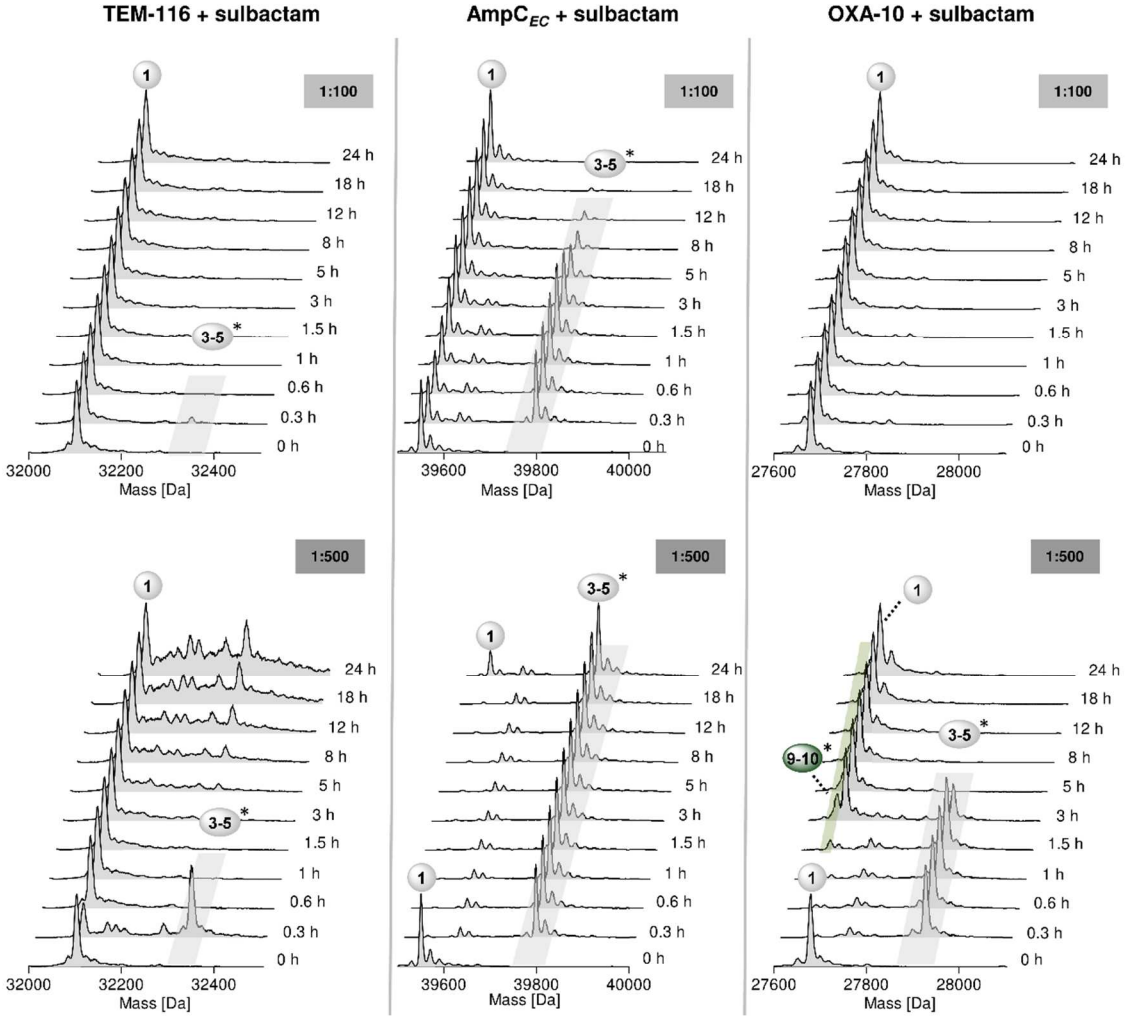


Figure 14: SPE-MS time courses of TEM-116, AmpC$_{EC}$, and OXA-10 modification by sulbactam. TEM-116, AmpC$_{EC}$, and OXA-10 (3 µM) were incubated with a 100- (top) or 500-fold (bottom) excess of sulbactam at r.t. Buffer: 50 mM Tris buffer pH 7.5. Mass spectra were acquired without the inhibitor (0 h) and after incubation for the indicated times. Deconvoluted spectra, obtained using the maximum entropy algorithm in the MassHunter Workstation Qualitative Analysis B.07.00 program (Agilent), are shown. Proposed structures corresponding to the labelled mass shifts are given in Figure 11. See Table 5 for a summary of the calculated and observed masses and mass shifts. *Note mass shifts may reflect more than one species, e.g. **2-5** as well as **9**-**10** give the same mass shift. The figure and figure legend are adopted with permission from Lang *et al.* Proc. Natl. Acad. Sci. U.S.A., 2022, *119*, e2117310119.

Overall, the differences between the results obtained via SPE-MS and reported LC-MS based studies[15,18-24] were striking. None of the efficient fragmentation to give the +52, +70, or +88 Da adducts (correlating to **6**, **7**, and **8**) was observed on a short time scale, both with enmetazobactam and the more extensively studied tazobactam and sulbactam.

Furthermore, the apparent fragmentation of the enmetazobactam derived acyl-enzyme complex to give a +169 Da mass species (tentatively assigned as alkene **11**), seemed intriguing, especially as such reaction was not observed with tazobactam.

Table 5: Modifications to AmpC$_{EC}$, TEM-116 and OXA-10 by reaction with enmetzobactam, tazobactam, or sulbactam as analysed by SPE-MS. All differences between measured and calculated masses / mass shifts are within experimental error. [a]Masses were derived from deconvolution of measured spectra using the maximum entropy algorithm in the MassHunter Workstation Qualitative Analysis B.07.00 programme (Agilent Technologies. [b]Relative to the measured unmodified protein mass. [c]Proposed product structures are defined in Figure 11.

		Mass observed[a] [Da]	Mass calculated [Da]	Mass shift observed[b] [Da]	Mass shift calculated [Da]	Assignment[c]	Comments
SPE-MS (4 s exposure to 0.1 % formic acid)	**AmpC$_{EC}$**	39551	39551			unmodified **1**	
	+ enmetazobactam	39718	39720	+167	+169	elimination product **11**	
		39865	39865	+314	+314	enamine **5**	or equal mass species
	+ tazobactam	39851	39851	+300	+300	enamine **5**	or equal mass species
	+ sulbactam	39784	39784	+233	+233	enamine **5**	or equal mass species
	OXA-10	27681	27682			unmodified **1**	
	+ enmetazobactam	27847	27851	+166	+169	elimination product **11**	
		27995	27996	+314	+314	enamine **5**	or equal mass species
		27662	27662	-19	-18	dehydroalanine **9**	or equal mass species
	+ tazobactam	27981	27982	+300	+300	enamine **5**	
		27662	27963	-19	-18	dehydroalanine **9**	or equal mass species
	+ sulbactam	27913	27915	+232	+233	enamine **5**	
		27662	27964	-19	-18	dehydroalanine **9**	or equal mass species
	TEM-116	32103	32103			unmodified **1**	
	+enmetazobactam	32270	32272	+167	+169	elimination product **11**	
		32417	32417	+314	+314	enamine **5**	or equal mass species
		32154	32155	+51	+52	crosslink **8**	or equal mass species
		32085	32085	-18	-18	dehydroalanine **9**	or equal mass species
	+ tazobactam	32404	32403	+301	+300	enamine **5**	or equal mass species
		32154	32155	+51	+52	crosslink **8**	or equal mass species
		32081	32085	-22	-18	dehydroalanine **9**	or equal mass species
	+ sulbactam	32336	32336	+233	+233	enamine **5**	or equal mass species

2.3.2.2. Acyl-enzyme fragmentation is induced during LC-MS analyses

LC-MS studies were carried out with support from Dr Patrick Rabe (Univeristy of Oxford).

To investigate the discrepancies between the SPE-MS studies and previous reports using LC-MS[15,18-24], equivalent samples were analysed using an LC-MS set-up comparable to those used in the previous reports. Samples were separated on a C4 column and eluted in a gradient of 5-95% (v/v) acetonitrile in water, supplemented with 0.1% (v/v) formic acid. All the β-lactamase complexes eluted within 4-5 min.

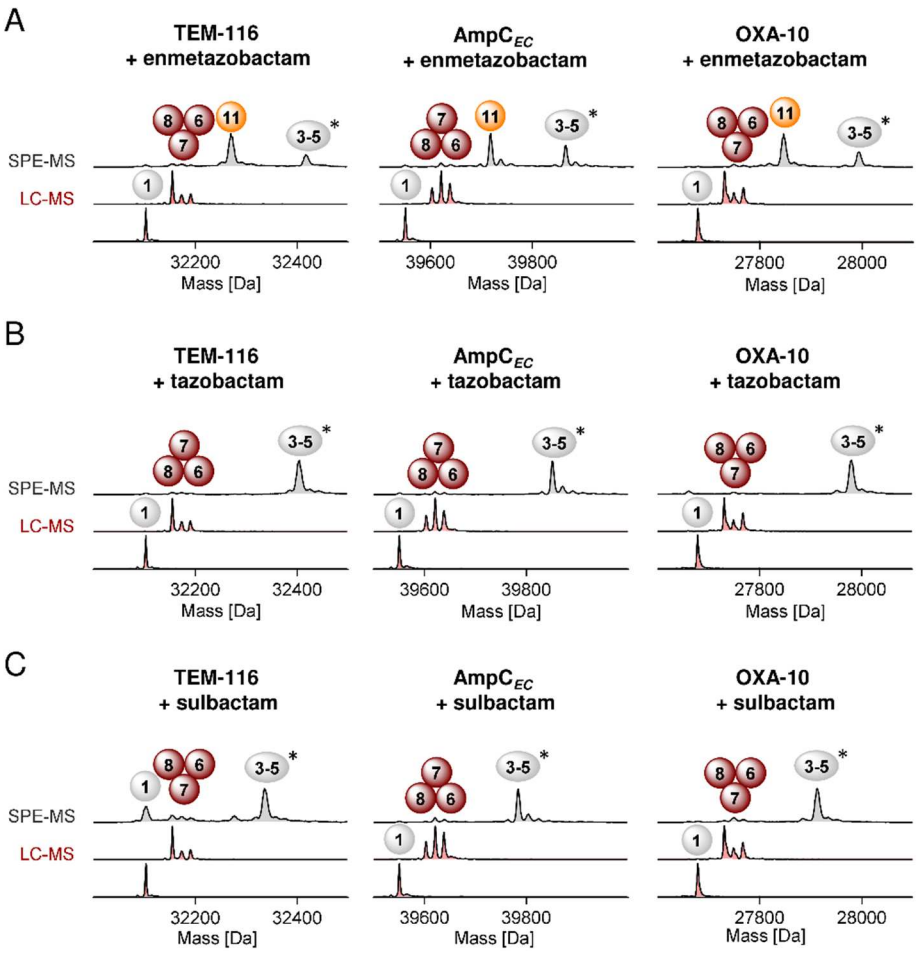


Figure 15: Protein-observed liquid chromatography (LC) and solid phase extraction (SPE) MS analysis of reactions of SBLs with enmetazobactam, tazobactam, or sulbactam, with 20 min pre-incubation time. (A) SBL reaction with enmetazobactam. (B) SBL reaction with tazobactam. (C) SBL reaction with sulbactam. For LC-MS, TEM-116, AmpC$_{EC}$ and OXA-10 (1 µM) were incubated with tazobactam (100 µM), enmetazobactam (100 µM), sulbactam (500 µM, 50 mM Tris, pH 7.5, 20 min, room temperature). For SPE-MS, TEM-116, AmpC$_{EC}$ and OXA-10 (3 µM) were incubated with tazobactam (300 µM), enmetazobactam (300 µM), or sulbactam (1.5 mM, 50 mM Tris, pH 7.5, 20 min, room temperature). See Table 6 for summary of the calculated and observed masses and mass shifts. *Note mass shifts may reflect more than one species, e.g. **2**-**5** and **9**-**10** give the same mass shift. The figure and figure legend are modified with permission from Lang *et al.* Proc. Natl. Acad. Sci. U.S.A., 2022, 119, e2117310119.

By contrast with the SPE-MS results and in agreement with previous LC-MS studies[15,18-24], TEM-116, $AmpC_{EC}$, and OXA-10 showed only +52, +70, and +88 Da adducts (correlating to **6**, **7**, and **8**) on incubation with enmetazobactam (100 equiv.), tazobactam (100 equiv.), or sulbactam (500 equiv.) for 20 min. The spectra appeared to show no evidence for adducts comprising the full mass of the inhibitor (as would be expected e.g. for *trans*-enamine **5**).

Table 6: Modifications to $AmpC_{EC}$, TEM-116 and OXA-10 by reaction with enmetzobactam, tazobactam, or sulbactam as analysed by LC-MS. All differences between measured and calculated masses / mass shifts are within experimental error. [a]Masses were derived from deconvolution of measured spectra using the maximum entropy algorithm in MassLynx V.4.1 (Waters). [b]Relative to the measured unmodified protein mass. [c]Proposed product structures are defined in Figure 11.

		Mass observed[a] [Da]	Mass calculated [Da]	Mass shift observed[b] [Da]	Mass shift calculated [Da]	Assignment[c]	Comments
LC-MS (4 min exposure to 0.1 % formic acid)	**$AmpC_{EC}$**	39552	39551			unmodified **1**	
	+enmetazobactam	39603	39603	+51	+52	crosslink **8**	or equal mass species
		39621	39621	+69	+70	aldehyde **7**	
		39640	39639	+88	+88	hydrated aldehyde **6**	
	+ tazobactam	39603	39603	+51	+52	crosslink **8**	or equal mass species
		39621	39621	+69	+70	aldehyde **7**	
		39640	39639	+88	+88	hydrated aldehyde **6**	
	+ sulbactam	39602	39603	+50	+52	crosslink **8**	or equal mass species
		39621	39621	+69	+70	aldehyde **7**	
		39640	39639	+88	+88	hydrated aldehyde **6**	
	OXA-10	27681	27682			unmodified **1**	
	+enmetazobactam	27732	27734	+51	+52	crosslink **8**	or equal mass species
		27750	27752	+69	+70	aldehyde **7**	
		27769	27770	+88	+88	hydrated aldehyde **6**	
	+ tazobactam	27732	27734	+51	+52	crosslink **8**	or equal mass species
		27750	27752	+69	+70	aldehyde **7**	
		27768	27770	+87	+88	hydrated aldehyde **6**	
	+ sulbactam	27732	27734	+51	+52	crosslink **8**	or equal mass species
		27750	27752	+69	+70	aldehyde **7**	
		27768	27770	+87	+88	hydrated aldehyde **6**	
	TEM-116	32104	32103			unmodified **1**	
	+enmetazobactam	32156	32155	+52	+52	crosslink **8**	or equal mass species
		32175	32173	+71	+70	aldehyde **7**	
		32193	32191	+89	+88	hydrated aldehyde **6**	
	+ tazobactam	32156	32155	+52	+52	crosslink **8**	or equal mass species
		32175	32173	+71	+70	aldehyde **7**	
		32193	32191	+89	+88	hydrated aldehyde **6**	
	+ sulbactam	32156	32155	+52	+52	crosslink **8**	or equal mass species
		32175	32173	+71	+70	aldehyde **7**	
		32193	32191	+89	+88	hydrated aldehyde **6**	

Both the LC- and the SPE-MS methods utilised the same mobile (as well as stationary) phase to separate proteins from the buffer components: aqueous acetonitrile solutions, supplemented with 0.1% (v/v) of formic acid (or an equivalent strong organic acid) to protonate the protein. One significant difference between the two methods lies in the contact time of the samples with this mobile phase, in particular before the protein is eluted into the spectrometer. In typical LC-MS protocols, like the ones employed here and in previous reports on SBLi inhibition by penam sulfones, proteins are in contact with the mobile phase for 1-10 min. With the SPE-MS workflow this contact time is drastically reduced to ~ 3-5 s. Therefore, the major difference between the analyses methods appeared to be in the exposure time to strongly acidic conditions.

To investigate the influence of formic acid on fragmentation of the enmetazobactam derived SBL-complexes, formic acid was added (to a final concentration of 0.1% (v/v)) to samples of TEM-116, AmpC$_{EC}$, and OXA-10 reacted with penam sulfones for 10 min and reactions were monitored using SPE-MS (Figure 16).

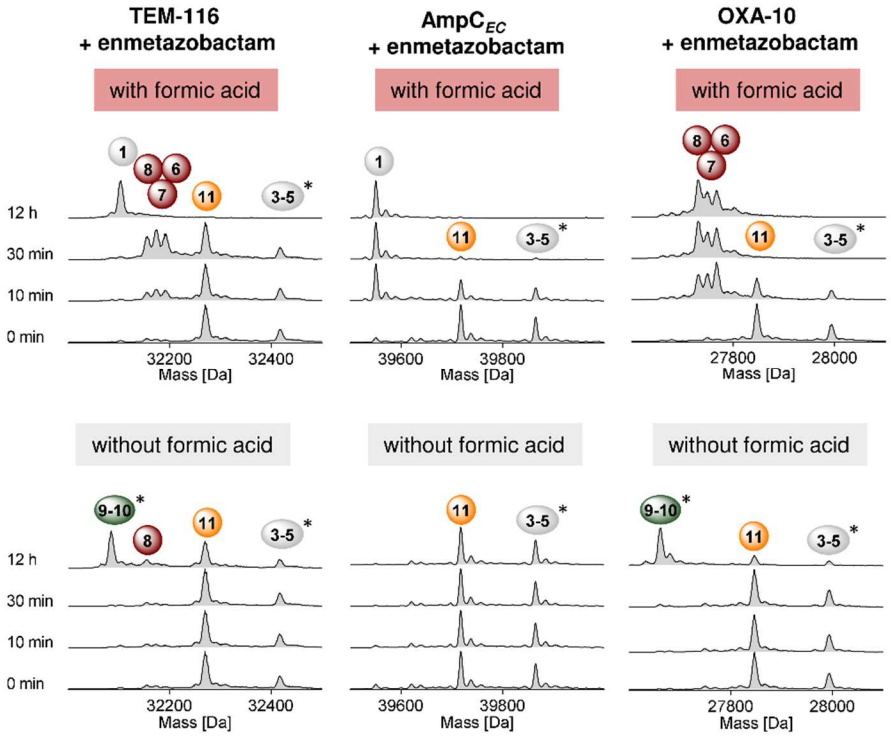


Figure 16: Effect of the addition of formic acid prior to SPE-MS analysis on modifications to TEM-116, AmpC$_{EC}$ and OXA-10 caused by reaction with enmetazobactam or tazobactam. TEM-116, AmpC$_{EC}$, and OXA-10 (3 µM) were reacted with a 100-fold excess of enmetazobactam in 50 mM Tris pH 7.5. Further reaction was induced by addition of formic acid to a final concentration of 0.1% (v/v). Samples were analysed using the SPE-MS method. Deconvoluted spectra, obtained using the maximum entropy algorithm in the MassHunter Workstation Qualitative Analysis B.07.00 programme (Agilent), are shown. The proposed structures of the labelled species are given in Figure 11. See Table 6 for summary of the calculated and observed masses and mass shifts. *Note mass shifts may reflect more than one species, e.g. **2**-**5** and **9**-**10** give the same mass shift.

TEM-116- and OXA-10-complexes showed efficient fragmentation to the +52, +70, and +88 Da species within 30 min of the formic acid addition, while such reaction was again not observed without formic acid addition over the same timeframe. For the AmpC$_{EC}$-complexes no fragmentation of the acyl-enzyme complexes was observed, but unmodified AmpC$_{EC}$ was recovered faster on formic acid treatment. The slower / less extensive fragmentation induced by adding formic acid to the sample prior to SPE-MS analysis compared to that observed during LC-MS analysis likely results from partial buffering under the assay conditions (50 mM Tris, pH 7.5) compared to the aqueous acetonitrile used as a mobile phase for LC-MS analysis.

Subsequent analogous experiments showed comparable results for tazobactam- and sulbactam derived SBL complexes on addition of 0.1% (v/v) formic acid, i.e. efficient

fragmentation to give +52, +70, and +88 Da species with TEM-116 and OXA-10 and accelerated regeneration of unmodified AmpC$_{EC}$ (Figure 17).

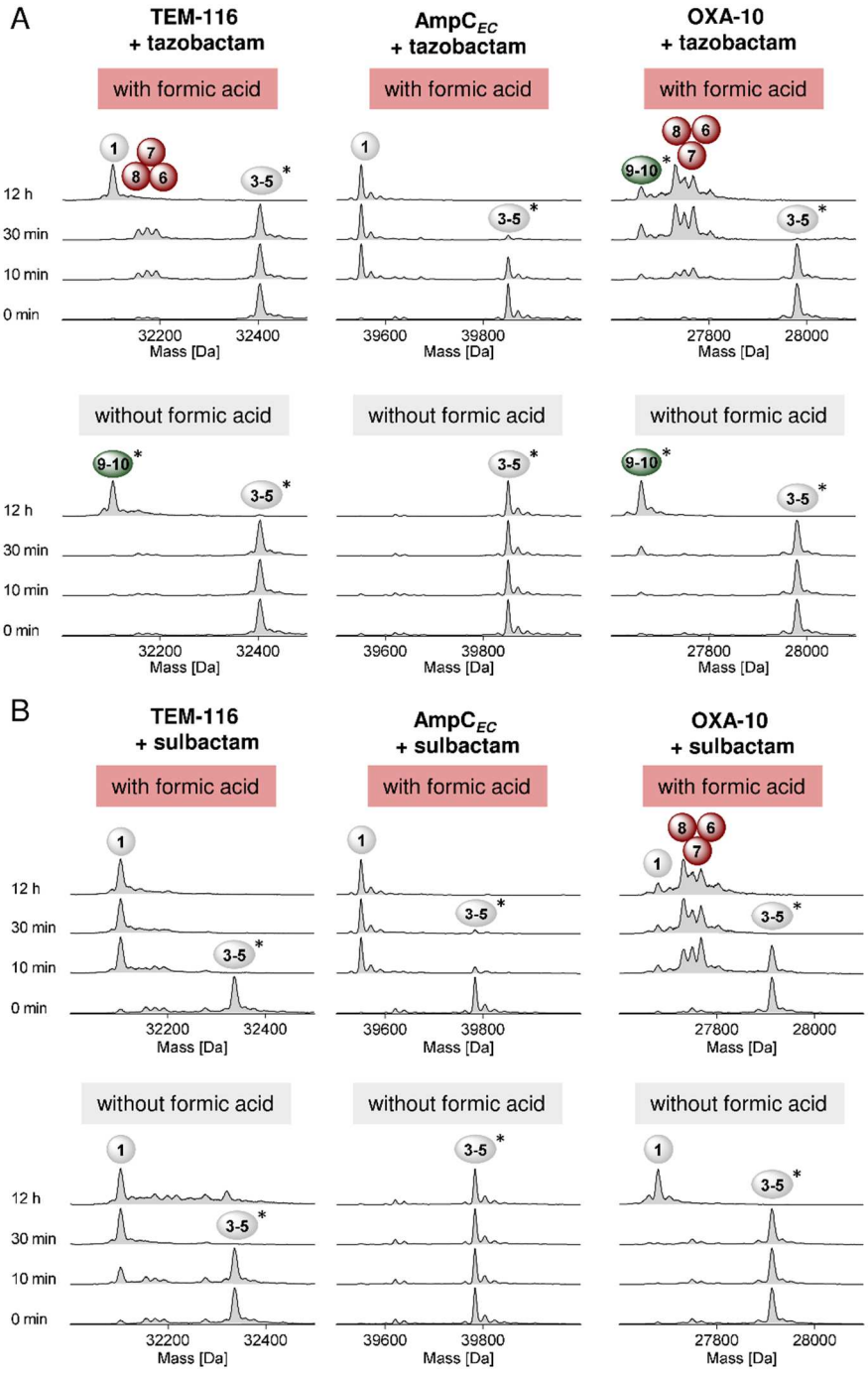


Figure 17: Effect of the addition of formic acid prior to SPE-MS analysis on modifications to TEM-116, AmpC$_{EC}$ and OXA-10 caused by reaction with tazobactam or sulbactam. TEM-116, AmpC$_{EC}$, and OXA-10 (3 µM) were reacted with tazobactam (300 µM) or sulbactam (1.5 mM) in 50 mM Tris pH 7.5. Further reaction was induced by addition of formic acid to a final concentration of 0.1 % (v/v). Samples were analysed using the SPE-MS method. Deconvoluted spectra, obtained using the maximum entropy algorithm in the MassHunter Workstation Qualitative Analysis B.07.00 programme (Agilent), are shown. The proposed structures of the labelled species are given in Figure 11. See Table 6 for summary of the calculated and observed masses and mass shifts. *Note mass shifts may reflect more than one species, e.g. **2**-**5** and **9**-**10** give the same mass shift.

2.3.2.3. Further investigations into the +169 Da species

Non-denaturing MS studies were carried out in collaboration with Dr Ritu Raj (Univeristy of Oxford).

To investigate the molecular basis of the +169 Da species observed using SPE-MS on reactions of TEM-116, AmpC$_{EC}$, and OXA-10 with enmetazobactam, first, structural studies were conducted. A crystal structure obtained from soaking crystals of unmodified AmpC$_{EC}$ with 200 mM enmetazobactam for 14 min (1.75 Å resolution, PDB: 6T35, Table 7) showed continuous electron density extending from the nucleophilic Ser64, which was refined as *trans*-enamine **5** (Figure 18).

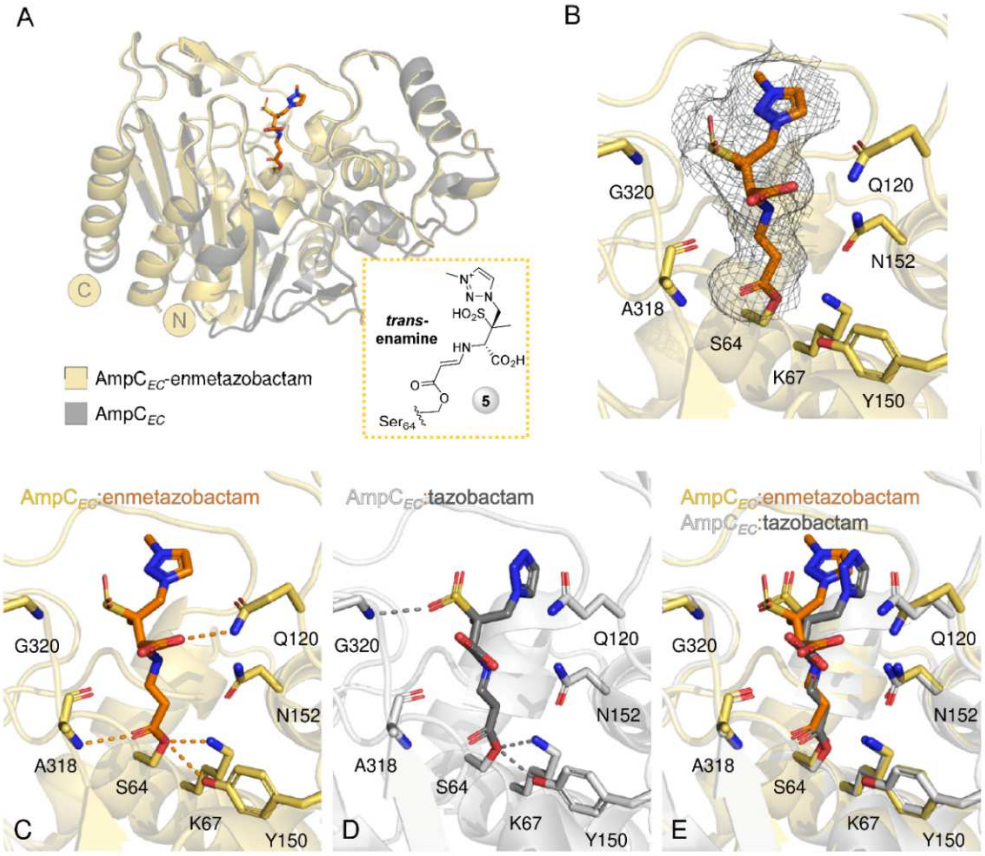


Figure 18: Views from crystal structures of AmpC$_{EC}$ reacted with enmetazobactam (PDB: 6T35) and tazobactam (PDB 6WA7 [57]) to give a *trans*-enamine bound to the active site Ser64. (A) Comparison of overviews of the unmodified AmpC$_{EC}$ fold (PDB: 6T3D [58], grey) and AmpC$_{EC}$ in complex with the enmetazobactam derived *trans*-enamine (yellow, **5** in Figure 11) shows no significant differences in the overall fold (backbone RMSD: 0.18 Å). (B) mF$_o$-DF$_c$ polder OMIT maps[59] contoured at 3.0 σ and carved around the enmetazobactam derived *trans*-enamine **5** bound to Ser64. (C) Interaction of AmpC$_{EC}$ with the enmetazobactam derived *trans*-enamine **5** (orange, PDB: 6T35). (D) Interaction of AmpC$_{EC}$ with the tazobactam derived *trans*-enamine **5** (dark gray, PDB 6WA7 [57]). Polar interactions are indicated as dashes. (E) Superimposition of the two *trans*-enamine complexes (colour coding as in (C) and (D). The figure and figure legend are modified with permission from Lang *et al.* Proc. Natl. Acad. Sci. U.S.A., 2022, *119*, e2117310119.

Note, at the given resolution this assignment is not unambiguous and while the conformation of the complex clearly excludes a substantial amount of the *cis*-configuration, the presence of

the *trans*-imine cannot be excluded. However, previous spectroscopic studies[8-15], support the assignment as the *trans*-enamine.

The β-lactam derived carbonyl of *trans*-enamine **5** is positioned to interact with the backbone NH of Ala318, (2.9 Å); one of its C-2 carboxylate oxygens is proximate to the sidechain amide nitrogen of Gln120 (2.5 Å) (Figure 18C). The triazole *N*-methyl group does not appear to interact directly with any active site residues; it is rotated by ~ 90° compared to the triazole motif as observed in a recently reported structure of an AmpC$_{EC}$-tazobactam *trans*-enamine complex (PDB 6WA7, Figure 18D-E)[57].

Table 7: Data collection and refinement statistics for the AmpC$_{EC}$ – enmetazobactam derived crystal.

Datasets	**AmpC$_{EC}$ –enmetazobactam** (PDB: 6T35)		
Data Collection		**Refinement**	PHENIX
Beamline (Wavelength, Å)	DLS I03 (0.9763)	R_{work}/R_{free}	0.1667/0.1844
Detector	Pilatus 6M-F	No. atoms	
Data Processing	Xia2	- Enzyme	2724
Space group	$P\,4_3\,3\,2$	- Ser64-enmetazobactam	28
Cell dimensions		- Water	258
- *a,b,c* (Å)	138.0, 138.0, 138.0	Average B-factors	
- α, β, γ (°)	90, 90, 90	- Enzyme	38.17
No. of molecules/ASU	1	- Ser64-enmetazobactam	59.29
No. reflections	45784 (3313)*	- Water	45.64
Resolution (Å)	56.34-1.75 (1.78-1.75)*	RMS$ deviations	
R_{merge}(I)	0.128 (5.437)*	- Bond lengths (Å)	0.005
I/σI	28.1 (1.3)*	- Bond angles (°)	0.80
$CC_{1/2}$	1.00 (0.53)*		
Completeness (%)	100 (100)*		
Multiplicity	77.5 (81.1)*		
Wilson B value (Å^2)	31.19		

ASU = asymmetric unit.
$ RMS = root mean square.
*Highest resolution shell in parentheses.

Importantly, these crystallographic studies did not show any evidence for elimination reactions to potentially give alkene **11** or other +169 Da species observed in the SPE-MS studies. To investigate the potential effects of the denaturing ESI-MS analyses on generation of the +169 Da species, non-denaturing MS experiments were carried out with TEM-116, AmpC$_{EC}$, and OXA-10 on reaction with enmetazobactam and tazobactam. By contrast to both LC- and SPE-MS, the non-denaturing MS analysis does not require acid promoted protonation of proteins and typically uses a lower energy input compared to conventional ESI-MS techniques.

Under non-denaturing MS conditions, predominantly species with the full mass of the inhibitors were observed both on reaction with enmetazobactam and tazobactam (+314 and +300 Da, respectively, Figure 19). By contrast with the SPE-MS studies (Figure 12), only low amounts of the +169 Da species (< 5%, compared to >50% in SPE-MS analyses) were observed on reaction of the SBLs with enmetazobactam (Figure 19A).

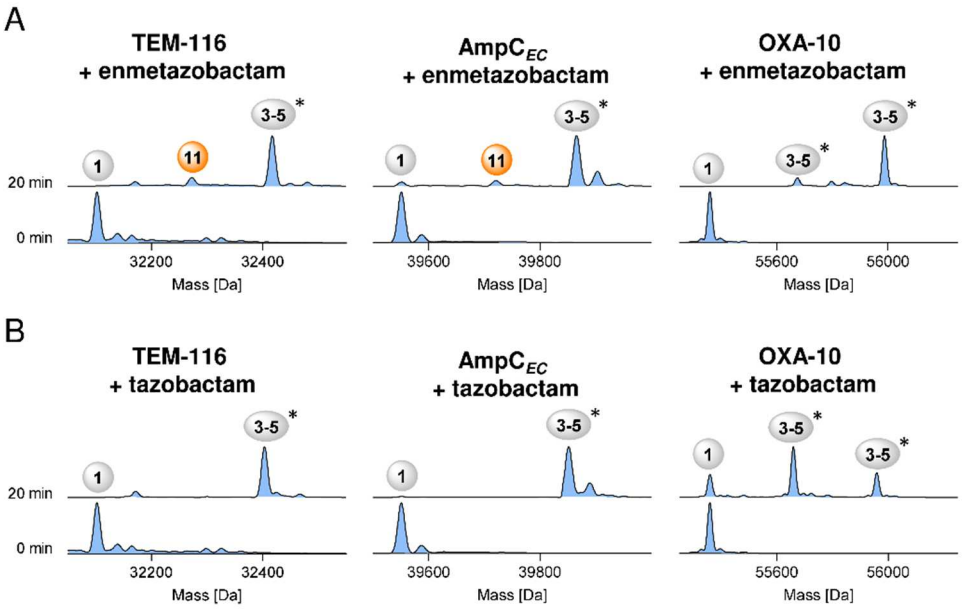


Figure 19: Native-MS studies showing lack of elimination from the enmetazobactam derived SBL complexes. TEM-116, AmpC$_{EC}$, or OXA-10 (10 µM) were incubated with (A) enmetazobactam or (B) tazobactam (1 mM) in 1 M ammonium acetate, pH 7.5 at room temperature for 20 min. Samples were desalted (using a Zeba micro spin desalting column, 7K MWCO, Thermo Fisher Scientific) immediately prior to analysis and sprayed directly into the mass-spectrometer. As reported[60] OXA-10 was predominantly dimeric. Non-deconvoluted spectra are shown in Appendix III, Figure S8-10. The proposed structures of the labelled species are given in Figure 11. See Table 8 for summary of the calculated and observed masses and mass shifts. *Note mass shifts may reflect more than one species, e.g. **2**-**5** give the same mass shift.

To investigate the apparent difference in the amounts of +169 Da species observed via the SPE-MS and non-denaturing MS techniques, subsequent studies were conducted to examine the impact of ESI properties on formation of the +169 Da species (Figure 20). For this the AmpC$_{EC}$-enmetazobactam complex was chosen for the long life time observed in SPE-MS studies (Figure 12) which is in agreement with the low de-acylation rates observed in competition studies (Figure 5 and Table 4) and facilitates detailed analysis of a single sample under multiple different conditions.

A clear dependence of the observed amount of +169 Da species could be demonstrated, both on the gas pressure in the spectrometer (Figure 20A) and the collision activation (Figure 20B). Small amounts of +169 Da species could also be observed on incubating AmpC$_{EC}$ with enmetazobactam at elevated temperature (> 45 °C) for 1 h prior to analysis (Figure 20C).

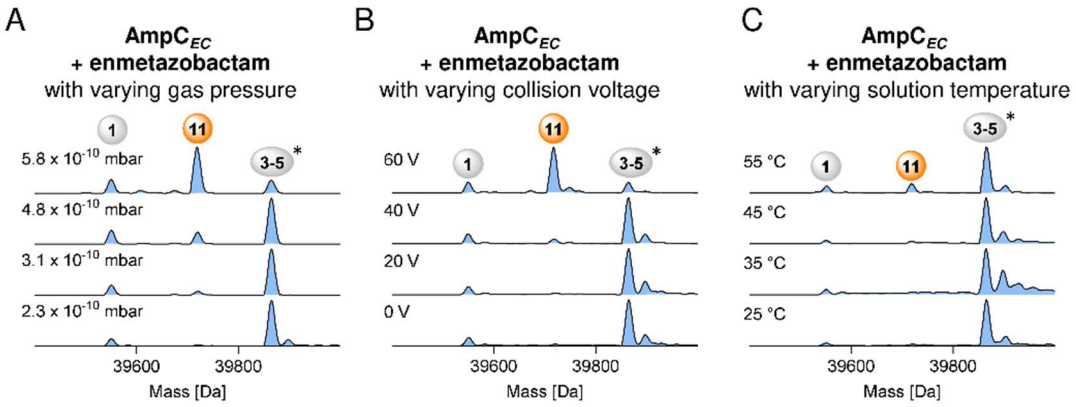


Figure 20: Native-MS studies showing the effect of gas pressure, collisional activation in the higher-energy C-trap dissociation (HCD) cell, and solution temperature on formation of elimination product 11 from the enmetazobactam derived AmpC$_{EC}$ complex. AmpC$_{EC}$ (10 µM) was incubated with enmetazobactam (1 mM) in 1 M ammonium acetate, pH 7.5 at r.t. for 20 min. The sample was desalted (using a Zeba micro spin desalting column, 7K MWCO, Thermo Fisher Scientific) immediately prior to analysis and sprayed directly into the mass-spectrometer. (A) Spectra were acquired without collisional activation and at the indicated UHV gas pressures. (B) Spectra were acquired with indicated collisional activation and low gas pressure (2.3 x 10^{-10} mbar). (C) Spectra of samples incubated at indicated temperatures for 1 h prior to analysis, acquired without collisional activation and at low gas pressure (2.3 x 10^{-10} mbar). Non-deconvoluted spectra are shown in Appendix III, Figure S11-13. Proposed structures corresponding to the labelled mass shifts are given Figure 11. *Note mass shifts may reflect more than one species, e.g. **2**-**5** give the same mass shift.

The results thus show that generation of the +169 Da species from the enmetazobactam derived SBL-acyl-enzyme complexes requires high energy conditions and therefore likely does not contribute towards SBL inhibition under biologically relevant conditions.

Table 8: Modifications to AmpC$_{EC}$, TEM-116 and OXA-10 by reaction with enmetzobactam, tazobactam, or sulbactam as analysed by native-MS. All differences between measured and calculated masses / mass shifts are within experimental error. [a]Masses were derived from deconvolution of measured spectra using the maximum entropy algorithm in MassLynx V.4.1 (Waters). [b]Relative to the measured unmodified protein mass. [c]Proposed product structures are defined in Figure 11.

		Mass observed[a] [Da]	Mass calculated [Da]	Mass shift observed[b] [Da]	Mass shift calculated [Da]	Assignment[c]	Comments
Non-denaturing MS (no exposure to formic acid)	**AmpC$_{EC}$**	39551	39551			unmodified **1**	
	+ enmetazobactam	39866	39865	+315	+314	enamine **5**	or equal mass species
	+ tazobactam	39851	39851	+300	+300	enamine **5**	or equal mass species
	OXA-10	55359	55364			unmodified **1**	dimer
	+ enmetazobactam	55989	55992	+630	+628	enamine **5**	dimer + 2 enmetazobactam
	+tazobactam	55957	55964	+598	+600	enamine **5**	dimer + 2 tazobactam
	TEM-116	32102	32103			unmodified **1**	
	+ enmetazobactam	32416	32417	+313	+314	enamine **5**	or equal mass species
	+ tazobactam	32404	32403	+301	+300	enamine **5**	or equal mass species

2.3.2.4. Prolonged reaction of SBLs with penam sulfones can lead to dehydration of the nucleophilic serine

Non-denaturing MS and LC-MS/MS studies were carried out in collaboration with Dr Ritu Raj (Univeristy of Oxford).

To investigate possible acid interference in generation of the -18 Da species, samples of TEM-116 and OXA-10, incubated overnight with enmetazobactam or tazobactam (100 equiv.) were analysed via non-denaturing MS. As observed via SPE-MS (Figure 12-13), incubation of TEM-116 with enmetazobactam let to ~ 45% conversion to the -18 Da species, while no such modification was observed on incubation with tazobactam (Figure 21). For OXA-10 -18 Da modification was observed both on reaction with enmetazobactam and tazobactam, but conversion appeared more efficient on incubation with tazobactam (~ 60% compared to ~ 45% for enmetazobactam and tazobactam, respectively, Figure 21).

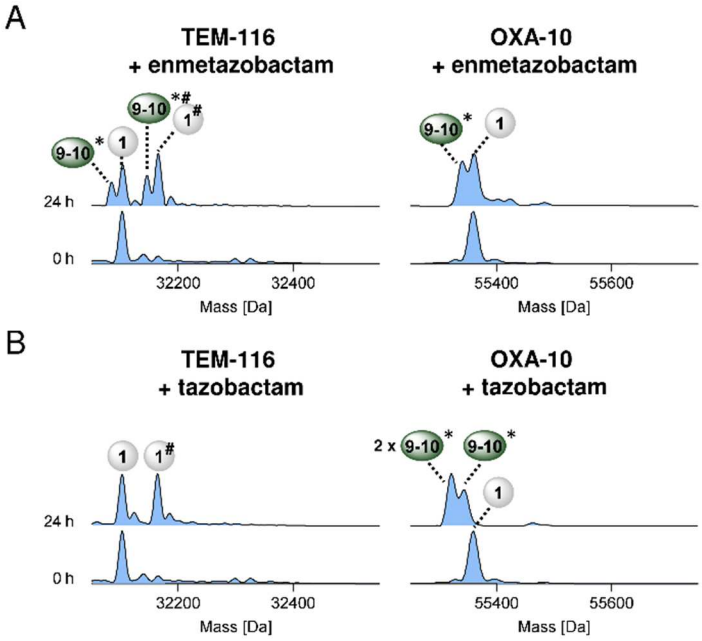


Figure 21: Native-MS studies on prolonged reaction of TEM-116 or OXA-10 with tazobactam or enmetazobactam. TEM-116 or OXA-10 (10 µM) were incubated with tazobactam or enmetazobactam (1 mM) in 50 mM Tris pH 7.5 at room temperature for 24 h. Samples were buffer exchanged into 1 M ammonium acetate, pH 7.5 (using a Zeba micro spin desalting column, 7K MWCO, Thermo Scientific) twice immediately prior to analysis and sprayed directly into the mass-spectrometer. #Corresponds to unmodified TEM-116 and -18 Da modified TEM-116 with an additional mass increase of +62 Da, likely reflecting non-covalent binding of a penam sulfone degradation product, i.e. hydrated acetaldehyde (**17** in Figure 30). Non-deconvoluted spectra are shown in Appendix III, Figure S26. Proposed structures of the labelled species are given in Figure 11. *Note mass shifts may reflect more than one species, e.g. **9**-**10** give the same mass shift.

Next, -18 Da modified TEM-116 and OXA-10 (with full conversion as indicated by SPE-MS) were tested for β-lactamase activity using FC-5[44]. In agreement with a previous report showing no catalytic activity of -18 Da modified SHV-1 and CTX-M-15 (both class A)[22], no

β-lactamase activity was observed for modified TEM-116 and OXA-10, when assayed with FC 5 (Figure 22).

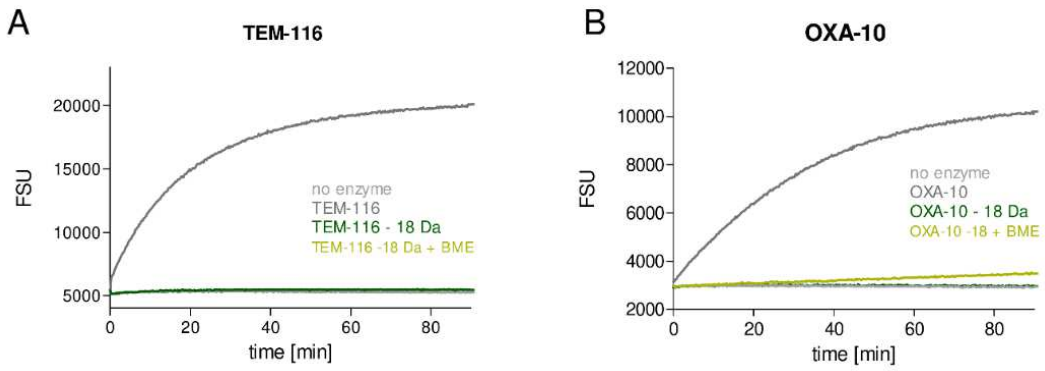


Figure 22: β-Lactamase activity assay for -18 Da modified TEM-116 and OXA-10. Prior to the assay TEM-116 (3 µM) was preincubated either without inhibitor, with enmetazobactam (900 µM), or with a combination of enmetazobactam (300 µM) and β-mercaptoethanol (BME, 3 mM) for 24 h in 50 mM Tris pH 7.5. OXA-10 116 (3 µM) was preincubated either without inhibitor, with tazobactam (300 µM), or with a combination of tazobactam (300 µM) and BME (3 mM). A) 100 pm TEM-116 was assayed using 5 µM FC-5[44]. (B) 300 pm OXA-10 was assayed using 5 µM FC-5[44]. Buffer: 50 mM phosphate buffer, pH 7.0, 7.5, or 8.0 and 0.01% (v/v) Triton X-100. Note, that the residual activity of the OXA-10 -18 Da +BME sample (< 5 % of activity of unmodified OXA-10) may be due to small amounts of unmodified enzyme in the sample. The figure and figure legend are reproduced with permission from Lang *et al.* Proc. Natl. Acad. Sci. U.S.A., 2022, *119*, e2117310119.

Dha **9** is a common intermediate in protein engineering, where it is reacted with thiols or other nucleophiles to introduce covalent modifications on proteins[61]. To investigate Dha **9** formation in the -18 Da modified TEM-116 and OXA-10 they were thus reacted with β-mercaptoethanol (BME, Figure 23-25).

On incubation of unmodified OXA-10 with BME (1,000 equiv.), no reaction was observed, as assessed by SPE-MS (Figure 23B). By contrast, after reaction of OXA-10 with 100 equivalents of tazobactam for 8 h, the subsequent addition of BME (1000 equiv.) resulted in ~ 80% conversion of -18 Da modified OXA-10 to give a +60 Da species (relative to unmodified OXA-10) within 2 hours (Figure 23A). This +60 Da species is in agreement with the addition of BME to Dha **9** to give 2-hydroxyethyl-cysteine (Dha-BME, **17**, Figure 23C). After the initial rapid conversion, the reaction did not progress further on prolonged reaction for 24 h, even with addition of more BME (Figure 23A). However, in subsequent studies conversion of the -18 Da species to the +60 Da species **17** could be increased to ≥ 98% by simultaneous addition of tazobactam and BME (Figure 23D-E and Figure 28). Conversely, generation of the +60 Da species was decreased by prolonged incubation with tazobactam prior to BME addition (Figure 23D-E), implying a slow inactivation of the initially formed Dha residue **9** towards reaction with BME.

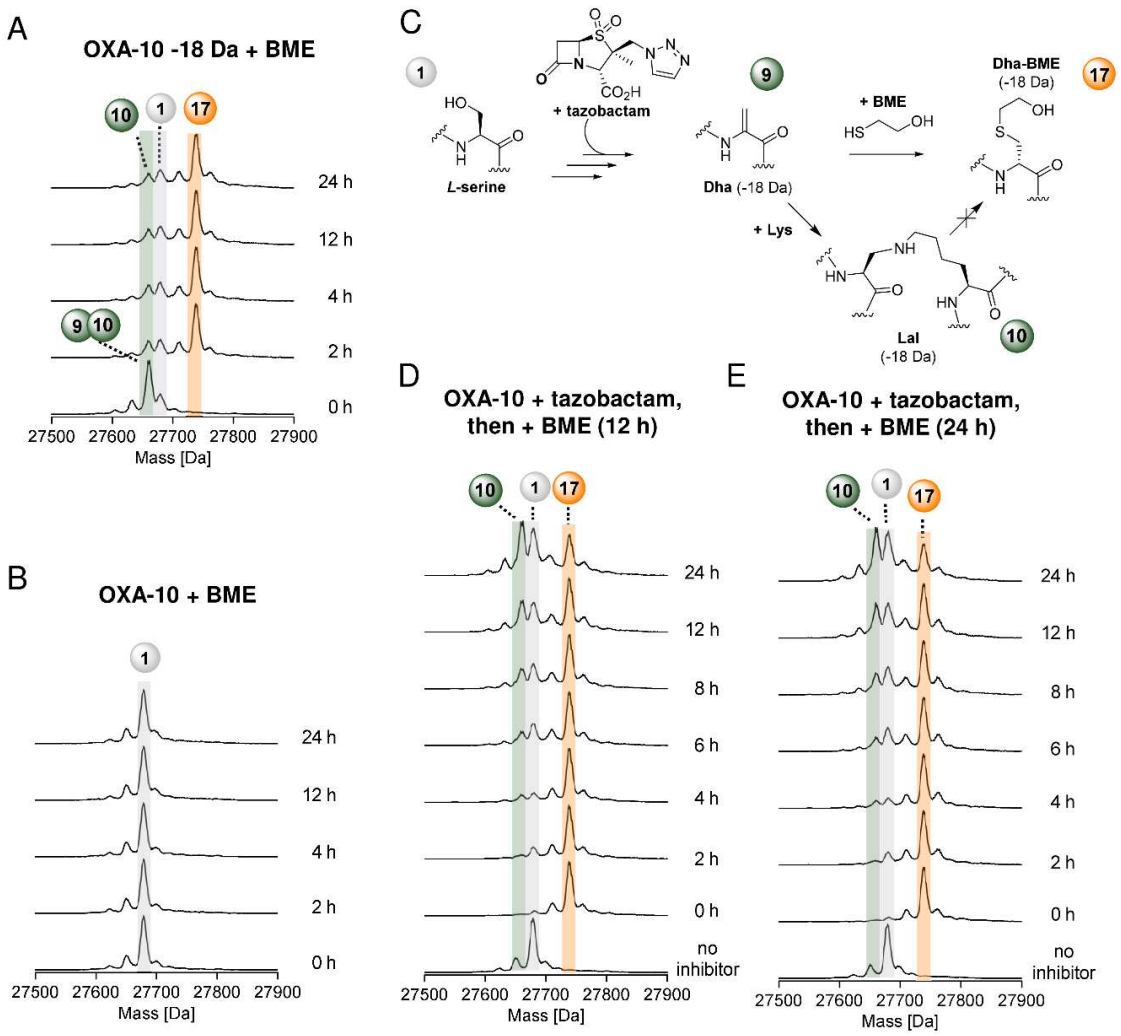


Figure 23: SPE-MS time courses for reaction of the OXA-10 S67Dha modified protein with β-mercaptoethanol (BME). OXA-10 (3 µM) was incubated with tazobactam (300 µM) and BME (3 mM) in 50 mM Tris pH 7.5 at r.t. The order and timing of the additions of tazobactam and BME were varied. (A) OXA-10 incubated with tazobactam leading to apparently complete conversion to the -18 Da modified protein (likely **9** or **10,** Figure 11), before addition of BME at t = 0 h. The results show ~80% addition of BME to the -18 Da modified OXA-10 within 2 h (likely to give **9** or **10**); no further progression of the reaction was observed over an additional 22 h. (B) BME was added to unmodified OXA-10 (in absence of tazobactam) at t = 0 h. No addition of BME to unmodified OXA-10 was observed over the duration of the experiment. (C) Proposed reaction scheme for OXA-10 modification on treatment with tazobactam and BME. (D) OXA-10 was incubated with tazobactam for the indicated time before addition of BME. Samples were then incubated for an additional 12 h with continuous rocking. The results show less addition of BME to the "aged" -18 Da modified protein, consistent with reaction of the S67Dha modified protein **9** to give the S67Dha-K70 Lal protein **10**, which does not react with BME to give an (2-hydroxyethyl)-cysteine residue (Dha-BME) **17**. (E) Samples from (D) measured after 24 h, showing no evidence for further reaction of any of the samples. The figure and figure legend are reproduced with permission from Lang *et al.* Proc. Natl. Acad. Sci. U.S.A., 2022, *119*, e2117310119.

By contrast with OXA-10, reaction of unmodified TEM-116 with BME (1,000 equiv.) resulted in slow addition of a single BME molecule over 24 h, likely via thiol disulfide exchange with one of the two disulfide-bound Cys residues (Figure 24). TEM-116 reacted with enmetazobactam to give -18 Da modified protein showed the same slow addition of a single BME, but no further addition of a second BME was observed, as would be expected for reaction of BME with Dha **9**

(Figure 24A). By contrast with OXA-10, reactivity of the TEM-116 derived -18 Da modified protein with BME was not increased by simultaneous addition of enmetazobactam and BME (Figure 24D-E).

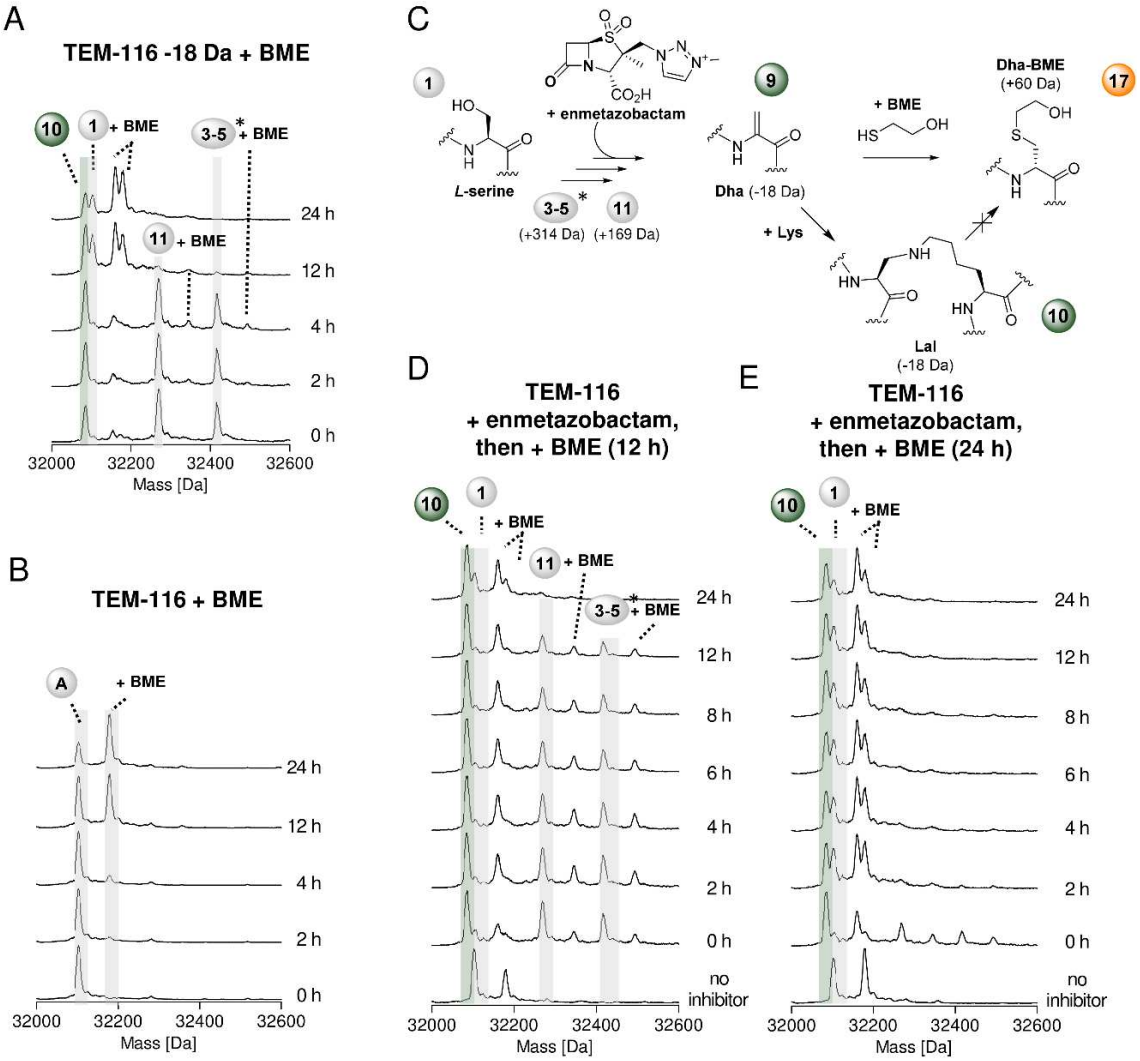


Figure 24: SPE-MS time courses for reaction of TEM-116 S70Dha modified protein with β-mercaptoethanol (BME). Unless stated otherwise, TEM-116 (3 µM) was incubated with enmetazobactam (300 µM) and BME (3 mM) in 50 mM Tris pH 7.5 at r.t. The order and timing of the additions of both enmetazobactam and BME were varied. (A) TEM-116 incubated with enmetazobactam for 8 h leads to partial conversion to the -18 Da modified protein (likely **9** or **10,** Figure 2), BME was then added at t = 0 h. The results indicate addition of BME to the -18 Da modified protein, as well as to unmodified TEM-116 and enmetazobactam modified TEM-116 (**3**-**5** and **11**, or equivalent mass species, Figure 11)). (B) BME added to unmodified TEM-116 (without tazobactam) at t = 0 h; addition of BME was observed. (C) Proposed reaction scheme for TEM-116 modification on treatment with enmetazobactam and BME. (D) TEM-116 was incubated with enmetazobactam for the indicated time; BME was then added and the samples were incubated for 12 h. The results show no evidence for addition of a second BME molecule, independent of pre-incubation time with enmetazobactam, suggesting efficient formation of the 70-73 Lal cross-link **10** following the formation of Dha **9**. (E) Samples from (D) measured after 24 h, showing no evidence for addition of a second BME molecule. The figure and figure legend are reproduced with permission from Lang *et al.* Proc. Natl. Acad. Sci. U.S.A., 2022, *119*, e2117310119.

The combined results from the BME derivatisation trials suggest that a Dha residue **9** is likely formed on -18 Da modification of OXA-10 observed on reaction with tazobactam, which is subsequently slowly inactivated towards reaction with BME, e.g. via an intramolecular cross-linking reaction within the OXA-10 active site (Figure 23C). If an equivalent Dha residue **9** is also formed on incubation of TEM-116 with enmetazobactam, this inactivation proceeds much faster and cannot be outcompeted by intermolecular reaction with BME.

To confirm location of the -18 and +60 Da modifications at the position of the nucleophilic Ser residues, modified OXA-10 and TEM-116 were subjected to tryptic proteolysis and analysed via LC-MS/MS. With +60 Da modified OXA-10 from simultaneous treatment with tazobactam and BME, the + 60 Da modification was located at Ser67, in agreement with formation of (Dha-BME, **17**, Figure 25).

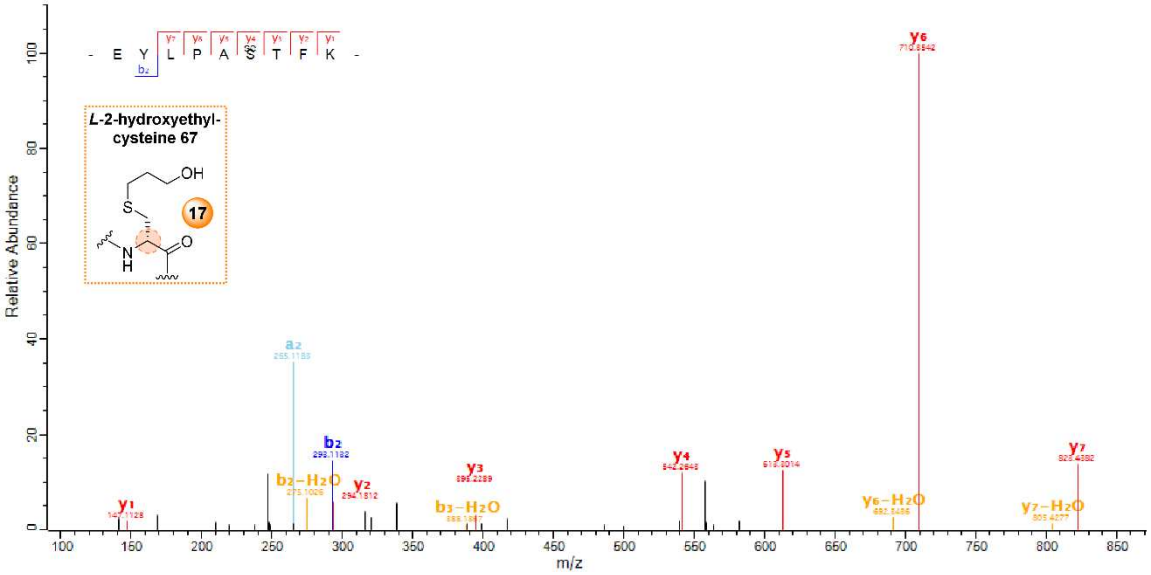


Figure 25: LC-MS/MS analysis of tryptic digest peptide of OXA-10 modified by reaction with tazobactam in the presence of β-mercaptoethanol (BME). OXA-10 (3 µM) was incubated with tazobactam (300 µM) and BME (3 mM) for 24 h in 50 mM Tris pH 7.5 at r. t., then desalted prior to trypsin digestion. MS/MS spectrum of the 62-EYLPASTFK-70 tryptic peptide (MH^{2+} ion), consistent with the Ser67 +60 Da modification **17** (resulting from Dha **9** formation, followed by BME addition to give (2-hydroxyethyl)-cysteine, Dha-BME **17**). The figure and figure legend are reproduced with permission from Lang *et al.* Proc. Natl. Acad. Sci. U.S.A., 2022, *119*, e2117310119.

MS/MS analysis of trypsin fragmented -18 Da modified TEM-116 confirmed a mass decrease of the nucleophilic Ser70. Importantly, while Ser70 containing peptides from unmodified TEM-116 showed complete backbone fragmentation (Figure 26A), no MS/MS fragmentation of the corresponding -18 Da modified peptide was observed beyond residues Lys73 or Ser70 (Figure 26B), consistent with crosslinking of the side chains of these residues (Figure 24C and see below).

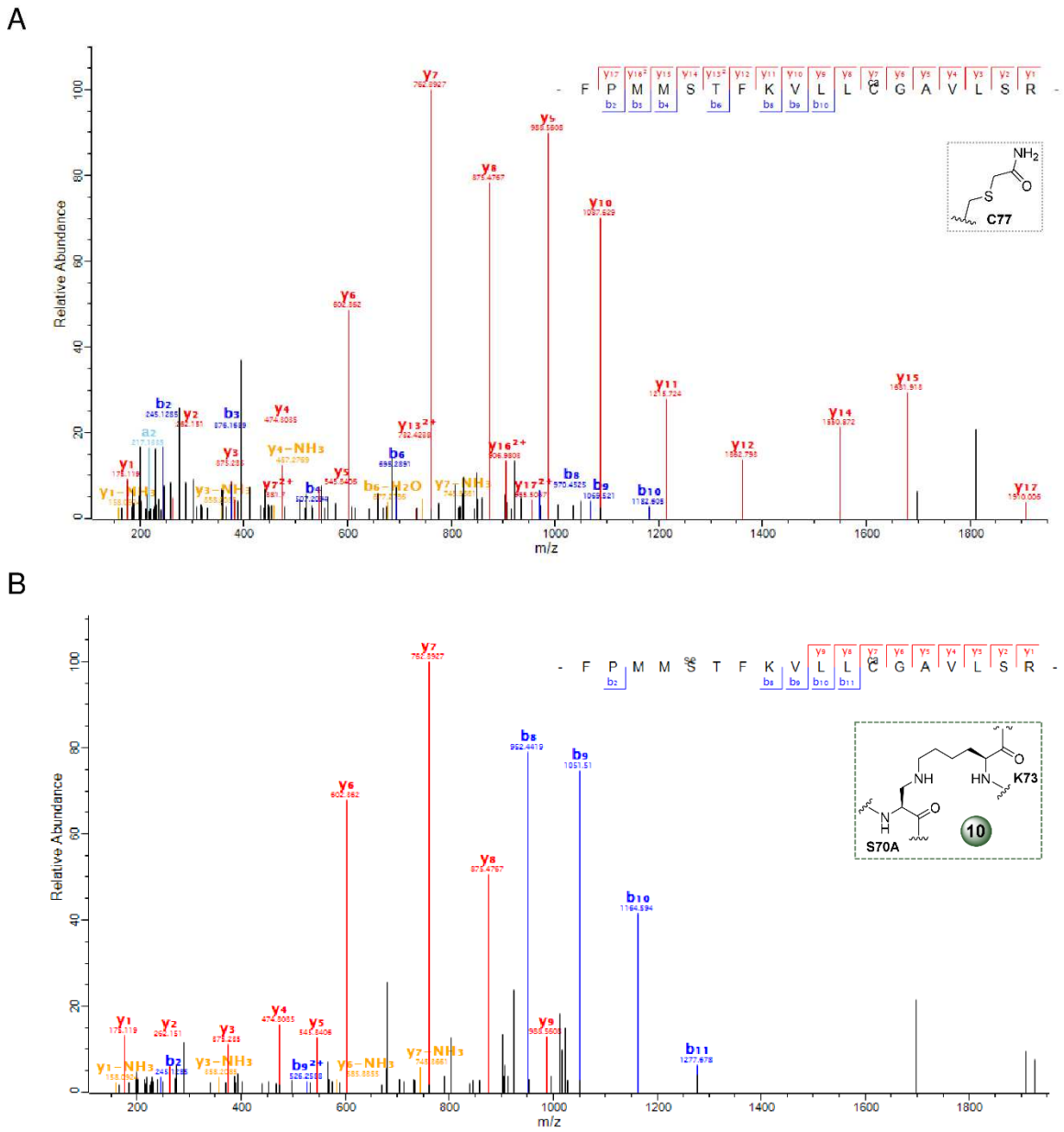


Figure 26: LC-MS/MS analysis of tryptic digest peptides of TEM-116 modified by reaction with enmetazobactam. TEM-116 (3 µM) was incubated with enmetazobactam (300 µM) for 24 h in 50 mM Tris pH 7.5 at r.t., then desalted prior to trypsin digestion. (A) MS/MS analysis of the 66-FPMMSTFKVLLCGAVLSR-83 tryptic peptide (MH^{3+} ion) consistent with an +58 Da acetamide modification at C77. (B) MS/MS analysis of the same peptide sequence with a -18 Da modification (likely **10**). The figure and figure legend are reproduced with permission from Lang *et al.* Proc. Natl. Acad. Sci. U.S.A., 2022, *119*, e2117310119.

To further investigate the structural basis of the -18 and +60 Da species, samples of OXA-10 reacted with either tazobactam or a combination of tazobactam and BME were crystallised using the Pact Premier suite (Molecular Dimensions). In all cases OXA-10 crystallised in similar conditions (see Materials and Methods) with two molecules in the ASU.

In both chains of a crystal structure of -18 Da modified OXA-10 (PDB: 7B3S, 1.85 Å resolution, Figure 27 and Table 9) planar geometry of the Cα atom and absence of electron density for

the Ser hydroxy oxygen (Figure 27E and I) compared to Ser67 of unmodified OXA-10 (PDB: 2X02[62], Figure 27D and H) clearly indicated dehydration of Ser67 to Dha **9**.

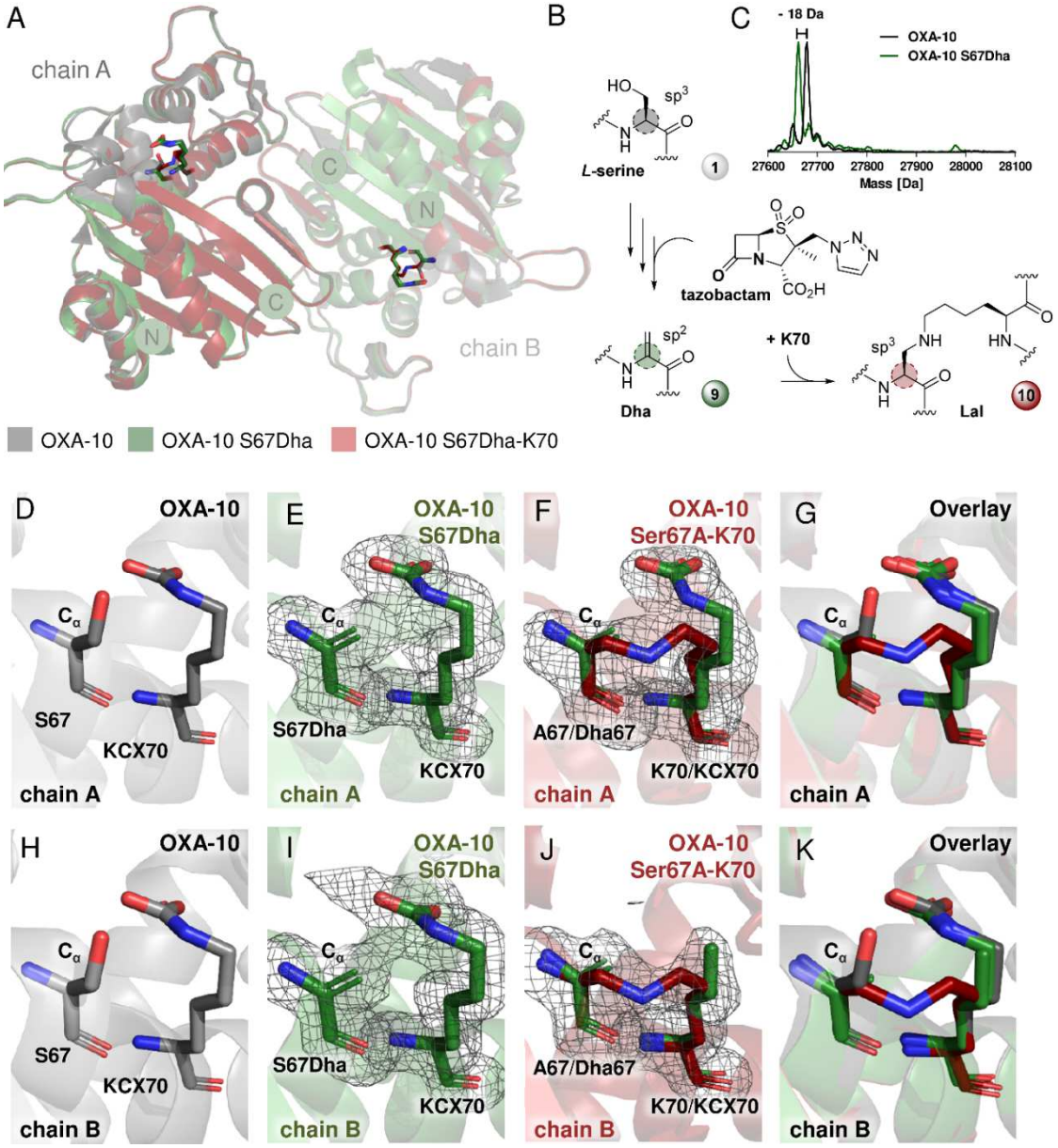


Figure 27: Views from crystal structures of OXA-10 after reaction with tazobactam to produce -18 Da mass shifts. (A) Overview of the fold of unmodified OXA-10 (PDB: 2X02[62], 1.35 Å resolution), OXA-10 S67Dha **9** (PDB: 7B3S, 1.85 Å resolution), and S67Dha OXA-10 in combination with a partial S67A-K70 Lal-crosslinked **10** OXA-10 structure (PDB: 7B3R, 1.83 Å resolution). (B) Reaction of OXA-10 with tazobactam. (C) SPE-ESI MS spectra of OXA-10 before and after modification by reaction with tazobactam. (D-G) Active site views of chain A. (H-K) Active site views of chain B. mF$_o$-DF$_c$ polder OMIT maps[59] are contoured at 3.0 σ and carved around active site residues. The figure and figure legend are reproduced with permission from Lang *et al.* Proc. Natl. Acad. Sci. U.S.A., 2022, *119*, e2117310119.

By contrast, examination of the electron density for active site residues in a second structure of -18 Da modified OXA-10 (PDB: 7B3R, 1.83 Å resolution, Figure 27 and Table 9), connecting electron density was observed between the C3 sidechain carbon of the original Ser67 and the

*N*ε-amine of Lys70 in both chains, indicating partial (~ 50%) formation of a lysinoalanine (Lal) crosslink **10**, which also manifests a -18 Da mass shift relative to the unmodified OXA-10 (Figure 27F and J). Notably, although generation of small amounts of the *D*(2*R*)-epimer cannot be ruled out, the new chiral centre formed by reaction of Lys70 with Dha **9** has, at least predominantly, the *L*(2*S*)-stereochemistry.

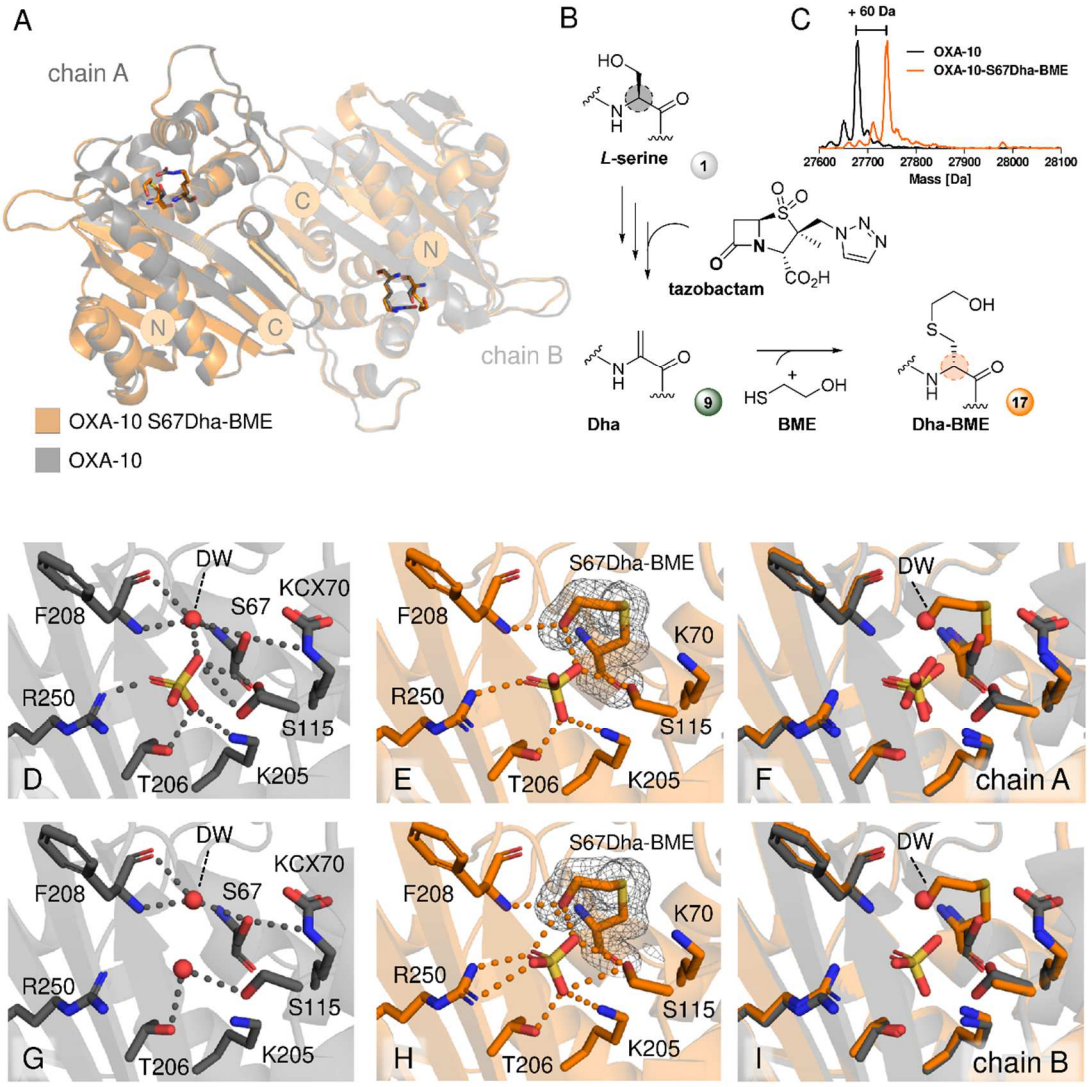


Figure 28: Views from a crystal structure of OXA-10 S67Dha reacted with β-mercaptoethanol (BME) to give (2-hydroxyethyl)-*D*-cysteine (Dha–BME). (A) Overview of OXA-10 fold of unmodified OXA-10 (PDB: 2X02[62], 1.35 Å resolution) and OXA-10 S67Dha-BME **17** (PDB: 7B3U, 1.60 Å resolution). (B) Reaction scheme for OXA-10 reaction with tazobactam, then BME. (C) SPE-ESI MS spectra of OXA-10 before and after reaction with tazobactam, then BME. (D-F) Active site interactions of chain A of unmodified OXA-10 (D), S67Dha-BME (E) mF_o-DF_c polder OMIT maps[59] contoured at 3.0 σ, carved around S67Dha-BME. (F) Superimposition of unmodified and S67Dha-BME **17** active site views. (G-I) Active site interactions of chain B of unmodified OXA-10 (G) and S67Dha-BME (H). (I) Superimposition of the unmodified and S67Dha-BME **17** active site views. Note that even though the generation of small amounts of the *L*-isomer cannot be excluded, the maps indicate formation of a (2-hydroxyethyl)-*D*-cysteine residue. The figure and figure legend are reproduced with permission from Lang *et al.* Proc. Natl. Acad. Sci. U.S.A., 2022, *119*, e2117310119.

A structure of OXA-10 reacted with tazobactam and BME to give a +60 Da species (PDB: 7B3U, 1.60 Å resolution, Figure 28 and Table 9) showed continuous electron density consistent with Dha-BME **17** formation, both in chain A and chain B (Figure 28E and H). By contrast with the intra-molecular addition of the *N*$^{\varepsilon}$-amine of Lys70 (Figure 27), only *D*(2S)-Dha-BME was observed. Addition of BME to Dha **9** thus also appears stereo-selective, although generation of minor amounts of *L(2R)*-Dha-BME cannot be ruled out. Interestingly, the Dha-BME hydroxyethyl oxygen is positioned in the same location as the de-acylating water (DW) in the active site of unmodified OXA-10 in both chains (Figure 28F and I).

Together, the combined SPE-MS, LC-MS/MS, and crystallographic studies suggest that on prolonged reaction of OXA-10 and TEM-116 with a large excess of tazobactam or enmetazobactam dehydration of the nucleophilic Ser may occur. In the case of OXA-10 this is followed by a slow, stereoselective addition of the Lys70 *N*$^{\varepsilon}$-amine to give a lysinoalainine crosslink **10**. As indicated by the unsuccessful BME derivatisation trials, formation of the Lal species is either substantially faster in the case of TEM-116, or occurs in a concerted reaction without intermediate generation of Dha **9**. The results are summarised in Figure 29.

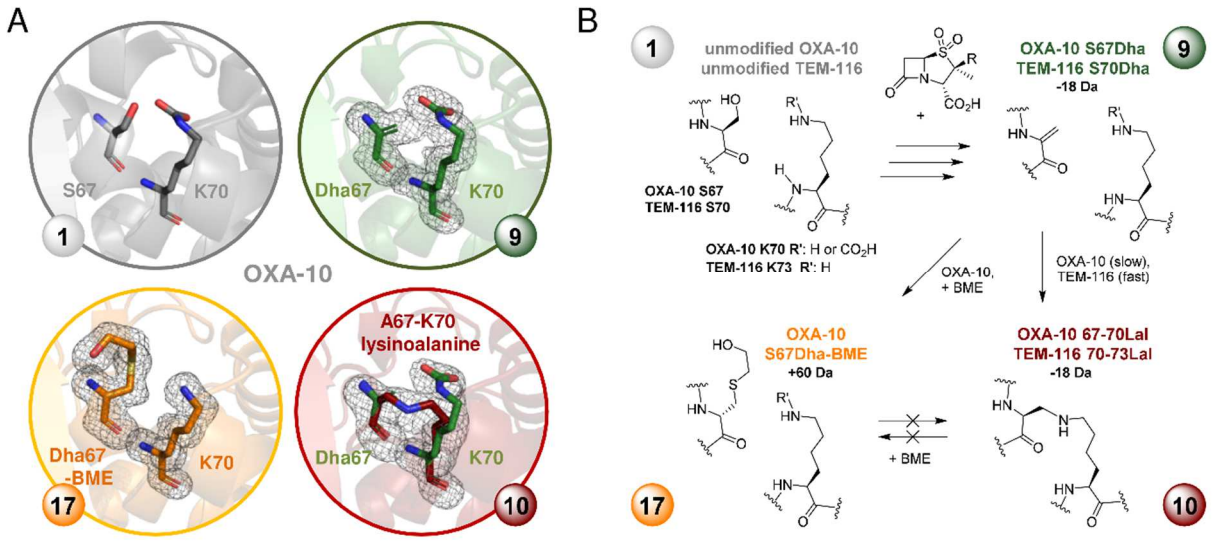


Figure 29: Reaction of SBLs with tazobactam or enmetazobactam produces a dehydroalanine (Dha) residue that reacts to give a crosslinked lysinoalanine (Lal) species. (A) Views from a crystal structure of unmodified OXA-10 **1** (PDB: 2X02[62], 1.35 Å resolution), -18 Da modified OXA-10, from incubation with tazobactam (100 equiv., 18 h, r.t.), showing either S67Dha **9** (PDB: 7B3S, 1.85 Å resolution) or S67Dha OXA-10 **9** together with partial formation of 67-70 Lal **10** (PDB: 7B3R, 1.83 Å resolution) and OXA10 S67Dha-BME species **17** (PDB: 7B3U, 1.60 Å resolution) derived from simultaneous incubation of OXA-10 with 100 equiv. tazobactam and 1000 equiv. β-mercaptoethanol (BME). mF$_o$-DF$_c$ polder OMIT maps[59] contoured at 3.0 σ, carved around active site residues from one (chain A) of two chains in the ASU are shown. See Figure 27-29 for mF$_o$-DF$_c$ polder OMIT maps for chain B. (B) Modifications observed on treatment of OXA-10 and TEM-116 with tazobactam, or enmetazobactam, with/without added BME. The figure and figure legend are reproduced with permission from Lang *et al.* Proc. Natl. Acad. Sci. U.S.A., 2022, *119*, e2117310119.

Table 9: Data collection and refinement statistics for OXA-10 crystals.

Datasets	**OXA10-BME** (PDB: 7B3U)	**OXA10-DHA** (PDB: 7B3S)	**OXA10-crosslink** (PDB: 7B3R)
Data Collection			
Beamline (Wavelength, Å)	DLS I24 (0.9686)	DLS I24 (0.9686)	DLS I24 (0.9686)
Detector	Pilatus3 6M	Pilatus3 6M	Pilatus3 6M
Data Processing	Xia2 dials	Xia2 dials	Xia2 dials
Space group	$P\,2_1\,2_1\,2_1$	$P\,2_1\,2_1\,2_1$	$P\,2_1\,2_1\,2_1$
Cell dimensions			
- *a,b,c* (Å)	48.9, 97.2, 126.0	48.9, 97.2, 125.9	48.6, 95.5, 126.2
- α, β, γ (°)	90, 90, 90	90, 90, 90	90, 90, 90
No. of molecules/ASU	2	2	2
No. reflections	80334 (3850)*	52193 (2503)*	52627 (2568)*
Resolution (Å)	76.97-1.60 (1.63-1.60)*	48.90-1.85 (1.88-1.85)*	63.09-1.83 (1.86-1.83)*
R_{merge}(I)	0.151 (1.185)*	0.275 (2.398)*	0.182 (1.544)*
I/σI	8.9 (1.6)*	7.1 (1.2)*	8.7 (1.8)*
CC-1/2	1.00 (0.82)*	0.99 (0.61)*	1.00 (0.85)*
Completeness (%)	99.9 (96.7)*	100 (97.6)*	99.8 (97.7)*
Multiplicity	12.7 (11.9)*	12.9 (12.9)*	12.9 (13.0)*
Wilson B value (Å^2)	14.95	9.58	21.27
Refinement	PHENIX	PHENIX	PHENIX
R_{work}/R_{free}	0.1551/0.1767	0.1649/0.2030	0.1698/0.1906
No. atoms	4571	4413	4202
- Enzyme	3937	3867	3747
- Ser64Dha	-	12	-
- Ser64Dha-Lys70 crosslink	-	-	60
- Ser64-BME species	18	-	-
- Water	576	507	396
Average B-factors	26.28	23.86	32.64
- Enzyme	24.59	22.34	32.12
- Ser64Dha	-	18.02	-
- Ser64Dha-Lys70 crosslink	-	-	25.89
- Ser64-DCys…	18.62	-	-
- Water	37.25	34.75	38.56
RMS[$] deviations			
- Bond lengths (Å)	0.006	0.009	0.005
- Bond angles (°)	0.885	1.004	0.861

[#] ASU = asymmetric unit.
[$] RMS = root mean square.
*Highest resolution shell in parentheses.

2.3.2.5. Solution based NMR studies show turn-over to fragmented products

NMR studies were carried out with support from Dr Christopher Lohans (University of Oxford).

The products of TEM-116, AmpC$_{EC}$, and OXA-10 catalysed hydrolysis of enmetazobactam, tazobactam, and sulbactam were investigated via NMR (Figure 30). While TEM-116 and OXA-10 efficiently degraded all penam sulfones, AmpC$_{EC}$ turn-over of 100 equivalents of enmetazobactam, tazobactam, or sulbactam was not completed within 18 h.

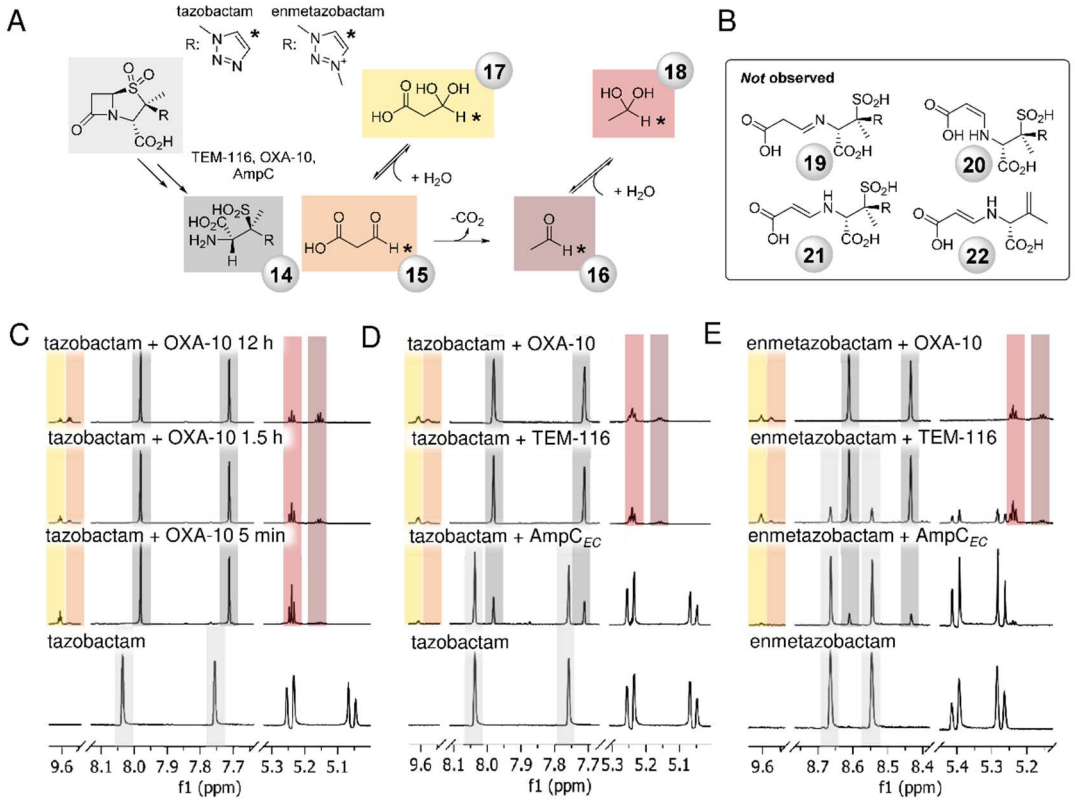


Figure 30: ^{1}H NMR analyses of the reaction of tazobactam and enmetazobactam with OXA-10, TEM-116, or AmpC$_{EC}$. (A) Products of reaction of tazobactam and enmetazobactam with serine β-lactamases and subsequent non-enzymatic reactions. (B) Compounds not observed in significant amounts. (C) ^{1}H NMR (750 MHz) time course showing reaction of tazobactam (5 mM) with OXA-10 (10 µM). (D) ^{1}H NMR analysis of reaction products of tazobactam (1 mM) with OXA-10, TEM-116, or AmpC$_{EC}$ (10 µM), incubated for 18 h. (E) ^{1}H NMR analysis of reaction products of enmetazobactam (1 mM) with OXA-10, TEM-116, or AmpC$_{EC}$ (10 µM), incubated for 18 h. All samples were setup in 50 mM phosphate buffer pH 7.5, 10 % D_2O and incubated at room temperature. Full spectra, including those of sulbactam degradation by TEM-116, OXA-10 and AmpC$_{EC}$, are shown in Appendix III, Figure S4-7. Chemical shift assignments are shown in Appendix III, Figure S3 and are consistent with previous reports[63].

Penam sulfone hydrolysis catalysed by all SBLs gave amines **14**, which appeared stable in solution over a period of 12 h, and aldehyde **15**, which underwent (presumably non-enzymatic) decarboxylation to give acetaldehyde **16**. As reported[63], both aldehydes were in equilibrium with the diols **17** and **18**, respectively. By contrast with the non-denaturing MS and SPE-MS results, no evidence of the hydrolysed *trans*-enamine **19** (or equivalent mass species **20**-**21**, Figure 30B) was found in solution.

Notably, the ^{1}H NMR analysis also showed no evidence of alkene **22** (Figure 30B), as would be expected on hydrolysis of the presumed elimination product **11** (Figure 9) correlating to the +169 Da species observed in the SPE-MS analysis on SBL inhibition by enmetazobactam (Figure 12), further supporting the non-denaturing MS and crystallographic studies which suggested no significant role of **11** for SBL in solution at room temperature.

2.4. SBL inhibition by clavulanic acid

Clavulanic acid is proposed to inhibit SBLs through a bifurcating reaction that is mechanistically related to SBL inhibition by penam sulfones, with the clavam furan ring opening analogously to the penam sulfone thiazolidine ring on opening of the β-lactam (Figure 31)[29].

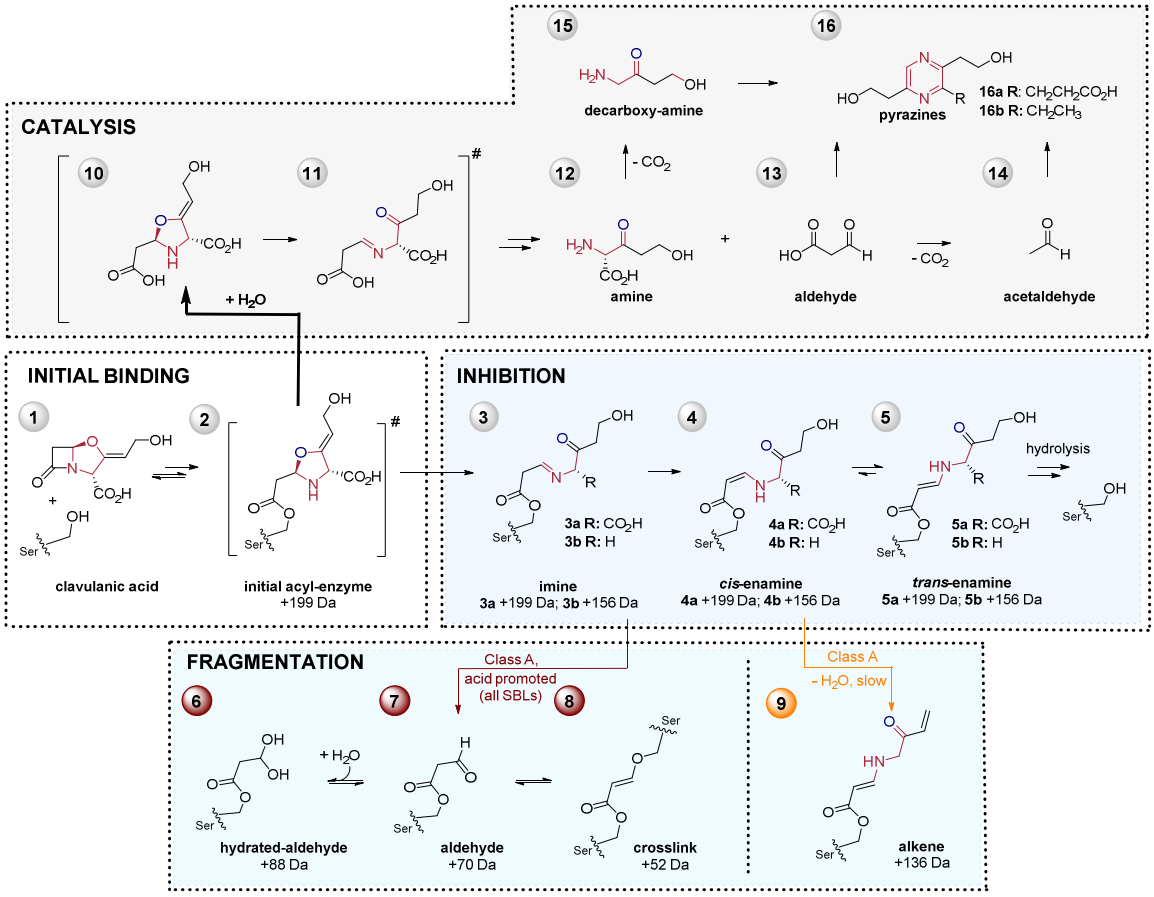


Figure 31: Pathways for reaction of clavulanic acid with SBLs. Following initial acyl-enzyme **2** formation the main transient inactivation pathway occurs via furan ring opening and decarboxylation to give species **3b**-**5b** which are relatively stable to hydrolysis. Fragmentation of **3b**-**5b** can occur in rare cases and is promoted by acid to give **6**-**8** or heat to give **11**. Dehydration of **3b**-**5b** can occur to give **9**. Efficient hydrolysis of the β-lactam occurs to give a β-amino acid product **10** which fragments in solution to give **12**-**16**. Our results imply biologically relevant inhibition involves **3b**-**5b** or equivalent mass species. Note that the numbering of species shown in this figure differs from that used for penam sulfone derived species as shown in Figure 9.

As a distinct difference to the penam sulfones, spectroscopic studies indicate that SBL inhibition by clavulanic acid involves decarboxylation of the α-keto acid resulting from oxazolidine ring opening (i.e. **3a**-**5a** in Figure 31), to give transiently stable de-carboxylated imine/enamine species (**3b**-**5b** in Figure 31)[29].

However, as with penam sulfones, previous LC-MS based protein observed ESI-MS studies[15,21,24,28-34] as well as some crystallographic studies[27,30,35] have suggested more substantial scaffold fragmentation of the acyl-enzyme complex, leading to +52, + 70, and +88 Da species (potentially correlating to **6**, **7**, and **8** in Figure 31, or equivalent mass species)[29,34], as also observed in LC-MS based studies on SBL inhibition by penam sulfones.

In light of the substantial differences observed on analysis of SBL inhibition by penam sulfones with different MS methods, we set out to reinvestigate the reaction of clavulanic acid with class A, C and D SBLs using a range of different biophysical techniques, including the SPE-MS method.

2.4.1. Kinetic analyses of transient SBL inhibition

2.4.1.1. Dose-dependence studies

Dose-dependence studies on SBL inhibition by clavulanic acid in competition with FC-5[44] (Table 10, Figure 32, and Appendix III, Figure S14) showed potent inhibition of TEM-116 (pIC_{50} 7.02) and OXA-10 (pIC_{50} 6.21) after 10 min of pre-incubation. By contrast, AmpC$_{EC}$ inhibition was very weak (pIC_{50} 2.78) under the same conditions.

Table 10: pIC_{50} values for clavulanic acid inhibition of TEM-116, AmpC$_{EC}$, and OXA-10. The enzymes (1 nM TEM-116, 500 pM AmpC$_{EC}$ or 250 pM OXA-10) in 50 mM phosphate buffer pH 7.5 (unless stated otherwise), 0.01% (v/v) Triton X-100 were pre-incubated with the inhibitors for the indicated times at room temperature, then assayed using 5 µM FC-5[44]. AmpC$_{EC}$ was screened at pH 7.0, 7.5, and 8.0. OXA-10 was also screened 100 mM $NaHCO_3$ added. pIC_{50}s as determined using non-linear regression (Appendix III, Figure S14). Errors are standard errors of four technical replicates.

		pIC_{50}[a]					
		AmpC$_{EC}$			OXA-10[a]	OXA-10[b]	TEM-116
	time	pH 7.0	pH 7.5	pH 8.0	pH 7.5	pH 7.5	pH 7.5
clavulanic acid	0 min	2.77 ± 0.08	2.37 ± 0.05	3.04 ± 0.02	5.75 ± 0.02	5.73 ± 0.02	6.95 ± 0.05
	10 min	2.82 ± 0.02	2.78 ± 0.02	3.31 ± 0.01	6.21 ± 0.02	6.28 ± 0.05	7.02 ± 0.03
	30 min	N/D	3.36 ± 0.03	N/D	6.55 ± 0.04	6.63 ± 0.03	7.21 ± 0.04
	60 min	3.11 ± 0.01	3.52 ± 0.03	3.31 ± 0.04	6.66 ± 0.04	6.93 ± 0.04	7.13 ± 0.09
	360	4.07 ± 0.03	4.22 ± 0.03	3.95 ± 0.01	6.88 ± 0.04	7.57 ± 0.03	6.96 ± 0.02

[a]With 100 mM added $NaHCO_3$.
[b]Without added $NaHCO_3$.

As with penam sulfones, addition of excess bicarbonate to ensure catalytically important Lys70 carbamylation[52] did not significantly influence clavulanic acid inhibition of OXA-10 (pIC_{50} 6.21 and 6.28 with and without added bicarbonate, respectively).

The potency of TEM-116 inhibition by clavulanic acid as measured by pIC_{50} was independent of the pre-incubation time (0-360 min), while with $AmpC_{EC}$ and OXA-10 clavulanic acid potency increased significantly with increased pre-incubation ($AmpC_{EC}$: pIC_{50} 2.37 and 4.22 with 0 min and 360 min, respectively; OXA-10: pIC_{50}: 5.75 and 6.88 with 0 min and 360 min, respectively) (Figure 32). This effect was more pronounced with a shorter pre-incubation time (0-60 min), with potency appearing to plateau on longer pre-incubation (60-360 min). By contrast with $AmpC_{EC}$ inhibition by penam sulfones, no clear pH dependence (pH 7.0-8.0) of clavulanic acid inhibition of $AmpC_{EC}$ was observed (Figure 32).

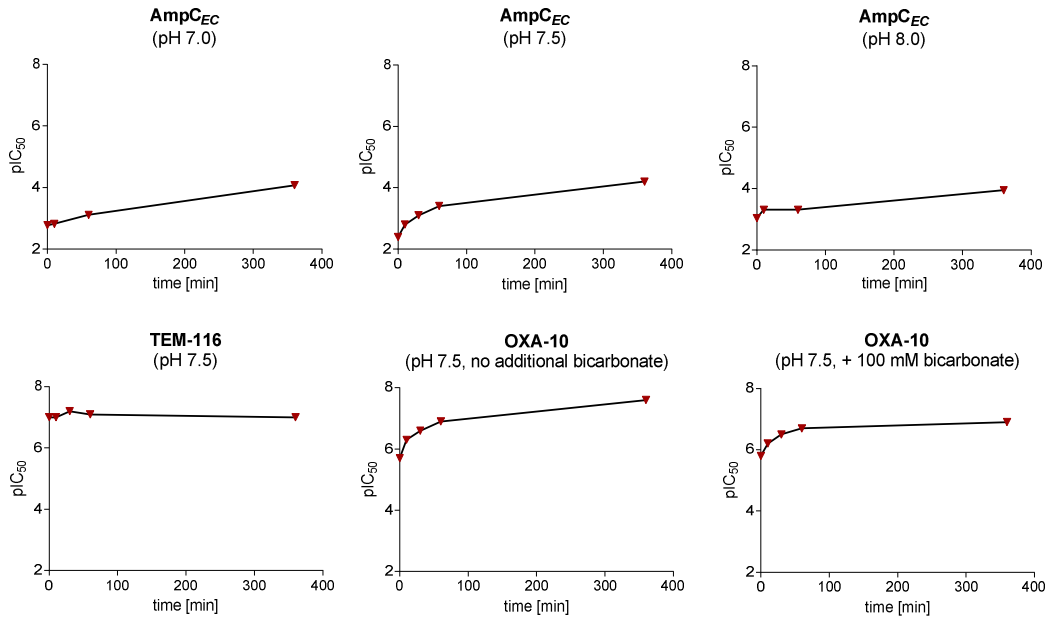


Figure 32: Time dependence of TEM-116, $AmpC_{EC}$, and OXA-10 inhibition by clavulanic acid. Graphical presentation of time-dependencies of pIC_{50}s summarised in Table 10.

2.4.1.2. Detailed kinetic analyses of transient SBL inhibition by clavulanic acid

Consistent with the time dependence of clavulanic acid conferred inhibition of $AmpC_{EC}$ and OXA-10 observed in the dose-dependence studies, significantly slower pseudo first-order rate constants (k_{inact}/K *or* k_2/K) were observed for $AmpC_{EC}$ and OXA-10 (3.0 ± 0.4 M^{-1} s^{-1} and 108.7 ± 3.7 M^{-1} s^{-1}, respectively) compared to TEM-116 (16.5 ± 0.3 x 10^3 M^{-1} s^{-1}) (Figure 33 and Table 11).

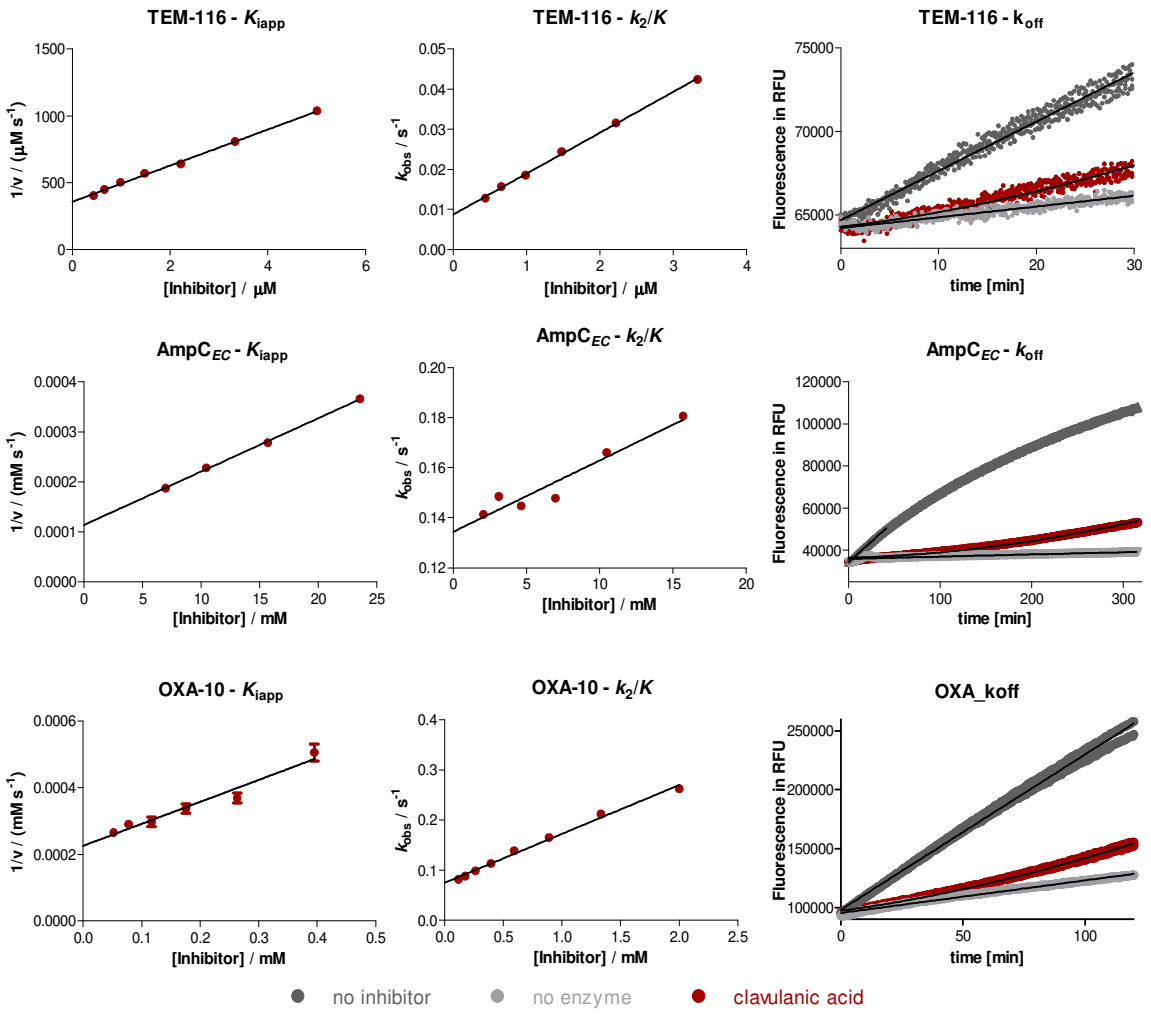


Figure 33: Kinetic characterisation of SBL inhibition by clavulanic acid. Left column: Determination of K_{iapp} values for TEM-116 (1 nM) assayed with NCF (50 µM), AmpC$_{EC}$ (100 nM) assayed with FC-5 (5 µM), and OXA-10 (50 nM) assayed with FC-5 (5 µM). Middle column: Determination of Pseudo first-order rate (k_2/K) determination assayed with the same conditions used for K_{iapp} determination. Right column: Dissociation after 'jump-dilution' of TEM-116, AmpC$_{EC}$, or OXA-10 (3 µM) pre-incubated with clavulanic acid, then diluted 100.000-300.000 fold and assayed with FC-5[44] (25 µM). Buffer: 50 mM phosphate buffer, pH 7.5, 0.01 % (v/v) Triton-X 100. For experiments with OXA-10 the buffer additionally contained 10 mM $NaHCO_3$.

The off-rates (k_{off}) for regeneration of transiently inhibited AmpC$_{EC}$ and OXA-10 were also significantly slower ((13.67 ± 0.04) x 10^{-6} s^{-1} and (61.57 ± 0.28) x 10^{-6} s^{-1}, for AmpC$_{EC}$ and OXA-10, respectively) compared to TEM-116 ((0.34 ± 0.01) x 10^{-3} s^{-1}), resulting in substantially increased half-lives of the inhibited species (845 ± 2 min and 188 ± 1 min for AmpC$_{EC}$ and OXA-10, respectively, compared to 34 ± 1 min for TEM-116) (Figure 33 and Table 11).

The partition ratio (k_{cat}/k_{inact}) for clavulanic acid inhibition of TEM-116 (Table 11) was comparable to those previously observed for tazobactam and enmetazobactam (11 compared to 9 and 4 for tazobactam and enmetazobactam, respectively, Table 4), while for OXA-10 the partition ratio was significantly improved (68 compared to 160 and 1700, respectively, Table 4). With AmpC$_{EC}$ binding of clavulanic acid was too slow to determine the partition ratio.

Table 11: Kinetic parameters for SBL inhibition by clavulanic acid. Values as determined from regressions in Figure 33**.** Buffer: 50 mM phosphate buffer, pH 7.5, 0.01% Triton X-100. For experiments with OXA-10 the buffer additionally contained 10 mM $NaHCO_3$.

	K_{iapp} (µM)	k_{inact}/K (M^{-1} s^{-1})	k_{off} (M^{-1} s^{-1})	$t_{1/2}$ (min)	k_{cat}/k_{inact}
TEM-116	1.63 ± 0.07	(16.5 ± 0.3) x 10^3	(0.34 ± 0.01) x 10^{-3}	34 ± 1	11
$AmpC_{EC}$	9964 ± 528	3.0 ± 0.4	(13.67 ± 0.04) x 10^{-6}	845 ± 2	N/D
OXA-10	342 ± 42	108.7 ± 3.7	(61.57 ± 0.28) x 10^{-6}	188 ± 1	68

2.4.2. Mechanistic studies with clavulanic acid

2.4.2.1. Covalently bound species depend on the mass spectrometric method

Samples of TEM-116, $AmpC_{EC}$, and OXA-10 reacted with 500 equivalents of clavulanic acid were analysed both via LC-MS and SPE-MS. As with the tested penicillanic acid sulfones, and in agreement with previous LC-MS studies with clavulanic acid[15,21,24,28-34], LC-MS analysis only showed +52, + 70, and +88 Da species (i.e. corresponding to **6**, **7**, or **8** in Figure 31 and Figure 34).

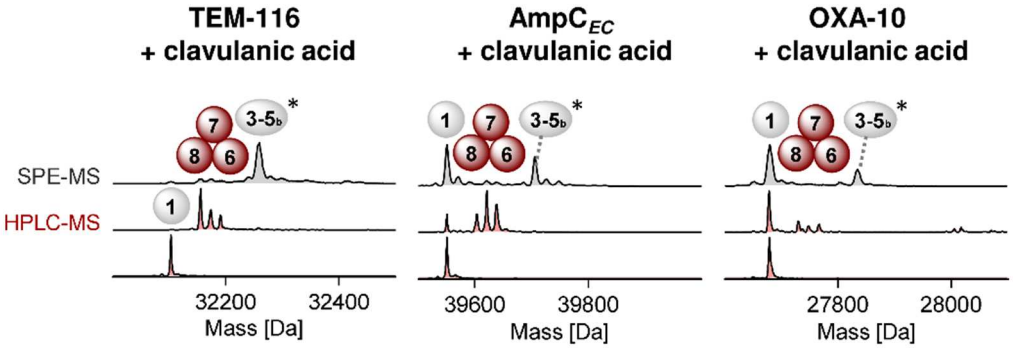


Figure 34: Results from protein-observed MS analysis of the reactions of serine-β-lactamases sulbactam and clavulanic acid. Spectra were acquired after incubation with clavulanic acid. For LC-MS TEM-116, $AmpC_{EC}$ and OXA-10 (1 µM) were incubated with clavulanic acid (500 µM) and for SPE-MS TEM-116, $AmpC_{EC}$ and OXA-10 (3 µM) were incubated with clavulanic acid (300 µM) in 50 mM Tris pH 7.5 at room temperature for 20 min. In the LC-method modified proteins were eluted using a mobile phase of 0.1 % (v/v) aqueous formic acid over approx. 4-5 min; elution using the SPE-method was done using the same mobile phase within 4 sec. See Materials and Methods for details.

By contrast, SPE-MS analysis of equivalent samples only showed +155 Da adducts (Figure 34), likely corresponding to de-carboxy *trans*-enamine **5b** (Figure 31) or equivalent mass species.

Table 12: Modifications to AmpC$_{EC}$, TEM-116, and OXA-10 observed on reaction with clavulanic acid as analysed by liquid chromatography (LC) MS and solid phase extraction (SPE) MS techniques. Differences between measured and expected masses / mass shifts are likely within experimental error. [a]Masses were derived from deconvolution of spectra using the maximum entropy algorithm either in MassLynx V.4.1 (Waters) for LC-MS, or the MassHunter Workstation Qualitative Analysis B.07.00 programme (Agilent Technologies) for SPE-MS. [b]Relative to the measured unmodified protein mass. [c]Proposed structures of the labelled species are given in Figure 31.

		Mass observed[a] [Da]	Mass calculated [Da]	Mass shift observed[b] [Da]	Mass shift calculated [Da]	Assignment[c]	Comments
AmpC$_{EC}$	**LC-MS**	39552	39551				
	+ clavulanic acid	39602	39603	+50	+52	crosslink **8**	or equal mass species
		39621	39621	+69	+70	aldehyde **7**	
		39640	39639	+88	+88	hydrated aldehyde **6**	
	SPE-MS	39551	39551				
	+ clavulanic acid	39706	39706	+155	+155	de-carboxy enamine **5b**	or equal mass species
		39748	39750	+197	+199	enamine **5a**	< 6 min, low abundance
OXA10	**LC-MS**	27681	27682				
	+ clavulanic acid	27732	27734	+51	+52	crosslink **8**	or equal mass species
		27750	27752	+69	+70	aldehyde **7**	
		27768	27770	+87	+88	hydrated aldehyde **6**	
	SPE-MS	27681	27682				
	+ clavulanic acid	27834	27837	+153	+155	de-carboxy enamine **5b**	or equal mass species
		27875	27881	+194	+199	enamine **5a**	or equal mass species
TEM-116	**LC-MS**	32104	32103				
	+ clavulanic acid	32156	32155	+52	+52	crosslink **8**	or equal mass species
		32175	32173	+71	+70	aldehyde **7**	
		32193	32191	+89	+88	hydrated aldehyde **6**	
	SPE-MS	32103	32103				
	+ clavulanic acid	32154	32155	+51	+52	crosslink **8**	> 6h, low abundance
		32187	32191	+84	+88	hydrated aldehyde **6**	
		32258	32258	+155	+155	de-carboxy enamine **5b**	or equal mass species
		32301	32302	+198	+199	enamine **5a**	< 6 min, low abundance

As observed with penam sulfones, addition of 0.1% (*v*/*v*, final concentration) formic acid to TEM-116 and OXA-10 samples reacted with clavulanic acid induced rapid fragmentation of the clavulanic acid derived +155 Da species to give +52, +70, and +88 Da species (likely corresponding to **6**-**8** in Figure 31) within 30 min of formic acid addition, as evident in SPE-MS analyses (Figure 35). In the case of AmpC$_{EC}$, addition of formic acid accelerated the recovery of the unmodified enzyme (Figure 35).

The discrepancies between the clavulanic acid derived covalently bound SBL species observed on short reaction times, using LC- and SPE-MS techniques thus appears to be a result of the milder sample preparation in the SPE-MS set-up.

Efficient fragmentation of the +155 Da species (likely corresponding to **5b** or equivalent mass species, Figure 31) is promoted by the acidic conditions during the chromatography step in the LC-MS workflow, but under neutral conditions fragmented products were not observed on short incubation times (< 20 min) with any of the tested SBLs.

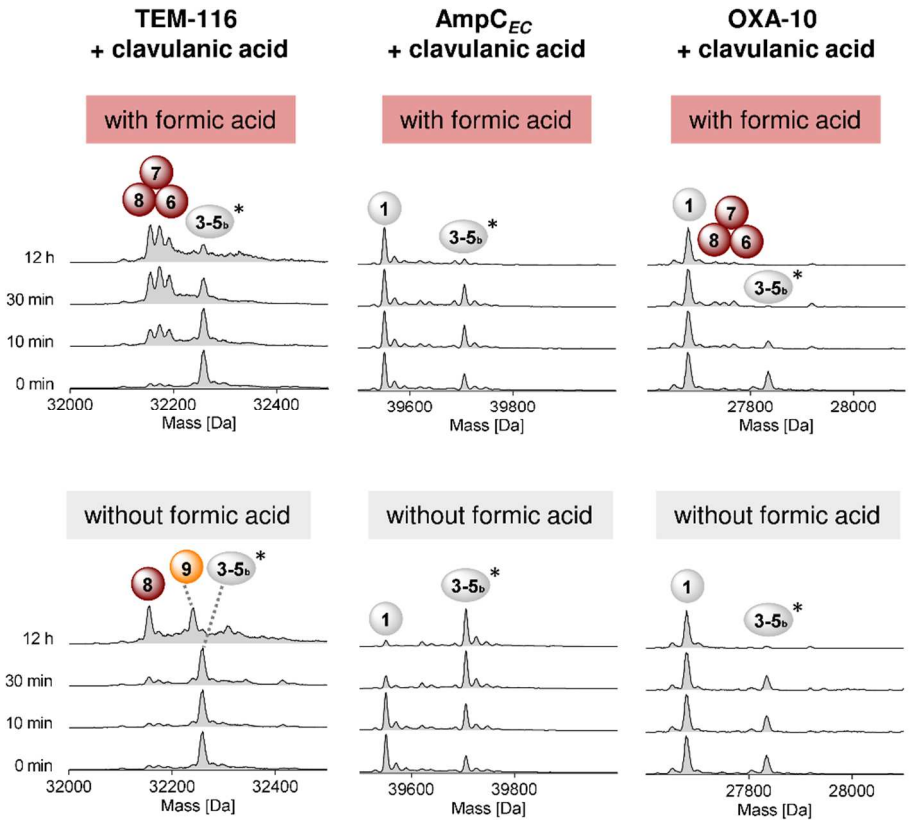


Figure 35: Effect of the addition of formic acid prior to SPE-MS analysis on modifications of TEM-116, AmpC$_{EC}$, and OXA-10 caused by reaction with clavulanic acid. TEM-116, AmpC$_{EC}$, and OXA-10 (3 µM) were reacted with a 500-fold excess of clavulanic acid in 50 mM Tris pH 7.5. Further reaction was induced by addition of formic acid to a final concentration of 0.1 % (v/v). Samples were analysed using the SPE-MS method. Deconvoluted spectra are shown, derived using the maximum entropy algorithm in the MassHunter Workstation Qualitative Analysis B.07.00 programme (Agilent). Proposed assignments are shown in Table 12. Proposed structures corresponding to the labelled mass shifts are given in Figure 31. *Note mass shifts may reflect more than one species, e.g. **3b**-**5b** give the same mass shift.

2.4.2.2. AEC fragmentation is observed on prolonged reaction of Class A SBLs with clavulanic acid

Non-denaturing MS studies were done in collaboration with Mariska de Munnik (University of Oxford).

Next, SPE-MS time-course studies were conducted to investigate potential clavulanic acid derived AEC fragmentation on prolonged reaction as observed on reaction of TEM-116 and OXA-10 with tazobactam and enmetazobactam.

In agreement with the faster binding rates of clavulanic acid inactivation of TEM-116 in the competition studies (Figure 33 and Table 11), modification of TEM-116 was significantly faster than with AmpC$_{EC}$ and OXA-10 (Figure 36). Notably, at early timepoints (5 s - 6 min) small amounts of a +199 Da species were observed, corresponding to a species with the full mass

of clavulanic acid (e.g. **2**-**5a** in Figure 31, or equivalent mass species), in addition to the +155 Da adduct (likely corresponding to a decarboxylated *trans*-enamine **5b**, or equivalent mass species), as previously reported for the Bla$_{MAB}$ β-lactamase from mycobacteria[64]. This is in agreement with a proposed bifurcation of the catalytic pathway, showing efficient turn-over of the carboxy-imine **3a** (or equivalent mass species) and transient inhibition on decarboxylation to give **3b**-**5b**. Notably, while only traces of the +199 Da species were observed on reaction with AmpC$_{EC}$ and OXA-10, a higher abundance was apparent with TEM-116 (Figure 36).

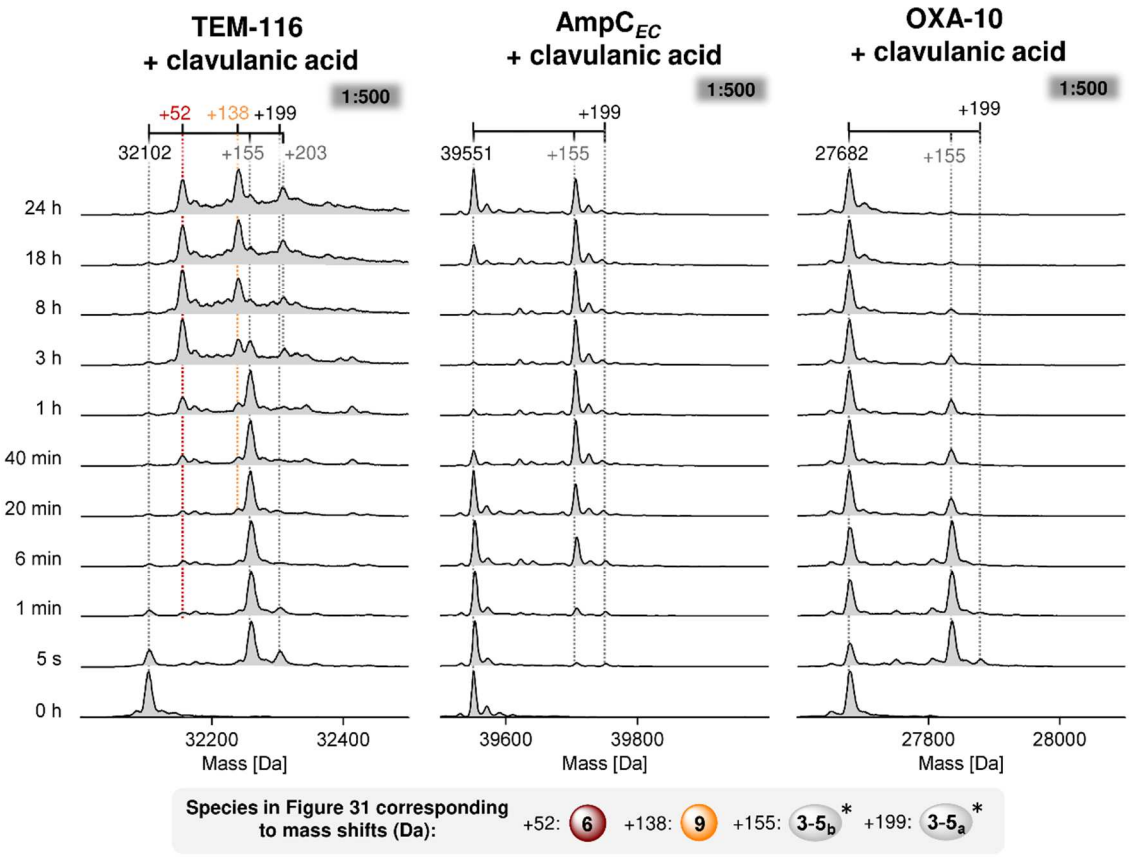


Figure 36: SPE-MS time courses of TEM-116, AmpC$_{EC}$, and OXA-10 modification by clavulanic acid. TEM-116, AmpC$_{EC}$, and OXA-10 (3 µM) were incubated with clavulanic acid (1.5 mM) at room temperature. Buffer: 50 mM Tris buffer pH 7.5. Mass-spectra were acquired without the inhibitor (0 h) and after the indicated times. Deconvoluted spectra are shown, obtained using the maximum entropy algorithm in the MassHunter Workstation Qualitative Analysis B.07.00 programme (Agilent). Proposed assignments are shown in Table 12. Proposed structures corresponding to the labelled mass shifts are given in Figure 31. *Note mass shifts may reflect more than one species, e.g. **3b**-**5b** give the same mass shift.

After ~6 min the +199 Da species was not observed anymore, with the +155 Da adduct dominating with all the tested SBLs. With AmpC$_{EC}$ and OXA-10, the +155 Da adduct slowly reacted to regenerate the unmodified enzyme within 8-18 h.

With the class A SBL TEM-116, some fragmentation of the +155 Da adduct was observed to give a +52 Da species (potentially corresponding to **8** in Figure 31) and +138 Da species,

potentially indicating dehydration of **5b** (or equivalent mass species) to give alkene **9** over the course of 8 h. While the +155 Da species appeared stable over the remaining time (24 h), the +52 Da species appeared to react (possibly, with clavulanic acid degradation products) to give an unidentified +203 Da species (Figure 36).

By contrast with the results for tazobactam and enmetazobactam (Figure 12-13), and reported work on TEM-2 and SHV-1 (both class A SBLs) inhibition by clavulanic acid[29,34], no dehydration of the enzyme to give –18 Da species (**9**-**10**, Figure 2) was observed on reacting TEM-116, $AmpC_{EC}$, or OXA-10 with clavulanic acid.

Non-denaturing MS time-courses on reaction of TEM-116 with 10 or 30 equivalents of lithium clavulanate confirmed +155 Da species as the major species on initial binding after 1 min (Figure 37). However, on prolonged incubation (4-20 min), additional species were observed with +52, +88, +241, and +306 Da mass increments.

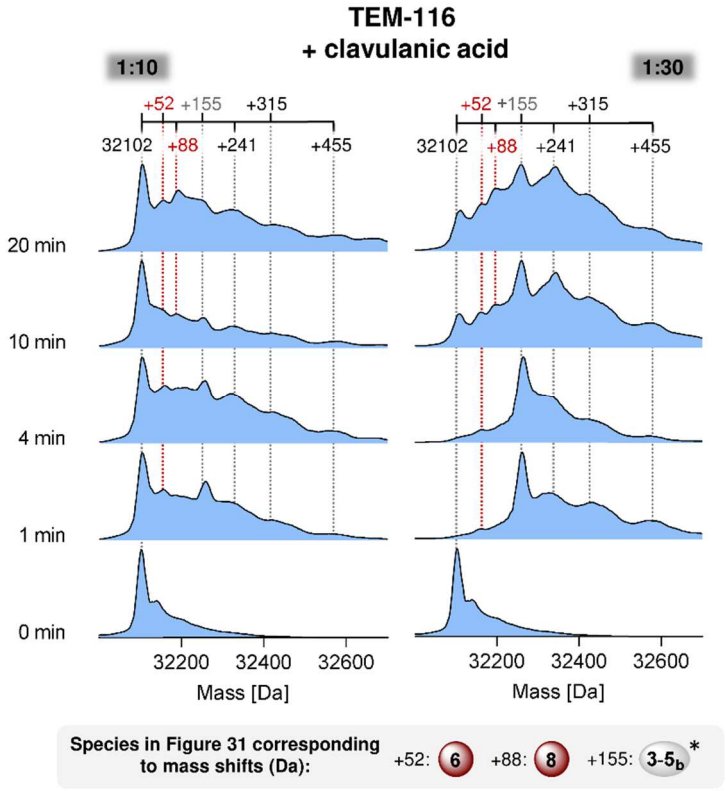


Figure 37: Non-denaturing MS time courses of TEM-116 modification by clavulanic acid. TEM-116 (10 µM) was incubated with lithium clavulanate (100 or 300 µM) at room temperature. Buffer: 50 mM ammonium acetate pH 7.0. Mass-spectra were acquired without the inhibitor (0 min) and after the indicated times. Deconvoluted spectra are shown, obtained using Bayesian deconvolution in UniDec[65]. Proposed assignments are shown in Table 13. Proposed structures corresponding to the labelled mass shifts are given in Figure 31. *Note mass shifts may reflect more than one species, e.g. **3b**-**5b** give the same mass shift.

It is unclear to which extend these species reflect covalently bound complexes, or non-covalent binding of lithium ions as well as one or multiple of the many clavulanic acid degradation products, e.g. the +88 Da and +241 Da species could indicate non-covalent binding of aldehyde **13** (Figure 38), to unmodified and +155 Da modified TEM-116, respectively. Alternatively, the +241 Da species may also result from non-covalent binding of the degradation pyrazine product **16a** (Figure 38) or reaction of multiple TEM-116 residues.

Table 13: Modifications to TEM-116 by reaction with lithium clavulanate as analysed by non-denaturing MS. All differences between measured and calculated masses / mass shifts are likely within experimental error. [a]Masses were derived from deconvolution of measured spectra using the maximum entropy algorithm in MassLynx V.4.1 (Waters). [b]Relative to the measured unmodified protein mass. [c]Proposed product structures are defined in Figure 11 and Figure 38A.

		Mass observed[a] [Da]	Mass calculated [Da]	Mass shift observed[b] [Da]	Mass shift calculated [Da]	Assignment[c]	Comments
Non-denaturing MS (no exposure to formic acid)	**TEM-116** + clavulanic	32108	32103				
		32165	32155	+ 54	+ 52	vinyl-ether crosslink **8**	or equal mass species
		32195	32191	+ 84	+ 88	hydrated aldehyde **6**	or non-covalent binding of **13**
		32259	32258	+ 148	+ 155	decarboxy *trans*-enamine **5b**	or equal mass species
		32343	32344	+ 232	+ 241	vinyl-ether crosslink **8 + 13**	or non-covalent binding of **16a**
		32417		+ 306			
		32557		+ 446			

2.4.2.3. Solution based NMR studies on clavulanic acid hydrolysis

NMR analyses were done in collaboration with Dr Christopher T. Lohans and Prof. Timothy D. W. Claridge (University of Oxford).

As with penam sulfones, no evidence for the non-fragmented species **19**-**21** (Figure 38) was found on SBL catalysed clavulanic acid hydrolysis in solution, as analysed via ^{1}H NMR. Instead, the fragmented amine **12** and aldehyde species **13** were observed (Figure 38A). This suggests that hydrolysis of the nascent acyl-enzyme **2** or imine/enamine intermediates (**3**-**5**, Figure 31) is likely followed by efficient fragmentation in solution which is not observed in the time-frame of NMR analysis and consistent with previous reports on non-enzymatic hydrolysis of clavulanic acid[66,67]. However, as more efficient fragmentation of the acyl-enzyme complex is observed with clavulanic acid than with penam sulfones, part of the observed products in solution may also result from hydrolysis of fragmented acyl-enzyme species (e.g. **6**, Figure 31).

At early time points (5 min), a mixture of both non-decarboxylated (**12**, Figure 38A) and decarboxylated (**15**, Figure 38A) amines was observed, with only the decarboxylated species observed on prolonged reaction (1.5-12 h, Figure 38C-D and Appendix III, Figure S15-16). Aldehyde **13** underwent de-carboxylation to give acetaldehyde **14**. Both aldehyde species were apparently in equilibrium with hydrated diols (**17** and **18,** respectively). The

decarboxylated amine **12** was observed to undergo condensation reactions with aldehydes **13** or **14** to give pyrazines (**16a** and **16b**, Figure 38A), also consistent with studies on the non-enzymatic hydrolysis of clavulanic acid[66,67].

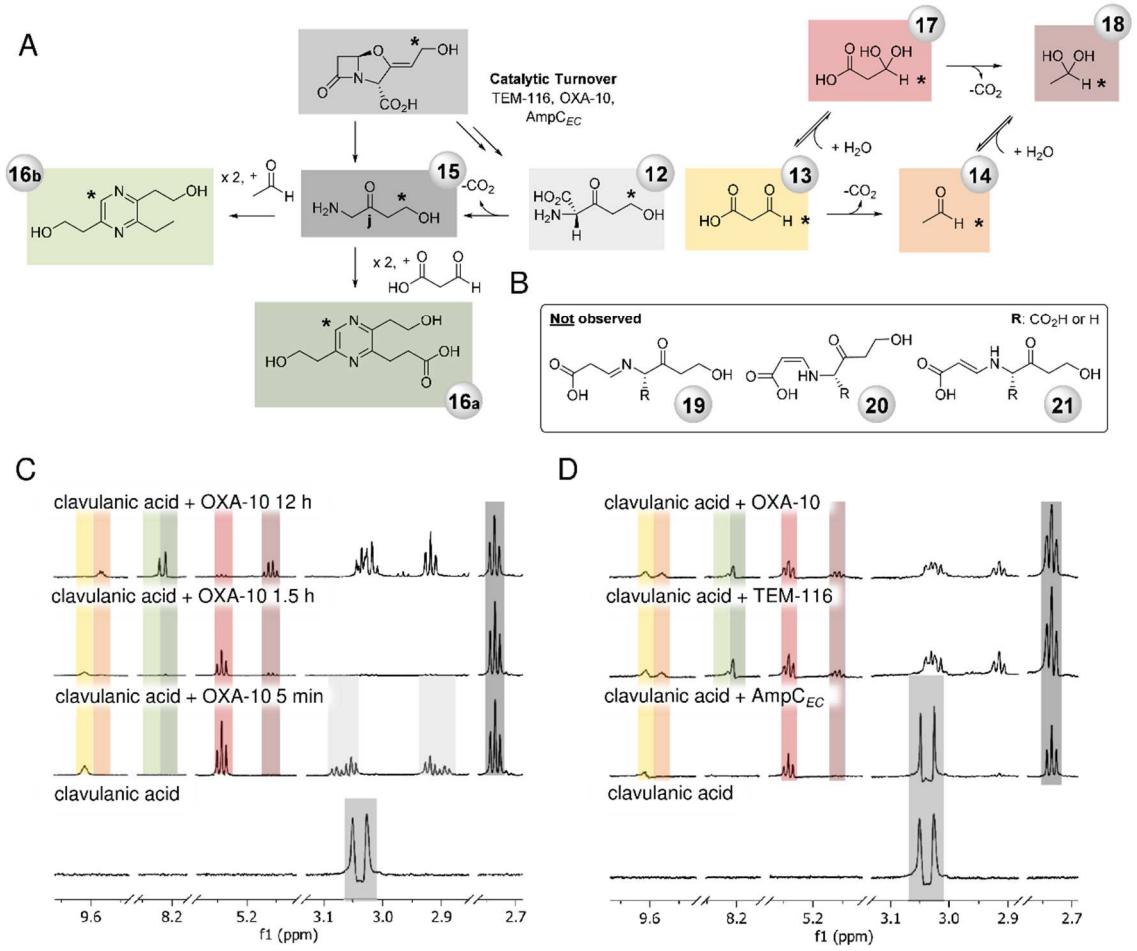


Figure 38: **^{1}H NMR analysis of the reaction of clavulanic acid with OXA-10, TEM-116, or AmpC$_{EC}$.** (A) Degradation products of clavulanic acid formed by reaction with serine β-lactamases and likely subsequent non-enzymatic reactions. *Indicate protons corresponding to shifts shown in (C-D). (B) Compounds not observed in significant amounts. (C) Time course of ^{1}H NMR Spectra (750 MHz) of clavulanic acid (5 mM) reaction with OXA-10 (10 µM). (D) ^{1}H NMR Spectra (750 MHz) of degradation products of clavulanic acid (1 mM) with OXA-10, TEM-116, or AmpC$_{EC}$ (10 µM), incubated for 18 h. All samples were setup in 50 mM phosphate buffer pH 7.5, 10 % D_2O and incubated at room temperature. Full spectra are shown in Appendix III, Figure S15. Chemical shift assignments are shown in Appendix III, Figure S16 and are consistent with previous reports[66,67].

Identification of the carboxy-amine **12** was further supported by HMBC studies showing correlation of the α-proton to both the carboxylic acid (C1 carbon, 168 ppm) and the ketone carbon (C3 carbon, 202 ppm) (Figure 39).

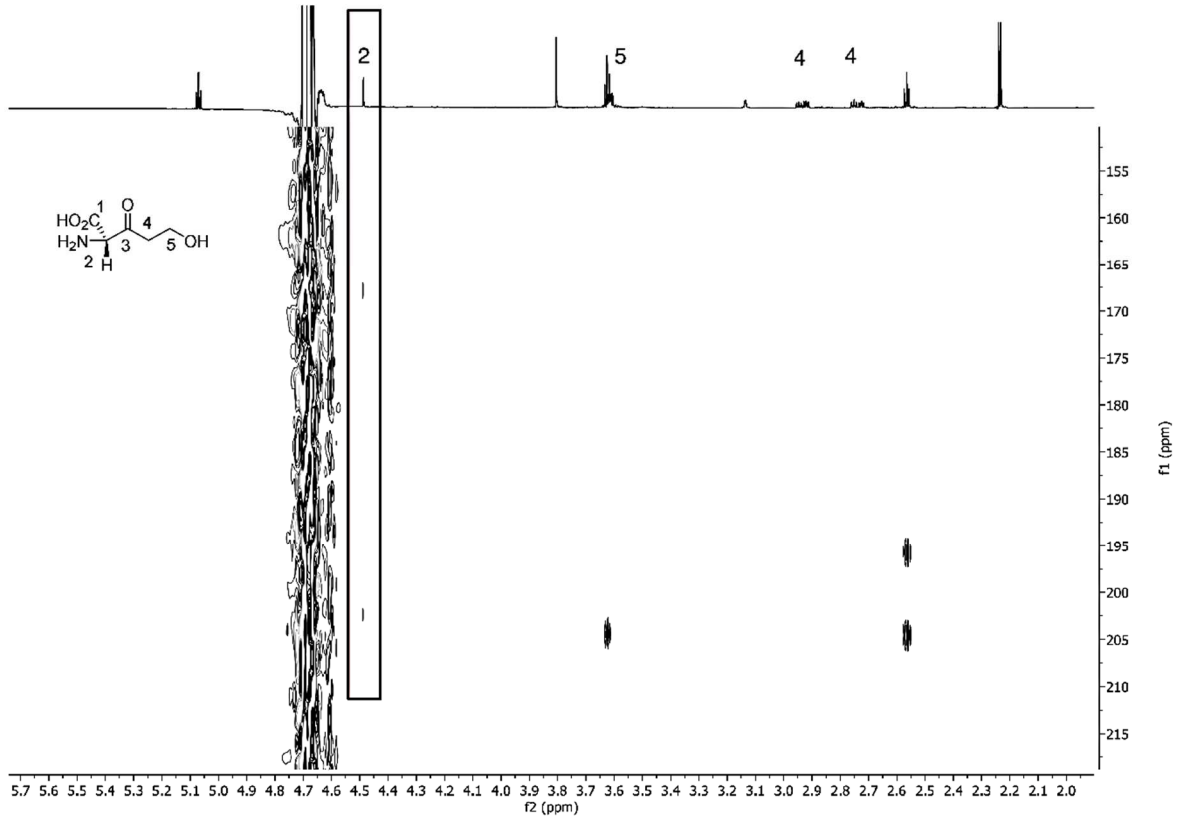


Figure 39: HMBC (700 MHz) analysis of the clavulanic acid derived carboxylated amine 15. Clavulanic acid (5 mM) was incubated with OXA-10 (10 µM) for 5 min at room temperature in 50 mM phosphate buffer, pH 7.5. Note, to differentiate the chemical shift of the α-proton of the carboxylate from the pre-saturation water-suppression and to increase the life-time of the carboxylated species, spectra were recorded at 8 °C, leading to a change in the chemical shift corresponding to the α-proton (4.49 ppm at 8 °C compared to 4.56 ppm at 25 °C).

The NMR studies thus further support efficient SBL catalysed hydrolysis to proceed via hydrolysis of species comprising the intact mass of clavulanic acid (e.g. **3**-**5a** in Figure 31), while transient inhibition is achieved through de-carboxylation to give **3**-**5b** (or equivalent mass species, Figure 31), as evident in the SPE- and non-denaturing-MS studies (Figure 37-38).

2.5. Summary and Conclusion

With the increasing dissemination of β-lactamases, combinations of β-lactam antibiotics with SBLi have become vitally important drugs[31]. However, with the emergence of ESBLs and inhibitor resistant β-lactamases, new and improved SBLi such as enmetazobactam are urgently needed[68]. For their development a detailed understanding of the mechanisms of inhibition will likely be important.

Previous reports on SBL inhibition by penam sulfones had shown partially contradicting results, with Raman[8-14] and UV/Vis[10,15] spectroscopy identifying *trans*-enamine **5**, resulting from opening of both β-lactam and thiazolidine rings, but without fragmentation, as the sole

transitory stable species. However, several ESI-MS studies imply efficient fragmentation of covalently bound sulfone inhibitors to give +52, +70 and +88 Da fragmented species (**6**, **7**, and **8** in Figure 9), with no (or little) evidence for species corresponding to the intact inhibitor mass[15,18-24].

The combined SPE-, LC-, and native-MS results presented in this chapter show that these discrepancies result from acid promoted fragmentation of the acyl-enzyme species (to give +52, +70, and +88 Da species) during LC-MS analysis (Figure 15-17) and that, under biologically relevant conditions and with short reaction times, all three penam sulfones react with $AmpC_{EC}$, TEM-116, and OXA-10 to give predominantly one or more transiently stable species with the full mass of the inhibitors (+314, +300, and +233 Da for enmetazobactam, tazobactam, and sulbactam respectively), likely indicating *trans*-enamine **5** (or an equivalent mass species, Figure 9).

While initial studies using the SPE-MS technique had indicated a unique +169 Da species on reaction of enmetazobactam with all tested SBLs (Figure 12-14), subsequent MS studies under non-denaturing conditions showed that generation of this species is promoted by the high energy applied during ESI-MS analysis (Figure 19-20). Such ESI-MS influenced fragmentation of covalent SBL-inhibitor complexes has also previously been reported with diazabicyclooctanes (see e.g. chapter 3 and ref. [69]). However, the +169 Da species was shown to also occur on incubation of the enmetazobactam derived AEC at increased temperature (>55 °C, Figure 20). This is notable, as a related fragmentation involving loss of SO_2 from 2β-alkenyl penam sulfones has previously been observed and linked to increased activity of these 2β-alkenyl penam sulfones compared to tazobactam against class A and C SBLs[70]. Further development may thus focus on modifying enmetazobactam to react to give the +169 Da species under biologically relevant conditions.

Further, on prolonged reaction of TEM-116 with enmetazobactam or tazobactam, small amounts of a +52 Da species were observed, which is generally thought to reflect a Ser-Ser vinyl-ether cross-linked species (**8** in Figure 9), though there are other possibilities[71-73]. While some previous studies had suggested +52 Da species to confer irreversible inhibition of the SBLs[71] the +52 Da species observed on reaction of TEM-116 with enmetazobactam or tazobactam were eventually hydrolysed and did not appear to lead to irreversible inactivation.

Interestingly, on prolonged reaction of the penam sulfones with TEM-116 and OXA-10 formation of the Dha residue **9** was observed, which can further react with a Lys amine-sidechain to give the cross-linked Lal species **10** (Figure 27). To date Lal **10** has only rarely been identified in natural protein structures under biological conditions (though there are examples, e.g. [74]), which may also be partially due to difficulties in its detection (as it cannot be directly distinguished from Dha **9** by intact protein MS). From the inhibition perspective, the

Dha **9** and Lal cross-linked species **10** are of particular interest as they are the only irreversible modification(s) we observed leading to inactivation of both class A and D SBLs. While a range of small molecules are routinely used in protein engineering to convert serine, or, more commonly, cysteine residues, to Dha **9,** these compounds generally lack sufficient selectivity to be useful for enzyme inhibition in a biological context[61]. Thus, the apparent differences in efficiency of Dha **9** formation between tazobactam and enmetazobactam are intriguing, as they suggest scope for penam sulfone optimisation to result in irreversible β-lactamase inhibition. This is further supported by the reported selective Dha formation on reaction of the class C β-lactamase P99 with β-sultams[75].

In the case of clavulanic acid, the combined SPE-, LC- and native-MS results suggest that rapid fragmentation to give +52, +70 and +88 Da species (with almost full completion within minutes) previously reported[15,21,24,28-34] is also promoted by acidic LC-MS conditions (Figure 34-35). However, while with AmpC$_{EC}$ and OXA-10, predominantly species with a +155 Da mass shift were observed (likely corresponding to the decarboxlated *trans*-enamine **5b**, or equivalent mass species, Figure 31) over 24 h, the SPE-MS results with TEM-116 give evidence for slow fragmentation of the +155 Da species, leading to +52 Da and +136 Da species, likely corresponding to a crosslinked species **8** and alkene **9** (Figure 31), respectively. While these fragmentation reactions are considerably slower than previously proposed[15,21,24,28-34], at least in the case of the +52 Da species, they occur on a faster time scale than the small amounts of fragmentation observed with the penam sulfones, and may be more biologically relevant for inhibition of TEM-116 and, by implication, other class A SBLs.

By contrast with the small amounts of +52 Da fragments observed on TEM-116 reaction with penam sulfones, the +52 Da species observed on reaction with clavulanic acid appeared resistant towards hydrolysis, which may support previous studies suggesting reaction of an initial, hydrolytically instable +52 Da species to give an equivalent mass species stable towards hydrolysis[71]. In the SPE-MS studies the +52 Da species does, however, appear to react to give a + 203 Da species which appears equally stable towards hydrolysis (the nature of this species is unclear and could result from reaction of a second clavulanate molecule).

In summary, the combined results give new insight into central aspects of the mechanisms of enmetazobactam and the widely clinically used drugs, tazobactam, sulbactam, and clavulanic acid. They clarify the fate of the penam sulfone and clavulanic acid derived acyl-enzyme complexes, which react under biologically relevant conditions and on a biologically relevant time scale under opening of the β-lactam fused rings, and, in the case of clavulanic acid, decarboxylation, but without efficient further fragmentation.

Further, the results reveal caveats on the use of established, and very widely used mass spectrometric techniques to study enzyme inhibition through covalent target modification. This is especially important as interest in development of new covalent drugs is continuously growing[76,77].

2.6. Materials and Methods

2.6.1. Materials

Inhibitors were from Sigma Aldrich (tazobactam), Molekula (sulbactam) and MedKoo Biosciences Inc. (enmetazobactam). Nitrocefin was from Toku-E. FC-5 was prepared (by Dr Anna Rydzik, University of Oxford) according to reported procedures[44]. The *E. coli* W3110 strain carrying the pAD7-AmpC$_{EC}$ plasmid was provided by Prof. Dr Malcolm G. P. Page (Jacobs University Bremen). The OXA-10 pET22b-OXA-10 plasmid was provided by Dr Jürgen Brem (Univeristy of Oxford).

2.6.2. Recombinant enzyme production and purification

Recombinant TEM-116 was expressed and purified by Dr Jürgen Brem (Univeristy of Oxford) according to reported procedures[40].

AmpC$_{EC}$ was expressed and purified according to modified reported procedures[42]. AmpC$_{EC}$ was expressed in *E. coli* W3110 using the pAD7 vector. Cells were grown for 9 h at 37 °C in 2TY media supplemented with 12.5 µg ml^{-1} tetracycline. AmpC$_{EC}$ containing cells were resuspended in 20 mM Tris, pH 7.5, supplemented with 10 mM $MgCl_2$, DNAse I (10 µg ml^{-1}, Roche), and a protease inhibitor cocktail (Thermo Fisher Scientific), lysed, centrifuged, filtered, and dialysed against 3 swaps of buffer A (10 mM Tris, pH 6.75). The lysate was loaded onto an SP Sepharose column (100 ml, equilibrated in Buffer A, GE Healthcare), the column was washed with buffer A until the UV trace returned to the initial level (ca. 7 CV), and AmpC$_{EC}$ was eluted in a gradient of 0-100% buffer B (100 mM Tris, pH 7.0, ca. 3 CV).

OXA-10 was expressed and purified according to reported procedures[43]. OXA-10 was expressed in *E. coli* BL21 (DE3) cells using a pET22b vector. Cells were grown in 2TY media supplemented with 25 mg ml^{-1} kanamycin at 37 °C to an OD_{600} of 0.6, then cooled to 18 °C. Protein production was induced by addition of 0.5 mM IPTG and the cells were incubated at 18 °C for 4 h. OXA-10 containing cells were resuspended in 50 mM MES, pH 6.0, supplemented with DNAse I (10 µg ml^{-1}, Roche) and a protease inhibitor cocktail (Thermo Fisher Scientific), lysed, centrifuged and the supernatant was filtered. OXA-10 was immobilised on a SP Sepharose column (100 ml, GE Healthcare) and washed until the UV

trace stabilised, before OXA-10 was eluted in a gradient of 0-100% buffer B (50 mM MES, pH 6.0, 1 M NaCl). The protein was further purified using a Superdex 75 column (300 ml, GE Healthcare), equilibrated in buffer C (50 mM MES, pH 6.0, 100 mM NaCl).

2.6.3. Kinetic assays under steady state conditions

Unless stated otherwise all assays were in 50 mM phosphate buffer, pH 7.5, supplemented with 0.01% (v/v) Triton X-100. Incubations were carried out at room temperature. Absorbance and fluorescent measurements were done with either PHERAstar or CLARIOstar platereaders (both BMG Labtech). Assays with nitrocefin were done in UV transparent plates (Bio-One UV-Star, COC, F-bottom, Greiner), with a total reaction volume of 200 µl. Absorbance was measured at λ_{abs} = 486 nm and using path-length correction. Assays with FC-5 were done in black-walled microplates (Greiner Bio-One µCLEAR, PS, F-bottom, black), with total reaction volumes of either 100 µl (96 well, half are-plates) or 25 µl (386 well plates). Fluorescence intensity was measured at λ_{ex} = 380 nm and λ_{em} = 460 nm. All measurements were done at least in triplicate. Non-linear regression was done using Prism (version 5 or 9, GraphPad Software).

2.6.3.1. Kinetic characterisation of reporter substrates

TEM-116 (1 nM), AmpC$_{EC}$ (500 pM), or OXA-10 (250 pM) were assayed with NCF or FC-5 in varying concentrations. Reaction velocities were obtained from regression of the initial linear slopes and correlated to product formation via linear regression of absorbance or fluorescent signal recorded on full turn-over of the substrate, as indicated by plateauing of the signal. Steady state kinetic parameters V_{max} and K_m were obtained using Michaelis-Menten equation (1).

$$v = V_{max} \frac{[S]}{Km + [S]} \quad (1)$$

with v: reaction velocity; V_{max}: maximum reaction velocity; [S]: substrate concentration proportional; K_m: Michaelis constant (substrate concentration leading to half maximal reaction velocity).

Turnover numbers (k_{cat}) were determined according to equation (2).

$$k_{cat} = \frac{V_{max}}{[E]} \quad (2)$$

with V_{max}: maximum reaction velocity; [E]: enzyme concentration.

2.6.3.2. Dose-dependence studies

For dose-dependence studies TEM-116 (1 nM), AmpC$_{EC}$ (500 pM), or OXA-10 (250 pM) were incubated with inhibitors at varying concentrations for the indicated time, then assayed with 5 µM FC-5. Reactions were initiated by addition of FC-5. Fluorescent intensity was measured in plate-mode in 2.5 min intervals. Reaction velocities were obtained from linear regression of initial slopes and normalised to no-inhibitor and no-enzyme controls. pIC$_{50}$s were determined by non-linear regression in Prism 5 (GraphPad Software).

2.6.3.3. Pseudo first order rate constants and apparent inhibition constants

Pseudo first order rate constants (k_2/K or k_{inact}/K) and apparent inhibition constants (K_{iapp}) were determined according to reported procedures[78]. TEM-116 (1 nM) was assayed with 50 µM NCF in the presence of inhibitors at varying concentrations. AmpC$_{EC}$ (100 nM) and OXA-10 (50 nM) were assayed with 25 µM FC-5. Reactions were initiated by addition of the enzyme using the build-in pump of the plate reader. Absorbance or fluorescent intensity were measured in well-mode in 1.2 s intervals until reactions plateaued.

$K_{iapp'}$ were inferred from the intercept divided by the slope of linear regression of reciprocals of the initial rates against inhibitor concentration [I] and corrected to account for the substrate concentration [I] and Michaelis-constant (K_m) according to equation (3), to give K_{iapp}.

$$K_{iapp} = \frac{{K_{iapp}}'}{1 + \left(\frac{[S]}{K_M}\right)} \tag{3}$$

Pseudo first-order rate constant k_{obs} were obtained fitting the full reaction curves to equation (4).

$$P = V_s t + (V_0 - V_S)\frac{\left(1 - e^{-k_{obs}t}\right)}{k_{obs}} + P_0 \tag{4}$$

with P: formed product, proportional to fluorescence signal; P_0: initial fluorescence; V_0: velocity of no-inhibitor control; V_S: velocity of no-enzyme control to estimate fully inhibited enzyme.

k_2/K' was inferred from linear regression of inhibitor concentration dependence of the resulting k_{obs}, according to equation (5).

$$k_{obs} = k_2 + {k_2}/{K'} * [I] \tag{5}$$

with K' representing the equilibrium coefficient of SBL inhibition in presence of substrate at the specific concentration.

k_2/K' was corrected to account for the substrate concentration [I] and Michaelis-constant (K_m) according to equation (6), to give k_2/K.

$$k_2/_K = \frac{k_2/_{K'}}{1 + \left(\frac{[S]}{K_M}\right)} \tag{6}$$

2.6.3.4. Dissociation rates

Dissociations rates (k_{off}) were determined via jump dilution[56]. TEM-116 (3 µM) was incubated with 300 µM inhibitor for 20 min at room temperature, then serially diluted 100,000 fold. AmpC$_{EC}$ (3 µM) was incubated with 900 µM inhibitor for 20 min at room temperature, then serially diluted 300,000 fold. OXA-10 (3 µM) was incubated with tazobactam (900 µM), enmetazobactam (900 µM), or sulbactam (3 mM) for 15 min at room temperature, then serially diluted 300,000 fold. Reactions were immediately assayed using 25 µM FC-5 and monitored for 30-400 min, then fitted to equation (7).

$$P = V_s t + (V_0 - V_S)\frac{\left(1 - e^{-k_{obs}t}\right)}{k_{obs}} + P_0 \tag{7}$$

with P: formed product, proportional to fluorescence signal; P_0: initial fluorescence; V_0: velocity of no-enzyme control to estimate fully inhibited enzyme; V_S: velocity of no-inhibitor control.

Half-lives for SBL inhibition ($t_{1/2}$) were obtained using equation (8).

$$t_{1/2} = \frac{\ln(2)}{k_{off}} \tag{8}$$

2.6.3.5. Partition ratios

Partition ratios (k_{cat}/k_{inact}) between efficient hydrolysis and transient inhibition were determined according to reported procedures[22]. TEM-116 (1 nM), AmpC$_{EC}$ (500 pM), or OXA-10 (250 pM) were incubated with inhibitors in varying concentrations for 60 min at room temperature, then assayed with FC-5 (5 µM). The partition ratio was estimated as the inhibitor-enzyme ratio resulting in ≥ 90% inhibition.

2.6.4. Mass spectrometry

2.6.4.1. Solid phase extraction mass spectrometry

SBLs (3 µM) in 50 mM Tris pH 7.5 were incubated at room temperature with tazobactam (30 µM or 300 µM), enmetazobactam (30 µM or 300 µM), sulbactam (300 µM or 1.5 mM), or clavulanic acid (300 µM or 1.5 mM). Mass spectra were acquired in positive ion mode using an integrated autosampler/solid phase extraction (SPE) RapidFire365 system (Agilent

Technologies) coupled to an Agilent 6550 Accurate Mass QTOF spectrometer. For the analyses, 50 µl of the solution was loaded onto a C4 SPE cartridge (Agilent Technologies). The cartridge was washed with buffer A (100% water, 0.1% (v/v) formic acid), then eluted into the mass spectrometer in buffer B (15% (v/v) water, 85% (v/v) acetonitrile 0.1% (v/v) formic acid). In between samples the cartridge was re-equilibrated in buffer A. Data were analysed using the maximum entropy deconvolution algorithm integrated in the MassHunter Qualitative Analysis software V.7 (Agilent Technologies).

2.6.4.2. Liquid chromatography mass spectrometry

SBLs (1 µM) in 50 mM Tris pH 7.5 were incubated at room temperature with tazobactam (100 µM), enmetazobactam (100 µM), sulbactam (500 µM), or clavulanic aid (500 µM). Samples were analysed using a Xevo G2-S mass spectrometer (Waters) coupled to an Acquity-UPLC system (Waters), equipped with a ProSwift™ RP-4H 1 mm 50 mm column (Thermo Fisher Scientific). 5 µl of the samples were loaded onto the column equilibrated in buffer A (95% (v/v) water, 5% (v/v) acetonitrile 0.1% (v/v) formic acid) and eluted using a gradient of 5-95% buffer B (5% (v/v) water, 95% (v/v) acetonitrile 0.1% (v/v) formic acid) over 10 min, then introduced directly into the ESI source. All proteins eluted within ~4-5 min. Data were analysed using MassLynx 4.1 (Waters), with deconvolution using the MaxEnt1 algorithm.

2.6.4.3. Non-denaturing mass spectrometry

Prior to use SBLs were dialysed against 1 M ammonium acetate pH 7.5 (3 swaps, overnight, 4 °C) using Slide-A-Lyzer dialysis cassettes (10K MWCO, Thermo Fisher Scientific).

In the case of penam sulfones, SBLs (10 µM) were incubated with tazobactam (200 µM) or enmetazobactam (200 µM) in 1 M ammonium acetate pH 7.5 or 50 mM Tris pH 7.5. Small molecules were removed using Zeba micro spin desalting columns (7K MWCO, pre-equilibrated in 1 M ammonium acetate solution, pH 7.5, Thermo Fisher Scientific) as described by the manufacturer. Samples (3 µl) were loaded into in-house prepared gold-coated capillary needles (Harvard Apparatus) and were injected into a Q-Exactive UHMR Hybrid Quadrupole-Orbitrap mass spectrometer (Thermo Fisher Scientific)[79]. Instrument parameters: capillary voltage 1.2 kV, S-lens RF 200%, mass range from 1,000 to 12,000 m/z, capillary temperature 60 °C, resolution of the instrument 17,500 at m/z = 200 (transient time: 64 ms). The noise level was lowered to 3 (default: 4.64). Where indicated, the HCD activation collisional energy and UHV gas pressure were varied. Calibration of the instruments was performed using a 10 mg ml^{-1} solution of CsI in water. Data were analysed using Xcalibur 4.1 (Thermo Fisher Scientific).

In the case of clavulanic acid, TEM-116 (10 µM) was incubated with lithium clavulanate (100 or 300 µM) in 50 mM ammonium acetate pH 7.0 at room temperature. Samples were directly sprayed into a Synapt HD mass spectrometer (Waters), using an automated chip-based nano-electrospray ion source (TriVersa Nanomate, Advion). Calibration was performed externally, using CsI in water. Data were analysed using MassLynx 4.1 (Waters) and with deconvolution in UniDec[65].

2.6.5. Crystallography

Unless stated otherwise crystallisation was achieved using the sitting drop vapour diffusion technique in low reservoir Intelli-Plates 93-3 (Art Robbins), set up using a Phoenix RE Drop setter instrument (Rigaku). Protein solutions were combined with precipitant solutions at different rations (1:2, 1:1, and 2:1) to give initial drop volumes of 200-300 nl and incubated at room temperature.

2.6.5.1. Crystallisation of AmpC$_{EC}$

AmpC$_{EC}$ (20 mg ml^{-1} in 50 mM Tris pH 7.5) was crystallised using condition B12 (10 mM zinc chloride, 100 mM MES pH 6.0 and 20% (w/v) PEG 6000) of the Pact Premier crystallisation suite (Molecular Dimensions). Optimised grid screens contained 22-27.5% PEG 6000, yielding crystals after 2-7 days of equilibration.

For the AmpC$_{EC}$-enmetazobactam complex crystals of unmodified AmpC$_{EC}$ were transferred into precipitant-solution supplemented with 200 mM enmetazobactam and incubated for 14 min at room temperature, then mounted on nylon loops, cryo cooled, and stored in liquid nitrogen.

2.6.5.2. Crystallisation of OXA-10

OXA-10 (3 µM in 50 mM Tris, pH 7.5) was incubated with tazobactam (300 µM) for 18 h at room temperature, with continuous rocking to achieve apparently complete modification to give the –18 Da species, as verified by SPE-MS. The sample was concentrated to a final OXA-10 concentration of 10 mg ml^{-1}. A broad screen using the Pact Premier suite (Molecular Dimensions) gave crystals in condition G8 (0.2 M sodium sulfate, 0.1 M Bis-Tris propane, pH 7.5, 20 % (w/v) PEG 3350) showing OXA-10 S70Dha modification (PDB: 7B3S) and condition F5 (0.2 M sodium nitrate, 0.1 M Bis-Tris propane pH 6.5, 20 % (w/v) PEG 3350) showing OXA-10 67-70Lal modification (PDB: 7B3R). Crystals appeared within 24 h, were mounted on nylon loops, cryo cooled, and stored in liquid nitrogen.

Crystals of OXA-10 S70Dha-BME (PDB: 7B3U) were obtained by incubating OXA-10 (3 µM) with tazobactam (300 µM) and β-mercaptoethanol (3 mM) in 50 mM Tris, pH 7.5 for 18 h at room temperature, with continuous rocking. Modification of OXA-10 to give the +60 Da species was verified by SPE-MS. Small molecules were removed using an Amicon concentrator (MWCO 10 kDa, Millipore) and the sample was washed with 50 mM Tris pH 7.5, then concentrated to 10 mg ml^{-1}. A broad screen using the Pact Premier suite (Molecular Dimensions) gave crystals in condition F8 (0.2 M sodium sulfate, 0.1 M Bis-Tris propane pH 6.5, 20 % (w/v) PEG 3350). Crystals appeared within 24 h, were mounted on nylon loops, cryo cooled, and stored in liquid nitrogen.

2.6.5.3. Data collection and processing

X-ray diffraction data were collected at 100 K at the MX beamlines at the Diamond Light Source (Didcot, United Kingdom) and were indexed, integrated, and scaled using the Xia2 pipeline[80]. Structures were solved by molecular replacement using Phaser[81] and reported structures of unmodified SBLs as starting models (PDB: 1IEM[47] for AmpC$_{EC}$ and PDB: 1K55[52] for OXA-10). Alternating cycles of refinement with phenix.refine[82] and manual model building in Coot[83] were performed until R_{work} and R_{free} converged.

2.6.6. Nuclear magnetic resonance spectrometry

^{1}H NMR spectra were recorded using a Bruker BioSpin Avance 750 MHz spectrometer or a Bruker Avance III 700 MHz spectrometer, both equipped with a 5 mm TCI cryoprobe. Water signal suppression was achieved using pre-saturation or excitation sculpting with the Perfect Echo pulse sequence[84]. Assays were performed using 10 µM SBL and 1 or 5 mM enmetazobactam, tazobactam, or sulbactam in 50 mM sodium phosphate, pH 7.5, 10% (v/v) D_2O. Chemical shift assignments were based on ^{1}H, COSY, HSQC, and HMBC spectra as well as previous reports[85].

2.6.7. Tryptic digestion and LC-MS/MS analyses

SBLs (3 µM) were incubated with tazobactam (300 µM) or enmetazobactam (300 µM) overnight under continuous rocking, both in the presence and absence of β-mercaptoethanol (1 mM). Conversion to the respective -18 and +60 Da modifications was verified by SPE-MS. Samples were exchanged into 50 mM $NaHCO_3$ using Amicon Ultra centrifugal filters (10 kDa MWCO, Merck Millipore) and concentrated to 8 µM. Proteins were denatured at 95 °C for 10 min, then cooled. DTT (4 mM) was added at room temperature. Then, samples were incubated for 25 min at 56 °C with continuous shaking. After cooling to room temperature

iodoacetamide (8 mM) was added and the samples were incubated in the dark for 30 min at room temperature. Then, residual iodoacetamide was quenched by addition of DTT (4 mM). Trypsin was added (160 nM, 1:50 trypsin:sample protein ratio) and samples were incubated overnight at 37 °C, then quenched with 10% (v/v) aqueous formic acid.

Samples were analysed using an UltiMate 3000 UHPLC coupled to an Orbitrap Eclipse Tribrid mass spectrometer (Thermo Fisher Scientific). Peptides were trapped on a guard column (Acclaim PepMap 100, 75 µm x 2 cm, nanoViper, C18, 3 µm, 100 Å, Thermo Fisher Scientific) using solvent A (0.1% (v/v) aqueous formic acid), then separated on an Acclaim PepMap analytical column (75 µm × 150 mm, RSLC C18, 3 µm, 100 Å, Thermo Fisher Scientific) using a linear gradient (6-45% solvent B (0.1% (v/v) formic acid, 80% acetonitrile, 20% water), flowrate: 300 nl/min, 90 min). Separated peptides were electrosprayed directly into the mass spectrometer operated in positive ion mode with data-dependent acquisition (3 s cycle time). Precursors and products were detected at a resolving power of 60,000 and 30,000 (at m/z 200), respectively. Precursor signals with an intensity >1.0 x 10^{-4} and charge state between 2-7 were isolated with the quadrupole using a 0.7 m/z isolation window (0.5 m/z offset) and subjected to MS/MS fragmentation using higher-energy collision induced dissociation with 30% relative fragmentation energy. MS/MS scans were collected at an AGC setting of 1.0 x 10^4 or a maximum fill time of 100 ms and precursors within 10 ppm were dynamically excluded for 30 s.

Generated raw data files were processed using the Andromeda search engine in MaxQuant (Version 1.6.3.4)[86,87]. Peak lists were searched against individual sequences and potential contaminant proteins. Carbamidomethylation was kept as a fixed modification whereas acetylation (protein *N*-terminus), oxidation (methionine), and dehydration (serine) and its corresponding adducts with BME and DTT were set as variable modifications. Peptide false discovery rate was kept at 1%. Trypsin was set as the protease and up to four missed cleavages were allowed. Spectra identifying crosslinked peptides were manually validated.

2.7. References

1. Lang, P.A.; Raj, R.; Tumber, A.; Lohans, C.T.; Rabe, P.; Robinson, C.V.; Brem, J.; Schofield, C.J. Studies on enmetazobactam clarify mechanisms of widely used β-lactamase inhibitors *Proc. Natl. Acad. Sci. U. S. A.* **2022**, *119* e2117310119.
2. Bush, K.; Bradford, P.A. Interplay between β-lactamases and new β-lactamase inhibitors. *Nat. Rev. Microbiol.* **2019**, *17*, 295-306.
3. Bush, K.; Bradford, P.A. β-Lactams and β-Lactamase Inhibitors: An Overview. *Cold Spring Harb. Perspect. Med.* **2016**, *6*.
4. Drawz, S.M.; Bonomo, R.A. Three decades of β-lactamase inhibitors. *Clin. Microbiol. Rev.* **2010**, *23*, 160-201.
5. Reading, C.; Cole, M. Clavulanic acid: a β-lactamase-inhibiting β-lactam from *Streptomyces clavuligerus*. *Antimicrob. Agents Chemother.* **1977**, *11*, 852-857.

6. English, A.R.; Retsema, J.A.; Girard, A.E.; Lynch, J.E.; Barth, W.E. CP-45,899, a β-Lactamase Inhibitor That Extends the Antibacterial Spectrum of β-Lactams: Initial Bacteriological Characterization. *Antimicrob. Agents Chemother.* **1978**, *14*, 414-419.
7. Aronoff, S.C.; Jacobs, M.R.; Johenning, S.; Yamabe, S. Comparative activities of the β-lactamase inhibitors YTR 830, sodium clavulanate, and sulbactam combined with amoxicillin or ampicillin. *Antimicrob. Agents Chemother.* **1984**, *26*, 580-582.
8. Padayatti, P.S.; Helfand, M.S.; Totir, M.A.; Carey, M.P.; Carey, P.R.; Bonomo, R.A.; van den Akker, F. High Resolution Crystal Structures of the *trans*-Enamine Intermediates Formed by Sulbactam and Clavulanic Acid and E166A SHV-1 β-Lactamase. *J. Biol. Chem.* **2005**, *280*, 34900-34907.
9. Totir, M.A.; Padayatti, P.S.; Helfand, M.S.; Carey, M.P.; Bonomo, R.A.; Carey, P.R.; van den Akker, F. Effect of the Inhibitor-Resistant M69V Substitution on the Structures and Populations of *trans*-Enamine β-Lactamase Intermediates. *Biochemistry* **2006**, *45*, 11895-11904.
10. Kalp, M.; Bethel, C.R.; Bonomo, R.A.; Carey, P.R. Why the Extended-Spectrum β-Lactamases SHV-2 and SHV-5 Are "Hypersusceptible" to Mechanism-Based Inhibitors. *Biochemistry* **2009**, *48*, 9912-9920.
11. Kalp, M.; Totir, M.A.; Buynak, J.D.; Carey, P.R. Different intermediate populations formed by tazobactam, sulbactam, and clavulanate reacting with SHV-1 β-lactamases: Raman crystallographic evidence. *J. Am. Chem. Soc.* **2009**, *131*, 2338-2347.
12. Helfand, M.S.; Taracila, M.A.; Totir, M.A.; Bonomo, R.A.; Buynak, J.D.; van den Akker, F.; Carey, P.R. Raman Crystallographic Studies of the Intermediates Formed by Ser130Gly SHV, a β-Lactamase that Confers Resistance to Clinical Inhibitors. *Biochemistry* **2007**, *46*, 8689-8699.
13. Totir, M.A.; Cha, J.; Ishiwata, A.; Wang, B.; Sheri, A.; Anderson, V.E.; Buynak, J.; Mobashery, S.; Carey, P.R. Why Clinically Used Tazobactam and Sulbactam Are Poor Inhibitors of OXA-10 β-Lactamase: Raman Crystallographic Evidence. *Biochemistry* **2008**, *47*, 4094-4101.
14. Heidari Torkabadi, H.; Che, T.; Shou, J.; Shanmugam, S.; Crowder, M.W.; Bonomo, R.A.; Pusztai-Carey, M.; Carey, P.R. Raman spectra of interchanging β-lactamase inhibitor intermediates on the millisecond time scale. *J. Am. Chem. Soc.* **2013**, *135*, 2895-2898.
15. Frase, H.; Smith, C.A.; Toth, M.; Champion, M.M.; Mobashery, S.; Vakulenko, S.B. Identification of products of inhibition of GES-2 β-lactamase by tazobactam by x-ray crystallography and spectrometry. *J. Biol. Chem.* **2011**, *286*, 14396-14409.
16. Power, P.; Sauvage, E.; Herman, R.; Galleni, M.; Gutkind, G.; Charlier, P.; Kerff, F. Crystal Structure of OXA-24 β-Lactamase Inhibited by Tazobactam. **2014**, 10.2210/pdb3ZNT/pdb.
17. Padayatti, P.S.; Helfand, M.S.; Totir, M.A.; Carey, M.P.; Hujer, A.M.; Carey, P.R.; Bonomo, R.A.; van den Akker, F. Tazobactam Forms a Stoichiometric *trans*-Enamine Intermediate in the E166A Variant of SHV-1 β-Lactamase: 1.63 Å Crystal Structure. *Biochemistry* **2004**, *43*, 843-848.
18. Yang, Y.; Janota, K.; Tabei, K.; Huang, N.; Siegel, M.M.; Lin, Y.I.; Rasmussen, B.A.; Shlaes, D.M. Mechanism of inhibition of the class A β-lactamases PC1 and TEM-1 by tazobactam. Observation of reaction products by electrospray ionization mass spectrometry. *J. Biol. Chem.* **2000**, *275*, 26674-26682.
19. Bonomo, R.A.; Liu, J.; Chen, Y.; Ng, L.; Hujer, A.M.; Anderson, V.E. Inactivation of CMY-2 β-lactamase by tazobactam: initial mass spectroscopic characterization. *Biochim. Biophys. Acta* **2001**, *1547*, 196-205.
20. Pagan-Rodriguez, D.; Zhou, X.; Simmons, R.; Bethel, C.R.; Hujer, A.M.; Helfand, M.S.; Jin, Z.; Guo, B.; Anderson, V.E.; Ng, L.M., et al. Tazobactam Inactivation of SHV-1 and the Inhibitor-resistant Ser^{130}-to-Gly SHV-1 β-Lactamase: Inisghts into the Mechanism of Inhibition. *J. Biol. Chem.* **2004**, *279*, 19494-19501.
21. Bethel, C.R.; Taracila, M.; Shyr, T.; Thomson, J.M.; Distler, A.M.; Hujer, K.M.; Hujer, A.M.; Endimiani, A.; Papp-Wallace, K.; Bonnet, R., et al. Exploring the Inhibition of

CTX-M-9 by β-Lactamase Inhibitors and Carbapenems. *Antimicrob. Agents Chemother.* **2011**, *55*, 3465-3475.
22. Papp-Wallace, K.M.; Bethel, C.R.; Caillon, J.; Barnes, M.D.; Potel, G.; Bajaksouzian, S.; Rutter, J.D.; Reghal, A.; Shapiro, S.; Taracila, M.A., et al. Beyond Piperacillin-Tazobactam: Cefepime and AAI101 as a Potent β-Lactam-β-Lactamase Inhibitor Combination. *Antimicrob. Agents Chemother.* **2019**, *63*, e00105-00119.
23. Thomson, J.M.; Distler, A.M.; Bonomo, R.A. Overcoming Resistance to β-Lactamase Inhibitors: Comparing Sulbactam to Novel Inhibitors against Clavulanate Resistant SHV Enzymes with Substitutions at Ambler Position 244. *Biochemistry* **2007**, *46*, 11361-11368.
24. Cheng, Q.; Xu, C.; Chai, J.; Zhang, R.; Wai chi Chan, E.; Chen, S. Structural Insight into the Mechanism of Inhibitor Resistance in CTX-M-199, a CTX-M-64 Variant Carrying the S130T Substitution. *ACS Infect. Dis.* **2020**, *6*, 577-587.
25. Sun, T.; Bethel, C.R.; Bonomo, R.A.; Knox, J.R. Inhibitor-Resistant Class A β-Lactamases: Consequences of the Ser130-to-Gly Mutation Seen in Apo and Tazobactam Structures of the SHV-1 Variant. *Biochemistry* **2004**, *43*, 14111-14117.
26. Kuzin, A.P.; Nukaga, M.; Nukaga, Y.; Hujer, A.; Bonomo, R.A.; Knox, J.R. Inhibition of the SHV-1 β-Lactamase by Sulfones: Crystallographic Observation of Two Reaction Intermediates with Tazobactam. *Biochemistry* **2001**, *40*, 1861-1866.
27. Tassoni, R.; Blok, A.; Pannu, N.S.; Ubbink, M. New Conformations of Acylation Adducts of Inhibitors of β-Lactamase from *Mycobacterium tuberculosis*. *Biochemistry* **2019**, *58*, 997-1009.
28. Sulton, D.; Pagan-Rodriguez, D.; Zhou, X.; Liu, Y.; Hujer, A.M.; Bethel, C.R.; Helfand, M.S.; Thomson, J.M.; Anderson, V.E.; Buynak, J.D., et al. Clavulanic Acid Inactivation of SHV-1 and the Inhibitor-resistant S130G SHV-1 β-Lactamase: Insights into the Mechanism of Inhibition. *J. Biol. Chem.* **2005**, *280*, 35528-35536.
29. Brown, R.P.A.; Aplin, R.T.; Schofield, C.J. Inhibition of TEM-2 β-Lactamase from *Escherichia coli* by Clavulanic Acid: Observation of Intermediates by Electrospray Ionization Mass Spectrometry. *Biochemistry* **1996**, *35*, 12421-12432.
30. Power, P.; Mercuri, P.; Herman, R.; Kerff, F.; Gutkind, G.; Dive, G.; Galleni, M.; Charlier, P.; Sauvage, E. Novel fragments of clavulanate observed in the structure of the class A β-lactamase from *Bacillus licheniformis* BS3. *J. Antimicrob. Chemother.* **2012**, *67*, 2379-2387.
31. Drawz, S.M.; Bethel, C.R.; Hujer, K.M.; Hurless, K.N.; Distler, A.M.; Caselli, E.; Prati, F.; Bonomo, R.A. The Role of a Second-Shell Residue in Modifying Substrate and Inhibitor Interactions in the SHV β-Lactamase: A Study of Ambler Position Asn276. *Biochemistry* **2009**, *48*, 4557-4566.
32. Papp-Wallace, K.M.; Taracila, M.A.; Smith, K.M.; Xu, Y.; Bonomo, R.A. Understanding the Molecular Determinants of Substrate and Inhibitor Specificities in the Carbapenemase KPC-2: Exploring the Roles of Arg220 and Glu276. *Antimicrob. Agents Chemother.* **2012**, *56*, 4428-4438.
33. Thomson, J.M.; Distler, A.M.; Prati, F.; Bonomo, R.A. Probing Active Site Chemistry in SHV β-Lactamase Variants at Ambler Position 244: Understanding unique Properties of Inhibitor Resistance. *J. Biol. Chem.* **2006**, *281*, 26734-26744.
34. Sulton, D.; Pagan-Rodriguez, D.; Zhou, X.; Liu, Y.; Hujer, A.M.; Bethel, C.R.; Helfand, M.S.; Thomson, J.M.; Anderson, V.E.; Buynak, J.D., et al. Clavulanic acid inactivation of SHV-1 and the inhibitor-resistant S130G SHV-1 β-lactamase. Insights into the mechanism of inhibition. *J. Biol. Chem.* **2005**, *280*, 35528-35536.
35. Tremblay, L.W.; Hugonnet, J.-E.; Blanchard, J.S. Structure of the Covalent Adduct Formed between *Mycobacterium tuberculosis* β-Lactamase and Clavulanate. *Biochemistry* **2008**, *47*, 5312-5316.
36. Chen, C.C.H.; Herzberg, O. Inhibition of β-lactamase by clavulanate: Trapped intermediates in cryocrystallographic studies. *J. Mol. Biol.* **1992**, *224*, 1103-1113.
37. Papp-Wallace, K.M.; Bethel, C.R.; Barnes, M.D.; Rutter, J.D.; Taracila, M.A.; Bajaksouzian, S.; Jacobs, M.R.; Bonomo, R.A. AAI101, a Novel β-Lactamase Inhibitor: Microbiological and Enzymatic Profiling. *Open Forum Infect. Dis.* **2017**, *4*, S375-S375.

38. Tselepis, L.; Langley, G.W.; Aboklaish, A.F.; Widlake, E.; Jackson, D.E.; Walsh, T.R.; Schofield, C.J.; Brem, J.; Tyrrell, J.M. *In vitro* efficacy of imipenem-relebactam and cefepime-AAI101 against a global collection of ESBL-positive and carbapenemase-producing *Enterobacteriaceae*. *Int. J. Antimicrob. Agents* **2020**, *56*, 105925.
39. Isler, B.; Harris, P.; Stewart, A.G.; Paterson, D.L. An update on cefepime and its future role in combination with novel β-lactamase inhibitors for MDR Enterobacterales and *Pseudomonas aeruginosa*. *J. Antimicrob. Chemother.* **2021**, *76*, 550-560.
40. Inglis, S.R.; Strieker, M.; Rydzik, A.M.; Dessen, A.; Schofield, C.J. A boronic-acid-based probe for fluorescence polarization assays with penicillin binding proteins and β-lactamases. *Anal. Biochem.* **2012**, *420*, 41-47.
41. Dubus, A.; Wilkin, J.M.; Raquet, X.; Normark, S.; Frère, J.M. Catalytic mechanism of active-site serine β-lactamases: role of the conserved hydroxy group of the Lys-Thr(Ser)-Gly triad. *Biochem. J.* **1994**, *301*, 485-494.
42. Page, M.G. The kinetics of non-stoichiometric bursts of β-lactam hydrolysis catalysed by class C β-lactamases. *Biochem. J.* **1993**, *295 (Pt 1)*, 295-304.
43. Baurin, S.; Vercheval, L.; Bouillenne, F.; Falzone, C.; Brans, A.; Jacquamet, L.; Ferrer, J.L.; Sauvage, E.; Dehareng, D.; Frere, J.M., et al. Critical role of tryptophan 154 for the activity and stability of class D β-lactamases. *Biochemistry* **2009**, *48*, 11252-11263.
44. van Berkel, S.S.; Brem, J.; Rydzik, A.M.; Salimraj, R.; Cain, R.; Verma, A.; Owens, R.J.; Fishwick, C.W.G.; Spencer, J.; Schofield, C.J. Assay platform for clinically relevant metallo-β-lactamases. *J. Med. Chem.* **2013**, *56*, 6945-6953.
45. Ghavami, A.; Labbé, G.; Brem, J.; Goodfellow, V.J.; Marrone, L.; Tanner, C.A.; King, D.T.; Lam, M.; Strynadka, N.C.J.; Pillai, D.R., et al. Assay for drug discovery: Synthesis and testing of nitrocefin analogues for use as β-lactamase substrates. *Anal. Biochem.* **2015**, *486*, 75-77.
46. Usher, K.C.; Blaszczak, L.C.; Weston, G.S.; Shoichet, B.K.; Remington, S.J. Three-Dimensional Structure of AmpC β-Lactamase from *Escherichia coli* Bound to a Transition-State Analogue: Possible Implications for the Oxyanion Hypothesis and for Inhibitor Design. *Biochemistry* **1998**, *37*, 16082-16092.
47. Powers, R.A.; Caselli, E.; Focia, P.J.; Prati, F.; Shoichet, B.K. Structures of Ceftazidime and Its Transition-State Analogue in Complex with AmpC β-Lactamase: Implications for Resistance Mutations and Inhibitor Design. *Biochemistry* **2001**, *40*, 9207-9214.
48. Crichlow, G.V.; Kuzin, A.P.; Nukaga, M.; Mayama, K.; Sawai, T.; Knox, J.R. Structure of the Extended-Spectrum Class C β-Lactamase of *Enterobacter cloacae* GC1, a Natural Mutant with a Tandem Tripeptide Insertion. *Biochemistry* **1999**, *38*, 10256-10261.
49. McDonough, M.A.; Anderson, J.W.; Silvaggi, N.R.; Pratt, R.F.; Knox, J.R.; Kelly, J.A. Structures of Two Kinetic Intermediates Reveal Species Specificity of Penicillin-binding Proteins. *J. Mol. Biol.* **2002**, *322*, 111-122.
50. Song, Y.; Schowen, R.L.; Borchardt, R.T.; Topp, E.M. Formaldehyde production by Tris buffer in peptide formulations at elevated temperature. *J. Pharm. Sci.* **2001**, *90*, 1198-1203.
51. Nassar, M.N.; Nesarikar, V.N.; Lozano, R.; Parker, W.L.; Huang, Y.; Palaniswamy, V.; Xu, W.; Khaselev, N. Influence of Formaldehyde Impurity in Polysorbate 80 and PEG-300 on the Stability of a Parenteral Formulation of BMS-204352: Identification and Control of the Degradation Product. *Pharm. Dev. Technol.* **2004**, *9*, 189-195.
52. Golemi, D.; Maveyraud, L.; Vakulenko, S.; Samama, J.-P.; Mobashery, S. Critical involvement of a carbamylated lysine in catalytic function of class D β-lactamases. *Proc. Natl. Acad. Sci. U. S. A.* **2001**, *98*, 14280-14285.
53. Cullmann, W. Interaction of β-Lactamase Inhibitors with Various β-Lactamases. *Chemotherapy* **1990**, *36*, 200-208.
54. Bernhard, F.; Odedra, R.; Sordello, S.; Cardin, R.; Franzoni, S.; Charrier, C.; Belley, A.; Warn, P.; Machacek, M.; Knechtle, P. Pharmacokinetics-Pharmacodynamics of Enmetazobactam Combined with Cefepime in a Neutropenic Murine Thigh Infection Model. *Antimicrob. Agents Chemother.* **2020**, *64*, e00078-00020.

55. Williams, J.W.; Morrison, J.F. The kinetics of reversible tight-binding inhibition. In *Methods in Enzymology*, Academic Press: **1979**; Vol. 63, pp. 437-467.
56. Copeland, R.A.; Basavapathruni, A.; Moyer, M.; Scott, M.P. Impact of enzyme concentration and residence time on apparent activity recovery in jump dilution analysis. *Anal. Biochem.* **2011**, *416*, 206-210.
57. Chang, C., Maltseva, N., Endres, M., Joachimiak, A., Center for Structural Genomics of Infectious Diseases (CSGID). Class C β-lactamase from *Escherichia coli* in complex with Tazobactam. **2020**, 10.2210/pdb6wa7/pdb.
58. Lang, P.A.; Parkova, A.; Leissing, T.M.; Calvopina, K.; Cain, R.; Krajnc, A.; Panduwawala, T.D.; Philippe, J.; Fishwick, C.W.; Trapencieris, P., et al. Bicyclic Boronates as Potent Inhibitors of AmpC, the Class C β-Lactamase from *Escherichia coli*. *Biomolecules* **2020**, *10*, 899.
59. Liebschner, D.; Afonine, P.V.; Moriarty, N.W.; Poon, B.K.; Sobolev, O.V.; Terwilliger, T.C.; Adams, P.D. Polder maps: improving OMIT maps by excluding bulk solvent. *Acta Crystallogr. D* **2017**, *73*, 148-157.
60. Danel, F.; Frère, J.-M.; Livermore, D.M. Evidence of dimerisation among class D β-lactamases: kinetics of OXA-14 β-lactamase. *Biochim. Biophys. Acta* **2001**, *1546*, 132-142.
61. Dadová, J.; Galan, S.R.G.; Davis, B.G. Synthesis of modified proteins via functionalization of dehydroalanine. *Curr. Opin. Chem. Biol.* **2018**, *46*, 71-81.
62. Vercheval, L., Kerff, F., Sauvage, E., Herman, R., Galleni, M., Charlier, P. Crystal structure of the class D β-lactamase OXA-10 at 1.35 Å resolution. **2010**, 10.2210/pdb2X02/pdb.
63. Poelarends, G.J.; Johnson, W.H., Jr.; Murzin, A.G.; Whitman, C.P. Mechanistic characterization of a bacterial malonate semialdehyde decarboxylase: identification of a new activity on the tautomerase superfamily. *J. Biol. Chem.* **2003**, *278*, 48674-48683.
64. Soroka, D.; Ourghanlian, C.; Compain, F.; Fichini, M.; Dubée, V.; Mainardi, J.-L.; Hugonnet, J.-E.; Arthur, M. Inhibition of β-lactamases of mycobacteria by avibactam and clavulanate. *J. Antimicrob. Chemother.* **2016**, *72*, 1081-1088.
65. Marty, M.T.; Baldwin, A.J.; Marklund, E.G.; Hochberg, G.K.A.; Benesch, J.L.P.; Robinson, C.V. Bayesian Deconvolution of Mass and Ion Mobility Spectra: From Binary Interactions to Polydisperse Ensembles. *Anal. Chem.* **2015**, *87*, 4370-4376.
66. Finn, M.J.; Harris, M.A.; Hunt, E.; Zomaya, I.I. Studies on the hydrolysis of clavulanic acid. *J. Chem. Soc., Perkin Trans. 1* **1984**, 1345-1349.
67. Haginaka, J.U.N.; Yasuda, H.; Uno, T.; Nakagawa, T. Degradation of Clavulanic Acid in Aqueous Alkaline Solution: Isolation and Structural Investigation of Degradation Products. *Chem. Pharm. Bull. (Tokyo)* **1985**, *33*, 218-224.
68. Tooke, C.L.; Hinchliffe, P.; Bragginton, E.C.; Colenso, C.K.; Hirvonen, V.H.A.; Takebayashi, Y.; Spencer, J. β-Lactamases and β-Lactamase Inhibitors in the 21st Century. *J. Mol. Biol.* **2019**, *431*, 3472-3500.
69. Ehmann, D.E.; Jahic, H.; Ross, P.L.; Gu, R.F.; Hu, J.; Durand-Reville, T.F.; Lahiri, S.; Thresher, J.; Livchak, S.; Gao, N., et al. Kinetics of avibactam inhibition against Class A, C, and D β-lactamases. *J. Biol. Chem.* **2013**, *288*, 27960-27971.
70. Richter, H.G.F.; Angehrn, P.; Hubschwerlen, C.; Kania, M.; Page, M.G.P.; Specklin, J.-L.; Winkler, F.K. Design, Synthesis, and Evaluation of 2β-Alkenyl Penam Sulfone Acids as Inhibitors of β-Lactamases. *J. Med. Chem.* **1996**, *39*, 3712-3722.
71. Heidari-Torkabadi, H.; Bethel, C.R.; Ding, Z.; Pusztai-Carey, M.; Bonnet, R.; Bonomo, R.A.; Carey, P.R. “Mind the Gap”: Raman Evidence for Rapid Inactivation of CTX-M-9 β-Lactamase Using Mechanism-Based Inhibitors that Bridge the Active Site. *J. Am. Chem. Soc.* **2015**, *137*, 12760-12763.
72. Helfand, M.S.; Bethel, C.R.; Hujer, A.M.; Hujer, K.M.; Anderson, V.E.; Bonomo, R.A. Understanding resistance to β-lactams and β-lactamase inhibitors in the SHV β-lactamase: lessons from the mutagenesis of Ser-130. *J. Biol. Chem.* **2003**, *278*, 52724-52729.

73. Brenner, D.G.; Knowles, J.R. Penicillanic acid sulfone: nature of irreversible inactivation of the RTEM β-lactamase from *Escherichia coli*. *Biochemistry* **1984**, *23*, 5833-5839.
74. Lynch, M.J.; Miller, M.; James, M.; Zhang, S.; Zhang, K.; Li, C.; Charon, N.W.; Crane, B.R. Structure and chemistry of lysinoalanine crosslinking in the spirochaete flagella hook. *Nat. Chem. Biol.* **2019**, *15*, 959-965.
75. Tsang, W.Y.; Ahmed, N.; Hinchliffe, P.S.; Wood, J.M.; Harding, L.P.; Laws, A.P.; Page, M.I. Different Transition-State Structures for the Reactions of β-Lactams and Analogous β-Sultams with Serine β-Lactamases. *J. Am. Chem. Soc.* **2005**, *127*, 17556-17564.
76. Scott, K.A.; Njardarson, J.T. Analysis of US FDA-Approved Drugs Containing Sulfur Atoms. In *Sulfur Chemistry*, Jiang, X., Ed. Springer International Publishing: Cham, **2019**; pp. 1-34.
77. Zhao, C.; Rakesh, K.P.; Ravidar, L.; Fang, W.-Y.; Qin, H.-L. Pharmaceutical and medicinal significance of sulfur (S^{VI})-Containing motifs for drug discovery: A critical review. *Eur. J. Med. Chem.* **2019**, *162*, 679-734.
78. Morrison, J.F.; Walsh, C.T. The behavior and significance of slow-binding enzyme inhibitors. *Advanc. Enzymol. Rel. Areas Molecular Biol.* **1988**, *61*, 201-301.
79. Hernandez, H.; Robinson, C.V. Determining the stoichiometry and interactions of macromolecular assemblies from mass spectrometry. *Nat. Protoc.* **2007**, *2*, 715-726.
80. Winter, G. xia2: an expert system for macromolecular crystallography data reduction. *J. Appl. Crystallogr.* **2010**, *43*, 186-190.
81. McCoy, A.J.; Grosse-Kunstleve, R.W.; Adams, P.D.; Winn, M.D.; Storoni, L.C.; Read, R.J. Phaser crystallographic software. *J. Appl. Crystallogr.* **2007**, *40*, 658-674.
82. Adams, P.D.; Grosse-Kunstleve, R.W.; Hung, L.W.; Ioerger, T.R.; McCoy, A.J.; Moriarty, N.W.; Read, R.J.; Sacchettini, J.C.; Sauter, N.K.; Terwilliger, T.C. PHENIX: building new software for automated crystallographic structure determination. *Acta Crystallogr. D* **2002**, *58*, 1948-1954.
83. Emsley, P.; Lohkamp, B.; Scott, W.G.; Cowtan, K. Features and development of Coot. *Acta Crystallogr. D* **2010**, *66*, 486-501.
84. Hwang, T.L.; Shaka, A.J. Water Suppression That Works. Excitation Sculpting Using Arbitrary Wave-Forms and Pulsed-Field Gradients. *J. Magn. Reson., Ser A* **1995**, *112*, 275-279.
85. Poelarends, G.J.; Johnson, W.H., Jr.; Murzin, A.G.; Whitman, C.P. Mechanistic characterization of a bacterial malonate semialdehyde decarboxylase: identification of a new activity on the tautomerase superfamily. *J. Biol. Chem.* **2003**, *278*, 48674-48683.
86. Cox, J.; Mann, M. MaxQuant enables high peptide identification rates, individualized p.p.b.-range mass accuracies and proteome-wide protein quantification. *Nat. Biotechnol.* **2008**, *26*, 1367-1372.
87. Cox, J.; Neuhauser, N.; Michalski, A.; Scheltema, R.A.; Olsen, J.V.; Mann, M. Andromeda: A Peptide Search Engine Integrated into the MaxQuant Environment. *J. Proteome Res.* **2011**, *10*, 1794-1805.

Chapter 3

AmpC$_{EC}$ interactions with Diazabicyclooctanes

The work in this chapter was carried out in conjunction with Dr Jürgen Brem, who advised on the experimental design, and Dr Thomas M. Leissing, who assisted with crystallographic experiments. KPC enzymes were produced by Catherine L. Tooke under supervision of Prof. James Spencer (University of Bristol). The work described herein has been reported in the academic literature[1,2].

Contents

3.1. Introduction 97
3.2. Steady-state kinetics of AmpC$_{EC}$ inhibition by diazabicyclooctanes 98
3.3. Microbiological analyses 101
3.4. Mass spectrometry 102
3.4.1. Analysis of SBL modifications observed on reaction with DBOs 102
3.4.2. Mass spectrometric assay to study relative thermodynamic stability of AmpC$_{EC}$-DBO complexes 106
3.5. Structural characterisation of AmpC$_{EC}$-DBO interactions 109
3.5.1. Crystal structure of AmpC$_{EC}$ in complex with avibactam 109
3.5.2. Crystal structure of AmpC$_{EC}$ in complex with relebactam 110
3.5.3. Crystal structure of AmpC$_{EC}$ in complex with nacubactam 111
3.5.4. Crystal structure of AmpC$_{EC}$ in complex with zidebactam 112
3.5.5. Comparison of DBO binding modes at AmpC$_{EC}$ active site 114
3.6. Summary and Conclusions 118
3.7. Materials and Methods 119
3.7.1. Materials 119
3.7.2. Recombinant enzyme production and purification 119
3.7.3. Kinetics 120
3.7.4. Mass spectrometry 120
3.7.5. Antimicrobial susceptibility testing 120
3.7.6. X-ray crystallography 120
3.8. References 121

3.1. Introduction

As shown in Chapter 2, a major drawback of the classical, β-lactam based, β-lactamase inhibitors is their low potency against class C serine β-lactamases, which renders them essentially ineffective against AmpC hyperproducing strains and other class C SBL harbouring bacteria[3]. The first clinically useful β-lactamase inhibitor with good potency against class C enzymes, avibactam (formerly NXL-104), was approved in 2015 to be used in combination with the third-generation cephalosporin ceftazidime (CZA, combination marketed as Avycaz), a preferred substrate of AmpC$_{EC}$[4].

Avibactam is a diazabicyclooctane (DBO) and was the first β-lactamase inhibitor that does not contain the β-lactam motif to acquire FDA approval[4]. Other than the β-lactam containing β-lactamase inhibitors, avibactam inhibits SBLs reversibly via reaction with the nucleophilic Ser residue (Ser64 in the case of AmpC$_{EC}$) under formation of a covalent carbamoyl-enzyme complex[5-7]. The detailed mechanism of both carbamoylation and de-carbamoylation of AmpC$_{EC}$ has not been fully elucidated yet. In general two different mechanisms are proposed: a) a two-base mechanism involving both Lys67 and Tyr150 for deprotonation of Ser64 to initiate carbamoylation and the *N*-sulfate nitrogen during de-carbamoylation (Figure 1) and b) a single base mechanism with deprotonation steps solely catalysed by Tyr150[8].

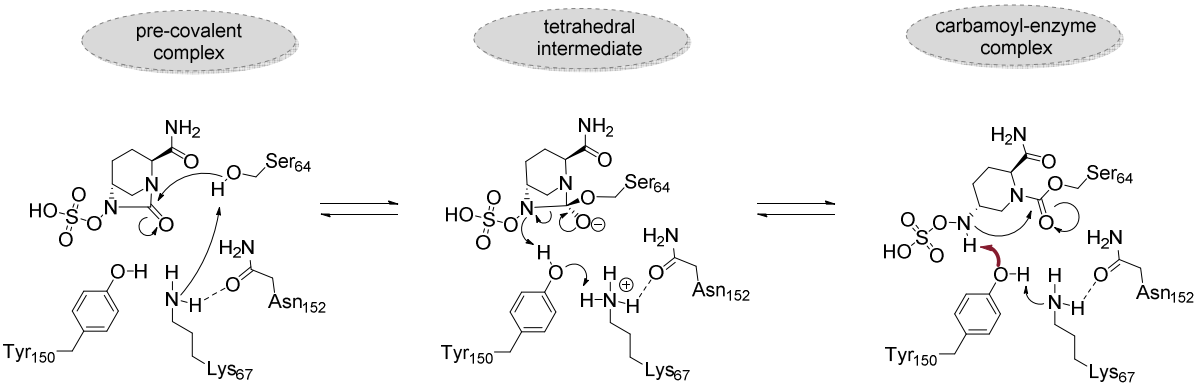


Figure 1: Proposed outline mechanism of AmpC$_{EC}$ inhibition by avibactam. Note: While either a two-base mechanism including Lys67 and Tyr150 (shown here) or a single-base mechanism involving only Tyr150 (not shown) have been proposed for deprotonation and reprotonation of Ser64, in both scenarios recyclisation requires deprotonation of the DBO *N*-sulfate nitrogen by Tyr150[8]. The figure and figure legend are modified with permission from Lang *et al*. Antimicrob. Agents Chemother. 65, e02073-20.

Since the clinical introduction of avibactam, many efforts have been made to optimise its relatively compact structure (MW: 265 Da). While modifications to the diazabicyclooctane core have also been explored (producing e.g. Durlobactam, formerly ETX-2514[9,10], see Chapter 1), much of these efforts have been focused on modification of the C2 amido sidechain (Figure 2), which is positioned similarly to the C6 or C7 sidechains of penicillins and cephalosporins on binding to SBLs. This has resulted in several new inhibitors being either

already approved for clinical use, or which are currently undergoing late-stage clinical testing. These include relebactam[11] (REL, formerly MK-7655, for use in combination with imipenem and cilastatin, marketed as Recarbrio), nacubactam[12] (NAC, formerly OP-0595 or RG6080, currently in Phase II in combination with meropenem), and zidebactam[13] (ZID, formerly WCK-5107, currently in Phase II in combination with cefepime).

By contrast with extensive studies on the structural basis of the inhibition of a wide variety of SBLs by avibactam (e.g. [14-20]), structural information on the binding of modified DBOs is more limited[2,8,12,21-23]. This Chapter aims to address this gap by studying AmpC$_{EC}$ inhibition by AVI, REL, NAC, and ZID, both from a kinetic and a structural perspective, to support SAR guided efforts for the further development of DBOs as class C β-lactamase inhibitors.

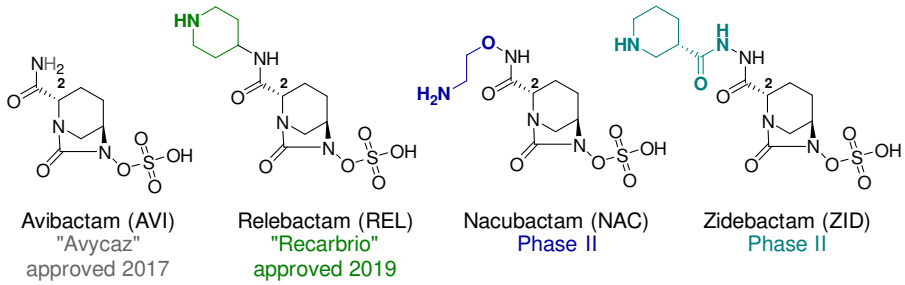


Figure 2: Diazabicyclooctane (DBO) β-lactamase inhibitors studied in this Chapter.

3.2. Steady-state kinetics of AmpC$_{EC}$ inhibition by diazabicyclooctanes

Initially, dose-dependence assays were carried out in competition with FC-5[24], with varying pre-incubation times (0 – 360 min) of AVI, REL, NAC, or ZID with AmpC$_{EC}$, and at pH 7.0, 7.5, and 8.0 (Figure 3 and Table 1).

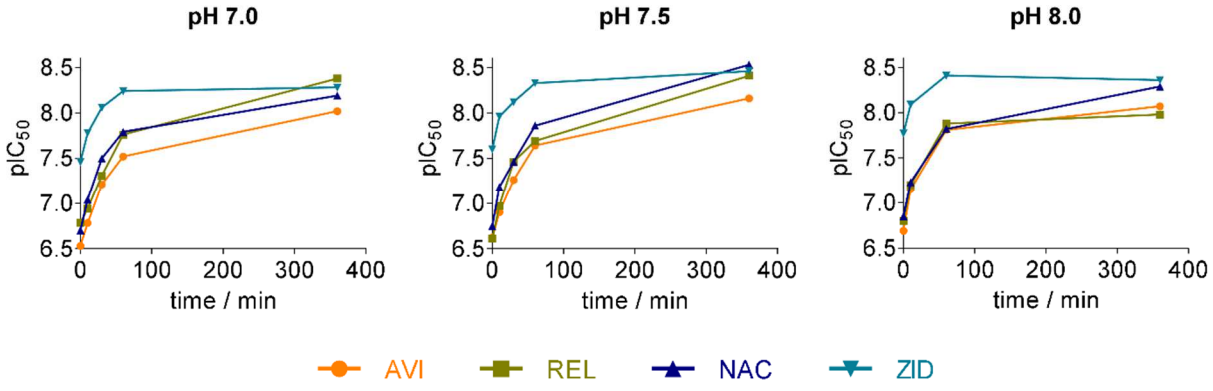


Figure 3: Time- and pH-dependence of AmpC$_{EC}$ inhibition by AVI, NAC, or ZID. pIC$_{50}$ values shown were determined via non-linear regression shown in Appendix IV, Figure S17 and summarised in Table 1. The figure is adopted with permission from Lang *et al.* Antimicrob. Agents Chemother. 2021, *65*, e02073-20.

All the tested DBOs were potent inhibitors of AmpC$_{EC}$, with pIC$_{50}$s > 6.5 under all the tested conditions. Notably, without pre-incubation time ZID was ~ 10-fold more potent than AVI, REL, and NAC (pIC$_{50}$ 7.60, compared to 6.63, 6.61, and 6.75, respectively, at pH 7.5, Figure 3B). The potency of all DBOs was increased on prolonged preincubation, before apparently reaching an equilibrium after 60 – 360 min. Interestingly, the differences in potency observed between ZID and the other DBOs diminished on equilibration, with all DBOs showing similar potency after 360 min of preincubation (pIC$_{50}$s of 8.46, 8.16, 8.41, and 8.53 for ZID, AVI, REL, and NAC, respectively, at pH 7.5, Figure 3).

Within the tested pH range (7.0 – 8.0), no strong effect on DBO inhibition was observed. However, a clear trend showed consistently improved potency of all DBOs at more basic pH when tested without preincubation, most strongly observed for ZID (pIC$_{50}$ 7.46 at pH 7.0, compared to 7.77 at pH 8.0, Figure 3). Under equilibrium conditions this effect again vanished (e.g. pIC$_{50}$ ZID: 8.28, 8.46, and 8.36, at pH 7.0, 7.5, and 8.0, respectively, after 360 min preincubation) suggesting a kinetic, rather than thermodynamic basis (Figure 3 and Table 1).

Table 1: pIC$_{50}$s for AmpC$_{EC}$ inhibition by AVI, NAC, or ZID, measured at varying pre-incubation time and pH. pIC$_{50}$ values as determined via non-linear regression shown in Appendix IV, Figure S17. AmpC$_{EC}$ (500 pM) was preincubated with the inhibitors for the indicated times at room temperature, then assayed using 5 µM FC-5[24]. Buffer: 50 mM phosphate buffer, pH 7.0, 7.5, or 8.0, containing 0.01% (*v*/*v*) Triton X-100. ND: Not determined.

		pIC$_{50}$ (mean ± SD)		
	time	**pH 7.0**	**pH 7.5**	**pH 8.0**
AVI	0 min	6.53 ± 0.06	6.62 ± 0.04	6.69 ± 0.02
	10 min	6.78 ± 0.04	6.90 ± 0.03	7.15 ± 0.03
	30 min	7.21 ± 0.08	7.26 ± 0.03	*ND*
	60 min	7.52 ± 0.05	7.64 ± 0.01	7.81 ± 0.04
	360 min	8.02 ± 0.04	8.16 ± 0.02	8.07 ± 0.06
REL	0 min	6.78 ± 0.08	6.61 ± 0.04	6.80 ± 0.02
	10 min	6.94 ± 0.05	6.97 ± 0.04	7.20 ± 0.02
	30 min	7.31 ± 0.04	7.46 ± 0.03	*ND*
	60 min	7.76 ± 0.05	7.69 ± 0.02	7.88 ± 0.05
	360 min	8.38 ± 0.03	8.41 ± 0.01	7.98 ± 0.08
NAC	0 min	6.70 ± 0.03	6.75 ± 0.04	6.85 ± 0.01
	10 min	7.04 ± 0.03	7.18 ± 0.01	7.23 ± 0.01
	30 min	7.50 ± 0.05	7.46 ± 0.02	*ND*
	60 min	7.79 ± 0.06	7.86 ± 0.02	7.82 ± 0.03
	360 min	8.19 ± 0.04	8.53 ± 0.02	8.29 ± 0.03
ZID	0 min	7.46 ± 0.03	7.60 ± 0.02	7.77 ± 0.02
	10 min	7.78 ± 0.02	7.96 ± 0.02	8.09 ± 0.02
	30 min	8.06 ± 0.02	8.12 ± 0.02	*ND*
	60 min	8.24 ± 0.02	8.33 ± 0.02	8.41 ± 0.02
	360 min	8.28 ± 0.07	8.46 ± 0.02	8.36 ± 0.03

To investigate the basis of the improved potency observed for ZID compared to AVI, REL, and NAC under non-equilibrium conditions, more detailed kinetic studies were conducted to determine the apparent inhibition constant (K_{iapp}), as well as the carbamoylation rate (k_2/K), and the de-carbamoylation rate (k_{off}) (Figure 4).

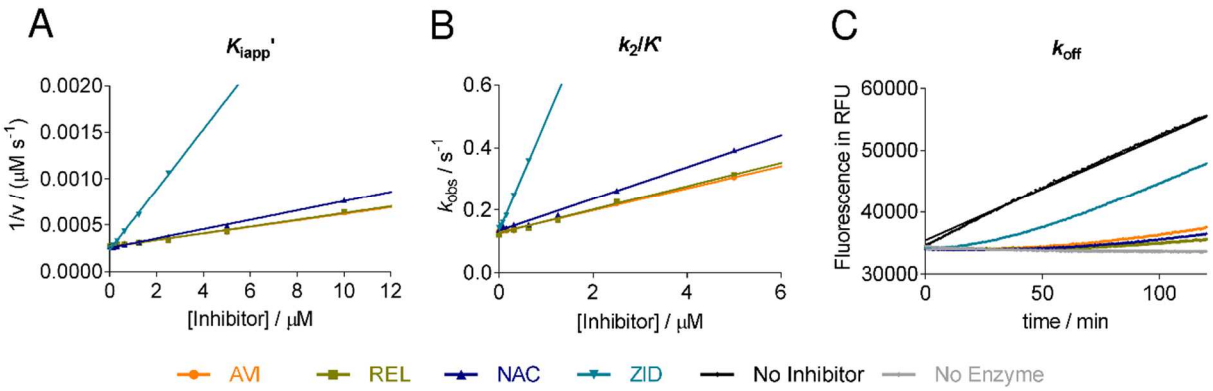


Figure 4: Kinetic analysis of AmpC$_{EC}$ inhibition by DBOs *in vitro*. (A-B) K_{iapp} values and pseudo first-order rates (k_2/K) were determined by assaying 100 nM AmpC$_{EC}$ with 5 µM FC-5[24]. (C) k_{off} rates were determined by jump-dilution (100,000-fold) of AmpC$_{EC}$ (1 µM) that had been pre-incubated with AVI, REL, NAC, or ZID (10 µM) at room temperature for 30 min, then assayed using 25 µM FC-5. Buffer: 50 mM Tris, pH 7.5, 0.01 % (*v*/*v*) Triton X-100. Data were analysed as described in Materials and Methods and as reported[25]. Kinetic constants are summarised in Table 2. The figure and figure legend are adopted with permission from Lang *et al*. Antimicrob. Agents Chemother. 2021, *65*, e02073-20.

In agreement with the improved potency observed for ZID without pre-incubation, the K_{iapp} of ZID, which is measured under non-equilibrium conditions, was improved ~ 10-fold compared to AVI, REL, and NAC (0.69 µM for ZID, compared to 7.4 µM, 7.1 µM, and 5.0 µM, for AVI, REL, and NAC, respectively, Figure 4A). This observation appears to result from an equally ~ 10-fold accelerated carbamoylation rate of ZID, compared to AVI, REL, and NAC (360 x 10^3 $M^{-1}s^{-1}$ compared to 36 x 10^3 $M^{-1}s^{-1}$, 38 x 10^3 $M^{-1}s^{-1}$ and 52 x 10^3 $M^{-1}s^{-1}$ for AVI, REL, and NAC, respectively, Figure 4B).

Table 2: Summary of kinetic constants of AmpC$_{EC}$ inhibition by AVI, NAC, or ZID. Constants were determined under steady-state conditions as shown in Figure 4.

	K_{iapp} (µM)	k_2/K ($M^{-1}s^{-1}$) x 10^3	k_{off} (s^{-1}) x 10^{-3}	$t_{1/2}$ (min)
AVI	7.4 ± 0.3	36 ± 1	0.060 ± 0.01	192 ± 1
REL	7.1 ± 0.3	38 ± 1	0.032 ± 0.01	364 ± 2
NAC	5.0 ± 0.1	52 ± 2	0.049 ± 0.01	236 ± 1
ZID	0.69 ± 0.04	360 ± 10	0.347 ± 0.01	39 ± 4

The similar potency observed for all tested DBOs under equilibrium conditions could be rationalised by jump-dilution experiments, showing a correspondingly accelerated de-carbamoylation rate of ZID compared to AVI, REL, and NAC (0.35 x 10^{-3} s^{-1} compared to 0.060 x 10^{-3} s^{-1}, 0.032 x 10^{-3} s^{-1} and 0.049 x 10^{-3} s^{-1} for AVI, REL, and NAC, respectively, Figure 4C).

3.3. Microbiological analyses

To investigate the activity of AVI, REL, NAC, and ZID against an AmpC$_{EC}$ hyper-expressing *E. coli* strain, the pAD7 plasmid[26], which was previously used for the expression and purification of recombinant AmpC$_{EC}$ (Chapter 2), was transformed into the *E. coli* DH5α lab strain. Both the wildtype and the AmpC$_{EC}$ expressing DH5α strains were then tested via broth microdilution for susceptibility towards ceftazidime (CAZ), a third-generation cephalosporin and preferred substrate of AmpC$_{EC}$. As expected, expression of AmpC$_{EC}$ conferred substantial resistance to CAZ, increasing the minimum inhibitory concentration (MIC) from 1 to 256 µg ml^{-1} (Table 3).

Table 3: Minimum inhibitory concentrations of ceftazidime against *E. coli* strains in the presence of varying concentrations of DBOs. See Materials and Methods for assay details. ND: Not determined.

		Minimum Inhibitory Concentration Ceftazidime [µg ml^{-1}]			
Strain	**[DBO] (µg ml^{-1})**	CAZ + AVI	CAZ + ZID	CAZ + NAC	CAZ + REL
DH5α wt	0	1			
DH5α	0	256			
pAD7	0.125	16	2	*ND*	*ND*
AmpC$_{EC}$	0.25	2	1	*ND*	*ND*
	0.5	2	≤ 0.25	*ND*	*ND*
	1	0.5	≤ 0.25	*ND*	*ND*
	2	0.5	≤ 0.25	*ND*	*ND*
	4	0.25	≤ 0.25	≤ 0.25	1
	8	0.5	≤ 0.25	*ND*	*ND*

Addition of AVI, REL, NAC, or ZID at a concentration of 4 µg ml^{-1} fully restored CAZ activity, with AVI, NAC, and ZID lowering MICs of CAZ below the 1 µg ml^{-1} observed against wildtype DH5α in the absence of DBOs. Experiments with varying concentrations (0.125 – 8 µg ml^{-1}) of AVI and ZID showed a clear dose-dependence. While 1 µg ml^{-1} AVI was required to restore the CAZ MIC to ≤ 1 µg ml^{-1}, the same effect was reached already with 0.25 µg ml^{-1} of ZID.

The DBOs were then tested for intrinsic antimicrobial activity, which had previously been described for other *E. coli* strains and has been attributed to inhibition of penicillin binding protein 2[12,27]. In agreement with those previous reports, and the observed ability to lower the CAZ MIC below the original level of the wildtype strain, substantial antimicrobial activity was observed for AVI, NAC, and ZID (MICs of 16 µg ml^{-1}, 2 µg ml^{-1}, and ≤ 0.25 µg ml^{-1}, respectively), while REL was less potent (MIC 128 µg ml^{-1}) (Table 4). Expression of AmpC$_{EC}$ did not show any substantial effect on the intrinsic antimicrobial activity of the DBOs.

Table 4: Minimum inhibitory concentrations of the DBOs as stand-alone antibacterials against *E. coli* strains. See Materials and Methods for assay details.

	Minimum Inhibitory Concentration DBOs [μg ml^{-1}]			
Strain	AVI	ZID	NAC	REL
DH5α wt	16	≤ 0.25	2	128
DH5α pAD7 AmpC$_{EC}$	16	≤ 0.25	4	128

3.4. Mass spectrometry

To investigate the mechanism of DBO-induced AmpC$_{EC}$ inhibition and the basis for the observed improved potency of ZID under non-equilibrium conditions compared to AVI, REL, and NAC, a range of denaturing protein-observed solid phase extraction-mass spectrometry (SPE-MS) based studies were carried out.

3.4.1. Analysis of SBL modifications observed on reaction with DBOs

Some serine β-lactamases, namely the *Klebsiella pneumoniae* carbapenamases (KPCs), have been reported to hydrolyse some DBOs via a three-step process involving carbamoylation, followed by de-sulfation of the carbamoyl-enzyme complex and subsequent hydrolysis (Figure 5)[5]. Other than the recyclization from the intact carbamoyl-enzyme complexes, this process is irreversible and leads to inactivation of the β-lactamase inhibitors.

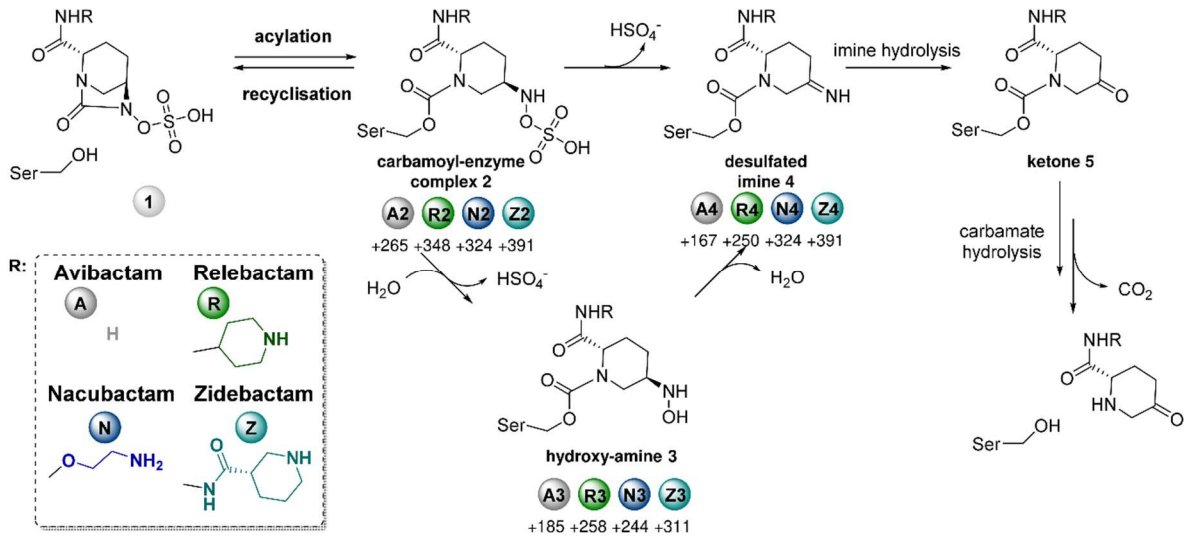


Figure 5: Fragmentation of DBO derived KPC-carbamoyl-enzyme complexes. Note that an analogous fragmentation can be induced under mass-spectrometry conditions[5].

To investigate potential de-sulfation of the carbamoyl-AmpC$_{EC}$ complexes, AmpC$_{EC}$ was incubated with AVI, REL, NAC, and ZID and analysed using SPE-MS after 1 min and 24 h (Figure 6). In agreement with the fast binding rates observed in competition studies with FC-5 (Table 2), apparently complete carbamoylation was observed with all DBOs within 1 min. While the major adducts observed indicated the intact carbamoyl-enzyme complexes (with mass increments of +265, +348, +324, and +391 Da for AVI, REL, NAC, and ZID, respectively, Table 5), small amounts of a species corresponding to loss of sulfate (- 80 Da) from the carbamoyl-enzyme complex (resulting in +185, +268, +244 or +311 Da species for AVI, REL, NAC and ZID, respectivley, Table 5) were also detected. While the relative abundancy of these species varied slightly between inhibitors (AVI 16 % abundancy, REL: 7 % abundancy, NAC 10 % abundancy, ZID: 6 % abundancy), in all cases the -80 Da species (relative to the carbamoyl-enzyme complex) were substantially less abundant than the intact carbamoyl-enzyme complex. Importantly, the ratios of de-sulfated complexes compared to the intact carbamoyl-enzyme complexes remained constant on analysis on incubation for 24 h. This suggests that de-sulfation likely occurs during ESI-MS analysis and does not reflect an enzymatic reaction, as has been previously reported on ESI-MS analysis of reaction of class C and D SBLs with AVI[5].

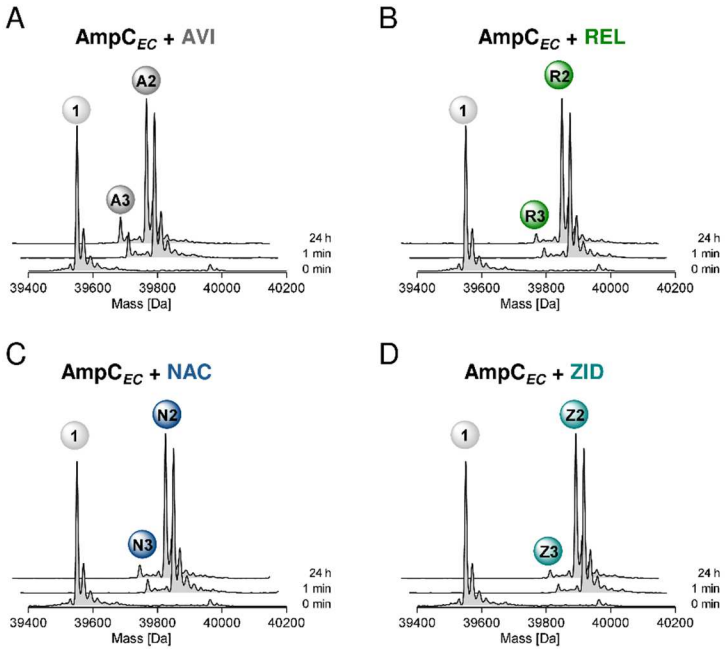


Figure 6: SPE-ESI MS time courses for AmpC$_{EC}$ modification by AVI, REL, NAC, or ZID. AmpC$_{EC}$ (3 µM) was incubated with (A) AVI, (B) REL, (C) NAC, or (D) ZID (3.3 µM) at room temperature. Buffer: 50 mM Tris, pH 7.5. Mass-spectra were acquired both before incubation with the inhibitor and after the indicated incubation times. Deconvoluted mass spectra are shown, as derived using the maximum entropy algorithm in the MassHunter Workstation Qualitative Analysis V.7 programme (Agilent Technologies). Proposed structures corresponding to the labelled mass shifts are given in Figure 5; observed and calculated mass-shifts are in Table 5.

Table 5: Observed and calculated masses of AmpC$_{EC}$ and KPC variants before and after modification due to reaction with AVI, REL, NAC, or ZID as analysed by SPE-MS. Differences between measured and calculated masses are all within the experimental error. [a]Masses derived from deconvolution of measured spectra using the maximum entropy algorithm in the MassHunter Workstation Qualitative Analysis V.7 programme (Agilent Technologies). [b]KPC masses were calculated based on protein sequences without an *N*-terminal methionine. [c]Relative to the measured unmodified protein mass. [d]Assignments correlate to species in Figure 5.

	Mass observed[a] [Da]	Mass calculated[b] [Da]	Mass shift observed[c] [Da]	Mass shift calculated [Da]	Assignment[d]
AmpC$_{EC}$	39551	39551			
+ AVI	39816	39816	+ 265	+ 265	A2
	39736	39736	+ 185	+ 185	A3 (minor, potential artefact)
+ REL	39899	39899	+ 348	+ 348	R2
	39816	39819	+ 265	+ 268	R3 (minor, potential artefact)
+ NAC	39875	39875	+ 324	+ 324	N2
	39796	39795	+ 245	+ 244	N3 (minor, potential artefact)
+ ZID	39942	39942	+ 391	+ 391	Z2
	39857	39862	+ 306	+ 311	Z3 (minor, potential artefact)
KPC-2	30640	30640			
+ AVI	30905	30905	+ 265	+ 265	A2
	30826	30825	+ 186	+ 185	A3
	30808	30807	+ 168	+ 167	A4
+ REL	30989	30988	+ 349	+ 348	R2
	30907	30908	+ 267	+ 268	R3
	30890	30890	+ 250	+ 250	R4
KPC-3	30665	30667			
+ AVI	30931	30932	+ 266	+ 265	A2
	30851	30852	+ 186	+ 185	A3
	30834	30834	+ 167	+ 167	A4
+ REL	31013	31015	+ 348	+ 348	R2
	30935	30935	+ 270	+ 268	R3
	30914	30917	+ 249	+ 250	R4
KPC-4	30657	30657			
+ AVI	30922	30922	+ 265	+ 265	A2
	30841	30842	+ 184	+ 185	A3
	30824	30824	+ 167	+ 167	A4
+ REL	31005	31005	+ 348	+ 348	R2
	30924	30925	+ 267	+ 268	R3
	30908	30907	+ 251	+ 250	R4

For comparison, SPE-MS time-courses were acquired for the reaction of KPC-2, -3, and -4 (*provided by Catherine Tooke, University of Bristol*) with AVI or REL over 37 h (Figure 7). As with AmpC$_{EC}$, apparently complete carbamoylation of all KPC variants was observed within 5 min of incubation with both AVI or REL. Initially no evidence for de-sulfation of this complex was observed at this point. However, on prolonged incubation (4-37 h), increasing amounts of the de-sulfated KPC carbamoyl-enzyme complex (with mass increments of +185 and +167 Da for AVI and +268, and + 250 Da for REL, Table 5) were observed. By contrast with the SPE-MS time-courses on reaction of AmpC$_{EC}$ with DBOs, the clear time-dependence of the observation of the de-sulfated species indicates their generation in solution as a result of an enzymatic reaction rather than through reactions initiated by the ESI-MS conditions.

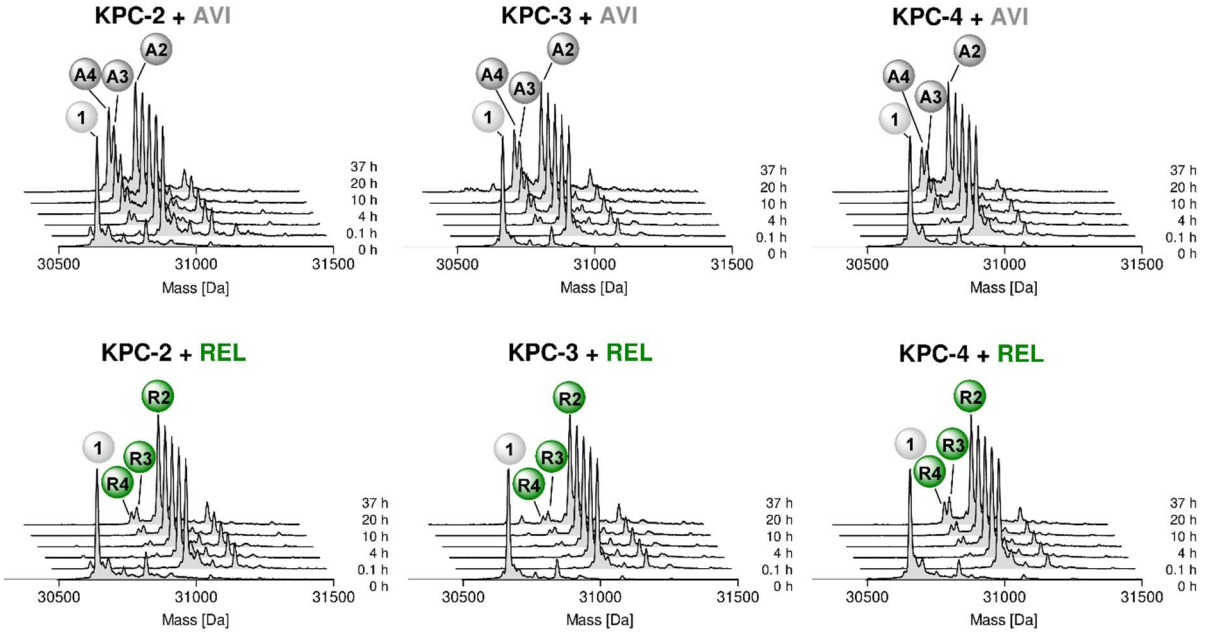


Figure 7: SPE-ESI MS time courses for KPC-2, -3, or -4 modification by AVI or REL. KPCs (3 µM) were incubated with AVI, REL, NAC, or ZID (6 µM) at room temperature. Buffer: 50 mM Tris, pH 7.5. Deconvoluted mass spectra are shown, as derived using the maximum entropy algorithm in the MassHunter Workstation Qualitative Analysis V.7 programme (Agilent Technologies). Proposed structures corresponding to the labelled mass shifts are given in Figure 5; observed and calculated mass shifts are in Table 5.

Subsequent studies also show clear pH dependence (pH 7.0-8.5) of the KPC-2 catalysed de-sulfation of both AVI- and REL-derived carbamoyl-enzyme complexes, with increased pH leading to slower de-sulfation (Figure 8).

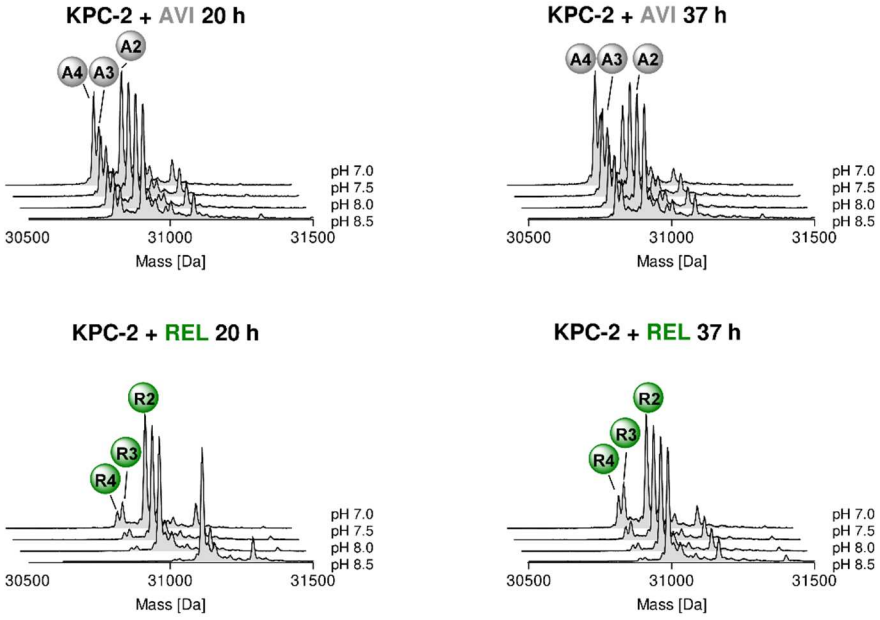


Figure 8: pH-dependence of KPC-2 catalysed de-sulfation of DBO derived carbamoyl-enzyme complexes. KPC-2 (3 µM) was incubated with AVI or REL (6 µM) at room temperature. Buffer: 50 mM Tris, pH 7.0-8.5. Deconvoluted mass spectra are shown, as derived using the maximum entropy algorithm in the MassHunter Workstation Qualitative Analysis V.7 programme (Agilent Technologies). Proposed structures corresponding to the labelled mass shifts are given in Figure 5; observed and calculated mass-shifts are in Table 5.

3.4.2. Mass spectrometric assay to study relative thermodynamic stability of $AmpC_{EC}$-DBO complexes

While the competition experiments under steady-state conditions described earlier are useful to characterise the kinetic profile of $AmpC_{EC}$ inhibition by the tested DBOs, they do not give any information on the thermodynamic stability of the respective carbamoyl-enzyme complexes. To study these, competition assays between two different DBOs were conducted and analysed via protein observed ESI-MS (Figure 9 and 10).

In all experiments $AmpC_{EC}$ was incubated with equal amounts of AVI and either REL, NAC, or ZID (1.1 equiv. each). Direct competition experiments (where the DBOs were added simultaneously, middle column in Figure 9B and Figure 10A-C) showed no preferential binding of REL or NAC over AVI after 1 min (44 : 56 (REL : AVI) and 49 : 51 (NAC : AVI), respectively), which is in agreement with the similar carbamoylation-rates observed for AVI, REL, and NAC binding in competition with FC-5 (Table 2). Equally in agreement with the kinetic data (showing a ~10-fold increase in the carbamoylation rate for ZID, Table 2), $AmpC_{EC}$ showed clear preferential binding of ZID over AVI (77 : 23) after 1 min. However, on apparently complete equilibration over a period of 12 h, ZID- and AVI- derived carbamoyl-enzyme complexes reached equal abundancy (51 : 49). REL and NAC abundancies remained at equal levels compared to AVI over the course of the experiment (49 : 51 (REL : AVI) and 53 : 47 (NAC : AVI), respectively, after 24 h).

Subsequent experiments, with successive addition of first AVI, followed by REL, NAC, or ZID, or vice versa, showed equilibration towards the same AVI : REL/NAC/ZID ratios over 12 – 24 h (left and right column in Figure 9B and Figure 10D-J).

Overall, the SPE-MS studies are thus in agreement with the inhibition studies showing enhanced potency of ZID compared to AVI, REL, and NAC with short, but not with prolonged, incubation times (Table 2).

Further, the results suggest that all the DBO derived carbamoyl-enzyme complexes are of similar energetic stability. The increased potency of ZID under pre-equilibrium conditions thus likely results from stabilisation of the tetrahedral intermediate common to both carbamoylation and de-carbamoylation, leading to a decrease in activation energy needed for both processes. The ZID-derived carbamoyl-enzyme complex therefore is likely not more energetically stabilised than the complexes derived from reaction of $AmpC_{EC}$ with AVI, REL, or NAC. The observed differences in the inhibition of ZID compared to AVI, REL, and NAC therefore appear to be based on a kinetic effect and not on improved thermodynamics.

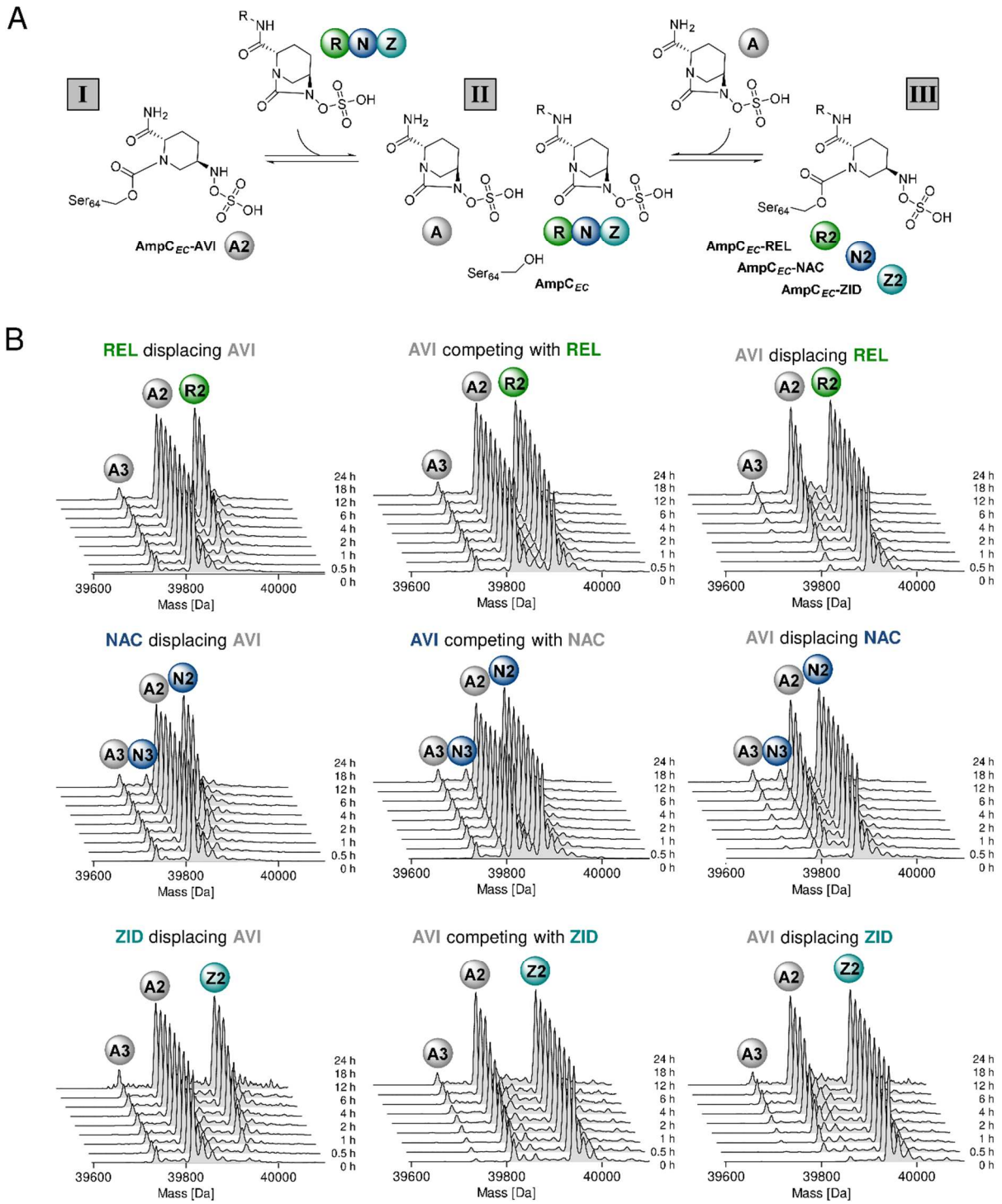


Figure 9: SPE-MS analyses on reversible DBO binding. (A) Schematic of intact protein SPE-MS observed DBO competition experiments. (B) SPE-MS analyses of competition exteriments. Left: AVI acyl-enzyme displacement by REL/NAC/ZID (I). Center: Direct competition between AVI and REL/NAC/ZID (II). Right: REL/NAC/ZID displacement by AVI (III). AmpC$_{EC}$ (3 µM) was incubated with 1.1 equiv DBO. For direct competition experiments (center) both DBOs were added simultaneously; for displacement experiments (left and right) the second DBO was added after 5 min incubation of AmpC$_{EC}$ with the first DBO. Buffer: 50 mM Tris, pH 7.5. Deconvoluted spectra are shown, as derived using the maximum entropy algorithm in the MassHunter Workstation Qualitative Analysis V.7 programme (Agilent Technologies). Proposed structures corresponding to the labelled mass shifts are given in Figure 5; observed and calculated mass-shifts are in Table 5. The figure and figure legend are adopted with permission from Lang *et al.* Antimicrob. Agents Chemother. 2021, *65*, e02073-20.

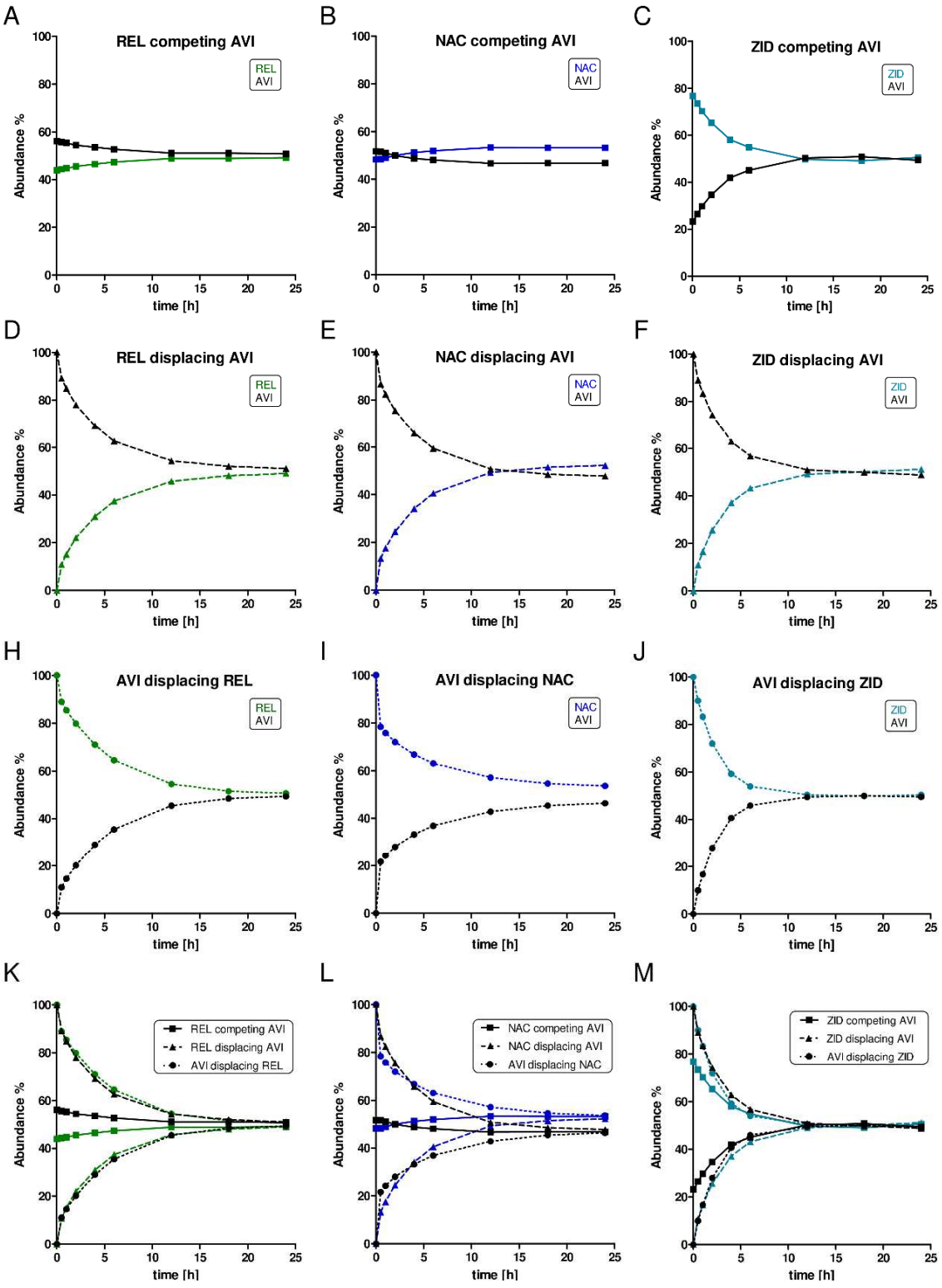


Figure 10: Binding to AmpC$_{EC}$ of AVI in competition with REL, NAC, or ZID as observed by SPE-MS. AmpC$_{EC}$ (3 µM) was incubated with 1.1 equiv DBOs in 50 mM Tris, pH 7.5. Experiments were performed in duplicate. Reactions were monitored via protein observed solid-phase extraction coupled with mass-spectrometry. Spectra were deconvoluted (Figure S4) using the maximum entropy algorithm in the MassHunter Workstation Qualitative Analysis V.7 programme (Agilent Technologies). The relative peak areas (in % abundance) of the +265 Da, + 338 Da, +324 Da or +391 Da adducts for AVI, REL, NAC, and ZID are shown. The figure and figure legend are adopted with permission from Lang *et al.* Antimicrob. Agents Chemother. 2021, *65*, e02073-20.

3.5. Structural characterisation of AmpC$_{EC}$-DBO interactions

To investigate the structural basis of AmpC$_{EC}$ inhibition by AVI, REL, NAC, and ZID, high resolution structures of the AmpC$_{EC}$-carbamoyl complexes were solved, obtained via soaking of DBOs into crystals of unmodified AmpC$_{EC}$ as described in Chapter 2. In all cases, analysis of electron density maps showed covalent modification of Ser64. Substantial changes of the overall fold of AmpC$_{EC}$ were not observed in any of these complexes (main-chain RMSDs of 0.12 Å (AmpC$_{EC}$-AVI), 0.14 Å (AmpC$_{EC}$-REL), 0.11 Å (AmpC$_{EC}$-NAC), and 0.15 Å (AmpC$_{EC}$-ZID) compared to unmodified AmpC$_{EC}$ (PDB: 6T3D, Chapter 2)).

3.5.1. Crystal structure of AmpC$_{EC}$ in complex with avibactam

A crystal structure of AmpC$_{EC}$ with AVI (1.51 Å resolution, PDB ID: 6TBW, Figure 11), showed AVI reacted with the nucleophilic Ser64 to form the ring-opened carbamoyl-complex, with the DBO-derived piperidine ring adopting a chair conformation, similar as observed in complex with the *Pseudomonas aeruginosa* derived AmpC β-lactamase (AmpC$_{PA}$, Figure 11D).

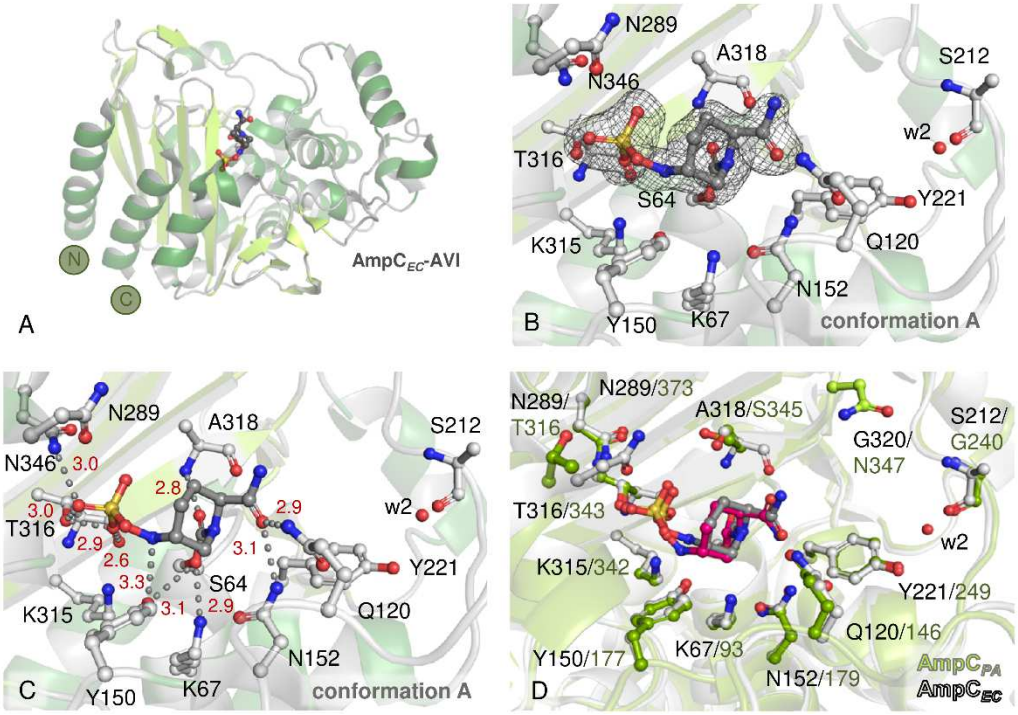


Figure 11: Views from a crystal structure of the AmpC$_{EC}$-AVI carbamoyl-enzyme complex (1.51 Å resolution, PDB: 6TBW). (A) Overview of AmpC$_{EC}$-AVI complex structure. (B) Active site view with mF$_o$-DF$_c$ polder OMIT map[28] contoured at 3.0 σ and carved around the AVI-derived carbamoyl. (C) Active site view with hydrogen-bonding interactions between AVI and AmpC$_{EC}$ active site residues shown as dashes. Distances (in Å) are indicated in red. (D) Overlay of AmpC$_{EC}$-AVI complex (white/grey) and AmpC$_{PA}$-AVI complex (green/pink, PDB: 4OOY[8]). The figure and figure legend are adopted with permission from Lang *et al*. Antimicrob. Agents Chemother. 2021, *65*, e02073-20.

The carbamoyl-carbonyl oxygen is positioned for polar interactions with Ala316 (2.8 Å). The *N*-sulfate group is positioned to interact with the sidechains of Asn346 (3.0 Å) and Thr316

(2.6 Å), as well as the Thr316 backbone carbonyl (2.9 Å). The *N*-sulfate nitrogen is further positioned in close proximity to Tyr150 (3.3 Å), which is proposed as the general base involved in re-cyclisation and de-carbonylation of DBOs from AmpC$_{EC}$ (Figure 1).

3.5.2. Crystal structure of AmpC$_{EC}$ in complex with relebactam

A structure of the AmpC$_{EC}$-REL complex (1.72 Å resolution, PDB: 6TPM, Figure 12) showed the DBO core of REL equally in the ring-opened form, covalently bound to Ser64. However, by contrast with the AmpC$_{EC}$-AVI structure, it was observed in two different conformations.

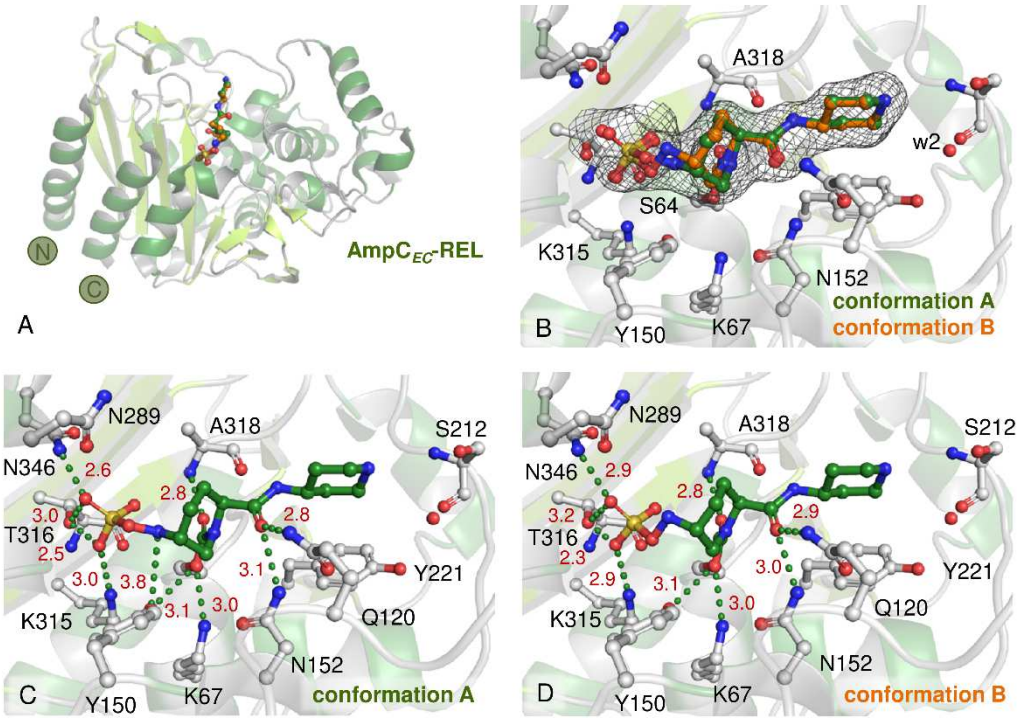


Figure 12: Views from a crystal structure of the AmpC$_{EC}$-REL carbamoyl-enzyme complex (1.72 Å resolution, PDB: 6TPM). (A) Overview of AmpC$_{EC}$-REL complex structure. (B) Active site view with mF_o-DF_c polder OMIT map[28] contoured at 3.0 σ and carved around the REL-derived carbamoyl, which was refined in two conformations. (C) Active site view with REL in conformation A. (D) Active site view with REL in conformation B. Hydrogen-bonding interactions are shown as dashes. Distances (in Å) are indicated in red. The figure and figure legend are adopted with permission from Lang *et al*. Antimicrob. Agents Chemother. 2021, *65*, e02073-20.

While in both conformations the DBO-derived piperidine ring adopts a chair-conformation, in conformation A, the *N*-sulfate nitrogen is in close proximity to the Tyr150 phenol (3.8 Å), as observed with AVI, while in the conformation B, the *N*-sulfate nitrogen is oriented away from Tyr150 (4.8 Å). The position of the sulfate is not substantially altered by the change of the nitrogen position, and it engages in hydrogen bonding interactions with Lys315 (2.9-3.0 Å), Asn346 (2.6-2.9 Å), as well as the sidechain (3.0-3.2 Å) and backbone carbonyl (2.3-2.5 Å) of Thr316. In both conformations the carbamoyl-carbonyl oxygen is positioned for polar interactions with Ala316 (2.8 Å). Positioning of the REL sidechain does not appear to be

influenced by the different conformations of the DBO core. As with AVI, the C2 amide-oxygen is positioned to engage in hydrogen bonding interactions with Asn152 (3.0-3.1 Å) and Gln120 (2.8-2.9 Å), while the piperidyl sidechain does not appear positioned to engage in additional hydrogen-bonding interactions.

3.5.3. Crystal structure of AmpC$_{EC}$ in complex with nacubactam

A structure of the AmpC$_{EC}$-NAC complex (1.47 Å resolution, PDB: 6T7L, Figure 13), shows NAC covalently bound to Ser64 and in a single conformation. As with AVI, the *N*-sulfate nitrogen is positioned in relatively close proximity to Tyr150 (3.8 Å).

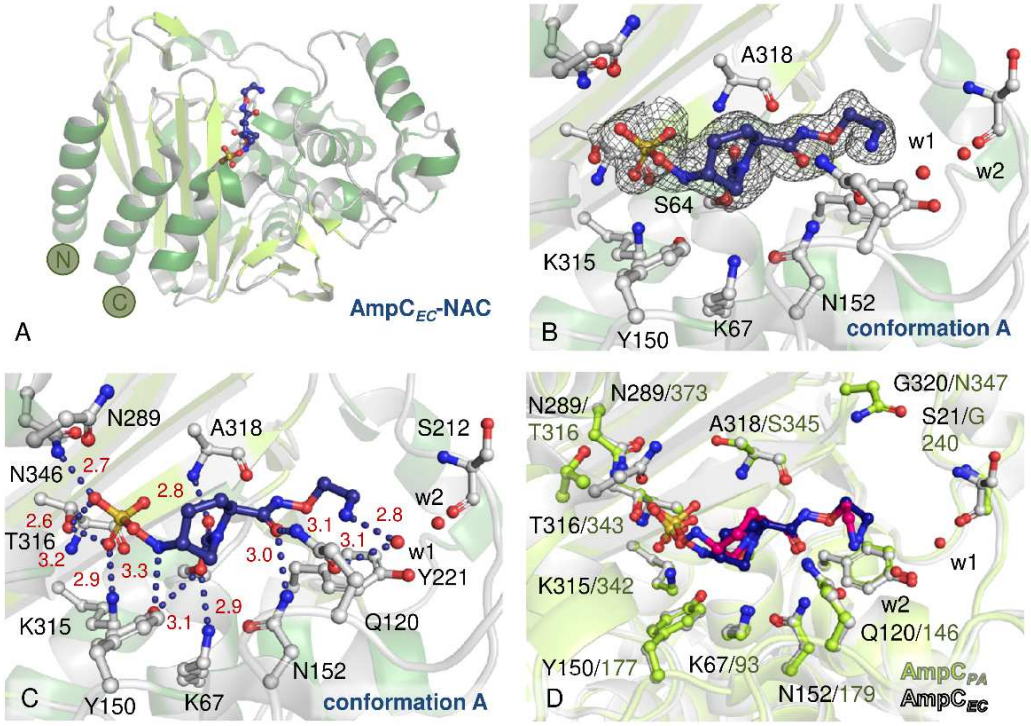


Figure 13: Views from a crystal structure of the AmpC$_{EC}$-NAC carbamoyl-enzyme complex (1.47 Å resolution, PDB: 6T7L). (A) Overview of AmpC$_{EC}$-NAC complex structure. (B) Active site view with mF_o-DF_c polder OMIT map[28] contoured at 3.0 σ and carved around the NAC-derived carbamoyl. (C) Active site view with hydrogen-bonding interactions between NAC and AmpC$_{EC}$ active site residues shown as dashes. Distances (in Å) are indicated in red. (D) Overlay of AmpC$_{EC}$-NAC complex (white/blue) and AmpC$_{PA}$-NAC complex (green/pink, PDB: 4X68[12]). The figure and figure legend are adopted with permission from Lang *et al*. Antimicrob. Agents Chemother. 2021, *65*, e02073-20.

The sulfate is positioned analogous as observed with AVI and REL, engaging in the hydrogen bonding interactions with Lys315 (2.9 Å), Asn346 (2.7 Å), and with the backbone carbonyl-oxygen of Thr316 (2.6 Å). The carbamoyl-carbonyl oxygen is again positioned for polar interactions with Ala316 (2.8 Å). The sidechain carbonyl engages in hydrogen bonding-interactions with Asn152 (3.0 Å) and Gln120 (3.1 Å), and, by contrast with REL, the terminal amine of the NAC sidechain is positioned to form an additional hydrogen bond with a water

molecule (2.8 Å, w1, Figure 13C), which is not observed in the structure of unmodified AmpC$_{EC}$, or in any of the other AmpC$_{EC}$-DBO complex structures. w1 is positioned for hydrogen bonding interaction with the sidechain of Gln120 (3.1 Å).

3.5.4. Crystal structure of AmpC$_{EC}$ in complex with zidebactam

In a similar manner as observed with REL, a crystal structure of AmpC$_{EC}$ reacted with ZID (1.30 Å resolution, PDB: 6T5Y, Figure 14) showed the ZID-derived carbamoyl-enzyme complex in two conformations which are refined in equal occupancy. In conformation A, the *N*-sulfate nitrogen is positioned for hydrogen-bonding interaction with Tyr150 (3.5 Å), while in conformation B it is distant from Tyr150 (4.8 Å). As with REL, the differences in the orientation of the *N*-sulfate nitrogen do not appear to substantially effect positioning of the sulfate, which engages in hydrogen bonding interactions with Lys315 (3.1 Å), Asn289 (3.1 Å), Asn346 (2.6 Å), and with the sidechain of Thr316 (2.7 Å).

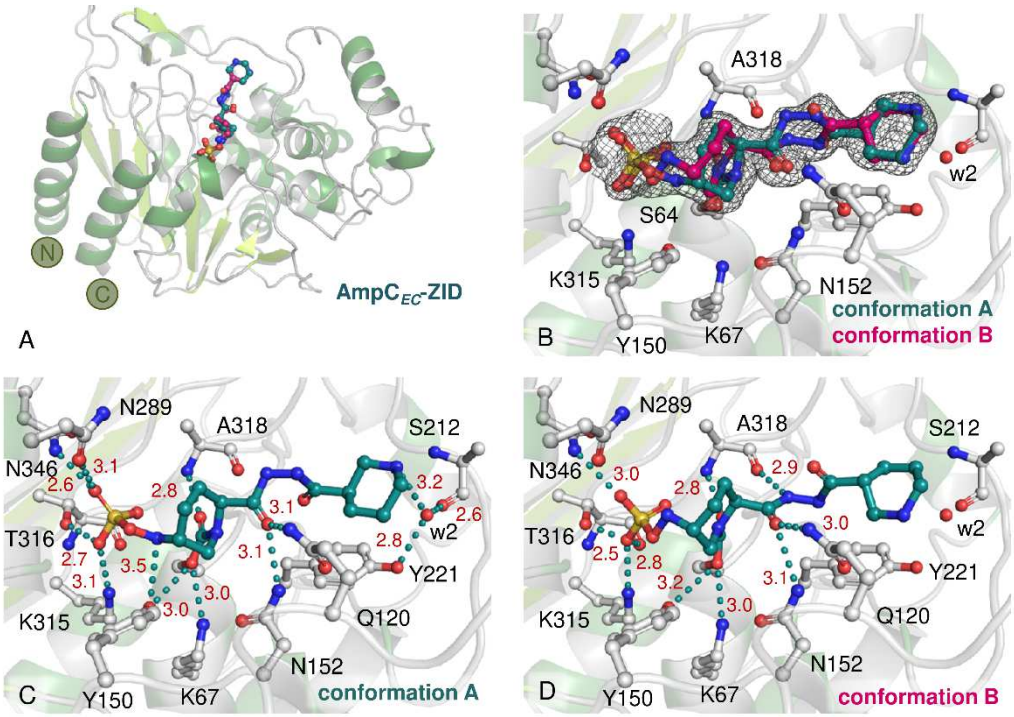


Figure 14: Views from a crystal structure of the AmpC$_{EC}$-ZID carbamoyl-enzyme complex (1.30 Å resolution, PDB: 6T5Y). (A) Overview of AmpC$_{EC}$-ZID complex structure. (B) Active site view with mF$_o$-DF$_c$ polder OMIT map[28] contoured at 3.0 σ and carved around the ZID-derived carbamoyl, which was refined in two conformations. (C) Active site view with ZID in conformation A. (D) Active site view with ZID in conformation B. Hydrogen-bonding interactions are shown as dashes. Distances (in Å) are indicated in red. The figure and figure legend are adopted with permission from Lang *et al.* Antimicrob. Agents Chemother. 2021, *65*, e02073-20.

As with AVI, REL, and NAC the carbamoyl-carbonyl oxygen is positioned to engage in polar interaction with the backbone nitrogen of Ala316 (2.8 Å) and the sidechain amide is positioned in close proximity to Asn152 (3.1 Å) and Gln120 (3.0-3.1 Å).

By contrast with REL and NAC, the acyl-hydrazide sidechain of ZID was observed in two different conformations. These two side-chain conformations are likely not affected by the two conformations observed for the *N*-sulfate nitrogen, resulting in a total of four distinct conformations of the ZID derived AmpC$_{EC}$-carbamoyl-enzyme complex. However, for the sake of clarity, only two conformations (representing both conformations of the *N*-sulfate nitrogen and the sidechain) were refined in equal occupancy.

In conformation A, the nitrogen of the piperidyl-ring of the ZID sidechain is positioned for hydrogen-bonding interactions with a conserved water molecule (3.2 Å, w2, Figure 14C), which is observed in all AmpC$_{EC}$-DBO complex structures described here (Figure 11-12), as well as the structure of unmodified AmpC$_{EC}$ (PDB: 6T3D). In all structures, w2 is positioned for hydrogen-bonding interactions with the sidechain of Tyr221 (2.8 Å) and the backbone carbonyl of Ser212 (2.6 Å).

In conformation B, the ZID piperidyl-ring does not engage in hydrogen-bonding interactions with w2, or any AmpC$_{EC}$ active site residues. Instead, one of the acyl-hydrazide nitrogen atoms is positioned for hydrogen-bonding interactions with the backbone carbonyl of Ala318 (2.9 Å), which is not observed in sidechain conformation A.

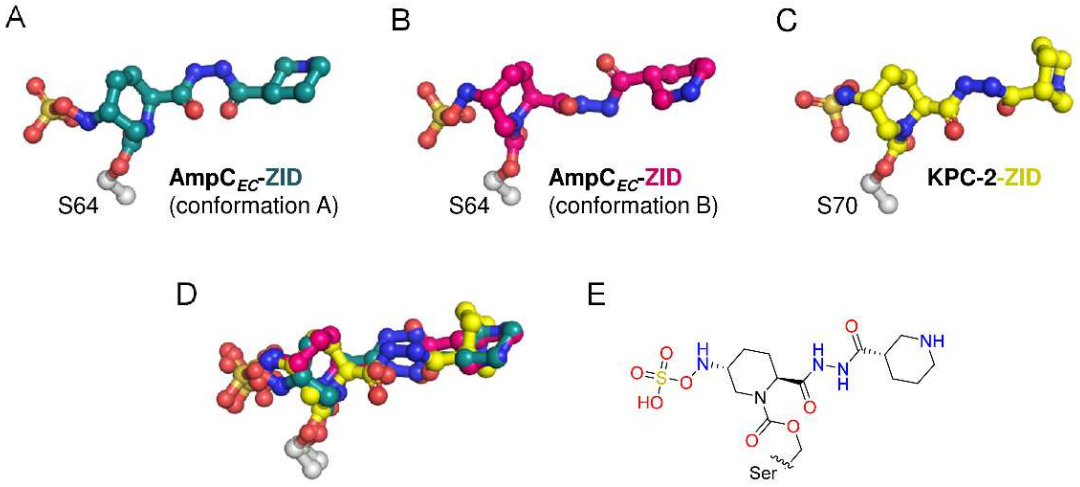


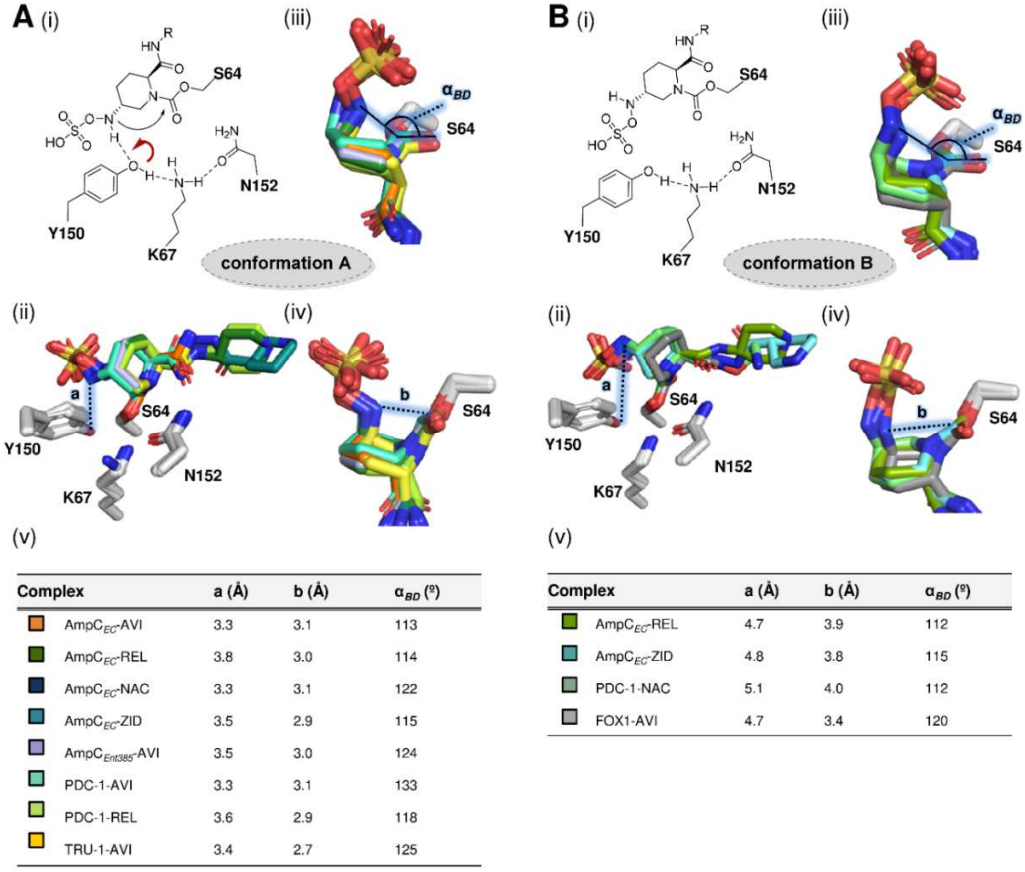
Figure 15: Comparison of ZID binding modes as observed in complex with AmpC$_{EC}$ and KPC-2. (A) Conformation A of the ZID binding mode at the AmpC$_{EC}$ active site. (B) Conformation B of the ZID binding mode at the AmpC$_{EC}$ active site. (C) The ZID binding mode at the KPC-2 active site (PDB: 6B1J) [22]. (D) Overlay of ZID binding modes, color-coded as in (A-C). (E) Structure of ring-opened ZID bound to the nucleophlic serine. The figure and figure legend are adopted with permission from Lang *et al.* Antimicrob. Agents Chemother. 2021, *65*, e02073-20.

To date no other structures of ZID in complex with a class C SBL have been reported. The only other available structure of ZID bound at the active site of an SBL shows ZID covalently bonded to Ser70 at the active-site of KPC-2 (PDB: 6B1J)[22]. While the *N*-sulfate conformation in this structure resembles conformation B observed at the AmpC$_{EC}$ active site, the sidechain

conformation observed on binding to KPC-2 reflects the sidechain conformation A observed at the AmpC$_{EC}$ active site (Figure 15).

3.5.5. Comparison of DBO binding modes at AmpC$_{EC}$ active site

Overall, the binding modes of the DBO core both observed for AVI-, REL-, NAC-, and ZID-derived carbamoyl-enzyme complexes with AmpC$_{EC}$ here, and in reported structures of class C SBL-DBO complexes, can be divided into two conformations (A and B in Figure 16).



Complex	a (Å)	b (Å)	α_{BD} (°)
AmpC$_{EC}$-AVI	3.3	3.1	113
AmpC$_{EC}$-REL	3.8	3.0	114
AmpC$_{EC}$-NAC	3.3	3.1	122
AmpC$_{EC}$-ZID	3.5	2.9	115
AmpC$_{Ent385}$-AVI	3.5	3.0	124
PDC-1-AVI	3.3	3.1	133
PDC-1-REL	3.6	2.9	118
TRU-1-AVI	3.4	2.7	125

Complex	a (Å)	b (Å)	α_{BD} (°)
AmpC$_{EC}$-REL	4.7	3.9	112
AmpC$_{EC}$-ZID	4.8	3.8	115
PDC-1-NAC	5.1	4.0	112
FOX1-AVI	4.7	3.4	120

Figure 16: Comparison of DBO derived AmpC$_{EC}$ complexes with DBO complexes of other class C SBLs. (i) (A) Conformation A: *N*-sulfate nitrogen in close proximity to Y150:O$_\eta$ and is oriented for nucleophilic reaction. (B) Conformation B: *N*-sulfate nitrogen oriented away from Y150:O$_\eta$ and unfavourable for nucleophilic reaction. (ii) Distance (a) between the DBO *N*-sulfate nitrogen and Y150:O$_\eta$ (iii) Bürgi-Dunitz angle (α_{BD}) for the *N*-sulfate nitrogen and the C=O of the carbonyl group. (iv) Distance (b) between carbonyl-carbon and *N*-sulfate nitrogen. (v) Summary of distances and angles. PDB codes: AmpC$_{Ent385}$-AVI[29] (6LC8), PDC-1-AVI[8] (4OOY), PDC-1-REL[11] (4NK3), TRU-1-AVI[20] (6FM7), PDC-1-NAC[12] (4X68), FOX-1-AVI[19] (5ZA2). Note: In the structure of the AmpC$_{Ent385}$-AVI complex, K67 is observed in two conformations, one of which is not positioned to interact with N152[29]. The figure and figure legend are adopted with permission from Lang *et al*. Antimicrob. Agents Chemother. 2021, *65*, e02073-20.

The main difference between the two conformations lays in the positioning of the *N*-sulfate nitrogen. This is important from a mechanistic perspective, as de-carbamylation via recyclization of the DBOs is likely initiated by deprotonation of the *N*-sulfate via Tyr150 (Figure 1)[8]. Thus, the Bürgi-Dunitz angle[30] (α_{BD}, preferred ~107°, Figure 16), as well as

both the distances between the Tyr150 phenol and the *N*-sulfate nitrogen (a in Figure 16) and the distance between the *N*-sulfate and the carbamoyl-carbonyl (b in Figure 16) are of stereoelectronical importance for recyclisation.

In most of the reported class C SBL-DBO complex structures, the DBO adopts conformation A, e.g. in structures of AmpC$_{PA}$ in complex with AVI (PDB: 4OOY)[8] and REL (PDB: 4NK3)[11], the *Enterobacter cloacae* AmpC$_{Ent385}$ in complex with AVI (PDB: 6LC8)[29], and the plasmid encoded TRU-1 with AVI (PDB: 6FM7)[20]. In this conformation the *N*-sulfate is in close proximity to Tyr150-O$_{\eta}$, and would thus appear 'primed' for recyclization.

By contrast, in structures of the plasmid encoded FOX-4 in complex with AVI (PDB: 5ZA2[19]) and PDC-1 in complex with NAC (PDB: 4X68)[12], the carbamoyl-enzyme complexes adopt conformation B, with the *N*-sulfate nitrogen positioned further away from Tyr150-O$_{\eta}$, pointing towards the opposite face of the active site, which would be unfavourable for recyclization according to the mechanism proposed in Figure 1.

In the AmpC$_{EC}$-DBO complex structures presented in this Chapters, all AVI-, REL-, NAC-, and ZID-derived carbamoyl-enzyme complexes are, either fully or partially, observed in conformation A, with the *N*-sulfate nitrogen positioned in close proximity to the phenolic oxygen of Tyr150 (3.3-3.8 Å) and the carbamoyl-carbon (2.9-3.1 Å, α_{BD} = 113-115°, with exception of NAC with α_{BD} = 122°, which deviates further from the preferred $\alpha_{BD,}$ Figure 16A).

However, while with AVI and NAC the carbamoyl-enzyme complex is solely observed in conformation A, with REL and ZID about 50% of the complex refined in conformation B, with the *N*-sulfate nitrogen positioned at the opposite face of the active site and further away from Tyr150:O$_{\eta}$ (4.7-4.8 Å) and the carbamoyl-carbon (3.8-3.9 Å, α_{BD} = 112-115°, Figure 16B).

Based on proposed de-carbamoylation mechanisms of DBOs from class C SBLs[8] (Figure 1), stereoelectronic considerations on the nucleophilic attack would thus suggest slower recyclization of the REL- and ZID-derived carbamoyl-enzyme complexes, compared to AVI- and NAC-derived complexes which appear in fully 'primed' conformation. However, this is in disagreement with the kinetic studies showing faster de-carbamoylation of ZID compared to other DBOs (Table 2). The structural observations thus do not obviously correlate with the kinetics of AmpC$_{EC}$ inhibition observed in solution. It should, however, be noted that the crystallographically observed binding modes may not accurately represent those in solution, where conformations A and B may be in dynamic equilibrium.

Table 6: Data collection and refinement statistics of AmpC$_{EC}$ crystals.

Datasets	**AmpC$_{EC}$-AVI** (PDB: 6TBW)	**AmpC$_{EC}$-REL** (PDB: 6TPM)
Data Collection		
Beamline (Wavelength, Å)	DLS I03 (0.9763)	DLS I03 (0.9763)
Detector	Eiger2 XE 16M	Pilatus 6M-F
Data Processing	Xia2 dials	Xia2 3dii
Space group	*P* 4_3 3 2	*P* 4_3 3 2
Cell dimensions		
a,b,c (Å)	138.1, 138.1, 138.1	138.5, 138.5, 138.5
α, β, γ (°)	90, 90, 90	90, 90, 90
No. of molecules/ASU	1	1
No. reflections	70726 (3475)*	48671 (2401)*
Resolution (Å)	69.10-1.51 (1.54-1.51)*	56.57 - 1.72 (1.75 -1.72)*
R_{meas}(I)	0.113 (2.848)*	0.113 (3.785)*
I/σI	29.0 (2.6)*	31.6 (1.7)*
$CC_{1/2}$	1.0 (0.8)*	1.00 (0.7)*
Completeness (%)	100 (100)*	100 (100)*
Multiplicity	77.6 (72.9)*	77.1 (74.8)*
Wilson B value (Å^2)	18.67	29.41
Refinement	PHENIX	PHENIX
R_{work}/R_{free}	0.1584/0.1808	0.1690/0.1953
No. atoms	3282	3224
- Enzyme	2863	2833
- DBO	17	46
- Water	389	313
Average B-factors	28.2	38.6
- Enzyme	26.6	37.4
- DBO	40.5	57.2
- Water	39.1	44.3
R.m.s deviations		
- Bond lengths (Å)	0.008	0.004
- Bond angles (°)	1.06	0.82

*Highest resolution shell in parentheses.

Table 6 continued.

Datasets	**AmpC$_{EC}$-NAC** (PDB: 6T7L)	**AmpC$_{EC}$-ZID** (PDB: 6T5Y)
Data Collection		
Beamline (Wavelength, Å)	DLS I03 (0.9763)	DLS I03 (0.9762)
Detector	Pilatus 6M-F	Pilatus 6M-F
Data Processing	Xia2 dials	Xia2 dials
Space group	*P* 4$_3$ 3 2	*P* 4$_3$ 3 2
Cell dimensions		
a,b,c (Å)	138.2, 138.2, 138.2	137.8, 137.8, 137.8
α, β, γ (°)	90, 90, 90	90, 90, 90
No. of molecules/ASU	1	1
No. reflections	76716 (4213)*	109248 (5376)*
Resolution (Å)	69.09-1.47 (3.99-1.47)*	68.9-1.30 (1.32-1.30)*
R_{meas}(I)	0.134 (3.003)*	0.085 (0.825)*
I/σI	25.9 (2.3)*	26.8 (2.4)*
$CC_{1/2}$	1.0 (0.8)*	1.0 (0.8)*
Completeness (%)	100 (100)*	100 (100)*
Multiplicity	75.8 (76.3)*	75.6 (71.7)*
Wilson B value (Å^2)	16.23	13.75
Refinement	PHENIX	PHENIX
R_{work}/R_{free}	0.1546/0.1823	0.1318/0.1487
No. atoms	3439	3387
- Enzyme	2929	2900
- DBO	21	52
- Water	459	419
Average B-factors	23.4	21.3
- Enzyme	21.4	19.4
- DBO	29.5	23.1
- Water	35.2	33.6
R.m.s deviations		
- Bond lengths (Å)	0.006	0.008
- Bond angles (°)	1.27	1.16

*Highest resolution shell in parentheses.

3.6. Summary and Conclusions

Collectively, the results show potent inhibition of AmpC$_{EC}$ by diazabicyclooctanes, both with isolated AmpC$_{EC}$ and in cells, and provide detailed insight into the mechanistic and structural basis of AmpC$_{EC}$ inhibition by AVI, REL, NAC, and ZID.

The kinetic studies reveal an unusual kinetic profile for ZID compared to other DBOs as manifested in accelerated on- and off-rate constants (Figure 4 and Table 2), which rationalise improved inhibition on short to no preincubation with AmpC$_{EC}$ in solution, together with no apparent increase of potency on equilibration after prolonged preincubation (Figure 3 and Table 2). These observations may suggest either (or a combination) of two different changes in the thermodynamic profile of the reaction of AmpC$_{EC}$ with ZID: a) improved energetic stabilisation of both ZID in solution and the AmpC$_{EC}$-ZID carbamoyl-enzyme complex or b) improved stabilisation of the tetrahedral intermediate involved in carbamoylation and de-carbamoylation.

To investigate the thermodynamic basis of the altered kinetic profiles, competition studies between two DBOs (AVI in combination with either REL, NAC, or ZID) were carried out via denaturing protein observed SPE-MS (Figure 9-10). The results show no evidence for preferential binding of ZID over AVI under equilibrium conditions, as would be expected on improved stabilisation of the AmpC$_{EC}$-ZID carbamoyl-enzyme complex. The distinctive kinetic profile for AmpC$_{EC}$ inhibition by ZID compared to the other DBOs thus likely results (at least predominantly) from improved thermodynamic stabilisation of the tetrahedral intermediate involved in both the carbamoylation and de-carbamoylation of AmpC$_{EC}$ with ZID.

The SPE-MS studies further show initial evidence for de-sulfation of the AmpC$_{EC}$-DBO carbamoyl-enzyme complexes (Figure 6), which had previously been described as an intermediate of DBO hydrolysis by KPC type serine β-lactamases[5]. However, as, other than with the KPC enzymes (Figure 7-8), the ratio of de-sulfated carbamoyl-AmpC$_{EC}$ complexes stayed constant over 24 h, de-sulfation of the AmpC$_{EC}$-DBO complexes likely does not result from an enzymatic reaction but is rather a product of reactions inducted under the ESI-MS conditions as reported previously on MS analysis of class C and D SBL reaction with AVI[5].

In accordance with the MS data, no substantial de-sulfation was observed in any of the crystal structures of AmpC$_{EC}$ reacted with AVI, REL, NAC, or ZID (Figure 11-14). By contrast with the reported structure for KPC-2[2], all structures showed the DBOs in their ring-opened form and with a fully intact *N*-sulfate moiety. Differences observed in the positioning of the *N*-sulfate nitrogen are notable as they do not obviously appear to correlate with the kinetic data which indicate more readily recyclisation and de-carbamoylation of ZID compared to the other DBOs. Based on the commonly proposed carbamoylation and de-carbamoylation mechanisms suggesting Tyr150 as the catalytic base initiating recyclisation[8] and the structural data

presented here, the partial re-orientation of the ZID *N*-sulfate nitrogen would suggest slower recyclisation / de-carbamoylation compared to e.g. AVI which appears 'fully primed' towards recyclisation with the *N*-sulfate nitrogen positioned in close proximity to Tyr150. Therefore, the structural data on AmpC$_{EC}$-DBO binding should be interpreted with caution as the binding mode in the crystalline state may not reflect those relevant in solution.

The binding-modes observed in the crystal structures are, however, in agreement with the protein observed SPE-MS competition experiments (Figure 9-10), showing no apparent improved stabilisation of the AmpC$_{EC}$-ZID carbamoyl-enzyme complex (Figure 14) compared to the respective AVI complex (Figure 11), as the ZID sidechain does not appear to engage in any strong polar interactions. Further, the ZID binding-mode appears more flexible compared to the other DBO-derived carbamoyl-enzyme complexes, as evident in four different observed binding modes, compared to one or two binding modes observed with the other carbamoyl-enzyme complexes (Figure 11-13).

While all tested DBOs show good potency against the single AmpC$_{EC}$ expressing *E. coli* lab strain tested, ZID outperforms AVI substantially under the fixed-concentration conditions in the *in vitro* experiments (Table 3), which may in part also result from the improved antimicrobial activity of ZID compared to the other DBOs (Table 4). The accelerated off-rate of ZID observed in solution (Table 2) may, however, have a stronger negative impact *in vivo* where antibiotic and β-lactamase inhibitor concentrations fluctuate and resistance mechanisms (e.g. efflux pumps) may increase the importance of the residency times of the target-inhibitor complex[31-33].

Overall, the combined results thus suggest room for further improvement of the DBO scaffold for AmpC$_{EC}$ inhibition via C2 sidechain-modification.

3.7. Materials and Methods

3.7.1. Materials

Avibactam (AVI, AstraZeneca), relebactam (REL, MedKoo Biosciences, Inc.), nacubactam (NAC, Advanced ChemBlocks, Inc.), and zidebactam (ZID, MedKoo Biosciences, Inc.) were obtained from commercial suppliers.

3.7.2. Recombinant enzyme production and purification

AmpC$_{EC}$ was expressed and purified as described in Chapter 2. KPC variants were provided by Catherine L. Tooke (University of Bristol).

3.7.3. Kinetics

Dose-dependence and detailed kinetic studies on $AmpC_{EC}$ inhibition by DBOs were carried out according to modified reported procedures[24,34,35] which are described in detail in Chapter 2. In short, pIC_{50}s were determined after incubating $AmpC_{EC}$ (500 pM) with AVI, REL, NAC, or ZID at varying concentrations for 0, 10, 30, 60, or 360 min at room temperature, followed by addition of FC-5 (5 µM) and monitoring of reactions for 30 min. To determine apparent inhibition constants K_{iapp} and second-order rate constants (k_2/K), 100 nM $AmpC_{EC}$ were assayed with FC-5 (5 µM) in the presence of varying concentration of AVI, REL, NAC, or ZID. Reactions were initiated by addition of $AmpC_{EC}$, then immediately monitored continuously for 30 s. For off-rates (k_{off}) $AmpC_{EC}$ (1 µM) was incubated with AVI, REL, NAC, or ZID (10 µM) for 30 min at room temperature, then diluted 100,000-fold and assayed with FC-5 (25 µM). All assays were in 50 mM phosphate buffer, pH 7.5 supplemented with 0.01% (*v*/*v*) Triton X-100. Data were analysed as described in Chapter 2.

3.7.4. Mass spectrometry

Unless stated otherwise, 3 µM $AmpC_{EC}$ or KPC-2, -3, or -4 were incubated with 3.3 µM or 6 µM AVI, REL, NAC, or ZID at room temperature in 50 mM Tris, pH 7.5. Samples were taken at indicated timepoints and analysed using SPE-MS as described in Chapter 2.

3.7.5. Antimicrobial susceptibility testing

The pAD7 plasmid[26] was transformed into chemically competent *E. coli* DH5α. Minimum inhibitory concentration (MICs) values were determined via broth microdilution (BMD) in Müller-Hinton broth (MH, Sigma Aldrich) according to guidelines of the Clinical and Laboratory Standards Institute (CLSI), both for *E. coli* DH5α pAD7 $AmpC_{EC}$ and the *E. coli* DH5α wildtype strain. Experiments were performed in technical triplicates in 96-well microtiter plates (Corning) containing MH supplemented with CAZ (0.125 - 256 µg ml^{-1}) as well as AVI (0.125, 0.25, 0.5, 1, 2, 4, or 8 µg ml^{-1}), REL (8 µg ml^{-1}), NAC (8 µg ml^{-1}), or ZID (0.125, 0.25, 0.5, 1, 2, 4, or 8 µg ml^{-1}). Plates were incubated for 18-24 h at 37 °C. Subsequently, absorbance was measured at 600 nm using a CLARIOstar plate-reader (BMG Labtech).

3.7.6. X-ray crystallography

$AmpC_{EC}$ was crystallised as described in Chapter 2. Crystals were transferred into well precipitant solution supplemented with AVI, REL, NAC, or ZID, then incubated at room temperature for 10, 6, 8, or 10 min, respectively. The crystals were then mounted on nylon loops, cryo-cooled, and stored in liquid nitrogen. X-ray diffraction data were collected at 100 K

using the i03 MX beamline at Diamond Light Source (DLS) and processed using the Xia2 pipeline[36]. Structures were solved by molecular replacement using Phaser[37] and the structure of unmodified AmpC$_{EC}$ (PDB: 6T3D, Chapter 2) as the starting model. Alternating cycles of refinement using phenix.refine[38] and manual model building using Coot[39] were performed until R_{work} and R_{free} converged.

3.8. References

1. Lang, P.A.; Leissing, T.M.; Page, M.G.P.; Schofield, C.J.; Brem, J. Structural Investigations of the Inhibition of *Escherichia coli* AmpC β-Lactamase by Diazabicyclooctanes. *Antimicrob. Agents Chemother.* **2020**, *65*, e02073-02020.
2. Tooke, C.L.; Hinchliffe, P.; Lang, P.A.; Mulholland, A.J.; Brem, J.; Schofield, C.J.; Spencer, J. Molecular Basis of Class A β-Lactamase Inhibition by Relebactam. *Antimicrob. Agents Chemother.* **2019**, *63*, e00564-00519.
3. Drawz, S.M.; Bonomo, R.A. Three decades of β-lactamase inhibitors. *Clin. Microbiol. Rev.* **2010**, *23*, 160-201.
4. Wang, D.Y.; Abboud, M.I.; Markoulides, M.S.; Brem, J.; Schofield, C.J. The road to avibactam: the first clinically useful non-β-lactam working somewhat like a β-lactam. *Future Med. Chem.* **2016**, *8*, 1063-1084.
5. Ehmann, D.E.; Jahic, H.; Ross, P.L.; Gu, R.F.; Hu, J.; Durand-Reville, T.F.; Lahiri, S.; Thresher, J.; Livchak, S.; Gao, N., et al. Kinetics of avibactam inhibition against Class A, C, and D β-lactamases. *J. Biol. Chem.* **2013**, *288*, 27960-27971.
6. Ehmann, D.E.; Jahic, H.; Ross, P.L.; Gu, R.F.; Hu, J.; Kern, G.; Walkup, G.K.; Fisher, S.L. Avibactam is a covalent, reversible, non-β-lactam β-lactamase inhibitor. *Proc. Natl. Acad. Sci. U. S. A.* **2012**, *109*, 11663-11668.
7. Choi, H.; Paton, R.S.; Park, H.; Schofield, C.J. Investigations on recyclisation and hydrolysis in avibactam mediated serine β-lactamase inhibition. *Org. Biomol. Chem.* **2016**, *14*, 4116-4128.
8. Lahiri, S.D.; Johnstone, M.R.; Ross, P.L.; McLaughlin, R.E.; Olivier, N.B.; Alm, R.A. Avibactam and class C β-lactamases: mechanism of inhibition, conservation of the binding pocket, and implications for resistance. *Antimicrob. Agents Chemother.* **2014**, *58*, 5704-5713.
9. Durand-Réville, T.F.; Guler, S.; Comita-Prevoir, J.; Chen, B.; Bifulco, N.; Huynh, H.; Lahiri, S.; Shapiro, A.B.; McLeod, S.M.; Carter, N.M., et al. ETX2514 is a broad-spectrum β-lactamase inhibitor for the treatment of drug-resistant Gram-negative bacteria including *Acinetobacter baumannii*. *Nat. Microbiol.* **2017**, *2*, 17104.
10. Shapiro, A.B.; Gao, N.; Jahić, H.; Carter, N.M.; Chen, A.; Miller, A.A. Reversibility of Covalent, Broad-Spectrum Serine β-Lactamase Inhibition by the Diazabicyclooctenone ETX2514. *ACS Infect. Dis.* **2017**, *3*, 833-844.
11. Blizzard, T.A.; Chen, H.; Kim, S.; Wu, J.; Bodner, R.; Gude, C.; Imbriglio, J.; Young, K.; Park, Y.-W.; Ogawa, A., et al. Discovery of MK-7655, a β-lactamase inhibitor for combination with Primaxin®. *Bioorg. Med. Chem. Lett.* **2014**, *24*, 780-785.
12. Morinaka, A.; Tsutsumi, Y.; Yamada, M.; Suzuki, K.; Watanabe, T.; Abe, T.; Furuuchi, T.; Inamura, S.; Sakamaki, Y.; Mitsuhashi, N., et al. OP0595, a new diazabicyclooctane: mode of action as a serine β-lactamase inhibitor, antibiotic and β-lactam 'enhancer'. *J. Antimicrob. Chemother.* **2015**, *70*, 2779-2786.
13. Moya, B.; Barcelo, I.M.; Bhagwat, S.; Patel, M.; Bou, G.; Papp-Wallace, K.M.; Bonomo, R.A.; Oliver, A. WCK 5107 (Zidebactam) and WCK 5153 are novel inhibitors of PBP2 showing potent "β-Lactam Enhancer" activity against *Pseudomonas aeruginosa*, including multidrug-resistant metallo-β-lactamase-producing high-risk clones. *Antimicrob. Agents Chemother.* **2017**, *61*, e02529-02516.

14. King, D.T.; King, A.M.; Lal, S.M.; Wright, G.D.; Strynadka, N.C.J. Molecular Mechanism of Avibactam-Mediated β-Lactamase Inhibition. *ACS Infect. Dis.* **2015**, *1*, 175-184.
15. Krishnan, N.P.; Nguyen, N.Q.; Papp-Wallace, K.M.; Bonomo, R.A.; van den Akker, F. Inhibition of Klebsiella β-Lactamases (SHV-1 and KPC-2) by Avibactam: A Structural Study. *PLoS One* **2015**, *10*, e0136813.
16. Lahiri, S.D.; Mangani, S.; Durand-Reville, T.; Benvenuti, M.; De Luca, F.; Sanyal, G.; Docquier, J.-D. Structural Insight into Potent Broad-Spectrum Inhibition with Reversible Recyclization Mechanism: Avibactam in Complex with CTX-M-15 and *Pseudomonas aeruginosa* AmpC β-Lactamases. *Antimicrob. Agents Chemother.* **2013**, *57*, 2496-2505.
17. Lahiri, S.D.; Mangani, S.; Jahić, H.; Benvenuti, M.; Durand-Reville, T.F.; De Luca, F.; Ehmann, D.E.; Rossolini, G.M.; Alm, R.A.; Docquier, J.-D. Molecular Basis of Selective Inhibition and Slow Reversibility of Avibactam against Class D Carbapenemases: A Structure-Guided Study of OXA-24 and OXA-48. *ACS Chem. Biol.* **2015**, *10*, 591-600.
18. Lohans, C.T.; Wang, D.Y.; Jorgensen, C.; Cahill, S.T.; Clifton, I.J.; McDonough, M.A.; Oswin, H.P.; Spencer, J.; Domene, C.; Claridge, T.D.W., et al. 13C-Carbamylation as a mechanistic probe for the inhibition of class D β-lactamases by avibactam and halide ions. *Org. Biomol. Chem.* **2017**, *15*, 6024-6032.
19. Nukaga, M.; Papp-Wallace, K.M.; Hoshino, T.; Lefurgy, S.T.; Bethel, C.R.; Barnes, M.D.; Zeiser, E.T.; Johnson, J.K.; Bonomo, R.A. Probing the Mechanism of Inactivation of the FOX-4 Cephamycinase by Avibactam. *Antimicrob. Agents Chemother.* **2018**, *62*, e02371-02317.
20. Pozzi, C.; Di Pisa, F.; De Luca, F.; Benvenuti, M.; Docquier, J.D.; Mangani, S. Atomic-Resolution Structure of a Class C β-Lactamase and Its Complex with Avibactam. *ChemMedChem* **2018**, *13*, 1437-1446.
21. Jin, W.; Wachino, J.-i.; Yamaguchi, Y.; Kimura, K.; Kumar, A.; Yamada, M.; Morinaka, A.; Sakamaki, Y.; Yonezawa, M.; Kurosaki, H., et al. Structural Insights into the TLA-3 Extended-Spectrum β-Lactamase and Its Inhibition by Avibactam and OP0595. *Antimicrob. Agents Chemother.* **2017**, *61*, e00501-00517.
22. Papp-Wallace, K.M.; Nguyen, N.Q.; Jacobs, M.R.; Bethel, C.R.; Barnes, M.D.; Kumar, V.; Bajaksouzian, S.; Rudin, S.D.; Rather, P.N.; Bhavsar, S., et al. Strategic Approaches to Overcome Resistance against Gram-Negative Pathogens Using β-Lactamase Inhibitors and β-Lactam Enhancers: Activity of Three Novel Diazabicyclooctanes WCK 5153, Zidebactam (WCK 5107), and WCK 4234. *J. Med. Chem.* **2018**, *61*, 4067-4086.
23. Ruggiero, M.; Papp-Wallace, K.M.; Brunetti, F.; Barnes, M.D.; Bonomo, R.A.; Gutkind, G.; Klinke, S.; Power, P. Structural Insights into the Inhibition of the Extended-Spectrum β-Lactamase PER-2 by Avibactam. *Antimicrob. Agents Chemother.* **2019**, *63*, e00487-00419.
24. van Berkel, S.S.; Brem, J.; Rydzik, A.M.; Salimraj, R.; Cain, R.; Verma, A.; Owens, R.J.; Fishwick, C.W.G.; Spencer, J.; Schofield, C.J. Assay platform for clinically relevant metallo-β-lactamases. *J. Med. Chem.* **2013**, *56*, 6945-6953.
25. Lang, P.A.; Parkova, A.; Leissing, T.M.; Calvopina, K.; Cain, R.; Krajnc, A.; Panduwawala, T.D.; Philippe, J.; Fishwick, C.W.; Trapencieris, P., et al. Bicyclic Boronates as Potent Inhibitors of AmpC, the Class C β-Lactamase from *Escherichia coli*. *Biomolecules* **2020**, *10*, 899.
26. Dubus, A.; Wilkin, J.M.; Raquet, X.; Normark, S.; Frère, J.M. Catalytic mechanism of active-site serine β-lactamases: role of the conserved hydroxy group of the Lys-Thr(Ser)-Gly triad. *Biochem. J.* **1994**, *301*, 485-494.
27. Livermore, D.M.; Mushtaq, S.; Warner, M.; Vickers, A.; Woodford, N. *In vitro* activity of cefepime/zidebactam (WCK 5222) against Gram-negative bacteria. *J. Antimicrob. Chemother.* **2017**, *72*, 1373-1385.
28. Liebschner, D.; Afonine, P.V.; Moriarty, N.W.; Poon, B.K.; Sobolev, O.V.; Terwilliger, T.C.; Adams, P.D. Polder maps: improving OMIT maps by excluding bulk solvent. *Acta Crystallogr. D* **2017**, *73*, 148-157.

29. Kawai, A.; McElheny, C.L.; Iovleva, A.; Kline, E.G.; Sluis-Cremer, N.; Shields, R.K.; Doi, Y. Structural basis of reduced susceptibility to ceftazidime-avibactam and cefiderocol in *Enterobacter cloacae* due to AmpC R2 loop deletion. *Antimicrob. Agents Chemother.* **2020**, *64*, 198-120.
30. Bürgi, H.B.; Dunitz, J.D.; Lehn, J.M.; Wipff, G. Stereochemistry of reaction paths at carbonyl centres. *Tetrahedron* **1974**, *30*, 1563-1572.
31. Copeland, R.A.; Pompliano, D.L.; Meek, T.D. Drug-target residence time and its implications for lead optimization. *Nat. Rev. Drug Discov.* **2006**, *5*, 730-739.
32. Lu, H.; Tonge, P.J. Drug-target residence time: critical information for lead optimization. *Curr. Opin. Chem. Biol.* **2010**, *14*, 467-474.
33. Tonge, P.J. Drug-Target Kinetics in Drug Discovery. *ACS Chem. Neurosci.* **2018**, *9*, 29-39.
34. Williams, J.W.; Morrison, J.F. The kinetics of reversible tight-binding inhibition. In *Methods in Enzymology*, Academic Press: **1979**; Vol. 63, pp. 437-467.
35. Copeland, R.A.; Basavapathruni, A.; Moyer, M.; Scott, M.P. Impact of enzyme concentration and residence time on apparent activity recovery in jump dilution analysis. *Anal. Biochem.* **2011**, *416*, 206-210.
36. Winter, G. xia2: an expert system for macromolecular crystallography data reduction. *J. Appl. Crystallogr.* **2010**, *43*, 186-190.
37. McCoy, A.J.; Grosse-Kunstleve, R.W.; Adams, P.D.; Winn, M.D.; Storoni, L.C.; Read, R.J. Phaser crystallographic software. *J. Appl. Crystallogr.* **2007**, *40*, 658-674.
38. Adams, P.D.; Grosse-Kunstleve, R.W.; Hung, L.W.; Ioerger, T.R.; McCoy, A.J.; Moriarty, N.W.; Read, R.J.; Sacchettini, J.C.; Sauter, N.K.; Terwilliger, T.C. PHENIX: building new software for automated crystallographic structure determination. *Acta Crystallogr. D* **2002**, *58*, 1948-1954.
39. Emsley, P.; Lohkamp, B.; Scott, W.G.; Cowtan, K. Features and development of Coot. *Acta Crystallogr. D* **2010**, *66*, 486-501.

Chapter 4

AmpC$_{EC}$ interactions with Cyclic Boronates

The work in this chapter was carried out in conjunction with Dr Jürgen Brem, who advised on the experimental design, expressed and purified recombinant TEM-116, and obtained the co-crystal structure of AmpC$_{EC}$ in complex with CB2, Dr Thomas M. Leissing, who assisted with the crystallographic experiments, and Dr Karina Calvopiña, who supported microbiological experiments. The bicyclic boronate inhibitors were synthesised by Anete Parkova under the supervision of Prof. Peteris Trapencieris (Latvian Institute of Organic Synthesis), Ricky Cain under the supervision of Prof. Colin Fishwick (University of Leeds), Alen Krajnc, and Dr Tharindi Panduwawala. The majority of the work described herein has been reported in the academic literature[1,2].

Contents

4.1. Introduction 127
4.2. Steady-state kinetics of SBL inhibition by cyclic boronates 129
4.2.1. Bicyclic boronates inhibit all classes of SBLs 129
4.2.2. Detailed kinetic studies for $AmpC_{EC}$ inhibition by cyclic boronates 130
4.3. Cyclic boronates restore ceftazidime activity in $AmpC_{EC}$ expressing *E. coli* 131
4.4. Structural characterisation of $AmpC_{EC}$-boronate interactions 132
4.4.1. Crystal structures of $AmpC_{EC}$-CB2 complex 132
4.4.2. Crystal structure of the $AmpC_{EC}$-CB3 complex 136
4.4.3. Crystal structure of $AmpC_{EC}$-TAN complex 138
4.4.4. Comparison of binding modes of bicyclic boronates 143
4.5. Summary and Conclusions 144
4.6. Materials and Methods 145
4.6.1. Materials 145
4.6.2. Recombinant enzyme production and purification 145
4.6.3. Kinetics 145
4.6.4. Antimicrobial Susceptibility Testing 146
4.6.5. Crystallography 146
4.7. References 146

4.1. Introduction

All β-lactamase inhibitors described in the previous chapters have one thing in common – while each of them shows potent inhibition of (at least a certain set of) SBLs, none display any clinically useful activity against any metallo-β-lactamases (MBLs). While much work has been focused on SBLs, which are presently the β-lactamases most commonly encountered in the clinic[3], it is important to note that MBL dissemination is increasing and developing into a major concern for the use of β-lactam antibiotics[4]. MBLs are not just resistant to inhibition by the β-lactam-based inhibitors described in Chapter 2, and the diazabicyclooctane based inhibitors described in Chapter 3, but have been shown to have potential to inactivate them (albeit slowly in the case of the diazabiocyclooctanes)[5-7]. While MBLs have long been known to be inhibited by metal-chelating agents such as EDTA and thiol-inhibitors such as captopril[8] and bisthiazolidines[9], it is likely none of those are sufficiently selective over other metallo-enzymes to be useful as drugs, leaving an urgent unmet clinical need for selective MBL inhibitors[4]. This was only changed in 2020 with the FDA approval of taniborbactam, the first clinically useful β-lactamase inhibitor, which is not only potent against SBLs, but also some MBLs[2,10-12].

MBLs are predominantly encoded on mobile plasmids and pathogenic strains producing both SBLs and MBLs, as well as other resistance mechanism (e.g. porins, efflux-pumps, etc.), are becoming increasingly prevalent[13]. Therefore, bicyclic boronates such as taniborbactam are of special interest because of their potential “dual-action” mode, i.e. of inhibiting both SBLs and MBLs. They further show some potential as inhibitors of penicillin binding proteins (PBPs), but the available inhibitors so far only show weak PBP inhibition which does not confer antimicrobial activity[14]. Therefore, bicyclic boronates are currently only used in combination with a β-lactam antibiotic.

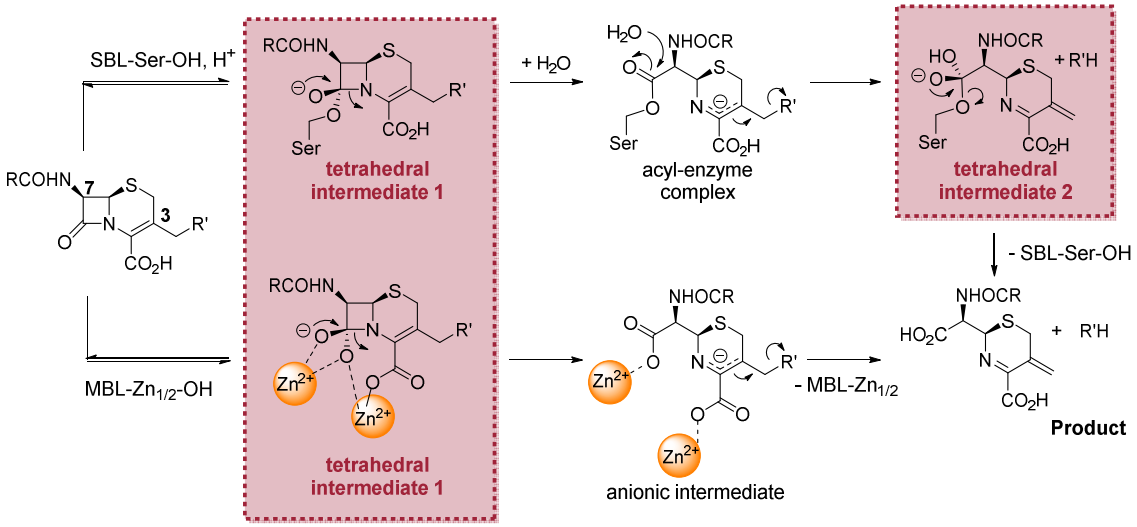


Figure 1: Serine- and metallo-β-lactamases catalysis both involves tetrahedral transition states.

Cyclic boronates are proposed to inhibit SBLs and MBLs (as well as PBPs) in part by imitation of tetrahedral intermediates common to catalysis of both classes of β-lactamase (Figure 1)[14].

This is possible through an equilibrium of sp^2- and sp^3-hybridised boronate species (Figure 2). In their sp^2-form boronates are thought to imitate the β-lactam substrates of β-lactamases, while the anionic tetrahedral sp^3-species show close resemblance of the tetrahedral transition states in β-lactamase catalysis (Figure 1)[15].

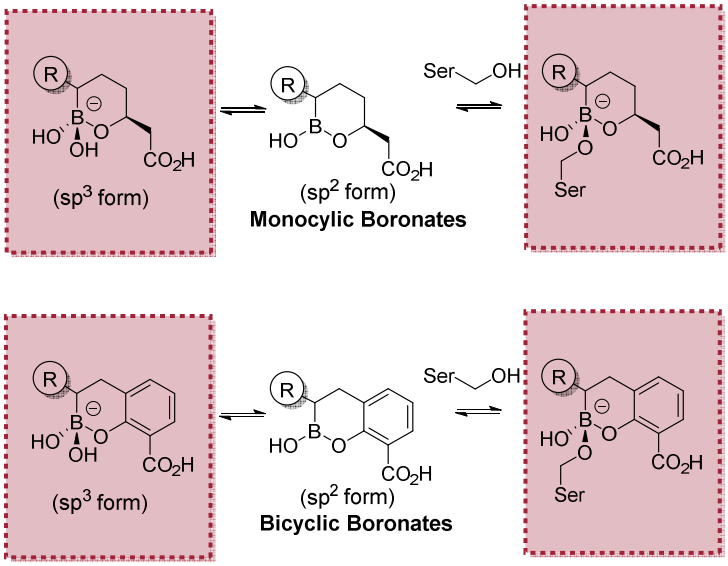


Figure 2: Mono- and bicyclic boronates both exist in sp^2- and sp^3-form and can thus imitate tetrahedral intermediates of both SBL- and MBL catalysis.

The work described in this chapter aimed to characterise the interactions of $AmpC_{EC}$ with taniborbactam and related bicyclic boronate inhibitors, i.e. previously reported model cyclic boronate 2 (CB2, Figure 3)[14,16-18] and a thioether bicyclic boronate derivative (CB3, Figure 3) which had previously reported to show enhanced potency against some SBLs and MBLs *in vitro*[17,19], to support structure-activity relationship (SAR) guided development of this scaffold for class C SBL inhibition.

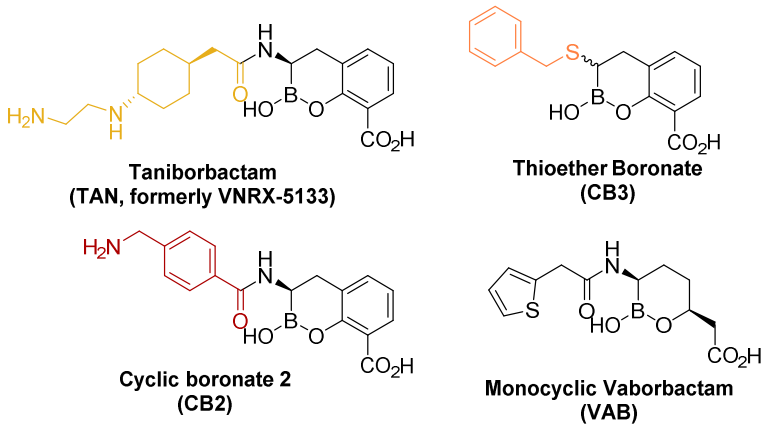


Figure 3: Cyclic boronates studied in this chapter.

4.2. Steady-state kinetics of SBL inhibition by cyclic boronates

4.2.1. Bicyclic boronates inhibit all classes of SBLs

CB2 and TAN were tested for inhibition against SBLs from all three Ambler classes: the class A SBL TEM-116 (*produced and purified by Dr. Jürgen Brem, University of Oxford*), AmpC$_{EC}$ from class C, and the two class D SBLs OXA-10 and OXA-48 (Figure 4).

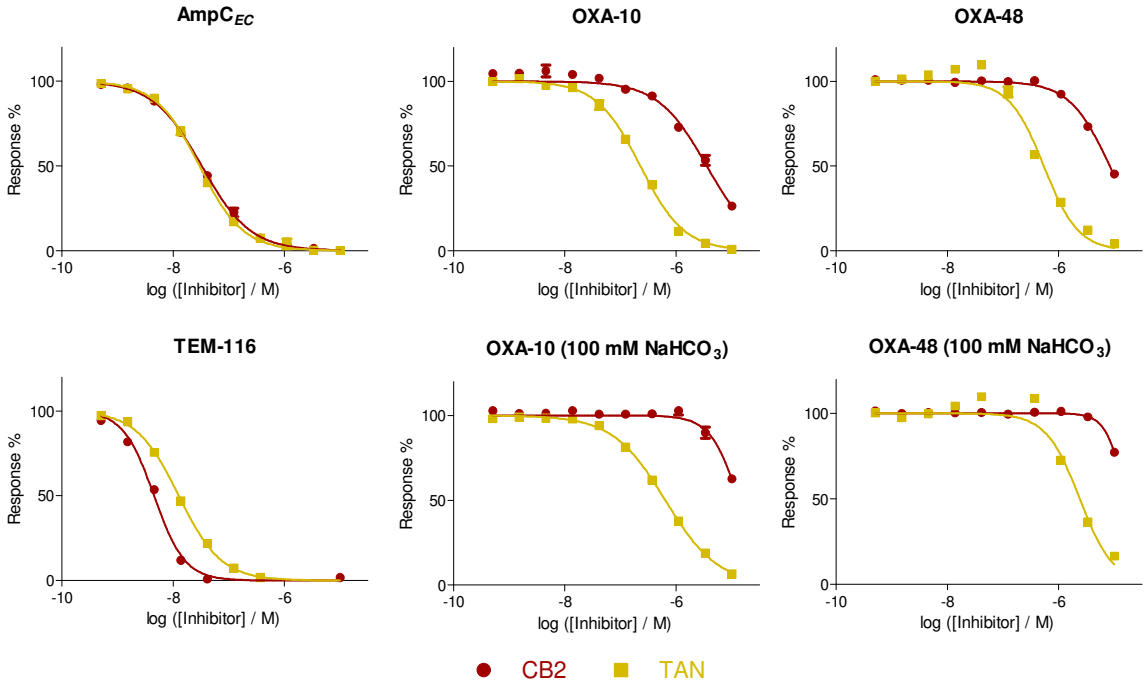


Figure 4: Dose-dependence of SBLs inhibition from Ambler classes A, C, and D by CB2 and TAN. AmpC$_{EC}$ (500 pM), TEM-116 (1 nM), OXA-10 (250 pM), and OXA-48 (250 pM) were incubated with inhibitors for 10 min at room temperature, then assayed with 5 µM FC-5[20]. Buffer: 50 mM phosphate buffer, pH 7.5, 0.01 % (v/v) Triton-X 100. In the case of class D SBLs assays were performed both with and without addition of 100 mM $NaHCO_3$.

With AmpC$_{EC}$, both boronates showed similarly potent inhibition (pIC_{50} 7.5, Table 1). By contrast, the different amido-side chains of CB2 and TAN appeared to substantially alter the inhibition profile towards the class A and D SBLs. While CB2 showed improved potency against TEM-116 compared to TAN (pIC_{50} 8.3 and 7.9, respectively), TAN was more potent compared to CB2 both against OXA-10 and OXA-48 (pIC_{50}s 5.6-6.6 compared to 4.8-5.5, as assayed with and without addition of 100 mM $NaHCO_3$ to ensure full Lys70 carbamylation, Table 1).

Table 1: pIC_{50}s for SBL inhibition by CB2 and taniborbactam. pIC_{50}s were determined from non-linear regression, as shown in Figure 4.

	pIC_{50}					
Inhibitor	**AmpC$_{EC}$**	**TEM-116**	**OXA-10**		**OXA-48**	
buffer	standard condition	standard condition	standard condition	+ 100 mM $NaHCO_3$	standard condition	+ 100 mM $NaHCO_3$
CB2	7.49 ± 0.01	8.34 ± 0.02	5.45 ± 0.03	4.87 ± 0.03	4.79 ± 0.03	5.08 ± 0.01
TAN	7.53 ± 0.01	7.90 ± 0.01	6.64 ± 0.02	6.19 ± 0.01	5.62 ± 0.03	6.27 ± 0.03

4.2.2. Detailed kinetic studies for AmpC$_{EC}$ inhibition by cyclic boronates

With AmpC$_{EC}$, detailed kinetics were determined with the different bicyclic boronates and the monocyclic VAB in competition with FC-5[20] (Figure 5 and Table 2). Initially the apparent inhibition constants (K_{iapp}) for all four inhibitors were determined (Figure 5A), showing superior potency of the three bicyclic boronates compared to VAB (K_{iapp} ~ 1–4 µM for the bicyclic boronates, compared to 19 µM for VAB). Out of the bicyclic boronates, CB3 showed ~ 2-fold improved inhibition compared to CB2 and TAN (K_{iapp} 1 µM for CB3, compared to 3 µM and 4 µM for CB2 and TAN, respectively). Interestingly, this effect was diminished in dose-response experiments which were carried out after a 10 min pre-incubation period with AmpC$_{EC}$, with CB2, TAN, and CB3 all showing equal potency (pIC$_{50}$ 7.5), while VAB remained less potent (pIC$_{50}$ 6.3, Figure 5D).

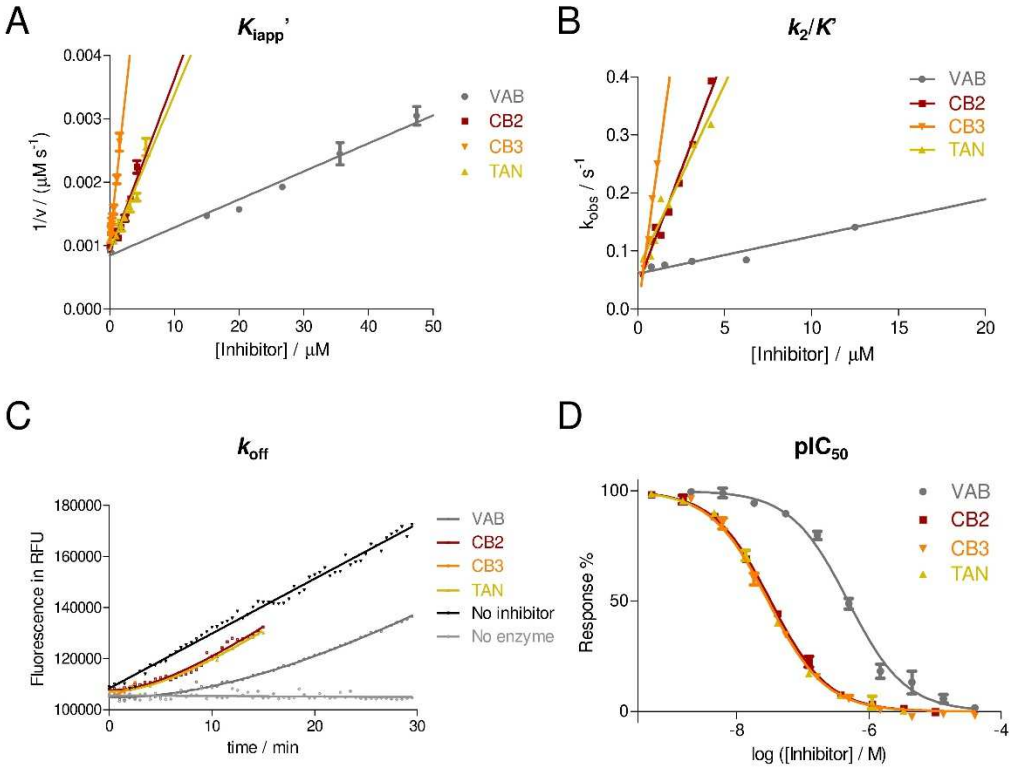


Figure 5: Kinetic characterisation of reversible AmpC$_{EC}$ inhibition by cyclic boronates. (A) Determination of the K_{iapp} value of AmpC$_{EC}$ inhibition by cyclic boronates. (B) Pseudo first-order rate (k_2/K) determination for AmpC$_{EC}$ (100 nM) with TAN, CB2, or CB3. (C) Dissociation after 'jump-dilution' of an AmpC$_{EC}$ solution (10 µM) pre-incubated with cyclic boronates (10 µM for TAN, CB2 and CB3 and 100 µM for VAB) at room temperature for 30 min, then diluted 100.000 fold and assayed with FC-5[20] (25 µM). (D) Dose-response curves for AmpC$_{EC}$ (500 pM) after 10 min inhibitor pre-incubation at room temperature, assayed using FC-5[20] (5 µM). Buffer: 50 mM phosphate buffer, pH 7.5, 0.01 % (v/v) Triton-X 100. The figure and figure legend are adopted with permission from Lang *et al*. *Biomolecules*, 2020, *10*, 899.

This difference can be rationalised by the observed 3-fold increased binding-rate for CB3, compared to CB2 and TAN, i.e. k_2/K ~ 224 × 10^3 M^{-1} s^{-1} for CB3 compared to ~ 80 × 10^3 M^{-1} s^{-1} for CB2 and TAN and ~ 7 × 10^3 M^{-1} s^{-1} for VAB, Figure 5B), but similarly accelerated off-rates

(21 × 10^{-3} s^{-1} for CB3, compared to 3 × 10^{-3} s^{-1} for CB2 and TAN and 0.7 × 10^{-3} s^{-1} for VAB, Figure 5C), resulting in a shorter half-life of the enzyme-inhibitor complex for CB3 (Table 2). These differences are consistent with the observed improved potency for CB3 when tested without pre-incubation with AmpC$_{EC}$ (as is the case in the K_{iapp} measurements), but not after a sufficient pre-incubation time (to allow equilibration).

Table 2: Steady-state kinetics of cyclic boronate inhibition of isolated AmpC$_{EC}$. K_{iapp} values and pseudo first-order rates (k_2/K) were determined by assaying 100 nM AmpC$_{EC}$ with 5 µM FC-5[36]. k_{off} rates were determined after jump-dilution (100,000 fold) of AmpC$_{EC}$ (1 µM) that had been pre-incubated with cyclic boronates (10 µM for TAN, CB2 and CB3 and 100 µM for VAB) at room temperature for 30 min, then assayed using 25 µM FC-5. pIC$_{50}$s were obtained from assays using 500 pM AmpC$_{EC}$ and 5 µM FC-5 following a 10 min inhibitor pre-incubation at room temperature. Buffer: 50 mM Tris, pH 7.5, 0.01% (v/v) Triton X-100. Data were analysed as described in Materials and Methods.

Inhibitor	K_{iapp} (µM)	k_2/K (M^{-1} s^{-1}) × 10^3	k_{off} (s^{-1}) x 10^{-3}	$t_{1/2}$ (min)	pIC$_{50}$
VAB	19.1 ± 1.32	6.55 ± 0.46	0.69 ± 0.03	16.8 ± 0.7	6.32 ± 0.03
TAN	3.73 ± 0.50	85.6 ± 9.2	2.54 ± 0.51	4.55 ± 0.91	7.53 ± 0.02
CB2	3.26 ± 0.40	81.0 ± 6.4	2.77 ± 0.27	4.18 ± 0.41	7.49 ± 0.01
CB3	1.16 ± 0.14	224 ± 21	20.9 ± 12.8	0.55 ± 0.34	7.53 ± 0.02

4.3. Cyclic boronates restore ceftazidime activity in AmpC$_{EC}$ expressing *E. coli*

Microbiological experiments were supported by Dr Karina Calvopiña (University of Oxford).

To investigate AmpC$_{EC}$ inhibition by VAB, CB2, CB3, and TAN in cells, they were tested against AmpC$_{EC}$ producing *E. coli* DH5α in combination with ceftazidime (CAZ) using the broth microdilution method. Wildtype DH5α cells were susceptible to CAZ (MIC 1 µg ml^{-1}), and production of cellular AmpC$_{EC}$ via the pAD7 plasmid[21] (see Chapter 3) conferred substantial resistance (MIC 256 µg ml^{-1}).

Table 2. Cyclic boronates restore ceftazidime (CAZ) activity against AmpC$_{EC}$ producing *E. coli*. All inhibitors were tested at a fixed concentration of 4 µg ml^{-1}.

		Minimal Inhibitory Concentration Ceftazidime (µg ml^{-1})				
Strain	Plasmid	CAZ	CAZ (+ **VAB**)	CAZ (+ **TAN**)	CAZ (+ **CB2**)	CAZ (+ **CB3**)
DH5α	-	1	-	-	-	-
DH5α	pAD7 AmpC$_{EC}$	256	1	1	0.5	4

At the fixed concentration of 4 µg ml^{-1}, all the tested boronates restored CAZ activity against the AmpC$_{EC}$ expressing strain. However, while VAB, CB2, and TAN fully restored the activity of CAZ to ≤ 1 µg ml^{-1}, CB3 reduced the MIC only to 4 µg ml^{-1}. This observation contrasts with

the improved activity observed for CB3 against isolated AmpC$_{EC}$ (Table 2) and likely reflects poorer cell penetration resulting from the increased hydrophobicity of the CB3 sidechain.

4.4. Structural characterisation of AmpC$_{EC}$-boronate interactions

After establishing distinctive differences in the kinetic profiles for AmpC$_{EC}$ inhibition of the different bicyclic boronates, it was aimed to obtain crystal structures of the AmpC$_{EC}$-boronate complexes to investigate a potential structural basis.

Most of the structures were obtained via soaking of the inhibitors into AmpC$_{EC}$ crystals with CB2 (1.73 Å resolution), TAN (1.42 Å resolution, PDB: 6YEN), and CB3 (1.60 Å resolution, PDB: 6YPD) were obtained by soaking of unmodified-AmpC$_{EC}$ crystals. Because of low density observed for the CB2 sidechain in the structure obtained via soaking, a second structure of the AmpC$_{EC}$-CB2 complex (2.03 Å resolution, PDB: 6YEO) was obtained by co-crystallisation (*by Dr Jürgen Brem, University of Oxford*).

In all the structures of the AmpC$_{EC}$-boronate complexes the overall AmpC$_{EC}$ fold remains unchanged (main chain RMSDs with respect to the unmodified AmpC$_{EC}$ structure (PDB: 6T3D) of 0.39 Å, 0.15 Å, 0.07 Å for CB2, TAN, and CB3 (chain A), respectively). Analysis of electron density maps at the AmpC$_{EC}$ active site indicates bicyclic boronates CB2, TAN, and CB3 reacted with the nucleophilic Ser64 to form an anionic tetrahedral species in which a sp^3 hybridised boron, as observed with other structures of bicyclic boronate-SBL complexes[12,14,16,22-24].

4.4.1. Crystal structures of AmpC$_{EC}$-CB2 complex

As the water solubility of CB2 and CB3 is substantially lower than that of other tested BLI (including TAN), DMSO had to be used to solubilise the inhibitors; however, DMSO had a detrimental impact on the AmpC$_{EC}$ crystals, as evidenced by the complete loss of X-ray diffraction on soaking crystals for longer than 10-15 min (see Chapter 2).

4.4.1.1. Crystal structure of AmpC$_{EC}$-CB2 complex obtained via soaking

A structure obtained by soaking a crystal of unmodified AmpC$_{EC}$ with CB2 for 10 min (10 mM, 1.73 Å resolution, not deposited in the PDB, Figure 6 and Table 3) showed clear density of the bicyclic boronate core of CB2 (Figure 6B). The boronate is positioned for hydrogen-bonding interactions with the backbone of Ala318 (3.0 Å), while the carboxylic acid is positioned to engage in polar interactions with the sidechain of The316 (2.7-3.0 Å).

The C3 amido side chain is positioned for polar interactions with the backbone of Ala318 (3.0 Å) and the sidechains of Asn152 (2.7 Å) and Gln120 (3.0 Å), in a similar manner as observed with the C2 amido sidechains of diazabicyclooctanes (Chapter 2). While the electron density observed for the benzyl-amine portion of the C3 amido side chain is insufficient to unambiguously assign its position (Figure 6B), the terminal amine is likely positioned for hydrogen-bonding interactions with a water molecule (w in Figure 6A, 2.5 Å), which in turn is in close proximity to the backbone nitrogen of Ser212 (2.8 Å).

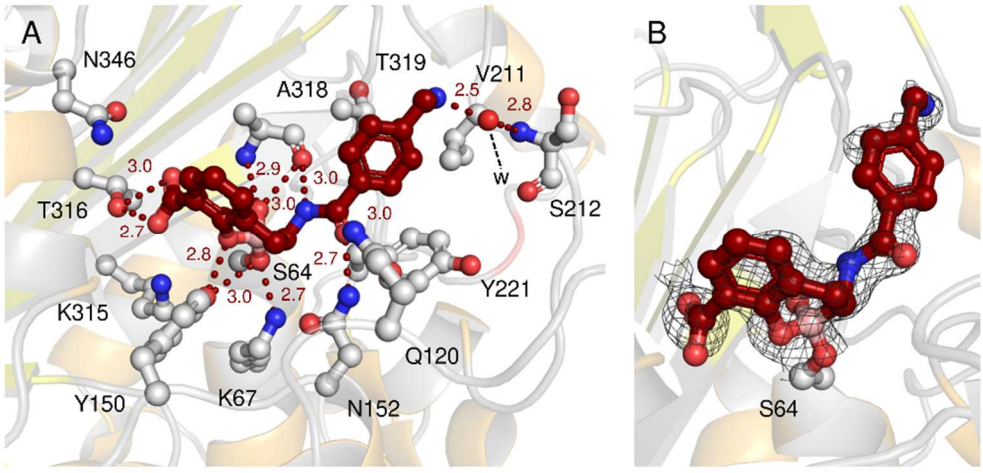


Figure 6: Views from a crystal structure of AmpC$_{EC}$ soaked with CB2. (A) Active site view showing CB2 covalently bound to Ser64. Hydrogen-bonding interactions are shown as dashed lines. Distances are indicated in Å. (B) $2mF_o$-DF_c map contoured at 1.0 σ and carved around CB2. Note that the electron density observed for the C3 amido sidechain is not sufficient to unambiguously indicate its position.

4.4.1.2. Co-crystallisation of AmpC$_{EC}$ with CB2

Because of the weak electron density observed for the C3 amido sidechain in structures obtained via soaking, co-crystallisation of AmpC$_{EC}$ with CB2 was investigated. As with the standard AmpC$_{EC}$ crystallisation conditions, co-crystallisation with CB2 prevented crystallisation (likely because of the added DMSO, 2% (v/v) final concentration), a broad screen was performed for the AmpC$_{EC}$-CB2 complex (*by Dr Jürgen Brem, University of Oxford*), which gave a structure of the complex with four molecules in the asymmetric unit (2.03 Å resolution, PDB: 6YEO, Figure 7 and Table 3).

In all four chains electron density was observed indicating covalently bound CB2 at the AmpC$_{EC}$ active site, with clear electron density for the C3 amido sidechain (Figure 7B). The overall fold (mainchain RMSD of chain B, C and D in relation to chain A: 0.31, 0.28, 0.33 Å respectively), as well as orientation of active site residues and CB2 (Figure 7D) are comparable in all chains. The carboxylic acid is positioned to engage in polar interactions with the sidechains of Gln346 (2.8 Å) and of Thr316 (2.8-3.0 Å).

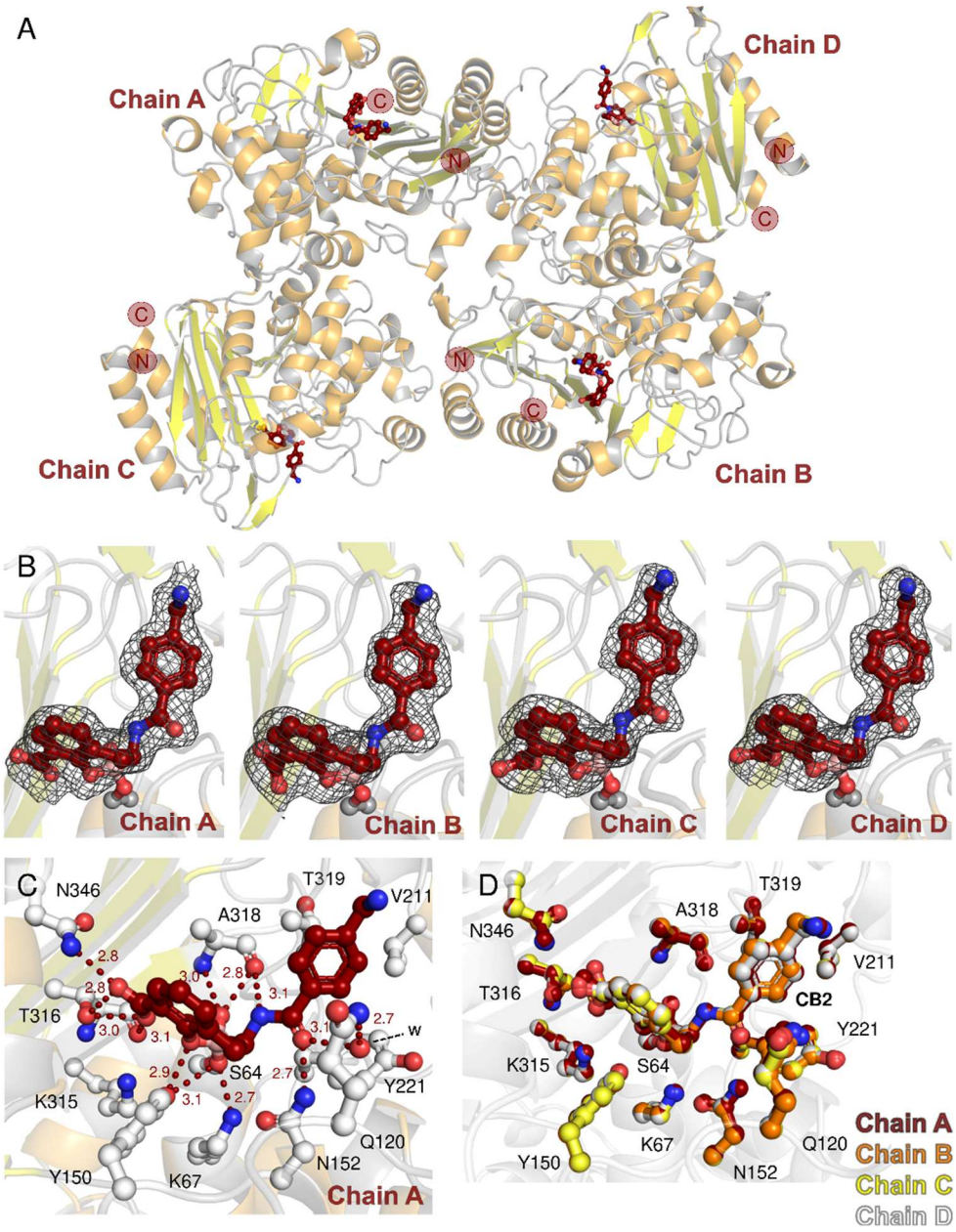


Figure 7: Views from a crystal structure obtained by co-crystallisation of AmpC*EC* with CB2. (A) Overview of the asymmetric unit (ASU) containing chains A-D. (B) mF_o-DF_c polder OMIT maps[25] contoured at 3.0 σ around CB2. (C) Structure of bound CB2 in its sp^3 form. (D) Overlay of colour coded active site residues and ligands in chains A-D shows no differences in the orientations of these residues and CB2. The figure and figure legend are adopted with permission from Lang *et al. Biomolecules*, 2020, *10*, 899.

Interestingly, while the C3 amido sidechain is positioned for polar interactions with the backbone of Ala318 (3.0 Å Å) and the sidechain of Asn152 (2.7 Å), in a similar manner as observed in the complex obtained via soaking (Figure 6A), in this structure the sidechain of Gln120 is positioned away from the active site in all four molecules (Figure 7C-D), preventing direct interaction with the C3 amide. Instead, a bridging water is observed, forming hydrogen bonds with both the Gln120 sidechain and the boronate C3 amide (w in Figure 7C, 3.1 Å and 2.7 Å, respectively).

4.4.1.3. Comparison of AmpC$_{EC}$-CB2 complex structures

Notably, the two structures of the AmpC$_{EC}$-CB2 complex were of crystals obtained in different crystallisation conditions (see Materials and Methods and Table 3), using precipitant solutions with different pH. The AmpC$_{EC}$-CB2 complex crystallised at pH 7.5, while unmodified AmpC$_{EC}$ crystallised at pH 6.0.

Table 3: Data collection and refinement statistics of AmpC$_{EC}$-CB2 complex crystals.

Datasets	**AmpC$_{EC}$-CB2 (soaked)**	**AmpC$_{EC}$-CB2 (co-crystallised)** (PDB ID: 6YEO)
Data Collection		
Beamline (Wavelength, Å)	DLS I03 (0.9686)	DLS I24 (0.9686)
Detector	Pilatus3 6M	Pilatus3 6M
Data Processing	Xia2 3dii	Xia2 dials
Space group	$P\,4_3\,3\,2$	$P\,2\,2\,2_1$
Cell dimensions		
- *a,b,c* (Å)	138.0, 138.0, 138.0	100.7, 179.6, 99.7
- α, β, γ (°)	90, 90, 90	90, 90, 90
No. of molecules/ASU	1	4
No. reflections	1820282 (87283)*	117532 (5616)*
Resolution (Å)	48.79-1.73 (1.76-1.73)*	100.68-2.03 (2.06-2.03)*
R_{meas}(I)	0.136 (3.396)*	0.368 (0.999)*
I/σI	18.4 (1.5)*	8.7 (2.7)*
$CC_{1/2}$	1.0 (0.6)*	1.0 (0.6)*
Completeness (%)	100 (100)*	100 (96.7)*
Multiplicity	38.4 (37.4)*	13.0 (13.1)*
Wilson B value (Å^2)	29.48	24.11
Refinement	PHENIX	PHENIX
R_{work}/R_{free}	0.1696/0.1959	0.1715/0.2027
No. atoms	3124	11915
- Enzyme	2807	10950
- Bound Inhibitor	27	101
- Water	279	864
Average B-factors	37.4	29.1
- Enzyme	36.4	28.3
- Bound Inhibitor	59.1	34.7
- Water	45.2	36.0
R.m.s deviations		
- Bond lengths (Å)	0.006	0.002
- Bond angles (°)	0.925	0.612

* Highest resolution shell in parentheses.

The two structures of the AmpC$_{EC}$-CB2 complex obtained via co-crystallisation and soaking do not show substantial differences in the AmpC$_{EC}$ fold (backbone RMSD of 0.38 Å for the soaked structure compared to chain A of the co-crystal) and active site residues other then Gln120 (Figure 8). Considering the varying pH between the two crystallisation conditions, the observed

differences in the orientation of the Gln120 side chain in the AmpC$_{EC}$-CB2 co-crystal may, however, result from an alternated protonation state of active site residues and not from CB2 binding.

While the binding mode of the boronate core is identical in both structures, differences are evident in the orientation of the terminal benzyl-amine of the C3 amido-sidechain (Figure 8). However, as the evidence for the sidechain in the electron density map is weak in the structure obtained via soaking (Figure 6B), the remaining discussion will focus on the CB2 binding mode as observed in the AmpC$_{EC}$-CB2-co-crystal structure.

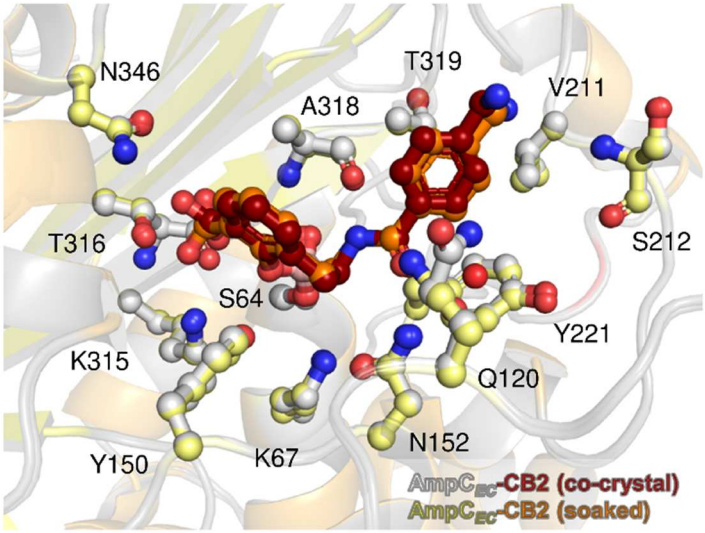


Figure 8: Comparison of crystal structures of AmpC$_{EC}$-CB2 complexes obtained via soaking and co-crystallisation. The co-crystallised AmpC$_{EC}$-CB2 complex (white and red) shows an unusual conformation of Gln120, not observed in a structure of the same complex obtained via soaking (yellow and orange).

4.4.2. Crystal structure of the AmpC$_{EC}$-CB3 complex

The AmpC$_{EC}$-CB3 complex structure was obtained via soaking of unmodified AmpC$_{EC}$ crystals (1.60 Å resolution, PDB ID: 6YPD, Figure 9 and Table 4). Compared to the other boronates, CB3 has a distinctive benzyl-thioether sidechain in place of the C3 amido sidechain. Further, CB3 was synthesized as a mixture of the (3*S*)- and (3*R*)-isomers with the (3*R*)-isomer in excess (~24:76 (*S*:*R*) ratio)[19].

However, in the crystal structure only the minor (3*S*)-isomer was observed bound to Ser64, suggesting preferential binding of this isomer, although elevated B-factors compared to the CB3 average indicate a partial disorder of the sidechain and minor amounts of bound (3*R*)-isomer can therefore not be ruled out.

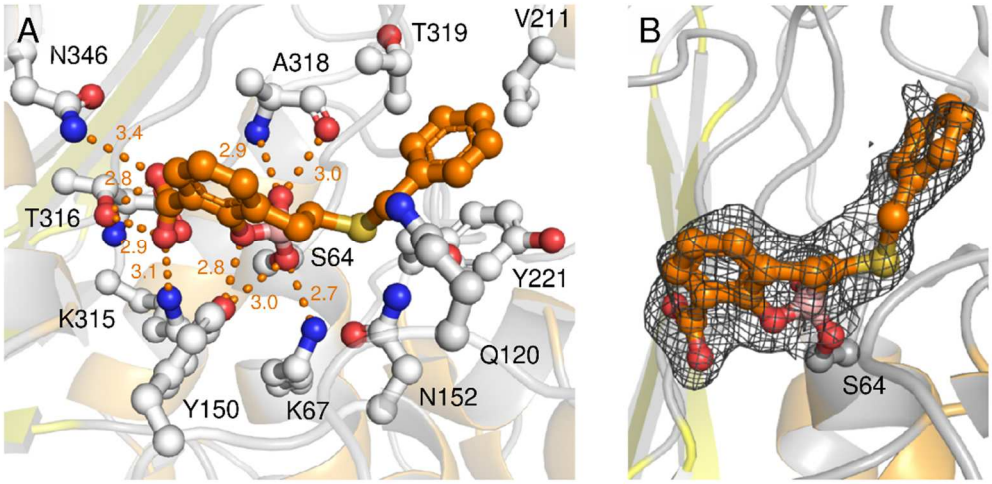


Figure 9: Views from a crystal structure of AmpC$_{EC}$ in complex with CB3. (A) Active site view showing CB3 covalently bound to Ser64. Hydrogen-bonding interactions are shown as dashed lines. Distances are indicated in Å. (B) mF$_o$-DF$_c$ polder OMIT map[25] contoured at 3.0 σ and carved around CB3. Figure and figure legend are adopted with permission from Lang *et al*. *Biomolecules*, 2020, *10*, 899.

The binding mode of the bicyclic boronate core of CB3 was comparable to the binding mode observed for CB2 core (Figure 6-7), with the carboxylic acid positioned for polar interactions with Lys 315 (3.1 Å), Thr316 (2.9 Å) and Gln356 (3.4 Å). Next to hydrophobic interactions with the side chains of V211 and T319 in the R1 pocket, the benzyl of the thioether sidechain of CB3 is also positioned for π-stacking interaction with Y221 (~ 4 Å distance to Y221 phenol ring).

Table 4: Data collection and refinement statistics for the AmpC$_{EC}$–CB3 crystal.

Datasets	**AmpC$_{EC}$-CB3** (PDB: 6YPD)		
Data Collection		**Refinement**	PHENIX
Beamline (Wavelength, Å)	DLS I03 (0.9762)	R_{work}/R_{free}	0.1709/0.1874
Detector	Eiger2 XE 16M	No. atoms	
Data Processing	dials	- Enzyme	2919
Space group	*P* 4$_3$ 3 2	- Bound Inhibitor	22
Cell dimensions		- Water	376
- *a,b,c* (Å)	139.0, 139.0, 139.0	Average B-factors	31.0
- α, β, γ (°)	90, 90, 90	- Enzyme	29.4
No. of molecules/ASU	1	- Bound Inhibitor	57.0
No. reflections	60941 (2948)*	- Water	40.2
Resolution (Å)	138.97-1.60 (1.63-1.60)*	R.m.s deviations	
R_{merge}(I)	0.166 (4.538)*	- Bond lengths (Å)	0.009
I/σI	22.1 (1.3)*	- Bond angles (°)	0.979
$CC_{1/2}$	1.0 (0.7)*		
Completeness (%)	100 (99.9)*		
Multiplicity	77.3 (67.4)*		
Wilson B value (Å^2)	23.35		

*Highest resolution shell in parentheses.

4.4.3. Crystal structure of AmpC$_{EC}$-TAN complex

Unexpectedly, in the crystal structure obtained by soaking TAN into crystals of unmodified AmpC$_{EC}$ (1.42 Å resolution, PDB ID: 6YEN), a second TAN molecule was observed. In addition to the expected bicyclic form of the inhibitor, which is covalently bound to the nucleophilic Ser64 at the active site, electron density was observed at the surface between two symmetry-related AmpC$_{EC}$ molecules indicating a non-covalently bound molecule of the inhibitor. This second molecule of TAN appeared to be in a tricyclic form (Figure 10), which has previously only been observed once before, i.e. in partial occupancy when bound at the active site of the MBL NDM-1[2].

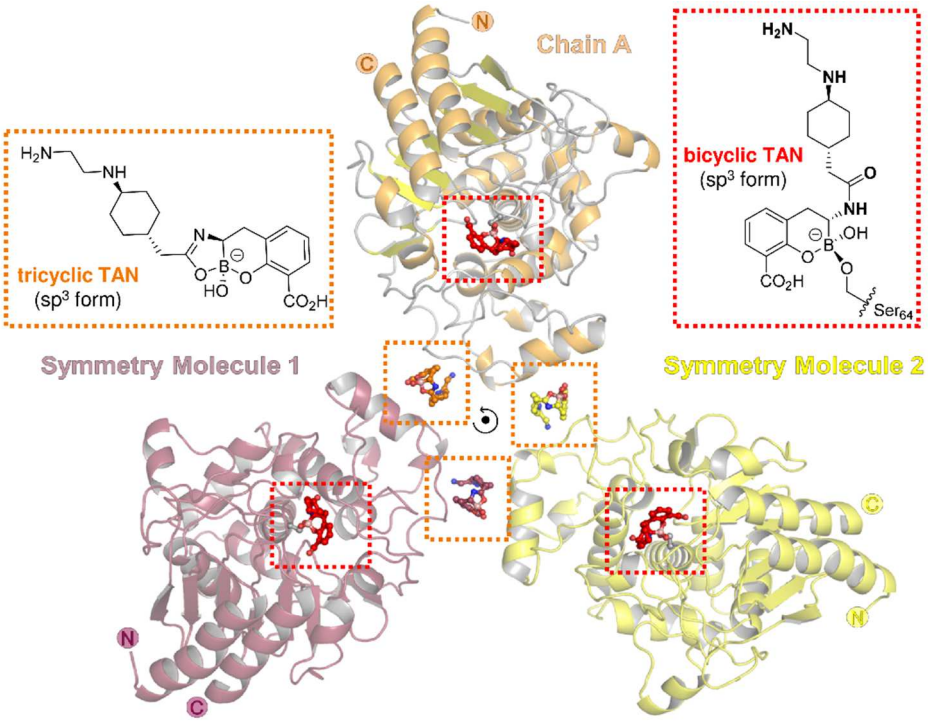


Figure 10: Overview of AmpC$_{EC}$-TAN complex crystal structure, showing both a bicyclic and a tricyclic molecule of TAN. Shown are symmetry related molecules around the 3-fold rotation axis, bicyclic TAN (red) bonded to the nucleophilic Ser64, and tricyclic TAN (colour coded by AmpC$_{EC}$ molecule) at the monomer interfaces. The figure and figure legend are adopted with permission from Lang *et al. Biomolecules*, 2020, *10*, 899.

4.4.3.1. Binding mode of bicyclic TAN at AmpC$_{EC}$ active site

At the AmpC$_{EC}$ active site, the bicyclic core of TAN was observed to be covalently bonded to Ser64 (Figure 11), i.e. it has a similar binding mode of the boronate core as observed with CB2 and CB3. The carboxylic acid is positioned for polar interactions with Thr316 (2.8-3.2 Å), Lys315 (3.1 Å), and Tyr150 (3.0 Å), while one of the boronate oxygen atoms is engaging in polar interactions with the backbone of Ala318 (2.9 Å, Figure 11).

The C3 amide of TAN is positioned in close proximity to the sidechains of Asn152 (2.9 Å) and Gln120 (3.0 Å). The cyclohexyl TAN sidechain is directed out of the active site and electron density maps showed only weak evidence for the terminal alkyl-amine, which is likely disordered and was therefore excluded from the final model.

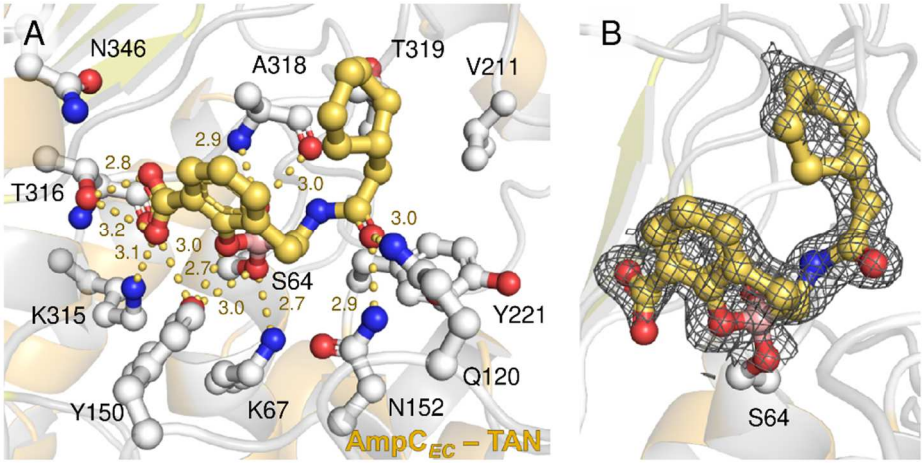


Figure 11: View from crystal structure of AmpC$_{EC}$-TAN complex showing bicyclic TAN molecule bound at AmpC$_{EC}$ active site. (A) Active site view showing bicyclic TAN covalently bound to Ser64. Hydrogen-bonding interactions are shown as dashed lines. Distances are indicated in Å. (B) mF$_o$-DF$_c$ polder OMIT map[25] contoured at 3.0 σ and carved around TAN. The figure is adopted with permission from Lang *et al*. *Biomolecules*, 2020, *10*, 899.

4.4.3.2. Tricyclic TAN on surface

The second TAN molecule was observed at the AmpC$_{EC}$ surface in a U-shaped conformation, with the C3 side chain folded over the bicyclic core (Figure 12); it is located between two symmetry related AmpC$_{EC}$ molecules, non-covalently bound through hydrogen-bonding interactions with multiple water molecules, which further interact with Pro140, Ala141, and Asn102 of one AmpC$_{EC}$ molecule, as well as hydrophobic interactions of the core benzyl ring with the sidechains of Ala143 and Ala98 of the second AmpC$_{EC}$ molecule (Figure 12A).

Interestingly, the amide sidechain of this TAN molecule is rotated compared to the bicyclic TAN molecule bound at the AmpC$_{EC}$ active site (Figure 11A), positioning the oxygen atom in very close proximity (1.5 Å) of the boron oxygen atom (Figure 12). Based on this very short distance between the boron and theoretical carbonyl oxygen, as well as the angle between this oxygen, the theoretical carbonyl carbon and the amide nitrogen (121.7°) this TAN derived molecule was modelled in a tricyclic form (Figure 12B) which had previously been observed crystallographically in complex with the B1 MBL NDM-1 (Figure 12C-D)[2].

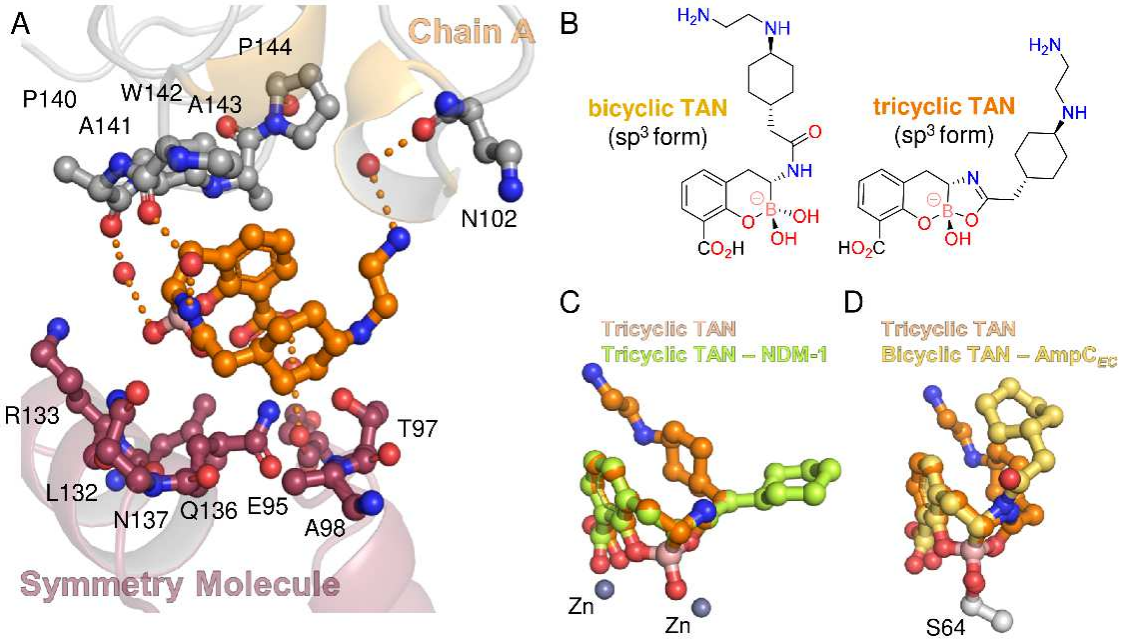


Figure 12: Views from AmpC$_{EC}$-TAN complex crystal structure showing tricyclic TAN molecule bound at AmpC$_{EC}$ surface. (A) Binding mode of tricyclic TAN at surface of two symmetry related AmpC$_{EC}$ molecules. Hydrogen bonding interactions are indicated as orange dashes. (B) Structures of proposed bi- and tricyclic sp^3 forms of TAN. (C) Overlay of tricyclic TAN observed at AmpC$_{EC}$ surface with tricyclic TAN observed at active site of NDM-1. (D) Overlay of tricyclic TAN observed at AmpC$_{EC}$ surface with bicyclic TAN bound to AmpC Ser64. The figure and figure legend are adopted with permission from Lang *et al*. *Biomolecules*, 2020, *10*, 899.

QPX7728 is a different tricyclic boronate currently in clinical trials, which shows broad spectrum SBL- and MBL-inhibition (see Chapter 1)[26]. However, by contrast with QPX7728, which contains a cyclopropyl group fused to the C2/C3 carbons, but otherwise no sidechain (Figure 13), TAN has a relatively bulky C3 side chain.

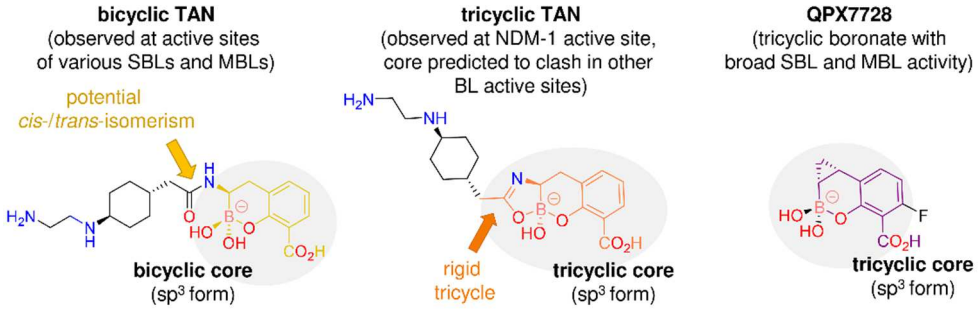


Figure 13: Structural comparison of tricyclic and bicyclic forms of TAN to the tricyclic boronate QPX7728. The figure is modified with permission from Lang *et al*. *Biomolecules*, 2020, *10*, 899.

Overlaying the tricyclic TAN core with the bicyclic TAN observed at the AmpC$_{EC}$ active site reveals a steric clash of the rigid tricycle core (Figure 14A-C). Overlays of tricyclic TAN with the bicyclic TAN observed at the active site of other SBLs (i.e. KPC-2[23] (PDB: 6TD1), CTX-M-15[12] (PDB: 6SP6), OXA-10[2] (PDB: 6RTN)) results in apparent similar steric clashes (Figure 14D-L). Assuming a conserved general binding mode of bicyclic TAN and no conformational changes of the SBL active sites on TAN binding, it is therefore unlikely that SBL active sites will accommodate the tricyclic form of TAN.

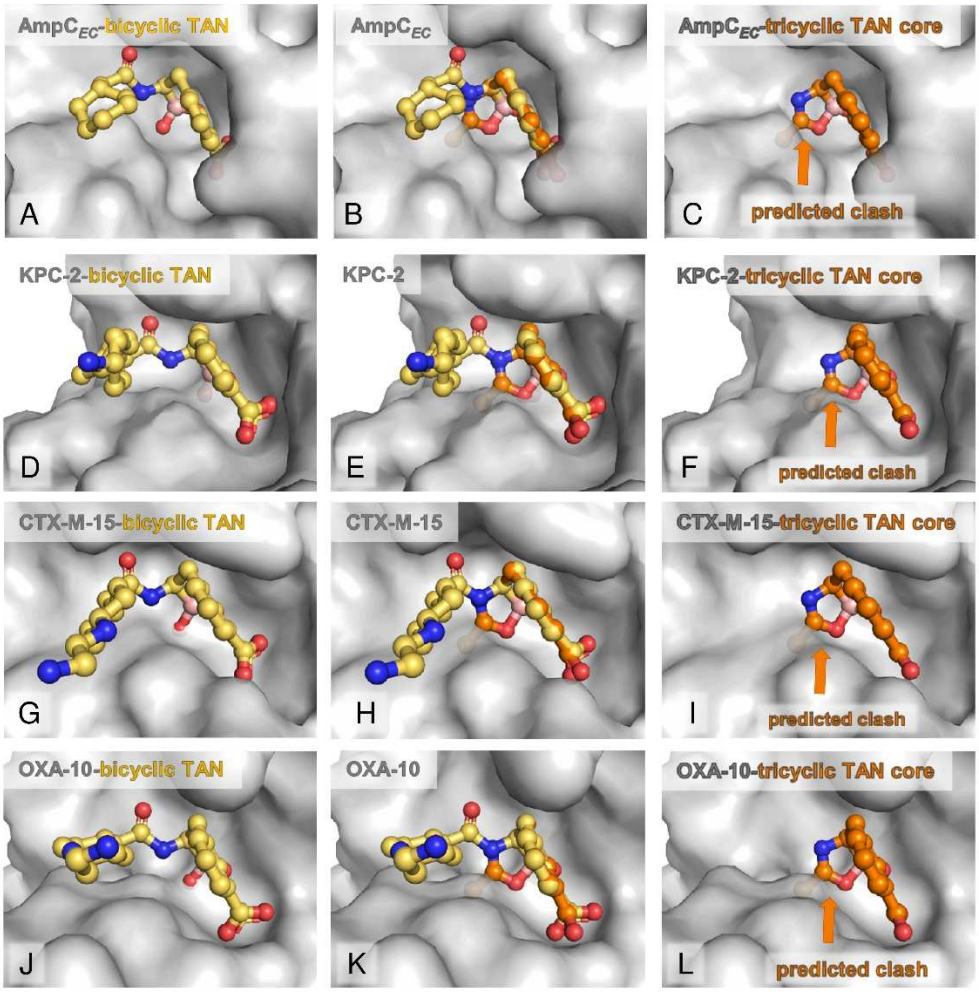


Figure 14: The tricyclic form of TAN likely cannot bind to some β-lactamases including members from Ambler Classes A, C, and D. Overlays of the tricyclic TAN core (orange, as observed at AmpC$_{EC}$ surface (Figure 4, PDB: 6YEN)) with bicyclic TAN complexes (yellow) as crystallographically observed at the active sites of KPC-2[23] (PDB: 6TD1), CTX-M-15[12] (PDB: 6SP6), and OXA-10[2] (PDB: 6RTN) reveals a likely steric clash of the rigid tricycle in the shown active sites. Left column: Observed conformations of the bicyclic form of TAN at the β-lactamase active sites; Middle column: Overlays of the tricyclic TAN and bicyclic TAN forms at the indicated active sites; Right column: The putative steric clashes of tricyclic TAN in the indicated β-lactamase active sites based on the overlays in the middle column. Note, the flexible parts of the tricyclic TAN inhibitor sidechain are not shown, but would result in a clear steric clash with the active site. The figure and figure legend are adopted with permission from Lang *et al*. *Biomolecules*, 2020, *10*, 899.

Tricyclic TAN had previously been observed bound at the active site of the NDM-1 MBL (PDB: 6RMF), together with a bicyclic form of TAN (with ~75% of TAN observed in the tricyclic and ~25% in the bicyclic form, Figure 15A-C)[2]. By contrast, overlay of the tricyclic TAN core with bicyclic TAN as previously observed bound at the active site of another MBL, VIM-2[12] (PDB: 6SP7), reveals another steric clash, making it unlikely that the VIM-2 active site will accommodate TAN in the tricyclic form (Figure 15D-F).

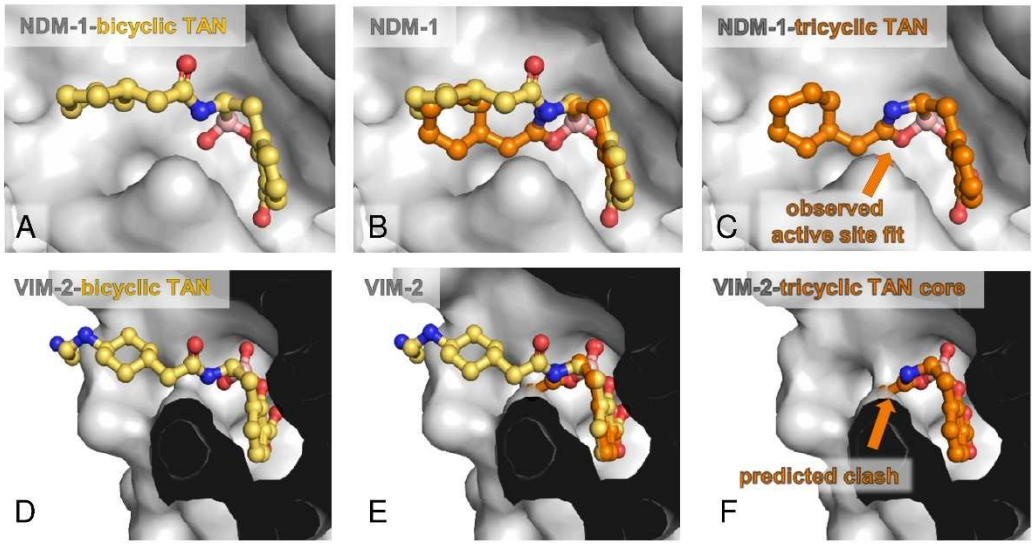


Figure 15: The tricyclic form of TAN likely can bind to the NDM-1 metallo β-lactamase, but not to the VIM-2 MBL. (A-C) Bi- (yellow) and tricyclic (orange) TAN as both observed crystallographically at the NDM-1 active site in different occupancy (~75% tricyclic and ~25% bicyclic, PDB: 6RMF)[2]. (D-F) Overlay of the tricyclic TAN core (orange, as observed at AmpC$_{EC}$ surface (Figure 4, PDB: 6YEN)) with bicyclic TAN complexes (yellow) as crystallographically observed at the active sites of VIM-2[12] (PDB: 6SP7). (D) Observed conformation of bicyclic TAN bound at VIM-2 active site. (E) Overlay of tricyclic TAN (as observed at the surface of AmpC$_{EC}$) with the bicyclic TAN observed at the VIM2-active site. (F) The putative steric clashes of tricyclic TAN in the VIM-2 active site based on the overlay in (E). The figure and figure legend are adopted with permission from Lang *et al*. *Biomolecules*, 2020, *10*, 899.

So far, the tricyclic form of TAN has only been observed crystallographically, both here and in one previous report[2]. Further studies will be needed to assess its origin and relevance in solution. An initially proposed β-lactamase catalysed reaction[2], however, appears unlikely to contribute towards tricycle formation in the AmpC$_{EC}$ crystal, in light of the steric clash predicted at the AmpC$_{EC}$ active site (Figure 14C). Tri-cyclisation thus likely occurs either during synthesis or in aqueous solution. Both the AmpC$_{EC}$ structure described here, and the previously reported structure of NDM-1 in complex with tricyclic TAN[2] were obtained at acidic pH (6.0 and 5.8, respectively), which may influence cyclisation. However, in subsequent studies tricyclic TAN was also observed crystallographically under basic conditions (pH 8.8, see Chapter 6), suggesting it may at least be stable at a broad pH-range.

Table 5: Data collection and refinement statistics for the AmpC$_{EC}$–taniborbactam crystal.

Datasets	**AmpC$_{EC}$-Taniborbactam** (PDB: 6YEN)		
Data Collection		**Refinement**	PHENIX
Beamline (Wavelength, Å)	DLS I03 (0.9787)	R_{work}/R_{free}	0.1442/0.1687
Detector	Pilatus 6M-F	No. atoms	
Data Processing	Xia2 autoPROC	- Enzyme	2941
Space group	$P\,4_3\,3\,2$	- Bound Inhibitor	24
Cell dimensions		- Unbound Inhibitor	28
- *a,b,c* (Å)	137.3, 137.2, 137.2	Water	349
- α, β, γ (°)	90, 90, 90	- Average B-factors	28.4
No. of molecules/ASU	1	- Enzyme	26.7
No. reflections	83449 (4083)*	- Bound Inhibitor	33.6
Resolution (Å)	97.04-1.42 (1.44-1.42)*	Unbound Inhibitor	51.2
R_{merge}(I)	0.135 (7.265)*	- Water	39.4
I/σI	26.6 (1.0)*	- R.m.s deviations	
$CC_{1/2}$	1.0 (0.4)*	Bond lengths (Å)	0.008
Completeness (%)	100 (100)*	Bond angles (°)	1.132
Multiplicity	76.9 (78.6)*		
Wilson B value (Å^2)	21.32		

*Highest resolution shell in parentheses.

4.4.4. Comparison of binding modes of bicyclic boronates

Overall, binding of the bicyclic boronate core of all three inhibitors in complex with AmpC$_{EC}$ is highly similar and similar to that observed for cyclic boronate 1 (CB1) in complex with the *Pseudomonas aeruginosa* AmpC (PDB: 6I30)[24].

Apart from the unusual orientation of the Gln120 sidechain in the AmpC$_{EC}$-CB2 co-crystal structure (Figure 7), which may be a result of the altered crystallisation condition, no apparent differences are observed in the orientation of active site residues on binding of CB2, CB3, and TAN (Figure 16).

The C3 boronate sidechains are oriented in a similar manner to that of the C6/C7 amido-sidechains of penicillins and cephalosporins at the AmpC$_{EC}$ active site. While the C3 amido sidechains of CB2 and TAN engage in similar polar interactions with Asn152 and Gln120, the benzyl-thioether sidechain of (3*S*)-CB3 is mainly positioned for hydrophobic interactions with residues within the Ω-loop (positions 185-225, Figure 16). As these residues are conserved in many chromosomal class C β-lactamases, this likely contributes towards the high potency of CB3 observed not just against AmpC$_{EC}$, but also the *P. aeruginosa* AmpC[19]. However, it should be noted that AmpC mutants showing a deletion of Y221 or other mutations within the Ω-loop have been observed to confer resistance to ceftazidime-avibactam[27] as well as reduced cefepime susceptibility[28], the proposed partner β-lactam for clinical use of TAN.

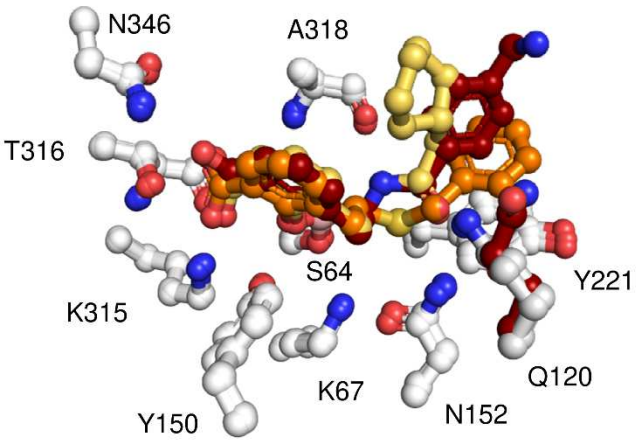


Figure 16: Comparison of bicyclic boronate binding modes at the AmpC$_{EC}$ active site. Shown is an overlay of views from crystal structures of AmpC$_{EC}$ in complex with CB2 (red), CB3 (orange), and TAN (yellow). The unusual conformation of the Gln120 sidechain observed in the co-crystallised AmpC$_{EC}$-CB2 complex structure is highlighted in red. The figure is adopted with permission from Lang *et al*. *Biomolecules*, 2020, *10*, 899.

4.5. Summary and Conclusions

While boron containing compounds have long been known to show antimicrobial properties[29], boronic acids / boronates have become increasingly popular in medicinal chemistry[30], including as antibacterials and β-lactamase inhibitors[15] following the clinical introduction of bortezomib (velcade), the first boronic acid containing drug to reach FDA approval (for multiple myeloma) in 2003.

The work described in this chapter comprises a detailed study of AmpC$_{EC}$ interactions with three (predominantly) bicyclic boronates. It demonstrates high potency of this class of inhibitors against AmpC$_{EC}$, adding to existing data on the potent inhibition of a range of other serine- and some metallo-β-lactamases[12,14,16,19]. The structural studies further support the proposal that bicyclic boronates inhibit β-lactamases by mimicking high-energy tetrahedral transition states in β-lactamase catalysis, with the binding modes of the sp^3 hybridised boron, as well as the 6,6-core ring system showing remarkable similarity to studies with SBLs from class A (e.g. CTX-M-15[12,16], L2[22], and KPC-2[23]), class D (e.g. OXA-10 [2,14]) and the class C AmpC from *Pseudomonas aeruginosa*[24] as well as PBP-5 from *Escherichia coli*[14].

The results show scope for further C3 side chain optimisation, with CB3, which contains an unusual thioether sidechain, showing improved AmpC$_{EC}$ inhibition compared to CB2 and TAN against the isolates enzyme, but not in cells, which likely reflects poor penetration of the hydrophobic CB3 into cells/the periplasm of the bacterial cell wall. Further optimisation of the thioether sidechain (e.g. by introduction of a terminal amine group, as with TAN[12]) should thus be carried out to improve not just inhibition against isolated enzymes, but also with respect to improved cell penetration.

While its exact origin is unclear, the observation of a tricyclic form of TAN is of potential interest, as it highlights the ability of boronate compounds to interchange between different forms which may contribute towards the unusual broad-range β-lactamase inhibition observed for TAN. While tricyclic TAN does not appear suitable to bind to most SBL active sites, it has been previously observed at the active site of the NDM-1 MBL[2] and may thus contribute towards inhibition of some MBLs. However, further studies will be needed to establish its relevance in solution.

4.6. Materials and Methods

4.6.1. Materials

VAB was obtained from Cayman Chemical. CB2 was synthesised by Anete Parkova under the supervision of Prof. Peteris Trapencieris (Latvian Institute of Organic Synthesis) as previously described[19]. CB2 was synthesised by Ricky Cain under the supervision of Prof. Colin Fishwick (University of Leeds) as previously described[14]. TAN was synthesised by Alen Krajnc and Dr Tharindi Panduwawala (University of Oxford) as previously described[2].

4.6.2. Recombinant enzyme production and purification

TEM-116 was expressed and purified by Dr. Jürgen Brem (University of Oxford) as previously described[31]. AmpC$_{EC}$ and OXA-10 were expressed and purified as described in Chapter 2. OXA-48 was expressed and purified as described in Chapter 5.

4.6.3. Kinetics

Dose-dependence and detailed kinetic studies on AmpC$_{EC}$ inhibition by DBOs were carried out according to modified reported procedures[20,32,33] which are described in detail in Chapter 2. In short, pIC$_{50}$s were determined after incubating AmpC$_{EC}$ (500 pM) with CB2, CB3, TAN, or VAB at varying concentrations for 10 min at room temperature, followed by addition of FC-5 (5 μM) and monitoring of reactions for 30 min. To determine apparent inhibition constants K_{iapp} and second-order rate constants (k_2/K), 100 nM AmpC$_{EC}$ were assayed with FC-5 (5 μM) in the presence of varying concentration of CB2, CB3, TAN, or VAB. Reactions were initiated by addition of AmpC$_{EC}$, then immediately monitored continuously for 30 s. For off-rates (k_{off}) AmpC$_{EC}$ (1 μM) was incubated with CB2, CB3, TAN (10 μM), or VAB (100 μM) for 30 min at room temperature, then diluted 100,000 fold and assayed with FC-5 (25 μM). All reactions were in 50 mM phosphate buffer, pH 7.5 supplemented with 0.01% (v/v) Triton X-100. Data were analysed as described in Chapter 2.

4.6.4. Antimicrobial Susceptibility Testing

Minimal inhibitory concentrations (MICs) values of CAZ were determined for wildtype *E. coli* DH5α and *E. coli* DH5α harbouring the pAD7-AmpC$_{EC}$ plasmid [21] via broth microdilution (BMD) according to guidelines of the Clinical and Laboratory Standards Institute (CLSI) as described in detail in Chapter 3. Cyclic boronates VAB, CB2, CB3, and TAN were tested at fixed a concentration of 4 µg ml^{-1}.

4.6.5. Crystallography

For soaking experiments AmpC$_{EC}$ was crystallised as described in Chapter 2. Crystals were transferred into precipitant solution supplemented with 10-20 mM CB2, CB3, or TAN, incubated at room temperature for 10-20 min, then mounted on nylon loops and cryo-cooled and stored in liquid nitrogen.

The co-crystal structure of AmpC$_{EC}$ in complex with CB2 was obtained via co-crystallisation. Sitting drop vapor-diffusion crystallisation in low reservoir Intelli-Plate 93-3 (Art Robbins Instruments) were set up using a Rigaku Phoenix RE Drop setter (Art Robbins Instrument). 200 nl AmpC$_{EC}$ (18 mg/mL in 50 mM Tris pH 7.5), preincubated with CB2 (20 mM, 30 min), were combined with 200 nl precipitant solution (150 mM HEPES pH 7.5, 60% (v/v) 2-methyl-2,4-pentanediol (MPD)). Crystals grew at room temperature over 1-2 weeks.

X-ray diffraction data were collected at 100 K using MX beamlines at Diamond Light Source (DLS) and processed using Xia2[34]. Structures were solved by molecular replacement using Phaser[35] and the structure of unmodified AmpC$_{EC}$ (PDB: 6T3D, Chapter 2) as the starting model. Alternating cycles of refinement using phenix.refine[36] and manual model building using Coot[37] were performed until R_{work} and R_{free} converged.

4.7. References

1. Lang, P.A.; Parkova, A.; Leissing, T.M.; Calvopina, K.; Cain, R.; Krajnc, A.; Panduwawala, T.D.; Philippe, J.; Fishwick, C.W.; Trapencieris, P., et al. Bicyclic Boronates as Potent Inhibitors of AmpC, the Class C β-Lactamase from *Escherichia coli*. *Biomolecules* **2020**, *10*, 899.
2. Krajnc, A.; Brem, J.; Hinchliffe, P.; Calvopina, K.; Panduwawala, T.D.; Lang, P.A.; Kamps, J.; Tyrrell, J.M.; Widlake, E.; Saward, B.G., et al. Bicyclic Boronate VNRX-5133 Inhibits Metallo- and Serine-β-Lactamases. *J. Med. Chem.* **2019**, *62*, 8544-8556.
3. Bush, K. Past and Present Perspectives on β-Lactamases. *Antimicrob. Agents Chemother.* **2018**, *62*, e01076-01018.
4. Mojica, M.F.; Rossi, M.-A.; Vila, A.J.; Bonomo, R.A. The urgent need for metallo-β-lactamase inhibitors: an unattended global threat. *Lancet Infect. Dis.* **2022**, *22*, e28-34.
5. Abboud, M.I.; Damblon, C.; Brem, J.; Smargiasso, N.; Mercuri, P.; Gilbert, B.; Rydzik, A.M.; Claridge, T.D.; Schofield, C.J.; Frere, J.M. Interaction of Avibactam with Class B Metallo-β-Lactamases. *Antimicrob. Agents Chemother.* **2016**, *60*, 5655-5662.

6. Lohans, C.T.; Brem, J.; Schofield, C.J. New Delhi Metallo-β-Lactamase 1 Catalyzes Avibactam and Aztreonam Hydrolysis. *Antimicrob. Agents Chemother.* **2017**, *61*, e01224-01217.
7. Prosperi-Meys, C.; Llabres, G.; de Seny, D.; Paul Soto, R.; Hernandez Valladares, M.; Laraki, N.; Frere, J.-M.; Galleni, M. Interaction between class B β-lactamases and suicide substrates of active-site serine β-lactamases. *FEBS Lett.* **1999**, *443*, 109-111.
8. Brem, J.; Berkel, S.S.v.; Zollman, D.; Lee, S.Y.; Gileadi, O.; McHugh, P.J.; Walsh, T.R.; McDonough, M.A.; Schofield, C.J. Structural Basis of Metallo-β-Lactamase Inhibition by Captopril Stereoisomers. *Antimicrob. Agents Chemother.* **2016**, *60*, 142-150.
9. Hinchliffe, P.; González, M.M.; Mojica, M.F.; González, J.M.; Castillo, V.; Saiz, C.; Kosmopoulou, M.; Tooke, C.L.; Llarrull, L.I.; Mahler, G., et al. Cross-class metallo-β-lactamase inhibition by bisthiazolidines reveals multiple binding modes. *Proc. Natl. Acad. Sci. U. S. A.* **2016**, *113*, E3745-3754.
10. Wang, X.; Zhao, C.; Wang, Q.; Wang, Z.; Liang, X.; Zhang, F.; Zhang, Y.; Meng, H.; Chen, H.; Li, S., et al. *In vitro* activity of the novel β-lactamase inhibitor taniborbactam (VNRX-5133), in combination with cefepime or meropenem, against MDR Gram-negative bacterial isolates from China. *J. Antimicrob. Chemother.* **2020**, *75*, 1850-1858.
11. Hamrick, J.C.; Docquier, J.D.; Uehara, T.; Myers, C.L.; Six, D.A.; Chatwin, C.L.; John, K.J.; Vernacchio, S.F.; Cusick, S.M.; Trout, R.E.L., et al. VNRX-5133 (Taniborbactam), a Broad-Spectrum Inhibitor of Serine- and Metallo-β-Lactamases, Restores Activity of Cefepime in *Enterobacterales* and *Pseudomonas aeruginosa*. *Antimicrob. Agents Chemother.* **2020**, *64*, e01963-01919.
12. Liu, B.; Trout, R.E.L.; Chu, G.-H.; McGarry, D.; Jackson, R.W.; Hamrick, J.C.; Daigle, D.M.; Cusick, S.M.; Pozzi, C.; De Luca, F., et al. Discovery of Taniborbactam (VNRX-5133): A Broad-Spectrum Serine- and Metallo-β-lactamase Inhibitor for Carbapenem-Resistant Bacterial Infections. *J. Med. Chem.* **2020**, *63*, 2789-2801.
13. Bahr, G.; González, L.J.; Vila, A.J. Metallo-β-lactamases in the Age of Multidrug Resistance: From Structure and Mechanism to Evolution, Dissemination, and Inhibitor Design. *Chem. Rev.* **2021**, *121*, 7957-8094.
14. Brem, J.; Cain, R.; Cahill, S.; McDonough, M.A.; Clifton, I.J.; Jimenez-Castellanos, J.C.; Avison, M.B.; Spencer, J.; Fishwick, C.W.; Schofield, C.J. Structural basis of metallo-β-lactamase, serine-β-lactamase and penicillin-binding protein inhibition by cyclic boronates. *Nat. Commun.* **2016**, *7*, 12406.
15. Krajnc, A.; Lang, P.A.; Panduwawala, T.D.; Brem, J.; Schofield, C.J. Will morphing boron-based inhibitors beat the β-lactamases? *Curr. Opin. Chem. Biol.* **2019**, *50*, 101-110.
16. Cahill, S.T.; Cain, R.; Wang, D.Y.; Lohans, C.T.; Wareham, D.W.; Oswin, H.P.; Mohammed, J.; Spencer, J.; Fishwick, C.W.; McDonough, M.A., et al. Cyclic Boronates Inhibit All Classes of β-Lactamases. *Antimicrob. Agents Chemother.* **2017**, *61*, e02260-02216.
17. Burns, C.J. Beta-lactamase inhibitors. WO 2010/130708 A1, **2010**.
18. Reddy, R.K. Boronic acid derivatives and therapeutic uses thereof. WO 2016/003929 A1, **2016**.
19. Parkova, A.; Lucic, A.; Krajnc, A.; Brem, J.; Calvopiña, K.; Langley, G.W.; McDonough, M.A.; Trapencieris, P.; Schofield, C.J. Broad Spectrum β-Lactamase Inhibition by a Thioether Substituted Bicyclic Boronate. *ACS Infect. Dis.* **2020**, *6*, 1398-1404.
20. van Berkel, S.S.; Brem, J.; Rydzik, A.M.; Salimraj, R.; Cain, R.; Verma, A.; Owens, R.J.; Fishwick, C.W.G.; Spencer, J.; Schofield, C.J. Assay platform for clinically relevant metallo-β-lactamases. *J. Med. Chem.* **2013**, *56*, 6945-6953.
21. Dubus, A.; Wilkin, J.M.; Raquet, X.; Normark, S.; Frère, J.M. Catalytic mechanism of active-site serine β-lactamases: role of the conserved hydroxy group of the Lys-Thr(Ser)-Gly triad. *Biochem J* **1994**, *301*, 485-494.
22. Calvopiña, K.; Hinchliffe, P.; Brem, J.; Heesom, K.J.; Johnson, S.; Cain, R.; Lohans, C.T.; Fishwick, C.W.G.; Schofield, C.J.; Spencer, J., et al. Structural/mechanistic insights into the efficacy of nonclassical β-lactamase inhibitors against extensively drug

resistant *Stenotrophomonas maltophilia* clinical isolates. *Mol. Microbiol.* **2017**, *106*, 492-504.
23. Tooke, C.L.; Hinchliffe, P.; Krajnc, A.; Mulholland, A.J.; Brem, J.; Schofield, C.J.; Spencer, J. Cyclic boronates as versatile scaffolds for KPC-2 β-lactamase inhibition. *RCS Med. Chem.* **2020**, *11*, 491-496.
24. Cahill, S.T.; Tyrrell, J.M.; Navratilova, I.H.; Calvopina, K.; Robinson, S.W.; Lohans, C.T.; McDonough, M.A.; Cain, R.; Fishwick, C.W.G.; Avison, M.B., et al. Studies on the inhibition of AmpC and other β-lactamases by cyclic boronates. *Biochim. Biophys. Acta Gen. Subj.* **2019**, *1863*, 742-748.
25. Liebschner, D.; Afonine, P.V.; Moriarty, N.W.; Poon, B.K.; Sobolev, O.V.; Terwilliger, T.C.; Adams, P.D. Polder maps: improving OMIT maps by excluding bulk solvent. *Acta Crystallogr D Struct Biol* **2017**, *73*, 148-157.
26. Hecker, S.J.; Reddy, K.R.; Lomovskaya, O.; Griffith, D.C.; Rubio-Aparicio, D.; Nelson, K.; Tsivkovski, R.; Sun, D.; Sabet, M.; Tarazi, Z., et al. Discovery of Cyclic Boronic Acid QPX7728, an Ultrabroad-Spectrum Inhibitor of Serine and Metallo-β-lactamases. *J. Med. Chem.* **2020**, *63*, 7491-7507.
27. Lahiri, S.D.; Walkup, G.K.; Whiteaker, J.D.; Palmer, T.; McCormack, K.; Tanudra, M.A.; Nash, T.J.; Thresher, J.; Johnstone, M.R.; Hajec, L., et al. Selection and molecular characterization of ceftazidime/avibactam-resistant mutants in Pseudomonas aeruginosa strains containing derepressed AmpC. *J. Antimicrob. Chemother.* **2015**, *70*, 1650-1658.
28. Haenni, M.; Châtre, P.; Madec, J.-Y. Emergence of *Escherichia coli* producing extended-spectrum AmpC β-lactamases (ESAC) in animals. *Front. Microbiol.* **2014**, *5*, 53.
29. A. Michaelis, P.B. Ueber Monophenylborchlorid und die Valenz des Bors. *Ber. Dtsch. Chem. Ges.* **1882**, *13*, 58-61.
30. Fernandes, G.F.S.; Denny, W.A.; Dos Santos, J.L. Boron in drug design: Recent advances in the development of new therapeutic agents. *Eur. J. Med. Chem.* **2019**, *179*, 791-804.
31. Inglis, S.R.; Strieker, M.; Rydzik, A.M.; Dessen, A.; Schofield, C.J. A boronic-acid-based probe for fluorescence polarization assays with penicillin binding proteins and β-lactamases. *Anal. Biochem.* **2012**, *420*, 41-47.
32. Williams, J.W.; Morrison, J.F. The kinetics of reversible tight-binding inhibition. In *Methods in Enzymology*, Academic Press **1979**, Vol. 63, pp. 437-467.
33. Copeland, R.A.; Basavapathruni, A.; Moyer, M.; Scott, M.P. Impact of enzyme concentration and residence time on apparent activity recovery in jump dilution analysis. *Anal. Biochem.* **2011**, *416*, 206-210.
34. Winter, G. xia2: an expert system for macromolecular crystallography data reduction. *J. Appl. Crystallogr.* **2010**, *43*, 186-190.
35. McCoy, A.J.; Grosse-Kunstleve, R.W.; Adams, P.D.; Winn, M.D.; Storoni, L.C.; Read, R.J. Phaser crystallographic software. *J. Appl. Crystallogr.* **2007**, *40*, 658-674.
36. Adams, P.D.; Grosse-Kunstleve, R.W.; Hung, L.W.; Ioerger, T.R.; McCoy, A.J.; Moriarty, N.W.; Read, R.J.; Sacchettini, J.C.; Sauter, N.K.; Terwilliger, T.C. PHENIX: building new software for automated crystallographic structure determination. *Acta Crystallogr. D* **2002**, *58*, 1948-1954.
37. Emsley, P.; Lohkamp, B.; Scott, W.G.; Cowtan, K. Features and development of Coot. *Acta Crystallogr. D* **2010**, *66*, 486-501.

Chapter 5

Interactions of AmpC$_{EC}$ with β-Lactam Antibiotics

Nuclear magnetic resonance spectroscopy assays were done in collaboration with Jos Kamps (University of Oxford). LTV-13 was synthesised by Dr Klaus-Daniel Umland (University of Oxford).

Contents

7.1. Introduction 151
7.2. AmpC$_{EC}$ interactions with penicillins 151
7.2.1. Nuclear magnetic resonance spectroscopy-based penicillin turnover assays 152
7.2.2. Structural studies 153
7.3. AmpC$_{EC}$ interactions with cephalosporins and cephamycins 157
7.3.1. Structure of cephamycin derived acyl-enzyme species 157
7.3.2. Structure of cephalosporin and cephamycin derived product complexes 159
7.4. AmpC$_{EC}$ interactions with penems and carbapenems 161
7.5. AmpC$_{EC}$ interactions with lactivicin derivative LTV-13 164
7.6. Summary and conclusions 166
7.7. Materials and Methods 167
7.7.1. Materials 167
7.7.2. Enzyme production and purification 167
7.7.3. Crystallography 167
7.7.4. NMR based turnover assays 168
7.8. References 168

7.1. Introduction

AmpC$_{EC}$ is predominantly a cephalosporinase, but also shows hydrolytic activity against a range of other β-lactam antibiotics, including cephamycins and most penicillins[1,2]. While the kinetics of AmpC$_{EC}$ and other class C SBLs with various β-lactam antibiotics have been studied in detail[1-3], structural information on the interaction of AmpC$_{EC}$ with β-lactams is more limited[4-7].

As is the case with all serine β-lactamases, AmpC$_{EC}$ catalysis proceeds via nucleophilic attack of the catalytic Ser residue, via a tetrahedral intermediate, to give an acyl-enzyme complex (AEC, see Chapter 1). Hydrolysis of the acyl-enzyme species is proposed to be aided by the conserved binding of a water molecule in close proximity to Tyr150 and the sidechain of Thr316, often referred to as the putative de-acylating water molecule[8,9]. The hydrolytic stability of this AEC varies between β-lactam antibiotics, with efficient hydrolysis occurring with some β-lactams and inhibition with others. Structural studies on AmpC$_{EC}$ interactions with β-lactam antibiotics have mainly focused on relatively hydrolytically stable acyl-enzyme species[4-7], with the exception of one study which employed mutagenesis of active site residues to capture the ES and EP complexes of AmpC$_{EC}$ hydrolysis derived from the cephalosporin cefalotin[7].

The following sections describe preliminary data on the interactions of AmpC$_{EC}$ with representative penicillins, cephalosporins, penems and carbapenems, as well as the structurally and mechanistically related lactivicin antibiotics (Figure 1). The results include structural information on β-lactam derived acyl-enzyme species and product complexes.

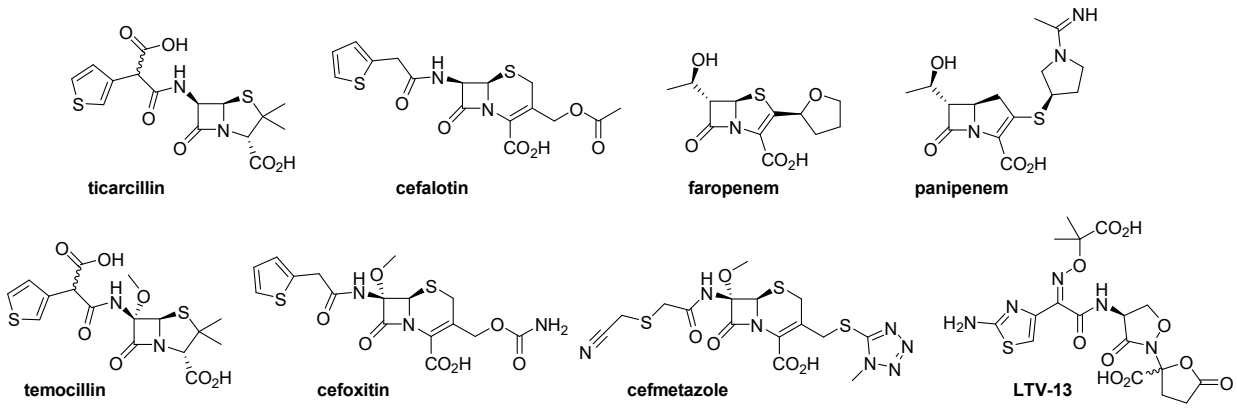


Figure 1: β-Lactam antibiotics studied in this chapter. LTV-13: a lactivicin derivative.

7.2. AmpC$_{EC}$ interactions with penicillins

Ticarcillin is a carboxypenicillin with a relatively broad antimicrobial spectrum, but which is vulnerable towards hydrolysis by most β-lactamases[10]. Temocillin (formerly BRL 17421) is

the 6-α-methoxy (6-OMe) derivative of ticarcillin and has been reported to show improved stability against some β-lactamases compared to ticarcillin[11-13]. Due to its relatively narrow spectrum of activity (mainly limited to *Enterobacteriaceae*, *H. influenzae*, and *Neisseria* [14]), clinical use of ticarcillin was initially limited, but its use has recently increased due to its β-lactamase stability[15,16]. More recently, temocillin has shown potential for treatment of urinary tract infections caused by third-generation cephalosporin-resistant pathogens[17] and multiple clinical trials are currently ongoing to evaluate temocillin as an alternative to carbapenems for the treatment of derepressed AmpC and ESBL producing *Enterobacteriaceae*[18].

For class A β-lactamases, it has been suggested that the observed differences in β-lactamase stability of 6-OMe penicillins results from a displacement of the de-acylating water molecule in the active site[19-21]. However, structural information on 6-OMe substituted penicillins is currently limited to a single structure of temocillin in complex with the class A β-lactamase CTX-M-14 and the *P. aeruginosa* penicillin binding protein-3 (PBP3)[20].

Both ticarcillin and temocillin differ only by the presence of a 6-OMe group in the latter, and are both mixtures of the (*R)*- and (*S)*-sidechain epimers (55:45 and 65:35 ratios, for ticarcillin and temocillin, respectively); the epimers have been separated via crystallisation and HPLC techniques[22,23]. In solution rapid epimerisation of both ticarcillin and temocillin occurs to give the thermodynamic epimeric mixture[22,23], but time-kill experiments have shown evidence for enhanced antimicrobial activity of the (*R)*-epimer of temocillin at early timepoints (when the extent of epimerisation was minimised)[24]. However, whilst it has been shown that the resolved epimers of both temocillin and other carboxypenicillins such as carbenicillin have different antimicrobial activities and pharmacodynamic properties[24-27], no biochemical information on the relative stabilities of the epimers towards β-lactamase catalysed hydrolysis has been reported.

7.2.1. Nuclear magnetic resonance spectroscopy-based penicillin turnover assays

Nuclear magnetic resonance spectrometry studies were done in collaboration with Jos Kamps (University of Oxford).

Turnover studies were caried out with $AmpC_{EC}$ in combination with both temocillin and ticarcillin (both used as mixtures of sidechain epimers), monitored by nuclear magnetic resonance (NMR) spectroscopy (Figure 2). The NMR spectra of the two epimers were assigned by comparison with reported data[22]. Efficient $AmpC_{EC}$ catalysed hydrolysis of 100 equivalents of ticarcillin was observed within 5 h. By contrast, only very slow turn-over was observed with

temocillin, an observation which is in agreement with the increased stability of the 6-OMe penicillins towards β-lactamase catalysed hydrolysis as reported previously[11-13].

Notably, with both temocillin and ticarcillin, preferential hydrolysis was observed for the (*S*)-epimer compared to the (*R*)-epimer. With ticarcillin, rapid hydrolysis of the (*S*)-epimer was observed in the initial 3 h, while only slow hydrolysis of the (*R*)-epimer was observed over the same period. On complete turnover of the (*S*)-epimer, however, the remaining (*R*)-epimer was hydrolysed within 1 h, suggesting that the slower hydrolysis of the (*R*)-epimer results from a lower binding affinity and not from generation of a more hydrolytically stable AEC compared to the (*S*)-epimer. With temocillin, almost no hydrolysis of the (*R*)-epimer was observed, and only very slow turnover of the (*S*)-epimer, which was not completed over the monitored time-frame (20 h).

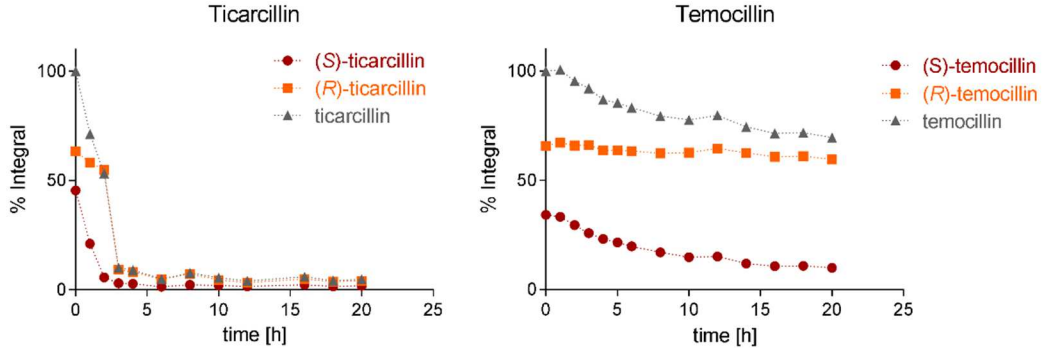


Figure 2: ^{1}H NMR time courses showing AmpC$_{EC}$ catalysed degradation of ticarcillin and temocillin. 25 µM AmpC$_{EC}$ were assayed with 2.5 mM ticarcillin or temocillin (both mixtures of sidechain epimers). Shown are normalised integrals of peaks corresponding to the thiophene C2-proton of the (*S*)-epimer (red, ticarcillin: 7.05 ppm, temocillin: 7.08 ppm), the (*R*)-epimer (orange, ticarcillin: 7.03 ppm, temocillin: 7.05 ppm) and the sum of both epimers (grey). Buffer: 100 mM phosphate buffer pH 7.5, 10 % D_2O.

The preliminary NMR results thus support the preferred conversion of the (*S*)-epimers for both ticarcillin and temocillin and that the presence of a 6-OMe groups slows β-lactamase catalysed hydrolysis. Crystallographic studies were then carried out to investigate the structural basis of these differences.

7.2.2. Structural studies

Electron density maps of a structure obtained from soaking crystals of unmodified AmpC$_{EC}$ with temocillin (10 min soak, 1.75 Å resolution, Figure 4 and Table 1) showed additional electron density indicating covalent modification of Ser64 to form a temocillin derived acyl-enzyme complex (Figure 4A and D).

While binding of small amounts of the (*S*)-epimer cannot be precluded, the electron density maps indicate the predominant presence of the (*R*)-temocillin epimer at the AmpC$_{EC}$ active site, suggesting either preferential reaction of (*R*)-temocillin or (perhaps more likely based on

the NMR studies) higher hydrolytic stability of the (*R*)-temocillin derived acyl-enzyme complex compared to that derived from (*S*)-temocillin (Figure 4D).

In the acyl-enzyme complex, the thiazolidine-carboxylate is positioned for polar interactions with the sidechains of Thr316 (2.8 Å) and Asn346 (3.0 Å) and the thiazolidine-nitrogen is in close proximity to the Tyr150 phenolic oxygen (3.2 Å). While the C6 amido sidechain is pointing out of the AmpC$_{EC}$ active site, the amide carbonyl is positioned for polar interactions with the sidechains of Asn152 (3.9 Å) and Gln120 (2.8 Å), and the amide nitrogen is positioned for hydrogen bonding with the backbone carbonyl of Ala318 (3.2 Å). The C6 methoxy-group in positioned for polar interactions with the sidechain of Gln152 (3.0 Å). The acyl-carbonyl is positioned in the oxyanion hole which is made up of the backbone nitrogen atoms of Ser64 and Ala318. Overall, the conformation of the temocillin derived AEC is in agreement with the expected binding mode of a penicillin derived AEC.

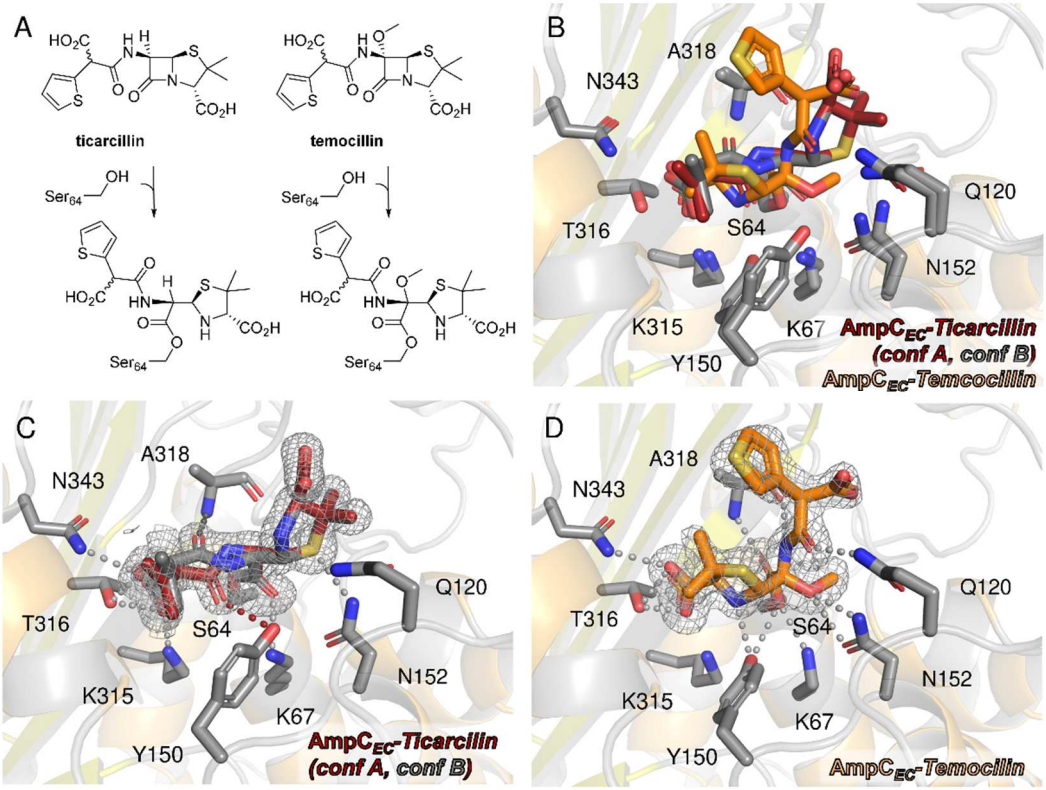


Figure 3: Views from crystal structures of AmpC$_{EC}$ reacted with ticarcillin or temocillin. (A) Reaction of AmpC$_{EC}$ with ticarcillin or temocillin. (B) Overlay of active site views from crystal structures of AmpC$_{EC}$ reacted with ticarcillin or temocillin. (C) Active site view from crystal structure of AmpC$_{EC}$ reacted with ticarcillin for 7 min. The ticarcillin derived acyl-enzyme species is observed in two conformations (A and B). White dashes represent polar interactions common to both conformations of the acyl-enzyme complex, red dashes are polar interactions only observed in conformation A, and grey dashes indicate polar interactions only observed with conformation B. Note, the observed differences in the orientation of Tyr150 and Lys67 in the AmpC$_{EC}$-ticarcillin structure (compared to both unmodified AmpC$_{EC}$ and to the AmpC$_{EC}$-temocillin complex shown in (D) result from cross-linking of the residues prior to reaction with ticarcillin (see Chapter 2). (D) Active site view from crystal structure of AmpC$_{EC}$ reacted with temocillin for 10 min. The temocillin derived acyl-enzyme species is observed in a single conformation. Polar interactions are indicated as white dashes. mF$_o$-DF$_c$ polder OMIT maps[28] are contoured at 3.0 σ and carved around the acyl-enzyme species.

Initial trials to soak ticarcillin into crystals of unmodified AmpC$_{EC}$ resulted in partial modification of the nucleophilic Ser (after soaking for 10 min, data not shown). While electron density maps did not give clear evidence for the amido sidechain of the ticarcillin derived AEC (which may reflect binding of a mixture of (*S*)- and (*R*)-epimers), clear additional electron density was evident for the thiazolidine ring portion of the AEC. Interestingly, with ticarcillin a clear change of position of the thiazolidine ring was evident compared to the conformation of the temocillin derived AEC; the thiazolidine ring in the acyl-enzyme complex is flipped by ~180° compared to that in the temocillin derived AEC, with the ticarcillin thiazolidine bound carboxylate positioned in the same way as the amido-sidechain carboxylate of the temocillin derived AEC (as also shown in Figure 3C).

To achieve crystals with a higher level of occupancy of the ticarcillin derived AEC, the soaking experiments were repeated with aged AmpC$_{EC}$ crystals which are de-acylation deficient due to a Tyr150-Lys67 crosslink, likely induced by reaction with formaldehyde from the crystallisation precipitant solution (see Chapter 2).

Analysis of the electron density maps of the structure of the crosslinked AmpC$_{EC}$ modified by reaction with ticarcillin to give an AEC (1.37 Å resolution, Figure 4C and Table 1) provided evidence for the binding modes of both the thiazolidine and the amido-sidechain portions of the AEC. As was observed with the catalytically viable AmpC$_{EC}$, the thiazolidine ring in the ticarcillin derived AEC was flipped ~180° compared to the temocillin derived AEC. Although binding of small amounts of the (*S*)-epimer cannot be precluded, the electron density maps indicated the predominant presence of the (*R*)-ticarcillin epimer at the AmpC$_{EC}$ active site. This likely suggests faster acylation of the (*S*)-epimer compared to the (*R*)-epimer.

The thiazolidine ring is positioned for polar interactions with the sidechain of Asn152 (3.3 Å), while the thiazolidine carboxylate is directed out of the AmpC$_{EC}$ active site and not engaging with active site residues. The C6 amido sidechain was refined in two conformations with the amide carbonyl either positioned for polar interaction with the backbone nitrogen of Ala318 (2.8 Å), or the phenol of Tyr150 (3.0 Å) at the opposite face of the active site. The position of the β-lactam derived carboxylate is apparently unaffected by the conformation of the amide and results in polar interactions with the sidechains of Lys315 (3.2 Å), Thr316 (2.5 Å), and Asn346 (3.1 Å).

In the structure of the cross-linked AmpC$_{EC}$ reacted with ticarcillin, the acyl-carbonyl of the ticarcillin derived AEC appears flipped out of the oxyanion pocket, pointing towards the opposite face of the AmpC$_{EC}$ active site. However, as this was not observed with the non cross-linked AmpC$_{EC}$, this observation may result from the conformational changes of Tyr150 and Lys67 induced by the cross-linking reaction. It is therefore unclear whether this represents a distinctive feature of the binding mode of the ticarcillin derived AEC.

Table 1: Data collection and refinement statistics for AmpC$_{EC}$-temocillin/ticarcillin derived structures.

Datasets	AmpC$_{EC}$-temocillin	AmpC$_{EC}$-ticarcillin
Data Collection	mx18069-27	mx18069-37
Beamline (Wavelength, Å)	DLS I03 (0.9686)	DLS I04-1 (0.9159)
Detector	Pilatus	Pilatus
Data Processing	Xia2-3dii	Xia2-dials
Space group	*P* 4_3 3 2	*P* 4_3 3 2
Cell dimensions		
a,b,c (Å)	137.7, 137.7, 137.7	13.5, 137.5, 137.5
α, β, γ (°)	90, 90, 90	90, 90, 90
No. of molecules/ASU	1	1
Total reflections	1672094 (77730)*	7168749 (357488)*
Unique reflections	45481 (2222)*	93002 (4585)*
Resolution (Å)	45.91-1.75 (1.78-1.75)*	79.37-1.37 (1.39-1.37)*
R_{meas}(I)	0.189 (4.012)*	0.146 (2.724)*
I/σI	14.6 (1.4)*	23.3 (2.5)*
$CC_{1/2}$	1.0 (0.5)*	1.0 (0.8)*
Completeness (%)	100 (100)*	100 (100)*
Multiplicity	36.8 (25.0)*	77.1 (78.0)*
Wilson B value (Å^2)	26.43	14.94
Refinement		
R_{work}/R_{free}	0.1815/0.2047	0.1543/0.1630
No. Atoms	3046	3211
- Enzyme	2717	2761
- Ligand	29	50
- Water	275	390
Average B-factors	31.5	20.49
- Enzyme	30.3	18.86
- Ligand	40.5	22.90
- Water	40.7	31.95
R.m.s deviations		
- Bond lengths (Å)	0.006	0.008
- Bond angles (°)	0.970	1.107

*Highest resolution shell in parentheses.

Overall, however, the results suggest that the introduction of the 6-OMe group in temocillin substantially changes the conformation of the AEC species bound at the AmpC$_{EC}$ active site. This contrasts with previous studies on the *P. aeruginosa* PBP3, in which no substantial differences were observed between acyl-enzyme species derived from both penicillins[20].

Notably, the putative de-acylating water molecule which is proposed to bind in close proximity to Tyr150 and the sidechain of Thr316 is not observed in either of the two penicillin derived AmpC$_{EC}$-acyl complexes. In both structures it appears to be displaced by carboxylic acid

motifs, either of the C6 amido sidechain (ticarcillin), or derived from opening of the β-lactam (temocillin). By contrast with studies on class A SBLs[20], the 6-OMe group thus does not appear to influence displacement of this water molecule at the AmpC$_{EC}$ active site.

7.3. AmpC$_{EC}$ interactions with cephalosporins and cephamycins

Cephalosporins are currently the most widely used β-lactam antibiotics[29]. They contain a dihydrothiazine ring fused to the β-lactam ring (Figure 4). As a distinctive feature compared to other β-lactam antibiotics, cephalosporins all contain a C3' sidechain which can contain a leaving group. On reaction with SBLs and opening of the β-lactam ring, the C3' group can be eliminated to give an exocyclic alkene (Figure 4).

Cephamycins are cephalosporins with a 7-OMe group (which is equivalent to the 6-OMe group of temocillin)[30]. Cephamycins are hydrolytically stable against a wider range of β-lactamases than cephalosporins, but are susceptible to hydrolysis by AmpC$_{EC}$ and other class C SBLs[31].

7.3.1. Structure of cephamycin derived acyl-enzyme species

Soaking the cephamycin cefmetazole into crystals of unmodified AmpC$_{EC}$, gave a crystal structure (5 min soak, 1.71 Å resolution, Figure 4 and Table 2) with additional electron density indicating covalent modification of Ser64 with the cefmetazole derived AEC.

Table 2: Data collection and refinement statistics for AmpC$_{EC}$-cefmetazole structure.

Dataset		**AmpC$_{EC}$-Cefmetazole**	
Data Collection	mx18069-27	**Refinement**	PHENIX
Beamline (Wavelength, Å)	DLS I03 (0.9686)	R_{work}/R_{free}	0.1575/0.1808
Detector	Pilatus3 6M	No. atoms	2997
Data Processing	Xia2-3dii	- Enzyme	2754
Space group	$P\,4_3\,3\,2$	- Ligand	25
Cell dimensions		- Water	212
- *a,b,c* (Å)	138.5, 138.5, 138.5	Average B-factors	39.02
- α, β, γ (°)	90, 90, 90	- Enzyme	38.38
No. of molecules/ASU	1	- Ligand	44.63
Total reflections	1894163 (90632)*	- Water	46.27
Unique reflections	49473 (2426)*	R.m.s deviations	
Resolution (Å)	46.15-1.71 (1.74-1.71)*	- Bond lengths (Å)	0.005
R_{meas}(I)	0.0091 (3.224)*	- Bond angles (°)	0.909
I/σI	24.9 (1.4)*		
$CC_{1/2}$	1.0 (0.5)*		
Completeness (%)	100 (100)*		
Multiplicity	38.3 (37.4)*		
Wilson B value (Å^2)	30.83		

*Highest resolution shell in parentheses.

The terminal nitrile of the C7 amido-sidechain is positioned for polar interactions with the sidechains of Gln120 (2.8 Å) and Asn152 (3.8 Å). The dihydrothiazine carboxylate is positioned to accept hydrogen bonds from the sidechains of Ly315 (3.2 Å) and Thr316 (2.8 Å). In agreement with elimination of this group on reaction with $AmpC_{EC}$, no electron density is evident for the C3' / R2 thioether tetrazole sidechain (Figure 4D).

The 7-OMe group of cefmetazole is positioned similarly as observed with the temocillin derived AEC (Figure 3D), but is not positioned for (direct) polar interactions with any $AmpC_{EC}$ active site residues. By contrast with the temocillin- and ticarcillin- derived AECs showing a 180° flip of the AEC (Figure 3), the binding mode of the cefmetazole derived AEC broadly resembles that of the reported cefalotin derived AEC (PDB: 1KVM, Figure 4B and C)[7]. However, in the reported structure the dihydrothiazine of the cefalotin derived AEC is rotated compared to its position observed in the cefmetazole derived AEC (Figure 4B). This results in re-positioning of the dihydrothiazine carboxylate out of the $AmpC_{EC}$ active site and allows binding of the putative de-acylating water molecule (Figure 4C), which is not observed in the $AmpC_{EC}$-cefmetazole derived acyl-enzyme complex (Figure 4D).

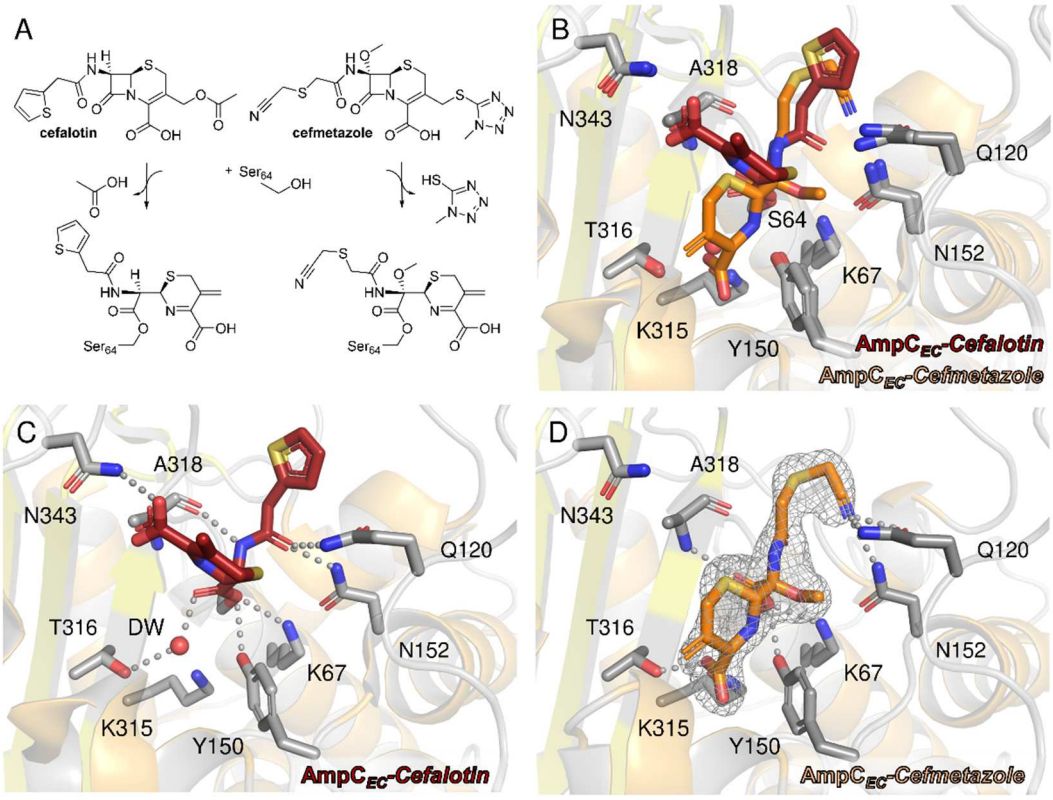


Figure 4: Views from crystal structures of $AmpC_{EC}$ reacted with cefmetazole or cefalotin. (A) Reaction of $AmpC_{EC}$ with cefalotin and cefmetazole. (B) Overlay of active site views from crystal structures of $AmpC_{EC}$ reacted with cefalotin or cefmetazole. (C) Active site view from a reported crystal structure of $AmpC_{EC}$ reacted with cefalotin (PDB: 1KVM[7]) showing the cefalotin derived acyl-enzyme species. (D) Active site view from a crystal structure of $AmpC_{EC}$ reacted with cefmetazole for 5 min showing the cefmetazole derived acyl-enzyme species. Polar interactions are indicated as white dashes. mF_o-DF_c polder OMIT maps[28] are contoured at 3.0 σ and carved around the cefmetazole derived acyl-enzyme species. DW: De-acylating water molecule.

7.3.2. Structure of cephalosporin and cephamycin derived product complexes

Product inhibition is generally not observed with class C SBLs[1,2], which may in part explain why structural information on product binding is so far limited to a single structure of an catalytically inactive S64G AmpC$_{EC}$ mutant in complex with hydrolysed cefalotin, a first-generation cephalosporin[7].

Soaking AmpC$_{EC}$ crystals obtained from the PEG condition with preferred substrates of AmpC$_{EC}$, resulted in complexes of AmpC$_{EC}$ with hydrolysis products derived from cefalotin and cefoxitin. Cefalotin and cefoxitin differ only by the presence of an additional 7-OMe group in cefoxitin and by a small change in the C3' / R2 leaving group (acetic acid and carbamic acid, for cefalotin and cefoxitin, respectively, Figure 5A).

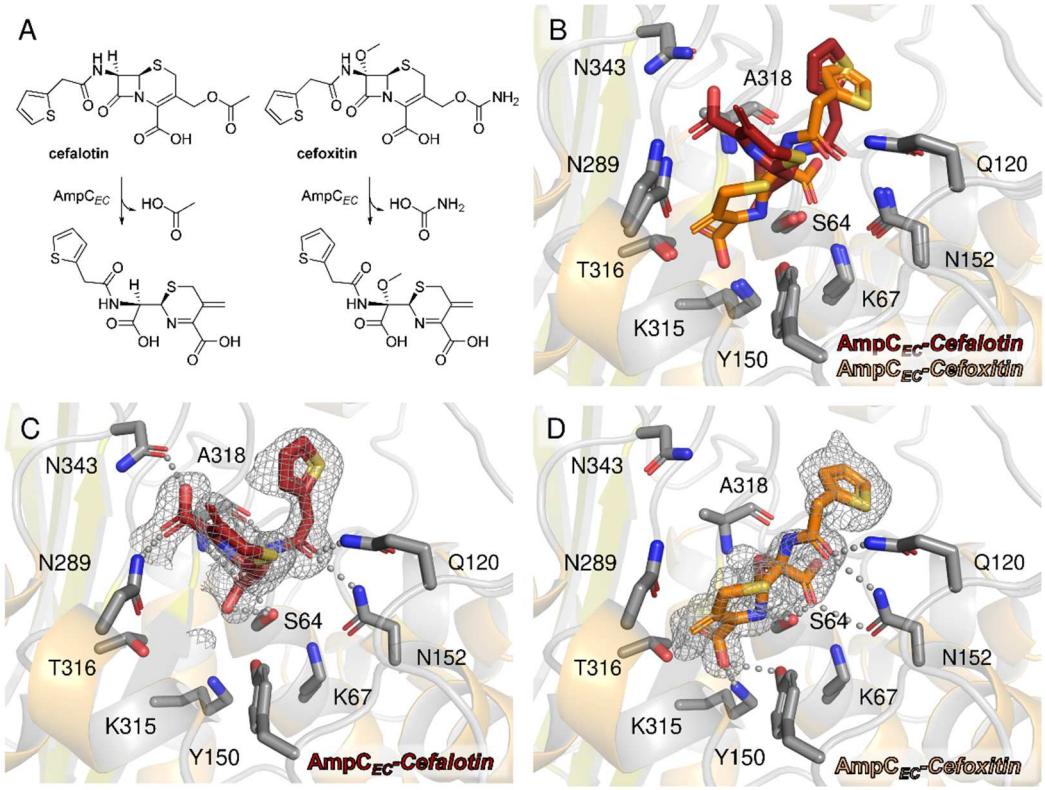


Figure 5: Views from crystal structures of AmpC$_{EC}$ in complex with cephalosporin derived hydrolysis products. (A) Reaction of AmpC$_{EC}$ with cefalotin or cefoxitin. (B) Overlay of active site views from crystal structures of AmpC$_{EC}$ in complex with hydrolysed cefalotin or cefoxitin. (C) Active site view from crystal structure of AmpC$_{EC}$ in complex with hydrolysed cefalotin. (D) Active site view from crystal structure of AmpC$_{EC}$ in complex with hydrolysed cefoxitin. Polar interactions are indicated as white dashes. mF$_o$-DF$_c$ polder OMIT maps[28] are contoured at 3.0 σ and carved around the cephalosporin derived hydrolysis products.

A structure of the AmpC$_{EC}$ complex with hydrolysed cefoxitin (9 min soak, 1.47 Å resolution, Figure 5 and Table 3) shows the β-lactam derived carboxylic acid out of the oxyanion-hole, positioned in close proximity to the side chains of Ser64 (2.4 Å), Lys67 (3.3 Å), and Asn152 (3.2 Å). While the dihydrothiazine ring is poisoned similarly as observed in the cefmetazole derived AEC (Figure 4A), the 7-OMe group is directed to the opposite face of the AmpC$_{EC}$

active site (compared to the cefmetazole derived AEC), pointing towards Ala318. The C7 amide carbonyl is positioned in close proximity to the sidechains of Gln120 (2.9 Å) and Asn152 (3.1 Å), while the thiophene portion of the sidechain is pointing out of the $AmpC_{EC}$ active site and is not engaging in interactions with $AmpC_{EC}$ residues

In the structure of $AmpC_{EC}$ in complex with hydrolysed cefalotin (5 min soak, 1.47 Å resolution, Figure 5 and Table 3), the β-lactam derived carboxylic acid is positioned in the oxyanion-hole in hydrogen bonding distance from the Ala318 backbone nitrogen (2.8 Å) and the Ser64 hydroxy group (2.6 Å) (Figure 5C). As observed with cefoxitin, the C7 amide carbonyl of the hydrolysed cephalosporin is positioned in close proximity to the sidechains of Gln120 (3.1 Å) and Asn152 (2.8 Å), while the thiophene portion of the sidechain is pointing out of the $AmpC_{EC}$ active site. Similarly as observed with the cephalosporin and cephamycin derived acyl-enzyme complexes (Figure 4), the dihydrothiazine carboxylate of the hydrolysed cefalotin is rotated compared to the cefoxitin derived hydrolysis product (Figure 5D) and positioned for hydrogen bonding with the sidechains of Asn289 (3.2 Å) and Asn343 (2.8 Å). Interestingly, this binding mode is different compared to that observed for hydrolysed cefalotin in complex with the $AmpC_{EC}$ S64G mutant (PDB: 1KVL[7]). In the reported structure of the catalytically impaired mutant, the dihydrothiazine carboxylate is pointing out of the $AmpC_{EC}$ active site and not positioned for interaction with any active site residues[7]. Importantly, the binding mode observed in this structure would also result in a steric clash of the β-lactam derived carboxylate with the sidechain of the nucleophilic Ser of the catalytically viable $AmpC_{EC}$. It is therefore likely that the crystal structure of wildtype $AmpC_{EC}$ in complex with hydrolysed cefalotin discussed here more closely represents a biologically relevant binding mode than the one observed at the active site of the S64G $AmpC_{EC}$ mutant.

By contrast with the studies on penicillins, the combined results suggest no substantial impact of the 7-OMe group on the conformation of the cephalosporin derived AEC. However, other than observed in the penicillin derived acyl-enzyme complexes, where the putative de-acylating water molecule was displaced also in the absence of the 6-OMe group, electron density maps indicate the putative water molecule bound at the $AmpC_{EC}$ active site on reaction with cefalotin, but not with cefmetazole. While the 7-OMe group of cefmetazole does not appear to directly displace the putative water molecule, it likely affects the positioning of the dihydrothiazine carboxylate in close proximity to the phenolic oxygen of Tyr150 and the sidechain of Thr316, resulting in the displacement. Further, the 7-OMe group of cephamycins does also appear to alter the binding mode of the hydrolysis product at the $AmpC_{EC}$ active site.

Further studies are needed to investigate potential kinetic consequences for $AmpC_{EC}$ hydrolysis of cephalosporins and cephamycins (e.g. hydrolytic stability of the AEC and potential product inhibition).

Table 3: Data collection and refinement statistics for AmpC$_{EC}$ complexes with hydrolysed cephalosporins.

Datasets	AmpC$_{EC}$-Cefalotin	AmpC$_{EC}$-Cefoxitin
Data Collection	mx19458-3	mx19458-3
Beamline (Wavelength, Å)	DLS I03 (0.9763)	DLS I03 (0.9763)
Detector	Pilatus3 6M	Pilatus3 6M
Data Processing	Xia2-dials	Xia2-dials
Space group	*P* 4_3 3 2	*P* 4_3 3 2
Cell dimensions		
- *a,b,c* (Å)	138.9, 138.9, 138.9	138.0, 138.0, 138.0
- α, β, γ (°)	90, 90, 90	90, 90, 90
No. of molecules/ASU	1	1
Total reflections	5940179 (294133)*	5442618 (264663)*
Unique reflections	77932 (3842)*	72058 (3527)*
Resolution (Å)	56.71-1.47 (1.50-1.47)*	56.35-1.50 (1.53-1.50)*
R_{meas}(I)	0.103 (3.107)*	0.139 (2.662)*
I/σI	33.4 (2.2)*	26.0 (2.5)*
$CC_{1/2}$	1.0 (0.7)*	1.0 (0.8)*
Completeness (%)	100 (100)*	100 (100)*
Multiplicity	76.2 (76.6)*	75.5 (75.1)*
Wilson B value (Å^2)	18.35	15.71
Refinement		
R_{work}/R_{free}	0.1400/0.1580	0.1500/0.1765
No. atoms	3187	3256
- Enzyme	2744	2812
- Ligand	24	26
- Water	419	417
Average B-factors	26.44	24.48
- Enzyme	24.35	22.70
- Ligand	41.68	35.48
- Water	39.31	35.92
R.m.s deviations		
- Bond lengths (Å)	0.010	0.013
- Bond angles (°)	1.173	1.429

*Highest resolution shell in parentheses.

7.4. AmpC$_{EC}$ interactions with penems and carbapenems

Clinically used carbapenems are synthetic β-lactam antibiotics with a pyrroline ring fused to the β-lactam ring (Figure 6A). Carbapenems are often considered as antibiotics of last-resort; as they are effective against a wide range of pathogens and relatively stable towards hydrolysis catalysed by most β-lactamases, including AmpC$_{EC}$[32]. Penems, which are more closely structurally related to penicillins with a thiazoline ring fused to the β-lactam ring

(Figure 6A), are similarly resistant towards hydrolysis catalysed by most β-lactamases, but are less commonly used[32].

A structure of $AmpC_{EC}$ reacted with panipenem (10 min soak, 1.33 Å resolution, Figure 6 and Table 4), a carbapenem, showed the panipenem derived AEC with the thiazolidine carboxylate positioned to form a salt bridge with the sidechain of Arg349 (3.0 Å), and further polar interactions with Asn346 (3.2 Å). The C6 hydroxy-ethyl sidechain is poisoned for polar interactions with the sidechains of Gln120 (3.5 Å) and Asn152 (3.0 Å). Notably, the carbonyl of the panipenem derived AEC, appears flipped out of the $AmpC_{EC}$ oxyanion hole and is directed towards the opposite face of the active site, in close proximity to Lys67 (2.7 Å). Such a flip has previously been observed with another carbapenem (imipenem) and was suggested to result from the steric influence of the hydroxy-ethyl group[4].

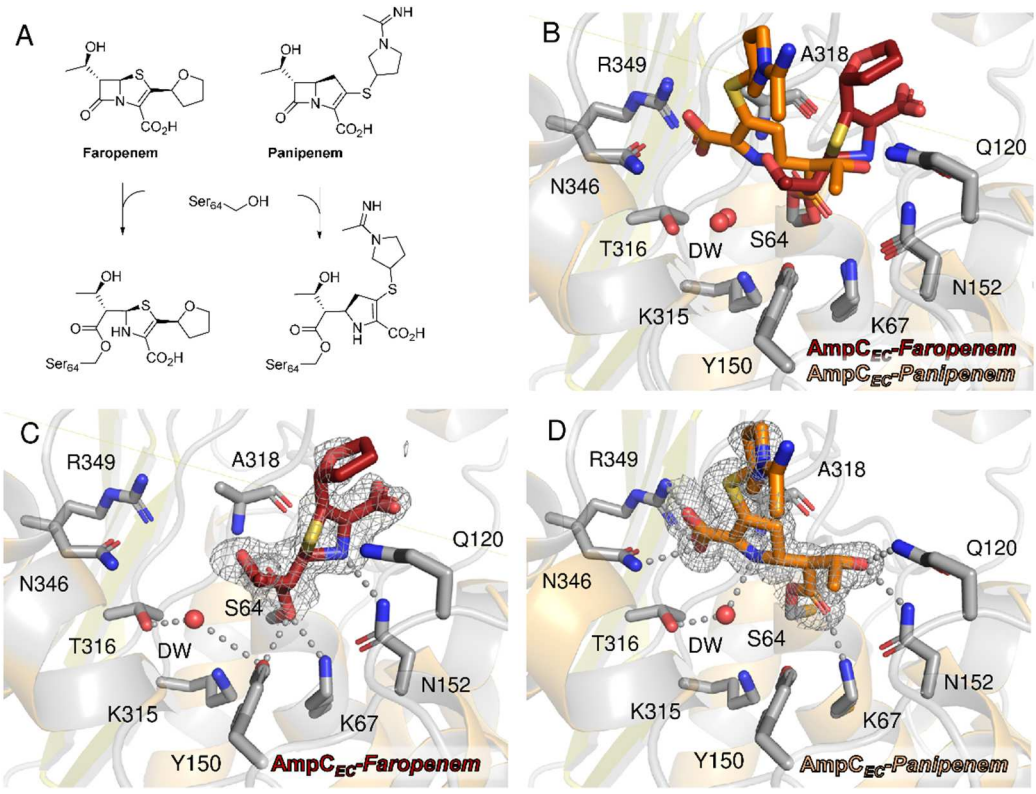


Figure 6: Views from crystal structures of $AmpC_{EC}$ reacted with (carba)penems. (A) Reaction of $AmpC_{EC}$ with faropenem and panipenem. (B) Overlay of active site views from crystal structures of $AmpC_{EC}$ reacted with faropenem or panipenem. (C) Active site view from crystal structure of $AmpC_{EC}$ reacted with faropenem for 10 min. (D) Active site view from crystal structure of $AmpC_{EC}$ reacted with panipenem for 10 min. Polar interactions are indicated as white dashes. mF_o-DF_c polder OMIT maps[28] are contoured at 3.0 σ and carved around the panipenem and faropenem derived acyl-enzyme species. DW: De-acylating water molecule.

By contrast with panipenem, in a crystal structure obtained from soaking crystals of unmodified $AmpC_{EC}$ with the penem faropenem (10 min soak, 1.83 Å resolution, Figure 6 and Table 4) examination of electron density maps indicated additional density extending from the nucleophilic Ser64, indicating the faropenem derived acyl-enzyme species. Interestingly, this

AEC appeared flipped ~180° compared to the expected binding mode of the β-lactam, with the thiazolidine ring oriented in a similar manner as observed with ticarcillin (Figure 3C), positioning the thiazolidine nitrogen in close proximity of the side chains of Gln120 (3.5 Å). The C6 hydroxy-ethyl sidechain is positioned at the opposite face of the AmpC$_{EC}$ active site and not positioned to engage in interactions with active site residues. Other than with the panipenem derived AEC, the acyl-carbonyl of the faropenem derived AEC is positioned in the oxyanion hole, near the backbone nitrogen of Ala318 (4.0 Å).

Table 4: Data collection and refinement statistics for AmpC$_{EC}$ structures with penems and carbapenems.

Datasets	**AmpC$_{EC}$-Panipenem**	**AmpC$_{EC}$-Faropenem**
Data Collection	mx180690-52	mx180690-52
Beamline (Wavelength, Å)	DLS I03 (0.9762)	DLS I03 (0.9762)
Detector	Eiger2 XE 16M	Eiger2 XE 16M
Data Processing	Xia2 dials	Xia2 dials
Space group	*P* 4$_3$ 3 2	*P* 4$_3$ 3 2
Cell dimensions		
- *a,b,c* (Å)	138.0, 138.0, 138.0	137.9, 137.9, 137,9
- α, β, γ (°)	90, 90, 90	90, 90, 90
No. of molecules/ASU	1	1
Total reflections	7706490 (381962)*	3027913 (152808)*
Unique reflections	102741 (5077)*	40091 (1958)*
Resolution (Å)	61.72-1.33 (1.35-1.33)*	97.52-1.83 (1.86-1.83)*
R_{meas}(I)	0.124 (2.962)*	0.164 (2.995)*
I/σI	28.4 (2.4)*	24.1 (2.0)*
$CC_{1/2}$	1.0 (0.8)*	1.0 (0.9)*
Completeness (%)	100 (100)*	100 (100)*
Multiplicity	75.0 (75.2)*	75.5 (78.0)*
Wilson B value (Å^2)	12.92	29.58
Refinement		
R_{work}/R_{free}	0.1334/0.1548	0.1813/0.2050
No. atoms	3372	3197
- Enzyme	2892	2882
- Ligand	25	21
- Water	422	288
Average B-factors	20.5	31.2
- Enzyme	18.7	30.2
- Ligand	21.0	58.2
- Water	31.8	39.3
R.m.s deviations		
- Bond lengths (Å)	0.010	0.017
- Bond angles (°)	1.152	1.339

*Highest resolution shell in parentheses.

Interestingly, the putative de-acylating water molecule was observed in both complexes derived from reaction of AmpC$_{EC}$ with faropenem or panipenem, bound in hydrogen bonding distance to the Tyr150 phenol and the Thr316 sidechain (Figure 6C and D). While this is notable, as both penems and carbapenems are thought to form hydrolytically stable complexes with AmpC$_{EC}$[32], it has also previously been observed in the imipenem derived AmpC$_{EC}$-acyl complex[4].

It should be noted that most other crystal structures obtained from soaking crystals of unmodified AmpC$_{EC}$ with faropenem, electron density was only evident for the hydroxy-ethyl sidechain and potentially some parts of the thiazolidine ring (data not shown). This may indicate fragmentation of the penem derived acyl-enzyme species as previously observed on reaction with some class C SBLs[33]. However, the additional electron density observed at the AmpC$_{EC}$ active site in the structures obtained from soaking trials with faropenem suggests larger portions of faropenem bound than reported in these previous studies. Further studies, e.g. using protein observed MS, will be needed to investigate the nature of these complexes and their relevance in AmpC$_{EC}$ catalysis or inhibition.

Overall, the results suggest that substitution of the penem sulfur to a carbon leads to differences in the conformation of the acyl-enzyme species on reaction with AmpC$_{EC}$, with potential mechanistic consequences (e.g. potential fragmentation reaction of the AEC) which will require further studies to clarify and investigate potential consequences for AmpC$_{EC}$ inhibition and catalysis.

7.5. AmpC$_{EC}$ interactions with lactivicin derivative LTV-13

Lactivicin (LTV, Figure 7) is a dicyclic dipeptide, containing a cyclo-serine and a γ-lactone ring[34]. It is the only naturally occurring non-β-lactam antibiotic known to act via inhibition of PBPs[34-36]. Lactivicin and lactivicin derivatives are reported to react with PBPs and SBLs through nucleophilic attack of the active-site Ser residue on the γ-lactone carbonyl, followed by opening of both the γ-lactone and cyclo-serine rings, leading to an acyclic acyl-enzyme species (Figure 7B)[37-39]. The resulting AECs have been shown to be relatively hydrolytically stable, both with PBPs and with SBLs[37-39].

Structural studies on lactivicin and lactivicin derivatives have, however, so far been limited to PBPs[37,38] and a single structure of the class A SBL BS3[39]. LTV-13 is a lactivicin derivative, modified with the amido-sidechain of the monobactam aztreonam at the C4 position (which is equivalent to C6 and C7 amido sidechains of penicillins and cephalosporins, respectively)[37].

A structure of AmpC$_{EC}$ in complex with LTV-13 was obtained via soaking (10 min soak, 1.84 Å resolution, Figure 7A and Table 5). Examination of electron density maps revealed additional electron density extending from Ser64 which is in agreement with formation of an AEC species (Figure 7).

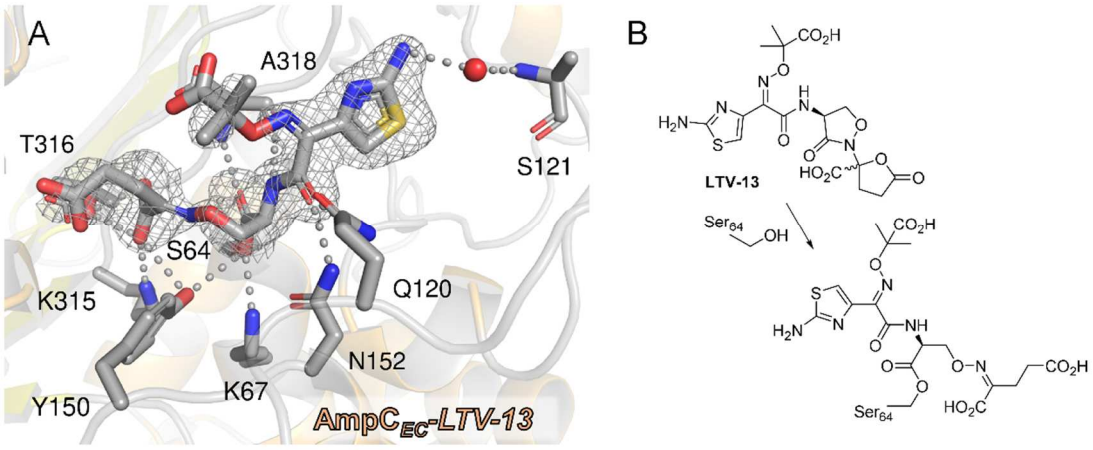


Figure 7: Structural basis of AmpC$_{EC}$ reaction with LTV-13. (A) Active site view from a crystal structure of AmpC$_{EC}$ reacted with LTV-13 for 10 min, showing the ring opened form of LTV-13 covalently bonded to the nucleophilic Ser64. Polar interactions are indicated as white dashes. mF$_o$-DF$_c$ polder OMIT maps[28] are contoured at 3.0 σ and carved around the LTV-13 derived acyl-enzyme species. (B) Reaction of AmpC$_{EC}$ with LTV-13.

As observed with most β-lactams, the acyl-enzyme carbonyl is positioned for polar interaction with the backbone of Ala318 (3.1 Å) and the C4 amido-sidechain amide is positioned in close proximity to Gln120 (2.8 Å) and Asn152 (2.9 Å). The terminal amine of the sidechain thiazole ring is positioned to interact with a water molecule (2.9 Å) which is within hydrogen bonding distance of the backbone nitrogen of Ser121 (2.9 Å), while the isobutyric acid portion of the amido-sidechain is pointing outwards of the active site and not engaging in interactions with active site residues. The cycloserine carboxylic acid is positioned in close proximity to Lys315 (2.8 Å) and Thr316 (3.0 Å), displacing the putative de-acylating water, as observed with the ticarcillin derived AEC (Figure 3). The terminal carboxylic acid derived from opening of the cycloserine ring is pointing outwards of the AmpC$_{EC}$ active site.

Overall, the structure thus gives evidence that LTV-13 reacts with AmpC$_{EC}$ to form at least a somewhat hydrolytically stable acyl-enzyme complexes arising from opening of both the γ-lactone and cycloserine rings. Further studies will be needed to investigate the kinetics of AmpC$_{EC}$ inhibition by LTV-13 and potential AmpC$_{EC}$ catalysed inactivation of LTV-13 and related lactivicin derivatives.

Table 5: Data collection and refinement statistics for AmpC$_{EC}$-LTV-13 structure.

Dataset	**AmpC$_{EC}$-LTV-13**		
Data Collection	mx18069-81	**Refinement**	PHENIX
Beamline (Wavelength, Å)	DLS I03 (0.9762)	R_{work}/R_{free}	0.1780/0.2032
Detector	Eiger2 XE 16M	No. atoms	3249
Data Processing	Xia2 3dii	- Enzyme	2889
Space group	$P\,4_3\,3\,2$	- Ligand	35
Cell dimensions		- Water	308
- *a,b,c* (Å)	138.8, 138.8, 138.8	Average B-factors	34.57
- α, β, γ (°)	90, 90, 90	- Enzyme	33.32
No. of molecules/ASU	1	- Ligand	66.26
Total reflections	2997277 (162114)*	- Water	41.99
Unique reflections	39464 (1976)*	R.m.s deviations	
Resolution (Å)	46.27-1.84 (1.87-1.84)*	- Bond lengths (Å)	0.008
R_{meas}(I)	0.122 (2.517)*	- Bond angles (°)	0.932
I/σI	36.7 (2.6)*		
$CC_{1/2}$	1.0 (0.9)*		
Completeness (%)	98.3 (100)*		
Multiplicity	75.9 (82.0)*		
Wilson B value (Å^2)	28.265		

*Highest resolution shell in parentheses.

7.6. Summary and conclusions

Structures of AmpC$_{EC}$ in complex with a range of different β-lactam antibiotics were obtained. While the data discussed is preliminary and requires further detailed solution studies to investigate potential consequences for AmpC$_{EC}$ catalysis and inhibition, they give some insight into interesting mechanistic considerations for AmpC$_{EC}$ interaction with a range of β-lactam antibiotics and the structurally related lactivicin derivative LTV-13.

They reveal that seemingly small alterations such as introduction of the 6-OMe/7-OMe group in penicillins and cephalosporins, or substitution of the penem sulfur to carbon, of the β-lactams can lead to substantial changes in the binding mode of the AmpC$_{EC}$ acyl-enzyme complexes or the corresponding product complexes. Potential consequences on the hydrolytic stability of those acyl-enzyme complexes should be investigated in solution studies.

Studies on class A SBLs have suggested that introduction of the 6-OMe/7-OMe group in penicillins and cephalosporins increases the stability of the AEC by displacement of the de-acylating water molecule[19-21]. The crystal structures shown here of AmpC$_{EC}$ reacted with temocillin and ticarcillin, however, reveal that the putative water molecule is displaced by both penicillins on formation of the AEC. Instead, the 6-OMe group appears to induce a 180° flip of the conformation of the AEC. By contrast, the putative de-acylating water molecule observed in the reported structure of the AmpC$_{EC}$ reacted with cefalotin, appears replaced in the structure

of the cefmetazole derived AmpC$_{EC}$-acyl complex reported here. However, the 7-OMe of cefmetazole does not appear to directly displace the water molecule, but instead to induce a conformational change of the AEC resulting in displacement of the water molecule by the dihydrothiazine carboxylate. The results thus raise the possibility, that conformational rearrangement of the AEC is a key reason why the 6-OMe/7-OMe substituted penicillins / cephalosporins manifest increased stability, rather than simple blockade of the approach of the hydrolytic water. Further SAR work on 6-OMe/7-OMe derivatives is clearly of interest to explore this, as are modelling studies to explore the precise mechanisms of the apparent conformational changes at the AEC stage. Evidence for conformational rearrangement to give a stable AEC complex comes from work on the inhibition of a serine protease (elastase) by a monocyclic β-lactam[40].

The apparent preferential hydrolysis of (*S*)-temocillin and -ticarcillin over the respective (*R*)-epimers is intriguing, especially in light of the reported enhanced antimicrobial activity of the (*R*)-epimers[24]. Those combined findings suggest potential in the development of carboxypenicillin derivatives with a resolved stereocenter, which may also be of relevance for other β-lactam antibiotics with unresolved chiral centres in the β-acyl side-chain such as carbenicillin[41], moxalactam[42], sulbenicillin[43], and cefsulodin[44]. Introduction of a Cα alkyl group (methyl in the first instance) on the side chain is of interest as it would enable locking of the side chain stereochemistry.

Overall, the presented results provide new insight into AmpC$_{EC}$ catalysed β-lactam hydrolysis and may represent a starting point for further SAR studies on the AmpC$_{EC}$ substrate scope and the development of new β-lactam antibiotics with improved stability towards AmpC$_{EC}$ hydrolysis.

7.7. Materials and Methods

7.7.1. Materials

β-Lactam antibiotics were from Carbosynth (temocillin), Global Life Sciences (ticarcillin), TOKU-E (cefmetazole and cefalotin), Sigma Aldrich (cefoxitin), Fluorochem (faropenem), and Ontario Chemicals (panipenem). LTV-13 was synthesised by Dr Klaus-Daniel Umland (University of Oxford) according to reported procedures[37].

7.7.2. Enzyme production and purification

AmpC$_{EC}$ was produced and purified as described in Chapter 2.

7.7.3. Crystallography

Unmodified AmpC$_{EC}$ was crystallised as described in Chapter 2. Crystals were transferred into the precipitant solution supplemented with the respective antibiotic and incubated at room

temperature for the indicated time, then cryo-cooled and stored in liquid nitrogen. Diffraction data were collected at the MX beamlines at Diamond Light Source. Structures were solved via molecular replacement with Phaser[45], using the structure of unmodified $AmpC_{EC}$ as the starting model (PDB: 6T3D, see Chapter 2). Alternating cycles of refinement with phenix.refine[46] and manual model building in Coot[47]were performed until R_{work} and R_{free} converged.

7.7.4. NMR based turnover assays

Spectra were recorded on a Bruker Avance III 700 MHz spectrometer equipped with a 5 mm inverse TCI cryo-probe and referenced to the residual deuterated solvent peak. The instrument was controlled by TopSpin software. All experiments were conducted at 298 K.

$AmpC_{EC}$ was exchanged to 100 mM phosphate buffer pH 7.5 using Micro Bio-Spin™ 6 columns (BIO-RAD). Reactions were set up in 100 mM phosphate buffer pH 7.5 containing 25 µM $AmpC_{EC}$ and 10 % D_2O in a final volume of 160 µL and initiated by addition of the β-lactam antibiotic substrate to a final concentration of 2.5 mM. The sample was immediately transferred to the spectrometers and spectra were recorded at the indicated time points.

7.8. References

1. Galleni, M.; Amicosante, G.; Frère, J.M. A survey of the kinetic parameters of class C β-lactamases. Cephalosporins and other β-lactam compounds. *Biochem. J.* **1988**, *255*, 123-129.
2. Galleni, M.; Frère, J.M. A survey of the kinetic parameters of class C β-lactamases. Penicillins. *Biochem. J.* **1988**, *255*, 119-122.
3. Bauvois, C.; Ibuka, A.S.; Celso, A.; Alba, J.; Ishii, Y.; Frère, J.-M.; Galleni, M. Kinetic Properties of Four Plasmid-Mediated β-Lactamases. *Antimicrob. Agents Chemother.* **2005**, *49*, 4240-4246.
4. Beadle, B.M.; Shoichet, B.K. Structural Basis for Imipenem Inhibition of Class β-Lactamases. *Antimicrob. Agents Chemother.* **2002**, *46*, 3978-3980.
5. Patera, A.; Blaszczak, L.C.; Shoichet, B.K. Crystal Structures of Substrate and Inhibitor Complexes with AmpC β-Lactamase: Possible Implications for Substrate-Assisted Catalysis. *J. Am. Chem. Soc.* **2000**, *122*, 10504-10512.
6. Powers, R.A.; Caselli, E.; Focia, P.J.; Prati, F.; Shoichet, B.K. Structures of Ceftazidime and Its Transition-State Analogue in Complex with AmpC β-Lactamase: Implications for Resistance Mutations and Inhibitor Design. *Biochemistry* **2001**, *40*, 9207-9214.
7. Beadle, B.M.; Trehan, I.; Focia, P.J.; Shoichet, B.K. Structural Milestones in the Reaction Pathway of an Amide Hydrolase: Substrate, Acyl, and Product Complexes of Cephalothin with AmpC β-Lactamase. *Structure* **2002**, *10*, 413-424.
8. Lobkovsky, E.; Moews, P.C.; Liu, H.; Zhao, H.; Frere, J.M.; Knox, J.R. Evolution of an enzyme activity: crystallographic structure at 2 Å resolution of cephalosporinase from the ampC gene of *Enterobacter cloacae* P99 and comparison with a class A penicillinase. *Proc. Natl. Acad. Sci. U. S. A.* **1993**, *90*, 11257-11261.
9. Bush, K. Past and Present Perspectives on β-Lactamases. *Antimicrob. Agents Chemother.* **2018**, *62*, e01076-01018.
10. Sutherland, R.; Beale, A.S.; Boon, R.J.; Griffin, K.E.; Slocombe, B.; Stokes, D.H.; White, A.R. Antibacterial activity of ticarcillin in the presence of clavulanate potassium. *Am. J. Med.* **1985**, *79*, 13-24.

11. Livermore, D.M.; Hope, R.; Fagan, E.J.; Warner, M.; Woodford, N.; Potz, N. Activity of temocillin against prevalent ESBL- and AmpC-producing *Enterobacteriaceae* from south-east England. *J. Antimicrob. Chemother.* **2006**, *57*, 1012-1014.
12. Phillips, I.; King, A.; Shannon, K.; Warren, C. Temocillin (BRL 17421): *In vitro* antibacterial activity and susceptibility to β-lactamases. *J. Antimicrob. Chemother.* **1982**, *10*, 271-278.
13. Jules, K.; Neu, H.C. Antibacterial activity and β-lactamase stability of temocillin. *Antimicrob. Agents Chemother.* **1982**, *22*, 453-460.
14. Van Landuyt, H.W.; Pyckavet, M.; Lambert, A.; Boelaert, J. *In vitro* activity of temocillin (BRL 17421), a novel β-lactam antibiotic. *Antimicrob. Agents Chemother.* **1982**, *22*, 535-540.
15. Alexandre, K.; Fantin, B. Pharmacokinetics and Pharmacodynamics of Temocillin. *Clin. Pharmacokinet.* **2018**, *57*, 287-296.
16. Livermore, D.M.; Tulkens, P.M. Temocillin revived. *J. Antimicrob. Chemother.* **2008**, *63*, 243-245.
17. Edlund, C.; Ternhag, A.; Skoog Ståhlgren, G.; Edquist, P.; Östholm Balkhed, Å.; Athlin, S.; Månsson, E.; Tempé, M.; Bergström, J.; Giske, C.G., et al. The clinical and microbiological efficacy of temocillin versus cefotaxime in adults with febrile urinary tract infection, and its effects on the intestinal microbiota: a randomised multicentre clinical trial in Sweden. *Lancet Infect. Dis.* **2022**, *22*, 390-400.
18. Lupia, T.; De Benedetto, I.; Stroffolini, G.; Di Bella, S.; Mornese Pinna, S.; Zerbato, V.; Rizzello, B.; Bosio, R.; Shbaklo, N.; Corcione, S., et al. Temocillin: Applications in Antimicrobial Stewardship as a Potential Carbapenem-Sparing Antibiotic. *Antibiotics* **2022**, *11*, 493.
19. Matagne, A.; Lamotte-Brasseur, J.; Dive, G.; Knox, J.R.; Frère, J.M. Interactions between active-site-serine β-lactamases and compounds bearing a methoxy side chain on the α-face of the β-lactam ring: kinetic and molecular modelling studies. *Biochem. J.* **1993**, *293*, 607-611.
20. Sacco, M.D.; Kroeck, K.G.; Kemp, M.T.; Zhang, X.; Andrews, L.D.; Chen, Y. Influence of the α-Methoxy Group on the Reaction of Temocillin with *Pseudomonas aeruginosa* PBP3 and CTX-M-14 β-Lactamase. *Antimicrob. Agents Chemother.* **2019**, *64*, e01473-01419.
21. Zeiser, E.T.; Becka, S.A.; Barnes, M.D.; Taracila, M.A.; LiPuma, J.J.; Papp-Wallace, K.M. Resurrecting Old β-Lactams: Potent Inhibitory Activity of Temocillin against Multidrug-Resistant *Burkholderia* Species Isolates from the United States. *Antimicrob. Agents Chemother.* **2019**, *63*, e02315-02318.
22. Bird, A.E.; Charsley, C.-H.; Jennings, K.R.; Marshall, A.C. High-performance liquid chromatographic assay of temocillin and epimerisation of its diastereoisomers. *Analyst* **1984**, *109*, 1209-1212.
23. Hoogmartens, J.; Roets, E.; Janssen, G.; Vanderhaeghe, H. Separation of the side-chain diastereoisomers of penicillins by high-performance liquid chromatography. *J. Chromatogr. A* **1982**, *244*, 299-309.
24. White, A.R.; Cooper, C.E.; Griffin, K.E.; Slocombe, B. Antibacterial activity of resolved temocillin epimers. *J. Antimicrob. Chemother.* **1986**, *18*, 335-343.
25. Guest, E.A.; Horton, R.; Mellows, G.; Slocombe, B.; Swaisland, A.J.; Tasker, T.C.G. Human pharmacokinetics of temocillin (BRL 17421) side chain epimers. *J. Antimicrob. Chemother.* **1985**, *15*, 327-336.
26. Itoh, T.; Nakashima, K.; Tsuda, Y.; Yamada, H. Stereoselective binding of carbenicillin epimers to human serum albumin. *Chirality* **1996**, *8*, 201-206.
27. Itoh, T.; Ishida, M.; Onuki, Y.; Tsuda, Y.; Shimada, H.; Yamada, H. Stereoselective renal tubular secretion of carbenicillin. *Antimicrob. Agents Chemother.* **1993**, *37*, 2327-2332.
28. Liebschner, D.; Afonine, P.V.; Moriarty, N.W.; Poon, B.K.; Sobolev, O.V.; Terwilliger, T.C.; Adams, P.D. Polder maps: improving OMIT maps by excluding bulk solvent. *Acta Crystallogr D Struct Biol* **2017**, *73*, 148-157.

29. Bush, K.; Bradford, P.A. β-Lactams and β-Lactamase Inhibitors: An Overview. *Cold Spring Harb. Perspect. Med.* **2016**, *6*, a025247.
30. Stapley, E.O.; Jackson, M.; Hernandez, S.; Zimmerman, S.B.; Currie, S.A.; Mochales, S.; Mata, J.M.; Woodruff, H.B.; Hendlin, D. Cephamycins, a New Family of β-Lactam Antibiotics I. Production by Actinomycetes, Including *Streptomyces lactamdurans*. *Antimicrob. Agents Chemother.* **1972**, *2*, 122-131.
31. Daoust, D.R.; Onishi, H.R.; Wallick, H.; Hendlin, D.; Stapley, E.O. Cephamycins, a New Family of β-Lactam Antibiotics: Antibacterial Activity and Resistance to β-Lactamase Degradation. *Antimicrob. Agents Chemother.* **1973**, *3*, 254-261.
32. Papp-Wallace, K.M.; Endimiani, A.; Taracila, M.A.; Bonomo, R.A. Carbapenems: Past, Present, and Future. *Antimicrob. Agents Chemother.* **2011**, *55*, 4943-4960.
33. Tanaka, R.; Namikawa, K.; Nakatsuka, T.; Adachi, H.; Yoshida, T.; Sugita, O.; Ishiguro, M. Novel carbon-carbon bond cleavage reaction of penem antibiotic by class C β-lactamases. *J. Antibiot.* **1994**, *47*, 945-948.
34. Harada, S.; Tsubotani, S.; Hida, T.; Ono, H.; Okazaki, H. Structure of lactivicin, an antibiotic having a new nucleus and similar biological activities to β-lactam antibiotics. *Tetrahedron Lett.* **1986**, *27*, 6229-6232.
35. Nozaki, Y.; Katayama, N.; Ono, H.; Tsubotani, S.; Harada, S.; Okazaki, H.; Nakao, Y. Binding of a non-β-lactam antibiotic to penicillin-binding proteins. *Nature* **1987**, *325*, 179-180.
36. Nozaki, Y.; Katayama, N.; Harada, S.; Ono, H.; Okazaki, H. Lactivicin, a naturally occurring non-β-lactam antibiotic having β-lactam-like action: biological activities and mode of action. *J. Antibiot.* **1989**, *42*, 84-93.
37. Starr, J.; Brown, M.F.; Aschenbrenner, L.; Caspers, N.; Che, Y.; Gerstenberger, B.S.; Huband, M.; Knafels, J.D.; Lemmon, M.M.; Li, C., et al. Siderophore Receptor-Mediated Uptake of Lactivicin Analogues in Gram-Negative Bacteria. *J. Med. Chem.* **2014**, *57*, 3845-3855.
38. Macheboeuf, P.; Fischer, D.S.; Brown, T.; Zervosen, A.; Luxen, A.; Joris, B.; Dessen, A.; Schofield, C.J. Structural and mechanistic basis of penicillin-binding protein inhibition by lactivicins. *Nat. Chem. Biol.* **2007**, *3*, 565-569.
39. Brown, T.; Charlier, P.; Herman, R.; Schofield, C.J.; Sauvage, E. Structural Basis for the Interaction of Lactivicins with Serine β-Lactamases. *J. Med. Chem.* **2010**, *53*, 5890-5894.
40. Wilmouth, R.C.; Westwood, N.J.; Anderson, K.; Brownlee, W.; Claridge, T.D.W.; Clifton, I.J.; Pritchard, G.J.; Aplin, R.T.; Schofield, C.J. Inhibition of Elastase by *N*-Sulfonylaryl β-Lactams: Anatomy of a Stable Acyl−Enzyme Complex. *Biochemistry* **1998**, *37*, 17506-17513.
41. Acred, P.; Brown, D.M.; Knudsen, E.T.; Rolinson, G.N.; Sutherland, R. New Semi-synthetic Penicillin active against *Pseudomonas pyocyanea*. *Nature* **1967**, *215*, 25-30.
42. Konaka, R.; Kuruma, K.; Nishimura, R.; Kimura, Y.; Yoshida, T. High-performance liquid chromatographic analysis of a new β-lactam antibiotic, 6059-s (moxalactam). *J. Chromatogr. B* **1981**, *225*, 169-178.
43. Eftimiadi, C.; De Leo, C.; Schito, G.C. Antibacterial activity *in vitro* of sulbenicillin against mucoid and non-mucoid strains of *Pseudomonas aeruginosa*. *Drugs Exp. Clin. Res.* **1985**, *11*, 241-245.
44. Wright, D.B. Cefsulodin. *Drug Intell. Clin. Pharm.* **1986**, *20*, 845-849.
45. McCoy, A.J.; Grosse-Kunstleve, R.W.; Adams, P.D.; Winn, M.D.; Storoni, L.C.; Read, R.J. Phaser crystallographic software. *J. Appl. Crystallogr.* **2007**, *40*, 658-674.
46. Adams, P.D.; Grosse-Kunstleve, R.W.; Hung, L.W.; Ioerger, T.R.; McCoy, A.J.; Moriarty, N.W.; Read, R.J.; Sacchettini, J.C.; Sauter, N.K.; Terwilliger, T.C. PHENIX: building new software for automated crystallographic structure determination. *Acta Crystallogr. D* **2002**, *58*, 1948-1954.
47. Emsley, P.; Lohkamp, B.; Scott, W.G.; Cowtan, K. Features and development of Coot. *Acta Crystallogr. D* **2010**, *66*, 486-501.

Chapter 6

Towards studying β-Lactamases with Time-Resolved Crystallography

The work described within this chapter was conducted within the context of a large, international, and multidisciplinary collaboration. Large scale protein expression and purification and crystallisation of OXA-48 was done in collaboration with Dr Patrick Rabe (University of Oxford). Fixed-target serial synchrotron (ft-SSX) data collection was done by Dr Robin Owen, Dr Pierre Aller, Dr Agata Butryn with guidance from Dr Allen M. Orville (all Diamond Light Source, DLS). Processing of ft-SSX data was done by Dr Pierre Aller, Dr Agata Butryn, and Dr Nicholas Devenish (all DLS). Drop-on-drop tr-SFX data collection was done by Dr Jan Kern, Dr Philipp Simon, Isabel Bogacz, Dr Hiroki Makita with support from Prof. Junko Yano and Prof. Vittal Yachandra (all Lawrence Berkeley National Laboratory, LBNL) controlling the ADE tape drive set-up and Dr Pierre Aller, Dr Agata Butryn (both DLS), and Gabriel Leen (PolyPico Technologies Ltd) with support from Dr Allen Orville (DLS) controlling the Poly Pico. Data collection at the SPring-8 Angstrom Compact free electron Laser (SACLA) was supported by Dr Shigeki Owada, Dr Kensuke Tono, Dr Rie Tanaka (all SACLA). Data collection at the Linac Coherent Light Source (LCLS) was supported by Dr Alex Batyuk, Dr Franklin Fuller, and Dr Roberto Alonso-Mori (all LCLS). Processing of tr-SFX data was done by Dr Aaron Brewster, Dr Asmit Bhowmick, and Dr Daniel Paley supervised by Dr Nicholas K. Sauter (all LBNL). Sample preparation and handling at LCLS was supported by Dr Medhanjali Dasgupta and Dr Steve Keable (both LBNL).

Contents

6.1. Introduction 173
6.1.1. Serial crystallography 173
6.1.2. Sample requirements, delivery and reaction initiation 174
6.1.3. Time-resolved serial crystallography studies on β-lactamases 176
6.2. First SACLA experiment 176
6.2.1. $AmpC_{EC}$ crystallisation 177
6.2.2. OXA-48 expression and purification 178
6.2.3. OXA-48 crystallisation 178
6.2.4. Data collection at SACLA 181
6.3. LCLS experiment 182
6.3.1. Establishing a second crystal form for $AmpC_{EC}$ 182
6.3.2. Single crystal soaking experiments 185
6.3.3. Fixed-target SSX experiments 191
6.3.4. Data collection at LCLS 196
6.4. Conclusions and Future work 202
6.5. Materials and Methods 203
6.7.1. Materials 203
6.7.2. Enzyme production and purification 203
6.7.1. Crystallisation 204
6.7.2. Data collection and processing 206
6.7.2. Data analysis 207
6.7. References 207

6.1. Introduction

The cryogenic freeze-trap X-ray crystallographic methods used in previous chapters are powerful tools to study enzyme-ligand interactions and have been one of the standard methods in structural biology over last four decades[1-3]. However, cryo-cooling may affect protein structures[4] and conventional freeze-trap methods suffer from poor time-resolution, often preventing characterisation of short lived intermediates and non-equilibrium states which are central to enzymatic reactions[5]. While other methods including stopped-flow rapid quench methods enable studies on such short-lived intermediates in specific detail[6], they require cryo-cooling and do not give broad structural information. Solution based methods such as nuclear magnetic resonance (NMR) spectroscopy[7] and Small Angle X-ray scattering (SAXS)[8] enable global structural studies at room temperature, but are limited by long measurement times, preventing insights into short lived intermediates. To address this gap, time-resolved serial crystallography approaches have been developed and, thanks to advances in radiation sources, sample delivery techniques, and data processing, are becoming more feasible and generally available[9-11]. In this chapter serial crystallography is used to attempt time-resolved structural studies on the interactions of $AmpC_{EC}$ with β-lactamase inhibitors and β-lactam antibiotics at room temperature.

6.1.1. Serial crystallography

Conventionally, macromolecular X-ray diffraction (MX) data is collected from a single (or small number of) large (µm-mm scale) protein crystal(s), mounted on a nylon loop and rotated within the X-ray beam to obtain a full data-set[12]. During this process, a significant amount of energy is deposited into the crystal, either by the total absorption or the inelastic scattering of a proportion of the X-rays. Thus, since the introduction of intense 3rd generation synchrotron sources, such data collection is usually conducted at 100 K (using a nitrogen cryo-stream for cooling), in an effort to reduce (but not fully prevent) radiation damage[13]. While historically large crystals were needed to generate high resolution diffraction data, recent decades have brought both advances in synchrotron X-ray sources and the introduction of X-ray free electron lasers (XFELs). Both generate much brighter, intense, and focused X-ray beams, thereby enabling the use of smaller crystals (nm-low µm[14])[9-11]. Additionally, the significantly shorter pulse duration generated by XFELs (fs range)[15] compared to synchrotrons (ms-ps range)[11] extends the scope of dynamic processes amenable to time-resolved serial crystallography studies.

With increasing intensity of the radiation sources and decrease of the crystal size, cryo-cooling is less sufficient in preventing radiation damage[13]. In the case of XFELs the beam intensity is so high, that the sample explodes on interaction with the X-ray beam[13,16]. Therefore,

instead of collecting a whole rotation set from one crystal, only a single diffraction image is obtained for each crystal[9-11]. Consequently, a very large number (usually >10,000) of crystals is required, which need to be continuously replaced in the X-ray beam. Collection of a full rotation-set is then achieved by sampling data from randomly oriented crystals. Both sample delivery and data processing thus require different approaches compared to conventional single crystal crystallography (see below). Using the single shot per crystals techniques in combination with fs X-ray pulses, radiation damage can be “outrun” as it propagates slower than diffracted X-rays[16], allowing to study even particularly radiation sensitive systems such a metallo proteins[13].

Another benefit of serial approaches lies in the smaller crystal size accessible for X-ray analysis, which reduces diffusion times of ligands into the crystals and thus allows more homogeneous reaction initiation compared to use of macrocrystals[17]. Together with sample delivery systems that allow the rapid renewal of the sample in the X-ray beam, this potentially enables a reduction in mixing times of the crystals with ligands to the sub-second range in which most enzymatic reactions, including β-lactamase catalysed β-lactam hydrolysis, proceed[14].

6.1.2. Sample requirements, delivery and reaction initiation

One of the challenges in the application of serial crystallography is in the need for continuous replacement of fresh crystal samples in the beam. Other than in cryogenic single crystal crystallography where nylon-loop, or in some cases nylon-mesh, mounts have long been the predominant carrier of choice[12], multiple different approaches are currently used in serial crystallography, each displaying different advantages and disadvantages[18,19].

Most commonly liquid jets are employed, which enable efficient mixing of crystal slurries with solutions of ligands to facilitate reaction initiation, but suffer from high sample consumption and strict sample requirements, limited to only very small crystals due to the narrow diameter of the capillaries used[20,21]. Viscous extruders such as liquid cubic phase (LCP) injectors use a similar continuous flow but are more sample efficient due to lower flow rates permitted by the viscous medium[22,23]. On the downside, as the high viscosity of the matrix prevents efficient mixing, this system is usually restricted to static structure determination of membrane proteins and time-resolved studies initiated via irradiation.

Fixed-targets, as used in this chapter to screen microcrystal slurries at Diamond Light Source (DLS), involve applying crystals to a grid, usually made of crystalline silicon or silicon nitride, and removal of excess precipitant solution via an external vacuum (Figure 1)[24,25]. The sample holders are then attached to a goniometer at the beamline end station and moved

through the X-ray beam. In the model used in this chapter the target holders are enclosed with mylar foil to prevent dehydration of the crystals during data collection. More recently, fixed-target techniques have emerged which do not require target enclosure and allow addition of ligand solution to the individual crystal-wells, thereby facilitating time-resolved mixing studies[19].

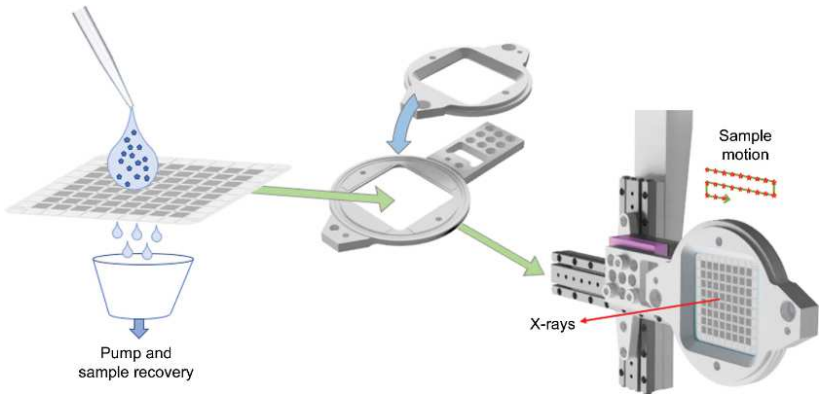


Figure 1: Experimental set-up for serial fixed-target X-ray diffraction data collection. Left: microcrystals are loaded on fixed target grids. Middle: Fixed target grids are mounted on sample holders. Right: Sample holders are mounted at the beamline end station and rastered through the beam during data collection. Image modified with permission from Ebrahim et al.[25]

The acoustic droplet ejection (ADE) sample delivery system[26] used for the time-resolved serial femtosecond crystallography (tr-SFX) experiments described in this chapter allows for effective sample use and a wide range of reaction initiation tools.

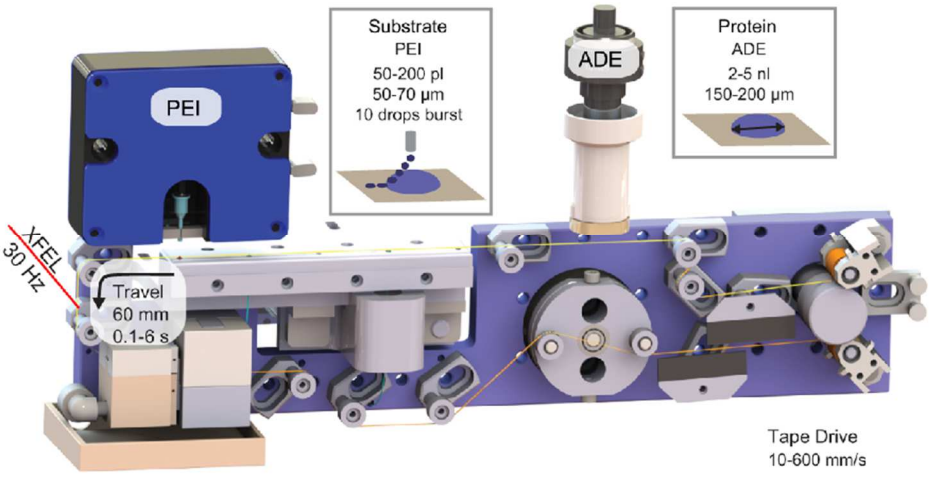


Figure 2: Experimental set up for drop-on-drop sample mix and delivery. nl sized drops of microcrystal slurry are deposited on a conveyer belt using acoustic droplet ejection (ADE), transferred first to a piezoelectric injector (PEI) which is depositing a burst of pl sized drops of ligand solution, then to the X-ray interaction zone. Image modified with permission from Buryn et al.[27]

In this set-up nanolitre volume sized microcrystal slurry droplets are dispensed on a Kapton belt which delivers the droplets to the X-ray interaction zone (Figure 2). On the way, reactions can be initiated via irradiation[28], gas diffusion[29], or, as recently described[27] and utilised in this work, via a “drop-on-drop” approach, adding ligand (or other) solutions using a second

droplet ejector (e.g. a piezoelectric injector, PEI in Figure 2). Reaction times can be easily varied by adjusting the speed of the conveyer belt (10–600 mm s^{-1}) and the position of the second droplet ejector, allowing reaction times of 0.1 - 6 s[27].

6.1.3. Time-resolved serial crystallography studies on β-lactamases

Structural information on substrate, intermediate, product, and inhibitor binding to β-lactamases may enable the development of β-lactamase resistant β-lactam antibiotics and β-lactamase inhibitors. However, most studies have so far been limited to relatively stable complexes such as those discussed in Chapters 2-5. Approximation of pre-acylation β-lactam binding to SBLs have been reported based on studies with inactivated β-lactamases either by mutation[30] or crosslinking of active site residues[31]. However, as such modifications perturb the β-lactamase active site, care must be taken when analysing such data as the binding modes may differ from those adopted with active β-lactamases (as demonstrated for example in Chapter 5).

While some initial serial crystallography studies with β-lactamases have been reported elsewhere[32-34] during the course of this work, involving studies on inhibitor and substrate interactions both on pre-equilibrated samples and in a time-resolved manner, this work has exclusively focused on the class A SBLs BlaC and CTX-M-14 and has predominantly used liquid-jet set-ups.

The work presented in this chapter aimed first to develop micro-crystallisation conditions for $AmpC_{EC}$ that are suitable for time-resolved serial crystallography studies. The crystal-slurries were then to be tested for structural studies on $AmpC_{EC}$ at room temperature using different sample-delivery techniques, with special emphasis on the drop-on-drop methodology[27], and both synchrotron and XFEL radiation. Finally, the work aimed to use the established methodology for time-resolved serial crystallographic studies on $AmpC_{EC}$ binding of and reaction with β-lactam antibiotics and β-lactamase inhibitors at room temperature in timeframes ranging from minutes to milliseconds.

6.2. First SACLA experiment

XFEL beamtime for first experiments to study β-lactamases via time-resolved serial crystallography studies using drop-on-drop techniques was awarded at the SPring-8 Angstrom Compact free electron Laser (SACLA) in Japan in July 2019. For these experiments it was attempted to modify the previously used $AmpC_{EC}$ conditions (see Chapter 2) for the production of microcrystal slurries. As a second option, the class D SBL OXA-48, which can be produced

and purified in gram-scale, was trialled for crystallisation conditions more suitable towards time-resolved experiments, e.g. in terms of viscosity of the sample.

6.2.1. AmpC$_{EC}$ crystallisation

For a first attempt to produce microcrystal slurries of AmpC$_{EC}$ modification of the crystallisation conditions used to produce macro-crystals as described in Chapter 2 was explored. While microcrystals could easily be obtained in the sitting-drop vapour diffusion set-up by increasing the PEG 6,000 content in the precipitate from typically 22-27% (*w*/*v*) to 35% (*w*/*v*), the volume of the drops was too small to be feasible to produce concentrated microcrystal slurry in a millilitre scale, as required for serial crystallography experiments. Further, harvesting the nanolitre sized drops proved inefficient, affording only small quantities of very dilute slurry, as most of the crystals were attached to the bottom of the crystallisation-wells. Therefore, the sitting-drop vapour diffusion setup, was scaled up. Using MRC-maxi-48-well-plates (Swissci), large macro-crystals (> 300 µm) could be obtained in 8 µl sized drops, using the original precipitant solution (22-27% (*w*/*v*) PEG 6,000, 10 mM $ZnCl_2$, 0.1 M MES pH 6.0). These crystals could then be used to produce concentrated micro-seed stocks, which were used to initiate nucleation in batch-crystallisation setups with a total volume of 100 µl. Varying the concentration of these seeds, as well as the ratio of precipitant solution and protein, batch crystallisation was established giving slurries of very uniform microcrystals of AmpC$_{EC}$ (see Materials and Methods for details, Figure 3). However, the crystals were very small (1-2 µm) and it was not possible to achieve larger crystals in this set-up.

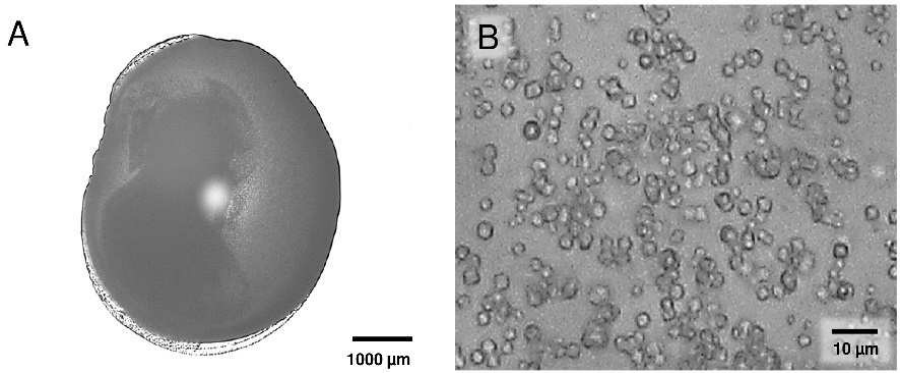


Figure 3: AmpC$_{EC}$ microcrystal slurry from batch set-up using the PEG condition. (A) 4 µl sized drop of microcrystal slurry. (B) Image at higher magnification showing individual microcrystals.

6.2.2. OXA-48 expression and purification

Expression and purification of OXA-48 were done in collaboration with Dr Patrick Rabe (University of Oxford).

Recombinant OXA-48 was produced with a TEV cleavable *N*-terminal His-tag using a pNIC28 vector and purified via nickel-affinity chromatography according to reported procedures[35]. Both constructs with and without the *N*-terminal His-tag were further purified via size exclusion chromatography (Figure 4). In total ~1.5 g of OXA-48 was produced and purified for serial crystallography experiments.

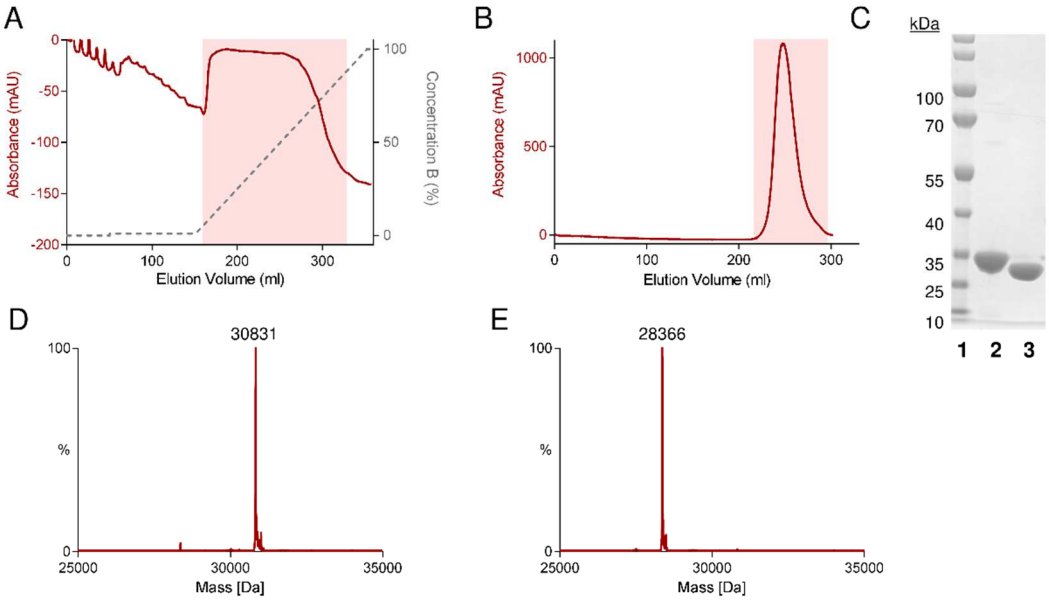


Figure 4: Purification of recombinant OXA-48. (A) UV-Trace of nickle affinity chromatography used to purify OXA-48 from cell lysate. Column: 2 × HisTrap HP, 2 × 5 ml; Buffer A: 50 mM MES, pH 7.5, 20 mM imidazole; Buffer B: 50 mM MES, pH 7.5, 500 mM imidazole. Highlighted elution volumes contained purified OXA-10. (B) UV-Trace of size exclusion chromatography used to purify OXA-48 after TEV cleavage and manual reverse Histrap chromatography. Column: Superdex 75, 300 mL Buffer: 50 mM MES, pH 6.0, 50 mM $NaHCO_3$. (C) SDS-PAGE analyses of purified OXA-48. Lane 1: PageRuler™. Lane 2: OXA-48 after TEV catalysed His-tag cleavage. Lane 3: OXA-48-HexaHis. (D) Solid-phase extraction-mass spectrometry (SPE-MS) analysis of purified OXA-48-HexaHis. (E) SPE-MS analysis of purified OXA-48-HexaHis.

6.2.3. OXA-48 crystallisation

Crystallisation of OXA-48 was optimised in collaboration with Dr Patrick Rabe (University of Oxford).

Constructs with and without the *N*-terminal His-tag were screened for crystallisation conditions. In both cases the protein was concentrated to ~ 10 mg/mL in 50 mM MES, pH 6.0, 50 mM $NaHCO_3$. Broad screens of crystallisation conditions gave a large number of hits showing crystals. However, when these crystals were screened for X-ray diffraction under cryogenic

conditions at the MX beamlines at DLS, the majority of crystals showed either no, or weak diffraction.

One high-resolution crystal structure with two molecules in the asymmetric unit (1.23 Å resolution, Table 1) was obtained from crystals of OXA-48 without the *N*-terminal His-tag, grown from condition D3 of the Morpheus Suite (Molecular Dimension, see Materials and Methods). Unfortunately, on examination of the electron density maps, additional electron density was observed indicating binding of MES buffer at the OXA-48 active site in both chains of the crystallographic dimer (Figure 7).

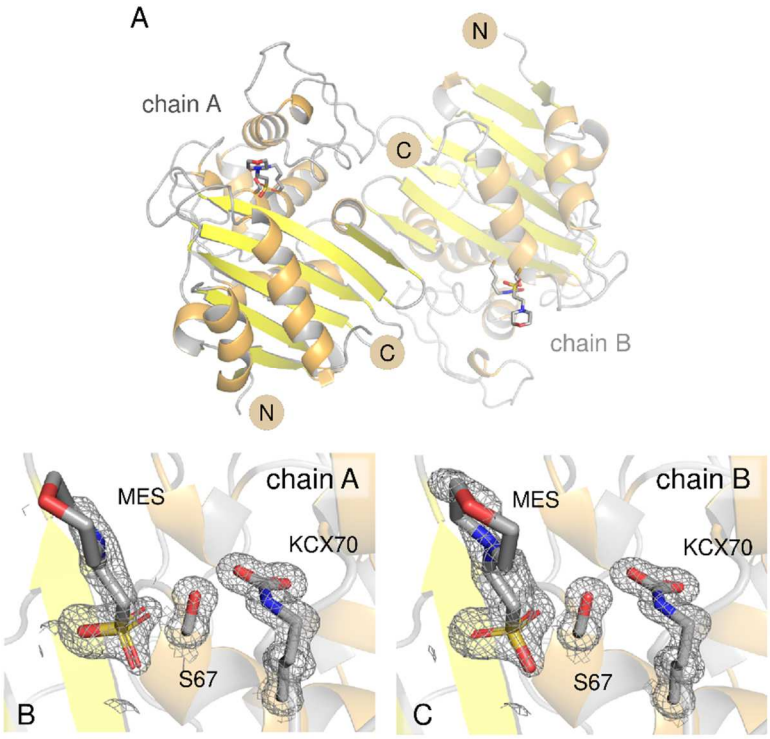


Figure 5: Views from crystal structure of OXA-48 in MES condition. (A) Overview of OXA-48 structure from MES condition. (B) Active sit view of chain A. (C) Active site view of chain B. Binding of MES buffer is observed in close proximity to the nucleophilic Ser67 and the carbamylated Lys70 (KCX70) in chain A and B. $2mF_o$-DF_c maps contoured at 1.0 σ and carved around active site residues and MES.

As an occupied active site, especially by a compound containing an electron rich sulfate motif, was considered non-optimal for time-resolved serial crystallography experiments, a second broad screen was carried out with OXA-48 in Tris buffer, to prevent binding of MES buffer at the active site. Significantly fewer crystals were obtained from this screen, suggesting a stabilising effect of the MES molecule bound at the active site of OXA-48, and many of the afforded hits were from crystallisation conditions using MES or similar buffers as precipitant, or showed a high content of viscose precipitants such as PEG.

A single condition was identified, giving macro crystals (~100 µm, Figure 6A) without the need of MES-type buffers or PEG (2.00 Å resolution, Table 1), i.e. condition B7 of the LMB

Crystallisation Screen (38% (*v*/*v*) 1,4-dioxane, Molecular Dimensions). Microcrystals of OXA-48 were grown using the dioxane-precipitant in batch set-up (100 µl, Figure 6B). By contrast with AmpC$_{EC}$, micro-seeding was not necessary to induce nucleation in batch set-up and did not improve crystal quality or density.

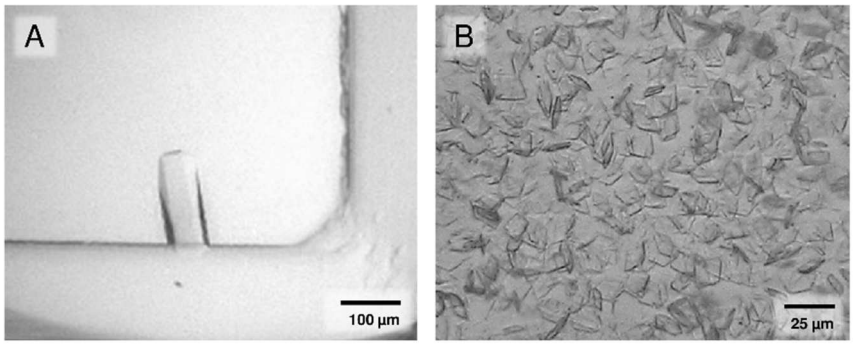


Figure 6: OXA-48 macro- and microcrystals from dioxane condition. Crystallisation conditions were identified from a LMB Crystallisation screen (condition B7, Molecular Dimensions), set up at 4 °C.

While in this structure 1,4-dioxane was observed bound at the OXA-48 active site in both chains of the crystallographic dimer (Figure 7), this condition appeared overall more suitable for time-resolved crystallography experiments, due to the lower electron density of dioxane compered to MES and a significantly lower viscosity of the precipitant.

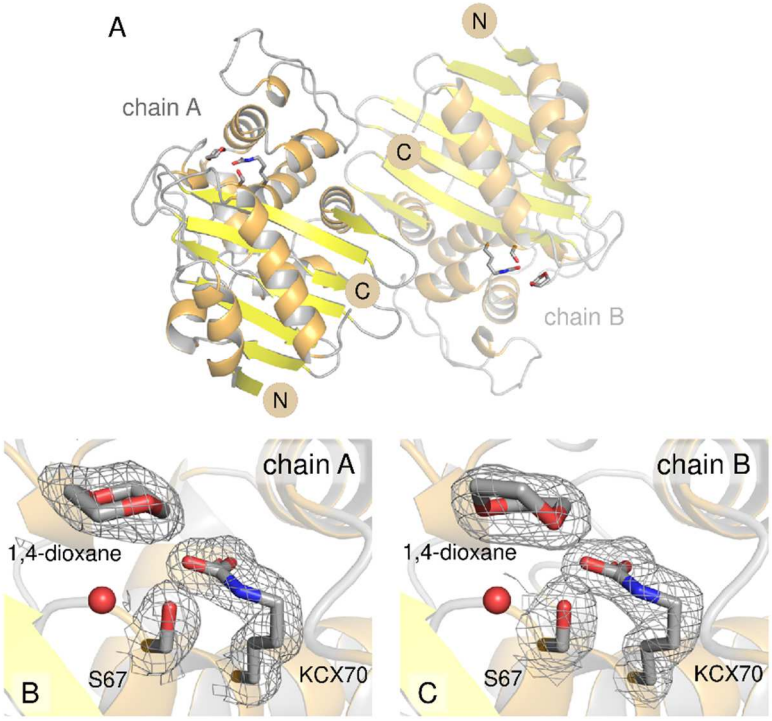


Figure 7: Views from crystal structure of OXA-48 in dioxane condition. (A) Overview of OXA-48 structure from dioxane condition. (B) Active site view of chain A. (C) Active site view of chain B. Binding of 1,4 dioxane from precipitant is observed in close proximity to the Ser67 and carbamylated Lys70 in both chains. 2mF_o-DF_c maps contoured at 1.0 σ and carved around active site residues and 1,4 dioxane.

Table 1: Data collection statistics for OXA-48 structures from single crystals.

Datasets	**OXA-48** (MES condition)	**OXA-48** (Dioxane condition)
Data Collection	mx18069-81	mx18069-84
Beamline (Wavelength, Å)	DLS I03 (0.9762)	DLS I04-1 (0.91587)
Detector	Eiger2 XE 16M	Pilatus 6M-F (25 Hz)
Data Processing	Xia2 autoproc+STARANISO	Xia2 dials
Space group	$P\,2_1\,2_1\,2_1$	$P\,6_5\,2\,2$
Cell dimensions		
a,b,c (Å)	70.4, 79.0, 126.2	121.1, 121.1, 161.0
α, β, γ (°)	90.0, 90,0, 90.0	90.0, 90.0, 120.0
No. of molecules/ASU	2	2
Total reflections	2182353 (83210)*	1819372 (77930)*
Unique reflections	170406 (8520)*	47683 (2240)*
Resolution (Å)	66.95-1.23 (1.31-1.23)*	161.04-2.00 (2.03-2.00)*
R_{meas}(I)	0.057 (1.197)*	0.460 (3.540)*
I/σI	19.9 (1.6)*	6.3 (1.2)*
$CC_{1/2}$	1.00 (0.70)*	1.00 (0.59)*
Completeness (%)	94.3 (59.1)*	99.9 (99.5)*
Multiplicity	12.8 (9.8)*	38.2 (34.8)*
Wilson B value (Å^2)	13.67	29.66

*Highest resolution shell in parentheses.

6.2.4. Data collection at SACLA

Experiments at SACLA were hampered by several technical problems. Shipments of liquid-nitrogen dewars containing proteins samples were thawed on prolonged delay at the Japanese customs, leading to a prolonged exposure of the proteins to room temperature prior to crystallisation. Further, ventilation within the experimental site was insufficient to compensate the high external temperatures (~30-38 °C) in combination with heat generated from the XFEL beam and equipment, leading to prolonged exposure of the crystal slurries to temperatures ranging between 34-36 °C during data-collection.

Under these non-ideal conditions $AmpC_{EC}$ crystal slurries showed diffraction (max. ~1.5 Å resolution), but the hit-rate was very low, and only 1505 indexed images were collected over 45 min of data collection, which was not enough to obtain a full data set. OXA-48 slurries did not show any diffraction and data collection was stopped after 25 min. Temperature induced degradation of the crystals under the exceptional conditions at SACLA was later ruled out in fixed-target serial crystallography experiments at DLS, which also showed no diffraction of the OXA-48 microcrystals. Thus, no full data sets of $AmpC_{EC}$ and OXA-48 were obtained at this first experiment at SACLA.

6.3. LCLS experiment

Based on more promising results obtained with the drop-on-drop methodology with other samples during the SACLA beamtime[27], subsequent beamtime was awarded at the Linac Coherent Light Source (LCLS, USA). However, given the disappointing performance of the OXA-48 and AmpC$_{EC}$ microcrystal slurries at SACLA they were not considered for further experiments. Instead, an alternative micro-crystallisation protocol was developed for AmpC$_{EC}$ and used for all following experiments.

6.3.1. Establishing a second crystal form for AmpC$_{EC}$

Most structures of AmpC$_{EC}$ which are deposited in the PDB are obtained using the original crystallisation condition used to first solve the AmpC$_{EC}$ structure[36-38]. The precipitant solution for this condition constitutes solely of a highly concentrated phosphate buffer (1.6-1.8 M, pH 8.7-8.8)[36-38], which is also more favourable for fast ligand diffusion than the highly viscous PEG-based condition discussed above.

In agreement with the original reports, no crystals could be obtained using hanging-drop vapour diffusion techniques when siliconized glass-cover slips or siliconized plastic cover-slips were used[36]. Changing to non-siliconized glass-cover slips gave clusters of crystals as shown in Figure 8A. These clusters were used to prepare microseed-stocks to grow crystals using siliconized glass-cover slips which showed a more defined morphology (Figure 8B), but showed space-group ambiguity and twinning on analysis of diffraction data. When micro-seeds prepared from these crystals were used in combination with siliconized glass-cover slips, clearly defined crystals were obtained (Figure 8C) which diffracted to high resolution in the reported *C* 1 2 1 space group (Table 2).

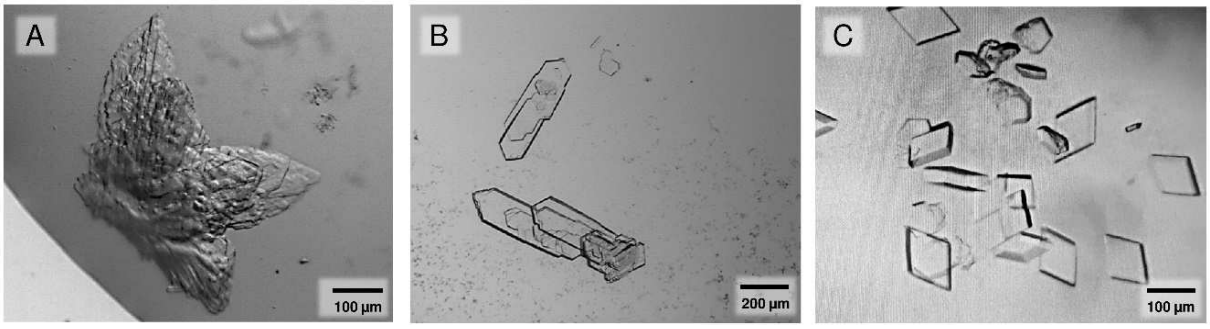


Figure 8: AmpC$_{EC}$ macro-crystal optimisation in phosphate condition. All crystals were grown via hanging-drop vapour diffusion technique with 1.6 M potassium phosphate pH 8.8 as the precipitant and an initial AmpC$_{EC}$ concentration of 6 mg ml^{-1}. Shown are images of (A) crystals obtained without seeding using non-siliconized glass coverslips, (B) crystals using siliconized glass cover-slips obtained after first round of seeding, and (C) crystals obtained using siliconized glass coverslips and optimised micro-seeds.

Trials to lower the pH of the precipitant solution to more biologically relevant conditions gave crystals in conditions with a pH as low as 7.8. However, on examination of data obtained from crystals grown at lower pH again space-group ambiguity and twinning was observed. Therefore, all following experiments were performed using crystals grown at pH 8.8. For future work, it may, however, be feasible to transfer crystals grown at pH 8.8 into precipitant solutions with lower pH to study the impact of the pH on AmpC$_{EC}$ reactivity.

Data from macro crystals were collected under cryogenic-conditions at DLS and a structure of AmpC$_{EC}$ in the phosphate condition (1.49 Å resolution, Table 2) was solved via molecular replacement using a reported structure of AmpC$_{EC}$ from similar crystallisation conditions (PDB: 2BLS[36]) as the starting model. Other than with AmpC$_{EC}$ crystal from the PEG condition, where the ASU contained only one molecule, in the phosphate condition AmpC$_{EC}$ crystallised with two molecules in the ASU (Figure 9A).

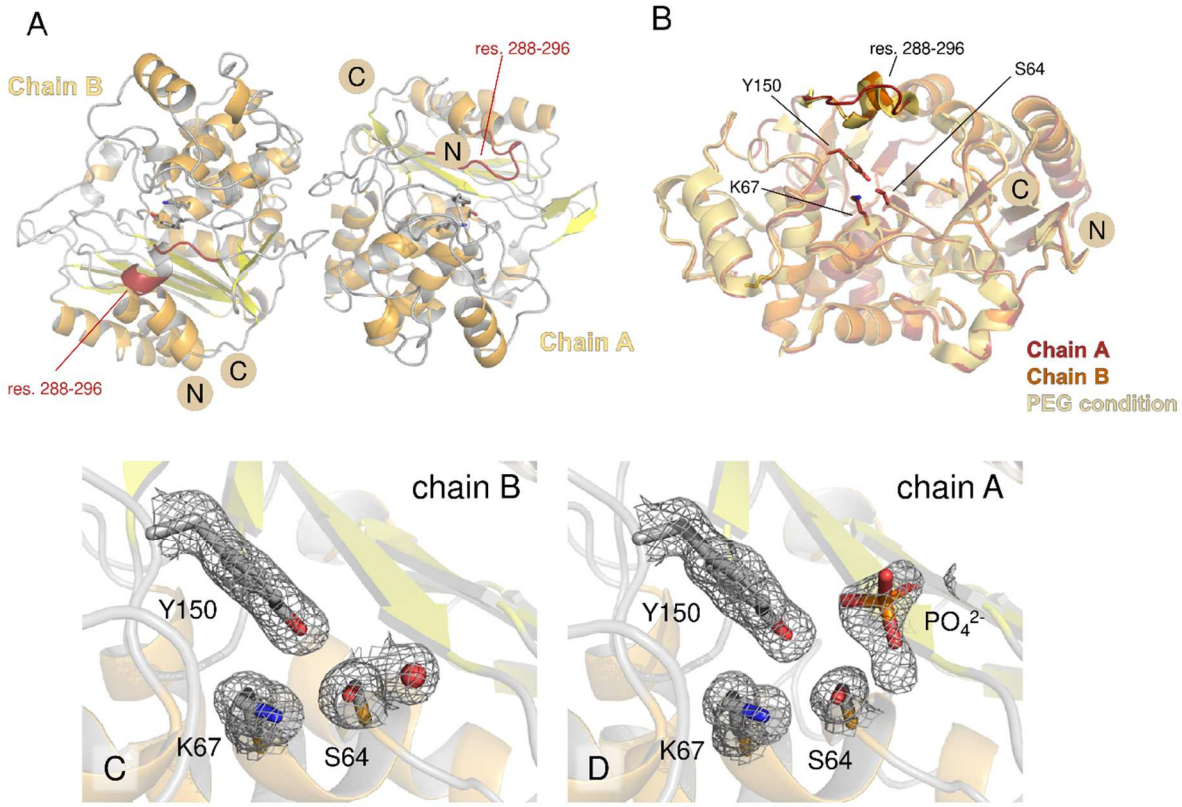


Figure 9: Views from crystal structure of AmpC$_{EC}$ in phosphate condition. (A) Overview of AmpC$_{EC}$ structure from phosphate condition. (B) Overlay of chain A and B from phosphate condition with chain A from PEG condition shows rearrangement of res. 288-296 in chain A, compared to chain A and PEG condition (PDB: 6T3D, Chapter 2). (C) Active site view of chain B. (D) Active site view of chain A. Binding of phosphate from precipitant solution is observed in close proximity to the nucleophilic Ser64 in chain A, but not in chain B. 2mF$_o$-DF$_c$ maps are contoured at 1.0 σ and carved around active site residues and the bound phosphate in chain A.

While the AmpC$_{EC}$ fold in chain B closely resembled that observed in AmpC$_{EC}$ crystals obtained from the PEG condition (PDB: 6T3D, Chapter 2, backbone RMSD: 0.33 Å) rearrangement of

residues 288-296 was observed in chain A (Figure 9B). While the loop is predominantly observed in this new conformation, additional electron density suggests partial occupancy for the standard conformation (< 30%), which is also reflected in elevated B-factors of the loop compared to the average of the structure (46.53 Å^2 compared to 25.89 Å^2 overall). While such loop rearrangements can be induced by crystal packing, the alternative loop conformation was not observed in previous structures of AmpC$_{EC}$ in the phosphate condition (e.g. PDB: 2BLS[36]). It's origin and biological relevance is thus unclear.

At the AmpC$_{EC}$ active site in chain A analysis of the electron density maps indicates a phosphate ion displacing the conserved water bound in the oxyanion hole, although likely in low occupancy (50 %, Figure 9D). By contrast, the active site in chain B appears un-occupied (Figure 9C).

Table 2: Data collection and Refinement statistics for AmpC$_{EC}$ structures from single crystals.

Datasets	**AmpC$_{EC}$ in phosphate condition** at 100 K		
Data Collection	mx23459-133	**Refinement**	PHENIX
Beamline (Wavelength, Å)	DLS I03 (0.97622)	R_{work}/R_{free}	0.1655/0.1857
Detector	Eiger2 XE 16M	No. atoms	6630
Data Processing	Xia2 dials-aimless	- Enzyme	5643
Space group	*C* 1 2 1	- Water	*977*
Cell dimensions		Average B-factors	27.58
- *a,b,c* (Å)	119.0 76.9, 97.8	- Enzyme	25.89
- α, β, γ (°)	90.0, 115.5, 90.0	- Water	37.29
No. of molecules/ASU	2	R.m.s deviations	
Total reflections	821417 (39678)*	- Bond lengths (Å)	0.005
Unique reflections	129684 (6216)*	- Bond angles (°)	0.763
Resolution (Å)	58.40-1.49 (1.51-1.49)*		
R_{meas}(I)	0.068 (1.070)*		
I/σI	12.2 (1.0)*		
$CC_{1/2}$	1.00 (0.79)*		
Completeness (%)	99.7 (96.5)*		
Multiplicity	6.3 (6.4)*		
Wilson B value (Å^2)	19.73		

*Highest resolution shell in parentheses.

After successful validation of the phosphate crystallisation condition for the production of macro crystals of AmpC$_{EC}$, methods were optimised to obtain microcrystal slurries in batch methods using micro-seeding (see Materials and Methods). AmpC$_{EC}$ crystallised reliably in 100 µl – 5 ml batches in a single tube within 2-4 h at room temperature, giving concentrated microcrystal slurries with crystals sized ~ 5-10 µm (Figure 10). The slurry was not further concentrated and used as crystallised for all further experiments.

Interestingly, while most other microcrystal slurries discussed in this chapter tended to show settling of micro-crystals over time (as seen e.g. in Figure 10C, left tube), most (but not all) slurries of $AmpC_{EC}$ microcrystals in the phosphate condition tended to float above the precipitate solution after prolonged time without agitation (Figure 10C, right tube).

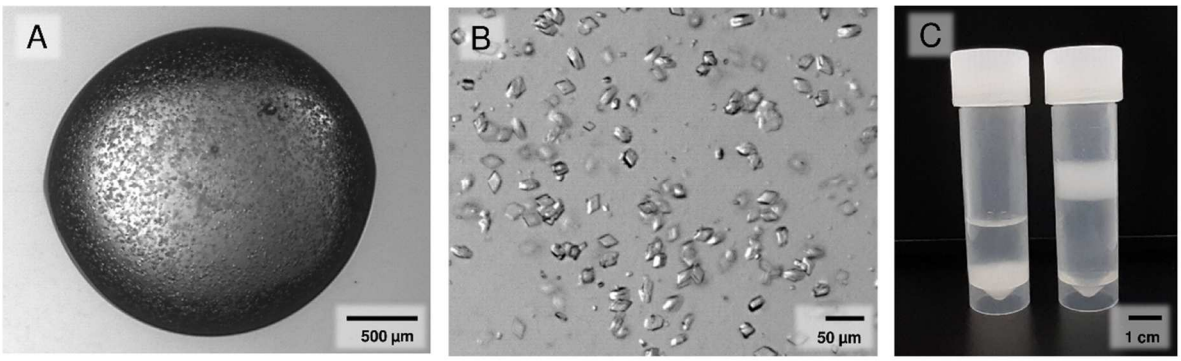


Figure 10: $AmpC_{EC}$ microcrystal optimisation in phosphate condition. (A) Drop (4 µl) of concentrated microcrystal slurry. (B) Magnified view of drop from microcrystal slurry showing microcrystal morphology. (C) Two batches of $AmpC_{EC}$ microcrystal slurry after 48 h without agitation showing either settling (left) or, as more commonly observed with this crystallisation condition, floating (right) of the microcrystals below or above the precipitant solution.

6.3.2. Single crystal soaking experiments

To test active site accessibility of $AmpC_{EC}$ crystallised in the phosphate conditions, three inhibitors were soaked into macro crystals: diazabicyclooctane avibactam (see also Chapter 3), bicyclic boronate taniborbactam (see also Chapter 4), and carbapenem ertapenem (see also Chapter 5). Multiple structures of $AmpC_{EC}$ crystals soaked with each of the inhibitors were obtained after different incubation times (1-30 min), followed by cryo-cooling. With all inhibitors modification of the nucleophilic Ser could be shown within < 5 min of incubation of crystals with the inhibitors. Shown in the following are representative structures of each $AmpC_{EC}$-inhibitor complex obtained, chosen based on resolution.

In a structure obtained from soaking with avibactam for 15 min (1.49 Å resolution, Table 3 and Figure 11) density extending from Ser64 indicated complete modification with the carbamoyl-enzyme complex resulting from covalent reaction of Ser64 with avibactam (Figure 11B and Chapter 3). The overall $AmpC_{EC}$ fold appeared unaffected by this modification, including residues 288-296 in chain A, which adopted the same unusual conformation as observed for unmodified $AmpC_{EC}$ in the phosphate condition (backbone RMSD 0.16 Å, compared to unmodified $AmpC_{EC}$ in phosphate condition, Figure 11A).

Notably, the avibactam derived carbamoyl-enzyme complex was observed solely in the conformation primed for de-carbamoylation (conformation A in Chapter 3), with the *N*-sulfate

nitrogen positioned in close proximity to the Tyr150 phenol (Figure 11C and D). This is in agreement with the conformation observed in the PEG condition (Figure 11E and Chapter 3).

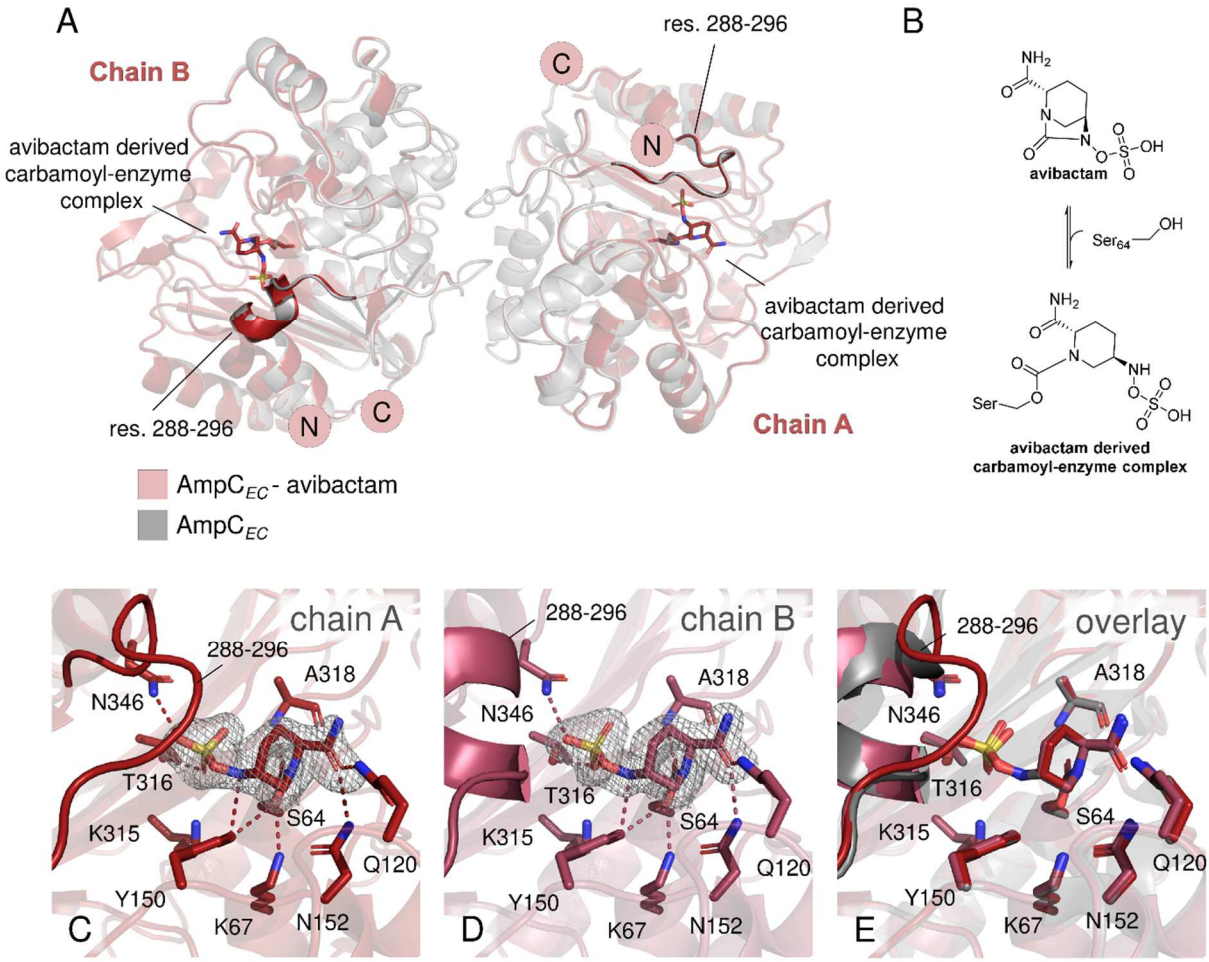


Figure 11: Crystal structure of AmpC$_{EC}$ obtained from singled crystal soaked with avibactam. AmpC$_{EC}$ was crystallised in the phosphate condition and soaked with 20 mM avibactam for 15 min. (A) Overlay with unmodified AmpC$_{EC}$ in phosphate condition. (B) Reaction of avibactam with SBLs. (C) Avibactam derived carbamoyl-enzyme complex observed covalently bonded to Ser64 in chain A. (D) Avibactam derived carbamoyl-enzyme complex observed covalently bonded to Ser64 in chain B. (E) Overlay of avibactam derived carbamoyl-enzyme complex observed covalently bonded in chain A (red), chain B (pink), and in a structure of AmpC$_{EC}$ in the PEG condition (PDB: 6TBW, grey, see Chapter 3). Polder OMIT maps[39] are contoured at 3.0 σ and carved around the avibactam derived carbamoyl-enzyme complex.

Structures from AmpC$_{EC}$ crystals soaked with the bicyclic boronate taniborbactam (shown in Figure 12 is a structure obtained after 21 min of soaking, 1.55 Å resolution, Table 3) equally showed electron density indicating covalent modification of the nucleophilic Ser64 with the bicyclic form of taniborbactam in its sp^3 state (Figure 12B and Chapter 4). Interestingly, while the overall AmpC$_{EC}$ fold was not alternated in chain B (overall backbone RMDS 0.21 Å, compared to unmodified AmpC$_{EC}$ in phosphate condition), residues 277-296 adopted the same

conformation in chain A as observed in chain B, and in the structures of $AmpC_{EC}$ obtained from crystals produced using the PEG condition (Figure 12A and Chapter 4).

The binding mode of the bicyclic taniborbactam both in chain A and B (Figure 12AD and E) is similar to that observed in the PEG condition (Figure 12F and Chapter 4); by contrast with the $AmpC_{EC}$-taniborbactam complex structure from crystals obtained from the PEG condition, electron density for the full C3 amido sidechain is evident in chain A (although not in chain B), and the benzyl-carboxylic acid both in chain A and in chain B is rotated 90° compared to the previously obtained structure from a crystal in the PEG condition (Figure 12F), which may result from different protonation states due to the increased pH (pH 8.8, compared to 6.0 in the PEG condition).

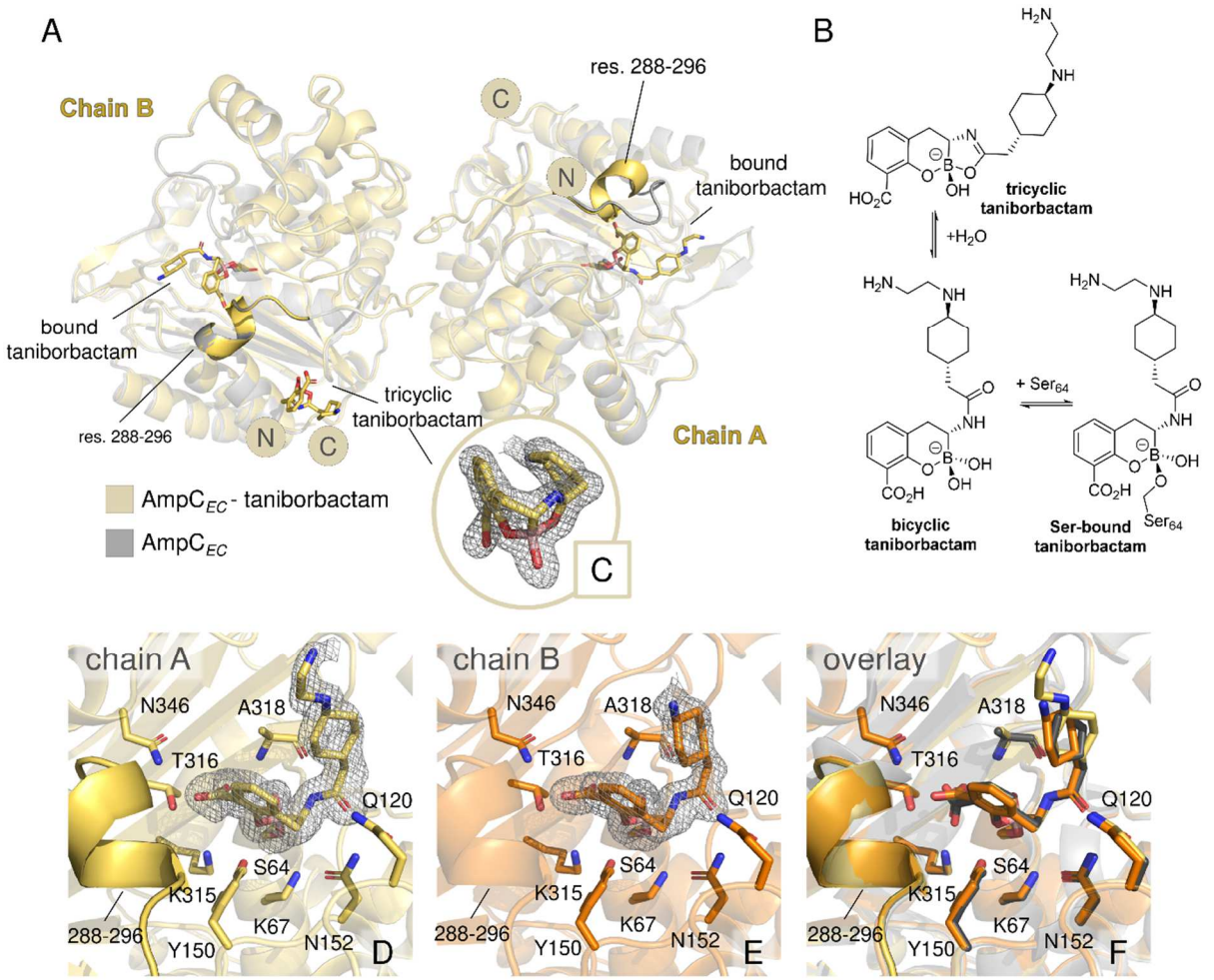


Figure 12: Crystal structure of $AmpC_{EC}$ obtained from singled crystal soaked with taniborbactam for 21 min. $AmpC_{EC}$ was crystallised in the phosphate condition and soaked with 20 mM taniborbactam for 21 min. (A) Overlay with unmodified $AmpC_{EC}$. (B) Reactions of taniborbactam in aquous solution and with SBLs. (C) Tricyclic taniborbactam observed at the $AmpC_{EC}$ surface. (D) Bicyclic taniborbactam observed covalently bonded to Ser64 in chain A. (E) Bicyclic taniborbactam observed covalently bonded to Ser64 in chain B. (F) Overlay of bicyclic taniborbactam observed covalently bonded in chain A (yellow), chain B (orange), and in a structure of $AmpC_{EC}$ in the PEG condition (grey, see Chapter 4). Polder OMIT maps[39] are contoured at 3.0 σ and carved around taniborbactam.

Notably, a second taniborbactam molecule was observed binding at the AmpC$_{EC}$ surface. As with the AmpC$_{EC}$ structure in the PEG condition (Chapter 4), the unbound taniborbactam appears in a tricyclic form (Figure 12B and C). This is notable, as it is the first observation of this tricyclic form of taniborbactam under basic conditions (pH 8.8, with previous crystallographic observations of tricyclic taniborbactam exclusively at pH 5.8-6.0, Chapter 4 and reference [40]). As the taniborbactam used for the studies described in this chapter is from a different source as the one used in Chapter 4, it also suggests reproducibility between different batches of the inhibitor. With enzymatic catalysis being unlikely to contribute towards generation of tricyclic taniborbactam (as discussed in Chapter 4), this suggests that tricyclisation of taniborbactam may occur in aqueous solution in a broad pH rage (5.8-8.8), which may support its relevance for β-lactamase inhibition under biological conditions.

A structure from an AmpC$_{EC}$ crystal soaked with ertapenem for 15 min (1.25 Å resolution, Table 3 and Figure 13) showed electron density extending from Ser64 indicating the ertapenem derived acyl-enzyme complex (AEC) in both AmpC$_{EC}$ chains in the ASU. While the overall AmpC$_{EC}$ fold appeared unaffected in chain B (main chain RMSD 0.28 Å compared to unmodified AmpC$_{EC}$ in phosphate condition), binding of ertapenem appeared to induce a partial re-arrangement of residues 288-296, with the normal conformation (i.e. as observed also in chain B and structures from crystals of the PEG condition) observed in ~ 35% occupancy, compared to < 30% in the structure of unmodified AmpC$_{EC}$. It should, however, be noted, that these are rough estimates which may also be (partially) bias by the higher resolution of the structure of AmpC$_{EC}$ in complex with ertapenem compared to unmodified AmpC$_{EC}$ (1.25 Å compared to 1.49 Å).

Next to the covalently bound ertapenem at the AmpC$_{EC}$ active sites, evidence for binding of three more ertapenem (derived) molecules were observed (Figure 13A), one within the AmpC$_{EC}$ active site in close proximity to the AEC in chain A (Figure 13C) and two at the AmpC$_{EC}$ surface (Figure 13F). While electron density for the whole, intact ertapenem was observed at the AmpC$_{EC}$ surface, for the additional molecule observed in the active site of chain A electron density was only observed for the C2-sidechain. Thus, it cannot be ruled out that this molecule may be hydrolysed.

Interestingly, all of the non-covalently bound ertapenem (derived) molecules showed additional electron density extending from the C2 side-chain pyrrolidine nitrogen, indicating carbamylation of the nitrogen (indicated with arrows in Figure 13F). This may be of interest from an inhibition perspective, as no such carbamylation was observed with the ertapenem derived AEC and carbamylation may thus prevent ertapenem binding to AmpC$_{EC}$. Further studies will be needed to examine the relevance of carbapenem sidechain carbamylation in solution and at physiological pH. This may be especially relevant to studies of OXA-type

carbapenemases, as these β-lactamases require carbamylation of an active site Lys residue to be catalytically active (see Chapter 1 and reference [41]), and are thus usually assayed in the presence of excess carbonate, which may also influence side-chain carbamylation of carbapenems as shown here.

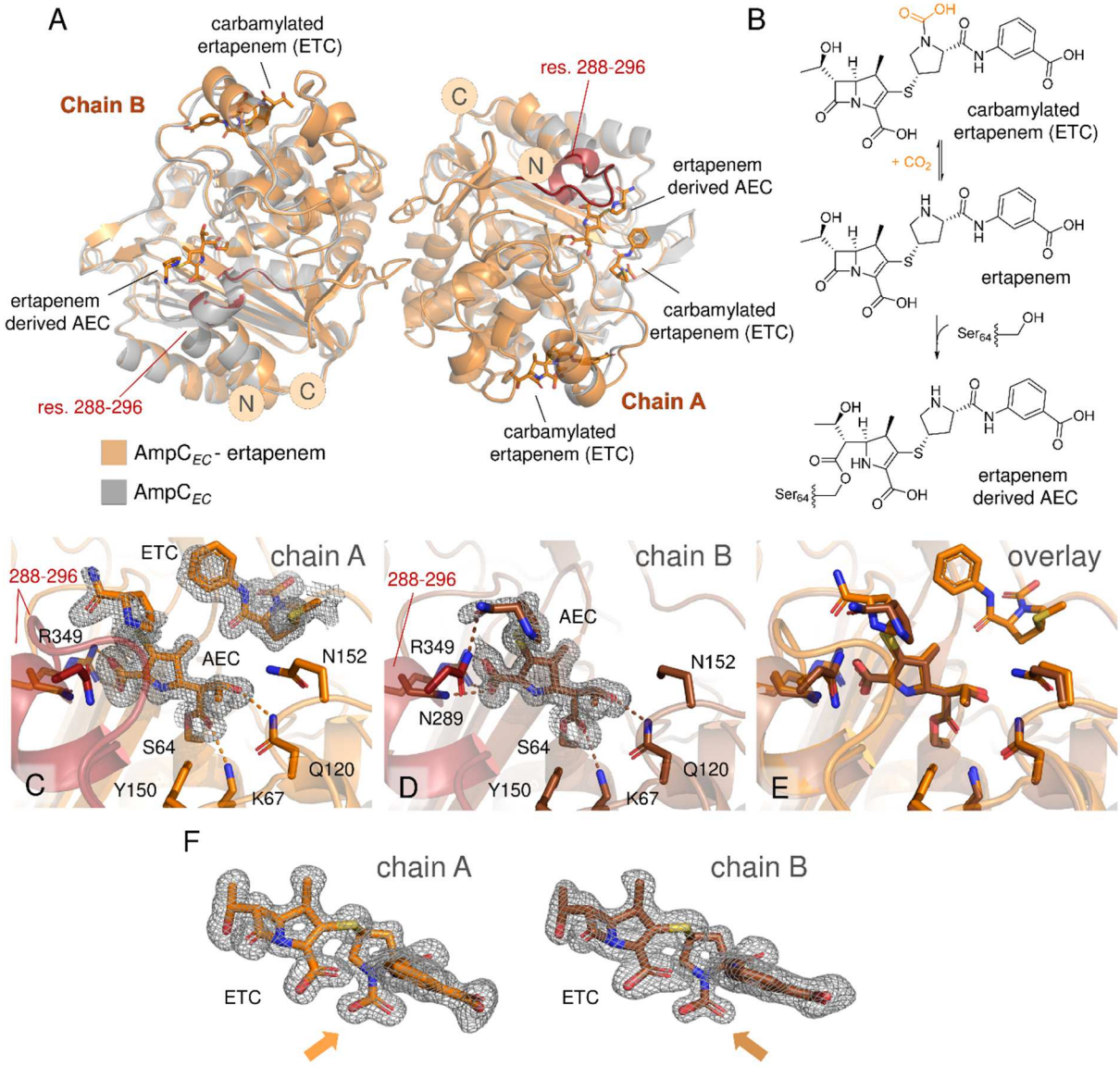


Figure 13: Crystal structure of AmpC$_{EC}$ obtained from singled crystal soaked with ertapenem. AmpC$_{EC}$ was crystallised in the phosphate condition and soaked with 20 mM ertapenem for 15 min. (A) Overlay with unmodified AmpC$_{EC}$. (B) Reactions of ertapenem in aqueous solution and with SBLs. (C) Active site view with ertapenem-derived acyl-enzyme complex (AEC) observed covalently bonded to Ser64 in chain A. (D) Active site view with ertapenem derived AEC observed covalently bonded to Ser64 in chain B. (E) Overlay of active site views from chain A and B. (F) Electron density maps of carbamylated ertapenem (ETC) observed at the AmpC$_{EC}$ surface in chain A (left) and chain B (right). Arrows indicate C2 sidechain carbamylation. Polder OMIT maps[39] are contoured at 3.0 σ and carved around taniborbactam.

Overall, the soaking experiments show that in crystals obtained from the phosphate condition the AmpC$_{EC}$ active site is well accessible for ligand binding in both chains of the crystallographic dimer, which is essential for tr-SFX studies initiated via ligand addition.

Table 3: Data collection and Refinement statistics for AmpC$_{EC}$ structures from single crystals.

Datasets	**AmpC$_{EC}$-AVI 15 min** (cryo)	**AmpC$_{EC}$-TAN 21 min** (cryo)	**AmpC$_{EC}$-ERT 15 min** (cryo)
Data Collection	mx23459-136	mx23459-136	mx23459-136
Beamline (Wavelength, Å)	DLS I24 (0.9763)	DLS I03 (0.9763)	DLS I03 (0.9763)
Detector	Eiger2 XE 16M	Eiger2 XE 16M	Eiger2 XE 16M
Data Processing	Xia2 fast_dp	Xia2 dials	Xia2 fast_dp
Space group	*C* 1 2 1	*C* 1 2 1	*C* 1 2 1
Cell dimensions			
- *a,b,c* (Å)	118.7, 76.2, 97.9	117.5, 77.9, 97.2	117.6, 78.1, 98.1
- α, β, γ (°)	90.0, 116.0, 90.0	90.0, 116.3, 90.0	90.0, 116.9, 90.0
No. of molecules/ASU	2	2	2
Total reflections	861431 (57494)*	764502 (37380)*	1474047 (97524)*
Unique reflections	126109 (8745)*	112287 (5428)*	218561 (15917)*
Resolution (Å)	29.59-1.49 (1.53-1.49)*	45.49-1.55 (1.58-1.55)*	29.69-1.25 (1.28-1.25)*
R_{meas}(I)	0.052 (1.397)*	0.052 (0.818)*	0.054 (1.033)*
I/σI	20.3 (1.4)*	20.9 (1.1)*	19.0 (1.8)*
$CC_{1/2}$	1.0 (0.7)*	1.0 (0.8)*	1.0 (0.7)*
Completeness (%)	99.4 (93.1)*	98.7 (95.9)*	99.8 (97.9)*
Multiplicity	6.8 (6.6)*	6.8 (6.9)*	6.7 (6.1)*
Wilson B value (Å^2)	21.34	22.57	14.07
Refinement	PHENIX	PHENIX	PHENIX
R_{work}/R_{free}	0.1410/0.1679	0.1591/0.1804	0.1378/0.1588
No. atoms	6512	6446	6991
- Enzyme	5604	5540	5819
- Ser-bound inhibitor	38	57	52
- unbound inhibitor	-	25	93
- Water	857	811	1009
Average B-factors	27.42	30.97	20.37
- Enzyme	25.70	29.72	18.32
- Ser-bound inhibitor	29.36	33.81	23.97
- unbound inhibitor	-	37.31	24.24
- Water	38.55	38.85	31.66
R.m.s deviations			
- Bond lengths (Å)	0.008	0.011	0.005
- Bond angles (°)	1.024	1.089	1.012

*Highest resolution shell in parentheses.

6.3.3. Fixed-target SSX experiments

Fixed-target serial synchrotron data collection was done by Dr Robin Owen, Dr Pierre Aller, Dr Agata Butryn with guidance from Dr Allen Orville (all Diamond Light Source). Data processing was done by Dr Pierre Aller, Dr Agata Butryn, and Dr Nicholas Devenish (all Diamond Light Source).

Slurries of $AmpC_{EC}$ microcrystals were initially tested for diffraction using a reported fixed-target serial synchrotron crystallography set-up (ft-SSX, see introduction to this chapter and reference [24]) at the I24 MX microfocus beamline at DLS. The crystals were loaded onto a silicon nitride chip with 7 × 7 µm cavities, excess precipitant solution was removed using negative pressure in a humidity-controlled environment, and the chip was enclosed in mylar and mounted at the beamline end station.

A data set complete to 2.0 Å resolution was obtained from the collection of 1 chip (loaded with 150 µl of crystal slurry (Table 4 and Figure 14).

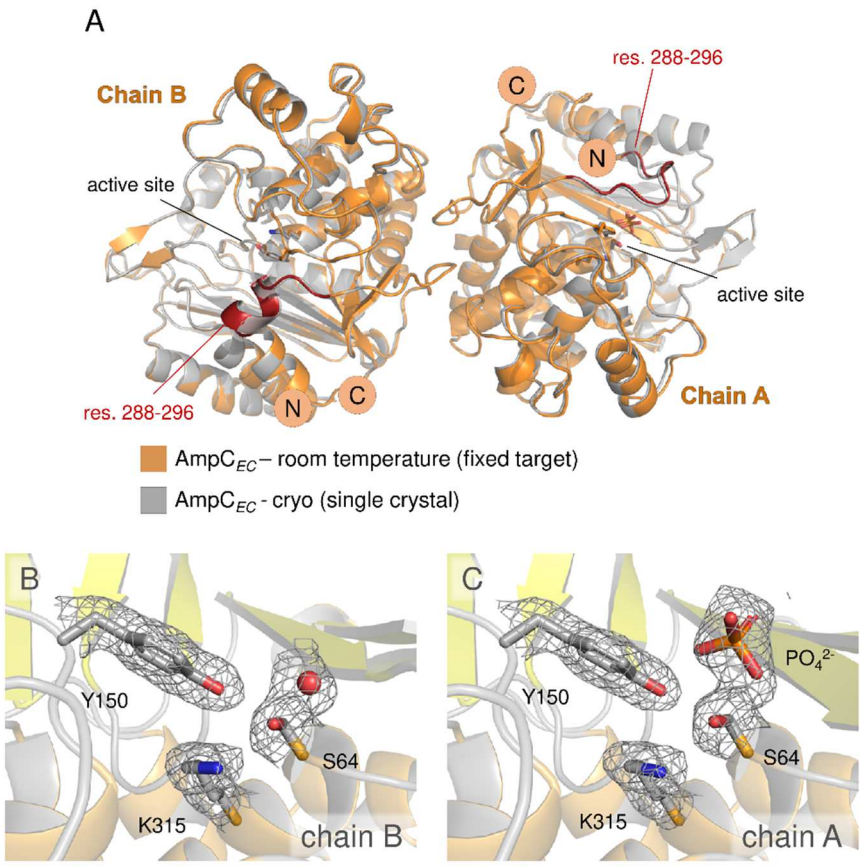


Figure 14: Room-temperature $AmpC_{EC}$ structure obtained via SSX. (A) Comparison of $AmpC_{EC}$ structures at 100 K (single crystal) and 278 K (SSX using fixed target). (B) Active site view of chain B of $AmpC_{EC}$ room temperature structure. (C) Active site view of chain A of $AmpC_{EC}$ room temperature structure. $2mF_o$-DF_c maps are contoured at 1.0 σ and carved around active site residues and the bound phosphate in chain A.

No significant changes in the overall fold and active site residues in the room temperature structure were observed compared to the AmpC$_{EC}$ structure obtained under cryogenic conditions (main chain RMSD 0.24 Å, between AmpC$_{EC}$ structures from fixed-target room temperature and single crystal cryogenic date-collection, Figure 14). The loop comprising residues 288-296 adopted predominantly the same alternative conformation in chain A, as observed under cryogenic conditions (Figure 14A). As observed under cryogenic conditions the de-acylating water was displaced by phosphate at the AmpC$_{EC}$ active site in chain A (Figure 14C), but not in chain B (Figure 14B).

Table 4: Data collection and Refinement statistics for AmpC$_{EC}$ structures from SSX.

Datasets	**AmpC$_{EC}$ in phosphate condition** at 298 K from fixed-target		
Data Collection		**Refinement**	PHENIX
Beamline (Wavelength, Å)	DLS I24 (1.000000)	R_{work}/R_{free}	0.1711/0.1958
Detector	Pilatus3 6M	No. atoms	5860
Data Processing		- Enzyme	5544
Space group	*C* 1 2 1	- Water	311
Cell dimensions		Average B-factors	32.29
- *a,b,c* (Å)	118.98, 77.96, 98.99	- Enzyme	32.10
- α, β, γ (°)	90, 115.97, 90	- Water	35.55
No. of molecules/ASU	2	R.m.s deviations	
Total Reflections	1566143 (43460)*	- Bond lengths (Å)	0.003
Unique reflections	47493 (2309)*	- Bond angles (°)	0.680
Resolution (Å)	89.0-2.10 (2.14-2.10)*		
R_{meas}(I)	24.2 (30.8)*		
I/σI	2.22 (1.09)*		
$CC_{1/2}$	0.60 (0.42)*		
Completeness (%)	100 (100)*		
Multiplicity	32.89 (18.64)*		
Wilson B value (Å^2)	30.84		

*Highest resolution shell in parentheses.

To verify AmpC$_{EC}$ active site accessibility in microcrystal slurry, three structures were collected of AmpC$_{EC}$ microcrystal slurries soaked with avibactam, taniborbactam, and ertapenem (Table 5 and Figure 15). Data collection was started after 10 min of incubation with the inhibitors. Due to an average duration of data-collection of ~15 min / chip, no exact time-point can be defined with this experimental set-up. However, based on the experiments in single crystals it is likely that equilibration is reached well within the initial 10 min pre-equilibration time-frame.

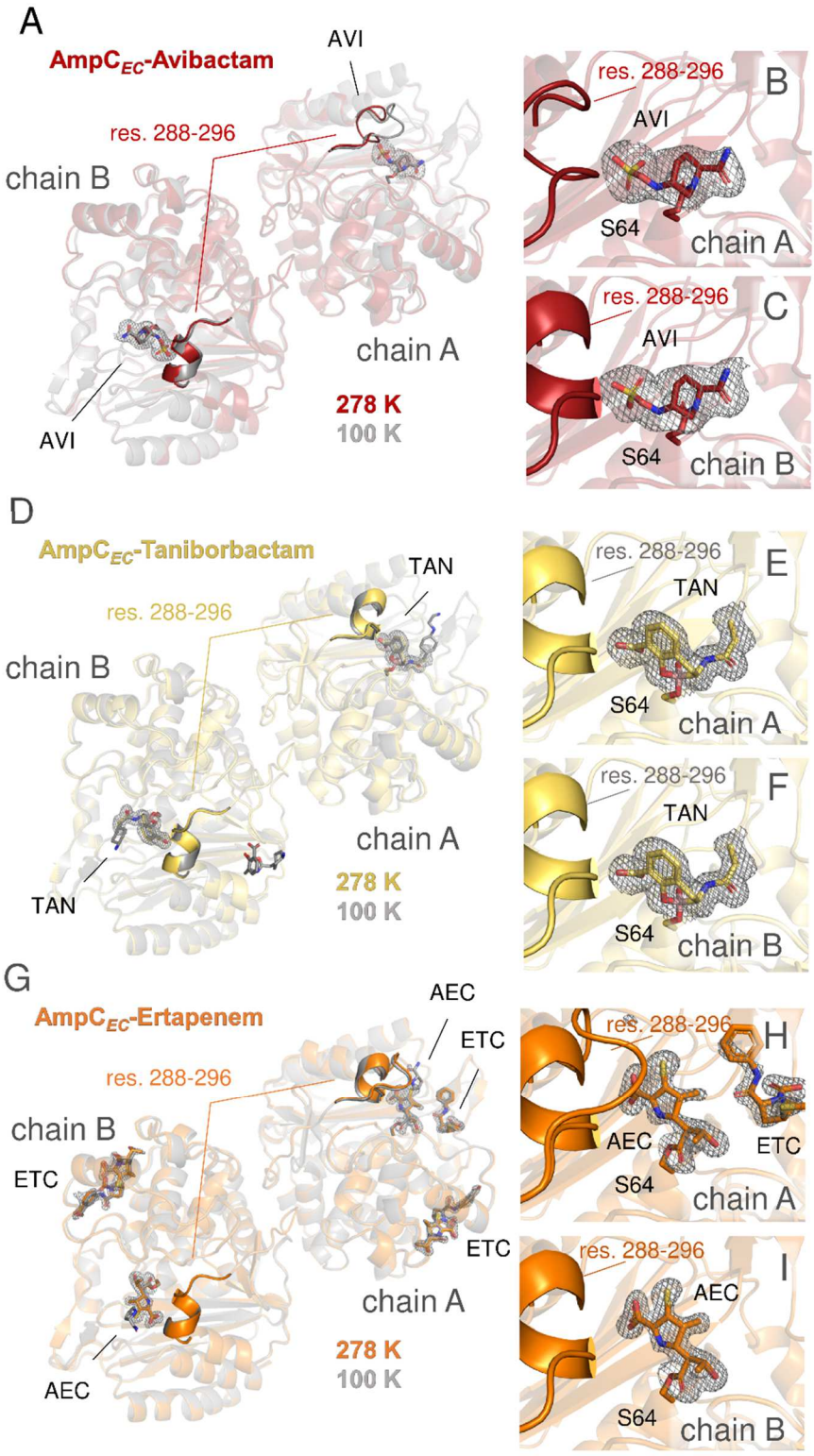


Figure 15: AmpC$_{EC}$-inhibitor complex structures determined in room temperature ft-SSX studies. (A) Overlay of AmpC$_{EC}$-avibactam complex structures from ft-SSX (278 K, red) and single crystal (100 K, grey) experiments. (B-C) Active site views of AmpC$_{EC}$-avibactam ft-SSX structure. (D) Overlay of AmpC$_{EC}$-taniborbactam complex structures from ft-SSX (278 K, yellow) and single crystal (100 K, grey) experiments. (E-F) Active site views of AmpC$_{EC}$-taniborbactam ft-SSX structure. (G) Overlay of AmpC$_{EC}$-ertapenem complex structures from ft-SSX (278 K, orange) and single crystal (100 K, grey) experiments. (H-I) Active site views of AmpC$_{EC}$-avibactam ft-SSX structure. Polder OMIT maps[39] are contoured at 3.0 σ and carved around inhibitors.

The obtained room temperature structures of AmpC$_{EC}$ in complex with avibactam (2.05 Å resolution, Table 5 and Figure 15A-C), taniborbactam (1.70 Å resolution, Table 5 and Figure 15D-F), and ertapenem (1.70 Å resolution, Table 5 and Figure 15G-I) all showed electron density indicating reaction of the nucleophilic Ser with the respective inhibitors.

The overall fold of all room temperature structures strongly represented those observed under cryogenic conditions (main chain RMSD of 0.47 Å, 0.24 Å, and 0.22 Å for room temperature structure compared to cryogenic structure for avibactam, taniborbactam, and ertapenem, respectively).

By contrast with the cryogenic structure of the AmpC$_{EC}$-avibactam structure, however, residues 288-296 adopted predominantly the same conformation in chain A as observed in chain B in all structures (Figure 15A-B), and not the alternate conformation observed in chain A in the structure of unmodified AmpC$_{EC}$ in the phosphate condition (Figure 14).

While full modification of Ser64 with bicyclic taniborbactam was observed at the AmpC$_{EC}$ active site in both chains, by contrast with the structure under cryogenic conditions (Figure 12), no electron density for the C3 sidechain was evident (Figure 15E-F), potentially suggesting higher disorder of the sidechain at room temperature (Figure 12C). Further, the tricyclic taniborbactam observed at the AmpC$_{EC}$ surface under cryogenic conditions, was not observed in the room temperature ft-SSX structure.

Similar to the room-temperature structure of AmpC$_{EC}$ in complex with taniborbactam, no electron density was observed for the C2 sidechain of the ertapenem derived acyl-enzyme complex at room temperature (Figure 15H-I). However, the additional non-covalent ertapenem molecules observed under cryogenic conditions at the active site in chain A and at the surface of both chain A and chain B were also evident in the ft-SSX structure obtained at room temperature (Figure 15G). As observed under cryogenic conditions, all the non-covalently bound ertapenem molecules showed additional electron density indicating carbamylation of the ertapenem C2 side-chain pyrrolidine nitrogen (Figure 15G and H).

Overall, the ft-SSX studies with AmpC$_{EC}$ microcrystal slurry pre-equilibrated with avibactam, taniborbactam, and ertapenem thus further demonstrate accessibility of AmpC$_{EC}$ active sites in microcrystals grown in the phosphate condition. However, the low time-resolution of the soaking technique used in this set-up excludes the observation of short-lived reaction intermediates.

Table 5: Data collection and Refinement statistics for AmpC$_{EC}$ structures from fixed-target SSX.

Datasets	**AmpC$_{EC}$-TAN** (fixed-target)	**AmpC$_{EC}$-AVI** (fixed-target)	**AmpC$_{EC}$-ERT** (fixed-target)
Data Collection			
Beamline (Wavelength, Å)	DLS I24 (0.9999)	DLS I24 (0.9999)	DLS I24 (0.9999)
Detector	Pilatus3 6M	Pilatus3 6M	Pilatus3 6M
Data Processing	dials.stills_process	dials.stills_process	dials.stills_process
Space group	*C* 1 2 1	*C* 1 2 1	*C* 1 2 1
Cell dimensions			
- *a,b,c* (Å)	118.74, 78.78, 99.04	118.9, 78.34, 99.24	118.7, 78.91, 99.23
- α, β, γ (°)	90, 116.1, 90	90, 116.0, 90	90, 116.4, 90
No. of molecules/ASU	2	2	2
Total reflections	8008168 (46584)*	3044205 (22880)*	2237143 (43807)*
Unique reflections	90125 (4451)*	51473 (2525)*	90045 (4424)*
Resolution (Å)	88.98-1.70 (1.73-1.70)*	89.2-2.05 (2.09-2.05)*	88.87-1.70 (1.73-1.70)*
R_{meas}(I)	8.0 (54.1)*	12.6 (59.7)*	19.9 (38.5)*
I/σI	5.37 (0.80)*	2.72 (0.64)*	2.94 (1.07)*
$CC_{1/2}$	0.99 (0.60)*	0.99 (0.54)*	0.93 (0.72)*
Completeness (%)	99.99 (99.82)*	99.98 (99.61)*	99.86 (98.99)*
Multiplicity	88.86 (10.47)*	59.14 (9.06)*	24.84 (9.90)*
Wilson B value (Å^2)	26.21	30.46	23.32
Refinement	PHENIX	PHENIX	PHENIX
R_{work}/R_{free}	0.1444/0.1652	0.1385/0.1792	0.1578/0.1870
No. atoms	5926	5874	6093
- Enzyme	5530	5556	5533
- Bound inhibitor	42	47	52
- Unbound inhibitor	-	-	73
- Water	346	272	407
Average B-factors	31.63	36.04	27.47
- Enzyme	31.09	35.70	26.35
- Bound inhibitor	28.65	42.46	40.92
- Unbound inhibitor	-	-	43.70
- Water	40.98	41.87	37.31
R.m.s deviations			
- Bond lengths (Å)	0.009	0.014	0.011
- Bond angles (°)	0.913	1.228	1.052

*Highest resolution shell in parentheses.

6.3.4. Data collection at LCLS

Drop-on-drop tr-SFX data collection was done by Dr Jan Kern, Dr Philipp Simon, Isabel Bogacz, Dr Hiroki Makita with support from Prof. Junko Yano and Prof. Vittal Yachandra (all Lawrence Berkeley National Laboratory, LBNL) controlling the ADE tape drive set-up and Dr Pierre Aller, Dr Agata Butryn (both Diamond Light source, DLS), and Gabriel Leen (PolyPico Technologies Ltd) with support from Dr Allen Orville (DLS) controlling the Poly Pico injector. Data collection at LCLS was supported by Dr Alex Batyuk, Dr Franklin Fuller, and Dr Roberto Alonso-Mori (all LCLS). Data processing was done by Dr Aaron Brewster, Dr Asmit Bhowmick, and Dr Daniel Paley supervised by Dr. Nicholas K. Sauter (all LBNL).

Due to the COVID-19 pandemic travel to LCLS from outside the US was not permitted. Therefore, samples were either prepared in advance and shipped to LCLS, or set up by local collaborators *(Dr Medhanjali Dasgupta and Dr Steve Keable, Berkeley, LBNL*), which was successful without advance training using the simple batch method set-up (see Materials and Methods). AmpC$_{EC}$ slurries both prepared in advance and additionally set up at LCLS were tested, showing no apparent loss of diffraction quality on shipment.

In total, eight room temperature structures of AmpC$_{EC}$ were obtained, including of AmpC$_{EC}$ in its unmodified form, seven structures obtained on addition of avibactam in varying concentrations with varying time delays of 0.1-2 s, and one structure obtained on addition of ertapenem with a 2 s delay. Structures ranged in resolution between 1.7-2.0 Å (Table 7 and Figure 16) and took ~ 30 min each to collect. A summary of the collected structures is given in Table 6.

Table 6: Room-temperature AmpC$_{EC}$ structures collected at LCLS. AVI: avibactam, ERT: ertapenem. Ligand occupancies were estimated based on visual inspection of electron density maps.

Structure (Ligand)	Time	ADE drop size	Number of 45 pl PEI drops merging	Ligand stock concentration (mM)	Final ligand concentration (mM)	Estimated ligand occupancy
1 (-)	-	-	-	-	-	-
2 (AVI)	0.1 s	2 nL	5-7	1000	167	< 10%
3 (AVI)	0.2 s	4 nL	4	1000	44	10-20%
4 (AVI)	0.2 s	2 nL	3	1000	122	20-30%
5 (AVI)	0.7 s	2 nL	3	1000	44	80-90%
6 (AVI)	2 s	3 nL	6	300	30	100%
7 (AVI)	2 s	3 nL	3	300	17	100%
8 (ERT)	2 s	2 nL	30	600	250	10-20%

Structure 1 shows the unmodified AmpC$_{EC}$, with phosphate bound at the active site in chain A, but not in chain B (Figure 16B and C), as observed in the single crystal (Figure 9) and ft-SSX studies (Figure 14).

In structures 2-4 (Table 6 and Figure 16), with reaction times ranging from 100-200 ms, additional electron density is apparent in isomorphous differences maps (compared to the SFX structure of unmodified AmpC$_{EC}$) indicating partial avibactam binding at the AmpC$_{EC}$ active site (Figure 16B and C). A clear dependence on the amount of additional electron density is evident on prolonged incubation time (i.e. 100 or 200 ms for structures 2 and 3, respectively), and, to a lesser extent, on the avibactam concentration added to the microcrystal slurry (e.g. 122 mM and 44 mM for structures 3 and 4, respectively). While, in these structures, the observed electron density clearly indicates partial covalent modification of Ser64 (as evident in electron density correlating to the carbamoyl carbonyl), it is insufficient to identify the avibactam binding mode which was therefore not included in the refined model. In all structures the additional electron density was stronger in chain B (Figure 16C), compared to chain A (Figure 16B), which may reflect slower binding of avibactam to the AmpC$_{EC}$ active site in chain A, potentially due to an inhibitory effect of the phosphate molecule bound in close proximity to Ser64.

In structures 5-7, with reaction times ranging from 700-2000 ms, sufficient electron density was observed to model the avibactam derived carbamoyl-enzyme complex (Figure 16B and C). In agreement with the single crystal (Figure 11) and ft-SSX studies (Figure 15) avibactam was observed solely in a confirmation primed for de-carbamoylation, with the *N*-sulfate nitrogen in close proximity to the Tyr150 phenol (see Chapter 2).

Interestingly, while in structure 1 residues 288-296 of chain A predominantly adopt the same unusual conformation as observed in the structures of unmodified AmpC$_{EC}$ from single crystal and ft-SSX studies (conformation B in Figure 16A), rearrangement of the loop to adopt predominantly the commonly observed conformation (A in Figure 16A) is observed in structure 2, on incubation with avibactam for 100 ms. Importantly, this precedes binding of avibactam in significant occupancy (Figure 16B and C). While in structures 2-3, both with 200 ms reaction time, but varying avibactam concentration (122 mM and 44 mM, for structures 2 and 3, respectively) the mobile loop is also predominantly observed in conformation A, increased B-factors indicate partial re-arrangement back to conformation B (Figure 16A). In structure 4, with 700 ms incubation with avibactam and Ser64 modification with the avibactam derived carbamoyl-enzyme complex with ~90% occupancy, the loop is observed both in conformation A and B and refined in ~50% occupancy each. In structures 6-7, with 2000 ms incubation with avibactam and full modification of S64 with the avibactam derived carbamoyl-enzyme complex, the loop is again predominantly observed in conformation B, as observed in structure 1 without addition of avibactam (Figure 16A).

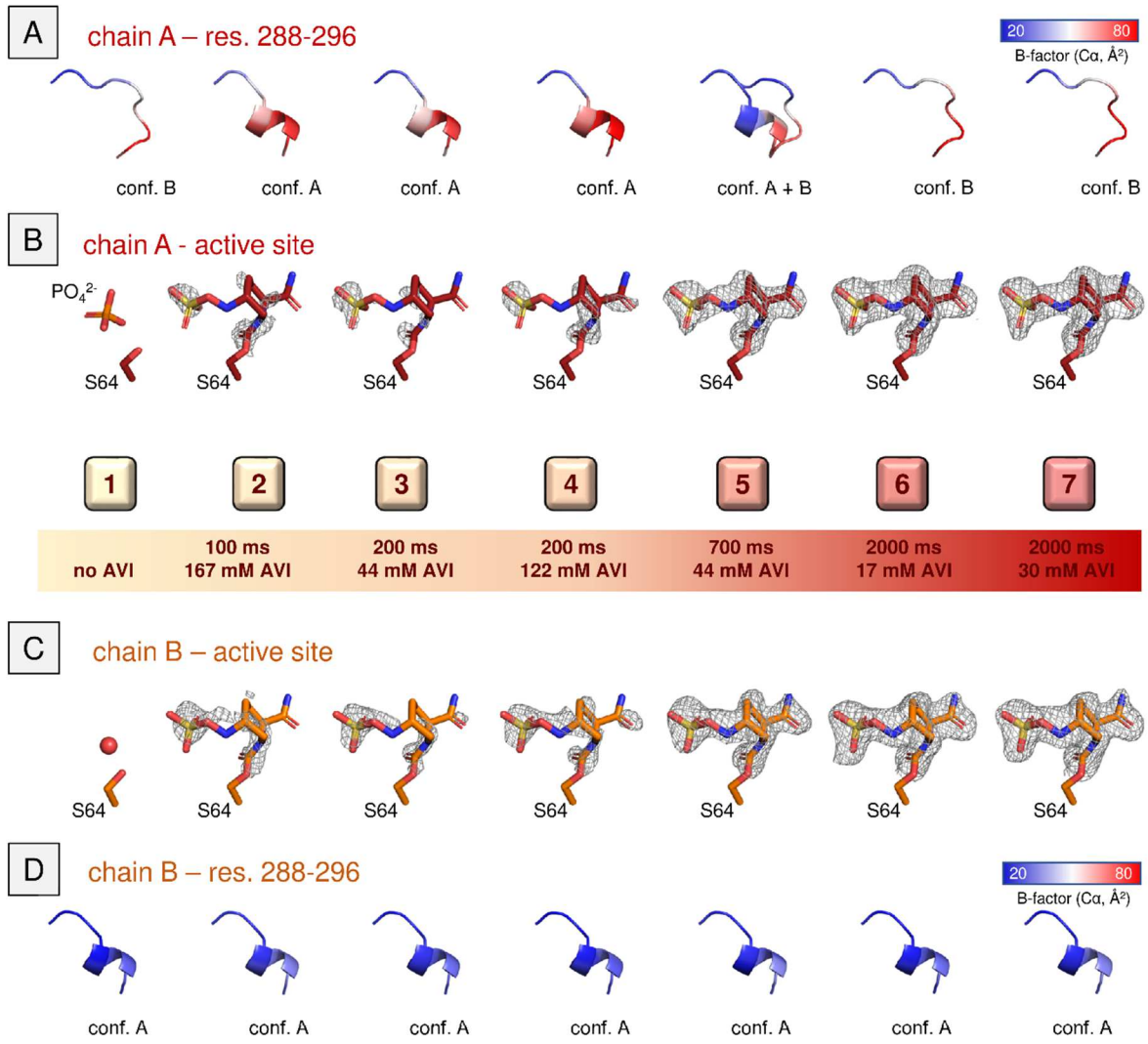


Figure 16: tr-SFX studies on avibactam binding to AmpC$_{EC}$. Views from crystal structures 1-7 (Table 6) obtained in tr-SFX studies at LCLS. (A) Res. 288-296 of chain A, colour coded by residue according to B-factors of C-α atom. (B) Active site view of chain A. Isomorphous F_o-F_o maps (relative to structure 1) are contoured at 3.0 σ and carved around the avibactam derived carbamoyl-enzyme complex as observed in structure 7. (C) Active site view of chain B. Isomorphous F_o-F_o maps (relative to structure 1) are contoured at 3.0 σ and carved around the avibactam derived carbamoyl-enzyme complex as observed in structure 7. (D) Res. 288-296 of chain B, colour coded by residue according to B-factors of Cα atom.

In chain B, consistent with the single crystal (Figure 11) and ft-SSX (Figure 15) studies, residues 288-296 are solely observed in conformation A in all structures. It should also be noted that the apparent return of residues 288-296 in chain A to conformation B 2 s after addition of avibactam is notable as this loop is being observed predominantly in conformation A in the ft-SSX studies on AmpC$_{EC}$ micro-crystals soaked with avibactam for prolonged time (10-30 min, Figure 15). Further investigations are required to evaluate the potential biological significance of the loop-rearrangement observed in chain A on binding of avibactam; the preliminary results, however, suggest that movement of the loop maybe important in inhibition and, maybe, catalysis, though further work is required, especially with respect to its relevance in solution.

Table 7: Data collection and Refinement statistics for AmpC$_{EC}$ structures from SFX. Note: Reprocessing of the data is required and resolution may be 0.1-0.3 Å lower than indicated. Structures are numbered as defined in Table 6 and Figure 16.

Datasets	**AmpC$_{EC}$ - 1 umodified** (LCLS)	**AmpC$_{EC}$-AVI - 2 100 ms, 150 mM** (LCLS)	**AmpC$_{EC}$-AVI - 3 200 ms, 40 mM** (LCLS)
Data Collection			
Beamline (Wavelength, Å)	LCLS MFX (1.301448)	LCLS MFX (1.300773)	LCLS MFX (1.301739)
Detector	RAYONIX MX340-HS	RAYONIX MX340-HS	RAYONIX MX340-HS
Data Processing	cctbx.xfel	cctbx.xfel	cctbx.xfel
Space group	*C* 1 2 1	*C* 1 2 1	*C* 1 2 1
Cell dimensions			
- *a,b,c* (Å)	119.2, 77.8, 99.1	119.3, 78.3, 99.3	119.5, 78.3, 99.4
- α, β, γ (°)	90, 116.0, 90	90, 116.0, 90	90.0, 115.9, 90.0
No. of molecules/ASU	2	2	2
Resolution (Å)	33.28-1.80 (1.83-1.80)*	(1.73-1.70)*	12.18-1.80 (1.83-1.80)*
R_{split}(I)	0.893 (0.137)*	0.156 (1.086)*	0.101 (0.820)*
I/σI	3.91 (0.66)*	2.50 (0.22)*	5.05 (0.76)*
$CC_{1/2}$	0.99 (0.24)*	0.98 (0.13)*	0.99 (0.33)*
Completeness (%)	100 (99.3)*	96.4 (61.4)*	99.7 (100)*
Multiplicity	57.32 (7.65)*	47.60 (3.04)*	110.9 (13.32)*
Wilson B value (Å^2)	25.06	28.91	26.39
Refinement	PHENIX	PHENIX	PHENIX
R_{work}/R_{free}	0.1601/0.1874	0.1697/0.1919	0.1542/0.1727
No. atoms	5914	5847	5972
- Enzyme	5551	5563	5562
- Ligand	-	-	-
- Water	358	284	410
Average B-factors	29.66	34.42	31.29
- Enzyme	29.11	34.25	30.71
- Ligand	-	-	-
- Water	37.8	37.85	39.16
R.m.s deviations			
- Bond lengths (Å)	0.004	0.003	0.003
- Bond angles (°)	0.753	0.653	0.647

*Highest resolution shell in parentheses.

Table 7 continued. Note: Reprocessing of the data is required and resolution may be 0.1-0.3 Å lower than indicated. Structures are numbered as defined in Table 6 and Figure 16.

Datasets	**AmpC$_{EC}$-AVI - 4** **200 ms, 110 mM** (LCLS)	**AmpC$_{EC}$-AVI - 5** **700 ms, 40 mM** (LCLS)	**AmpC$_{EC}$-AVI - 6** **2s, 17 mM (3d)** (LCLS)
Data Collection			
Beamline (Wavelength, Å)	LCLS MFX (1.301754)	LCLS MFX (1.301577)	LCLS MFX (1.301457)
Detector	RAYONIX MX340-HS	RAYONIX MX340-HS	RAYONIX MX340-HS
Data Processing	cctbx.xfel	cctbx.xfel	cctbx.xfel
Space group	*C* 1 2 1	*C* 1 2 1	*C* 1 2 1
Cell dimensions			
- *a,b,c* (Å)	119.5, 78.1, 99.4	119.4, 78.3, 99.4	119.1, 77.9, 99.1
- α, β, γ (°)	90.0, 115.9, 90.0	90.0, 115.9, 90.0	90.0, 116.0, 90.0
No. of molecules/ASU	2	2	2
Resolution (Å)	33.38-1.70 (1.73-1.70)*	33.38-1.85 (1.88-1.85)*	32.76-1.80 (1.83-1.80)*
R_{split}(I)	0.117 (1.001)*	0.154 (0.968)*	0.126 (0.869)*
I/σI	4.35 (0.51)*	3.58 (0.52)*	4.22 (0.69)*
$CC_{1/2}$	0.99 (0.17)*	0.98 (0.24)*	0.99 (0.28)*
Completeness (%)	99.9 (97.9)*	99.9 (99.1)*	100 (99.8)*
Multiplicity	87.07 (6.39)*	50.04 (7.55)*	67.20 (9.15)*
Wilson B value (Å^2)	24.14	27.21	25.22
Refinement	PHENIX	PHENIX	PHENIX
R_{work}/R_{free}	0.1610/0.1855	0.1665/0.1810	0.1553/0.1799
No. atoms	5959	5955	5943
- Enzyme	5575	5601	5519
- Ligand	-	38	38
- Water	384	308	378
Average B-factors	31.03	31.70	30.23
- Enzyme	30.46	31.25	29.59
- Ligand	-	50.73	39.63
- Water	39.34	37.93	38.84
R.m.s deviations			
- Bond lengths (Å)	0.013	0.005	0.005
- Bond angles (°)	1.367	0.829	0.794

*Highest resolution shell in parentheses.

Table 7 continued. Note: Reprocessing of the data is required and resolution may be 0.1-0.3 Å lower than indicated. Structures are numbered as defined in Table 6 and Figure 16.

Datasets	**AmpC$_{EC}$-AVI - 7 2s, 30 mM (6d)** (LCLS)	**AmpC$_{EC}$-ERT - 8 2 s,** (LCLS)
Data Collection		
Beamline (Wavelength, Å)	LCLS MFX (1.301490)	LCLS MFX (1.300773)
Detector	RAYONIX MX340-HS	RAYONIX MX340-HS
Data Processing	cctbx.xfel	cctbx.xfel
Space group	*C* 1 2 1	*C* 1 2 1
Cell dimensions		
- *a,b,c* (Å)	119.1, 78.0, 99.2	118.9, 79.0, 99.4
- α, β, γ (°)	90.0, 116.0, 90.0	90, 115.9, 90
No. of molecules/ASU	2	2
Resolution (Å)	33.30-1.80 (1.83-1.80)*	33.34-1.70 (1.73-1.70)*
R_{split}(I)	0.127 (0.902)*	0.189 (1.098)*
I/σI	4.14 (0.65)*	2.78 (0.31)*
$CC_{1/2}$	0.99 (0.09)	0.25 (0.04)*
Completeness (%)	100 (99.7)*	95.9 (62.6)*
Multiplicity	68.46 (8.66)*	36.72 (1.89)*
Wilson B value (Å^2)	26.29	26.64
Refinement	PHENIX	PHENIX
R_{work}/R_{free}	0.1555/0.1827	-
No. atoms	5903	-
- Enzyme	5519	-
- Ligand	38	-
- Water	338	-
Average B-factors	31.90	-
- Enzyme	31.38	-
- Ligand	38.78	-
- Water	39.93	-
R.m.s deviations		
- Bond lengths (Å)	0.013	-
- Bond angles (°)	1.128	-

*Highest resolution shell in parentheses.

Despite the addition of a very high concentration of ertapenem (250 mM, crystal structure 8 in Table 6 and 7), obtained after 2 s incubation with ertapenem, only very weak evidence for ertapenem binding at the $AmpC_{EC}$ active site in both chains was observed (data not shown), suggesting significantly slower diffusion and / or binding of ertapenem compared to avibactam. No rearrangement of residues 288-296 in chain A was observed compared to unmodified $AmpC_{EC}$.

6.4. Conclusions and Future work

Dynamic structural biology using serial crystallography is a rapidly growing field, offering opportunities to gain global structural insight into short lived intermediates in enzyme catalysis which have long been inaccessible. However, while the field has made significant advances in the past decade, many of the processes such as optimal sample preparation, sample delivery and data processing are still cutting-edge and under continued development.

As shown here in the case of OXA-48, extensive screening did not afford any conditions satisfying all the requirements for optimal microcrystal samples such as low viscosity, unperturbed active sites, small and uniform crystal dimensions and high diffraction quality of microcrystals. In the future new methods such as *in situ* data collection[42] may facilitate identification of micro crystallisation conditions, but it is likely that crystallisation will remain one of the bottle necks of serial crystallography for many macromolecular samples.

When suitable crystallisation conditions can be identified via broad screens or from literature, as in the case of $AmpC_{EC}$, serial crystallography approaches can enable more homogenous reaction initiation through ligand soaking compared to single crystal approaches which require larger crystals, as reduction of the crystal volume significantly reduces diffusion times. The work described in this chapter shows proof-of-principle for reaction initiation with the drop-on-drop system in a sub-second time-frame, which is considerably faster than initial results reported with this system[27].

The conformational changes of the loop comprised of residues 288-296, which is part of helix 10 and in close proximity to the $AmpC_{EC}$ active site, apparently induced by avibactam addition, are intriguing, especially as they appear to precede covalent binding of avibactam to Ser64 which would potentially indicate an involvement in initial non-covalent binding or transition states. However, further studies are required to investigate relevance of the alternative loop conformation (which is only observed in one out of two chains in the ASU) in solution.

Overall, the data does, however, also suggest that reaction of $AmpC_{EC}$ with avibactam in microcrystal slurries occurs in an even faster timescale than that accessible using the drop-

on-drop approach (which is consistent with the kinetic studies discussed in Chapter 2). As the remaining diffusion time imposed by the drop-on-drop approach appears to preclude the study of timepoints shorter than 100 ms (as indicated by the partial electron density for the carbamoyl-enzyme complex), alternative sample-delivery systems should be considered to study $AmpC_{EC}$ reactions such as liquid jets, which have recently been reported to introduce β-lactam ligands into β-lactamase active sites within 10 ms[33]. Another option lays in drop-on-fixed target approaches[19], which preclude larger amounts of mother liquor around the crystals (as in the drops) and may thus facilitate faster initiation due to shorter diffusion distances and higher ligand concentrations.

Alternatively, modification of β-lactams with photocleavable protecting groups could be explored to allow light activated reaction initiation such as described previously for other systems which are not natively initiable via irradiation[43,44].

The crystallisation conditions developed for $AmpC_{EC}$ should enable to study $AmpC_{EC}$ with any of these systems, and in combination with a wide range of β-lactams and β-lactamase inhibitors.

6.5. Materials and Methods

6.7.1. Materials

Ertapenem was from Biosynth-Carbosynth. Taniborbactam was from medchemexpress. Avibactam was gifted by Prof. Mike Page (University of Huddersfield). The pNIC28 plasmid used to express OXA-48 was provided by Dr Christopher Lohans (University of Oxford). TEV protease was provided by Dr Jürgen Brem (University of Oxford).

6.7.2. Enzyme production and purification

$AmpC_{EC}$ was produced and purified as described in Chapter 2.

Recombinant OXA-48 was produced and purified according to reported procedures[35]. OXA-48 (conjugated to a 6xHis tag) was expressed in *E.coli* BL21 (DE3) cells using a pNIC28 vector. Cells were grown in 2TY media supplemented with 50 µg ml^{-1} kanamycin at 37 °C until OD_{600} of 0.6-1.0, then cooled to 18 °C. OXA-48 expression was induced via addition of 0.6 mM IPTG and the culture was incubated overnight at 18 °C.

OXA-48 containing cells were resuspended in buffer A (50 mM MES, pH 7.5, 20 mM imidazole), lysed, and centrifuged. The filtered supernatant was loaded onto two combined 5 ml HisTrap HP columns (GE Healthcare) equilibrated in buffer A, the columns were washed with buffer A until the UV signal stabilised, and OXA-48 was eluted in a gradient of 0-100%

buffer B (50 mM MES, pH 7.5, 500 mM imidazole). Fractions containing OXA-48 were concentrated and exchanged to buffer C (50 mM MES, pH 6.0), TEV protease was added (1:100 weight ratio), and the reaction was left at 4 °C overnight, with continuous rocking. TEV and the cleaved His-tag were removed via a second His-affinity column, and the protein was further purified via size-exclusion chromatography using a Superdex 75 column (300 ml, Amersham Pharmacia Biosciences), pre-equilibrated in buffer D (50 mM MES, pH 6.0, 50 mM $NaHCO_3$).

6.7.1. Crystallisation

6.7.1.1. AmpC$_{EC}$ crystallisation in PEG condition

Macro crystals were obtained via sitting-drop vapour diffusion technique using MRC-maxi 48-well plates (Swissci). AmpC$_{EC}$ (3 µl, 20 mg ml^{-1}, in 50 mM Tris pH 7.0) was mixed with precipitant solution (22-27% (w/v) PEG 6,000, 10 mM $ZnCl_2$, 100 mM MES pH 6.0) and equilibrated at room temperature against wells filled with 200 µl precipitant solution. Drops containing crystals were harvested, and diluted in precipitant solution to a final volume of 100 µl, then crushed using seed-bead kits (PTFE beads, Hampton Research) according to the manufacturer's instructions, with alternate cycles of vortexing (15 s) and cooling on ice (15 s) for 15 min.

Microcrystals were prepared in batch set-up. In a typical set-up, 400 µl of precipitant solution (35% (w/v) PEG 6,000, 10 mM $ZnCl_2$, 100 mM MES pH 6.0) are added quickly to 100 µl AmpC$_{EC}$ (20 mg ml^{-1}, in 50 mM Tris pH 7.5) and immediately mixed thoroughly by pipetting up and down. 50 µl micro seed stock are added and the crystallisation solution is mixed, then divided into 100 µl aliquots and incubated in a 96-well plate at room temperature for 18-24 h. After crystallisation, slurries from individual wells were combined in an Eppendorf tube and left to settle for 24-48 h, then ~50% of the supernatant were removed. Immediately before use, crystals were resuspended by pipetting.

6.7.1.2. OXA-48 crystallisation

Broad-screens with OXA-48 (either with or without *N*-terminal His-tag, 10 mg ml^{-1}, either in 50 mM MES pH 6.0, or 50 mM Tris pH 7.5) were set up using either a Phoenix RE Drop setter instrument (Rigaku) and low reservoir Intelli-Plates 93-3 plates (Art Robbins), or a TTP Mosquito HTS nanolitre liquid handler (SPT Labtech) and low profile SWISSCI 96-3 plates. Crystallisation conditions were identified using commercial screens from Molecular Dimensions (Morpheus, Morpheus II, JCSG Plus, LMB, PACT premier, Wizard, SG1, BCS, and PGA), or Hampton Research (Index, Crystal Screen, PEGRx, PEG/Ion, SaltRx, and MPD

Screen). Protein solutions were combined with precipitant solutions at different rations (1:2, 1:1, and 2:1) to give initial drop volumes of 200-300 nl and incubated either at room temperature or 4 °C.

Crystals in MES condition were obtained by crystallising OXA-48 without *N*-terminal His-tag (in 50 mM MES pH 6.0) in condition D3 of the Morpheus Crystallisation Screen (0.12 M alcohols (1,6-hexanediol, 1-butanol, 1,2-propanediol, 2-propanol, 1,4-butanediol, 1,3-propanediol), 0.1 M buffer system 1 (imidazole, MES monohydrate (acid), pH 6.5), 30% (v/v) Precipitant Mix 3 (40% (v/v) glycerol; 20% (w/v) PEG 4000)) at room temperature. Crystals appeared within 1-2 weeks.

Crystals in Dioxane condition were obtained by crystalising OXA-48 without His-tag (in 50 mM Tris pH 7.5) in condition LMB Crystallisation Screen, condition B7 (38% (*v*/*v*) 1,4-dioxane) at 4 °C. Crystals appeared within 1-2 weeks.

6.7.1.3. AmpC$_{EC}$ crystallisation in phosphate condition

Initial clusters of crystals were obtained using hanging drop vapour diffusion techniques. AmpC$_{EC}$ (1.5 µl, 25 mg ml^{-1} in 50 mM potassium phosphate buffer, pH 7.0) was combined with 1.6 M potassium phosphate pH 8.8 (4.5 µl, precipitant solution), the resulting drop was equilibrated over 500 µl precipitant solution in pre-greased 24 well Combo Plate (SBS format, Greiner), using un-siliconized glass coverslips (MD4-08, Molecular Dimensions). Clusters of crystals grew over 1-2 weeks at room temperature, were harvested, diluted in precipitant solution to a final volume of 100 µl, then used to prepare micro seeds as described for PEG condition.

The resulting micro-seed stock was diluted 10-10,000 fold in precipitant solution, then mixed with AmpC$_{EC}$ instead of precipitant solution to set-up analogous crystallisation trials as described above, but with siliconized glass-coverslips (Hampton Research). More defined clusters of AmpC$_{EC}$ appeared over 3-4 days at room temperature, and were used to prepare a new seed stock as described above.

Crystallisation with this new micro seed stock gave single crystals of ~ 100-150 µm size when the seeds were diluted 1,000-10,000 fold in precipitant solution and used in the hanging-drop vapour diffusion set-up described above. Less diluted seed stock (~10-100 fold diluted in precipitant solution) was used to obtain microcrystals, which were used to prepare more concentrated micro-seed stock as described above. Macro-crystals generally grew over 3-4 days, while micro-crystals appeared within 18 h at room temperature.

A concentrated seed stock obtained from micro crystal slurries (either from vapour diffusion experiments described above, or from batch methods described below) was used for batch-set ups. In a typical set-up, 900 µl of 1.9 M potassium phosphate pH 8.8 are added quickly to 100 µl $AmpC_{EC}$ (50 mg ml^{-1}, in 50 mM sodium phosphate, pH 7.0) and immediately mixed thoroughly by pipetting up and down, to give a cloudy solution. 50 µl micro seed stock are added and the crystallisation solution is mixed, then incubated at room temperature for 2-4 h to give a concentrated microcrystal slurry. Slurries were used without further concentration.

6.7.2. Data collection and processing

6.7.1.4. Single crystal experiments

Crystals were cryo-protected using precipitant solution supplemented with either 20% (*v*/*v*) glycerol (OXA-48 in dioxane condition) or 25% (*w*/*v*) sucrose ($AmpC_{EC}$ in phosphate condition), mounted on nylon-loops, cryo-cooled, and stored in liquid nitrogen. X-ray diffraction data from single crystals were collected at 100 K at the MX beamlines at Diamond Light Source and processed using the Xia2 pipeline[45].

6.7.1.5. Fixed target serial synchrotron experiments

Data collection was done by Dr Robin Owen, Dr Pierre Aller, Dr Agata Butryn with guidance from Dr Allen Orville (all Diamond Light Source). Data processing was done by Dr Pierre Aller, Dr Agata Butryn, and Dr Nicholas Devenish (all Diamond Light Source).

Data collection was performed at beamline I24 at Diamond Light Source according to reported procedures[24,25]. In short micro-crystal slurry (100-200 µl) was loaded onto a chip (made of crystalline silicon and containing 11259 aperture sized 7 x 7 µm) in a humidity controlled environment, sealed with Mylar, enclosed in a metal frame and mounted at the beamline. Chips were aligned using three corner fiducials. During data collection the chip was moved to position each aperture in the path of the beam once.

Diffraction images were processed using dials.stills_process[46,47] and the data was merged using PRIME[48-50] with the cryo structure of $AmpC_{EC}$ in the phosphate condition used as the reference model.

6.7.1.6. Drop on drop ADE tape drive experiments

Data collection was done by Dr Jan Kern, Dr Philipp Simon, Isabel Bogacz, Hiroki Makita with support from Prof. Junko Yano and Prof. Vittal Yachandra (all Lawrence Berkeley National Laboratory) controlling the ADE tape drive set-up and Dr Pierre Aller, Dr Agata Butryn (both

Diamond Light source), and Gabriel Leen (PolyPico Technologies Ltd) with support from Dr Allen Orville (Diamond Light Source) controlling the Poly Pico. Data collection at SACLA was supported by Dr Shigeki Owada, Dr Kensuke Tono, and Dr Rie Tanaka (all SACLA). Data collection at LCLS was supported by Dr Alex Batyuk, Dr Franklin Fuller, and Dr Roberto Alonso-Mori (all LCLS). Data processing was done by Dr Aaron Brewster, Dr Asmit Bhowmick, and Dr Daniel Paley supervised by Dr Nicholas N. Sauter (all Lawrence Berkeley National Laboratory).

Data injection and mixing was performed according to reported procedures[26,27]. In short, microcrystal slurry was loaded into a Hamilton syringe, which was rotated during the whole course of the data collection to prevent crystal settling. From the syringe the slurry was fed into the ADE, from which ~3 nl sized droplets of crystal slurry were deposited to the Kapton conveyer belt at a frequency of 30 Hz, which was synchronised to the XFEL master clock. A piezoelectric injector (PEI, PolyPico Technologies, Ireland, equipped with a disposable cartridge which was refilled using a second syringe pump) was used to deposit bursts of ~120 pl droplets of ligand solutions on the conveyer belt, synchronised to the ADE droplets. A camera was used to visually inspect the number of drops generated by the PEI that merged with the crystal slurry drop. The PEI was installed at a fixed position, and soak times of the ligands with the microcrystals were varied solely by changing the speed of the conveyer belt.

Data were processed with hit-finding using Cheetah[51], followed by data reduction with cctbx.xfel[28,47,50] and indexing with dials.stills_process[46]. Data were merged using cxi.merge[28,47,50] with the fixed-target room temperature structure of $AmpC_{EC}$ in the phosphate condition used as the reference model.

6.7.2. Data analysis

Structures were solved via molecular replacement with Phaser[52] using reported structures of $AmpC_{EC}$ in the phosphate condition (PDB: 2BLS[36]) and OXA-48 (PDB: 4S2P[53]) as starting models. Alternating cycles of refinement with phenix.refine[54] and manual model building in Coot[55] were performed until R_{work} and R_{free} converged.

6.7. References

1. Moffat, K.; Henderson, R. Freeze trapping of reaction intermediates. *Curr. Opin. Struct. Biol.* **1995**, *5*, 656-663.
2. Stoddard, B.L. Trapping Reaction Intermediates in Macromolecular Crystals for Structural Analyses. *Methods* **2001**, *24*, 125-138.
3. Moffat, K. Time-Resolved Crystallography. *Acta Crystallogr. A* **1998**, *54*, 833-841.
4. Weik, M.; Colletier, J.-P. Temperature-dependent macromolecular X-ray crystallography. *Acta Crystallogr. D* **2010**, *66*, 437-446.

5. Moffat, K. Time-Resolved Biochemical Crystallography: A Mechanistic Perspective. *Chem. Rev.* **2001**, *101*, 1569-1582.
6. Barman, T.E.; Bellamy, S.R.W.; Gutfreund, H.; Halford, S.E.; Lionne, C. The identification of chemical intermediates in enzyme catalysis by the rapid quench-flow technique. *Cell. Mol. Life Sci.* **2006**, *63*, 2571-2583.
7. Markwick, P.R.L.; Malliavin, T.; Nilges, M. Structural Biology by NMR: Structure, Dynamics, and Interactions. *PLoS Comput. Biol.* **2008**, *4*, e1000168.
8. Brosey, C.A.; Tainer, J.A. Evolving SAXS versatility: solution X-ray scattering for macromolecular architecture, functional landscapes, and integrative structural biology. *Curr. Opin. Struct. Biol.* **2019**, *58*, 197-213.
9. Orville, A.M. Recent results in time resolved serial femtosecond crystallography at XFELs. *Curr. Opin. Struct. Biol.* **2020**, *65*, 193-208.
10. Šrajer, V.; Schmidt, M. Watching proteins function with time-resolved x-ray crystallography. *J. Phys. D: Appl. Phys.* **2017**, *50*, 373001.
11. Pearson, A.R.; Mehrabi, P. Serial synchrotron crystallography for time-resolved structural biology. *Curr. Opin. Struct. Biol.* **2020**, *65*, 168-174.
12. Rodgers, D.W. Cryocrystallography. *Structure* **1994**, *2*, 1135-1140.
13. Garman, E. Radiation damage in macromolecular crystallography: what is it and why should we care? *Acta Crystallogr. D* **2010**, *66*, 339-351.
14. Wolfenden, R.; Snider, M.J. The Depth of Chemical Time and the Power of Enzymes as Catalysts. *Acc. Chem. Res.* **2001**, *34*, 938-945.
15. Spence, J. XFELs for structure and dynamics in biology. *IUCrJ* **2017**, *4*, 322-339.
16. Stan, C.A.; Milathianaki, D.; Laksmono, H., et al. Liquid explosions induced by X-ray laser pulses. *Nat. Phys.* **2016**, *12*, 966-971.
17. Schmidt, M. Mix and Inject: Reaction Initiation by Diffusion for Time-Resolved Macromolecular Crystallography. *Adv. Condens. Matter Phys.* **2013**, *2013*, 167276.
18. Cheng, R.K. Towards an Optimal Sample Delivery Method for Serial Crystallography at XFEL. *Crystals* **2020**, *10*, 215.
19. Mehrabi, P.; Schulz, E.C.; Agthe, M., et al. Liquid application method for time-resolved analyses by serial synchrotron crystallography. *Nat. Methods* **2019**, *16*, 979-982.
20. Weierstall, U. Liquid sample delivery techniques for serial femtosecond crystallography. *Philos. Trans. R. Soc. B* **2014**, *369*, 20130337.
21. Oberthuer, D.; Knoška, J.; Wiedorn, M.O., et al. Double-flow focused liquid injector for efficient serial femtosecond crystallography. *Sci. Rep.* **2017**, *7*, 44628.
22. Weierstall, U.; James, D.; Wang, C., et al. Lipidic cubic phase injector facilitates membrane protein serial femtosecond crystallography. *Nat. Commun.* **2014**, *5*, 3309.
23. Sugahara, M.; Mizohata, E.; Nango, E., et al. Grease matrix as a versatile carrier of proteins for serial crystallography. *Nat. Methods* **2015**, *12*, 61-63.
24. Owen, R.L.; Axford, D.; Sherrell, D.A.; Kuo, A.; Ernst, O.P.; Schulz, E.C.; Miller, R.J.D.; Mueller-Werkmeister, H.M. Low-dose fixed-target serial synchrotron crystallography. *Acta Crystallogr. D* **2017**, *73*, 373-378.
25. Ebrahim, A.; Appleby, M.V.; Axford, D.; Beale, J.H.; Moreno-Chicano, T.; Sherrell, D.A.; Strange, R.W.; Hough, M.A.; Owen, R.L. Resolving polymorphs and radiation-driven effects in microcrystals using fixed-target serial synchrotron crystallography. *Acta Crystallogr. D* **2019**, *75*, 151 - 159.
26. Fuller, F.D.; Gul, S.; Chatterjee, R., et al. Drop-on-demand sample delivery for studying biocatalysts in action at X-ray free-electron lasers. *Nat. Methods* **2017**, *14*, 443-449.
27. Butryn, A.; Simon, P.S.; Aller, P., et al. An on-demand, drop-on-drop method for studying enzyme catalysis by serial crystallography. *Nat. Commun.* **2021**, *12*, 4461.
28. Kern, J.; Chatterjee, R.; Young, I.D., et al. Structures of the intermediates of Kok's photosynthetic water oxidation clock. *Nature* **2018**, *563*, 421-425.
29. Rabe, P.; Kamps, J.J.A.G.; Sutherlin, K.D., et al. X-ray free-electron laser studies reveal correlated motion during isopenicillin *N* synthase catalysis. *Sci. Adv.* **2021**, *7*, eabh0250.

30. Beadle, B.M.; Trehan, I.; Focia, P.J.; Shoichet, B.K. Structural Milestones in the Reaction Pathway of an Amide Hydrolase: Substrate, Acyl, and Product Complexes of Cephalothin with AmpC β-Lactamase. *Structure* **2002**, *10*, 413-424.
31. Rodkey, E.A.; Drawz, S.M.; Sampson, J.M.; Bethel, C.R.; Bonomo, R.A.; van den Akker, F. Crystal Structure of a Preacylation Complex of the β-Lactamase Inhibitor Sulbactam Bound to a Sulfenamide Bond-Containing Thiol-β-lactamase. *J. Am. Chem. Soc.* **2012**, *134*, 16798-16804.
32. Olmos, J.L.; Pandey, S.; Martin-Garcia, J.M., et al. Enzyme intermediates captured "on the fly" by mix-and-inject serial crystallography. *BMC Biol.* **2018**, *16*, 59.
33. Pandey, S.; Calvey, G.; Katz, A.M., et al. Observation of substrate diffusion and ligand binding in enzyme crystals using high-repetition-rate mix-and-inject serial crystallography. *IUCrJ* **2021**, *8*, 878-895.
34. Wiedorn, M.O.; Oberthür, D.; Bean, R., et al. Megahertz serial crystallography. *Nat. Commun.* **2018**, *9*, 4025.
35. van Groesen, E.; Lohans, C.T.; Brem, J.; Aertker, K.M.J.; Claridge, T.D.W.; Schofield, C.J. ^{19}F NMR Monitoring of Reversible Protein Post-Translational Modifications: Class D β-Lactamase Carbamylation and Inhibition. *Chem. Eur. J.* **2019**, *25*, 11837-11841.
36. Usher, K.C.; Blaszczak, L.C.; Weston, G.S.; Shoichet, B.K.; Remington, S.J. Three-Dimensional Structure of AmpC β-Lactamase from *Escherichia coli* Bound to a Transition-State Analogue: Possible Implications for the Oxyanion Hypothesis and for Inhibitor Design. *Biochemistry* **1998**, *37*, 16082-16092.
37. Powers, R.A.; Shoichet, B.K. Structure-Based Approach for Binding Site Identification on AmpC β-Lactamase. *J. Med. Chem.* **2002**, *45*, 3222-3234.
38. Powers, R.A.; Caselli, E.; Focia, P.J.; Prati, F.; Shoichet, B.K. Structures of Ceftazidime and Its Transition-State Analogue in Complex with AmpC β-Lactamase: Implications for Resistance Mutations and Inhibitor Design. *Biochemistry* **2001**, *40*, 9207-9214.
39. Liebschner, D.; Afonine, P.V.; Moriarty, N.W.; Poon, B.K.; Sobolev, O.V.; Terwilliger, T.C.; Adams, P.D. Polder maps: improving OMIT maps by excluding bulk solvent. *Acta Crystallogr. D* **2017**, *73*, 148-157.
40. Krajnc, A.; Brem, J.; Hinchliffe, P., et al. Bicyclic Boronate VNRX-5133 Inhibits Metallo- and Serine-β-Lactamases. *J. Med. Chem.* **2019**, *62*, 8544-8556.
41. Golemi, D.; Maveyraud, L.; Vakulenko, S.; Samama, J.-P.; Mobashery, S. Critical involvement of a carbamylated lysine in catalytic function of class D β-lactamases. *Proc. Natl. Acad. Sci. U. S. A.* **2001**, *98*, 14280-14285.
42. Sanchez-Weatherby, J.; Sandy, J.; Mikolajek, H.; Lobley, C.M.C.; Mazzorana, M.; Kelly, J.; Preece, G.; Littlewood, R.; Sorensen, T.L.-M. VMXi: a fully automated, fully remote, high-flux in situ macromolecular crystallography beamline. *J. Synchrotron Radiat.* **2019**, *26*, 291-301.
43. Schulz, E.C.; Mehrabi, P.; Müller-Werkmeister, H.M., et al. The hit-and-return system enables efficient time-resolved serial synchrotron crystallography. *Nat. Methods* **2018**, *15*, 901-904.
44. Tosha, T.; Nomura, T.; Nishida, T., et al. Capturing an initial intermediate during the P450nor enzymatic reaction using time-resolved XFEL crystallography and caged-substrate. *Nat. Commun.* **2017**, *8*, 1585.
45. Winter, G. xia2: an expert system for macromolecular crystallography data reduction. *J. Appl. Crystallogr.* **2010**, *43*, 186-190.
46. Winter, G.; Waterman, D.G.; Parkhurst, J.M., et al. DIALS: implementation and evaluation of a new integration package. *Acta Crystallogr. D* **2018**, *74*, 85-97.
47. Brewster, A.S.; Waterman, D.G.; Parkhurst, J.M., et al. Improving signal strength in serial crystallography with DIALS geometry refinement. *Acta Crystallogr. D* **2018**, *74*, 877-894.
48. Hattne, J.; Echols, N.; Tran, R., et al. Accurate macromolecular structures using minimal measurements from X-ray free-electron lasers. *Nat. Methods* **2014**, *11*, 545-548.

49. Uervirojnangkoorn, M.; Zeldin, O.B.; Lyubimov, A.Y.; Hattne, J.; Brewster, A.S.; Sauter, N.K.; Brunger, A.T.; Weis, W.I. Enabling X-ray free electron laser crystallography for challenging biological systems from a limited number of crystals. *eLife* **2015**, *4*, e05421.
50. Sauter, N. XFEL diffraction: developing processing methods to optimize data quality. *J. Synchrotron Radiat.* **2015**, *22*, 239-248.
51. Barty, A.; Kirian, R.A.; Maia, F.R.N.C.; Hantke, M.; Yoon, C.H.; White, T.A.; Chapman, H. Cheetah: software for high-throughput reduction and analysis of serial femtosecond X-ray diffraction data. *J. Appl. Crystallogr.* **2014**, *47*, 1118-1131.
52. McCoy, A.J.; Grosse-Kunstleve, R.W.; Adams, P.D.; Winn, M.D.; Storoni, L.C.; Read, R.J. Phaser crystallographic software. *J. Appl. Crystallogr.* **2007**, *40*, 658-674.
53. King, D.T.; King, A.M.; Lal, S.M.; Wright, G.D.; Strynadka, N.C.J. Molecular Mechanism of Avibactam-Mediated β-Lactamase Inhibition. *ACS Infect. Dis.* **2015**, *1*, 175-184.
54. Adams, P.D.; Grosse-Kunstleve, R.W.; Hung, L.W., et al. PHENIX: building new software for automated crystallographic structure determination. *Acta Crystallogr. D* **2002**, *58*, 1948-1954.
55. Emsley, P.; Lohkamp, B.; Scott, W.G.; Cowtan, K. Features and development of Coot. *Acta Crystallogr. D* **2010**, *66*, 486-501.

Chapter 7

Summary and Conclusions

Contents

7.1. $AmpC_{EC}$ inhibition by clinically relevant β-lactamase inhibitors 213
7.2. $AmpC_{EC}$ interactions with β-lactam antibiotics 214
7.3. Serial crystallography approaches to study $AmpC_{EC}$ 215
7.4. Conclusions.....216
7.5. References.....216

The discovery of widely useful antibiotics in the 20th century revolutionised treatment of infections and enabled one of the cornerstones of modern medicine[1]. Today antimicrobial resistance is arguably one of the major challenges to global health in the 21st century[2]. Due to their excellent potency against a wide range of pathogens, combined with low toxicity, β-lactam antibiotics remain the most important class of antibiotics in clinical use[3]. However, resistance to β-lactams is growing, predominantly through β-lactamase catalysed hydrolysis[4].

Escherichia coli is one the most common pathogens causing infections and is the leading pathogen for deaths associated with resistance[2]. Most *E. coli* have a chromosomally encoded class C AmpC serine β-lactamase ($AmpC_{EC}$), which under normal conditions is produced at low levels, but production may be increased drastically on mutations in the promoter or attenuator regions[5,6]. Hyperproduction of $AmpC_{EC}$ then leads to β-lactam resistance in pathogenic *E. coli*[7].

The work presented in this thesis aimed to characterise $AmpC_{EC}$ using a range of biophysical and biochemical techniques to study both $AmpC_{EC}$ catalysis and inhibition.

7.1. $AmpC_{EC}$ inhibition by clinically relevant β-lactamase inhibitors

One of the most successful strategies employed to combat antimicrobial resistance conferred by β-lactamases is the co-administration of a β-lactam with a β-lactamase inhibitor[8]. In Chapters 2-4 studies on the inhibition of $AmpC_{EC}$ by all major classes of currently clinically relevant β-lactamases are described. All these inhibitors act by covalent reaction with the active site nucleophilic Ser residue.

Chapter 2 focuses on describing work on penam sulfones (including sulbactam, tazobactam, and the more recently introduced enmetazobactam) and clavulanic acid, which were the first serine β-lactamase inhibitors (SBLi) to be used in medical treatment and which remain the most commonly used. All of these SBLi contain a β-lactam ring and are proposed to inhibit SBLs via formation of transiently stable acyl-enzyme species resulting from substantial scaffold fragmentation of the enzyme-bound inhibitor species[8]. In agreement with previous studies[8], $AmpC_{EC}$ inhibition by these compounds is much weaker than for the class A SBL TEM-116 and the class D SBL OXA-10. However, by contrast with previous studies, the results reveal that penam sulfone inhibition of $AmpC_{EC}$, as well as TEM-116 and OXA-10, involves transiently stable species with the full mass of the inhibitors (likely *trans*-enamine species resulting from opening of the oxidised thiazolidine ring), and which do not involve the reported scaffold fragmentation. Instead, the results shown that scaffold fragmentation is induced under the acidic conditions encountered during established and widely used LC-MS based analysis. On

prolonged reaction of TEM-116 and OXA-10 with an excess of the penam sulfones dehydration of the nucleophilic Ser residue was observed, together with formation of a previously unobserved lysinoalanine crosslink at the SBL active sites. These observations are of interest as they result in irreversible SBL inhibition. While generation of these species is not efficient enough with the currently available inhibitors to be biologically relevant, they suggest scope for the optimisation of penam sulfones for irreversible SBL inhibition.

The results presented in Chapter 3 show, by contrast with the β-lactam based inhibitors, potent inhibition of AmpC$_{EC}$ by the diazabicyclooctane SBLis avibactam, relebactam, nacubactam, and zidebactam, which have a range of different C2 amido side chains. SBL inhibition by DBOs proceeds via reversible covalent reaction with the nucleophilic Ser residues leading to carbamoyl-enzyme complexes[9]. The results show that the nature of the C2 DBO amido sidechain can impact on both the carbamoylation- and decarbamoylation rates of the equilibrium reaction, with zidebactam showing ~ 10-fold increased reaction rates for both processes compared to the other DBOs. Protein observed SPE-MS studies suggests that this is likely due to improved stabilisation of the tetrahedral intermediate involved in both carbamoylation- and decarbamoylation with zidebactam. The resulting improved potency of zidebactam against AmpC$_{EC}$ thus likely reflects a kinetic effect rather than improved thermodynamic stabilisation of the zidebactam derived AmpC$_{EC}$-carbamoyl complex

Studies on AmpC$_{EC}$ inhibition by bicyclic boronates, including the clinically used taniborbactam, described in Chapter 4 show similarly good potency as observed with the DBOs. Structural studies on AmpC$_{EC}$ interactions with bicyclic boronates further support inhibition via formation of covalent complexes mimicking the tetrahedral intermediate common to both SBL and MBL catalysis. Next to the bicyclic form of taniborbactam observed at the AmpC$_{EC}$ active site, a second molecule of the inhibitor in a tricylic form was observed crystallographically, non-covalently bonded to the surface of the β-lactamase. This is of interest, as structural comparison suggests that this tricyclic form likely cannot contribute towards inhibition of AmpC$_{EC}$ and other SBLs but may play a role in the inhibition of certain MBLs.

7.2. AmpC$_{EC}$ interactions with β-lactam antibiotics

The structural work on interactions of AmpC$_{EC}$ with β-lactam antibiotics described in Chapter 5 demonstrates substantial conformational changes of the acyl-enzyme and product complex induced by relatively small changes in the β-lactam core.

Crystal structures of AmpC$_{EC}$ reacted with the penicillin ticarcillin and it's 6-OMe analogue temocillin reveal substantial conformational changes of the AmpC$_{EC}$ bonded acyl-enzyme species, potentially rationalising the increased stability towards AmpC$_{EC}$ catalysed hydrolysis

of temocillin compared to ticarcillin. The results further imply preferential hydrolysis of the (*S*)-side chain epimers of the carboxypenicillins compared to the respective (*R*)-epimers, which is of interest especially due to the equally improved antimicrobial activity of the (*R*)-epimer compared to the (*S*)-epimer[10]. Structural studies with faropenem and panipenem show similar conformational differences between penem and carbapenem derived acyl-enzyme species on reaction with AmpC$_{EC}$.

Further studies will be needed to establish the relevance of the crystallographically observed conformation differences in acyl-enzyme and enzyme-product complexes in solution.

7.3. Serial crystallography approaches to study AmpC$_{EC}$

Time-resolved serial crystallography is a new and promising tool to study the structural basis of enzyme catalysis at a global macromolecular level[11]. However, the results presented in Chapter 6 highlight challenges in establishing suitable micro-crystallisation conditions for such experiments, as especially evident in the crystallisation trials with the class D SBL OXA-48.

A suitable crystallisation system was successfully established for AmpC$_{EC}$. The microcrystals were used for time-resolved serial crystallography studies on reaction of AmpC$_{EC}$ with the diazabicyclooctane SBLi avibactam. Binding of the inhibitor was demonstrated in the sub-second timeframe (700 ms) using a drop-on-drop approach. However, while the observed ms time-frame for the diffusion of the SBLi is a substantial improvement compared to previous studies using the drop-on-drop methodology[12], it is still too slow to resolve avibactam binding in the pre-covalent complex as evident by electron density indicating partial (10%) covalent modification of the nucleophilic Ser after incubation of the AmpC$_{EC}$ crystal slurry with avibactam for 100 ms. However, the studies do reveal potential correlated motions of residues 288-296 on reaction of AmpC$_{EC}$ with avibactam. Such motions of a relatively large loop (which is in close proximity to the AmpC$_{EC}$ active site) may be slower than the covalent reaction and thus more attainable to time-resolved studies.

Further studies are needed to establish a potential biological function of the loop-re-arrangement. Efforts should also be directed towards exploring alternative sample-deliver and mixing methodologies such as drop-on-fixed-target[13] and liquid jets[14], which may facilitate faster diffusion of the SBLi and β-lactam antibiotics. Alternatively, modification of the carboxylic acid of β-lactam antibiotics with photocleavable protection groups could be used to allow pre-saturation of the crystal slurry with the substrate, followed by homogeneous activation of the reaction via irradiation.

7.4. Conclusions

Overall, the results give detailed insight into the mechanisms and structural basis of interactions of $AmpC_{EC}$, a clinically relevant SBL, with all presently used classes of clinically relevant SBLi, as well as different β-lactam antibiotics. The results may inform structure activity relationship guided efforts to design improved SBLi and more hydrolytically stable β-lactam antibiotics to counteract antimicrobial resistance.

7.5. References

1. White, A.R.; Blaser, M.; Carrs, O.; Cassell, G.; Fishman, N.; Guidos, R.; Levy, S.; Powers, J.; Norrby, R.; Tillotson, G., et al. Effective antibacterials: at what cost? The economics of antibacterial resistance and its control. *J. Antimicrob. Chemother.* **2011**, *66*, 1948-1953.
2. Murray, C.J.L.; Ikuta, K.S.; Sharara, F.; Swetschinski, L.; Robles Aguilar, G.; Gray, A.; Han, C.; Bisignano, C.; Rao, P.; Wool, E., et al. Global burden of bacterial antimicrobial resistance in 2019: a systematic analysis. *Lancet* **2022**, *399*, 629-655.
3. Bush, K.; Bradford, P.A. β-Lactams and β-Lactamase Inhibitors: An Overview. *Cold Spring Harb. Perspect. Med.* **2016**, *6*, a025247.
4. Bush, K. Past and Present Perspectives on β-Lactamases. *Antimicrob. Agents Chemother.* **2018**, *62*, e01076-01018.
5. Jaurin, B.; Grundström, T.; Edlund, T.; Normark, S. The *E. coli* β-lactamase attenuator mediates growth rate-dependent regulation. *Nature* **1981**, *290*, 221-225.
6. Nelson, E.C.; Elisha, B.G. Molecular Basis of AmpC Hyperproduction in Clinical Isolates of *Escherichia coli*. *Antimicrob. Agents Chemother.* **1999**, *43*, 957-959.
7. Jacoby, G.A. AmpC β-Lactamases. *Clin. Microbiol. Rev.* **2009**, *22*, 161-182.
8. Drawz, S.M.; Bonomo, R.A. Three decades of β-lactamase inhibitors. *Clin. Microbiol. Rev.* **2010**, *23*, 160-201.
9. Ehmann, D.E.; Jahic, H.; Ross, P.L.; Gu, R.F.; Hu, J.; Kern, G.; Walkup, G.K.; Fisher, S.L. Avibactam is a covalent, reversible, non-β-lactam β-lactamase inhibitor. *Proc. Natl. Acad. Sci. U. S. A.* **2012**, *109*, 11663-11668.
10. White, A.R.; Cooper, C.E.; Griffin, K.E.; Slocombe, B. Antibacterial activity of resolved temocillin epimers. *J. Antimicrob. Chemother.* **1986**, *18*, 335-343.
11. Orville, A.M. Recent results in time resolved serial femtosecond crystallography at XFELs. *Curr. Opin. Struct. Biol.* **2020**, *65*, 193-208.
12. Butryn, A.; Simon, P.S.; Aller, P.; Hinchliffe, P.; Massad, R.N.; Leen, G.; Tooke, C.L.; Bogacz, I.; Kim, I.-S.; Bhowmick, A., et al. An on-demand, drop-on-drop method for studying enzyme catalysis by serial crystallography. *Nat. Commun.* **2021**, *12*, 4461.
13. Mehrabi, P.; Schulz, E.C.; Agthe, M.; Horrell, S.; Bourenkov, G.; von Stetten, D.; Leimkohl, J.-P.; Schikora, H.; Schneider, T.R.; Pearson, A.R., et al. Liquid application method for time-resolved analyses by serial synchrotron crystallography. *Nat. Methods* **2019**, *16*, 979-982.
14. Pandey, S.; Calvey, G.; Katz, A.M.; Malla, T.N.; Koua, F.H.M.; Martin-Garcia, J.M.; Poudyal, I.; Yang, J.-H.; Vakili, M.; Yefanov, O., et al. Observation of substrate diffusion and ligand binding in enzyme crystals using high-repetition-rate mix-and-inject serial crystallography. *IUCrJ* **2021**, *8*, 878-895.

Appendix

Contents

Appendix I – Summary of non-β-lactamase related work 219
8.1. Structural studies on the *Escherichia coli* AlkB DNA demethylase....219
8.2. Structural and functional studies on the phytanoyl-CoA hydroxylase....222
8.3. Structural studies on the *Petersilium crispum* phenylalanine ammonia-lyase 223
8.4. Materials and Methods 224
8.4.1. Materials 224
8.4.2. Enzyme production and purification....224
8.4.3. RapidFire MS based PAHX activity assay 225
8.4.4. X-ray Crystallography....226
8.4.4.1. Crystallisation of AlkB....226
8.4.4.1.1. Generation of apo AlkB 226
8.4.4.1.2. Crystallisation....227
8.4.4.1.3. Data collection, processing, and analysis....228
8.4.4.2. Crystallisation of PAHX 228
8.4.4.2.1. Generation of apo PAHX....228
8.4.4.2.2. Thermal shift assays 228
8.4.4.2.3. Anaerobic PAHX crystallisation 229
8.4.4.2.4. Aerobic PAHX crystallisation....229
8.4.4.2.5. Data collection, processing, and analysis....229
8.4.4.3. Crystallisation of pcPAL 230
Appendix II – General Methods....231
9.1. General 231
9.2. Microbiology 231
9.2.1. Bacterial Growth Media 231
9.2.2. Plasmid DNA isolation....231
9.2.3. Agarose Gel Electrophoresis....231
9.3. Protein Production and Purification 232
9.3.1. Preparation of competent cells 232
9.3.2. Transformation....232
9.3.3. Starter cultures....232
9.3.4. Glycerol Stocks 232
9.3.5. Bacterial growth and expression 232
9.3.6. Purification 233
9.3.7. SDS-PAGE 233
Appendix III – Supplementary Information for Chapter 2 234
Appendix IV – Supplementary Information for Chapter 3 251
Appendix V – Sequences of protein constructs....252
References 254

Appendix I – Summary of non-β-lactamase related work

In addition to work on β-lactamases, I carried out work on other projects during the course of the DPhil research, the results of which are summarised below.

8.1. Structural studies on the *Escherichia coli* AlkB DNA demethylase

Work on AlkB was carried out in conjunction with Dr Patrick Rabe (University of Oxford) who advised on experimental design and collaborated on large scale protein production, the UK XFEL hub at Diamond Light Source (DLS), led by Dr Allen M. Orville and I24 beamline staff led by Dr Robin Owen (DSL), who conducted SSX experiments, the group of Dr Jan Kern (Lawrence Berkely National Laboratory, LBNL) who conducted ADE tr-SFX experiments and the MX beamline scientists at the Linac Coherent Light Source (LCLS) and Pohang Accelerator Laboratory X-ray Free Electron Laser (PAL-XFEL). Processing of serial crystallography data was done by members of the UK XFEL hub and the research group of Dr Nicholas K. Sauter (LBNL). The work builds on previous work conducted by Dr Thomas M. Leissing (University of Oxford)[1]. Part of this work has been reported in the academic literature[2].

The *Escherichia coli* protein AlkB is a mononuclear iron (II), 2-oxoglutarate (2OG), and dioxygen dependent oxygenase that catalyses the removal of DNA alkylation damage through oxidative demethylation[3]. AlkB is relatively promiscuous, catalysing the oxidation of a range of methyl adducts and larger alkylation lesions from all endocyclic positions on both purine and pyrimidine bases, although with varying efficiency[4]. The exact mechanism of AlkB is still debated. Like with other 2OG oxygenases, the reaction is proposed to proceed via oxygen activation to give a reactive Fe(IV)═O intermediate[5]. Structural studies on AlkB-substrate complexes under anaerobic conditions have shown the 2OG C1 carboxylate to coordinate the active site Fe(II) in close proximity to the substrate, with an apparently available Fe(II) coordination sphere for O_2 binding distal to the substrate and occupied by a water molecule[4,6]. To position a potential reactive oxo-ferryl intermediate adjacent to the oxidised substrate C-H bond thus requires either a re-arrangement of the 2OG carboxylate prior to O_2 binding, a “ferryl flip” following the formation of the oxo-ferryl species, or a variation of the consensus mechanism[7]. This research aimed to study the mechanism of AlkB catalysis using reaction intermediate mimics and time-resolved serial crystallography.

In total ~ 800 mg of recombinant AlkB was produced in *E. coli* and purified according to reported procedures[8]. Initial crystallisation of the AlkB:Fe^{2+}:2OG:T-1-meA-T complex was achieved under anaerobic conditions according to reported procedures[1,6]. By contrast with previous reports[6], but in agreement with previous work in the group[1], AlkB crystallised with low symmetry (space group *P*1), but crystals diffracted to very high resolution (max. 1.0 Å).

Exposure of the crystals to molecular oxygen led to disappearance of the substrate from the AlkB active site after presumed turn-over, as previously reported[1,6]. A crystal structure (1.20 Å resolution) obtained after exposing anaerobically grown crystals of the AlkB:Fe^{2+}:2OG:T-1-meA-T complex with nitric oxide (1000 ppm NO for 45 min) to imitate oxygen binding gave evidence for binding of nitric oxide distal to the substrate with replacement of the Fe(II) ligating water molecule. This observation contrasts with previous studies on NO binding to clavaminate synthase, another 2OG oxygenase, which showed rearrangement of the coordination position of the 2OG C1 carboxylate by NO[9]. A structure obtained from co-crystallisation of AlkB with vanadium oxide, succinate, and the substrate (imitating the Fe(IV)═O intermediate[10], 1.10 Å resolution) showed orientation of the vanadium oxide oxygen in close proximity to the substrate C-H bond. Interestingly, on incubation of anaerobic crystals with NO, in addition to NO binding at the active site, rearrangement of residues 70-76 was observed (compared to the anaerobic ground state); these residues are in close proximity of the AlkB active site. The rearrangement (which is not observed on completed oxygen induced turn-over of the substrate) may indicate correlated motion within the AlkB molecule, similar to that recently observed on oxygen binding to the structurally related isopenicillin N synthase (IPNS) during catalysis[11].

Micro-crystallisation conditions of AlkB were established (see Materials and Methods) to study the AlkB:Fe^{2+}:2OG:T-1-meA-T complex at room temperature using serial crystallography. Structures of AlkB were obtained using fixed-target serial crystallography (ft-SX) at DLS, both under aerobic (1.90 Å resolution) and anaerobic (1.75 Å resolution) conditions. These showed little difference to the structures obtained under cryogenic conditions from single crystals. The microcrystal slurries were then used for time-resolved serial femtosecond crystallography (tr-SFX) experiments at LCLS, using the ADE tape-drive system (see Chapter 6) and reaction initiation via incubation in an oxygen enriched atmosphere as previously described[11]. In total five room temperature structures of AlkB (1.4-1.5 Å resolution) were obtained with reaction times varying from 0-10 s). While no reaction was observed within 0.4-4 s of incubation with oxygen, apparently full turnover was observed on prolonged reaction for 10-30 s, suggesting oxygen diffusion to the AlkB active site in the microcrystal slurry and enzymatic reaction proceed within a timeframe of 4-10 s. Reaction resulted in substantial changes in the *P*1 unit cell (β: 78.3° and 76.9°, for unreacted and reacted complexes, respectively).

The reaction time was substantially slower than observed with other samples[11], potentially due to the high viscosity of the AlkB sample (25% (*w*/*v*) PEG 3350, 5% (*v*/*v*) glycerol, see Materials and Methods) which may hamper diffusion of oxygen. Thus, the crystallisation system was optimised for lower viscosity. Using cross-seeding, microcrystal slurries were obtained in precipitant solution lacking viscous components (but otherwise equalling the

previous conditions, see Materials and Methods), with crystal morphology, symmetry, and diffraction unaffected. When these slurries were used in ADE tape-drive experiments at LCLS, preliminary data from two partial data sets (complete to 2.1-2.5 Å resolution) suggests that reactions are manifest within 2-4 s of incubation with oxygen, as evident in changes in the electron density maps in the iron-coordination sphere indicate partial decarboxylation of 2OG after 2s and partial reorientation of the generated succinate after 4s. Further, changes in the unit-cell distribution were apparent, showing ~30% of crystals with the reduced β angle observed on reaction with oxygen. Notably, the structure obtained on 4 s incubation with O_2 showed increased B-factors for residues 70-76 (compared to a structure obtained under anaerobic conditions), suggesting potential conformational changes on O_2 binding to AlkB, similar to those observed on binding of the O_2 surrogate NO.

In the structure of the AlkB:VO:SIN:T-1-meA-T complex obtained from single crystals under cryogenic conditions (see above), the observed vanadium oxide bond length was significantly longer (~ 1.8 Å) than expected for the vanadyl double bond (1.58–1.63[12]). This is in agreement with previously reported X-ray irradiation induced photoreduction of the vanadyl species to an oxidation state ≤ +3[10]. To study the AlkB:VO complex under radiation damage reduced conditions, serial crystallography was pursued. The impact of X-ray irradiation on the VO-bond length was studied in ft-SX experiments at DLS and PAL-XFEL. In addition to studies on the AlkB:VO:SIN:T-1-meA-T complex, AlkB:VO complexes with thiol containing SIN and 2OG analogues were studied to investigate potential impact of the coordinating ligands on VO reduction. Data analysis for the results of these experiments is ongoing.

During the studies on AlkB, an unusual blue colour of AlkB crystal was observed on multiple occasions; anaerobically grown colourless crystals turned blue on prolonged exposure to oxygen. The blue appearance of AlkB has previously been suggested to result from self-hydroxylation of Tyr178 in the absence of substrate, leading to inactivation of AlkB[13], but in some cases blue AlkB crystals were also observed under anaerobic conditions. In my work, no additional electron density for such hydroxylation was evident in the electron density maps obtained from blue AlkB crystals. While studies were occasionally hindered by inactive AlkB complexes (both observed with blue and colourless AlkB crystals), the blue microcrystal slurry used in the initial LCLS experiments showed activity of the AlkB complex on incubation with oxygen for 10 s. The origin and potential biological role of “blue AlkB” thus remains unclear.

Overall, the results provide new structural insight into reaction intermediates of AlkB catalysis. Future work should focus on using the new crystallisation conditions to collect data on AlkB catalysis with different substrates, including substrates with deuterated methyl groups employing a potential kinetic isotope effect, on oxygen exposure with a range of different reaction times.

8.2. Structural and functional studies on the phytanoyl-CoA hydroxylase

The work on phytanoyl-CoA hydroxylase was carried out in conjunction with Dr Zhihong Zhang (University of Oxford) who advised on protein production and purification, Dr Anthony Tumber (University of Oxford) who advised on SPE-MS based PAHX activity and inhibition assays, and Dr Jurgen Brem, Dr Thomas Leissing, and Dr Michael McDonough (all University of Oxford) who advised on crystallographic studies.

Phytanoyl-CoA hydroxylase (PAHX) is a clinically relevant human 2OG-oxygenase that catalyses α-hydroxylation of phytanic acid, an essential step in the human metabolism of phytanic acid[14]. Phytanic acid is a product of the metabolism of chlorophyll in ruminants, resulting in an average daily human intake of phytanic acid of about ~ 50-100 mg through the consumption mainly of marine foods, beef and dairy products[15]. Unless treated by diet therapy, inactivation of PAHX leads to the accumulation of this fatty acid and eventually to Refsum's disease, a severe neurological disorder[14,16]. Patients with Refsum's disease suffer multiple complex symptoms, the molecular origins of which are still in part unclear[17]. Over the past decade great efforts have been put into the development of inhibitors of other 2OG oxygenases for clinical applications[18,19]. Most of these inhibitors are 2OG-analogues[18] and therefore could potentially inhibit PAHX. The project aimed to establish a medium-throughput assay to test clinically used 2OG-oxygenase inhibitors for inhibition of PAHX to investigate PAHX-related possible complications of long-term clinical use and to further investigate the mechanistic basis of PAHX catalysis.

Recombinant PAHX with an SenP2 proteinase cleavable *N*-terminal SUMO-His-fusion tag was produced in *E. coli* and purified according to protocols established by Dr Zhihong Zhang (University of Oxford). To study the effect of (potential) clinically relevant 2OG oxygenase inhibitors a new assay was established using solid-phase extraction mass-spectrometry (SPE-MS) to directly monitor phytanoyl-CoA hydroxylation. To validate the assay a small array of sample compounds was screened. The results showed inhibition of PAHX by some clinically used 2OG oxygenase/HIF prolyl hydroxylases (PHD) inhibitors, i.e. Daprodustat[20] (GSK1278863, $pIC_{50} = 5.98 \pm 0.11$) and Roxadustat[21] (FG4592, $pIC_{50} = 5.99 \pm 0.08$), but not by mildronate, an antiischemic drug and 2OG analogue developed for the inhibition of butyrobetaine dehydrogenase which catalyses β-oxidation of fatty acids during carnitine biosynthesis[22]. To investigate potential alternative, physiological relevant, roles of PAHX, acyl-CoA esters structurally related to phytanoyl-CoA were incubated with PAHX. Contrary to the published data[23] no hydroxylation of isovaleryl-CoA (an intermediate of the branched chain amino acid (BCAA) metabolism) was observed under the tested conditions. However, PAHX catalysed hydroxylation was observed with palimitoleoyl-CoA and arachidonoyl-CoA which are intermediates in the metabolism of polyunsaturated fatty acids (PUFAs)[24].

Initial crystallisation of PAHX under anaerobic conditions using previously reported conditions[25] failed to produce higher resolution data than the reported structure (2.50 Å resolution, see Materials and Methods). New crystallisation conditions were identified in a broad screen with PAHX under aerobic conditions in the presence of Mn^{2+} (see Materials and Methods). On optimisation of the crystallisation conditions, a higher resolution structure (2.00 Å resolution, space-group *H*3, 1 molecule per ASU) could be obtained. Interestingly, in this new crystal form the PAHX structure is altered compared to the reported structure, leaving the active site and metal chelation motif impaired. Further studies in solution will be needed to establish potential physiological relevance of this alternative fold.

Overall, the results demonstrate the feasibility of SPE-MS based PAHX assays to study off-target effects of clinically relevant 2OG oxygenase inhibitors by PAHX inhibition and give new insight into the substrate scope of PAHX beyond phytanoyl-CoA. More studies will be needed to investigate potential biological relevance of the apparently different PAHX conformation observed in the crystallographic studies.

8.3. Structural studies on the *Petersilium crispum* phenylalanine ammonia-lyase

The work on phenylalanine ammonia-lyase was carried out in collaboration with the group of Dr László C. Bencze (Babes-Bolyai University), who produced and purified wildtype and mutant pcPAL and conducted biotransformation, kinetic, and preparative scale ammonia addition experiments. Part of the work has been reported in the academic literature[26].

Phenylalanine ammonia-lyases (PALs) catalyse the stereoselective addition of ammonia to cinnamic acid to give phenylalanine, or eliminate ammonia from phenylalanine to give cinnamic acid, depending to the environmental ammonia concentration and pH[27,28]. Engineered PALs are promising biocatalysts to produce optically pure D- and L-phenylalanine derivatives which are used in the synthesis as peptidomimetics e.g. in the synthesis of antimicrobial peptides[27]. The project aimed to provide structural insight into the extended substrate scope of engineered variants of PAL from *Petroselinum crispum* (pcPAL), as well as new mechanistic insight in PAL catalysis through structural studies on PAL in complex with substrate analogues.

Crystallisation conditions for pcPAL were identified in a broad screen, giving crystals diffracting to a maximal resolution of ~1.6 Å. Structures of pcPAL were solved via molecular replacement and contained two molecules in the ASU, with symmetry related molecules completing the catalytic tetramer observed in solution and previous crystallographic studies[29].

A structure of I460V pcPAL in complex with *p*-methoxy cinnamic acid (2.42 Å resolution, PDB: 6RGS) rationalises the enhanced activity of the pcPAL variant towards *p*-substituted cinnamic acid derivatives[26], by showing positioning of the *p*-methoxy group in the additional

cavity created by the I460V substitution. Importantly, the structure is the first structure of any catalytically active PAL with a ring-substituted substrate/product complexed in the active site. Using the same crystallisation condition, further structures of pcPAL variants in complex with substituted cinnamic acid were obtained. Structures of I460V pcPAL in complex with *p*-nitro cinnamic acid (1.95 Å resolution) and *m*-CF_3 cinnamic acid (derived from co-crystallisation with *m*-CF_3-D-Phe, 1.80 Å resolution) give further insight into the structural basis of the reported enhanced substrate scope of I460V pcPAL[26]. A structure of the double mutant F137A/I460V pcPAL in complex with *p*-phenyl cinnamic acid (1.80 Å resolution) rationalised the unexpected high activity towards the substrate through a rearrangement of the aromatic sidechain of Tyr453 (compared to the structure of I460V pcPAL) into the free cavity left by the F137A mutation, resulting in improved hydrophobic interactions with the biphenyl substrate.

Co-crystallisation trials with a range of cinnamic acid analogues gave a crystal structure of I460V pcPAL in complex with *N*-phenyl glycine (1.9 Å resolution). Interestingly, in this structure the complete pcPAL protein appeared highly ordered, including multiple loops (residues 105–127, 332-345, and 550-555) which had not been observed in previous structures, likely due to high mobility. Some of these loops are in close proximity to the pcPAL active site and have a potential role in catalysis. Further studies will be needed to investigate relevance of the ordered conformation of the loops for pcPAL catalysis.

Overall, the results give new insight into cinnamic acid binding to wildtype and engineered pcPAL and will help guide the further development of engineered PALs as biocatalysts for the production of unnatural amino acids.

8.4. Materials and Methods

8.4.1. Materials

The methylated trinucleotide T-1-meA-T was from Keck Oligos Service (Yale University). T-1-d_3(me)A-T was synthesised by Dr Alistair Farley and Dr Afaf El-Sagheer (both University of Oxford) according to reported procedures[30,31]. 4-Mercapto-4-oxobutanoic acid (4SH) was synthesised by Dr Alistair Farley (University of Oxford). Phytanoyl-CoA was from Sigma Aldrich. Isovaleryl-CoA, palimitoleoyl-CoA, and arachidonoyl-CoA were from Insight Biotechnology Ltd. Cinnamic acid and D-phenylalanine derivatives were provided by Dr László C. Bencze (Babes-Bolyai University). *N*-phenyl glycine was from Fluorochem.

8.4.2. Enzyme production and purification

AlkB was produced and purified according to modified reported procedures[8]. AlkB was produced in *E.coli* BL21 (DE3) cells and grown at 37°C in 2TY supplemented with 30 µg ml^{-1}

kanamycin until optical density (OD_{600}) reached ~0.8. The cells were cooled to 15 °C, before protein production was induced for 16 h by addition of 0.2 mM IPTG. Cells were harvested via centrifugation and stored at -80 C. AlkB containing cells were resuspended in 100 mM MES, pH 5.8 (binding buffer). After lysis and centrifugation, the supernatant was loaded onto an SP Sepharose column (100 ml), the column was washed with binding buffer until the UV trace returned to its initial level, and AlkB was eluted in a gradient of 0-1 M NaCl. After concentration the protein was further purified via size exclusion chromatography (SEC) using a Superdex S75 column (300 ml, Amersham Pharmacia Biosciences), pre-equilibrated in 50 mM Tris, pH 7.5, 100 mM NaCl.

PAHX (conjugated to a SUMO-His-tag) was produced in *E. coli* BL21 (DE3) cells. Cells were grown in 2TY supplemented with 30 µg ml^{-1} kanamycin at 37 °C until OD_{600} reached 1.4-1.6. The temperature was then lowered to 27 °C before protein production was induced by addition of IPTG to a final concentration of 0.5 µM, followed by another 3 h of growth at 27 °C. PAHX-SUMO-His containing cells were resuspended in 20 mM Tris pH 7.8, 500 mM NaCl, 40 mM imidazole (binding buffer). The supernatant was loaded onto a 5 ml HisTrap HP column (GE Healthcare) at a flowrate of 1 ml min^{-1}. After complete loading, the column was washed with binding buffer until a stable UV signal was seen (ca. 10 CV), then the protein was eluted in approx. 3 CV of 20 mM Tris pH 7.8, 500 mM NaCl, 500 mM imidazole (elution buffer). Fractions containing protein were pooled and concentrated to 5 ml before exchanging to binding buffer, using PD-10 desalting columns (GE Healthcare) pre-equilibrated with gel filtration buffer (25 mM Tris pH 7.8, 150 mM NaCl). SenP2 proteinase (provided by Dr Zhihong Zhang, University of Oxford) was added in a ratio of 1:1500 and the reaction was left to incubate under constant mixing at 4 °C overnight. The cleaved His-SUMO-Tag was separated from the protein by a reverse His-tag column. The protein was loaded onto the column and the unbound protein fractions were collected. The fractions containing protein were pooled and concentrated. The protein was further purified using a Superdex 75 SEC column (300 ml, Amersham Pharmacia Biosciences).

Wildtype pcPAL and pcPAL mutants were produced and purified by Alina Filip (Babes-Bolyai University) according to reported procedures[32].

8.4.3. RapidFire MS based PAHX activity assay

Initial conditions used for assay optimisation were based on reported UV-based LC PAHX activity assays[33,34], which had to be modified to prevent initially observed rapid hydrolysis of the substrate and to facilitate better ionisation of phytanoyl-CoA. The optimised concentrations for PAHX, substrate, and co-factors are given in Table S1.

Table S1: Assay conditions used for the PAHX screening.

	Final concentration
PAHX	1 µM
Phytanoyl-CoA	10 µM
Guanosine-5'-triphosphate (GTP)	1000 µM
L-ascorbic acid	200 µM
Ferric ammonium sulfate (FAS)	20 µM
2-oxoglutaric acid (2OG)	20 µM
50 mM Tris pH 7.5	

Reactions were initiated by addition of the substrate and samples were quenched by addition of the reported 2OG oxygenase inhibitor[18] 2.4-PDCA (100 µM final concentration). Mass spectra were acquired using either a RapidFire360 (Agilent Technologies) integrated autosampler/solid phase extraction (SPE) system (Agilent Technologies) coupled to an API40000 triple quadrupole mass spectrometer (Applied Biosystems) or a RapidFire365 coupled to an Agilent 6550 Accurate Mass QTOF mass spectrometer (Agilent Technologies). The sample in the reaction buffer was loaded onto a phenyl SPE cartridge (Agilent Technologies) to remove buffer salts, then eluted to the mass spectrometer in 15% water, 85% acetonitrile, 5 mM ammonium formate (buffer A). The cartridge was cleaned by washing with both buffer A and buffer B (5 mM ammonium formate) in between samples. Data was analysed using the RapidFire peak integration software and MassLynx V4.1 (Waters).

8.4.4. X-ray Crystallography

8.4.4.1. Crystallisation of AlkB

8.4.4.1.1. Generation of apo AlkB

To remove co-purified metals from the AlkB sample, the sample was first dialyzed using Slide-A-Lyzer™ Dialysis Cassettes (10 kDa MWCO, Thermo Fisher Scientific) against size exclusion buffer (50 mM Tris, pH 7.5, 100 mM NaCl) supplemented with 10 mM phenantroline and 50 mM EDTA. The sample was dialysed against three swaps of this buffer, twice for 3 h and once overnight. To remove the chelators, the sample was then dialysed against size exclusion buffer suspended over Chelex-100 resin (2 swaps, 3 h each, Bio-Rad).

For protein sample used for time-resolved experiments, residual EDTA was removed using Amicon Ultra Centrifugal filters (10 kDa MWCO) to concentrate the sample to ~20 mg ml^{-1} protein concentration, then diluted 10-fold in size exclusion buffer. The EDTA concentration

was monitored using a chromogenic plate reader assay as reported[35]. Alternate cycles of dilution in size exclusion buffer and concentration via ultracentrifugation filters were performed until no residual EDTA was detected.

8.4.4.1.2. Crystallisation

Anaerobic crystallisation of AlkB was performed within an anaerobic chamber (oxygen concentration ≤ 2 ppm, Belle Technology). Before use all precipitant solutions and plastic consumables were equilibrated under anaerobic conditions for at least 18 h. Protein and substrate solutions as well as co-factors were equilibrated under anaerobic conditions for 30 min prior to use.

Unless stated otherwise, AlkB (461 µM) was incubated with iron (II) ammonium sulfate (576 µM, FAS), 2OG (1 mM) and methylated trinucleotide T-1-meA-T (1 mM) in 50 mM Tris, pH 7.5 at room temperature for 15 min prior to crystallisation to give the protein solution. For co-crystallisation with vanadium oxide, excess metal was used (2.2 mM VO) and succinate or succinate analogous (4.5 mM) were used instead of 2OG.

Macro-crystals were obtained via hanging-drop vapour diffusion technique using pre-greased 24 well Combo Plate (SBS format, Greiner). 4 µl protein solution was mixed with 4 µl precipitant solution (0-25% (w/v) PEG 3350, 0-5% (v/v) glycerol, 200 mM sodium formate) on siliconized plastic-cover slips (Molecular Dimensions) and equilibrated over wells filled with 500 µl precipitant at room temperature. Without micro-seeding crystals appeared within ~7 days using precipitants with high PEG3350 (25% (w/v)) and glycerol (5% (v/v)) content. When micro-seeding was used crystals grew over 48 h, using precipitant solutions with and without PEG and glycerol.

In the batch set-up the protein solution was mixed in a 1:1 ratio with precipitant solution and concentrated seed stock (final concentration: 230 µM AlkB, 288 µM FAS, 500 µM 2OG, 500 µM T-1-meA-T, 0-12.5% (w/v) PEG 3350, 0-2.5% (v/v) glycerol, 10-fold diluted seed stock). The crystallisation solution was mixed carefully, then split into 100 µl aliquots and incubated in 96-well plates, which were sealed (Polyolefin StarSeal, Starlab, UK) and incubated at room temperature without shaking. Microcrystals, with an average size of approximately 5 µm, appeared within 24 h. The wells were combined and left to settle for 6-18 h. Before use, ~80% of the supernatant was removed and the settled crystals were resuspended to give a concentrated microcrystalline slurry.

8.4.4.1.3. Data collection, processing, and analysis

Single crystals were mounted on nylon loops and cryo-cooled and stored in liquid nitrogen. Crystals grown using non-viscous precipitants were briefly transferred into a viscous precipitant solution (25% (w/v) PEG 3350, 5% (v/v) glycerol, 200 mM sodium formate) prior to cryo-cooling. X-ray diffraction data was collected at 100 K at the MX beamlines at Diamond Light Source (DLS) and processed using Xia2[36].

Serial Synchrotron X-ray diffraction experiments under aerobic conditions were conducted at the I24 beamline at DLS as described in Chapter 6. Anaerobic data was collected using a clipless-chip set-up prepared under anaerobic conditions as reported[2]. Serial femtosecond X-ray crystallography (SFX) experiments on the AlkB:VO complexes were conducted at PAL-XFEL using a similar chip-less chip system[37]. Time-resolved SFX experiments on AlkB catalysis were conducted at LCLS using the ADE tape-drive system described in Chapter 6. Reactions were initiated via an oxygen enriched atmosphere as previously reported[11]. Data from serial-experiments were processed as described in Chapter 6.

Structures were solved via molecular replacement with Phaser[38] using a reported structure of AlkB (PDB: 2FDJ[6]) as the starting model. Alternating cycles of refinement with phenix.refine[39] and manual model building in Coot[40] were performed until R_{work} and R_{free} converged.

8.4.4.2. Crystallisation of PAHX

8.4.4.2.1. Generation of apo PAHX

Apo-PAHX was generated using Slide-A-Lyzer™ Dialysis Cassettes (10 kDa MWCO, Thermo Fisher Scientific). The protein solutions were dialysed at 4 °C against 3 swaps of 200 x access volume of buffer supplemented with 20 mM EDTA over 24 h and subsequently against three swaps of 200 x access volume of EDTA-free buffer over 24 h.

8.4.4.2.2. Thermal shift assays

Apo-PAHX (4 µM) was incubated with different additives for 5 min at room temperature before addition of SyproOrange dye (5x concentrated according to manufacturer's definition, Thermo Fisher Scientific) in 96 well white PCR plates (25 µl final volume, StarLabs). Melting point (Tm) values were assessed using a CFX96 Touch™ real-Time PCR Detection System (BIO-RAD). The temperature was increased in steps of 0.2 °C from 20 °C to 95 °C and fluorescence was monitored (excitation at ƛ = 492 nm and emission at ƛ = 610 nm). A reading was taken at each temperature. The Rubic Buffer Screen, Rubic Additive Screen, and Durham pH Screen (Molecular Dimensions) were screened, as well as a range of transition-metal salts.

8.4.4.2.3. Anaerobic PAHX crystallisation

Anaerobic crystallisation of PAHX was performed within an anaerobic chamber (oxygen concentration ≤ 2 ppm, Belle Technologies, UK) according to reported procedures[25]. Before use all precipitant solutions and plastic consumables were equilibrated under anaerobic conditions for at least 18 h. Protein solutions and co-factors were equilibrated under anaerobic conditions for 90 min prior to use. Protein solutions were incubated at 4 °C.

PAHX was buffer exchanged into 25 mM Tris buffer pH 7.8 and concentrated to 6.5 mg/ml. The protein was incubated under anaerobic conditions at 4 °C with 1 mM FAS and 2 mM 2OG for 30 min prior to setting up the crystallisation plate to give the protein solution. PAHX was crystallised via hanging-drop vapour diffusion technique using pre-greased 24 well Combo Plate (SBS format, Greiner). 2 µl of the protein solution was mixed with 2 µl of the precipitant solution-solution (18-25% (w/v) PEG 3350, 0.1-0.2 M ammonium citrate) on siliconized plastic cover slips (Molecular Dimensions) and equilibrated over wells filled with 500 µl precipitant solution. Crystals appeared within 2-5 days.

8.4.4.2.4. Aerobic PAHX crystallisation

PAHX was either a) buffer exchanged into 25 mM Tris buffer pH 7.8 supplemented with 50 mM NaCl and incubated with 2 mM $MnCl_2$ or 2 mM $MnCl_2$ and 4 mM 2,4-PDCA (from 100 mM DMSO-stock) for 30 min on ice or b) buffer exchanged into 100 mM citrate buffer pH 6.0 and incubated with 2 mM $Zn(OAc)_2$ or with 2 mM $Zn(OAc)_2$ and 4 mM 2,4-PDCA for 30 min on ice. Crystallisation plates (low reservoir Intelli-Plate 93-3, Art Robbins Instruments) were set up with a Rigaku Phoenix RE Drop setter instrument (Art Robbins Instrument) and crystals were grown via vapor diffusion technique at 25 °C or 4 °C.

The optimised condition used PAHX in 100 mM citrate buffer pH 6.0, pre-incubated on ice with 5 mM Mn^{2+} and were based on condition D12 (0.22 M ammonium citrate dibasic, 12% (w/v) PEG 3350) of the PegIon broad screen (Hampton Research), incubated at room temperature. Crystals appeared within 7 days.

8.4.4.2.5. Data collection, processing, and analysis

Single crystals were briefly transferred into precipitant solution supplemented with 25% (v/v) glycerol, mounted on nylon loops, and cryo-cooled and stored in liquid nitrogen. X-ray diffraction data was collected at 100 K at the MX beamlines at Diamond Light Source (DLS) and processed using Xia2[36]. Structures were solved via molecular replacement with Phaser[38] using the reported structure of PAHX (PDB: 2A1X [25]) as the starting model.

Alternating cycles of refinement with phenix.refine[39] and manual model building in Coot[40] were performed until R_{work} and R_{free} converged.

8.4.4.3. Crystallisation of pcPAL

A solution of pcPAL (10 mg ml^{-1}, in 20 mM Tris, 100 mM NaCl, pH 8.0) was saturated with the respective substrate and left to incubate at 4 °C for 1-24 h prior to crystallisation. Crystallisation was performed at 4 °C using the sitting-drop vapor diffusion method. Initial crystallisation conditions were identified using the PegIon screen (Hampton Research) set up in low reservoir Intelli-Plate 93-3 (Art Robbins Instruments) using a Rigaku Phoenix RE Drop setter instrument (Art Robbins Instrument) mixing 100 nl of protein solution with 100 nl of precipitant. Small crystals were obtained after 2 weeks in condition C6 (0.2 M ammonium acetate, 20% (w/v) PEG 3350). A grid screen (0.05-0.2 M ammonium acetate, 15-25% (w/v) PEG 3350) gave larger crystals which appeared with 2-8 weeks. Crystals were transferred into precipitant solution supplemented with 25% (v/v) glycerol, then mounted on nylon loops and cryo-cooled and stored in liquid nitrogen.

Single crystals were briefly transferred into precipitant solution supplemented with 25% (v/v) glycerol, mounted on nylon loops, and cryo-cooled and stored in liquid nitrogen. X-ray diffraction data were collected at 100 K at the MX beamlines at DLS and processed using Xia2[36]. Structures were solved via molecular replacement with Phaser[38] using a reported structure of pcPAL (PDB: 1W27[29]) as the starting model. Alternating cycles of refinement with phenix.refine[39] and manual model building in Coot[40] were performed until R_{work} and R_{free} converged.

Appendix II – General Methods

9.1. General

Unless stated otherwise all chemicals were purchased from Sigma Aldrich and used without further purification. Enzymes used for microbiology were purchased from New England Biolabs. Water was purified using a Millipore Milli-Q system containing a 0.22 µm filter. Equipment used for biological procedures was sterilized by autoclaving at 121 °C for 20 min. Oligonucleotides were purchased from Sigma Aldrich.

9.2. Microbiology

9.2.1. Bacterial Growth Media

2 Trypton Yeast Extract (2TY) bacterial growth medium, super optimal broth with Catabolite Repression (SOC) medium, and Lysogeny broth (LB) Agar were prepared as shown below. All media was autoclaved at 121 °C for 20 min prior to use.

Table 2: Content of different used bacterial growth media

	2 Trypton Yeast Extract (2TY)	Super optimal broth with Catabolite Repression (SOC)	Lysogeny broth (LB) Agar
Tryptone	16.0 g/L	2.0 g/L	10.0 g/L
Yeast extract	10.0 g/L	0.50 g/L	5.0 g/L
NaCl	5.0 g/L	0.58 g/L	10.0 g/L
KCl	-	0.19 g/L	-
$MgCl_2$	-	1.96 g/L	-
Glucose		3.60 g/L	
Agar	-	-	20.0 g/L

9.2.2. Plasmid DNA isolation

Plasmids were purified using a GeneJET Plasmid Miniprep Kit (Thermo Fisher Scientific) or a GeneJET Plasmid Midiprep Kit (Thermo Fisher Scientific) following the protocols given by the supplier.

9.2.3. Agarose Gel Electrophoresis

Agarose gels for purification of nucleic acids were prepared by heating 0.8-1.0 % agarose (Bioline) in TAE buffer (40 mM Tris-Acetate pH 8.0, 1 mM EDTA) to give a clear solution. After the solution was cooled to approx. 50 °C, SYBR safe DNA stain (4 µl for 100 ml, Invitrogen) was added and the cast gel was left to solidify at rt. Prior to loading DNA samples were mixed with loading buffer (Fermentas). Separation was achieved by electrophoresis in TAE buffer at 80-100 V for 30 - 45 min.

9.3. Protein Production and Purification

9.3.1. Preparation of competent cells

E. coli (BL21 (DE3) or XLGold) cells were grown on LB Agar at 37 °C overnight. Single colonies were picked and transferred into 100 ml of 2TY media and incubated overnight at 37 °C and 180 rpm. 0.4 ml of the overnight culture was used to inoculate 100 ml of media and cells were grown to OD_{600}= 0.45 – 0.55. Subsequently the cell suspension was cooled on ice for 15 min before the cells were harvested by centrifugation (3750 rpm, 4 °C, 10 min). The supernatant was removed and the cells were suspended in 30 ml of 0.1 M $MgCl_2$ solution. After centrifugation (3750 rpm, 4 °C, 5 min), the supernatant was again removed and the cells were resuspended in 40 ml of cold 0.1 M $CaCl_2$ solution and incubated on ice for 20 min. Finally, cells were harvested via centrifugation (3750 rpm, 4 °C, 5 min), the supernatant was removed and the cells were resuspended in 12 ml of 0.1 M $CaCl_2$ solution supplemented with 15 % glycerol, before they were shock-frozen in liquid nitrogen and stored at -80 °C until further use.

9.3.2. Transformation

Competent *E. coli* BL21(DE3) cells (50 µl) were thawed and added to 1.0 µl of plasmid DNA (~ 100 ng). After resting for 30 min on ice the bacteria were heat shocked at 42 °C for 45 s. After being left to rest again on ice for 10 min 450 µl of 2TY growth media was added and the bacteria were incubated at 37 °C and 180 rpm for 40 min. Subsequently 100 µl of the solution was spread onto LB Agar-plates which were supplemented with appropriate antibiotics and bacterial colonies were grown at 37 °C overnight.

9.3.3. Starter cultures

Cells were transformed with the plasmid of interest, a single colony was picked and used to inoculate 100 ml 2TY media supplemented with the appropriate antibiotic. Cultures were grown at 37 °C overnight.

9.3.4. Glycerol Stocks

Glycerol Stocks for long term storage were prepared by gently mixing 1.6 ml of starter culture with 0.4 ml of sterile glycerol and stored at -80 °C.

9.3.5. Bacterial growth and expression

All recombinant proteins were produced in *E.coli* cells. Starter cultures of bacterial cells were diluted 1:100 in fresh 2TY media supplemented with the appropriate antibiotics. After expression cells were harvested by centrifugation (8,000 xg, 8 min, 4 °C) and stored at -80 °C.

9.3.6. Purification

Cells containing the protein of interest were resuspended in the stated buffer (5 x of the cell mass), supplemented with DNaseI from bovine pancreas (Roche) and protease inhibitor PMSF. The suspension was stirred at rt for 20 min and then at 4 °C for another 20 min. Cells were either lysed via sonification (5-6 x 10 s at 60% amplitude, Sonics Vibracell VCX750 Ultrasonic Cell Disruptor) or homogenisation. After lysis the lysate supernatant was separated from the cell debris via centrifugation (22,000 rpm, 4 °C, 20 min), filtered (0.45 µm syringe filter) and purified as described below. All of the protein purification steps took place at 4 °C using an AKTA FPLC system. Fractions containing protein were analysed via SDS-PAGE (see 9.3.7), before pooling and concentrating using Amicon concentrators (Millipore). Purified protein solutions were aliquoted, shock-frozen in liquid nitrogen and stored at – 80 °C until further use.

9.3.7. SDS-PAGE

SDS-PAGE Gels were either purchased from Thermo Fisher Scientific (NuPAGE Novex 4-12% Bis-Tris Protein Gels) or prepared using the recipe shown in Table S3. Prior to loading protein samples were heated in SDS loading buffer (Life Technologies) for 10 min at 100 °C. Gels were run at 180 V in a Mini-Protean Tetra Cell (Bio-Rad) filled with running buffer (25 mM Tris pH 8.8, 0.04% SDS) until sufficient separation was achieved. Subsequently gels were rinsed with water and stained with coommassie stain (40% methanol, 10% acetic acid, 0.05% Coommassie Blue R) for 5-10 min and destained with destain solution (10% methanol, 10% acetic acid) for 2-24 h.

Table S3: Recipe for SDS-PAGE gels

	Separating Gel			Stacking Gel
	V ml for 6%	V ml for 8%	V ml for 12 %	V ml
H_2O	5.3	4.6	3.3	2.1
30% acrylamide mix	2.0	2.7	4.0	0.5
1.5 M Tris-HCl pH 8.8	2.5	2.5	2.5	
10% SDS	0.1	0.1	0.1	0.03
10% ammonium persulphate	0.1	0.1	0.1	0.03
TEMED	0.008	0.006	0.004	0.003
1.5 M Tris-HCl pH 6.8				0.38

Appendix III – Supplementary Information for Chapter 2

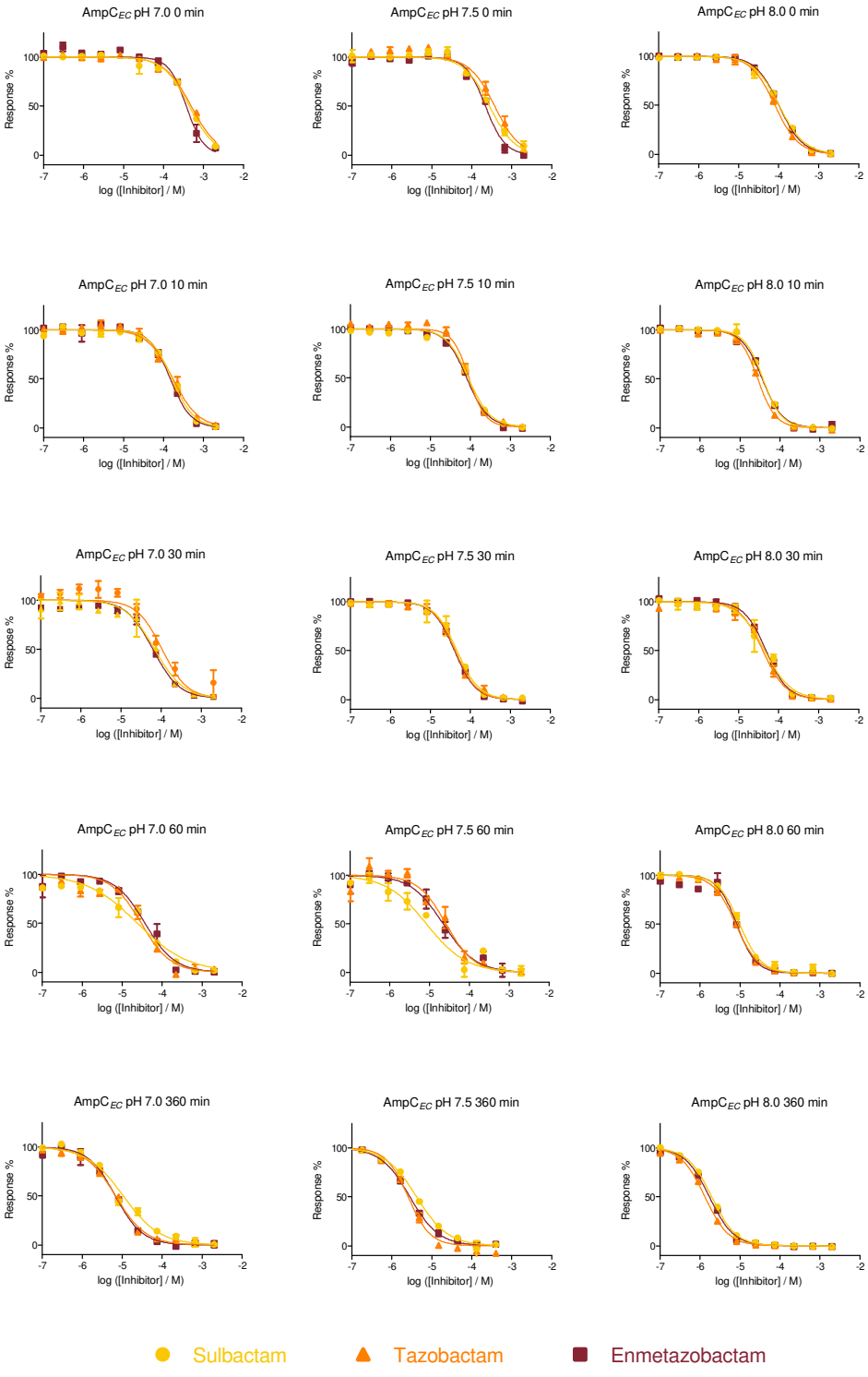


Figure S1: Dose dependence curves for AmpC$_{EC}$ inhibition by tazobactam, enmetazobactam, or sulbactam. AmpC$_{EC}$ (500 pM) was pre-incubated with the inhibitors for the indicated time at room temperature and assayed using 5 µM FC-5[41]. Buffer: 50 mM phosphate buffer, pH 7.0, 7.5, or 8.0 and 0.01% (v/v) Triton X-100. pIC$_{50}$s were determined using non-linear regression and are given in Table S1 and S2. Error bars indicate standard errors of four technical replicates. The figure and figure legend are adopted with permission from Lang *et al.* Proc. Natl. Acad. Sci. U.S.A., 2022, *119*, e2117310119.

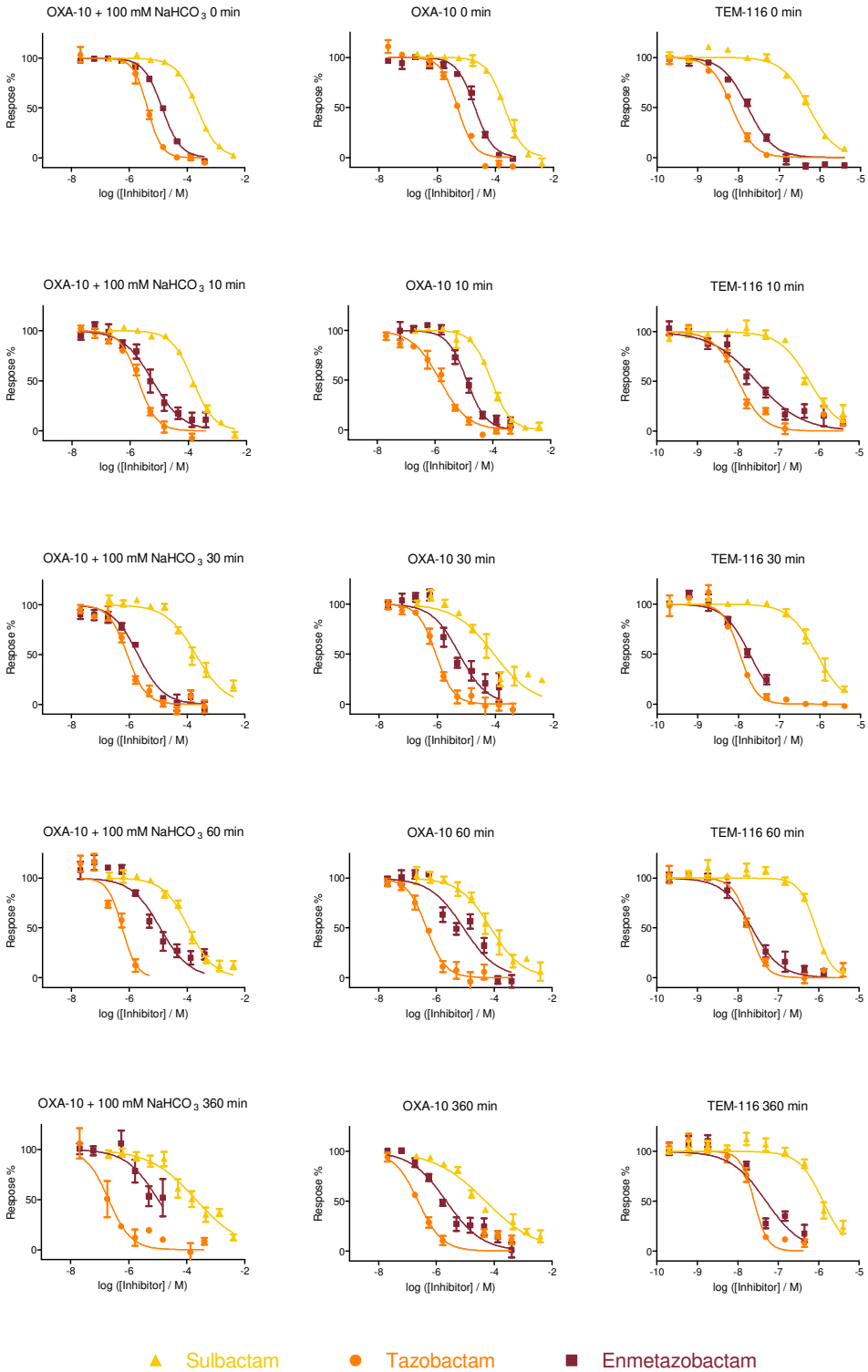
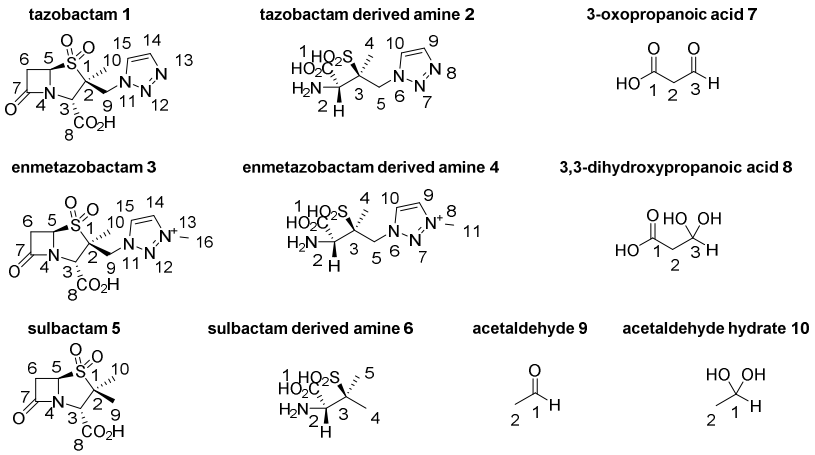


Figure S2: Dose dependence curves for OXA-10 and TEM-116 inhibition by tazobactam, enmetazobactam, or sulbactam. The enzymes (1 nM TEM-116 or 250 pM OXA-10) in 50 mM phosphate buffer pH 7.5, 0.01% (v/v) Triton X-100 were pre-incubated with the inhibitors for the indicated times at room temperature, then assayed using 5 μM FC-5[41]. OXA-10 was additionally screened in the presence of added 100 mM $NaHCO_3$. pIC_{50}s were determined using non-linear regression and are given in Table S1. Error bars indicate standard errors of four technical replicates. The figure and figure legend are adopted with permission from Lang *et al.* Proc. Natl. Acad. Sci. U.S.A., 2022, *119*, e2117310119.

A



B

tazobactam 1

Position	^{1}H (ppm)
1	-
2	-
3	4.37 (s)
4	-
5	4.93 (d, *J* = 4.3 Hz)
6	3.59 (dd, *J* = 17.2, 4.3 Hz), 3.37 (dd, *J*= 17.4, 1.4 Hz)
7	-
8	-
9	5.24 (d, *J* = 16.0 Hz), 5.06 (d, *J* = 16.0 Hz)
10	1.31 (s)
11	-
12	-
13	-
14	7.76 (d, *J* = 1.1 Hz)
15	8.04 (d, *J* = 1.1 Hz)

enmetazobactam 3

Position	^{1}H (ppm)
1	-
2	-
3	4.44 (s)
4	-
5	5.00 (s)
6	3.63 (dd, *J* = 18.3, 3.5 Hz), 3.39 (d, *J* = 18.3 Hz)
7	-
8	-
9	5.40 (d, *J* = 15.4 Hz), 5.27 (d, *J* = 15.6 Hz)
10	1.43 (s)
11	-
12	-
13	-
14	8.66 (s)
15	8.55 (s)
16	4.31 (s)

sulbactam 5

Position	^{1}H (ppm)
1	-
2	-
3	4.1 (s)
4	-
5	4.90 (s)
6	3.55 (dd, *J* = 18.0, 3.8 Hz), 3.30 (d, *J* = 18.1 Hz)
7	-
8	-
9	1.35 (s)
10	1.49 (s)

3-oxopropanoic acid 7 (reported[42])

Position	^{1}H (ppm)
1	-
2	3.31 (d, *J* = 2.9 Hz)
3	9.61 (t, *J* = 2.9 Hz)

tazobactam derived amine 2

Position	^{1}H (ppm)
1	-
2	4.11 (s)
3	-
4	1.09 (s)
5	-
6	-
7	-
8	-
9	7.71 (d, *J* = 1.1 Hz)
10	7.98 (d, *J* = 1.1 Hz)

enmetazobactam derived amine 4

Position	^{1}H (ppm)
1	-
2	4.04 (s)
3	-
4	1.12 (s)
5	-
6	-
7	-
8	-
9	8.61 (s)
10	8.43 (s)
11	4.27 (s)

sulbactam derived amine 6

Position	^{1}H (ppm)
1	-
2	3.91 (s)
3	-
4	1.00 (s)
5	1.07 (s)

3,3-dihydroxypropanoic acid 8 (reported[42])

Position	^{1}H (ppm)
1	-
2	2.41 (d, *J* = 5.6 Hz)
3	5.24 (t, *J* = 5.6 Hz)

acetaldehyde 9 (reported[42])

Position	^{1}H (ppm)
1	9.58 (q, *J* = 3.0 Hz)
2	2.14, (d, *J* = 3.1 Hz)

acetaldehyde hydrate 10 (reported[42])

Position	^{1}H (ppm)
1	5.16 (q, *J* = 5.3 Hz)
2	1.23 (d, *J* = 5.3 Hz)

Figure S3: Chemical shift assignments for tazobactam, enmetazobactam, sulbactam and their products. (A) Structures of inhibitors and assigned products. (B) Chemical shift assignments. Spectra (750 MHz) were recorded in 50 mM phosphate buffer, pH 7.5, 10 % D_2O. Chemical shifts and assignments for 3-oxopropanoic acid 7, 3,3-dihydroxypropanoic acid 8, acetaldehyde 9 and acetaldehyde hydrate 10 are in agreement with reported data[42]. The figure and figure legend are adopted with permission from Lang *et al.* Proc. Natl. Acad. Sci. U.S.A., 2022, *119*, e2117310119.

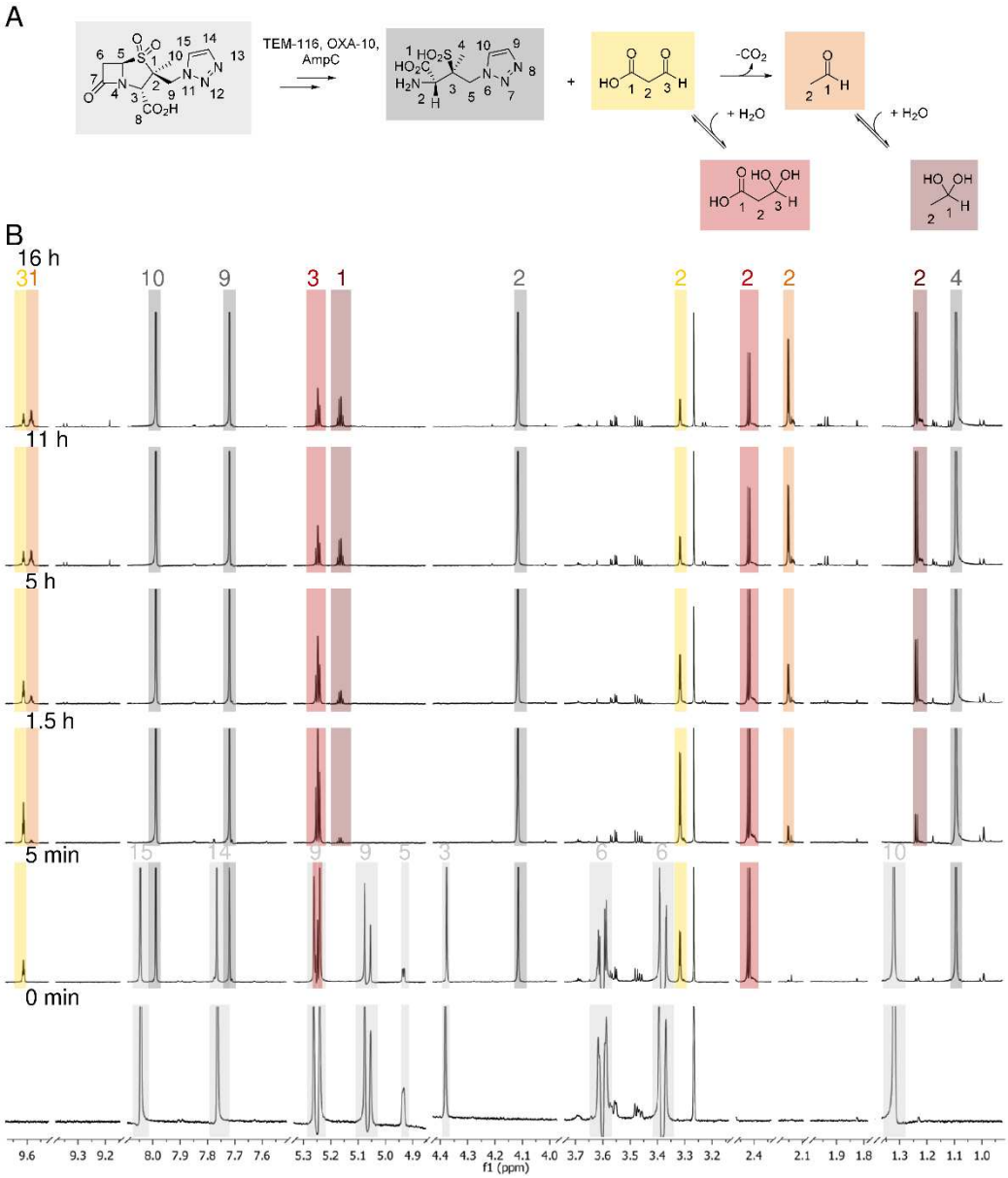


Figure S4: ^{1}H NMR analysis of the reaction of tazobactam with OXA-10. ^{1}H NMR Spectra (750 MHz) showing the products of tazobactam formed by reaction with OXA-10 and likely subsequent non-enzymatic reactions. OXA-10 (10 µM) was incubated with tazobactam (5 mM, room temperature, 50 mM phosphate buffer pH 7.5, 10 % D_2O). Chemical shift assignments are shown in Figure S3. The figure and figure legend are adopted with permission from Lang *et al.* Proc. Natl. Acad. Sci. U.S.A., 2022, *119*, e2117310119.

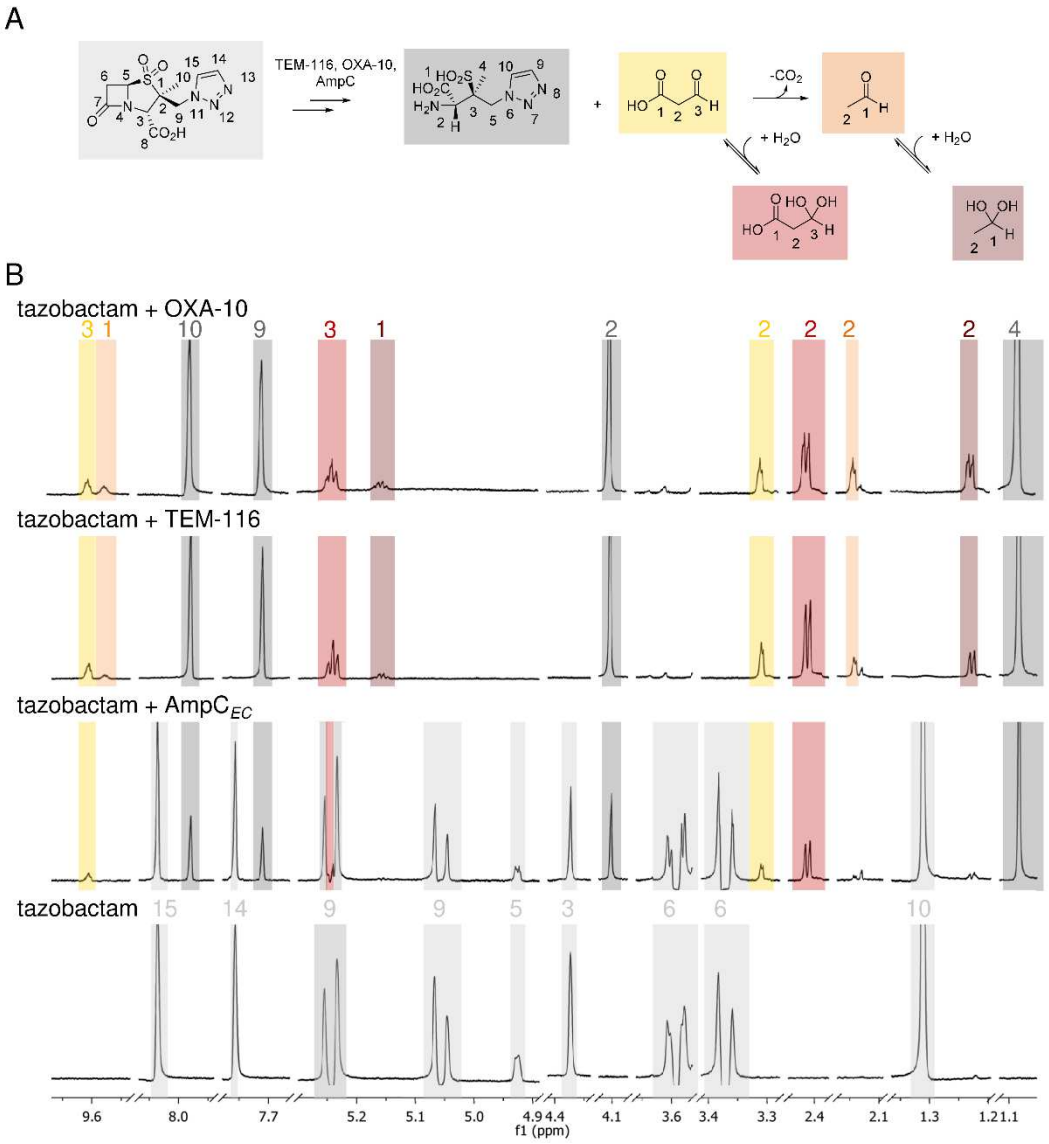


Figure S5: ^{1}H NMR analysis of the reaction of tazobactam with OXA-10, TEM-116, or AmpC$_{EC}$. ^{1}H NMR spectra (750 MHz) showing the products of tazobactam formed by reaction with SBLs and likely subsequent non-enzymatic reactions. OXA-10, TEM-116, or AmpC$_{EC}$ (10 µM) were incubated with tazobactam (1 mM, 18 h, room temperature, 50 mM phosphate buffer pH 7.5, 10 % D_2O). In all cases the inhibitors gave the same major reaction products. Chemical shift assignments are shown in Figure S3. The figure and figure legend are adopted with permission from Lang *et al.* Proc. Natl. Acad. Sci. U.S.A., 2022, *119*, e2117310119.

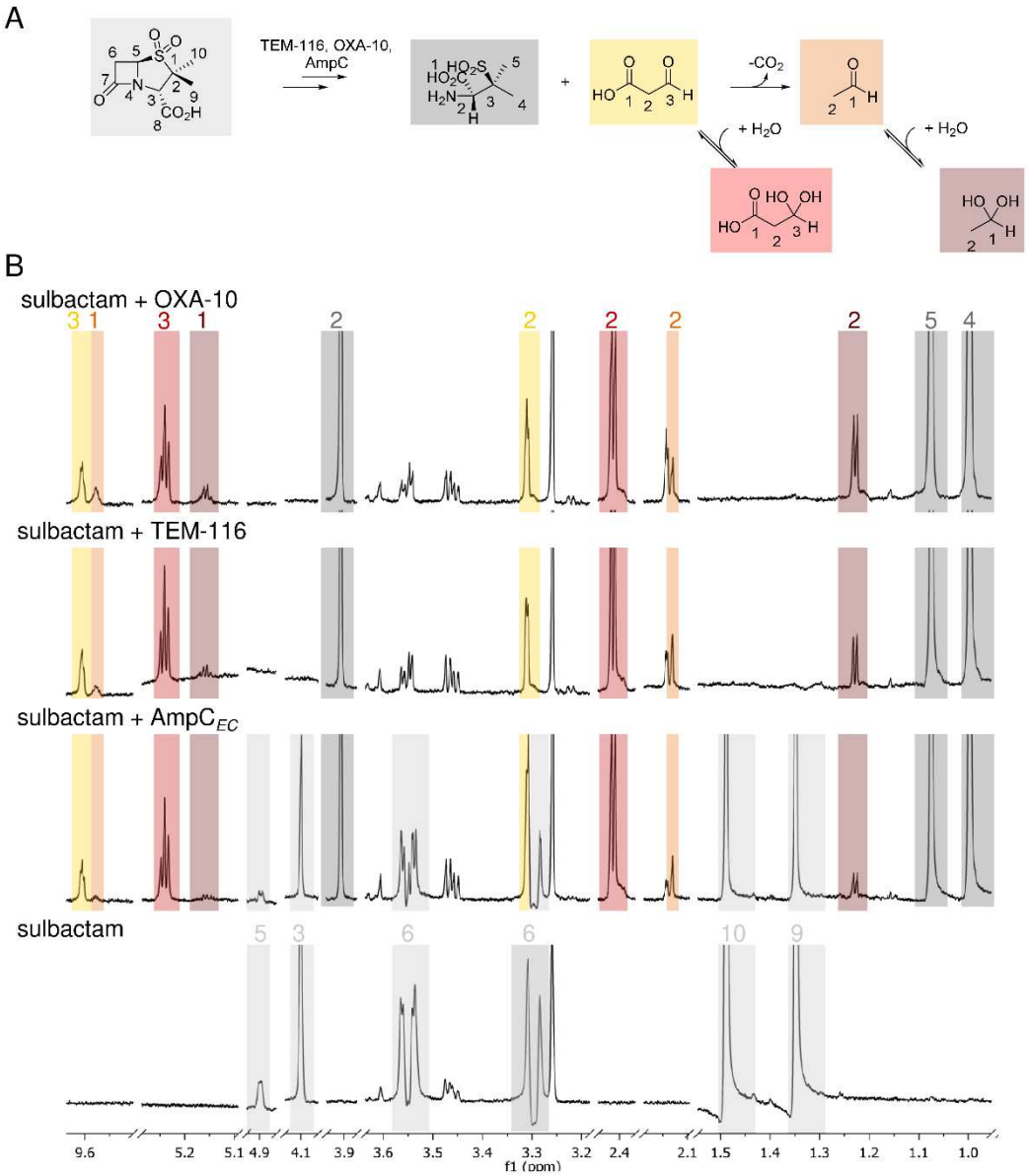


Figure S6: ^{1}H NMR analysis of the reaction of sulbactam with OXA-10, TEM-116, or AmpC$_{EC}$. ^{1}H NMR spectra (750 MHz) showing the products of sulbactam formed by reaction with SBLs and likely subsequent non-enzymatic reactions. OXA-10, TEM-116, or AmpC$_{EC}$ (10 µM) were incubated with sulbactam (1 mM, 18 h, room temperature, 50 mM phosphate buffer pH 7.5, 10 % D_2O). In all cases the inhibitors gave the same major products. Chemical shift assignments are shown in Figure S3. The figure and figure legend are adopted with permission from Lang *et al.* Proc. Natl. Acad. Sci. U.S.A., 2022, *119*, e2117310119.

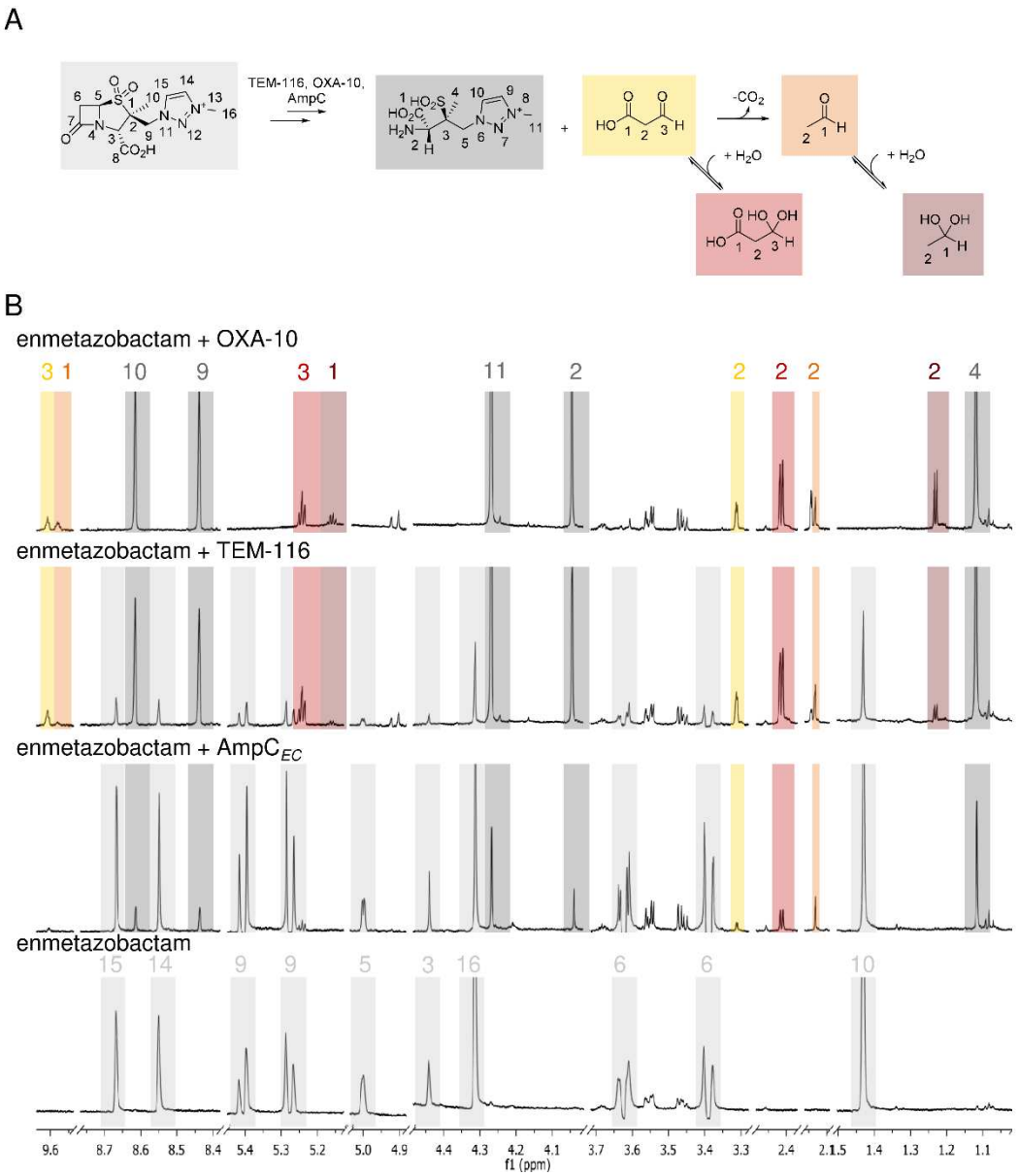


Figure S7: ^{1}H NMR analysis of the reaction of enmetazobactam with OXA-10, TEM-116, or AmpC$_{EC}$. ^{1}H NMR spectra (750 MHz) showing the products of enmetazobactam formed by reaction with SBLs and likely subsequent non-enzymatic reactions. OXA-10, TEM-116, or AmpC$_{EC}$ (10 µM) were incubated with enmetazobactam (1 mM, 18 h, room temperature, 50 mM phosphate buffer pH 7.5, 10 % D_2O). In all cases the inhibitors gave the same major products. Chemical shift assignments are shown in Figure S3. The figure and figure legend are adopted with permission from Lang *et al.* Proc. Natl. Acad. Sci. U.S.A., 2022, *119*, e2117310119.

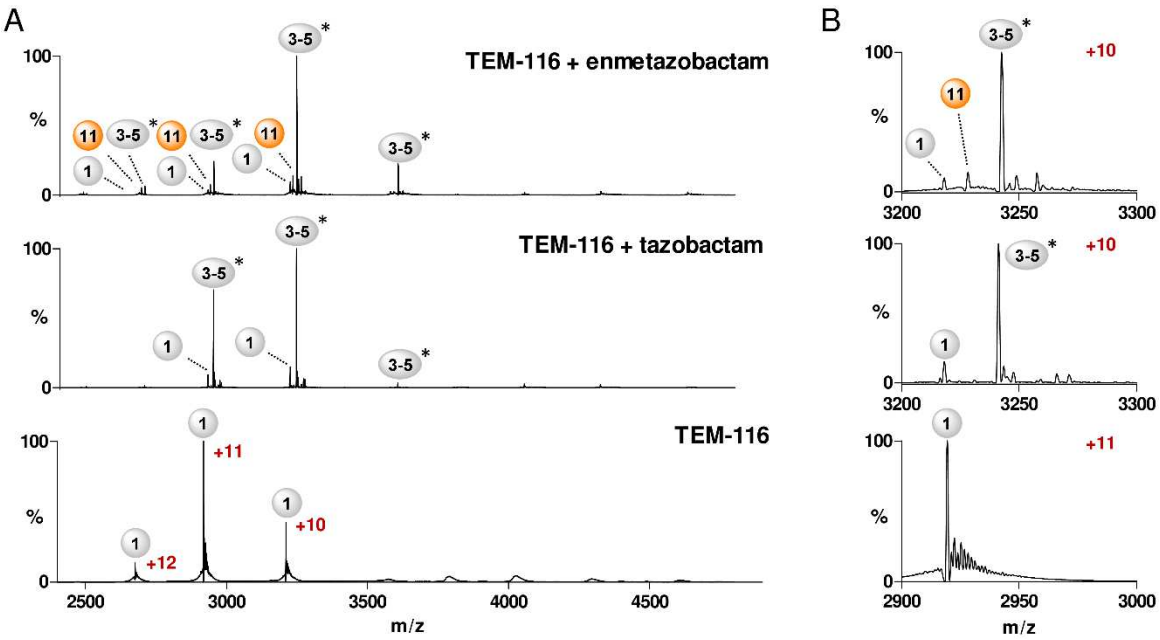


Figure S8: Native-MS studies on the interaction of TEM-116 with tazobactam and enmetazobactam after 20 min incubation. TEM-116 (10 µM) was incubated with tazobactam or enmetazobactam (1 mM) in 1 M ammonium acetate, pH 7.5 at r.t. for 20 min. Samples were desalted (using a Zeba micro spin desalting column, 7K MWCO, Thermo Scientific) immediately prior to analysis, then sprayed directly into the mass-spectrometer. (A) Mass spectra of unmodified TEM-116, with tazobactam, and with enmetazobactam. Charge states are in red. Note: The lower charge state observed on binding of tazobactam and enmetazobactam (major charge state: +10) compared to unmodified TEM-116 (major charge state: +11) indicates binding of the inhibitors may lead to a different conformation conformation. (B) Magnification of the major charge states of the respective spectra in (A). Proposed structures corresponding to the labelled mass shifts are given in Chapter 2, Figure 11. *Note mass shifts may reflect more than one species, e.g. **2**-**5** give the same mass shift. The figure and figure legend are adopted with permission from Lang *et al.* Proc. Natl. Acad. Sci. U.S.A., 2022, *119*, e2117310119.

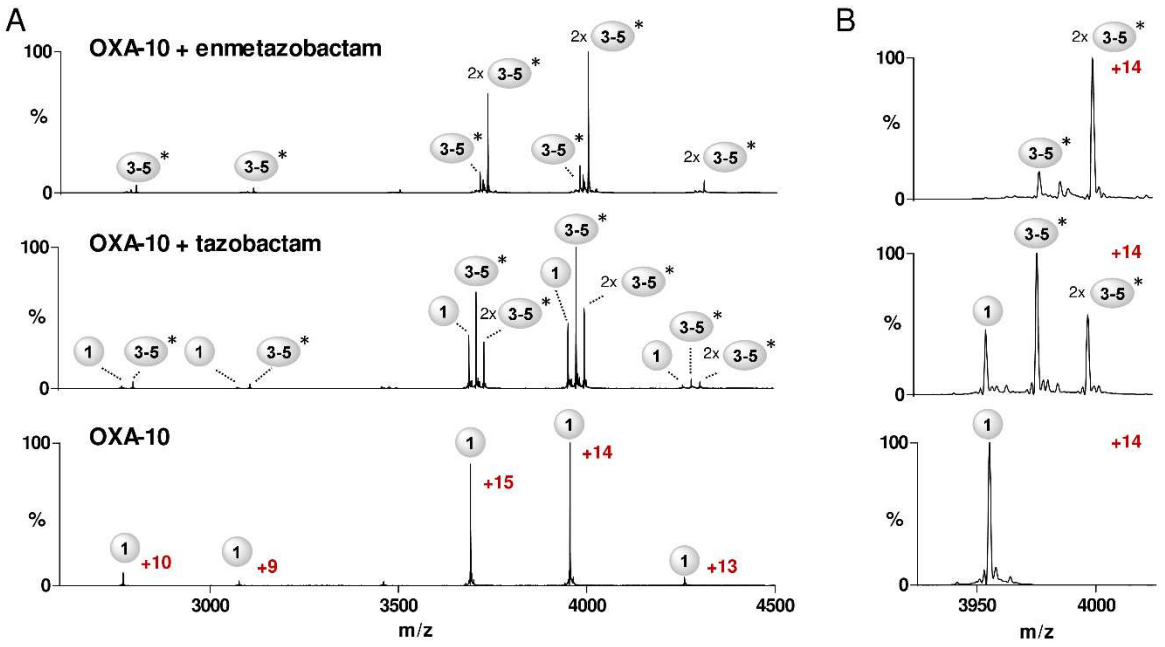


Figure S9: Native-MS studies on the interaction of OXA-10 with tazobactam and enmetazobactam after 20 min incubation. OXA-10 (10 µM) was incubated with tazobactam or enmetazobactam (1 mM) in 1 M ammonium acetate, pH 7.5 at r.t. for 20 min. Samples were desalted (using a Zeba micro spin desalting column, 7K MWCO, Thermo Scientific) immediately prior to analysis, then sprayed directly into the mass-spectrometer. (A) Mass spectra of unmodified OXA-10, with tazobactam, and with enmetazobactam. Charge states are in red. Note: In agreement with reported studies(3) OXA-10 was observed in a predominantly dimeric form. (B) Magnification of the major charge state (+ 14) of the respective spectra in (A). Proposed structures corresponding to the labelled mass shifts are given in Chapter 2, Figure 11. *Note mass shifts may reflect more than one species, e.g. **2-5** give the same mass shift. The figure and figure legend are adopted with permission from Lang *et al.* Proc. Natl. Acad. Sci. U.S.A., 2022, *119*, e2117310119.

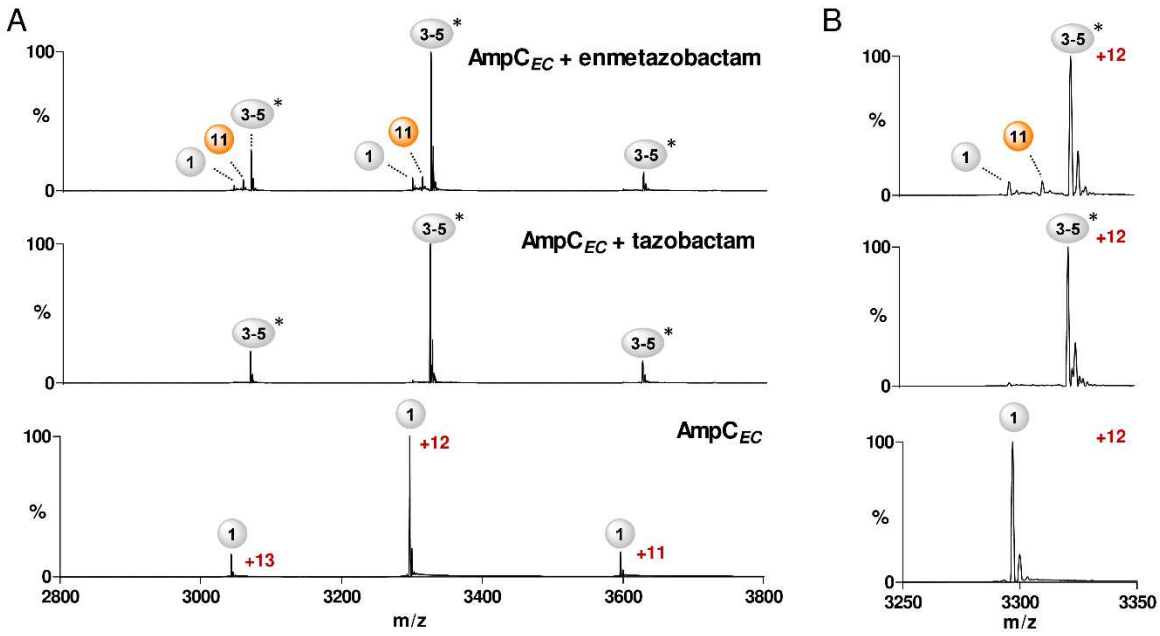


Figure S10: Native-MS studies on the interaction of AmpC$_{EC}$ with tazobactam and enmetazobactam after 20 min incubation. AmpC$_{EC}$ (10 µM) was incubated with tazobactam or enmetazobactam (1 mM) in 1 M ammonium acetate, pH 7.5 at r.t. for 20 min. Samples were desalted (using a Zeba micro spin desalting column, 7K MWCO, Thermo Scientific), immediately prior to analysis, then sprayed directly into the mass-spectrometer. (A) Mass spectra of unmodified AmpC$_{EC}$, with tazobactam, and with enmetazobactam. Charge states are in red. (B) Magnification of the major charge state (+ 12) of the respective spectra in (A). Proposed structures corresponding to the labelled mass shifts are given in Chapter 2, Figure 11. *Note mass shifts may reflect more than one species, e.g. **2-5**, give the same mass shift. The figure and figure legend are adopted with permission from Lang *et al.* Proc. Natl. Acad. Sci. U.S.A., 2022, *119*, e2117310119.

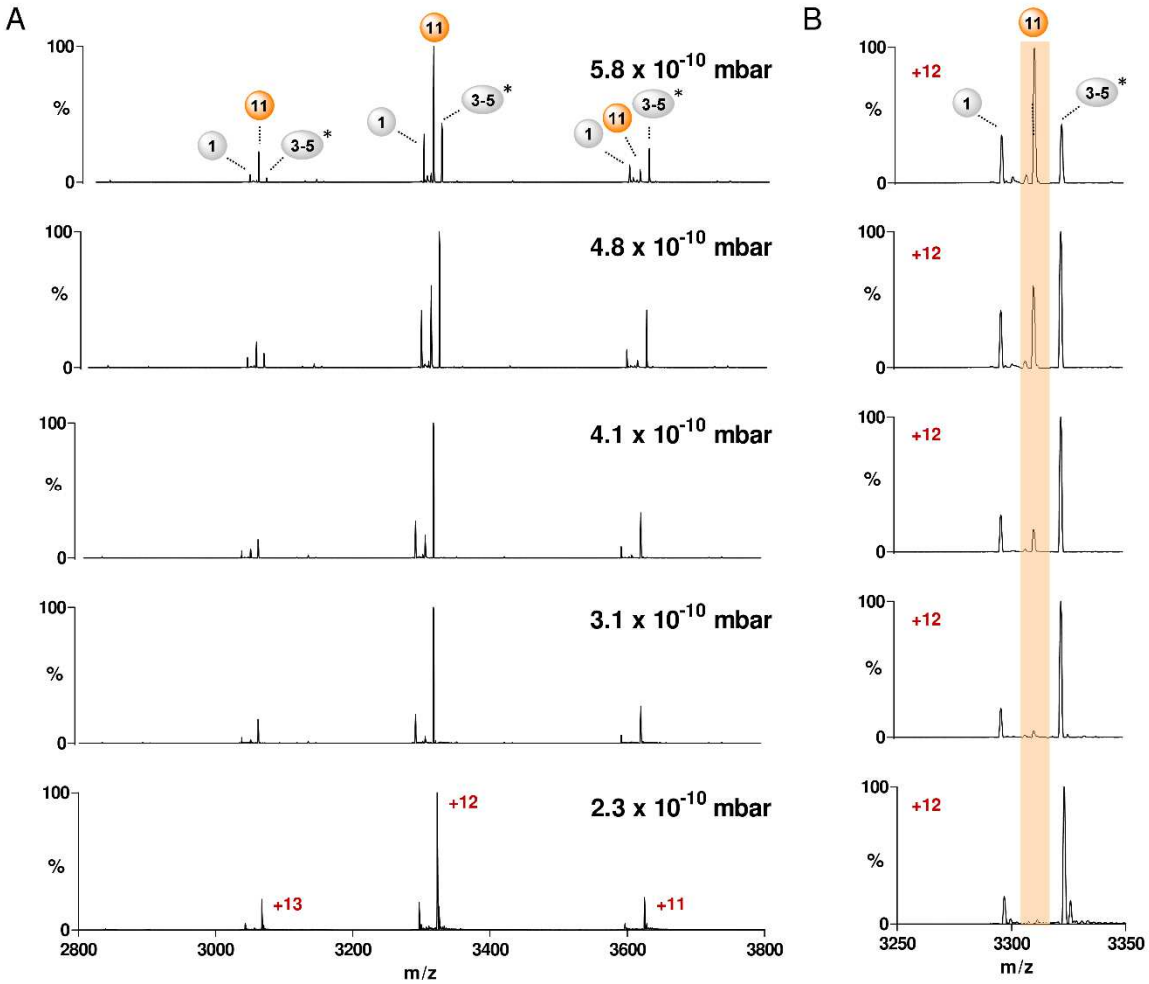


Figure S11: Native-MS studies showing the dependence of elimination from the AmpC$_{EC}$-enmetazobactam derived complex on gas-pressure. AmpC$_{EC}$ (10 µM) was incubated with enmetazobactam (1 mM) in 1 M ammonium acetate, pH 7.5 at r.t. for 20 min. The sample was desalted (using a Zeba micro spin desalting column, 7K MWCO, Thermo Scientific) immediately prior to analysis, then sprayed directly into the mass-spectrometer. Spectra were acquired without collisional activation and at the indicated UHV gas pressures. (A) Mass spectra of the AmpC$_{EC}$-enmetazobactam derived complex with varying UHV gas pressures. Charge states are in red. (B) Magnification of the major charge state (+ 12) of the respective spectra in (A). Proposed structures corresponding to the labelled mass shifts are given in Chapter 2, Figure 11. *Note mass shifts may reflect more than one species, e.g. **2-5** give the same mass shift. The figure and figure legend are adopted with permission from Lang *et al.* Proc. Natl. Acad. Sci. U.S.A., 2022, *119*, e2117310119.

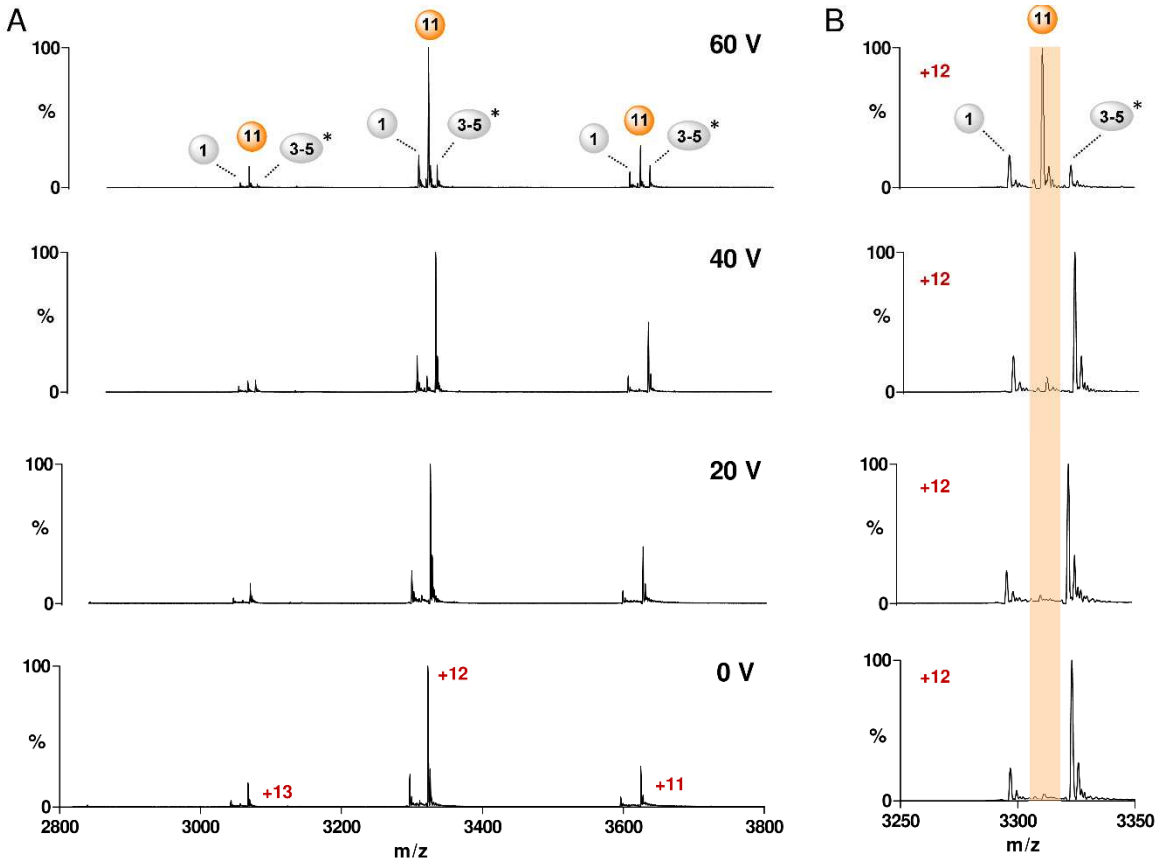


Figure S12: Native-MS studies showing the effect of collisional activation in the higher-energy C-trap dissociation (HCD) cell on formation of elimination product 11 from the AmpC$_{EC}$-enmetazobactam derived complex. AmpC$_{EC}$ (10 µM) was incubated with enmetazobactam (1 mM) in 1 M ammonium acetate, pH 7.5 at r.t. for 20 min. The sample was desalted (using a Zeba micro spin desalting column, 7K MWCO, Thermo Scientific) immediately prior to analysis, then sprayed directly into the spectrometer. Spectra were acquired at a constant UHV gas-pressure of 2.7 x 10^{-10} mbar and at the indicated HCD collisional activation energy. (A) Mass spectra of the AmpC$_{EC}$-enmetazobactam derived complex at a constant gas pressure and varying collisional activation energy. Charge states are in red. (B) Magnification of the major charge state (+ 12) of the respective spectra in (A). Proposed structures corresponding to the labelled mass shifts are given in Chapter 2, Figure 11. *Note mass shifts may reflect more than one species, e.g. **2-5** give the same mass shift. The figure and figure legend are adopted with permission from Lang *et al.* Proc. Natl. Acad. Sci. U.S.A., 2022, *119*, e2117310119.

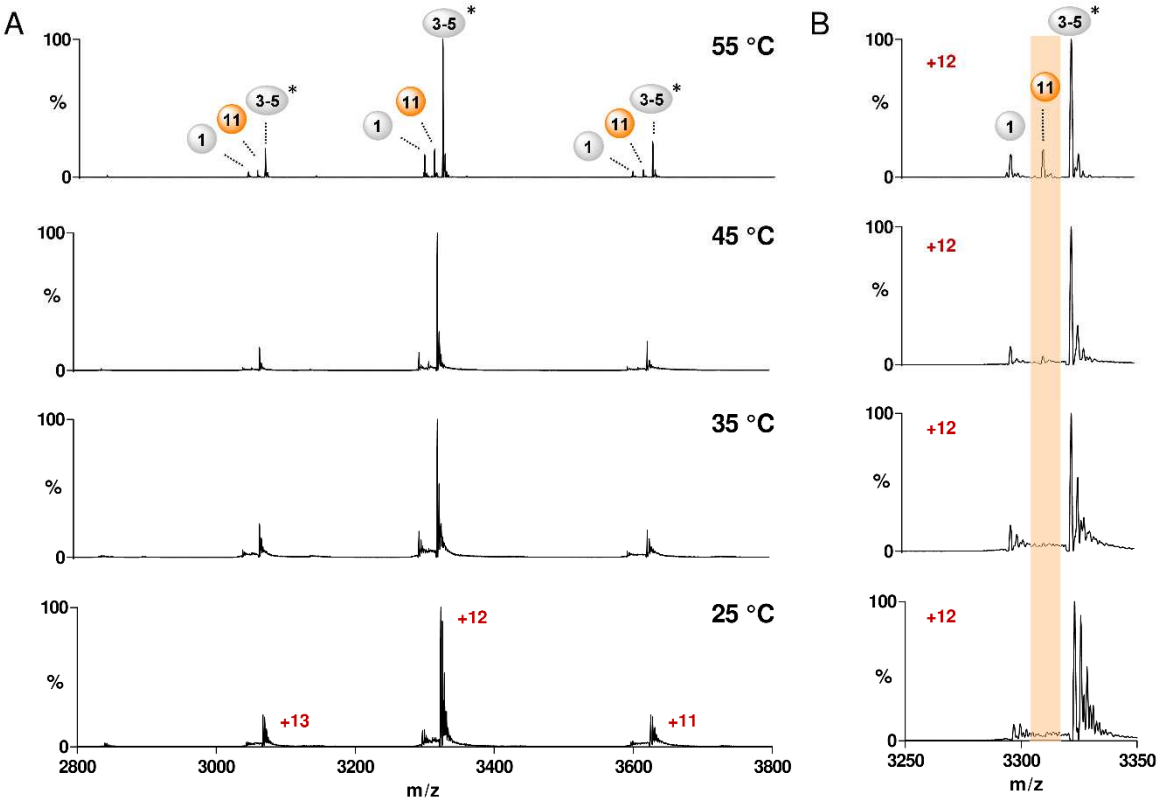


Figure S13: Native-MS studies showing the dependence of elimination from the AmpC$_{EC}$-enmetazobactam derived complex on solution temperature. AmpC$_{EC}$ (10 µM) was incubated with enmetazobactam (1 mM) in 1 M ammonium acetate, pH 7.5 at r.t. for 20 min, then for 1 h at the indicated temperatures. Samples were desalted (using a Zeba micro spin desalting column, 7K MWCO, Thermo Scientific) immediately prior to analysis, then sprayed directly into the mass-spectrometer. Spectra were acquired without collisional activation at a constant UHV gas-pressure of 2.7 x 10^{-10} mbar. (A) Mass spectra of AmpC$_{EC}$-enmetazobactam derived complex incubated at the indicated temperatures. Charge states are in red. (B) Magnification of the major charge state (+ 12) of the respective spectra in (A). Proposed structures corresponding to the labelled mass shifts are given in Chapter 2, Figure 11. *Note mass shifts may reflect more than one species, e.g. **2-5** give the same mass shift. The figure and figure legend are adopted with permission from Lang *et al.* Proc. Natl. Acad. Sci. U.S.A., 2022, *119*, e2117310119.

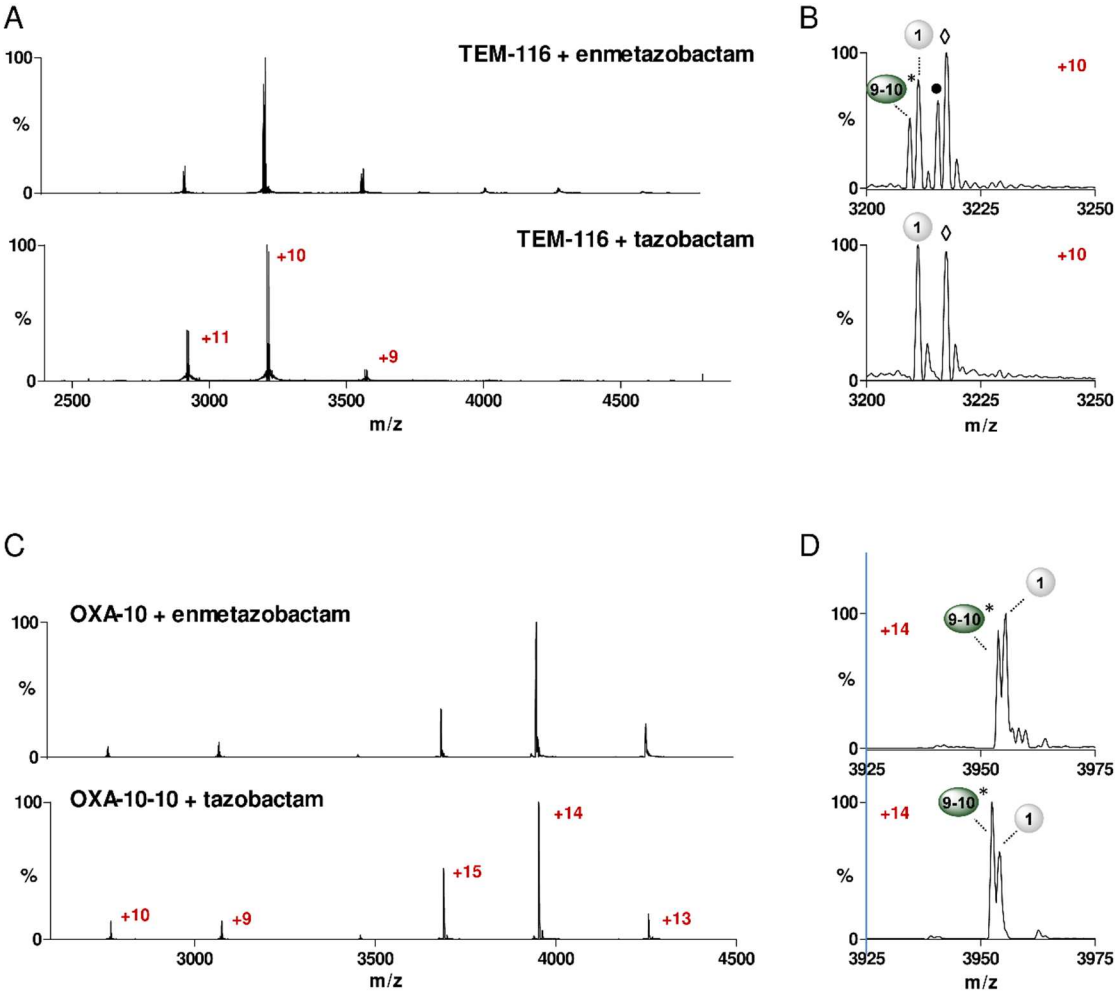


Figure S26: Non-denaturing (native) MS studies on TEM-116 or OXA-10 interactions with tazobactam and enmetazobactam after prolonged incubation. TEM-116 or OXA-10 (10 µM) were incubated with tazobactam or enmetazobactam (1 mM) in 50 mM Tris pH 7.5 at r.t. for 24 h. Prior to analysis samples were buffer exchanged into 1 M ammonium acetate, pH 7.5 ((using a Zeba micro spin desalting column, 7K MWCO, Thermo Scientific) twice immediately prior to analysis and sprayed directly into the mass-spectrometer. (A) Mass spectra of TEM-116 incubated with enmetazobactam or tazobactam. Charge states are in red. (B) Magnification of the major charge state (+10) of the respective spectra in (A). Note that in the case of TEM-116 on incubation with both tazobactam and enmetazobactam an additional adduct of +62 Da was observed, both for the unmodified and the dehydrated protein. This species may result from binding of a penam degradation product, i.e. hydrated acetaldehyde. ● Corresponds to **9** or **10** + 62 Da and ◊ corresponds to **1** + 62 Da. (C) Mass spectra of OXA-10 incubated with enmetazobactam, or tazobactam. Charge states are indicated in red. (D) Magnification of the major charge state (+14) of the respective spectra in (C). Proposed structures of the labelled species are given in Chapter 2, Figure 11. *Note mass shifts may reflect more than one species, e.g. **9**-**10** give the same mass shift.

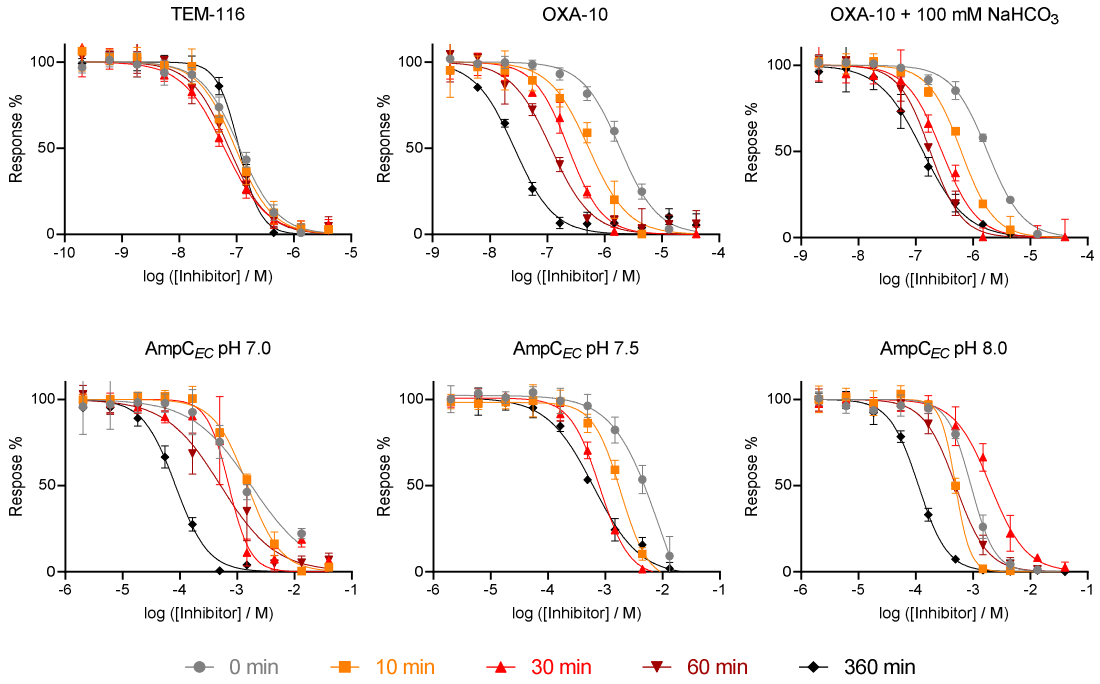


Figure S14: Dose dependence curves for TEM-116, OXA-10 and AmpC$_{EC}$ inhibition by clavulanic acid. The enzymes (1 nM TEM-116, 250 pM OXA-10, or 500 pM AmpC$_{EC}$) in 50 mM phosphate buffer pH 7.5, 0.01% (v/v) Triton X-100 were pre-incubated with clavulanic acid for the indicated times at room temperature, then assayed using 5 µM FC-5[41]. OXA-10 was additionally screened in the presence of added 100 mM $NaHCO_3$. AmpC$_{EC}$ was additionally screened at pH 7.0 and pH 8.0. pIC$_{50}$s were determined using non-linear regression and are given in Chapter 2, Table 10. Error bars indicate standard errors of four technical replicates.

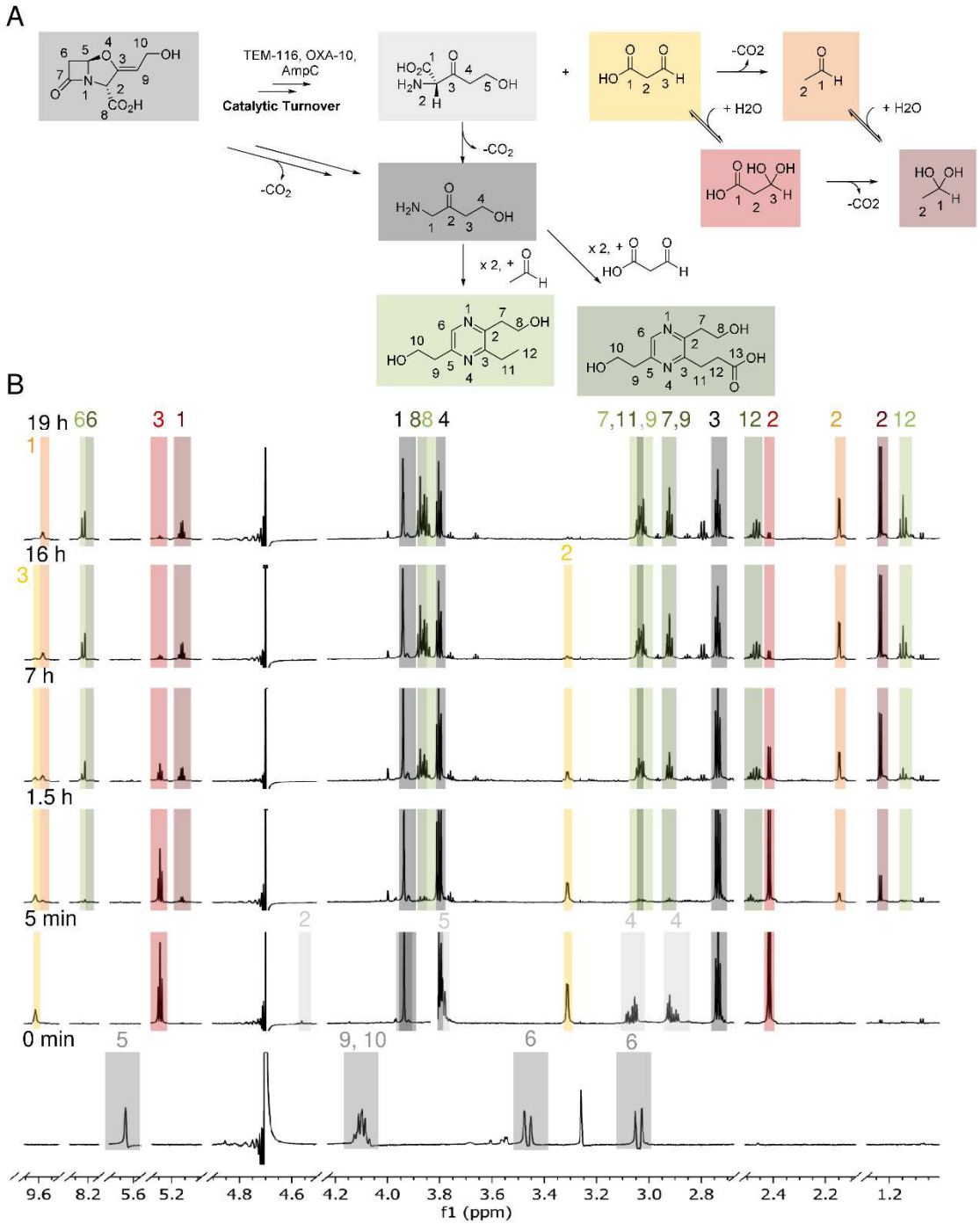
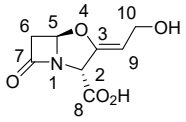


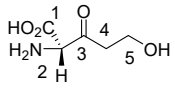
Figure S15: ^{1}H-NMR analysis of the reaction of clavulanic acid with OXA-10 over time. ^{1}H-NMR spectra (750 MHz) showing the degradation products of clavulanic acid formed by reaction with OXA-10 and likely subsequent non-enzymatic reactions. OXA-10 (10 µM) was incubated with clavulanic acid (5 mM) at room temperature in 50 mM phosphate buffer pH 7.5, 10 % D_2O. Chemical shift assignments are shown in Figure S16 and are consistent with previous reports[43,44].

A

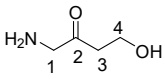
Clavulanic Acid 1



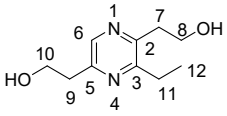
Clavulanic Avid derived Amine 2



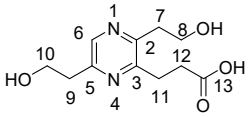
Decarboxylated Amine 3



Ethyl-Pyrazine 5



Ethyl-Pyrazine 6



B

Clavulanic Acid 1

Position	^{1}H (ppm)
1	-
2	4.85 (s)
3	-
4	-
5	5.63 (s)
6	3.46 (d, *J* = 18.7 Hz), 3.04 (d, *J* = 18.7 Hz)
7	-
8	-
9	4.10 (m)
10	4.10 (m)

Clavulanic Acid derived Amine 2

Position	^{1}H (ppm)
1	-
2	4.56 (s)
3	-
4	3.06 (dt, *J* = 18.3, 6.0 Hz), 2.91 (dt, *J* = 18.1, 6.0 Hz)
5	3.80 (t, *J* = 6.1 Hz)

Decarboxylated Amine 3 (reported[43])

Position	^{1}H (ppm)
1	3.94 (s)
2	-
3	2.73 (t, *J* = 6.0 Hz)
4	3.80 (t, *J* = 6.1 Hz)

Ethyl-Pyrazine 5 (reported[44])

Position	^{1}H (ppm)
1	-
2	-
3	-
4	-
5	-
6	8.22 (s)
7	3.03 (m)
8	3.85 (m)
9	3.03 (m)
10	3.85 (m)
11	2.79 (q, *J* = 8.0 Hz)
12	1.15 (t, *J* = 7.9 Hz)

Carboxy-Pyrazine 6 (reported[44])

Position	^{1}H (ppm)
1	-
2	-
3	-
4	-
5	-
6	8.21 (s)
7	2.92 (t, *J* = 6.5 Hz)
8	3.87 (t, *J* = 6.7 Hz)
9	2.92 (t, *J* = 6.5 Hz)
10	3.87 (t, *J* = 6.7 Hz)
11	3.03 (m)
12	2.46 (m)
13	-

Figure S16: Chemical shift assignments for clavulanic acid and its degradation products. (A) Structures of inhibitors and assigned products. (B) Chemical shift assignments. Spectra (750 MHz) were recorded in 50 mM phosphate buffer, pH 7.5, 10 % D_2O. Chemical shifts and assignments for decarboxylated amine 3, pyrazine 4, ethyl-pyrazine 5 and carboxy-pyrazine 6 are in agreement with previous reports[43,44]. The assignment of clavulanic acid derived amine 2 was supported by HMBC data (see Chapter 2, Figure 39).

Appendix IV – Supplementary Information for Chapter 3

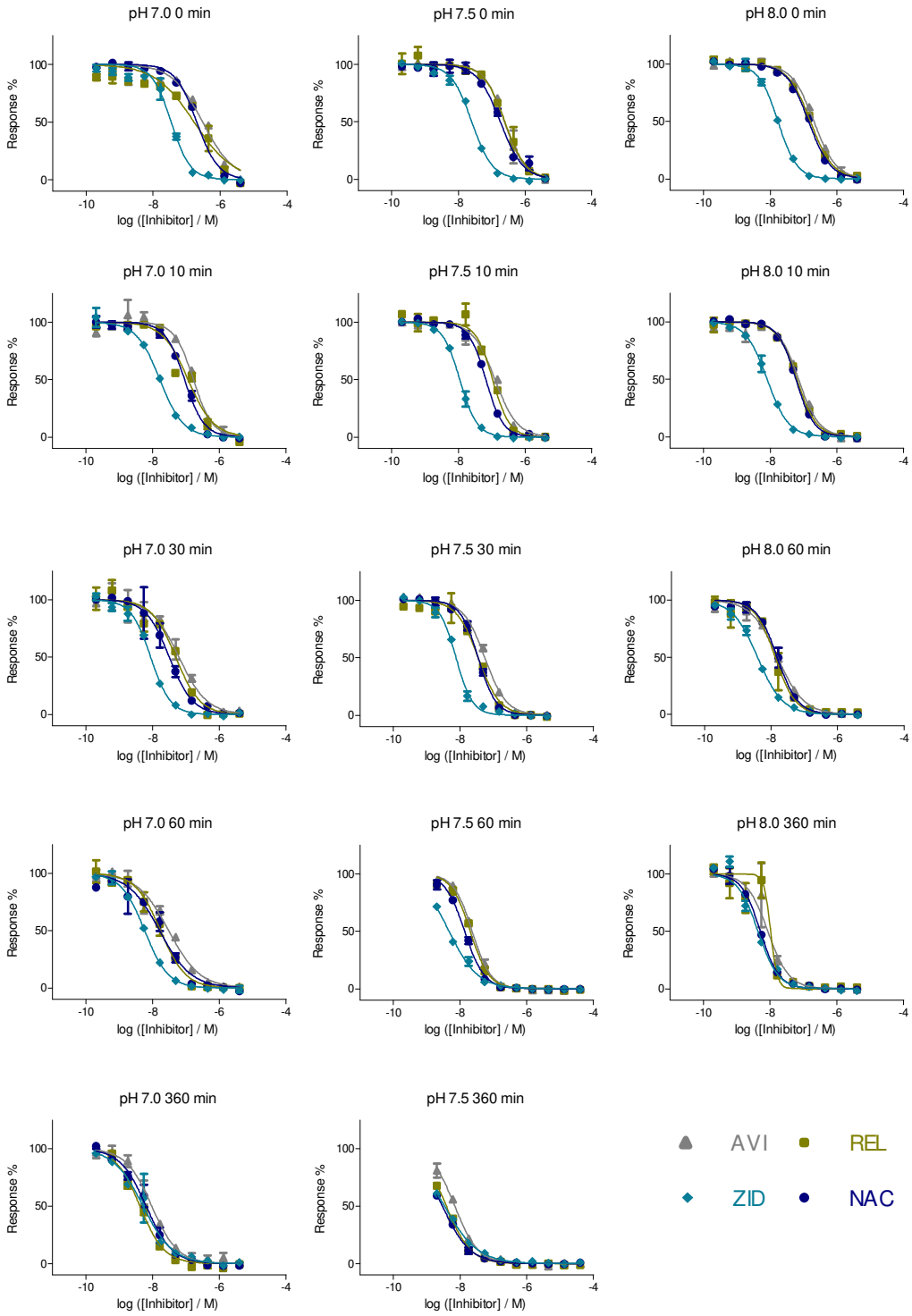


Figure S17: Dose dependence curves for AmpC$_{EC}$ inhibition by AVI, REL, NAC, or ZID. AmpC$_{EC}$ (500 pM) was pre-incubated with the inhibitors for the indicated times at room temperature and assayed using 5 µM FC-5[41]. Buffer: 50 mM phosphate buffer, pH 7.0, 7.5, or 8.0, containing 0.01% (v/v) Triton X-100. pIC$_{50}$s were determined using non-linear regression and summarised in Chapter 3, Table 1. The figure and figure legend are adopted with permission from Lang *et al*. Antimicrob. Agents Chemother. *65*, e02073-20

Appendix V – Sequences of protein constructs

OXA-48 and PAHX were produced with an N-terminal HisTag which was removed during purification. TEM-116 and pcPAL were produced and purified with an N-terminal HisTag. Note that all pcPAL variants were produced with two mutation of surface Cys residues (C704S/C716S) to reduce aggregation[32]. Molecular weights (MW) and extinction coefficients (ε) were calculated using the ProtParam tool.

AmpC*EC* (MW: 39551.14 Da, ε: 93850 M^{-1} cm^{-1}, at 280 nm)

APQQINDIVHRTITPLIEQQKIPGMAVAVIYQGKPYYFTWGYADIAKKQPVTQQTLFELGSVS
KTFTGVLGGDAIARGEIKLSDPTTKYWPELTAKQWNGITLLHLATYTAGGLPLQVPDEVKSS
SDLLRFYQNWQPAWAPGTQRLYANSSIGLFGALAVKPSGLSFEQAMQTRVFQPLKLNHTWI
NVPPAEEKNYAWGYREGKAVHVSPGALDAEAYGVKSTIEDMARWVQSNLKPLDINEKTLQ
QGIQLAQSRYWQTGDMYQGLGWEMLDWPVNPDSIINGSDNKIALAARPVKAITPPTPAVRA
SWVHKTGATGGFGSYVAFIPEKELGIVMLANKNYPNPARVDAAWQILNALQ

OXA-10 (MW: 27681.60 Da, ε: 47565 M^{-1} cm^{-1}, at 280 nm)

MGSITENTSWNKEFSAEAVNGVFVLCKSSSKSCATNDLARASKEYLPASTFKIPNAIIGLETG
VIKNEHQVFKWDGKPRAMKQWERDLTLRGAIQVSAVPVFQQIAREVGEVRMQKYLKKFSY
GNQNISGGIDKFWLEGQLRISAVNQVEFLESLYLNKLSASKENQLIVKEALVTEAAPEYLVHS
KTGFSGVGTESNPGVAWWVGWVEKETEVYFFAFNMDIDNESKLPLRKSIPTKIMESEGIIGG

OXA-48 (MW: 28367.27 Da, ε: 63940 M^{-1} cm^{-1}, at 280 nm)

SMKEWQENKSWNAHFTEHKSQGVVVLWNENKQQGFTNNLKRANQAFLPASTFKIPNSLIA
LDLGVVKDEHQVFKWDGQTRDIATWNRDHNLITAMKYSVVPVYQEFARQIGEARMSKMLH
AFDYGNEDISGNVDSFWLDGGIRISATEQISFLRKLYHNKLHVSERSQRIVKQAMLTEANGD
YIIRAKTGYSCRIEPKIGWWVGWVELDDNVWFFAMNMDMPTSDGLGLRQAITKEVLKQEKII
P

TEM-116 with an *N*-terminal HisTag (MW 32103.48 Da, ε: 31065 M^{-1} cm^{-1}, at 280 nm)

MKHHHHHHHSDYDIPTTENLYFQGSHPETLVKVKDAEDQLGARVGYIELDLNSGKILESFRP
EERFPMMSTFKVLLCGAVLSRIDAGQEQLGRRIHYSQNDLVEYSPVTEKHLTDGMTVRELC
SAAITMSDNTAANLLLTTIGGPKELTAFLHNMGDHVTRLDRWEPELNEAIPNDERDTTMPVA
MATTLRKLLTGELLTLASRQQLIDWMEADKVAGPLLRSALPAGWFIADKSGAGERGSRGIIA
ALGPDGKPSRIVVIYTTGSQATMDERNRQIAEIGASLIKHWC

AlkB (MW: 22786.06, ε: 27180 M^{-1} cm^{-1}, at 280 nm)

QEPLAAGAVILRRFAFNAAEQLIRDINDVASQSPFRQMVTPGGYTMSVAMTNCGHLGWTTH
RQGYLYSPIDPQTNKPWPAMPQSFHNLCQRAATAAGYPDFQPDACLINRYAPGAKLSLHQ
DKDEPDLRAPIVSVSLGLPAIFQFGGLKRNDPLKRLLLEHGDVVVWGGESRLFYHGIQPLKA
GFHPLTIDCRYNLTFRQAGKKE

PAHX (MW: 35435.63, ε: 30285 M^{-1} cm^{-1}, at 280 nm)

SGTISSASFHPQQFQYTLDNNVLTLEQRKFYEENGFLVIKNLVPDADIQRFRNEFEKICRKEV
KPLGLTVMRDVTISKSEYAPSEKMITKVQDFQEDKELFRYCTLPEILKYVECFTGPNIMAMHT
MLINKPPDSGKKTSRHPLHQDLHYFPFRPSDLIVCAWTAMEHISRNNGCLVVLPGTHKGSLK
PHDYPKWEGGVNKMFHGIQDYEENKARVHLVMEKGDTVFFHPLLIHGSGQNKTQGFRKAI
SCHFASADCHYIDVKGTSQENIEKEVVGIAHKFFGAENSVNLKDIWMFRARLVKGERTNL

pcPAL with an *N*-terminal HisTag (MW: 80923.04 Da, ε: 46215 M^{-1} cm^{-1}, at 280 nm)

MGHHHHHHHHHHSSGHIDDDDKHMLEMENGNGATTNGHVNGNGMDFCMKTEDPLYWGI
AAEAMTGSHLDEVKKMVAEYRKPVVKLGGETLTISQVAAISARDGSGVTVELSEAARAGVK
ASSDWVMDSMNKGTDSYGVTTGFGATSHRRTKQGGALQKELIRFLNAGIFGNGSDNTLPH
SATRAAMLVRINTLLQGYSGIRFEILEAITKFLNQNITPCLPLRGTITASGDLVPLSYIAGLLTGR
PNSKAVGPTGVILSPEEAFKLAGVEGGFFELQPKEGLALVNGTAVGSGMASMVLFEANILAV
LAEVMSAIFAEVMQGKPEFTDHLTHKLKHHPGQIEAAAIMEHILDGSAYVKAAQKLHEMDPL
QKPKQDRYALRTSPQWLGPQIEVIRSSTKMIEREINSVNDNPLIDVSRNKAIHGGNFQGTPIG
VSMDNTRLAIAAIGKLMFAQFSELVNDFYNNGLPSNLSGGRNPSLDYGFKGAEVAMASYCS
ELQFLANPVTNHVQSAEQHNQDVNSLGLISSRKTSEAVEILKLMSTTFLVGLCQAIDLRHLEE
NLKSTVKNTVSSVAKRVLTMGVNGELHPSRFCEKDLLRVVDREYIFAYIDDPCSATYPLMQK
LRQTLVEHALKNGDNERNLSTSIFQKIATFEDELKALLPKEVESARAALESGNPAIPNRIEECR
SYPLYKFVRKELGTEYLTGEKVTSPGEEFEKVFIAMSKGEIIDPLLESLESWNGAPLPIS

References

1. Leissing, T. Studies on FIH interactions. University of Oxford, **2018**.
2. Rabe, P.; Beale, J.H.; Butryn, A.; Aller, P.; Dirr, A.; Lang, P.A.; Axford, D.N.; Carr, S.B.; Leissing, T.M.; McDonough, M.A., et al. Anaerobic fixed-target serial crystallography. *IUCrJ* **2020**, *7*, 901-912.
3. Falnes, P.Ø.; Johansen, R.F.; Seeberg, E. AlkB-mediated oxidative demethylation reverses DNA damage in *Escherichia coli*. *Nature* **2002**, *419*, 178-182.
4. Yu, B.; Hunt, J.F. Enzymological and structural studies of the mechanism of promiscuous substrate recognition by the oxidative DNA repair enzyme AlkB. *Proc. Natl. Acad. Sci. U. S. A.* **2009**, *106*, 14315-14320.
5. Martinez, S.; Hausinger, R.P. Catalytic Mechanisms of Fe(II)- and 2-Oxoglutarate-dependent Oxygenases. *J. Biol. Chem.* **2015**, *290*, 20702-20711.
6. Yu, B.; Edstrom, W.C.; Benach, J.; Hamuro, Y.; Weber, P.C.; Gibney, B.R.; Hunt, J.F. Crystal structures of catalytic complexes of the oxidative DNA/RNA repair enzyme AlkB. *Nature* **2006**, *439*, 879-884.
7. Waheed, S.O.; Ramanan, R.; Chaturvedi, S.S.; Lehnert, N.; Schofield, C.J.; Christov, C.Z.; Karabencheva-Christova, T.G. Role of Structural Dynamics in Selectivity and Mechanism of Non-heme Fe(II) and 2-Oxoglutarate-Dependent Oxygenases Involved in DNA Repair. *ACS Cent. Sci.* **2020**, *6*, 795-814.
8. Woon, E.C.Y.; Demetriades, M.; Bagg, E.A.L.; Aik, W.; Krylova, S.M.; Ma, J.H.Y.; Chan, M.; Walport, L.J.; Wegman, D.W.; Dack, K.N., et al. Dynamic Combinatorial Mass Spectrometry Leads to Inhibitors of a 2-Oxoglutarate-Dependent Nucleic Acid Demethylase. *J. Med. Chem.* **2012**, *55*, 2173-2184.
9. Zhang, Z.; Ren, J.-s.; Harlos, K.; McKinnon, C.H.; Clifton, I.J.; Schofield, C.J. Crystal structure of a clavaminate synthase-Fe(II)-2-oxoglutarate-substrate-NO complex: evidence for metal centred rearrangements. *FEBS Lett.* **2002**, *517*, 7-12.
10. Mitchell, A.J.; Dunham, N.P.; Martinie, R.J.; Bergman, J.A.; Pollock, C.J.; Hu, K.; Allen, B.D.; Chang, W.-c.; Silakov, A.; Bollinger, J.M., et al. Visualizing the Reaction Cycle in an Iron(II)- and 2-(Oxo)-glutarate-Dependent Hydroxylase. *J. Am. Chem. Soc.* **2017**, *139*, 13830-13836.
11. Rabe, P.; Kamps, J.J.A.G.; Sutherlin, K.D.; Linyard, J.D.S.; Aller, P.; Pham, C.C.; Makita, H.; Clifton, I.; McDonough, M.A.; Leissing, T.M., et al. X-ray free-electron laser studies reveal correlated motion during isopenicillin *N* synthase catalysis. *Sci. Adv.* **2021**, *7*, eabh0250.
12. Krakowiak, J.; Lundberg, D.; Persson, I. A Coordination Chemistry Study of Hydrated and Solvated Cationic Vanadium Ions in Oxidation States +III, +IV, and +V in Solution and Solid State. *Inorg. Chem.* **2012**, *51*, 9598-9609.
13. Henshaw, T.F.; Feig, M.; Hausinger, R.P. Aberrant activity of the DNA repair enzyme AlkB. *J. Inorg. Biochem.* **2004**, *98*, 856-861.
14. Jansen, G.A.; Oftnan, R.; Ferdinandusse, S.; Ijlst, L.; Muijsers, A.O.; Skjeldal, O.H.; Stokke, O.; Jakobs, C.; Besley, G.T.N.; Wraith, J.E., et al. Refsum disease is caused by mutations in the phytanoyl-CoA hydroxylase gene. *Nat. Genet.* **1997**, *17*, 190-193.
15. Roca-Saavedra, P.; Mariño-Lorenzo, P.; Miranda, J.M.; Porto-Arias, J.J.; Lamas, A.; Vazquez, B.I.; Franco, C.M.; Cepeda, A. Phytanic acid consumption and human health, risks, benefits and future trends: A review. *Food Chem.* **2017**, *221*, 237-247.
16. Wanders, R.J.A.; Komen, J.; Ferdinandusse, S. Phytanic acid metabolism in health and disease. *Biochim. Biophys. Acta* **2011**, *1811*, 498-507.
17. Aubourg, P.; Wanders, R. Chapter 163 - Peroxisomal disorders. In *Handbook of Clinical Neurology*, Dulac, O., Lassonde, M., Sarnat, H.B., Eds. Elsevier: **2013**; Vol. 113, pp. 1593-1609.
18. Rose, N.R.; McDonough, M.A.; King, O.N.F.; Kawamura, A.; Schofield, C.J. Inhibition of 2-oxoglutarate dependent oxygenases. *Chem. Soc. Rev.* **2011**, *40*, 4364-4397.
19. Yeh, T.-L.; Leissing, Thomas M.; Abboud, M.I.; Thinnes, C.C.; Atasoylu, O.; Holt-Martyn, J.P.; Zhang, D.; Tumber, A.; Lippl, K.; Lohans, C.T., et al. Molecular and

cellular mechanisms of HIF prolyl hydroxylase inhibitors in clinical trials. *Chem. Sci.* **2017**, *8*, 7651-7668.
20. Ariazi, J.L.; Duffy, K.J.; Adams, D.F.; Fitch, D.M.; Luo, L.; Pappalardi, M.; Biju, M.; DiFilippo, E.H.; Shaw, T.; Wiggall, K., et al. Discovery and Preclinical Characterization of GSK1278863 (Daprodustat), a Small Molecule Hypoxia Inducible Factor-Prolyl Hydroxylase Inhibitor for Anemia. *J. Pharmacol. Exp. Ther.* **2017**, *363*, 336-347.
21. Provenzano, R.; Besarab, A.; Sun, C.H.; Diamond, S.A.; Durham, J.H.; Cangiano, J.L.; Aiello, J.R.; Novak, J.E.; Lee, T.; Leong, R., et al. Oral Hypoxia-Inducible Factor Prolyl Hydroxylase Inhibitor Roxadustat (FG-4592) for the Treatment of Anemia in Patients with CKD. *Clin. J. Am. Soc. Nephrol.* **2016**, *11*, 982-991.
22. Sjakste, N.; Gutcaits, A.; Kalvinsh, I. Mildronate: An Antiischemic Drug for Neurological Indications. *CNS Drug Rev.* **2005**, *11*, 151-168.
23. Mukherji, M.; Kershaw, N.J.; Schofield, C.J.; Wierzbicki, A.S.; Lloyd, M.D. Utilization of Sterol Carrier Protein-2 by Phytanoyl-CoA 2-Hydroxylase in the Peroxisomal α Oxidation of Phytanic Acid. *Chem. Biol.* **2002**, *9*, 597-605.
24. Berquin, I.M.; Edwards, I.J.; Kridel, S.J.; Chen, Y.Q. Polyunsaturated fatty acid metabolism in prostate cancer. *Cancer Metastasis Rev.* **2011**, *30*, 295-309.
25. McDonough, M.A.; Kavanagh, K.L.; Butler, D.; Searls, T.; Oppermann, U.; Schofield, C.J. Structure of Human Phytanoyl-CoA 2-Hydroxylase Identifies Molecular Mechanisms of Refsum Disease. *J. Biol. Chem.* **2005**, *280*, 41101-41110.
26. Nagy, E.Z.A.; Tork, S.D.; Lang, P.A.; Filip, A.; Irimie, F.D.; Poppe, L.; Toşa, M.I.; Schofield, C.J.; Brem, J.; Paizs, C., et al. Mapping the Hydrophobic Substrate Binding Site of Phenylalanine Ammonia-Lyase from *Petroselinum crispum*. *ACS Catal.* **2019**, *9*, 8825-8834.
27. Kong, J.-Q. Phenylalanine ammonia-lyase, a key component used for phenylpropanoids production by metabolic engineering. *RSC Adv.* **2015**, *5*, 62587-62603.
28. Lovelock, S.L.; Lloyd, R.C.; Turner, N.J. Phenylalanine Ammonia Lyase Catalyzed Synthesis of Amino Acids by an MIO-Cofactor Independent Pathway. *Angew. Chem. Int. Ed.* **2014**, *53*, 4652-4656.
29. Ritter, H.; Schulz, G.E. Structural Basis for the Entrance into the Phenylpropanoid Metabolism Catalyzed by Phenylalanine Ammonia-Lyase. *Plant Cell* **2004**, *16*, 3426-3436.
30. Timofeev, E.N.; Mikhailov, S.N.; Zuev, A.N.; Efimtseva, E.V.; Herdewijn, P.; Somers, R.L.; Lemaitre, M.M. Oligodeoxynucleotides Containing 2′-Deoxy-1-methyladenosine and Dimroth Rearrangement. *Helv. Chim. Acta* **2007**, *90*, 928-937.
31. Mikhailov, S.N.; Rozenski, J.; Efimtseva, E.V.; Busson, R.; Van Aerschot, A.; Herdewijn, P. Chemical incorporation of 1-methyladenosine into oligonucleotides. *Nucleic Acids Res.* **2002**, *30*, 1124-1131.
32. Dima, N.A.; Filip, A.; Bencze, L.C.; Olah, M.; Satorhelyi, P.; Vértessy, B.G.; Poppe, L. Expression and purification of recombinant phenylalanine ammonia-lyase from *Petroselinum crispum*. *Studia UBB Chemia* **2016**, *2*, 21-34.
33. Foulon, V.; Asselberghs, S.; Geens, W.; Mannaerts, G.P.; Casteels, M.; Van Veldhoven, P.P. Further studies on the substrate spectrum of phytanoyl-CoA hydroxylase: implications for Refsum disease? *J. Lipid Res.* **2003**, *44*, 2349-2355.
34. Mukherji, M.; Chien, W.; Kershaw, N.J.; Clifton, I.J.; Schofield, C.J.; Wierzbicki, A.S.; Lloyd, M.D. Structure-function analysis of phytanoyl-CoA 2-hydroxylase mutations causing Refsum's disease. *Hum. Mol. Genet.* **2001**, *10*, 1971-1982.
35. Mónico, A.; Martínez-Senra, E.; Cañada, F.J.; Zorrilla, S.; Pérez-Sala, D. Drawbacks of Dialysis Procedures for Removal of EDTA. *PLoS One* **2017**, *12*, e0169843.
36. Winter, G. xia2: an expert system for macromolecular crystallography data reduction. *J. Appl. Crystallogr.* **2010**, *43*, 186-190.
37. Lee, D.; Baek, S.; Park, J.; Lee, K.; Kim, J.; Lee, S.J.; Chung, W.K.; Lee, J.-L.; Cho, Y.; Nam, K.H. Nylon mesh-based sample holder for fixed-target serial femtosecond crystallography. *Sci. Rep.* **2019**, *9*, 6971.

38. McCoy, A.J.; Grosse-Kunstleve, R.W.; Adams, P.D.; Winn, M.D.; Storoni, L.C.; Read, R.J. Phaser crystallographic software. *J. Appl. Crystallogr.* **2007**, *40*, 658-674.
39. Adams, P.D.; Grosse-Kunstleve, R.W.; Hung, L.W.; Ioerger, T.R.; McCoy, A.J.; Moriarty, N.W.; Read, R.J.; Sacchettini, J.C.; Sauter, N.K.; Terwilliger, T.C. PHENIX: building new software for automated crystallographic structure determination. *Acta Crystallogr. D* **2002**, *58*, 1948-1954.
40. Emsley, P.; Lohkamp, B.; Scott, W.G.; Cowtan, K. Features and development of Coot. *Acta Crystallogr. D* **2010**, *66*, 486-501.
41. van Berkel, S.S.; Brem, J.; Rydzik, A.M.; Salimraj, R.; Cain, R.; Verma, A.; Owens, R.J.; Fishwick, C.W.G.; Spencer, J.; Schofield, C.J. Assay platform for clinically relevant metallo-β-lactamases. *J. Med. Chem.* **2013**, *56*, 6945-6953.
42. Poelarends, G.J.; Johnson, W.H., Jr.; Murzin, A.G.; Whitman, C.P. Mechanistic characterization of a bacterial malonate semialdehyde decarboxylase: identification of a new activity on the tautomerase superfamily. *J. Biol. Chem.* **2003**, *278*, 48674-48683.
43. Finn, M.J.; Harris, M.A.; Hunt, E.; Zomaya, I.I. Studies on the hydrolysis of clavulanic acid. *J. Chem. Soc., Perkin Trans. 1* **1984**, 1345-1349.
44. Haginaka, J.U.N.; Yasuda, H.; Uno, T.; Nakagawa, T. Degradation of Clavulanic Acid in Aqueous Alkaline Solution: Isolation and Structural Investigation of Degradation Products. *Chem. Pharm. Bull. (Tokyo)* **1985**, *33*, 218-224.